

BEYOND STANDARD MODEL PHYSICS AT CURRENT AND FUTURE COLLIDERS

by

Zhen Liu

Bachelor in Science, Zhejiang University, 2009

Master in Science, University of Wisconsin-Madison, 2011

Submitted to the Graduate Faculty of
the Kenneth P. Dietrich School of Arts and Sciences
in partial fulfillment
of the requirements for the degree of
Doctor of Philosophy

University of Pittsburgh

2015

UNIVERSITY OF PITTSBURGH
KENNETH P. DIETRICH SCHOOL OF ARTS AND SCIENCES

This dissertation was presented

by

Zhen Liu

It was defended on

April 24th 2015

and approved by

Tao Han, Distinguished Professor/Director of PITT PACC, University of Pittsburgh

Joseph Boudreau, Professor, University of Pittsburgh

Adam Leibovich, Associate Professor/Associate Chair, University of Pittsburgh

Ira Rothstein, Professor, Carnegie Mellon University

Michael Wood-Vasey, Associate Professor, University of Pittsburgh

Dissertation Director: Tao Han, Distinguished Professor/Director of PITT PACC,

University of Pittsburgh

BEYOND STANDARD MODEL PHYSICS AT CURRENT AND FUTURE COLLIDERS

Zhen Liu, PhD

University of Pittsburgh, 2015

The Large Hadron Collider (LHC), a multinational experiment which began running in 2009, is highly expected to discover new physics that will help us understand the nature of the universe and begin to find solutions to many of the unsolved puzzles of particle physics. For over 40 years the Standard Model has been the accepted theory of elementary particle physics, except for one unconfirmed component, the Higgs boson. The experiments at the LHC have recently discovered this Standard-Model-like Higgs boson. This discovery is one of the most exciting achievements in elementary particle physics. Yet, a profound question remains: Is this rather light, weakly-coupled boson nothing but a Standard Model Higgs or a first manifestation of a deeper theory? Also, the recent discoveries of neutrino mass and mixing, experimental evidences of dark matter and dark energy, matter-antimatter asymmetry, indicate that our understanding of fundamental physics is currently incomplete. For the next decade and more, the LHC and future colliders will be at the cutting-edge of particle physics discoveries and will shed light on many of these unanswered questions. There are many promising beyond-Standard-Model theories that may help solve the central puzzles of particle physics. To fill the gaps in our knowledge, we need to know how these theories will manifest themselves in controlled experiments, such as high energy colliders. I discuss how we can probe fundamental physics at current and future colliders directly through searches for new phenomena such as resonances, rare Higgs decays, exotic displaced signatures, and indirectly through precision measurements on Higgs in this work. I explore beyond standard model physics effects from different perspectives, including explicit models

such as supersymmetry, generic models in terms of resonances, as well as effective field theory approach in terms of higher dimensional operators. This work provides a generic and broad overview of the physics potentials of different particle physics experiments, supported by several detailed studies on characteristic physics cases to highlight the special features. The studies presented in this work provide timely and crucial knowledge highly demanded for our understanding and planning for future experiments.

TABLE OF CONTENTS

I.	INTRODUCTION	1
A.	DIJET RESONANCES	1
B.	ELECTROWEAK RESONANCES	2
C.	SUPERSYMMETRY	6
1.	SUSY Higgs Sector	8
2.	SUSY Dark Matter	11
3.	SUSY Displaced Decays	14
D.	HIGGS BOSON	16
1.	Higgs Boson at the LHC	17
2.	Higgs Width at the ILC	19
3.	Higgs Couplings from ZZ-fusion at the ILC	20
4.	Higgs Boson at Muon Collider	24
II.	BSM PHYSICS AT THE LHC	27
A.	DIJET RESONANCES	27
1.	Classification of Resonant Particles in Hadronic Collisions	28
2.	Parton-Resonance Interactions	29
a.	$\mathbf{3} \otimes \mathbf{3}$	31
b.	$\mathbf{3} \otimes \mathbf{8}$	33
c.	$\mathbf{8} \otimes \mathbf{8}$	34
d.	$\mathbf{3} \otimes \bar{\mathbf{3}}$	35
3.	Resonance Production at The LHC	36
a.	Quark-Quark Annihilation	41

b. Quark-Gluon Annihilation	43
c. Gluon-Gluon Annihilation	45
d. Quark-Antiquark Annihilation	46
4. Bounds from the LHC Dijet Spectrum	49
5. Summary and Outlook	55
B. ELECTROWEAK RESONANCES	56
1. LHC Searches	57
2. Leptonic Final States	59
3. Hadronic Final States	62
4. Summary and Outlook	65
C. SUSY HIGGS PHYSICS IN NMSSM	65
1. NMSSM Higgs Sector and the Low- m_A Region	66
a. Masses	67
b. Couplings	72
2. Parameter Scan and Constrained Regions	73
3. H_1 as the SM-like Higgs Boson	78
a. Parameter Regions	78
b. Production and Decays of the SM-like H_1	84
c. Wave Function Overlap	87
4. H_2 as the SM-like Higgs Boson	90
a. Parameter Regions	90
b. Production and Decays for the SM-like H_2	93
c. Wave Function Overlap	95
5. LHC Phenomenology for the Non-SM-like Higgs Bosons	96
a. H_1 as the SM-like Higgs Boson	96
b. H_2 as the SM-like Higgs Boson	103
6. Summary and Outlook	104
D. SUSY DARK MATTER IN MSSM	105
1. The MSSM Parameters Relevant to DM studies	106
2. Current Constraints and the Scanning Results	108

a.	Constraints from the Higgs Searches and the Flavor Sector	109
b.	Confronting the Direct and Indirect Searches	112
c.	Scanning Results	112
3.	Discussions	119
a.	The Nature of the DM	119
b.	Lower Limit on the Spin-Independent Cross Section	121
c.	Connection to the Indirect Searches	123
d.	Implication of LSP for Higgs Physics	123
e.	Consequences of Co-annihilation	125
4.	Summary and Outlook	127
E.	SUSY DARK MATTER IN NMSSM	130
1.	Light Neutralino Dark Matter	132
a.	Neutralino Sector in the NMSSM	132
b.	Parameters and Constraints	134
c.	Highlights from Experimental Bounds	137
d.	DM Properties	141
2.	LHC Observables	150
a.	Modifications to the SM-like Higgs Boson Properties	150
b.	Non-SM Light Higgs Bosons	153
c.	Light Sfermions	157
3.	Summary and Outlook	160
F.	SUSY DISPLACED DECAYS	162
1.	The LHC Searches Under Consideration	164
a.	CMS Heavy Stable Charged Particles	166
b.	CMS Displaced Dijets	168
c.	CMS Displaced Dileptons	170
d.	CMS Displaced Electron and Muon	172
e.	ATLAS Muon Spectrometer	173
f.	ATLAS Low-EM Jets	175
g.	ATLAS Displaced Muon Plus Tracks	176

2.	Models and Limits	177
a.	Baryonic R-Parity Violation	180
b.	General Gauge Mediation	188
c.	Mini-Split SUSY	197
3.	Summary and Outlook	199
III.	BSM PHYSICS AT THE ILC AND CEPC	206
A.	ELECTROWEAK RESONANCES AT THE ILC	206
1.	Z' observables at the ILC	206
2.	Z' Beyond the LHC Reach	210
3.	Summary of the Z' at the ILC	210
B.	HIGGS WIDTH AT THE ILC	211
1.	Formalism for Higgs Width Determination	212
a.	General Approach to the Higgs Width	212
b.	The ILC at 250 GeV	214
c.	The ILC at 500 GeV and Beyond	216
2.	Simulations	217
a.	Invisible Decays of the Higgs at 250 GeV	217
b.	Estimated Sensitivity for σ_{ZW} at 500 GeV	220
c.	Fully Hadronic Reconstruction	222
d.	Semi-leptonic Reconstruction	223
e.	Sensitivity	226
3.	Achievable Accuracies at the ILC	227
a.	Model-Independent Fitting	227
b.	Model-Dependent Constraints	232
4.	Summary and Outlook	235
C.	HIGGS COUPLINGS AT THE ILC	237
1.	Sensitivity Analysis	238
a.	Simulation Framework	241
b.	500 GeV Analysis	243
c.	1-TeV Analysis	245

d. Multivariate Log-Likelihood Analyses	246
2. Impact on Higgs Physics	249
a. Higgs Width and Coupling Fits	249
b. Operator Analysis	251
3. Summary and Outlook	254
D. HIGGS WIDTH AND COUPLINGS AT THE CEPC	255
IV. BSM PHYSICS AT VLHC AND MUON COLLIDER	264
A. ELECTROWEAK RESONANCES AT VLHC	264
1. Gold-plated Modes: Leptonic Final States	268
a. Dilepton Invariant Mass	269
b. Forward-backward Asymmetry	270
c. Weak Boson Radiation	273
2. Crucial Modes for Coupling Determination: Hadronic Final States	274
3. Diagnosis Power of the VLHC	275
4. In the Presence of $Z - Z'$ Mixing	278
B. HIGGS WIDTH AT A MUON COLLIDER	280
1. Resonant Profile for a Higgs Boson	280
2. Width Determination for the SM Higgs Boson	283
3. Width Determination for a Broader Higgs Boson	287
4. Summary and Outlook	290
C. HIGGS FROM RADIATIVE RETURN AT A MUON COLLIDER	291
1. Production Mechanisms	291
2. Radiative Return	295
a. Signal and Background	295
b. Estimated Sensitivities	298
3. ZH Associated Production and HA Pair Production	298
4. Comparison of Different Modes	300
5. Summary and Outlook	302
V. CONCLUSIONS	305
VI. APPENDIX	312

A. Clebsch-Gordan Coefficients	312
B. Feynman Rules	313
C. Consideration of One Photon Sensitivity	315
D. Z' at the LHC	316
1. Narrow Width Approximation	318
2. Angular Distribution	320
3. Final State Polarization	321
4. Beyond the Narrow Width Approximation	322
E. Z' at the ILC	323
1. No Polarization	323
2. Fixed Initial State Polarization	324
3. Polarization Asymmetries	325
4. CMS Heavy Stable Charged Particles	327
5. CMS Displaced Dijets	327
6. CMS Displaced Dileptons	332
7. CMS Displaced Electron and Muon	336
8. ATLAS Muon Spectrometer	337
9. ATLAS Low-EM Jets	339
10. ATLAS Displaced Muon Plus Tracks	341
F. Relic Density Calculation	343
G. Combination Method and χ^2 Definition	346
H. Analysis for $b\bar{b}$ Backgrounds	347
BIBLIOGRAPHY	350

LIST OF TABLES

I.1	Benchmark models and couplings.	5
I.2	Branching ratios in % for benchmark models.	7
I.3	Possible solutions for light (< 40 GeV) neutralino DM in MSSM and NMSSM.	13
II.1	Quantum numbers of possible dijet resonant states	30
II.2	Summary for resonance particles.	37
II.3	The minimal widths for the benchmark Z' models and the cross sections.	59
II.4	Z' Parton level cross sections at the LHC 14 TeV.	63
II.5	Cut flow table and significance S/\sqrt{B} for $Z' \rightarrow b\bar{b}$ processes at LHC 14 TeV.	64
II.6	Reduced Higgs couplings at tree level.	73
II.7	NMSSM Parameter regions for the H_1 -126 case.	81
II.8	NMSSM Parameter region for the H_2 -126 case.	91
II.9	Connection between the SUSY DM properties and the Higgs bosons.	128
II.10	Possible solutions for light (< 40 GeV) neutralino DM in MSSM and NMSSM.	130
II.11	The parameters and ranges considered.	135
II.12	Collider constraints on the sbottom and stau.	139
II.13	Summary of our signal rate with the ATLAS sbottom search selections.	158
II.14	A summary of the LHC searches recast in this section.	165
III.1	Expected number of events in invisible Higgs searches.	220
III.2	Cuts applied in hadronic and semi-leptonic analysis.	224
III.3	Expected number of events from $h \rightarrow WW$ signal and backgrounds.	225
III.4	Estimated relative errors for various cross sections at the ILC.	228
III.5	Relative uncertainties from projections of ATLAS and CMS experiments.	229

III.6	Model-independent precisions (1σ) of the width and couplings constants. . .	230
III.7	Model-dependent precisions for coupling constants achievable at the ILC. . .	233
III.8	Cut flow table for singal and background at 500 GeV and 1 TeV.	240
III.9	Cuts applied at ILC 500 GeV.	243
III.10	Cross sections for signal and background processes at ILC 500 GeV.	245
III.11	Cuts applied at ILC 1 TeV.	246
III.12	Cross sections for signal and background processes at ILC 1 TeV.	248
III.13	The improvement on selected coupling precisions by our ZZ fusion analysis. . .	250
III.14	Estimated precisions of Higgs boson property measurements at the CEPC. . .	255
III.15	Coupling measurement precision in percent from the 10 parameter fit. . . .	262
III.16	Coupling measurement precision in percent from the 7 parameter fit	263
IV.1	The comparison of leptonic forward-backward asymmetry.	272
IV.2	The results of the initial state W -boson radiation.	274
IV.3	The hadronic cross sections for benchmark models and SM background. . .	276
IV.4	Effective cross sections at the resonance.	282
IV.5	Fit accuracies for one standard deviation of Γ_h , B , and m_h of the SM Higgs. .	286
IV.6	The effective cross sections for the exotic Higgs	287
IV.7	Fitting accuracies for the exotic Higgs properties.	289
IV.8	Parametrization and their 2HDM models correspondence.	293
IV.9	Muon Collider Parameters.	294
VI.1	Additional events expected from $h \rightarrow b\bar{b}$ with cuts.	348

LIST OF FIGURES

I.1	The effect of adding the singlet to the MSSM CP-even Higgs boson spectrum.	10
I.2	Higgs production and decay branching fractions.	18
I.3	Feynman diagram of the ZZ fusion signal process.	22
I.4	Total cross section for $e^-e^+ \rightarrow e^-e^+ + h$ at ILC.	23
II.1	Parton Luminosities at the LHC.	38
II.2	Rapidity distributions of possible resonances.	40
II.3	Color-sextet vector cross sections at the LHC	42
II.4	Color-octet fermion cross sections at the LHC	44
II.5	Color-sextet scalar cross sections at the LHC	47
II.6	Color-octet vector cross sections at the LHC	48
II.7	95% confidence level upper limits on dijet production cross sections.	51
II.8	Bounds on the products of SM parton couplings and branching ratios.	53
II.9	The invariant mass and angular distribution of the dielectron system.	60
II.10	The precisions for $pp \rightarrow Z' \rightarrow e^-e^+$	62
II.11	Lines for $m_{h_v}^2 = m_{H_v}^2$ for different values of $\tan \beta$ in the λ versus m_A plane.	71
II.12	Allowed mass regions of the Higgs bosons versus m_{H^\pm} for various scenarios.	76
II.13	The dependence of m_{H_1} on selected NMSSM parameters.	79
II.14	Viable NMSSM parameter regions in the H_1 -126 case	82
II.15	The normalized cross sections for the SM-like Higgs boson for H_1 -126 case.	84
II.16	The correlation for production and decay modes for the SM-like Higgs.	86
II.17	The normalized $\sigma \times \text{Br}/\text{SM}$ for $gg \rightarrow H_1 \rightarrow \gamma\gamma$	86
II.18	$ \xi_{H_i}^S ^2$ versus $ \xi_{H_i}^{h_v} ^2$ for H_1 (a), H_2 (b) and H_3 (c) in the H_1 -126 case.	88

II.19	A_v -fraction in the light CP-odd Higgs A_1 : $ \xi_{A_1}^{A_v} ^2 = 1 - \xi_{A_2}^{A_v} ^2 = 1 - \xi_{A_1}^{A_s} ^2$.	88
II.20	Viable NMSSM parameter regions in the H_2 -126 case	92
II.21	The normalized cross sections for the SM-like Higgs boson for H_2 -126 case.	94
II.22	The correlation for production and decay modes for the SM-like Higgs.	94
II.23	$ \xi_{H_i}^S ^2$ versus $ \xi_{H_i}^{h_v} ^2$ for H_1 (a), H_2 (b) and H_3 (c) in the H_2 -126 case.	95
II.24	Higgs boson cross sections at the 14 TeV LHC in the H_1 -126 case.	97
II.25	Decay branching fractions for Higgs bosons in the case of H_1 -126.	98
II.26	Decay branching fractions for Higgs bosons in the case of H_1 -126.	99
II.27	Higgs boson cross sections at the 14 TeV LHC in the H_2 -126 case.	100
II.28	Decay branching fractions for Higgs bosons in the case of H_2 -126.	101
II.29	Decay branching fractions for Higgs bosons in the case of H_2 -126.	102
II.30	Allowed mass and parameter regions.	111
II.31	Allowed branching fraction regions.	112
II.32	Allowed parameter regions.	113
II.33	Spin-independent cross section.	117
II.34	The annihilation cross section and spin-dependent cross section.	119
II.35	DM gaugino and Higgsino components.	120
II.36	The annihilation cross section and spin-dependent cross section.	122
II.37	Branching fractions to neutralinos and charginos.	124
II.38	Spin-independent cross section as a function of neutralino components.	126
II.39	Z boson partial decay widths (left panel) and coupling parameters.	137
II.40	Relic density versus scaled spin-independent cross section and DM masses.	142
II.41	Validation of various light DM scenarios.	144
II.42	The LSP DM candidate components.	145
II.43	The LSP DM candidate components.	146
II.44	The spin-dependent direct detection rate and the indirect detection rate.	148
II.45	The correlation of SM-like Higgs production rates for various channels.	152
II.46	Branching fractions of the SM-like Higgs.	152
II.47	The couplings and decay branching fractions of the light Higgs boson.	154
II.48	Total cross sections at the 14 TeV LHC for the light A_1 and H_1 .	155

II.49	Neutralino DM production from Higgs decays at the 14 TeV LHC.	156
II.50	Displaced dijet acceptance for RPV stop.	179
II.51	Recast constraints on displaced $\tilde{t} \rightarrow \bar{d}_j \bar{d}_k$ via baryonic RPV.	182
II.52	Recast constraints on displaced $\tilde{t} \rightarrow \bar{b} \bar{b}$ in the Dynamical RPV framework. .	183
II.53	Recast constraints on displaced $\tilde{g} \rightarrow jjj$ via baryonic RPV.	185
II.54	Recast constraints on displaced $\tilde{H}^0 \rightarrow jjj$ via baryonic RPV.	186
II.55	Recast constraints on displaced $\tilde{q} \rightarrow q\tilde{G}$ in general GMSB.	191
II.56	Recast constraints on displaced $\tilde{g} \rightarrow g\tilde{G}$ in general GMSB.	192
II.57	Recast constraints on displaced $\tilde{t} \rightarrow t^{(*)}\tilde{G}$ in general GMSB.	193
II.58	Recast constraints on displaced \tilde{H}^0 decays via GMSB.	195
II.59	Recast constraints on displaced $\tilde{g} \rightarrow q\bar{q}\tilde{B}$ in mini-split SUSY.	198
III.1	The accuracies of ILC observables for a 500 GeV ILC.	207
III.2	The exclusion reach of the 500 GeV (1 TeV) ILC.	209
III.3	Recoil mass distributions for the invisible decay of the Higgs boson.	219
III.4	Kinematic distributions for the signal.	221
III.5	nvariant mass of the 4 jets identified with a Higgs in the all-hadronic analysis.	222
III.6	Model-independent uncertainties of the Higgs boson couplings.	231
III.7	Model-dependent uncertainties of the Higgs boson couplings.	234
III.8	Angles θ_1 , θ_2 and ϕ as defined in the text.	238
III.9	Differential distributions for singal and background for 500 GeVILC.	244
III.10	Differential distributions for singal and background for 1000 TeVILC. . . .	247
III.11	Log-likelihood as a function of the relative cross section.	248
III.12	Constraints on coefficients of dimension-six operators \bar{c}_H and \bar{c}_{HB}	253
III.13	The 7 parameter fit result, and comparison with the HL-LHC.	260
III.14	The 10 parameter fit result and comparison with the ILC.	261
IV.1	Production rates and discover/exclusion power at different c.m. energy. . .	265
IV.2	The ratios of $2 \rightarrow 3(4)$ process over $2 \rightarrow 2$ process cross sections.	266
IV.3	The invariant mass distribution and fit results for the Z'	269
IV.4	Angular distribution observables for Z'	271
IV.5	The transverse mass distribution of the $e^\pm + \cancel{E}_T$ system.	273

IV.6	5(6)-parameter fit contour at 68% C.L. for our benchmark models.	277
IV.7	Clustered transverse mass distribution of the signal and background.	278
IV.8	Effective cross section for $\mu^+\mu^- \rightarrow h$ versus the collider energy \sqrt{s}	282
IV.9	Simulated signal and backgrounds with fluctuations.	285
IV.10	Fitted values and errors for the SM Higgs width.	286
IV.11	Simulated signal and backgrounds with fluctuations.	288
IV.12	Fitted values and errors for the Higgs width versus the input values.	289
IV.13	Main production mechanisms of heavy Higgs.	292
IV.14	Total width of heavy Higgs boson.	294
IV.15	Signal and background for RR heavy Higgs.	297
IV.16	Estimated exclusion and discovery limits of heavy Higgs.	299
IV.17	Sensitivity to the Higgs coupling through associated production.	301
IV.18	Comparison of sensitivities between different production mechanisms.	304
VI.1	Feynman rules for the vertices of resonant particle couplings to partons.	314
VI.2	Comparison of our simulation to the CMS displaced dijet analysis.	330
VI.3	Comparison of our simulation to the CMS displaced dijet analysis.	333
VI.4	Comparison of our simulation to the CMS displaced dilepton analysis.	335
VI.5	Comparison of our simulation to the CMS displaced electron and muon analysis.	336
VI.6	Comparison of our simulation to the ATLAS muon chamber analysis.	338
VI.7	Comparison of our simulation to the ATLAS low-EM jet analysis.	340
VI.8	Comparison of our simulation to the ATLAS muon plus tracks analysis.	342
VI.9	Evolution with temperature and yielding the correct WIMP relic density.	345

I. INTRODUCTION

The Standard Model (SM) of particle physics is a successful theory describing the microscopic world. With the predicted particle—the Higgs boson—discovered at the Large Hadron Collider, the Standard Model is complete. The SM crystallizes over a hundred years of continuous development in our understanding of the physics world as the cutting edge tested theory of microscopic physics up to the highest energies accessible today. A few clouds are hanging over the SM as a fundamental theory, urging the need for Beyond Standard Model (BSM) physics. In this thesis, we explore possible probes for BSM physics at different colliders. I first introduce the topics studies in this thesis.

A. DIJET RESONANCES

While much of the attention for new physics discovery has centered on theories associated with electroweak symmetry breaking, most initial states at hadron colliders are composed of colored particles with the strong interactions of quantum chromodynamics (QCD). Hence, any new colored resonances will be produced with favorable rates at the LHC since their couplings may be typically of the strength of the strong-interaction.

Beyond the SM, there are many possible exotic colored states that can be produced at the LHC. Besides being phenomenologically interesting and experimentally important to search for, many of the exotic states are also theoretically motivated. For example, color-antitriplet scalars may be produced via quark-quark annihilation as squarks in R-parity violating supersymmetric (SUSY) theories [1], or as “diquarks” in E_6 grand unified theories [2]. Color-sextet scalars can arise in partially unified Pati-Salam theories [3] and

be produced also via quark-quark annihilation. Color-triplet fermions can be produced via quark-gluon annihilation as “excited quarks” in composite models [4, 5]. Sextet fermions, the so-called “quixes”, associated with chiral color [6] and top quark condensate models [7] may also be produced via quark-gluon annihilation. Color-octet scalars that are $SU(2)_L$ singlets can arise in technicolor models [8], and in universal extra dimensions [9]. Color-octet vectors have been extensively explored as axigluons [6, 10] and colorons [11, 12]. There has also been much recent interest in studying the similar states in the context of Kaluza-Klein gluons [13], and low-scale string resonances [14–16] via gluon-gluon, or quark-antiquark annihilation.

Any new resonant states produced at the LHC through interactions with light partons will contribute to the dijet production, leading to one of the simplest signal topologies.

Motivated by the above considerations, we study the colored resonances in a most general way. We classify them according to their couplings to light partons, solely based on group theory decomposition. Among those possible colored resonances, we focus on those produced by the leading parton luminosities directly from valence quarks or gluons. We apply the new ATLAS and CMS data to put bounds on various possible colored resonant states and derive LHC limits on these states. Our study has been included in the LHC experimental searches. Studies on generic resonance of this type will be best tested at hadron colliders such as the LHC and VLHC. We discuss the details of LHC searches in section II.A.

B. ELECTROWEAK RESONANCES

Additional colorless vector gauge bosons (Z') occur in many extensions of the Standard Model (SM), in part because it is generically harder to break additional abelian $U(1)'$ factors than non-abelian ones¹. The existence of a Z' could have many other possible implications, including an Next-to-Minimal-Supersymmetric-Standard-Model(NMSSM)-like solution to the μ problem (and the possibility of electroweak baryogenesis), new F and D term contributions to the lightest scalar mass, an additional Higgs singlet, additional neutralinos (with collider and dark matter consequences), new vector (under the SM) fermions for anomaly cancella-

¹For reviews, see [2, 17–19]. Specific properties are reviewed in [20–26].

tion, and many possibilities for neutrino mass. Other possibilities involve interactions with dark matter, the mediation of supersymmetry breaking, Flavor Changing Neutral Current (FCNC) (for family non-universal couplings), associated charged W' s, and the production of superpartners and exotics. The Z' couplings could also give clues about a possible embedding of the $U(1)'$ into a more fundamental underlying theory. Although Z' s can occur at any scale and with couplings ranging from extremely weak to strong, we concentrate here on TeV-scale masses with couplings not too different from electroweak, which might therefore be observable at the LHC or future colliders.

A $U(1)'$ or Z' is generic in many scenarios of physics beyond the Standard Model, such as string theory compactifications, GUTs, extra-dimensions, compositeness, dynamical electroweak symmetry breaking, dark-sector models, etc. We study the potential of probing a TeV-scale Z' with electroweak couplings in future high energy pp collider. Our study aim at a comprehensive study of the discovery and diagnosis power of such machine for the Z' . We study the leptonic and hadronic decay modes of the Z' as well as the W^+W^- decay mode in presence of $Z - Z'$ mixing. We show that a 100 TeV VLHC could potentially discover a Z' up to 28 TeV and determine the Z' mass, width, and especially the coupling strengths well enough under very minimalistic assumptions to distinguish different Z' models well.

Following the notation in [17], we define the couplings of the SM and additional neutral gauge bosons to fermions by

$$-L_{NC} = eJ_{em}^\mu A_\mu + g_1 J_1^\mu Z_{1\mu}^0 + g_2 J_2^\mu Z_{2\mu}^0, \quad (\text{I.B.1})$$

with

$$J_\alpha^\mu = \sum_i \bar{f}_i \gamma^\mu [\epsilon_L^{\alpha i} P_L + \epsilon_R^{\alpha i} P_R] f_i. \quad (\text{I.B.2})$$

The SM (Z_1^0) parameters are $g_1 = g/\cos\theta_W$ and $\epsilon_L^{1i} = t_{3L}^i - \sin^2\theta_W q^i$, $\epsilon_R^{1i} = -\sin^2\theta_W q^i$, where q^i is the electric charge of f_i in units of $|e|$ and $t_{3L}^i = \pm 1/2$ is the third component of weak isospin. We will absorb g_α into the chiral charges² by defining

$$g_{L,R}^{1i} \equiv g_1 \epsilon_{L,R}^{1i}, \quad g_{L,R}^{2i} \equiv g_2 \epsilon_{L,R}^{2i}. \quad (\text{I.B.3})$$

²The gauge coupling g_2 is not really a separate parameter, because it can be absorbed in the chiral couplings, as in (I.B.3). However, the separate extraction of g_2 would become meaningful if the charges were established to correspond to an embedding in a nonabelian group of some other model with well-defined normalization, such as the E_6 and LR models.

When it does not cause confusion we will drop the superscript 2 on $g_{L,R}^{2i}$. It will also be convenient to define the vector and axial couplings and the asymmetry parameters

$$g_{V,A}^i \equiv g_L^i \pm g_R^i, \quad A_i \equiv \frac{g_L^{i2} - g_R^{i2}}{g_L^{i2} + g_R^{i2}} = \frac{2g_V^i g_A^i}{g_V^{i2} + g_A^{i2}}, \quad (\text{I.B.4})$$

for $i = u, d, e, \nu, \dots$. Analogous definitions hold for the $g_{L,R}^{1i}$.

Assuming negligible (mass and kinetic) $Z-Z'$ mixing [21, 25, 26]) and family universality, the relevant Z' parameters are $M_{Z'}$, $\Gamma_{Z'}$, and the chiral couplings $g_{L,R}^i$ for $i = u, d, e$, and ν . A lower bound on $\Gamma_{Z'}$ (the “minimal” width) can be calculated in terms of the other parameters from the decays into the SM fermions, but a larger $\Gamma_{Z'}$ is possible due to decays into Higgs particles, superpartners, right-handed neutrinos, exotic fermions (such as those needed in some Z' models for anomaly cancellation), or other BSM particles [27, 28]. We will usually assume as well that the $U(1)'$ charges commute³ with $SU(2)$, so that there are only five relevant chiral charges,

$$g_L^u = g_L^d \equiv g_L^q, \quad g_R^u, \quad g_R^d, \quad g_L^e = g_L^\nu \equiv g_L^\ell, \quad g_R^e. \quad (\text{I.B.5})$$

Ideally, one would like to determine these, as well as $M_{Z'}$ and $\Gamma_{Z'}$, in a model-independent way from collider as well as existing and future precision data. In practice, the existing limits are sufficiently stringent that we may have to resort to considering specific benchmark models. For illustration, we will consider the well-known χ , ψ , and LR models, associated with the breakings $SO(10) \rightarrow SU(5) \times U(1)_\chi$, $E_6 \rightarrow SO(10) \times U(1)_\psi$, and $SU(2)_L \times SU(2)_R \times U(1)_{B-L} \rightarrow SU(2) \times U(1)_Y \times U(1)_{LR}$ (for $g_R = g$), respectively. We will also consider $Z_\eta = \sqrt{\frac{3}{8}}Z_\chi - \sqrt{\frac{5}{8}}Z_\psi$, associated with a certain compactification of the heterotic string, and the B-L model⁴ with charge $(B-L)/2$. The charges for these benchmark models are listed in Table I.1. For the E_6 , LR, and B-L models we will take for the reference value of g_2 the GUT-normalized hypercharge coupling

$$g_2 = \sqrt{\frac{5}{3}} g \tan \theta_W \sim 0.46, \quad (\text{I.B.6})$$

³One exception is the benchmark sequential model, in which $g_{L,R}^{2i} = g_{L,R}^{1i}$. This could possibly emerge from a diagonal embedding of the SM in a larger group, or for Kaluza-Klein excitations in an extra-dimensional theory.

⁴The $B-L$ charge usually occurs in a linear combination with $T_{3R} = Y - \frac{B-L}{2}$, where $Y = Q - T_{3L}$, as in the χ and LR models. Here we consider a simple $B-L$ charge as an example of a purely vector coupling.

Table I.1: Benchmark models and couplings, with $\epsilon_{L,R}^i \equiv \hat{\epsilon}_{L,R}^i/D$. The last row shows the total width of a 10 TeV Z' , including only fermion pair decay modes.

	χ	ψ	η	LR	B-L	SSM	
D	$2\sqrt{10}$	$2\sqrt{6}$	$2\sqrt{15}$	$\sqrt{5/3}$	1	1	
$\hat{\epsilon}_L^q$	-1	1	-2	-0.109	1/6	$\hat{\epsilon}_L^u$	$\frac{1}{2} - \frac{2}{3}\sin^2\theta_W$
						$\hat{\epsilon}_L^d$	$-\frac{1}{2} + \frac{1}{3}\sin^2\theta_W$
						$\hat{\epsilon}_R^u$	$-\frac{2}{3}\sin^2\theta_W$
						$\hat{\epsilon}_R^d$	$\frac{1}{3}\sin^2\theta_W$
$\hat{\epsilon}_L^l$	3	1	1	0.327	-1/2	$\hat{\epsilon}_L^\nu$	$\frac{1}{2}$
						$\hat{\epsilon}_L^e$	$-\frac{1}{2} + \sin^2\theta_W$
						$\hat{\epsilon}_R^e$	$\sin^2\theta_W$
\hat{Q}_u	2	-2	4	0.765	0	$-\frac{1}{2}$	
\hat{Q}_d	-2	-2	1	-0.765	0	—	
$\Gamma_{Z'} \text{ (GeV)}$	116	52	63	205	91	296	

which is an approximation to the simplest E_6 prediction [29] for the GUT models and follows for $g_R = g$ in $SU(2)_L \times SU(2)_R \times U(1)_{B-L}$. We will also consider the sequential model with $g_2 = g_1$ and $\epsilon_{LR}^{2i} = \epsilon_{LR}^{1i}$.

In this table, we also list the total width of these benchmark models for 10 TeV Z' . We note here this only includes the fermion pair decay modes, as for the bosonic decay modes, additional inputs of mixing angles are needed. These widths can be viewed as the minimal widths of these models. The typical total width for Z' varies from ≈ 50 GeV (for Z'_ϕ) to ≈ 300 GeV (for Z'_{SSM}) for 10 TeV Z' , manifesting the validity of narrow width approximation for weakly interacting Z' searches at hadron colliders.

The Z' could mix with the SM Z boson, bridged by mass mixing and kinetic mixing. This $Z - Z'$ mixing gives rise to hZZ' coupling and $Z'W^+W^-$ coupling, introducing additional decay channels of Z' into Zh and W -boson pair. The mixing is strongly constrained by the precision electroweak data (for a recent review, see, e.g., Ref. [17]). The mass mixing between Z and Z' introduces the SM-like Higgs to $Z'Z'$ coupling proportional to the (milli-) $U(1)'$ charge of the SM-like Higgs boson, and the $Z'W^+W^-$ coupling proportional to the mixing as well. With further gauge kinetic mixing, the mixing is further shifted and new hZZ' vertices will emerge.

We discuss the details of LHC searches in section II.B, ILC searches in section III.A, and VLHC searches in section IV.A.

C. SUPERSYMMETRY

SUSY solves the Higgs hierarchy problem in an elegant way, features gauge coupling unification, provides a viable dark matter candidate and potentially generate the baryon-antibaryon asymmetry through electroweak baryogenesis. The Minimal Supersymmetric Standard Model (MSSM) remains one of the most appealing models that leads to a more complete theory beyond the Standard Model (SM). Its simplest extension, the NMSSM [30, 31] introduces additional appealing features. Among the most notable is that it provides an attractive solution to the SUSY μ problem [32]. Furthermore, it is widely believed

Table I.2: Branching ratios in % for benchmark models. The fermion branching ratios are for each family, but three families are included in the total width. The diboson modes are in the decoupling limit $\sin\beta = \cos\alpha \rightarrow 1$ with heavy H, H^\pm, A , for which the Zh width is the same as that for W^+W^- . The W , Z , and t masses are ignored. The last row shows $\Gamma_{Z'}/M_{Z'}$.

	χ	ψ	η	LR	B-L	SSM
u	3.6	12.2	15.9	10.4	5.1	9.9
d	17.8	12.2	9.9	18.2	5.1	12.8
e	5.9	4.1	3.3	2.3	15.4	2.9
ν	5.3	2.0	0.7	0.8	7.	5.8
W^+W^-	1.12	4.1	5.3	2.3	0.	2.9
$\Gamma_{Z'}/M_{Z'}$	0.012	0.006	0.007	0.021	0.009	0.032

that the discovery of a Standard Model-like Higgs boson [33, 34] strongly supports the idea of weak-scale supersymmetry based on the “naturalness” argument. However, in the context of the MSSM, a Higgs mass of $m_h \sim 126$ GeV still requires a significant degree of fine tuning [35–38]. In contrast, the NMSSM largely alleviates the tuning required to achieve this rather high mass value [39, 40].

1. SUSY Higgs Sector

The Higgs sector of the MSSM consists of two $SU(2)_L$ doublets. After electroweak symmetry breaking (EWSB), there are five physical states left in the spectrum, two CP-even states h^0 and H^0 with $m_{h^0} < m_{H^0}$, one CP-odd state A^0 , and two charged scalar states H^\pm . At tree-level, it is customary to use the mass m_A and the ratio of the vacuum expectation values $\tan \beta = v_u/v_d$ as the free parameters to determine the other masses. These masses receive large radiative corrections from the top-stop sector due to the large top Yukawa coupling. If we categorize these Higgs bosons according to their couplings to the electroweak gauge bosons, there are two distinct regions in the MSSM [41]:

- (i) The “decoupling region”: For a relatively heavy A^0 ($m_A \gtrsim 300$ GeV), the lighter CP-even state h^0 is the SM-like Higgs and the others H^0 , A^0 , and H^\pm are heavy and nearly degenerate.
- (ii) The “non-decoupling region”: For $m_A \sim m_Z$, the heavier CP-even Higgs H^0 is the SM-like Higgs, while h^0 and A^0 are light and nearly degenerate. The mass of the charged Higgs H^\pm is typically around 140 GeV.

The decoupling scenario comfortably accommodates the current searches due to the effective absence of the non-SM-like Higgs states. In fact, it would be very difficult to observe any of the heavy MSSM Higgs bosons at the LHC if $m_A \gtrsim 400$ GeV for a modest value of $\tan \beta \lesssim 10$ [42–45]. The non-decoupling scenario, on the other hand, would lead to a rich LHC phenomenology due to the existence of multiple light Higgs bosons. Although this latter scenario would be more tightly constrained by current experiments, it would correspondingly have greater predictive power for its phenomenology.

In the NMSSM, one complex $SU(2)_L \times U(1)_Y$ singlet scalar field is added to the Higgs sector. As a result, after the scalar fields acquire vacuum expectation values, one new CP-even and one new CP-odd state are added to the MSSM spectrum, resulting in three CP-even mass eigenstates (denoted by H_1 , H_2 , H_3), two CP-odd mass eigenstates (A_1 , A_2), plus a pair of charged states (H^\pm).

The masses of the CP-even scalars can be better understood by considering what happens when the singlet is added to the MSSM spectrum. The masses of the MSSM Higgs bosons can be in one of two scenarios: the SM-like Higgs of the MSSM can either be the lighter eigenstate or the heavier eigenstate, as illustrated in the top row of Fig. 1.1. After adding the singlet scalar, the two panels of the MSSM give rise to six possible scenarios in the NMSSM, as illustrated in the lower row of Fig. 1.1.

In reality, the mass eigenstates are admixtures of the gauge interaction eigenstates, and thus cannot be labelled as simply as in Fig. 1.1. Nevertheless, these graphs give us an intuitive picture of the result of adding the singlet field of the NMSSM.

Recently, many analyses of the NMSSM have been performed in light of the recent Higgs searches at the LHC, focusing on the large m_A region. References [46–48] showed the compatibility of the NMSSM with an enhanced $\gamma\gamma$ rate, while Reference [49] studied the stringent flavor and muon $g - 2$ constraints on the model. Moreover, the NMSSM may include many interesting features, that include grand unification of gauge couplings [50], naturalness for the Higgs mass [39, 40, 51–53], neutralino Dark Matter [54–56], and possible accommodation of multiple nearly degenerate Higgs bosons [57–59].

These low- m_A parameter regions of the NMSSM have unique properties and offer rich phenomenology, providing complementary scenarios to the existing literature for the large- m_A case, as mentioned above. The production cross section and decay branching fractions for the SM-like Higgs boson may be modified appreciably and new Higgs bosons may be readily produced at the LHC.

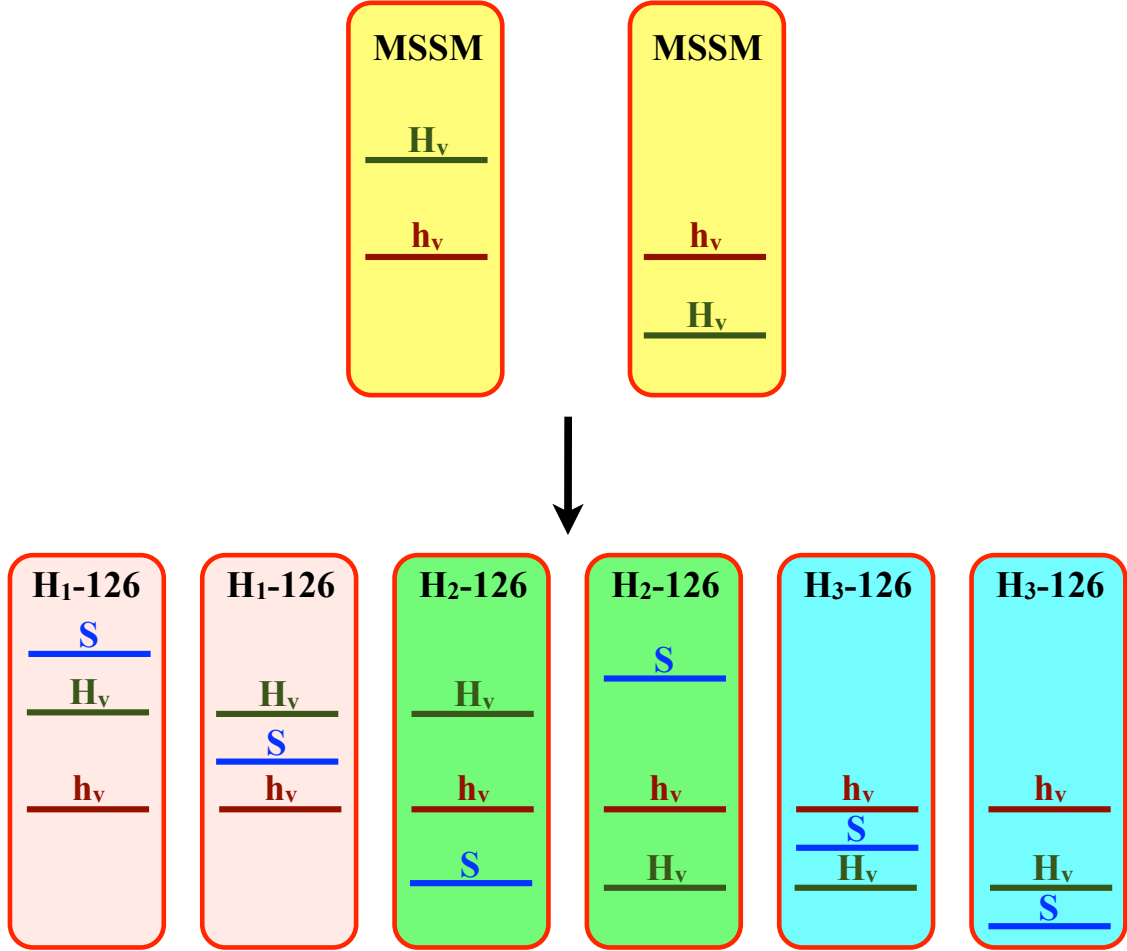


Figure I.1: Illustration of the effect of adding the singlet to the MSSM CP-even Higgs boson spectrum before mixing.

2. SUSY Dark Matter

Observations of the cosmic microwave background, gravitational lensing, clustering of galaxies, galactic rotation curves, etc. have provided compelling evidence for the existence of Dark Matter (DM), which is likely to be of particle origin.

One of the best motivated candidates for DM is the Weakly Interacting Massive Particle (WIMP), a good example of which is the Lightest Supersymmetric Particle (LSP) (for reviews, see [60–62]).

The identification of the particle DM is one of the most challenging tasks in theoretical and experimental particle physics. From the theoretical point of view, the weakly interacting massive particle remains to be a highly motivated candidate (for a recent review, see, e.g., Ref. [61]). To reach the correct relic abundance in the current epoch, a WIMP mass is roughly at the order

$$M_{\text{WIMP}} \lesssim \frac{g^2}{0.3} 1.8 \text{ TeV}. \quad (\text{I.C.7})$$

The upper bound miraculously coincides with the new physics scale expected based on the “naturalness” argument for electroweak physics. There is thus a high hope that the search for a WIMP dark matter may be intimately related to the discovery of TeV scale new physics. However, the precise value of the WIMP mass and the exact relic abundance heavily depend on the dynamics in a specific model. If WIMPs exist in the Galaxy, they may be detected through direct search experiments [63–70]. The DAMA experiment [63] has detected an annual modulation in the measured recoil spectrum at the 8.9σ level, consistent with the presence of WIMP DM in the Galaxy. More recently, the CoGeNT [64], CRESST [65] and CDMS [66] experiments have also obtained results that are consistent with low mass WIMP DM. On the other hand, these results have been challenged by other experiments such as XENON-10 [67], XENON-100 [68] and more recently TEXONO [71], which have excluded the parameter space favored by the DAMA, CoGeNT, CRESST and CDMS experiments. Complementary to the direct searches, indirect detection experiments include the Fermi gamma ray space telescope [72], Alpha Magnetic Spectrometer [73], Air Cherenkov Telescopes [74–76], and CMB experiments such as Planck [77], and the Wilkinson Microwave

Anisotropy Probe (WMAP) [78, 79]. The WMAP observations place a lower limit on the particle mass $m_\chi \gtrsim 10$ GeV, assuming a velocity-independent annihilation cross section $\langle\sigma_a v\rangle = 1 \text{ pb}\times c$ [80–85]. The non-observation of gamma rays from DM annihilation in the nearby dwarf galaxies [72, 86] has been used to place constraints on the DM particle mass $m_\chi \gtrsim 40$ GeV, for neutralino annihilation to the $b\bar{b}$ channel with a velocity-independent cross section $\langle\sigma_a v\rangle = 1 \text{ pb}\times c$, although these bounds would be relaxed with a more general analysis including the velocity-dependent contributions [87–90].

On the other hand, the LHC experiments have made a historic discovery of the long-sought-after Higgs boson predicted by the SM. The experiments also show no evidence for Beyond-SM Higgs bosons, nor other new physics such as SUSY etc. with the current data, seemingly in favor of heavy colored sparticles [91–95]. Several authors have studied the present LHC data and the implications for DM, as well as the possibility that future LHC data will provide information to the DM puzzle [37, 96–118]. Although the SUSY parameter space has been significantly reduced due to the absence of a SUSY signal at the LHC and due to the constraining properties of the SM-like Higgs boson, a dark matter candidate can still be readily accommodated in SUSY theories.

It is interesting to understand the viable WIMP mass range under current experimental constraints. While the dark matter direct detection experiments probe the dark matter at around a few hundred GeV with high sensitivity, the sensitivity drops significantly for the light dark matter given the limitation from the energy threshold of a given experiment. Light WIMP dark matter and its related sector, on the other hand, typically receive strong experimental constraints from various dark matter related searches, especially direct searches at lepton colliders. These factors make proper light WIMP DM candidate in a given model very restricted, sometimes tuned to rely on specific kinematics and dynamics. A comprehensive examination of light DM candidates in the low mass range is then in demand. Indeed, there have been interesting excesses in annual modulation by the DAMA collaboration [63], and in direct measurements by CoGeNT [64]⁵, CRESST [65] and CDMS [120] experiments that could be interpreted as signals from a low mass dark matter.

The tantalizing events from the gamma ray spectrum from the Galactic Center in the

⁵For a recent independent analysis, see Ref. [119].

Fermi-LAT data could also be attributed to contributions from low mass dark matter annihilation [121]. To convincingly establish a WIMP DM candidate in the low mass region, it is ultimately important to reach consistent observations among the direct detection, indirect detection and collider searches for the common underlying physics such as mass, spin and coupling strength.

Table I.3: Possible solutions for light (< 40 GeV) neutralino DM in MSSM and NMSSM.

	Models	DM (< 40 GeV)	Annihilation
Funnels	NMSSM	Bino/Singlino	$\tilde{\chi}_1^0 \tilde{\chi}_1^0 \rightarrow A_1, H_1 \rightarrow SM$
Co-ann.	MSSM & NMSSM	Bino/Singlino	$\tilde{\chi}_1^0 \tilde{\chi}_1^0 \rightarrow f \bar{f}; \tilde{\chi}_1^0 \tilde{f} \rightarrow V f; \tilde{f} \tilde{f}' \rightarrow f f'$

In section II.E, we explore the implications of a low mass neutralino LSP dark matter in the mass window $2 - 40$ GeV in the framework of the NMSSM (see Ref. [122] for a recent review). The robust bounds on the chargino mass from LEP experiments disfavored the Wino-like and Higgsino-like neutralinos, and forced a light LSP largely Bino-like or Singlino-like, or an admixture of these two. However, those states do not annihilate efficiently to the SM particles in the early universe. Guided by the necessary efficient annihilation to avoid overclosing the universe, we tabulate in table II.10 the potentially effective processes, where the first row indicates the funnel processes near the light Higgs resonances, and the second row lists the coannihilation among the light SUSY states. There is another possibility of combined contributions from the s -channel Z -boson and SM-like Higgs boson, as well as the t -channel light stau (~ 100 GeV).

With a comprehensive scanning procedure, we confirm three types of viable light DM solutions consistent with the direct/indirect searches as well as the relic abundance considerations: (i) A_1, H_1 -funnels, (ii) LSP-stau coannihilation and (iii) LSP-sbottom coannihilation. Type-(i) may take place in any theory with a light scalar (or pseudo-scalar) near the LSP pair threshold; while Type-(ii) and (iii) could occur in the framework of MSSM as well. These possible solutions all have very distinctive features from the perspective of DM astrophysics and collider phenomenology. We present a comprehensive study on the properties of these solutions and focus on the observational aspects of them at colliders, including new

phenomena in Higgs physics, missing energy searches and light sfermion searches. The decays of the SM-like Higgs boson may be modified appreciably and the new decay channels to the light SUSY particles may be sizable. The new light CP-even and CP-odd Higgs bosons will decay to a pair of LSPs as well as other observable final states, leading to rich new Higgs phenomenology at colliders. For the light sfermion searches, the signals would be very difficult to observe at the CERN Large Hadron Collider when the LSP mass is nearly degenerate with the parent. However, a lepton collider, such as the International Linear Collider (ILC), would be able to uncover these scenarios benefited from its high energy, high luminosity, and the clean experimental environment.

3. SUSY Displaced Decays

In spite of progressively tightening limits [123, 124], supersymmetry continues to serve as one of the most compelling scenarios for new physics at the LHC. In the absence of traditional signals below about 1 TeV, there has been a growing interest in exploring models in which superparticles are light enough for the 8 TeV LHC to produce, but somehow manage to evade the existing searches. Indeed, this situation remains a strong possibility, in large part because the observable signatures of SUSY depend extremely sensitively on the details of the spectrum and on the decays of the lightest superparticles. In particular, a broad class of highly-motivated scenarios that has so far received relatively limited dedicated attention in LHC searches includes superparticles with macroscopic decay lengths spanning from sub-mm to tens of meters. Such “displaced” particles can occur in models with R-parity violation (RPV) [1] or gauge mediated SUSY breaking (GMSB) [125], and also in mini-split spectra where all squarks are at roughly the 1000 TeV scale [126, 127] and the gluino lifetime becomes extended.

However, displaced decay signals occupy a subtle place in collider phenomenology. At the high end of the above lifetime range, long-lived charged particle searches [128–130] may become appropriate if the displaced particle is charged or has a nontrivial chance to form charged hadrons, but the efficiency drops exponentially for lower lifetimes. At the low end of the lifetime range, any number of prompt searches or searches involving bottom or

charm hadrons might pick up the signals [131], but may subject them to unnecessarily large backgrounds. Many different targeted strategies have been applied to search the broad range lifetimes in between [132–145]. Because energetic particle production originating in the bulk of the detector is extremely rare, most of these searches benefit from tiny backgrounds, often $O(1)$ event or smaller while maintaining good signal efficiency. The non-observation of excesses in such clean searches then begs the question of their implications for more general classes of models, where even very low efficiency can still lead to significant limits. Several recent phenomenological works have investigated the power of these searches, or proposed new searches for similarly striking signals [146–159].

In section II.F, we attempt to develop a more refined understanding of the status of SUSY scenarios with displaced decays, in light of the small but powerful collection of existing LHC displaced particle searches. Most of the models that we study have either never been searched for at nonzero lifetime, or explicit searches cover only one possible signature out of several. In practice, it is typical for each highly specialized displaced decay search to phrase its results in terms of only one or a handful of highly specialized new physics models. This is understandable, given the vast range of possible interesting models and the computational overhead required to fully simulate and interpret them. However, inferring the implications of those searches for a different model, and in particular how they might interplay with each other in covering the parameter space of that different model, then requires careful recastings. We present here, what we believe to be for the first time in the context of our chosen SUSY models, a comprehensive set of such recastings for multiple displaced particle searches simultaneously. Our results highlight the strengths and weaknesses of the various searches, and give a clear indication of what regions may currently be lacking in sensitivity. The process of undertaking these recastings also illustrates some of the difficulties and ambiguities that can arise when attempting to extrapolate the results of displaced decay searches beyond their original target models, especially given the unconventional approaches to event reconstruction. A saving feature is that total rates near the boundaries of sensitivity are usually very strong functions of both mass and lifetime, such that even $O(1)$ uncertainties in our estimation of experimental acceptance can still lead to only $O(10\%)$ uncertainties in model reach. Nonetheless, where possible we point out aspects of the searches that could be

particularly prone to mismodeling by recasters. We also make several suggestions for how some of these searches might be adapted to serve as more powerful probes of SUSY or other models beyond their original targets.

Of course, even restricting ourselves to simple variations on the particle content of the MSSM, the variety of possible displaced final-state signatures is extremely rich. To narrow down the possibilities to a manageable level, we first of all focus on simplified models where only one type of superparticle is produced, and undergoes a single-stage displaced decay back into SM particles and/or the LSP. These simplified models can generally be embedded into a variety of more complete spectra with additional production channels, such that our results are both broad in applicability and conservative within any given model. (For a more inclusive survey approach, see [157].) Within the still rather large set of possible simplified models, we focus on ones that have a sizable fraction of hadronic visible decays, either directly or due to subsequent decays of electroweak bosons. Such hadronic signals are nominally the most challenging and the least constrained by explicit displaced searches, and in some cases unconstrained or only mildly constrained even in prompt decay searches. Significantly, some of the simplified models that are most motivated by naturalness [160–164] can fall into this category, including direct production of the lightest stop eigenstate or of a quasi-degenerate multiplet of Higgsinos.

D. HIGGS BOSON

The discovery of a Higgs boson at the LHC [33, 34] completes the simple structure of the SM. Yet, a profound question remains: Is this rather light, weakly-coupled boson nothing but a SM Higgs, or it is a first manifestation of a deeper theory? While the LHC certainly will take us to a long journey on seek for new physics beyond the SM, it would be very important to determine the Higgs boson’s properties as accurately as possible at the LHC and future collider facilities, whether or not there are other particles directly associated with the Higgs sector observed at the LHC. In the following sections, we will briefly introduce the Higgs phenomenology at different collider facilities.

1. Higgs Boson at the LHC

The LHC facilitates the discovery of the SM-like Higgs boson at around 126 GeV. A huge number of Higgs bosons could be produced through various channels, including Glu-Glu Fusion (GGF), Weak-Boson Fusion (WBF, or VBF), weak-boson associated production, heavy fermion associated production ($t\bar{t}h$, $b\bar{b}h$, etc.) and so on. The corresponding production rates for the SM Higgs boson at 8 TeV LHC are shown in the upper panel of Fig. 1.2 from Ref. [165]. We also show the Higgs decay branching fractions as a function of the would-be SM Higgs mass in the lower panel of Fig. 1.2. Due to the off-shell suppression of the decay width to weak bosons, other decay models, especially decays to fermion pairs and diphoton become sizable for a 126 GeV Higgs boson. This enables us to learn Higgs properties from different decay modes comparing to a heavier one. In the meantime, the hadron collider provide a very complex environment for Higgs studies, resulting in specific designs and searching strategies for the Higgs boson.

The LHC as a high energy hadron machine, facilitates large gluon and valence quark parton luminosities. This leads to the leading production mode of the Higgs boson to be through top-loop induced GGF process. The LHC is also QCD background rich. The GGF produced Higgs then decay into, though with 10^{-3} or below branching fractions, diphoton or four charged leptons from ZZ^* to stand out of the background. These two channels are the leading channels contributing to the Higgs discovery and later detailed studies on its properties such as CP at the LHC. The electroweak background for four charged leptons are small at the LHC, resulting in small signal and background interference. As for the diphoton final state, the background is well understood but non-negligible. These signal and background differences cause invariant mass peak shift for the Higgs decay products, which can be taken advantage of to bound the Higgs boson width [166]. Another interesting application from the Higgs to four charged lepton final states is to compare the off-shell Higgs contribution and on-shell Higgs contribution. This can also lead to some interesting bounds on the Higgs boson total width, though some careful treatment of the interpretation need to be taken into account.

The Higgs to fermion decay channels will provide direct evidence of Higgs's role in chiral-

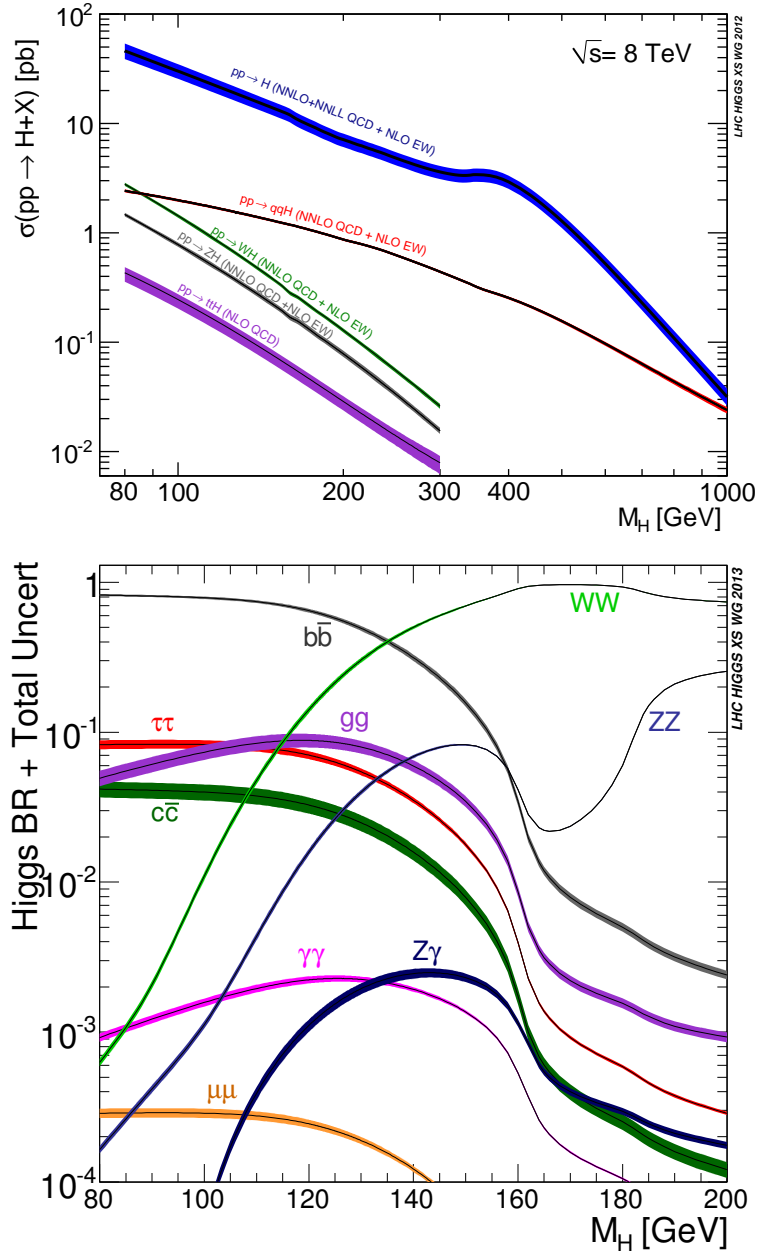


Figure I.2: Higgs production and decay branching fractions from Ref. [165].

symmetry breaking in the fermion sector. The dominate production rate of the Higgs from GGF can be viewed as an indirect evidence of such couplings, but such effects can also arise from BSM physics effects, e.g. heavy fermion loops. The two dominate fermion pair decay modes of the Higgs boson are to bottom pairs and tau lepton pairs. The QCD-rich hadron collider environment made these two decay modes hard to observe from GGF. Instead, one can rely on the weak boson associated production, where the leptonic decaying Z boson can significantly increase the signal to background ratios. So far we have seen evidence for both decays through this channel. The muon Yukawa coupling of the Higgs boson can be probed at the LHC, benefited from the clean muon chamber. However, the process is signal statistics limited. Similarly, slightly indirect probe of the charm Yukawa through J/ψ meson plus photon decay modes are proposed. Amongst these SM Yukawa couplings, the top Yukawa is probably one of the most important ones, such decay is kinematically forbidden. The LHC could probe such coupling through $t\bar{t}h$ production mode. After the LHC 7 and 8 TeV run, the ATLAS (CMS) put an upper bound on the cross section 6.7 (4.4) times the SM value [167, 168]. In addition, the BSM flavor changing fermion decays of the Higgs boson can be interesting and observed, which will certainly reveal Higgs's role in flavor violation. Upcoming LHC run II will certainly improve the situation.

Higgs exotic decays such as invisible decays can be probed at the LHC through ZH associated production, which can limit the Higgs invisible branching fractions to 40%. There are many other interesting and challenging Higgs decays modes, especially these inspired by SUSY as discussed in section I.C.1, for a rather comprehensive review, see Ref. [169].

2. Higgs Width at the ILC

The discovery of a Higgs boson at the LHC [33, 34] completes the simple structure of the SM. While we look forward to a long and hopefully fruitful run at the LHC as it continues to search for direct evidence of new physics beyond the SM, it will be very important to determine the Higgs boson's properties as accurately as possible at the LHC and future collider facilities. It may be that the Higgs itself is our first access to the next regime of physics.

The key properties of the Higgs boson are the strengths of its couplings to other particles. The overall strength of these couplings, at least to particles lighter than the Higgs itself, is characterized by the total width Γ_h . Because of the broad spread of the partonic energy distribution, limited energy-momentum resolution for final state particles, and the large SM backgrounds in the LHC environment, there is essentially no way to measure its total width or any partial width to a *desirable accuracy* without additional theoretical assumptions [170–172]. Assuming an upper limit for a Higgs coupling, such as that of hWW and hZZ , then an upper bound for the total width can be inferred [172]. Around $(10 - 40) \times \Gamma_h$ accuracy can be achieved by measuring the interference effect which shifts the invariant mass distribution of the $ZZ/\gamma\gamma$ mode [166], and by measuring $pp \rightarrow ZZ$ differential cross sections with $m_{ZZ} > 300$ GeV [173, 174]. At a lepton collider optimized for Higgs boson studies, such as ILC or a circular e^+e^- collider (TLEP) [175], the hZZ coupling, and thus the partial decay width $\Gamma(h \rightarrow ZZ)$ can be measured to a good accuracy [176] by measuring inclusive Higgs cross sections. The total decay width then can be indirectly determined. For review on ILC, see the ILC Technical Design Report (TDR) [177]. See, e.g., [178] for an estimate of sensitivity in a 2-Higgs Doublet Model.

3. Higgs Couplings from ZZ-fusion at the ILC

We evaluate the $e^-e^+ \rightarrow e^-e^+h$ process through the ZZ fusion channel at the ILC operating at 500 GeV and 1 TeV center of mass energies. We perform realistic simulations on the signal process and background processes. With judicious kinematic cuts, we find that the inclusive cross section can be measured to 2.9% after combining the 500 GeV at 500 fb⁻¹ and 1 TeV at 1 ab⁻¹ runs. A multivariate log-likelihood analysis further improves the precision of the cross section measurement to 2.3%. We discuss the overall improvement to model-independent Higgs width and coupling determinations and demonstrate the use of different channels in distinguishing new physics effects in Higgs physics. Our study demonstrates the importance of the ZZ fusion channel to Higgs precision physics, which has often been neglected in the literature.

The discovery of a 126 GeV Higgs Boson at the LHC completes the roster of particles

predicted by the SM. High energy experiments now continue their search for physics beyond the Standard Model in light of this new era. A major new avenue for pursuing this search is the detailed study of the Higgs itself. While the mass of the Higgs boson is a free parameter in the SM, its couplings to other particles are dictated by the gauge and Yukawa interactions. The observations of this particle are so far consistent with the SM expectations, but there is considerable room for new physics to reveal itself in deviations of the Higgs properties from the SM. There are also many theoretical scenarios in which such deviations would arise at a potentially detectable level. Hence, a precise measurement of those couplings is a key tool in establishing a departure from the SM, and in characterizing any sign of new physics which may be discovered.

The LHC will continue to accumulate a large amount of data at unprecedented energies for many years, which will improve on current understanding of Higgs physics. It also faces certain limitations intrinsic to a hadron collider, including the uncertainty of large QCD-related backgrounds. The LHC can measure particular channels involving specific modes of production and decay in combination, and thus constrain combinations of coupling constants and the unknown width. Unfortunately, because it cannot measure a single coupling independent of the width, it cannot place strong bounds on the absolute values of couplings, nor on the total width unless additional, model-dependent, assumptions are made [170–172, 179–181]. A “Higgs factory” such as the International Linear Collider has the potential to make precision measurements of Higgs physics that take advantage of the simple reconstructable kinematics and clean experimental environment. One especially appealing feature of the ILC is the ability to accurately extract the Higgs width in a model-independent manner.

The key feature of a lepton collider in making model-independent measurements is the ability to determine the inclusive Higgs production rate. This is done using processes such as $e^-e^+ \rightarrow h + X$ where X represents additional measurable particles. Since the initial state, including longitudinal momentum, is well-known we can infer the Higgs momentum without specifying the decay of the Higgs:

$$p_h = p_{e^-e^+} - p_X. \tag{I.D.8}$$

This complete kinematical reconstruction allows us to discriminate the inclusive Higgs signal from background and measure the couplings of the relevant production mechanism independently of the width. Once this is done, measurements of additional specific decay channels can be used to determine the total width and the absolute values of other couplings. In a previous study we discussed this general strategy in detail [182]. Based on available analyses the model-independent Higgs width Γ_h can be measured at the level of $\delta_{\Gamma_h} \simeq 5\%$ relative to the true width. Most of this error derives from the uncertainty on the inclusive cross section. Thus, any substantial improvement of the total width measurement depends critically on improving the precision on the inclusive cross section. Currently, the inclusive cross section sensitivity is estimated for the ‘‘Higgsstrahlung’’ channel $e^-e^+ \rightarrow Zh$. The cross section for this channel is largest just above the threshold at a center of mass energy $\sqrt{s} \simeq 250$ GeV, where it can be measured using the Z decay to electrons and muons with a relative error $\delta\sigma_{Zh}^{inc} \simeq 2.6\%$ [183, 184]. At $\sqrt{s} = 500$ GeV the Higgsstrahlung rate is substantially reduced but using hadronic decays of the Z may allow one to measure the cross section at $\delta\sigma_{Zh}^{inc} \simeq 3\%$ [185].

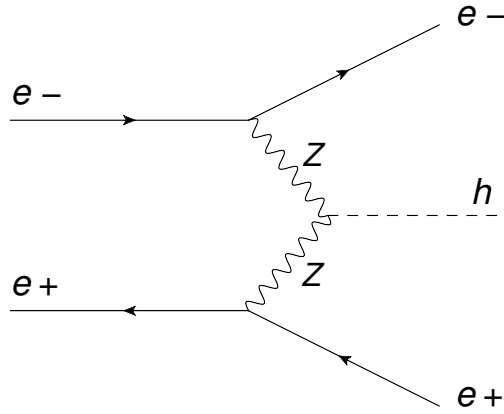


Figure I.3: Feynman diagram of the ZZ fusion signal process.

Further improvements can be made by examining the alternate production mechanism of ZZ fusion

$$e^-e^+ \rightarrow e^-e^+Z^*Z^* \rightarrow e^-e^+h, \quad (\text{I.D.9})$$

as depicted in Fig. I.3, which has often been neglected in the literature. This mode has a

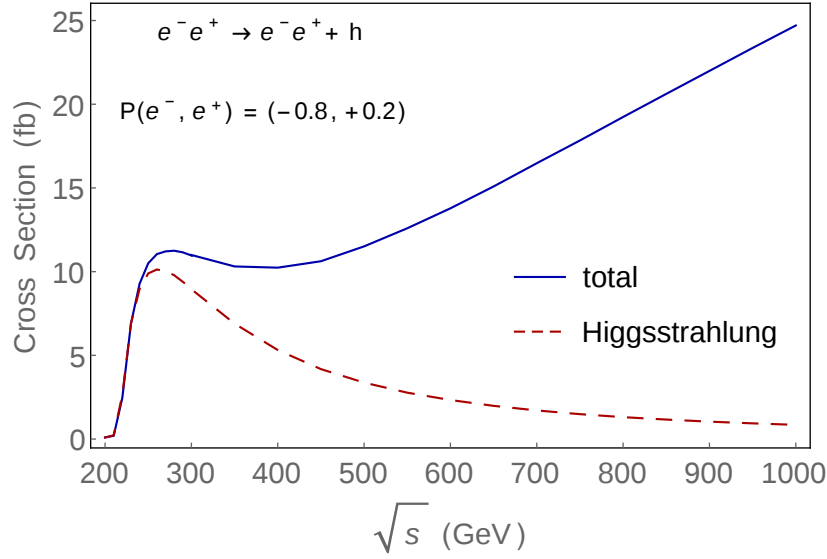


Figure I.4: Total cross section (in fb) for $e^-e^+ \rightarrow e^-e^+ + h$ at ILC versus \sqrt{s} . The dashed curve is for Higgsstrahlung mode only.

small rate at 250 GeV but grows with energy as $\ln^2(s/M_Z^2)$. At 500 GeV it already contributes roughly twice as much to the final state e^-e^+h as the Higgsstrahlung process $Zh \rightarrow e^-e^+h$, which falls roughly as $1/s$, as can be seen in Fig. I.4. At 1 TeV this ratio grows to almost a factor of twenty. Thus, although the Higgsstrahlung process benefits from a sharp kinematic on-shell Z peak through the reconstructible final states into which the Z decays, the ZZ fusion channel, which features two energetic forward/backward electrons, should also be exploited to make maximal use of the high-energy reach of the ILC.

In section III.C we perform a fast detector simulation analysis of the inclusive ZZ fusion channel measurement at 500 GeV and 1 TeV. We simulate the predominant backgrounds and a SM-like Higgs signal and calculate the signal sensitivity using a cut-based analysis and multivariate log-likelihood analysis. We find that with the cut-based analysis, we can reach a sensitivity on the cross section to 2.9% level. The multivariate analysis further improves the precision of the cross section measurement to 2.3%.

4. Higgs Boson at Muon Collider

In the light of the discovery of a 126 GeV Standard-Model-like Higgs boson at the LHC, we evaluate the achievable accuracies for direct measurements of the width, mass, and the s -channel resonant production cross section of the Higgs boson at a proposed muon collider. We find that with a beam energy resolution of $R = 0.01\%$ (0.003%) and integrated luminosity of 0.5 fb^{-1} (1 fb^{-1}), a muon collider would enable us to determine the Standard-Model-like Higgs width to $\pm 0.35 \text{ MeV}$ ($\pm 0.15 \text{ MeV}$) by combining two complementary channels of the WW^* and $b\bar{b}$ final states. A non-Standard-Model Higgs with a broader width is also studied. The unparalleled accuracy potentially attainable at a muon collider would test the Higgs interactions to a high precision.

Of all properties of the Higgs boson, its total decay width (Γ_h) is perhaps of the most fundamental importance since it characterizes the overall coupling strength. Once it is determined, the partial decay widths to other observable channels would be readily available. Because of the broad spread of the partonic energy distribution, limited energy-momentum resolution for final-state particles and the large SM backgrounds in the LHC environment, there is essentially no way to measure its total width or any partial width to a desirable accuracy without additional theoretical assumptions [170, 179, 180]. Assuming an upper limit for a Higgs coupling, such as that of hWW , then an upper bound for the total width can be inferred [171, 172]. At a muon collider, however, due to the much stronger coupling for the Higgs to the muons than to the electrons, an s -channel production of a Higgs boson [186] will likely lead to clear signal for several channels, and thus its total decay width may be directly measured by fitting its scanned data.

In section IV.B, we propose a realistic scanning and fitting procedure to determine the Higgs boson width at a muon collider. We demonstrate the complementarity for the two leading signal channels $h \rightarrow b\bar{b}$, WW^* . The combined results lead to a highly accurate determination for the width, mass and the s -channel production cross section. This is undoubtedly invaluable for determining the Higgs interactions and testing the theory of the electroweak symmetry breaking to an unparalleled precision.

Higgs boson properties could be studied with a high accuracy at a muon collider via the

s -channel resonant production. It is a possible situation where the center-of-mass energy of the muon collider is off the resonance above the Higgs mass. The discovery potential for a generic heavy Higgs boson (H) and compare different production mechanisms, including the “radiative return” (γH), Z -boson associated production (ZH) and heavy Higgs pair production (HA). These production mechanisms do not sensitively rely on *a priori* knowledge of the heavy Higgs boson mass. We include various types of Two Higgs Doublet Models for the comparison. We conclude that the radiative return process could provide an important option for both the heavy Higgs discovery and direct measurement of invisible decays at a high energy muon collider.

With the discovery of the SM-like Higgs boson (h) at the LHC [33, 34], the follow-up examinations of its properties at the LHC and future colliders will be of high priority for collider physics.

The Higgs sector may not be as simple as it is in the minimal electroweak theory. A wide class of new physics scenarios, ranging from supersymmetry [187] to models of neutrino mass generation [188–192], postulates the existence of an extended sector of fundamental scalars. While such an extension could leave some imprint on the properties of the recently discovered Higgs boson, it is also imperative that the proposed future colliders should have the potential to identify additional scalars that could be produced within its kinematic reach. Due to the rather weak couplings and the large SM backgrounds, the LHC will have limited coverage for such search [193–197]. At a future lepton collider, on the other hand, due to the clean experimental environment, it would be straightforward to identify a heavy Higgs signal once it is copiously produced on resonance [198].

The exact center-of-mass energy required for an optimal heavy Higgs signal depends on the unknown heavy Higgs mass, in particular for the s -channel resonant production at a muon collider. The situation may be remedied if instead we consider associated production of a Higgs boson with other particles. A particularly interesting process is the “radiative return” (RR) process. In the case of the Higgs boson production, the processes under consideration are

$$\mu^+\mu^- \rightarrow \gamma H, \gamma A, \tag{I.D.10}$$

where H (A) is a heavy neutral CP-even (CP-odd) state, respectively. When the center of mass energy of the muon collider is above the heavy Higgs resonance, the photon emission from the initial state provides an opportunity of the heavy Higgs boson “back” to the resonance. For this, one does not need to know the mass of the (unknown) heavy scalar. This mechanism alone could also provide an excellent channel to measure the invisible decay of the heavy Higgs boson.

II. BSM PHYSICS AT THE LHC

A. DIJET RESONANCES

The CERN Large Hadron Collider is pushing the energy frontier and taking the field of high energy physics to a new era. While much of the attention for new physics discovery has centered on theories associated with electroweak symmetry breaking, most initial states at hadron colliders are composed of colored particles. Hence, any new colored resonances will be produced with favorable rates at the LHC since their couplings may be typically of the strength of the strong-interaction.

Beyond the SM, there are many possible exotic colored states that can be produced at the LHC. Besides being phenomenologically interesting and experimentally important to search for, many of the exotic states are also theoretically motivated. For example, color-antitriplet scalars may be produced via quark-quark annihilation as squarks in R-parity violating SUSY theories [1], or as “diquarks” in E_6 grand unified theories [2]. Color-sextet scalars can arise in partially unified Pati-Salam theories [3] and be produced also via quark-quark annihilation. Color-triplet fermions can be produced via quark-gluon annihilation as “excited quarks” in composite models [4, 5]. Sextet fermions, the so-called “quixes”, associated with chiral color [6] and top quark condensate models [7] may also be produced via quark-gluon annihilation. Color-octet scalars that are $SU(2)_L$ singlets can arise in technicolor models [8], and in universal extra dimensions [9]. Color-octet vectors have been extensively explored as axigluons [6, 10] and colorons [11, 12]. There has also been much recent interest in studying the similar states in the context of Kaluza-Klein gluons [13], and low-scale string resonances [14–16] via gluon-gluon, or quark-antiquark annihilation.

Any new resonant states produced at the LHC through interactions with light partons

will contribute to the dijet production, leading to one of the simplest signal topologies. Both the ATLAS and CMS collaborations have recently searched for this class of signal and obtained 95% confidence level limits on the production cross section of such resonant states. From these limits they were able to already put the most stringent bound on the mass of an excited quark of 1.53 TeV from ATLAS [199] and 1.58 from CMS [200], and on a string resonance [200] of 2.5 TeV.

Motivated by the above considerations, we study the colored resonances in a most general way. We classify them according to their couplings to light partons, solely based on group theory decomposition as shown in section II.A.1. Among those possible colored resonances, we focus on those produced by the leading parton luminosities directly from valence quarks or gluons. We then construct their couplings to light partons and describe their general features in section II.A.2. In section II.A.3 we calculate the cross sections for their resonant production at the LHC with c.m. energies of 7 and 14 TeV. We apply the new ATLAS and CMS data to put bounds on various possible colored resonant states in section II.A.4. Finally, we conclude in section II.A.5. A few appendices contain the QCD color treatment, and a list of Feynman rules for the resonance couplings to the initial state light partons VI.AVI.B.

1. Classification of Resonant Particles in Hadronic Collisions

The resonance structures can be classified according to the spin (J) and the quantum numbers under the SM gauge group $SU(3)_C \times SU(2)_L \times U(1)_Y$. We adopt a notation of group structure

$$(SU_3, SU_2)_{Q_e}^J, \tag{II.A.1}$$

where Q_e indicates the electric charge ($T_3 + Y$).

In pp collisions at the LHC, we consider the dominant partons participating in the heavy resonance production to be the valence quarks and gluons. We express them with our

notation as

$$\begin{array}{lll}
Q & (\mathbf{3}, \mathbf{2})_{2/3, -1/3}^{1/2} & \text{Left - handed doublet} \\
U & (\mathbf{3}, \mathbf{1})_{2/3}^{1/2} & \text{Right - handed singlet} \\
D & (\mathbf{3}, \mathbf{1})_{-1/3}^{1/2} & \text{Right - handed singlet} \\
A & (\mathbf{8}, \mathbf{1})_0^1 & \text{vector.}
\end{array} \tag{II.A.2}$$

We can thus classify the single particle production via the annihilation of any two partons above. Table II.1 lists the quantum numbers of possible resonances in our notation from two initial partons. Since the LHC is a “QCD machine”, it is natural to start primarily based on the $SU(3)_C$ quantum numbers of the two initial states. We thus have partonic collisions of quark-quark: $\mathbf{3} \otimes \mathbf{3}$; quark-gluon: $\mathbf{3} \otimes \mathbf{8}$; gluon-gluon: $\mathbf{8} \otimes \mathbf{8}$; and quark-antiquark: $\mathbf{3} \otimes \bar{\mathbf{3}}$.

Possible spins and the electric charges are also given in Table II.1. In principle, neutral particles may be further classified by the discrete symmetries according to their parity (P), charge conjugation (C), and CP properties if these quantum numbers are conserved in their interactions. We will discuss them in the next section. In the last column, we add baryon numbers (B) carried by the initial state partons. Depending on the underlying theory for the new resonances, baryon number may or may not be conserved in their interactions.

2. Parton-Resonance Interactions

We now construct the interaction Lagrangians for the resonances and partons guided by the SM gauge symmetry. We limit our consideration only to those colored states listed in Table II.1. We will not postulate their interactions with other particles (leptons, electroweak bosons, or even new particles beyond the SM). Although an incomplete description for a resonant particle as a full interacting theory, this minimal approach is sufficient for evaluating the production rate at the LHC. Assuming these interactions dominate, then their decay to dijets would also be the leading channel. Furthermore, we will not consider higher dimensional color representations beyond $\mathbf{8}$ again due to the minimality considerations. Should there exist a color “ $\mathbf{15}$ -tet” fermion, a simple calculation of the QCD beta-function would indicate the loss of the asymptotic freedom of QCD [201].

Table II.1: The $SU(3)_C \times SU(2)_L \times U(1)_Y$ quantum numbers and spins (J) of possible resonant states created by initial state quarks and gluons. The electric charge ($Q_e = T_3 + Y$) and baryon number (B) carried by the two initial state partons are also provided.

initial state	J	$SU(3)_C$	$SU(2)_L$	$U(1)_Y$	$ Q_e $	B
QQ	0	$\bar{\mathbf{3}} \oplus \mathbf{6}$	$\mathbf{1} \oplus \mathbf{3}$	$\frac{1}{3}$	$\frac{4}{3}, \frac{2}{3}, \frac{1}{3}$	$\frac{2}{3}$
QU	1	$\bar{\mathbf{3}} \oplus \mathbf{6}$	$\mathbf{2}$	$\frac{5}{6}$	$\frac{4}{3}, \frac{1}{3}$	$\frac{2}{3}$
QD	1	$\bar{\mathbf{3}} \oplus \mathbf{6}$	$\mathbf{2}$	$-\frac{1}{6}$	$\frac{2}{3}, \frac{1}{3}$	$\frac{2}{3}$
UU	0	$\bar{\mathbf{3}} \oplus \mathbf{6}$	$\mathbf{1}$	$\frac{4}{3}$	$\frac{4}{3}$	$\frac{2}{3}$
DD	0	$\bar{\mathbf{3}} \oplus \mathbf{6}$	$\mathbf{1}$	$-\frac{2}{3}$	$\frac{2}{3}$	$\frac{2}{3}$
UD	0	$\bar{\mathbf{3}} \oplus \mathbf{6}$	$\mathbf{1}$	$\frac{1}{3}$	$\frac{1}{3}$	$\frac{2}{3}$
QA	$\frac{1}{2}, \frac{3}{2}$	$\mathbf{3} \oplus \bar{\mathbf{6}} \oplus \mathbf{15}$	$\mathbf{2}$	$\frac{1}{6}$	$\frac{2}{3}, \frac{1}{3}$	$\frac{1}{3}$
UA	$\frac{1}{2}, \frac{3}{2}$	$\mathbf{3} \oplus \bar{\mathbf{6}} \oplus \mathbf{15}$	$\mathbf{1}$	$\frac{2}{3}$	$\frac{2}{3}$	$\frac{1}{3}$
DA	$\frac{1}{2}, \frac{3}{2}$	$\mathbf{3} \oplus \bar{\mathbf{6}} \oplus \mathbf{15}$	$\mathbf{1}$	$\frac{1}{3}$	$\frac{1}{3}$	$\frac{1}{3}$
AA	0, 1, 2	$\mathbf{1} \oplus \mathbf{8} \oplus \mathbf{8} \oplus \mathbf{10} \oplus \bar{\mathbf{10}} \oplus \mathbf{27}$	$\mathbf{1}$	0	0	0
$Q\bar{Q}$	1	$\mathbf{1} \oplus \mathbf{8}$	$\mathbf{1} \oplus \mathbf{3}$	0	1, 0	0
$Q\bar{U}$	0	$\mathbf{1} \oplus \mathbf{8}$	$\mathbf{2}$	$-\frac{1}{2}$	1, 0	0
$Q\bar{D}$	0	$\mathbf{1} \oplus \mathbf{8}$	$\mathbf{2}$	$\frac{1}{2}$	1, 0	0
$U\bar{U}, D\bar{D}$	1	$\mathbf{1} \oplus \mathbf{8}$	$\mathbf{1}$	0	0	0
$U\bar{D}$	1	$\mathbf{1} \oplus \mathbf{8}$	$\mathbf{1}$	1	1	0

A similar approach to ours has been carried out to construct the potentially large signals at the early run of the LHC with minimal model input [202, 203]. There has also been previous work on classifying exotic particles at the LHC [204].

a. $\mathbf{3} \otimes \mathbf{3}$ At the LHC the valence-valence initial states consist of two quarks, uu , dd , or ud . Hence, the production cross section of a heavy particle that couples to two quarks will receive an enhancement from the parton luminosity of the initial state. As listed on the top section of Table II.1, such states can be color-antitriplets or sextets. They also carry an exotic baryon number of $2/3$ (if B is conserved) and thus are often referred to “diquarks”.¹ According to their electroweak (EW) quantum numbers under $SU(2)_L \otimes U(1)_Y$, there are 6 such states. We denote them by the notation in Eq. (II.A.1) as

$$\begin{aligned}\Phi &\sim (\mathbf{3} \oplus \bar{\mathbf{6}}, \mathbf{3})_{-4/3, 2/3, -1/3}^0, & \Phi_q &\sim (\mathbf{3} \oplus \bar{\mathbf{6}}, \mathbf{1})_q^0 \quad (q = -1/3, 2/3, -4/3), \\ V_U^\mu &\sim (\mathbf{3} \oplus \bar{\mathbf{6}}, \mathbf{2})_{-1/3, -4/3}^1 & V_D^\mu &\sim (\mathbf{3} \oplus \bar{\mathbf{6}}, \mathbf{2})_{2/3, -1/3}^1.\end{aligned}\tag{II.A.3}$$

We construct the gauge invariant Lagrangian as follows

$$\begin{aligned}\mathcal{L}_{qqD} \sim & K_{ab}^j \left[y_{\alpha\beta} \overline{Q_{\alpha a}^C} i\sigma_2 \Phi^j Q_{\beta b} + \kappa_{\alpha\beta} \Phi_{-1/3}^j \overline{Q_{\alpha a}^C} i\sigma_2 Q_{\beta b} \right. \\ & + \lambda_{\alpha\beta}^{1/3} \Phi_{-1/3}^j \overline{D_{\alpha a}^C} U_{\beta b} + \lambda_{\alpha\beta}^{2/3} \Phi_{2/3}^j \overline{D_{\alpha a}^C} D_{\beta b} + \lambda_{\alpha\beta}^{4/3} \Phi_{-4/3}^j \overline{U_{\alpha a}^C} U_{\beta b} \\ & \left. + \lambda_{\alpha\beta}^U \overline{Q_{\alpha a}^C} i\sigma_2 \gamma_\mu V_U^{j\mu} U_{\beta b} + \lambda_{\alpha\beta}^D \overline{Q_{\alpha a}^C} i\sigma_2 \gamma_\mu V_D^{j\mu} D_{\beta b} \right] + \text{h.c.},\end{aligned}\tag{II.A.4}$$

where $\Phi^j = \frac{1}{2}\sigma_k \Phi_k^j$ with σ_k the $SU(2)_L$ Pauli matrices and K_{ab}^j are $SU(3)_C$ Clebsch-Gordan coefficients with the quark color indices $a, b = 1-3$, and the diquark color index $j = 1-N_D$. N_D is the dimension of the ($N_D = 3$) triplet or ($N_D = 6$) antisextet representation. C denotes charge conjugation, and α, β are the fermion generation indices. The color factor K_{ab}^j is symmetric (antisymmetric) under ab for the $\mathbf{6}$ ($\bar{\mathbf{3}}$) representation. Their normalization convention is given in Appendix VI.A.

¹This should not be confused with a possible two-light-quark bound state as “diquark”. We are talking about a new state at a TeV mass scale with a quantum number similar to two quarks.

After electroweak symmetry breaking, the states in Eq. (II.A.3) mix and reclassify themselves according to color (**3**, $\bar{\mathbf{6}}$) and electric charges ($-4/3$, $2/3$, $-1/3$), denoted by $E_{N_D}, U_{N_D}, D_{N_D}$. The relevant interactions among the physical states are then

$$\begin{aligned}\mathcal{L}_{qqD} = & K_{ab}^j \left[\lambda_{\alpha\beta}^E E_{N_D}^j \overline{u_{\alpha a}^C} P_\tau u_{\beta b} + \lambda_{\alpha\beta}^U U_{N_D}^j \overline{d_{\alpha a}^C} P_\tau d_{\beta b} + \lambda_{\alpha\beta}^D D_{N_D}^j \overline{d_{\alpha b}^C} P_\tau u_{\alpha a} \right. \\ & + \lambda_{\alpha\beta}^{E'} E_{N_D}^{j\mu} \overline{u_{\alpha a}^C} \gamma_\mu P_R u_{\beta b} + \lambda_{\alpha\beta}^{U'} U_{N_D}^{j\mu} \overline{d_{\alpha a}^C} \gamma_\mu P_R d_{\beta b} \\ & \left. + \lambda_{\alpha\beta}^{D'} D_{N_D}^{j\mu} \overline{u_{\alpha a}^C} \gamma_\mu P_\tau d_{\beta b} \right] + \text{h.c.}\end{aligned}\tag{II.A.5}$$

where $P_\tau = \frac{1}{2}(1 \pm \gamma_5)$ with $\tau = R, L$ for the right- and left-chirality projection operators. Here and henceforth, we include a superscript μ to indicate a vector state.

Naively, the strength of these Yukawa interactions can be naturally of the order of unity, since the interactions among colored states are likely to be similar to QCD strong interaction with a coupling constant $g_s^2 = 4\pi\alpha_s \sim \mathcal{O}(1)$. However, many of them are tightly constrained by flavor physics. A commonly adopted solution is the “minimal flavor violation” (MFV) [205]. This assumption makes the couplings align with the SM Yukawa matrices, and they only become significant when involving heavier quarks such as the top [206]. In some specific model realizations, the MFV is not necessary and certain individual operators involving light flavors can be sizable [207]. We do not introduce additional couplings for those new colored states and thus the baryon number is conserved. In fact, the baryon number can be made a conserved quantum number for the above interactions by the SM gauge symmetry along with a simple extension to the lepton sector [206].

We note that the color-triplet scalars (U_3, D_3) resemble scalar quarks (\tilde{u}, \tilde{d}) in SUSY and the interactions (with the chirality $\tau = L$) are directly analogous to R-parity violating operators of the λ'' terms [1], or the “diquarks” [2]. Color-triplet scalars at the TeV scale have also been considered in SUSY models to present a unified explanation of dark matter and baryogenesis [208]. The color-sextet scalars possess similar nature of “diquark Higgs” in some unified theories [3] or some exotic diquarks [209]. The vector states, on the other hand, are more exotic in terms of connections with an underlying model. There has been previous interest in the resonant production of diquark scalars and vectors at the LHC [210].

b. $3 \otimes 8$ A gluon and a quark can yield large partonic luminosity, and may couple to exotic fermion states. For simplicity, we only consider spin-1/2 states, with quantum numbers as

$$(\mathbf{3} \oplus \bar{\mathbf{6}}, \mathbf{1} \oplus \mathbf{2})_{-1/3, 2/3}^{1/2}.$$

We have not included the $\mathbf{15}$ since, as mentioned previously in this section, a $\mathbf{15}$ fermion would spoil the asymptotic freedom of the strong coupling.

Instead of writing down the complete SM gauge invariant operators, we consider the interactions after electroweak symmetry breaking with physical mass eigenstates. These two states are fermionic and of electric charges $-1/3$ and $2/3$. We denote them generically by $q_{N_D}^*$, or specifically by $d_{N_D}^*$ and $u_{N_D}^*$, where $N_D = 3$ or 6 for the dimension of their color representation. The $SU(3)_C$ gauge invariance requires the interactions to start with dimension-five, and are of the color-magnetic dipole form. The Lagrangian for these physical states is then

$$\begin{aligned} \mathcal{L}_{qgF} = \frac{g_s}{\Lambda} F^{A,\mu\nu} & \left[\bar{u} \bar{K}_{N_D,A} (\lambda_L^U P_L + \lambda_R^U P_R) \sigma_{\mu\nu} u_{N_D}^* \right. \\ & \left. + \bar{d} \bar{K}_{N_D,A} (\lambda_L^D P_L + \lambda_R^D P_R) \sigma_{\mu\nu} d_{N_D}^* \right] + \text{h.c.} \end{aligned} \quad (\text{II.A.6})$$

where $F^{A,\mu\nu}$ is the gluon field strength tensor with the adjoint color index $A = 1, \dots, 8$, and \bar{K}_A are $3 \times N_D$ matrices of Clebsch-Gordan coefficients connecting the color indices of the different representations. If the new fermion field is a $\mathbf{3}$, then $\bar{K}_A^\dagger = K^A = \sqrt{2} T^A$, where T^A are the fundamental $SU(3)$ representation matrices. Due to the presence of a gluon field, we naturally include a QCD coupling g_s . The new physics scale Λ is at least $M_{q_j^*}$ or higher. In a strongly interacting theory, we expect that the strength of the couplings $\lambda_{L,R}^U$ and $\lambda_{L,R}^D$ should be typically of the order of unity. However, if the operators are from one-loop contributions in a weakly coupled theory, then one would expect to have a suppression factor of the order $1/16\pi^2$ [202].

The color-triplet states resemble the excited quarks. They could also be string excitations in a low scale string scenarios [14–16]. The color-sextet fermions arise in theories of chiral color [6] and top quark condensate models [7], the so-called “quixes”. There has been previous interest in the color-sextet fermion production at hadron colliders [211].

c. $8 \otimes 8$ LHC is often referred to as a “gluon machine” since it has a large parton luminosity for gluon-gluon initial states. Among the bosonic states from the $8 \otimes 8$ decompositions, many higher dimensional color representations can be embedded into larger theories, unlike the 15-tet fermion states that spoil the asymptotic freedom. We only focus on the color-octet resonances that can result from gluon-gluon fusion. They may carry the quantum numbers

$$(\mathbf{8}_S \oplus \mathbf{8}_A, \mathbf{1})_0^{0,1,2}. \quad (\text{II.A.7})$$

The symmetric and antisymmetric representations can be utilized with the algebraic relations of the fundamental representation matrices

$$[T^A, T^B] = if^{ABC}T^C, \quad \{T^A, T^B\} = \frac{1}{N_C}\delta^{AB} + d^{ABC}T^C, \quad (\text{II.A.8})$$

and $N_C = 3$ is the dimension of the $SU(3)_C$ fundamental representation.

The leading operators start from dimension-five. Two possible interactions between gluons and a spin zero octet and spin two octet are

$$\mathcal{L}_{gg8} = g_s d^{ABC} \left(\frac{\kappa_S}{\Lambda_S} S_8^A F_{\mu\nu}^B F^{C,\mu\nu} + \frac{\kappa_T}{\Lambda_T} (T_8^{A,\mu\sigma} F_{\mu\nu}^B F_{\sigma}^{C\ \nu} + f T_8^{A,\rho} F^{B,\mu\nu} F_{\mu\nu}^C) \right), \quad (\text{II.A.9})$$

where S_8 (T_8) is a scalar (tensor) octet. We again assume that the couplings κ_S, κ_T of the order of unity. The relative coupling factor f is more likely to be 1. If the operators are from one-loop contributions in a weakly coupled theory, then one would expect to have a suppression factor of the order $1/16\pi^2$.

It is also possible to couple two gluons and a CP-odd octet scalar or tensor. The couplings of the CP odd states are identical in form to those in Eq. (II.A.9) with the replacement of one field strength tensor with its dual:

$$\tilde{F}_{\mu\nu}^A = \frac{1}{2} \varepsilon^{\mu\nu\rho\sigma} F_{\rho\sigma}^A, \quad (\text{II.A.10})$$

where $\varepsilon^{\mu\nu\rho\sigma}$ is the four dimensional antisymmetric tensor.

Finally, the antisymmetric structure constants f^{ABC} can also be used to construct interactions with CP-odd color octets. However, since the color structure is antisymmetric, the Lorentz structure must also be antisymmetric. Hence, terms proportional to $F_{\mu\nu} \tilde{F}^{\mu\nu}$ are zero and the only surviving term is $\tilde{T}_8^{\mu\sigma} \tilde{F}_{\mu\nu} F_{\sigma}^{\ \nu}$, where \tilde{T}_8 is the CP-odd color-octet tensor.

Color-octet (pseudo)scalars can arise in technicolor models [8, 212], and in universal extra dimensions [9]. There has been much recent interest in the gluon fusion production of color-octet scalars at the LHC [213, 214]. These interactions were induced via loops which are parameterized by the octet-scalar coupling in Eq. (II.A.9) with an additional suppression from the loop factor. Color-octet vector states have also been studied in the context of low-scale string resonances [15, 16] via gluon-gluon annihilation, but it typically leads to a suppressed rate.

d. $\mathbf{3} \otimes \bar{\mathbf{3}}$ Although the quark-antiquark annihilation would not result in the largest partonic luminosity at high energies in pp collisions, we include some discussions for resonant production from $\mathbf{3} \otimes \bar{\mathbf{3}}$ for completeness. The resonances may carry the quantum numbers

$$(\mathbf{1} \oplus \mathbf{8}, \mathbf{1} \oplus \mathbf{3})_{-1,0,1}^1, \quad (\mathbf{1} \oplus \mathbf{8}, \mathbf{2})_{0,1}^0. \quad (\text{II.A.11})$$

Once again, we focus on the color-octet states and ignore the well-known color-singlet states such as Z' 's, W' 's, and Kaluza-Klein gravitons.

We first consider the color-octet vector states. We denote them according to their color and electric charges V_8^0 , V_8^\pm . We write their interactions with quarks as

$$\begin{aligned} \mathcal{L}_{q\bar{q}V} = & g_s \left[V_8^{0,A,\mu} \bar{u} T^A \gamma_\mu (g_L^U P_L + g_R^U P_R) u + V_8^{0,A,\mu} \bar{d} T^A \gamma_\mu (g_L^D P_L + g_R^D P_R) d \right. \\ & \left. + \left(V_8^{+,A,\mu} \bar{u} T^A \gamma_\mu (C_L V_L^{CKM} P_L + C_R V_R^{CKM} P_R) d + \text{h.c.} \right) \right], \end{aligned} \quad (\text{II.A.12})$$

where $V_{L,R}^{CKM}$ are the left- and right-handed CKM matrices. Due to the stringent constraints from flavor physics, we have assumed that there is no FCNC, and the charged current aligns with the SM CKM. The couplings $C_{L,R}$ and $g_{L,R}$ are thus diagonal and naturally order of unity. Well-known examples of color-octet vectors coupled to $q\bar{q}$ include the axigluon [6, 10], a coloron or Techni- ρ [11, 12], a Kaluza-Klein gluon [13], and low-scale string resonances [14–16] via $q\bar{q}$ annihilation.

As for the color-octet scalar states, we note that the renormalizable interactions between a color-octet scalar and two quarks are Yukawa type interactions, and the SM gauge invariant interactions require the scalar to be a doublet [215] under $SU(2)_L$. Once again, due to the assumption of MFV, their couplings to light quarks would be small, and the only significant

coupling would be to the top or bottom quarks. The single production of charged and neutral scalars through initial state bottom quarks has been studied previously [216]. However, similar to Higgs production, the dominant resonant production of the scalar states would be via gluon fusion through top quark loops due to the increased parton luminosity and enhanced couplings. The effective couplings should be of the same form as in Eq. (II.A.9) for S_8 , but with a suppressed coupling.

We summarize the resonant states of our phenomenological interests in Table II.2. We propose notations for their names, give their conserved quantum numbers, leading couplings to initial state partons, and related theoretical models.

3. Resonance Production at The LHC

We will now give analytical formulas and present the expected numerical values of the production cross sections of the colored resonances at the LHC with 7 and 14 TeV hadronic center of momentum (c.m.) energies. The hadronic cross sections are computed by calculating the partonic cross section (σ_{ij}) and convolving it with the parton distribution functions (pdfs). We write the formula as

$$\sigma(S) = \sum_{ij} \int d\tau \frac{dL_{ij}}{d\tau} \sigma_{ij}(s), \quad (\text{II.A.13})$$

$$\frac{dL_{ij}}{d\tau} \equiv (f_i \otimes f_j)(\tau) = \int_0^1 dx_1 \int_0^1 dx_2 f_i(x_1) f_j(x_2) \delta(x_1 x_2 - \tau), \quad (\text{II.A.14})$$

where S (s) is hadronic (partonic) c.m. energy squared, f_i the parton i 's distribution function with a momentum fraction x_i , and $\tau = s/S$. For all numerical results here and henceforth, we have used the CTEQ6L1 pdfs [217] and set the factorization and renormalization scales the same at the resonance mass ($Q^2 = M^2$).

For a resonant production, the on-shell condition forces the partonic cross section to go like $\sigma_{ij} \sim \delta(s - M^2)$. Thus the hadronic cross section will be evaluated with the parton luminosity at $\tau = M^2/S$. We first show the partonic luminosities versus the scale at the resonance mass in Fig. II.1 for the parton combinations of $u_1 u_2$, $d_1 d_2$, $u_1 d_2 + d_1 u_2$, $g_1 g_2$, $g_1 u_2 + u_1 g_2$, $g_1 d_2 + d_1 g_2$, $u_1 \bar{u}_2 + \bar{u}_1 u_2$, and $d_1 \bar{d}_2 + \bar{d}_1 d_2$ at (a) 7 and (b) 14 TeV LHC. As expected, initial states involving valence quarks and gluons will have the largest parton luminosities.

Table II.2: Summary for resonant particle names, their quantum numbers, and possible underlying models.

Particle Names (leading coupling)	J	$SU(3)_C$	$ Q_e $	B	Related models
$E_{3,6}^\mu (uu)$	0, 1	3 , $\bar{\mathbf{6}}$	$\frac{4}{3}$	$-\frac{2}{3}$	scalar/vector diquarks
$D_{3,6}^\mu (ud)$	0, 1	3 , $\bar{\mathbf{6}}$	$\frac{1}{3}$	$-\frac{2}{3}$	scalar/vector diquarks; \tilde{d}
$U_{3,6}^\mu (dd)$	0, 1	3 , $\bar{\mathbf{6}}$	$\frac{2}{3}$	$-\frac{2}{3}$	scalar/vector diquarks; \tilde{u}
$u_{3,6}^* (ug)$	$\frac{1}{2}, \frac{3}{2}$	3 , $\bar{\mathbf{6}}$	$\frac{2}{3}$	$\frac{1}{3}$	excited u ; quixes; stringy
$d_{3,6}^* (dg)$	$\frac{1}{2}, \frac{3}{2}$	3 , $\bar{\mathbf{6}}$	$\frac{1}{3}$	$\frac{1}{3}$	excited d ; quixes; stringy
$S_8 (gg)$	0	8 _S	0	0	π_{TC}, η_{TC}
$T_8 (gg)$	2	8 _S	0	0	stringy
$V_8^0 (u\bar{u}, d\bar{d})$	1	8	0	0	axigluon; g_{KK}, ρ_{TC} ; coloron
$V_8^\pm (u\bar{d})$	1	8	1	0	ρ_{TC}^\pm ; coloron

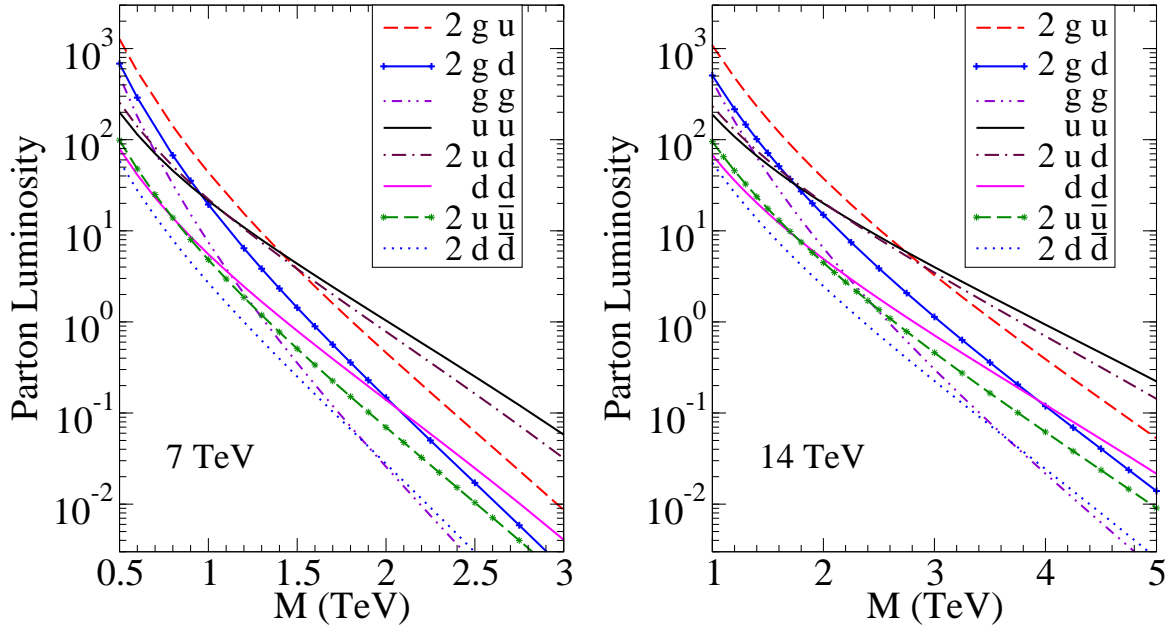


Figure II.1: The parton luminosities $dL_{ij}/d\tau$ versus resonance mass at the (a) 7 TeV and (b) 14 TeV LHC.

In particular, gluons dominate at lower masses, while valence quarks take over at higher masses. The cross-over between gg and uu occurs near $M = 0.75$ (1.2) TeV at the 7 (14) TeV LHC. Not only the u quark pdf is about twice as much as that of d at low masses, but also it falls much more slowly at high masses than d . For completeness, we also include \bar{q} initial state when relevant. In fact, the cross-over of the partonic luminosities between gg and $u\bar{u}$ occurs near $M = 1.2$ (2.2) TeV at the 7 (14) TeV LHC.

The rapidity of the partonic c.m. system is also of significant interest, which is defined as

$$y_{CM} = \frac{1}{2} \ln \frac{x_1}{x_2}. \quad (\text{II.A.15})$$

We show the y_{CM} distributions at the 7 and 14 TeV LHC for $M = 1.5$ TeV in Figs. II.2(a) and II.2(b) respectively. These distributions measure the longitudinal boost due to the asymmetry between the two parton energies. The gg and uu initial states are symmetric and hence peaked at zero rapidity. Due to the up-quark being valence with a broader distribution in x , the uu initial state develops a larger discrepancy between parton momentum fractions than the gg initial state and is therefore broader. Also, the $u\bar{u}$, $u\bar{d}$ and ug initial states have a large imbalance in the momentum fractions and are broader than the uu and gg initial states. In fact, at the 14 TeV LHC the imbalance is so pronounced for ug that the rapidity distribution peaks at $|y_{CM}| \approx 0.9$. Since the 14 TeV LHC probes lower τ than the 7 TeV LHC, a larger discrepancy between the parton momentum fractions can develop and the rapidity distributions are considerably broader than at the 7 TeV LHC. This fact will have an impact on the experimental acceptance for the final state jets.

We consider the leading production with the resonances as listed in Table II.2. We do not attempt to calculate the decay of the resonances. Instead, we parameterize the production rate to dijets simply by a branching fraction (BR). Thus the total signal cross section will be governed by a coupling constant to the initial state partons, a branching fraction, and the resonance mass.

In the following calculations we employ the narrow width approximation, which is valid for $\Gamma \ll M$, where Γ and M are the total width and mass of the resonant particle, respectively. Using the interactions listed in section II.A.2, for a resonance mass on the order of a

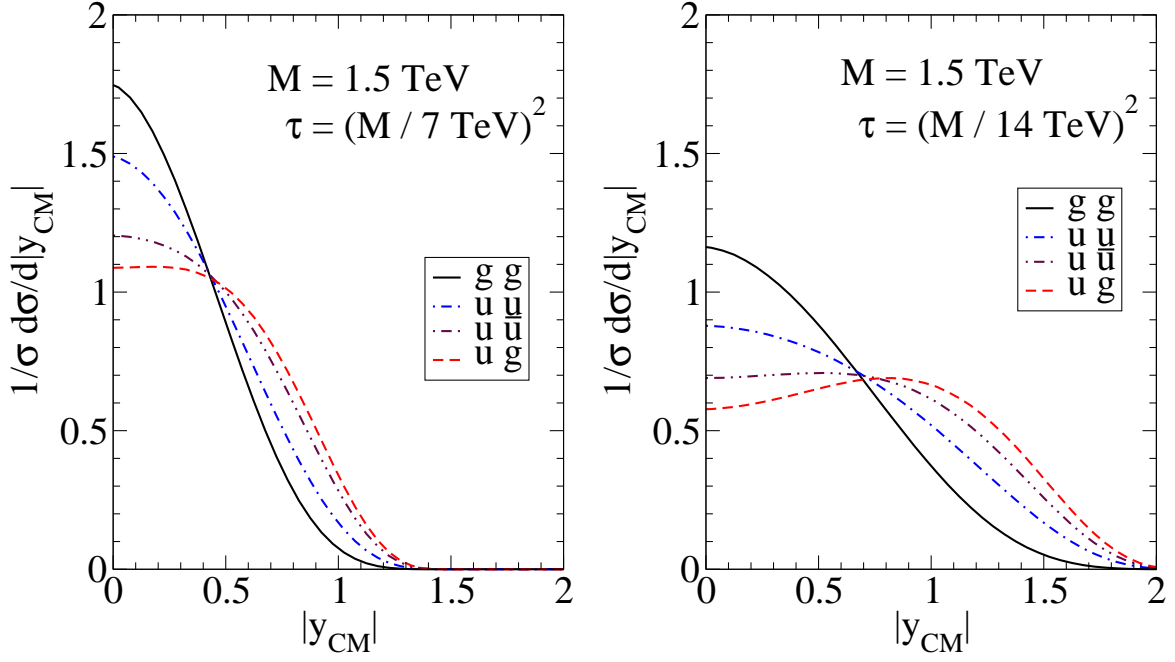


Figure II.2: Center of momentum system rapidity distributions for resonance mass of 1.5 TeV and initial states $gg, uu, u\bar{u}$ and ug at the (a) 7 and (b) 14 TeV LHC.

TeV and order one couplings between the new resonance and SM partons we find $\Gamma \lesssim 0.15 M$. However, if the couplings of the resonance are large or there are many additional decay channels, the width may be sizeable and its effects will have to be included.

a. Quark-Quark Annihilation The uu , dd , and ud initial states can annihilate into color-antitriplet and sextet spin 0 and spin 1 particles, often referred as diquarks. Based on the interactions of section II.A.2.a and using the Feynman rules in the appendix, for a resonant diquark mass of M the hadronic cross section from uu and dd initial states is found to be

$$\sigma_{qq} = \lambda^2 \frac{\pi N_D}{N_C^2} \frac{1}{S} (q \otimes q)(\tau_0) \quad (\text{II.A.16})$$

for both scalar and vector diquarks and for the ud initial state

$$\sigma_{ud} = \lambda^2 \frac{\pi N_D}{2^2 N_C^2} \frac{1 + \delta_{1J}}{S} ((u \otimes d)(\tau_0) + (d \otimes u)(\tau_0)), \quad (\text{II.A.17})$$

where the coupling constant λ specifies the resonance as in Eq. (II.A.5) and J is the spin of the resonance. N_D is the dimension of the antitriplet ($N_D = 3$) or sextet ($N_D = 6$) representation. Here and henceforth, $\tau_0 = M^2/S$.

The production cross sections of the color-sextet vector diquarks to dijet at a 7 TeV and 14 TeV LHC are shown in Figs. II.3(a) and II.3(b), respectively. The production cross sections of the scalars E_6, U_6 are the same as those for the vectors E_6^μ, U_6^μ while the production rate for the scalar D_6 is half that of D_6^μ .

Due to the antisymmetric factor on the quark color indices, the only non-zero valence quark configuration to give a antitriplet scalar diquark is the flavor-off diagonal contribution $ud \rightarrow \bar{D}_3$. However, the antitriplet vector diquarks can be produced from both the flavor diagonal $uu \rightarrow \bar{E}_3^\mu$, $dd \rightarrow \bar{U}_3^\mu$ and flavor-off diagonal $ud \rightarrow \bar{D}_3^\mu$ contributions from valence quarks. Also, since the cross section is proportional to the dimension of the diquark representation, the production cross sections for the antitriplet diquarks are half that of the respective sextet diquarks.

Besides the leading contribution from the valence quarks, we have also included the anti-quark contributions for the conjugate particle production in the numerical results presented

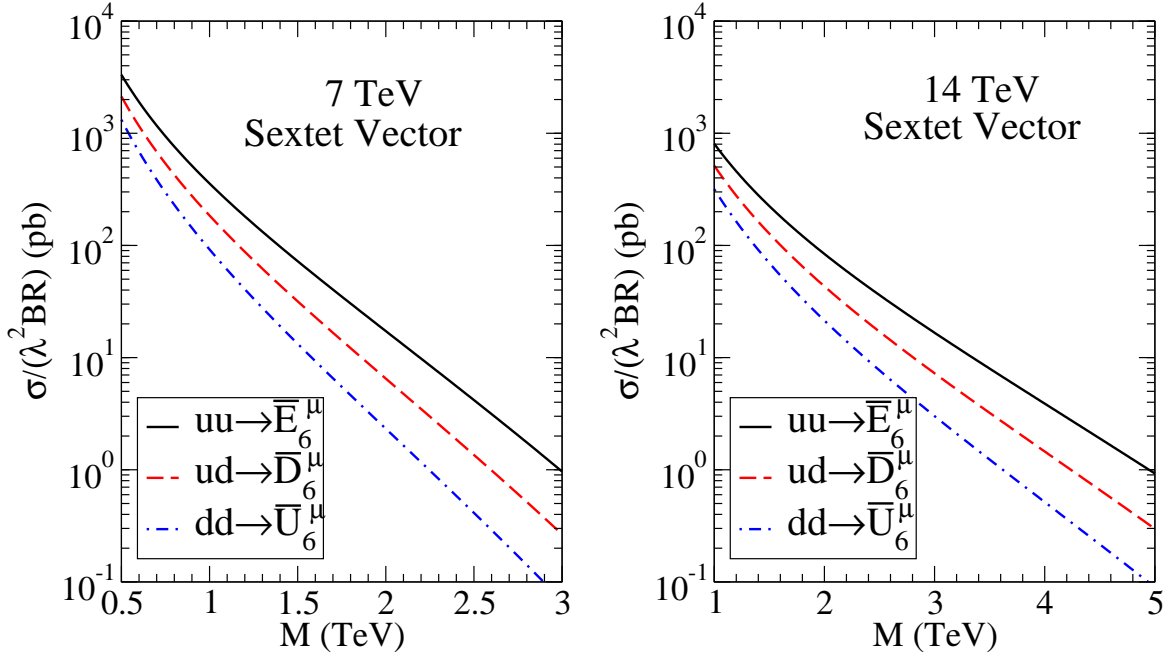


Figure II.3: Dijet cross sections for color-sextet vector production via uu, ud and dd initial states versus its mass at the LHC for (a) 7 TeV and (b) 14 TeV. Subleading contributions from antiquarks for the conjugate particle production are also included. The coupling constant to initial state partons and the branching fraction to dijet have been factorized out.

here. We summarize a few representative cross sections for the color-sextet vector diquarks, along with the percentage contribution from the antiquarks.

7 TeV LHC :	\bar{E}_6^μ	\bar{D}_6^μ	\bar{U}_6^μ
$\sigma(\text{pb}) \ M = 0.5 \text{ TeV}$	3400	2100	1300
$\bar{q}\bar{q}'$	2.8%	5.6%	11%
$\sigma(\text{pb}) \ M = 3 \text{ TeV}$	0.96	0.27	0.064
$\bar{q}\bar{q}'$	0.011%	0.028%	0.068%
14 TeV LHC :	\bar{E}_6^μ	\bar{D}_6^μ	\bar{U}_6^μ
$\sigma(\text{pb}) \ M = 1 \text{ TeV}$	800	510	320
$\bar{q}\bar{q}'$	2.8%	5.5%	11%
$\sigma(\text{pb}) \ M = 5 \text{ TeV}$	0.92	0.30	0.090
$\bar{q}\bar{q}'$	0.026%	0.075%	0.21%

Once again, we have pulled out the coupling constant λ^2 and the branching fraction (or equivalent to setting $\lambda^2 = \text{BR} = 1$).

The next-to-leading order (NLO) QCD corrections to scalar diquark production have been previously calculated [218] and sizable corrections were found. For instance, the cross section with masses between 0.5 and 1.5 TeV can be increased by about 20% for U_6 and 30–35% for D_3 . It is expected that the corrections to the other color-sextets and antitriplets should be similar to the above.

b. Quark-Gluon Annihilation The ug and dg initial states can produce color-triplet and sextet excited quarks. Using the Feynman rules in the appendix, the hadronic cross section for excited quarks of mass M is

$$\sigma_{qg} = 8\pi^2 \lambda^2 \frac{\alpha_s}{N_C} \frac{M^2}{\Lambda^2} \frac{1}{S} (g \otimes q)(\tau_0), \quad (\text{II.A.18})$$

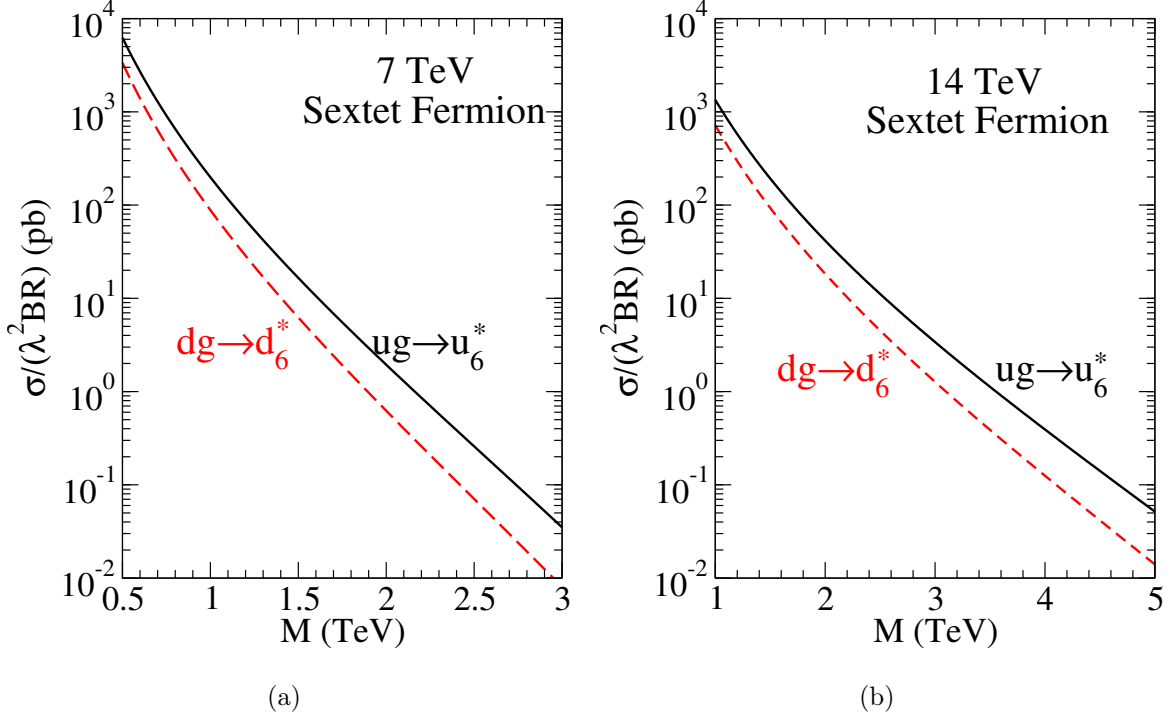


Figure II.4: Dijet cross sections for color-sextet fermion production via ug and dg initial states versus its mass at the LHC for (a) 7 TeV and (b) 14 TeV. Subleading contributions from antiquarks for the conjugate particle production are also included. The coupling constant to initial state partons and the branching fraction to dijet have been factorized out. The new physics scale, Λ , has been set equal to $2M$.

where $\lambda^2 = \lambda_L^2 + \lambda_R^2$ and $\lambda_{L,R}$ specify the interactions as in Eq. (II.A.6). Since the Clebsch-Gordan coefficients for the color-triplet and sextet states are normalized the same it follows that the production cross sections are the same. Comparing with the convention in Ref. [5], the new physics scale Λ here corresponds to twice the excited quark mass.

Figure II.4 presents the production cross section of excited sextet quarks u_6^* and d_6^* produced from ug and dg initial states, respectively, at the (a) 7 and (b) 14 TeV LHC. The u_6^* production rate is larger than the d_6^* production rate by about a factor of two at low mass, due to the larger u quark pdf. We have taken the cutoff $\Lambda = 2M$ in the numerical evaluation. With our CG coefficient normalization, our results should be a factor of two larger than that using the convention of [5].

For the numerical results we have once again included the conjugates, produced from $\bar{u}g, \bar{d}g \rightarrow \bar{u}^*, \bar{d}^*$. Representative results for the total cross section and the percentage contribution from antiquarks, after factorizing out the overall constants, are

7 TeV LHC :	u_6^*	d_6^*
$\sigma(\text{pb})$ $M = 0.5$ TeV	6200	3400
$\bar{q}g$	8.5%	20%
$\sigma(\text{pb})$ $M = 3$ TeV	0.035	0.0080
$\bar{q}g$	0.82%	2.6%
14 TeV LHC :	u_6^*	d_6^*
$\sigma(\text{pb})$ $M = 1$ TeV	1300	720
$\bar{q}g$	8.4%	20%
$\sigma(\text{pb})$ $M = 5$ TeV	0.052	0.014
$\bar{q}g$	1.2%	4.2%

c. Gluon-Gluon Annihilation Gluon-gluon annihilation can result in color-octet scalars and tensors. Using the parameterization of Eq. (II.A.9) and Feynman rules in the appendix,

the hadronic production cross section of a color-octet scalar and tensor of mass M from gluon-gluon fusion is

$$\sigma_{gg} = 4\pi^2 \alpha_s \kappa^2 \frac{N_C^2 - 4}{N_C(N_C^2 - 1)} \frac{M^2}{\Lambda^2} \frac{1 + \delta_{0J}}{S} (g \otimes g)(\tau_0), \quad (\text{II.A.19})$$

where κ and Λ are specified by the interaction. Since on-shell tensor polarizations are traceless, the $T_8^\rho{}_\rho$ term in Eq. (II.A.9) does not contribute to the resonant production of the color-octet tensor.

The production cross sections for the color-octet scalar to dijets are presented in Fig. II.5 for the LHC at 7 TeV (dashed curve) and 14 TeV (solid curve). For the numerical results presented the new physics scale Λ has been set equal to the resonant mass. The color-octet tensor cross section is one half that of the the color-octet scalar. Since the gluon luminosity falls fast at a higher mass, the cross section at 7 TeV LHC drops by more than five orders of magnitude from 6000 pb at $M = 0.5$ TeV to 0.02 pb at $M = 2.5$ TeV, and at 14 TeV LHC by about five orders of magnitude from 1200 pb at $M = 1$ TeV to 0.01 pb at $M = 4.6$ TeV. The production cross section of an octet tensor is half that of the octet scalar.

The next-to-leading logarithm (NLL) soft-gluon resummation correction to scalar octet production via gluon fusion has been previously calculated and sizable corrections were found [214]. The cross section can be increased by a factor of 2.4 at mass 0.5 TeV and 3.5 at a mass of 2.5 TeV.

d. Quark-Antiquark Annihilation Although the parton luminosity is lower than the previously discussed initial states, we also include resonant production from $u\bar{u}$, $d\bar{d}$, $u\bar{d}$, and $d\bar{u}$ initial states. These states can couple to color-octet vectors. Using the interactions in Eq. (II.A.12), the production cross section for a color-octet vector of mass M from $q\bar{q}'$ initial states is

$$\sigma_{q\bar{q}} = 4\pi^2 g^2 \alpha_s \frac{C_F}{N_C} \frac{1}{S} (q \otimes \bar{q}')(\tau_0) \quad (\text{II.A.20})$$

where

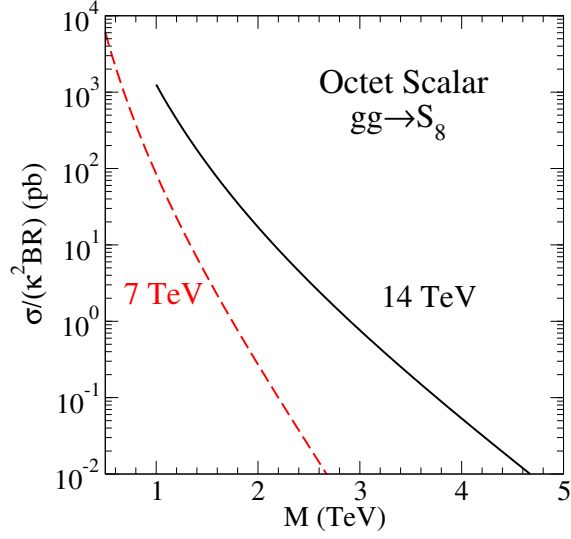


Figure II.5: Dijet cross sections for color-octet scalar production via gg initial states versus its mass at the LHC for 7 TeV (dashed curve) and 14 TeV (solid curve). The coupling constant to initial state partons and the branching fraction to dijet have been factorized out. The new physics scale, Λ , has been set equal to M .

$$g^2 = \begin{cases} \frac{1}{2}(|C_L V_L^{CKM}|^2 + |C_R V_R^{CKM}|^2) & \text{for charged states,} \\ \frac{1}{2}(|g_L^{U,D}|^2 + |g_R^{U,D}|^2) & \text{for neutral states.} \end{cases}$$

The color factor $C_F = (N_C^2 - 1)/2N_C = 4/3$.

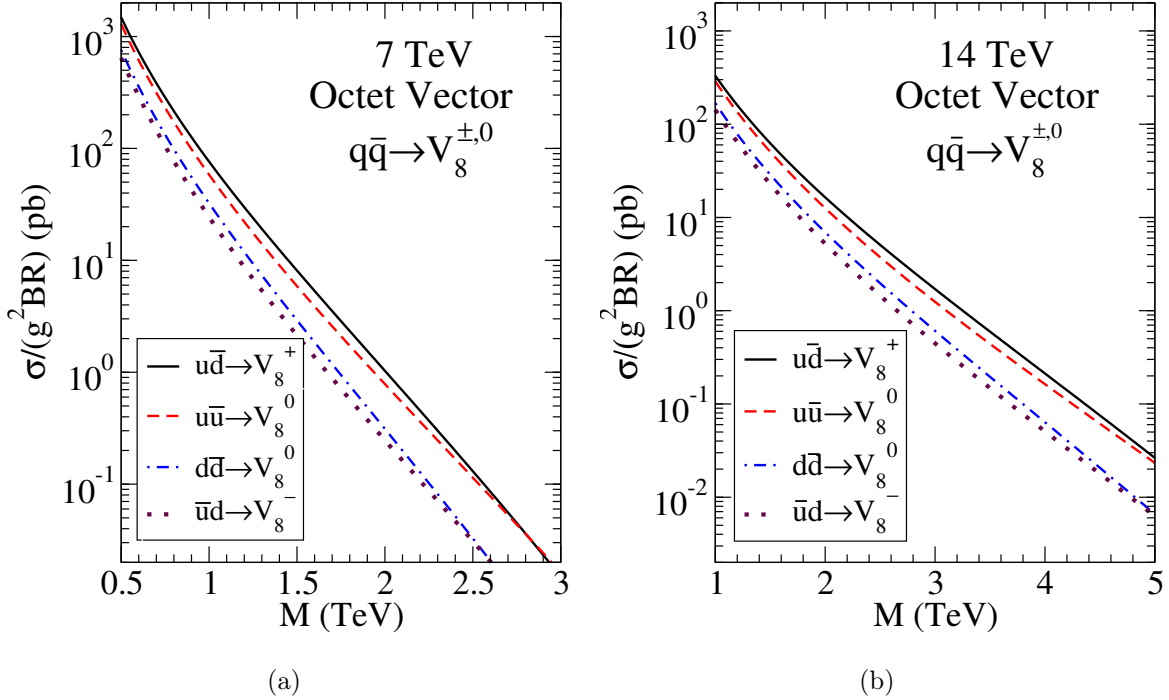


Figure II.6: Dijet cross sections for color-octet vector production via $u\bar{d}$, $u\bar{u}$, $d\bar{d}$, and $d\bar{u}$ initial states versus its mass at the LHC for (a) 7 TeV and (b) 14 TeV. The coupling constant to initial state partons and the branching fraction to dijet have been factorized out.

The cross sections for color-octet vectors are presented in Fig. II.6 for the (a) 7 TeV and (b) 14 TeV LHC. Since the u quark pdf is greater than the d quark pdf, the neutral vectors are produced more favorably by the $u\bar{u}$ initial state than by $d\bar{d}$. Due to the \bar{d} quark pdf being larger than the \bar{u} quark pdf, the production of V_8^+ is larger than the production rate of V_8^0 from $u\bar{u}$ initial state and V_8^0 production rate from $d\bar{d}$ initial state is larger than the

production rate of V_8^- . Some representative cross sections values are listed below.

7 TeV LHC :	$u\bar{d} \rightarrow V_8^+$	$d\bar{u} \rightarrow V_8^-$	$u\bar{u} \rightarrow V_8^0$	$d\bar{d} \rightarrow V_8^0$
$\sigma(\text{pb})$ $M = 0.5$ TeV	1500	640	1300	760
$\sigma(\text{pb})$ $M = 3$ TeV	0.015	0.0037	0.016	0.0030
14 TeV LHC :	$u\bar{d} \rightarrow V_8^+$	$d\bar{u} \rightarrow V_8^-$	$u\bar{u} \rightarrow V_8^0$	$d\bar{d} \rightarrow V_8^0$
$\sigma(\text{pb})$ $M = 1$ TeV	330	140	290	170
$\sigma(\text{pb})$ $M = 5$ TeV	0.026	0.0063	0.023	0.0066

Once again, we have pulled out the coupling constant λ^2 and the branching fraction (or equivalent to setting $\lambda^2 = \text{BR} = 1$).

All the cross sections presented in this section are at leading order in QCD. The production cross section of colored resonance can receive sizable QCD corrections as shown for the color-triplet and sextet scalar diquarks [218] and color octet scalars [214]. We will take this into account when setting the bounds.

Throughout this study, we neglect the color-singlet states, such as Z' , W' or KK gravitons. Our formalism for is equally applicable to those by adjusting the couplings $g_s \rightarrow e/\sin\theta_W$ and setting the color factor C_F to 1. Before folding in the decay branching fraction to the final state, the production rates for a color-singlet state would be smaller than the colored resonance by roughly about a factor of 30.

4. Bounds from the LHC Dijet Spectrum

Searching for new physics signals in the dijet spectrum at hadron colliders has been long carried out. The standard form of the four-fermion contact interaction in the literature is [219]:

$$\mathcal{L}_{4q} = \frac{2\pi}{\Lambda^2} \bar{q}_L \gamma^\mu q_L \bar{q}_L \gamma_\mu q_L \quad (\text{II.A.21})$$

For a sufficiently high mass, the new resonant states can be integrated out and the $\mathbf{3} \otimes \mathbf{3}$ and $\mathbf{3} \otimes \bar{\mathbf{3}}$ vector interactions can produce similar interactions to Eq. (II.A.21). The bounds

on the four fermion interactions can be roughly translated into bounds on our interactions with the identification

$$\frac{2\pi}{\Lambda^2} \sim \frac{\lambda^2}{2M^2}, \quad (\text{II.A.22})$$

where M is the mass of the resonant state of our current interest. Assuming a coupling constant of unity, the current LHC bound of $\Lambda \geq 4$ TeV translates into

$$M \gtrsim 1.1 \text{ TeV}.$$

Note this bound is only a rough estimate since one would have to be careful in computing the color factor and counting the contributing light partons.

Using measurements of dijet production rates at 7 TeV LHC, the ATLAS and CMS collaborations have recently released bounds on the dijet production cross sections as a function of resonance mass based on the first data of 3.1 pb^{-1} [199] and 2.9 pb^{-1} [200], respectively. Even with such small amount of initial data, the LHC experiments have gone beyond the existing Tevatron results, pushing the LHC to the phase of discovery for new physics.

We model the experimental efficiencies by a simple parameterization. The detector acceptance for dijet events at ATLAS was about 31% for an excited quark mass around 300 GeV, and about 48% around 1700 GeV. For our study we model this acceptance as

$$\mathcal{A}_{ATLAS} = \begin{cases} \frac{0.17}{1400 \text{ GeV}}(m - 300 \text{ GeV}) + 0.31 & m \leq 1700 \text{ GeV} \\ 0.48 & m > 1700 \text{ GeV} \end{cases} \quad (\text{II.A.23})$$

To model the CMS detector acceptances we compared our results for dijet production cross section without detector acceptance to the the CMS results including detector acceptance. Using their axigluon and excited quark results, we model the CMS detector acceptance as

$$\mathcal{A}_{CMS} = \frac{\Delta}{2100 \text{ GeV}}(m - 500 \text{ GeV}) + 0.47, \quad (\text{II.A.24})$$

where $\Delta = 0.08$ for the quark-quark final state and $\Delta = 0.17$ for the quark-gluon final state. There was no analogous data to find the acceptance for gluon-gluon final states. We therefore also use the quark-gluon acceptance for the gluon-gluon final state.

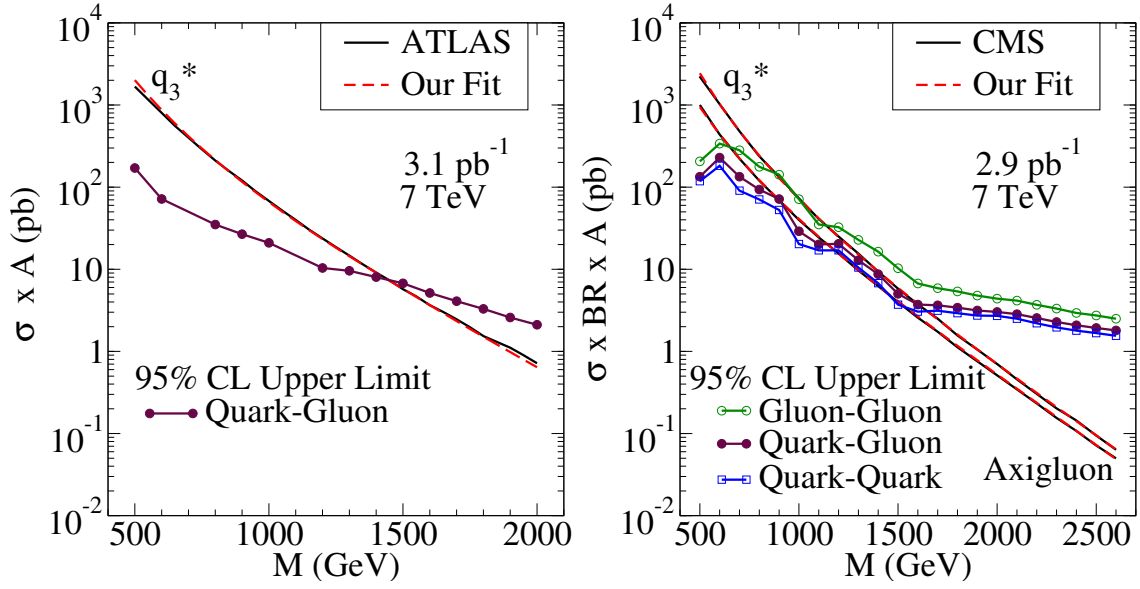


Figure II.7: 95% confidence level upper limits on dijet production cross sections versus resonant mass for (a) ATLAS results (solid circles) and (b) CMS results from the contributions of gluon-gluon (open circles), quark-gluon (solid circles), and quark-quark (open boxes). Our fits (dashed curve) almost overlap with the theoretical predictions (solid curves) provided by ATLAS for q_3^* and CMS for q_3^* and axigluon.

The predicted dijet cross sections for triplet excited quarks at ATLAS and triplet excited quarks and axigluons at CMS are presented by the solid curves in Figs. II.7(a) and II.7(b), respectively. To reproduce their results for the triplet excited quark production, we set $\lambda = 1$ in Eq. (II.A.18) and summed over all possible initial state quarks. As can be seen, using the acceptances in Eqs. (II.A.23) and (II.A.24), our simulations (dashed curves) fit well the results provided by the ATLAS and CMS collaborations (solid curves). The current 95% confidence level upper limits for dijet production cross sections at both ATLAS and CMS are also presented in Fig. II.7.

All of the colored resonances presented in the previous sections can contribute to the dijet signal; hence, the ATLAS and CMS dijet cross section bounds can be used to place limits on the mass and couplings of these new particles. We consider the current bounds on those colored resonances as summarized in Table II.2. In presenting our results for the current bound, we once again parameterize the signal rates by an overall coupling to the initial state partons and a branching fraction to decay to the final state dijets. The limits on the product of the two constants of new colored resonances as a function of the resonant mass are shown in Fig. II.8. The color-sextet vector diquark and color-octet scalar bounds are based on the leading order QCD calculations presented here with K-factors from QCD corrections, while all other bounds are based solely on the leading order calculations. The regions above the corresponding curves are excluded, thus providing meaningful upper bounds for the couplings and lower bounds for the resonant masses. The zigzag shapes of the curves are due to the non-smooth experimental bounds for different masses as in Fig. II.7(b).

Figure II.8(a)² shows the CMS bounds on the sextet vector diquarks with a NLO K-factor of 1.2 included [218]. The bounds on the scalar U_6, E_6 couplings are the same as those on vector U_6^μ, E_6^μ and the bounds on the D_6 couplings are twice weaker than the bound on D_6^μ . Furthermore, taking into account the different K-factors of 1.3 for triplets and 1.2 for sextets, the bound on the antisextet vectors are 1.8 times stronger than the bounds on the triplet vectors and the bounds on D_6^μ are 3.7 times stronger than D_3 .

Figure II.8(b) shows the bounds on the excited quarks. Results based on the ATLAS

²We have extended the E_6^μ bound beyond the CMS data point at 2.6 TeV, assuming there has been no event observed.

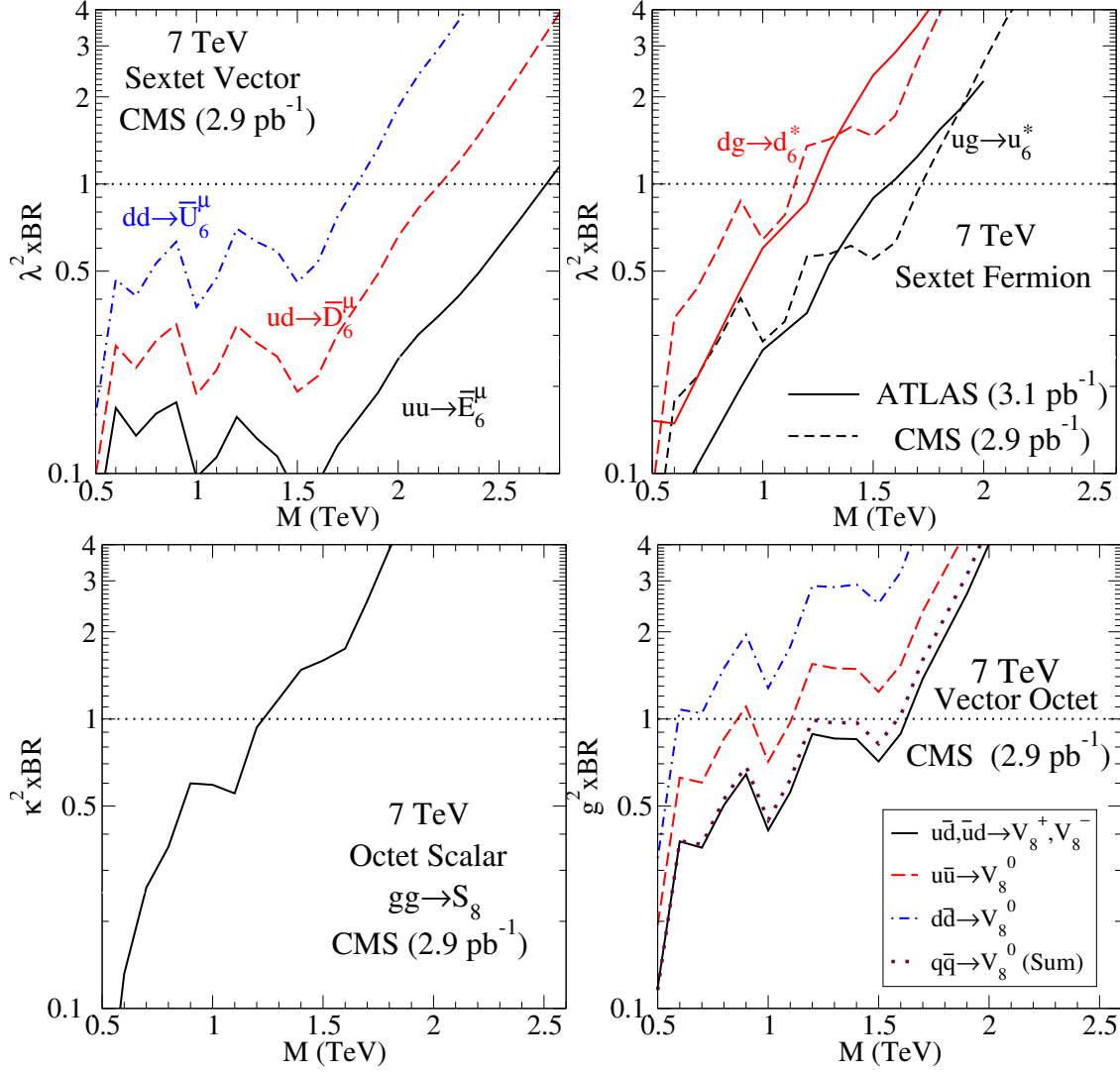


Figure II.8: Bounds on the products of SM parton couplings to the resonances and dijet branching ratios (vertical axis) versus the resonant mass for (a) color-sextet vector diquarks, (b) color-sextet (or color-triplet) excited quarks, (c) color-octet scalar, and (d) color-octet vectors from (a,b,c,d) CMS and (b) ATLAS.

data (solid curves) and CMS data (dashed curves) are comparable. Following the convention in Ref. [5], we have set $\Lambda = 2M$. As noted earlier, the results for a color-triplet and sextet are the same. The bounds obtained here are stronger than those for the diquarks above.

Figure II.8(c) shows the bounds on octet scalar couplings including NLL K-factors running from 2.4 at resonance mass 0.5 TeV and 3.5 at 2.5 TeV [214]. Even with the K-factor, the weakest bound of all studied are the gg initial processes. This is due to the sharp fall of gg luminosity at higher masses. The bounds on the coupling constants of the T_8 are a factor of two weaker than those of the S_8 .

Although not as large as uu , dd initial states, the $q\bar{q}$ annihilation provides reasonable sensitivity to the colored resonances. In comparison with the Tevatron as a $p\bar{p}$ collider, the LHC is somewhat in a disadvantageous situation with respect to the valence quark dominance. Nevertheless, the LHC results currently have slightly extended the Tevatron bounds on axigluons and universal colorons [200]. We also obtain significant bounds for the color-octet resonances based on the CMS data as seen in Fig. II.8(d). However, due to the much larger data sample, the Tevatron dijet bounds for color-singlet vectors (Z' , W' etc.) are much more stringent than those from the LHC.

Assuming a coupling constant and branching ratio of unity as indicated by the horizontal dotted lines in Fig. II.8, the current mass lower bounds on the colored resonant states are

summarized as

E_6^μ	2.7 TeV (CMS)	E_6	2.7 TeV
D_6^μ	2.3 TeV (CMS)	D_6	1.9 TeV
U_6^μ	1.8 TeV (CMS)	U_6	1.8 TeV
E_3^μ	2.5 TeV (CMS)	U_3^μ	0.8, 1.0 – 1.2, 1.4 – 1.6 TeV
D_3^μ	1.9 TeV (CMS)	D_3	0.8, 0.9 – 1.2, 1.3 – 1.7 TeV
u_6^*	1.7 TeV (CMS), 1.6 TeV (ATLAS)	d_6^*	1.1 TeV, 1.2 TeV
V_8^\pm	1.6 TeV (CMS)	V_8^0	1.6 TeV
S_8	1.2 TeV (CMS)	T_8	0.9 TeV ,

where the mass bounds have been rounded to the nearest tenth of a TeV. All of the bounds obtained here are beyond the existing Tevatron analyses.

It should be noted that there are small uncertainties associated with the results above. For instance, the bounds presented above have been obtained by utilizing the narrow width approximation. Also, the detector acceptances are somewhat dependent on the spin of the resonance.

5. Summary and Outlook

Experiments at the LHC have opened up the energy frontier for TeV scale new physics searches. Motivated by the recent ATLAS and CMS dijet analyses, we study the possible colored resonances in a most general approach. We classify the colored resonances based on group theory decomposition of QCD $SU(3)_C$ interaction as well as other quantum numbers, as listed in Table II.1. These resonances may carry exotic SM quantum numbers, but all of them find their interesting roles in certain theories beyond the SM.

We then construct their effective couplings to light partons. Based on those features, we name them and list them in Table II.2. We calculate their resonant production cross section at the LHC. The production rates may be as large as 400 pb (1000 pb) at the c.m. energy of 7 (14) TeV for a mass of 1 TeV, leading to the largest production rates for new physics at the TeV scale, and simplest event topology with dijet final states. Our approach is quite general and applicable to other possible signals of resonant particles other than dijets at the LHC.

We applied the new ATLAS/CMS dijet data to have put bounds on various possible colored resonant states. We obtained the lower bounds on their masses ranging from 0.9 to 2.7 TeV, if their couplings are of the order of unity. The results obtained here are beyond the existing Tevatron analyses. In an optimal situation, if a signal above the SM backgrounds is established in the near future, it is then the exciting time to determine the nature of the resonance particle and to untangle the new underlying theory as commented in the text and in Table II.2. With the anticipated increase of integrated luminosity and c.m. energy, experiments at the LHC will undoubtedly take our understanding of particle physics to an unprecedented level.

B. ELECTROWEAK RESONANCES

A $U(1)'$ or Z' is generic in many scenarios of physics beyond the Standard Model, such as string theory compactifications, GUTs, extra-dimensions, compositeness, dynamical electroweak symmetry breaking, dark-sector models, etc. We study the potential of probing a TeV-scale Z' with electroweak couplings in future experiments. In particular, we focus on two scenarios: (1) If a Z' is discovered at the LHC, what is the potential of measuring its mass and width and to distinguish between benchmark models utilizing various observables, especially asymmetries, at a high luminosity LHC and the ILC. (2) If the Z' is not accessible as a clear resonance signal, what is the exclusion reach at the ILC.

Typical Z' models with electroweak couplings should be observable³ at the LHC as reso-

³The reach is reduced if the dilepton branching ratios are significantly reduced due to BSM decay chan-

nances in the dilepton channels for masses up to $\sim 4\text{--}5$ TeV for $\sqrt{s} = 14$ TeV and an integrated luminosity of 100 fb^{-1} . There have been extensive studies of diagnostic possibilities⁴ of the Z' couplings at the LHC utilizing the cross sections

$$\sigma^f \equiv \sigma[f\bar{f}] \equiv \sigma_{pp \rightarrow Z' \rightarrow f\bar{f}} = \sigma_{Z'} B(Z' \rightarrow f\bar{f}) \quad (\text{II.B.25})$$

for decays into the final state $f\bar{f}$ for $f = \ell, \tau, t, b$ (with $\ell = e, \mu$), as well as forward-backward or charge asymmetries, rapidity distributions, and possible final state polarizations for $\tau^-\tau^+$ or $t\bar{t}$. Other possible probes include $\Gamma_{Z'}$ from the lineshape, and various rare decay modes and associated productions. It was generally concluded that significant diagnostic probes of the couplings would be possible for Z' masses up to around 2.5 TeV.

However, ATLAS [240] and CMS [241] have already excluded dilepton resonances corresponding to standard benchmark Z' 's below $\sim 2.5\text{--}2.9$ TeV, so even if a Z' is observed in future LHC running it will be difficult to carry out detailed diagnostics. We have therefore re-examined what might be learned for a relatively heavy Z' , allowing for high integrated luminosities of 300 and 3000 fb^{-1} at the LHC, in combination with observations at the ILC with $\sqrt{s} = 500$ GeV and integrated luminosity of 500 fb^{-1} , or at 1 TeV with 1000 fb^{-1} , for fixed e^\pm polarizations. We also consider the possibility of additional ILC running with reversed polarizations. We consider two illustrative cases: (1) a 3 TeV Z' observed directly at the LHC and indirectly at the ILC; (2) a more massive Z' observed only by indirect effects at the ILC. Future studies will also include indirect constraints from existing and future precision experiments.

1. LHC Searches

The formalism relevant to the production and decay of a Z' at the LHC is summarized in Appendix VI.D. We assume in this section that a narrow colorless resonance has been observed as a peak in the $\ell^-\ell^+$ distribution at the LHC at mass $M_{Z'}$, and that the lepton angular distribution has identified that the resonance has spin-1 [225, 230]. Assuming family universal couplings and neglecting $Z - Z'$ mixing (known to be small from precision

nels [27, 28].

⁴See, for example, [27, 28, 220–239]. Other studies are reviewed in [17, 19, 23].

electroweak studies [21, 25, 26]), there remain to be determined the five chiral couplings in (I.B.5) as well as $\Gamma_{Z'}$. Ideally, one would like to determine these in as model-independent a way as possible.

The simplest observables (other than $M_{Z'}$) are the cross sections $\sigma^f = \sigma_{Z'} B(Z' \rightarrow f\bar{f})$ after subtracting backgrounds, especially for $f = e, \mu$. However, the cross sections have uncertainties from the parton distribution functions (PDFs), higher-order terms, and the luminosity. Furthermore, they are inversely proportional to $\Gamma_{Z'}$, as in (VI.D.19), so they do not allow a determination of the absolute couplings, even in principle. Also, the leptonic rates depend only on a linear combination of the u and d couplings (roughly 2 to 1 at the LHC), unless there is significant information from the rapidity distribution (which is unlikely at the LHC).

The $\Gamma_{Z'}$ ambiguity can be eliminated and the PDF/higher order uncertainties can be reduced by considering ratios of observables. If one can tag the $f = b$ and t final states well enough then the ratios of the rates for $f = \ell, b, t$ could in principle determine the ratios of $g_L^{q2} + g_R^{u2}, g_L^{q2} + g_R^{d2}$, and $g_L^{\ell2} + g_R^{e2}$ (again assuming family universality). These could be promoted to absolute measurements if $\Gamma_{Z'}$ can be extracted from the lineshape, since the product $\sigma^f \Gamma_{Z'} = \sigma_{Z'} \Gamma(Z' \rightarrow f\bar{f})$ depends only on the absolute couplings.

Forward-backward or charge asymmetries could yield additional information. From (VI.D.25) we see that g_R^{f2}/g_L^{f2} can be determined for $f = \ell, u, d$ if charge identification is available for ℓ, t, b , respectively. This is again independent of $\Gamma_{Z'}$ and involves reduced PDF uncertainties. Final state polarization effects for $f = \tau$ or t could carry complementary information, which could increase the accuracies of the determinations and/or help to test our assumption of family universality. Off-pole interference with standard model (mainly γ and Z) backgrounds could also in principle yield information such as the signs of the couplings [235, 238].

As stated previously, however, the existing LHC limits are sufficiently strong that it will most likely not be possible to obtain significant model-independent determinations of the couplings from the LHC alone. Nevertheless, some of the observables could at least allow discrimination between the benchmark models.

2. Leptonic Final States

The leptonic final states are very clean at the LHC. The standard model dilepton background is at the attobarn level, negligible compared to the femtobarn-level signal. We tabulate the cross sections and total widths for our benchmark models in Table II.3 for $M_{Z'} = 3$ TeV. These widths are “minimal”; if the Z' can decay into final states other than standard model fermions, the total width will increase, resulting in a suppression of the standard model fermion branching fractions as well as the appearance of new visible (invisible) final states like $W_R^+ W_R^-$ (sterile $\nu_R^e \nu_R$).

Table II.3: The minimal widths for the benchmark Z' models and the cross sections $\sigma^e = \sigma[e^- e^+] = \sigma_{Z'} B(Z' \rightarrow e^- e^+)$ at the (14 TeV) LHC for dielectron final states in the mass window $2.8 - 3.2$ TeV. The acceptance of the electron-positron pair is taken to be 78%.

	χ	ψ	η	LR	B-L	SSM
width (3 TeV Z') (GeV)	34.7	15.7	18.9	61.4	27.4	88.7
σ^e (fb)	0.850	0.430	0.503	1.006	1.004	1.602

We simulate the signal and background events using MadGraph5 [242] with input model files generated by FeynRules [243], using proton parton distribution functions (PDF) set CTEQ611 [217]. The generated events then pass through Pythia6 [244] to perform parton showers and then Delphes [245] for detector simulation using the Snowmass Delphes3 card. We show the invariant mass distributions and the angular distributions in the center of mass (CM) frame of the dielectron system for these benchmark models in Fig. II.9. One can extract the mass, width, and total rate σ^e from the invariant mass distribution as shown in the left panel⁵. The dimuon final state is similar. The energy resolution for high energy muons is worse than for electrons according to the Snowmass detector simulation. As a result, dimuon final states will provide additional statistics for Z' discovery but won't contribute much to the mass and width determinations.

⁵The rapidity distribution of the dielectron pair could in principle be useful for separating the effects of the u and d . In practice, however, there is little sensitivity for $M_{Z'} \gtrsim 3$ TeV.

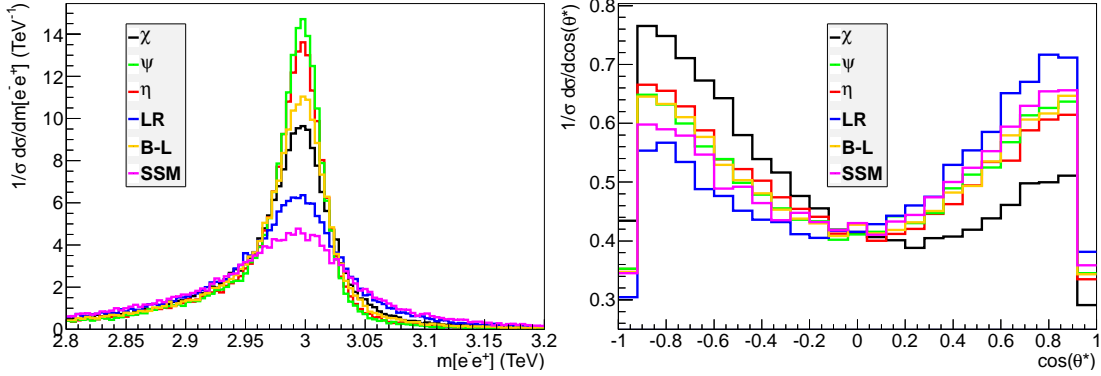


Figure II.9: *Left panel:* the invariant mass distribution of the dielectron system for the benchmark models for a 3 TeV Z' at the LHC at 14 TeV; *Right panel:* the angular distribution of the electrons in the CM frame with respect to the rapidity (boost) direction of the system in the lab frame, integrated over the dielectron rapidity y .

The forward-backward asymmetry A_{FB} , defined in (VI.D.25) (which is equivalent to the charge asymmetry A_c in (VI.D.26)), can be obtained directly by counting, from the charge asymmetry, or by fitting to the angular distribution shown in the right panel of Fig. II.9 for the benchmark models. From (VI.D.25) one sees that A_{FB} is sensitive to the difference between the left and right- chiral couplings-squared of the leptons and of the quarks. Of course, there is no forward-backward asymmetry in a pp collider at zero Z' rapidity y , but there can be an asymmetry for nonzero y . We define the forward direction with respect to the rapidity (boost) direction of the Z' or equivalently of the dielectron system. The (mainly valence) quark direction is usually the same as the boost direction at the LHC. However, around 20% of the events have the anti-quark direction along the boost direction (the contamination factor). This contamination factor varies for different PDF sets, adding additional theoretical uncertainties. It also varies somewhat with the Z' model because of the different relative couplings of up-type and down-type quarks.

In order to estimate the sensitivity to the Z' parameters, we have simulated the line-

shape and angular distributions for each of our benchmark models, assuming the minimal width, and then “fit” to the simulated data to determine the uncertainties in the extracted parameters. We show the fitting results for the masses and widths of the Z' in the left panel of Fig. II.10, and the simulated cross section and forward-backward asymmetries in the right panel. The two contours are for the LHC at 14 TeV and 300 fb^{-1} (blue) and 3000 fb^{-1} (red). The fitting for the mass and width is model-independent. We fit the invariant mass distribution by a Breit-Wigner resonance convoluted with a Gaussian distribution for the smearing from the electron energy resolution. We assume 0.7% systematic uncertainties for the mass and width ($\sqrt{2}$ times the electron energy resolution 0.5%). We see that $M_{Z'}$ can be reproduced to around 10 GeV, i.e., better than one percent. $\Gamma_{Z'}$ can also be determined to around 10 GeV, but from Table II.3 and Fig. II.10 this is very crude (e.g., 30-60%) for the minimal widths in most of the benchmark models. The total width and mass precision is dominated by systematic uncertainties: one can see that the improvement from 300 fb^{-1} to 3000 fb^{-1} is not significant. Nevertheless, the LHC is the only planned facility that can measure these quantities to any precision⁶.

We also show the forward-backward asymmetry and cross section determinations⁷. In addition to the statistical uncertainties, we take the systematic uncertainties $10\% \oplus 2\%$ ($6\% \oplus 2\%$) for the cross section for the LHC at 300 fb^{-1} (3000 fb^{-1}). The 10% (6%) are the correlated uncertainties (e.g., PDF and luminosity uncertainties) that will cancel when taking the ratios of cross sections, leaving 2% systematics for the forward-backward asymmetry. A_{FB} can be determined very well for asymmetric models such as the Z_χ and Z_{LR} , approximately 20% (5%) at the LHC 14 TeV with 300 fb^{-1} (3000 fb^{-1}). The absolute error is comparable for the other (more symmetric) models. The contours in Fig. II.10 indicate that there is some reasonable possibility of distinguishing some of the benchmark models with minimal width at the LHC 14 TeV. However, there is not much possibility for model-independent studies based on the dielectron observables alone.

⁶In principle the mass could be determined indirectly, e.g., by comparing results from the ILC at different energies. However, the ILC sensitivity is small for a multi-TeV Z' mass.

⁷The uncertainties in $\Gamma_{Z'}$ are too large to obtain useful model-independent constraints from $\sigma^e \Gamma_{Z'}$.

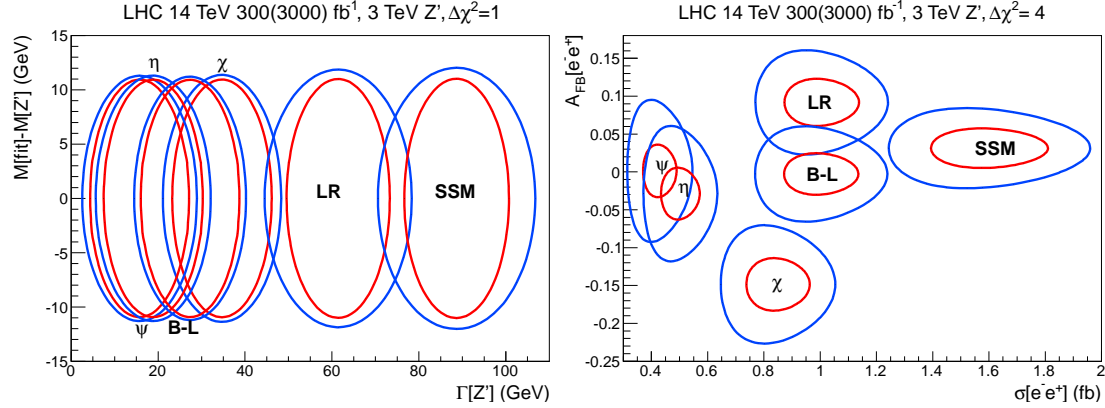


Figure II.10: The results for $pp \rightarrow Z' \rightarrow e^-e^+$ with dielectron invariant mass from 2.8 – 3.2 TeV. *Left panel:* $\Delta\chi^2 = 1$ contours for the fitted width versus mass for the LHC at 300 fb $^{-1}$ and 3000 fb $^{-1}$. *Right panel:* $\Delta\chi^2 = 4$ contours of the simulated forward-asymmetry versus the cross section.

3. Hadronic Final States

The hadronic final states of the 3 TeV Z' are particularly important. Once combined with the leptonic channels, under the assumption of family universality, one can in principle obtain the absolute values of the Z' coupling strength to both leptons and hadrons. On the other hand, one faces the difficulties of huge QCD backgrounds. In this section we discuss the possibility of observing these channels at the LHC.

We list the parton level cross section for both signal and irreducible background at the LHC 14 TeV in Table II.4. The cross sections for these models for the dijet final state, including up, down, charm and strange quarks, are at the femtobarn level. The QCD background, after preliminary cuts, is ~ 1000 times larger than the signal. More strict cuts and selection criteria may help improve this channel, but nevertheless the dijet channel is not promising.

We are particularly interested in the third generation final states. Heavy quark tagging techniques make it possible to observe these channels. Moreover, they can determine the

(family universal) Z' couplings to up-type quarks and down-type quarks. In the case that top quark charge and/or polarization tagging is available, one would be able to obtain constraints on the chiral couplings of the Z' . On the other hand, the top quark signal is statistically very limited, as shown in the table. The top tagging and mis-tagging rates in this highly boosted scenario require further investigation. Thus we only list its parton level cross section and not discuss backgrounds.

Table II.4: Parton level cross sections at the LHC 14 TeV. We only select events with final state dijet and bottom pair invariant mass in the window $2.9 - 3.1$ TeV. $\sigma_{2j;\text{cut}}^{SM}$ are with cuts h_t (scalar sum of jets' p_{Ts}) > 500 GeV, $p_T > 200$ GeV, and $y_j < 2$.

	χ	ψ	η	LR	B-L	SSM
σ_{2j}^{SM} (fb)	1.4×10^6					
$\sigma_{2j;\text{cut}}^{SM}$ (fb)	5.1×10^3					
$\sigma_{2j}^{Z'}$ (fb)	6.0	5.6	8.3	21	1.4	19
$\sigma_{2b}^{Z'}$ (fb)	2.9	1.6	1.9	7.8	0.4	6.2
$\sigma_{2b}^{SM+Z'}$ (fb)	5.5	3.7	3.9	10	2.3	8.7
$\sigma_{2t}^{Z'}$ (fb)	0.7	1.7	3.2	5.8	0.5	7.0

For the bottom pair final state we include both the QCD dijet background and the SM bottom pair irreducible background. We show the cut flow effective acceptance ϵ and final significance at LHC 14 TeV in Table II.5. The QCD dijets are required to be in the mass window of $2.5 - 3.5$ TeV, with $h_t > 500$ GeV and leading jet $p_t > 200$ GeV at the parton level. The cross section is 36 pb, but tight b -tagging criteria that have a 0.1% fake rate from light quark jets can reduce it greatly. Both the signal and irreducible bottom pair background require $b\bar{b}$ invariant mass in the same window. The effective invariant mass m_{eff} is the invariant mass of all the jets with $p_t > 100$ GeV. After these series of cuts, we will be able to establish three sigma significance for the excess for the benchmark models Z_χ , Z_{LR} and Z_{SSM} in the $b\bar{b}$ final state at LHC 14 TeV with 3000 fb^{-1} .

Table II.5: Cut flow table and significance S/\sqrt{B} for $Z' \rightarrow b\bar{b}$ processes at LHC 14 TeV. The cross sections σ before cuts are for bottom pair (dijet) invariant mass from 2.5 – 3.5 TeV. ϵ_b represents the percentage acceptance of at least one tagged b -jet. $\epsilon_{P_t^b}$ represents the percentage acceptance also requiring the p_T of the leading b -jet to be greater than 1.2 TeV. σ_{eff} is the cross section after these cuts.

	QCD Dijet	SM $b\bar{b}$	χ	ψ	η	LR	B-L	SSM
σ (fb)	36300	12.1	3.44	1.73	2.03	10.8	0.45	9.74
ϵ_b (%)	0.561	27.6	30.7	30.1	30.2	29.7	30.7	28.7
$\epsilon_{P_t^b}$ (%)	0.0365	6.80	9.07	9.14	9.34	8.15	9.56	7.63
σ_{eff} (fb)	11.78	0.82	0.31	0.16	0.19	0.88	0.04	0.74
$\frac{S}{\sqrt{B}} @ 0.3 \text{ ab}^{-1}$			1.5	0.8	0.9	4.3	0.2	3.6
$\frac{S}{\sqrt{B}} @ 3 \text{ ab}^{-1}$			4.8	2.4	2.9	14	0.7	11

4. Summary and Outlook

We study and discuss the Z' discovery and model discrimination potential of the LHC and ILC, using the benchmark models Z'_χ , Z'_ψ , Z'_η , Z'_{LR} , Z'_{B-L} , and Z'_{SSM} . We discuss two scenarios: (1) a 3 TeV Z' that can be resonantly produced at the LHC; (2) a Z' that is too massive to observe as a clear resonance signal.

We discuss the potential of the LHC at 14 TeV with integrated luminosity of 300 fb^{-1} and 3000 fb^{-1} in both leptonic and hadronic final states. The leptonic final states have low background and provide the best sensitivity for discovery. The excellent lepton energy resolution allows them to probe the Z' mass and width. We show in the left panel of Fig. II.10 that for 300 fb^{-1} (and 3000 fb^{-1}), one can reach around 10 GeV precision for each at $\sim 1\sigma$. Unfortunately, the width uncertainty is a significant fraction of the width itself for typical models with electroweak-scale couplings, limiting the possibility of constraining the absolute magnitudes of the couplings. The leptonic forward-backward asymmetry, combined with the cross section would have some sensitivity to the chiral couplings, and in particular would allow discrimination between benchmark models (with minimal width) at a reasonable level. We also discuss the hadronic Z' modes at the LHC. We study the sensitivity of the bottom pair final state in detail. Although there is a large background from mis-tagged light jets as shown in Table II.5, a 3σ excess can be achieved for certain benchmark models, such as Z'_χ , Z'_{LR} and Z'_{SSM} .

The inclusion of additional observables (such as heavy particle final states, additional asymmetries and polarizations, and precision electroweak constraints), a global χ^2 study for model discrimination, the possibility of model-independent coupling extractions, and the implications of departing from such assumptions as family universality are under investigation.

C. SUSY HIGGS PHYSICS IN NMSSM

These low- m_A parameter regions of the NMSSM have unique properties and offer rich phenomenology, providing complementary scenarios to the existing literature for the large- m_A

case, as mentioned above. The production cross section and decay branching fractions for the SM-like Higgs boson may be modified appreciably and new Higgs bosons may be readily produced at the LHC. We evaluate the production and decay of the Higgs bosons in this model and propose further searches at the LHC to probe the Higgs sector of the NMSSM.

The rest of this section is organized as follows. In Sec. II.C.1, we present a short, self-contained introduction to the Higgs sector of the NMSSM. In Sec. II.C.2, we discuss our parameter scanning scheme and the current constraints applied. We then discuss the resulting constraints and correlations for the NMSSM parameter space in Sec. II.C.3 for the case that the SM-like Higgs is the lightest CP-even scalar and in Sec. II.C.4 when the SM-like Higgs is the second lightest CP-even scalar. In Sec. II.C.5, we consider the basic LHC phenomenology for our results. Finally, we summarize and conclude in Sec. II.F.3.

1. NMSSM Higgs Sector and the Low- m_A Region

In the NMSSM [30, 31, 246, 247], a new gauge singlet chiral superfield $\hat{\mathcal{S}}$ is added to the MSSM Higgs sector resulting in a superpotential of the form

$$W_{\text{NMSSM}} = Y_u \hat{u}^c \hat{H}_u \hat{Q} + Y_d \hat{d}^c \hat{H}_d \hat{Q} + Y_e \hat{e}^c \hat{H}_d \hat{L} + \lambda \hat{\mathcal{S}} \hat{H}_u \hat{H}_d + \frac{1}{3} \kappa \hat{\mathcal{S}}^3 \quad (\text{II.C.26})$$

with an explicit \mathbb{Z}_3 symmetry. Additionally, the soft-SUSY breaking Higgs sector of the NMSSM is:

$$V_{H,\text{Soft}} = m_{H_u}^2 H_u^\dagger H_u + m_{H_d}^2 H_d^\dagger H_d + M_S^2 |\mathcal{S}|^2 + \left(\lambda A_\lambda (H_u^T \epsilon H_d) \mathcal{S} + \frac{1}{3} \kappa A_\kappa \mathcal{S}^3 + c.c. \right). \quad (\text{II.C.27})$$

After the singlet obtains a vacuum expectation value (VEV) $\langle \mathcal{S} \rangle = v_s / \sqrt{2}$, an effective μ term is generated: $\mu = \lambda v_s / \sqrt{2}$, which solves the so-called μ -problem of the MSSM. An effective b -term $b_{\text{eff}} = \mu(A_\lambda + \frac{\kappa}{\lambda} \mu)$ is also generated at tree level.

In this work, we assume a CP-conserving Higgs potential with all the coefficients being real. We further take λ and κ to be positive, unless otherwise stated. For the VEVs, we use the convention $\langle H_u^0 \rangle = v_u / \sqrt{2}$, $\langle H_d^0 \rangle = v_d / \sqrt{2}$, with $v_u^2 + v_d^2 = v^2 = (246 \text{ GeV})^2$ and $\tan \beta = v_u / v_d$. After electroweak symmetry breaking, we are then left with three CP-even Higgs states H_1, H_2, H_3 , two CP-odd Higgs states A_1, A_2 , and a pair of charged Higgs states H^\pm .

a. Masses CP-odd Higgs Bosons For the CP-odd Higgs bosons, we define the mixing states

$$A_v = \sqrt{2} \left(\text{Im}(H_d^0) \sin \beta + \text{Im}(H_u^0) \cos \beta \right), \quad A_s = \sqrt{2} \text{Im}(\mathcal{S}). \quad (\text{II.C.28})$$

The relevant parameters of our interest are the diagonal elements of the mass matrix in the basis of (A_v, A_s) as

$$m_A^2 = \frac{2\mu}{\sin 2\beta} \left(A_\lambda + \frac{\kappa}{\lambda} \mu \right) = \frac{2b_{\text{eff}}}{\sin 2\beta}, \quad (\text{II.C.29})$$

$$m_{A_s}^2 = \frac{\lambda^2 v^2}{8\mu^2} \left(m_A^2 \sin 2\beta + 6 \frac{\kappa}{\lambda} \mu^2 \right) \sin 2\beta - 3 \frac{\kappa}{\lambda} \mu A_\kappa. \quad (\text{II.C.30})$$

The full mass matrix expression can be found in Ref. [246]. In the limit of zero mixing between A_v and A_s , m_A is the mass of the CP-odd Higgs A_v , as in the case of the MSSM. However, in the NMSSM, the mass eigenstates are typically a mixture of A_v and A_s , resulting in a more complicated mass spectrum and parameter dependence. Although m_A is not a mass eigenvalue in the NMSSM, it takes the same form in terms of b_{eff} as in the MSSM [see Eq. (II.C.29)]. We also note that $m_{A_s}^2$ has the contribution $-3 \frac{\kappa}{\lambda} \mu A_\kappa$. As a result, to obtain positive mass squared eigenvalues, the combination μA_κ can not be too large and positive, in particular, for the small m_A region that we consider in section II.C. We denote the mass eigenstates as A_1 and A_2 , where $m_{A_1} \leq m_{A_2}$.

Charged Higgs Bosons The charged Higgs bosons H^\pm in the NMSSM have the same definition as in the MSSM, but a new contribution to their mass

$$H^\pm = H_d^\pm \sin \beta + H_u^\pm \cos \beta, \quad m_{H^\pm}^2 = m_A^2 + m_W^2 - \frac{1}{2}(\lambda v)^2. \quad (\text{II.C.31})$$

The extra λ -dependent term leads to a reduction of the charged Higgs mass compared to its MSSM value. Requiring $m_{H^\pm}^2 \geq 0$ gives an upper bound for λ as a function of m_A

$$\lambda \leq \frac{\sqrt{2}}{v} \sqrt{m_A^2 + m_W^2}. \quad (\text{II.C.32})$$

The LEP search limit $m_{H^\pm} \gtrsim 80$ GeV [248, 249], as well as the bounds from the Tevatron and LHC charged Higgs boson searches, strengthen this upper limit even further, depending on the value of $\tan \beta$.

CP-even Higgs Bosons The CP-even Higgs sector is much more complicated compared to that of the MSSM. It is advantageous to define the basis as:

$$\begin{pmatrix} h_v \\ H_v \end{pmatrix} = \begin{pmatrix} \cos \beta & \sin \beta \\ -\sin \beta & \cos \beta \end{pmatrix} \begin{pmatrix} \sqrt{2} (\text{Re}(H_d^0) - v_d) \\ \sqrt{2} (\text{Re}(H_u^0) - v_u) \end{pmatrix}, \quad S = \sqrt{2} (\text{Re}(\mathcal{S}) - v_s). \quad (\text{II.C.33})$$

The benefit of using this basis is that the couplings of h_v to the gauge sector and the fermion sector are exactly *the same* as that of the SM Higgs. On the other hand, H_v does *not* couple to pairs of gauge bosons at all, and its coupling to the up-type quarks (down-type quarks and charged leptons) is proportional to $\frac{1}{\tan \beta} (\tan \beta)$ with respect to the SM values. The singlet, S , does not couple to either the gauge bosons or the fermions. While the mass eigenstates $H_{1,2,3}$ (with $m_{H_1} \leq m_{H_2} \leq m_{H_3}$) are typically mixtures of h_v , H_v and S , by knowing the fraction of h_v , H_v , and S in the mass eigenstates, we have a better understanding of their interactions with the gauge bosons and fermions.

The diagonal entries of the mass matrix for the CP-even Higgs bosons in the basis of (h_v, H_v, S) are given by [246]

$$m_{h_v}^2 = m_Z^2 + \left[\frac{1}{2}(\lambda v)^2 - m_Z^2 \right] \sin^2 2\beta, \quad (\text{II.C.34})$$

$$m_{H_v}^2 = m_A^2 - \left[\frac{1}{2}(\lambda v)^2 - m_Z^2 \right] \sin^2 2\beta, \quad (\text{II.C.35})$$

$$m_S^2 = \frac{\lambda^2 v^2}{8\mu^2} \left(m_A^2 \sin 2\beta - 2\frac{\kappa}{\lambda} \mu^2 \right) \sin 2\beta + \frac{\kappa}{\lambda} \mu \left(A_\kappa + 4\frac{\kappa}{\lambda} \mu \right). \quad (\text{II.C.36})$$

Note that the combination $\frac{\kappa}{\lambda} \mu A_\kappa$, that appear in m_S^2 , also appeared in $m_{A_s}^2$ [see Eq. (II.C.29)]. While $\frac{\kappa}{\lambda} \mu A_\kappa$ could not be too large and positive in order for $m_{A_s}^2$ to be positive, we see that it also can not be too large and negative in order for m_S^2 to be positive. This term also introduces certain correlation between μ and A_κ , as discussed in Secs. II.C.3 and II.C.4. For large m_A , we see that $m_{H_v}^2$ grows with m_A , while m_{h_v} remains around the electroweak scale. The singlet, on the other hand, is determined by a combination of μ , A_κ , and m_A , as well as the dimensionless quantities κ , λ , and $\tan \beta$.

The first and foremost effect of the introduction of the singlet and its couplings to the MSSM Higgs sector is the extra λ -term in Eqs. (II.C.34) and (II.C.35), which lifts up the

mass of the SM-like Higgs $m_{h_v}^2$, in particular, for small $\tan\beta$, while reducing $m_{H_v}^2$. In the MSSM, for the SM-like Higgs to have a mass of approximately 126 GeV typically requires the tree-level Higgs mass-squared $m_Z^2 \cos^2 2\beta$ to be maximized, which prefers large $\tan\beta$. In the NMSSM, by contrast, the contribution from $\frac{1}{2}(\lambda v)^2 \sin^2 2\beta$ results in small values of $\tan\beta$ being favored, especially for large λ . Consequently, the contribution to the Higgs mass from stop sector loop corrections can be relaxed. The left-right mixing in the stop sector is no longer required to be near maximal ($|A_t| \sim \sqrt{6M_{3SQ}M_{3SU}}$ in the MSSM).

The mixture of the singlet with the MSSM Higgs sector, in particular with h_v , could further affect the SM-like Higgs mass. If we consider only the h_v - S mixing for simplicity, when $m_{h_v}^2 > m_S^2$, the mass eigenvalues for the SM-like Higgs is pushed up after the diagonalization of the 2×2 mass matrix. This is the so-called “push-up” scenario described in the literature. On the other hand, when $m_{h_v}^2 < m_S^2$, the mass eigenvalue for the SM-like Higgs is pushed down due to the mixing, and is, thus, called the “push-down” scenario. Such effects have been discussed extensively in the literature [40, 48], considered almost exclusively in the limit of $m_A \gg m_Z$, which decouples the effect of the MSSM non-SM like Higgs H_v , while focusing only on the mixture of h_v and S . The low-lying spectrum in such cases includes two CP-even Higgs bosons, H_1 and H_2 , as a mixture of h_v and S , with either H_1 or H_2 being the 126 GeV SM-like Higgs, corresponding to the push-down or push-up scenario, respectively. In this large- m_A scenario, only one CP-odd Higgs A_s might be light, while A_v and H^\pm are heavy and decouple. Both the push-up and push-down scenarios, however, suffer from a certain degree of fine-tuning for the NMSSM parameters if the stop masses are relatively light and the left-right mixing in the stop sector is not large [40].

Low- m_A Region

In this section, we consider the region of the NMSSM with relatively small m_A ($m_A \lesssim 2m_Z$). In this region, all the MSSM-type Higgs bosons are relatively light, with $m_{h_v}^2$ and $m_{H_v}^2$ relatively close to each other. With an appropriate choice of other NMSSM parameters, m_S^2 and $m_{A_s}^2$ can be light as well. This could lead to potentially large mixing effects in the Higgs mass eigenstates, resulting in possible deviations of the SM-like Higgs couplings to the gauge boson and fermion sectors.

The low- m_A region of the MSSM (the so-called “non-decoupling” region) has been studied

in Refs. [45, 250–255]. It was pointed out that for $m_A \sim m_Z$, the heavy CP-even Higgs, H^0 in the usual MSSM notation, is the SM-like Higgs. On the other hand, for the light CP-even Higgs h^0 to be SM-like, m_A is typically large: $m_A \gtrsim 300$ GeV, in the so-called “decoupling” region of the MSSM. However, these observations do not necessarily hold in the NMSSM, due to the singlet-induced λ -term contribution to $m_{h_v}^2$ and $m_{H_v}^2$, as well as the singlet mixing effects in the mass matrix.

If we ignore the singlet mixture with h_v and H_v for the moment, and study the consequence of the extra λ -term in the 2×2 (h_v, H_v) system in the NMSSM, then, to have the heavy CP-even MSSM Higgs be SM-like, $m_{h_v}^2 \geq m_{H_v}^2$, requires

$$m_A^2 \leq m_Z^2 \cos 4\beta + (\lambda v)^2 \sin^2 2\beta. \quad (\text{II.C.37})$$

Fig. II.11 shows the lines in the λ versus m_A plane when $m_{h_v}^2 = m_{H_v}^2$, for various values of $\tan \beta$. For regions above the lines, $m_{h_v}^2 > m_{H_v}^2$, and the heavy CP-even MSSM Higgs is SM-like (up to mixing and loop corrections). For regions below the lines, $m_{h_v}^2 < m_{H_v}^2$, and the light CP-even MSSM Higgs is SM-like. All the lines cross the point $m_A = m_Z$ and $\lambda = \sqrt{2}m_Z/v \sim 0.5$. For small $\tan \beta \sim 1$, large λ (above the $\tan \beta = 1$ line) is preferred to realize $m_{h_v} > m_{H_v}$, while small λ gives rise to $m_{h_v} < m_{H_v}$. For larger values of $\tan \beta$, the curve tilts more and more vertically. For $\tan \beta \gtrsim 10$, the λ dependence becomes rather weak and the separation of the two regions is governed by the value of m_A : $m_A \lesssim m_Z$ for $m_{h_v} > m_{H_v}$ and $m_A \gtrsim m_Z$ for $m_{h_v} < m_{H_v}$, which is similar to the usual MSSM case. In Fig. II.11, we also include the m_{H^\pm} contours as dashed lines, with the shaded area indicating the region ruled out by $m_{H^\pm}^2 < 0$. Taking into account the LEP bound of $m_{H^\pm} \gtrsim 80$ GeV [248, 249] limits us to the right of the $m_{H^\pm} = 80$ GeV contour. Therefore, requiring $m_{h_v} > m_{H_v}$ while satisfying the experimental charged Higgs bounds restricts us to two regions: large $\lambda \gtrsim 0.5$, $m_A \gtrsim m_Z$ for small $\tan \beta \sim 1 - 2$, or small $\lambda \lesssim 0.5$, $m_A \lesssim m_Z$ for $\tan \beta \gtrsim 2$. Imposing a stronger bound on m_{H^\pm} from $t \rightarrow bH^\pm$ searches at the Tevatron and the LHC [256–258] further narrows down the $m_{h_v} > m_{H_v}$ region, resulting in a fine-tuned region to realize.

On the other hand, $m_{h_v} < m_{H_v}$ is much easier to realize in the NMSSM. In contrast to the MSSM, where being deep into the decoupling region $m_A \gtrsim 300$ GeV is typically required to satisfy both the mass window and the cross section requirement (i.e. for h^0 to obtain

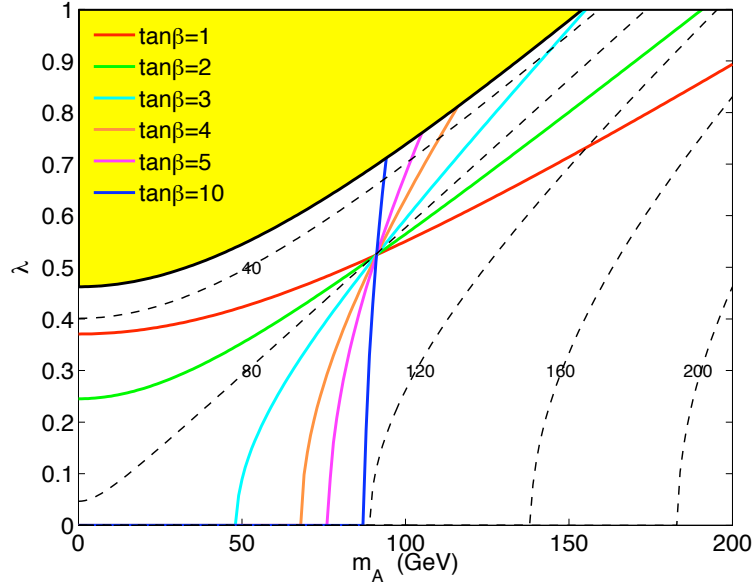


Figure II.11: Lines for $m_{h_v}^2 = m_{H_v}^2$ for different values of $\tan \beta$ in the λ versus m_A plane. $m_{h_v}^2 > m_{H_v}^2$ above the lines and $m_{h_v}^2 < m_{H_v}^2$ below the lines. Also shown by the dashed lines are the mass contours for the tree-level value of m_{H^\pm} . The shaded region corresponds to the excluded region with $m_{H^\pm}^2 < 0$.

SM-like couplings to the gauge bosons), in the NMSSM, with the mixture of the singlet and the possible suppressed couplings to $b\bar{b}$, even a suppressed coupling to the gauge sector could be accommodated while satisfying the experimentally observed cross section range. Note that our discussions are based on tree level expression for the Higgs masses. While including loop corrections shifts all the masses, our statements are still qualitatively valid.

Including the extra singlet in the spectrum gives three distinct cases, as sketched in Fig. I.1, corresponding to either H_1 , H_2 , or H_3 being SM-like:

- H_1 SM-like: $m_{h_v} \lesssim m_{H_v}, m_S$,
- H_2 SM-like: $m_S \lesssim m_{h_v} \lesssim m_{H_v}$ or $m_{H_v} \lesssim m_{h_v} \lesssim m_S$,
- H_3 SM-like: $m_{H_v}, m_S \lesssim m_{h_v}$.

With the off-diagonal mixing in the mass matrix, the separation of these regions becomes less distinct while the above relations still approximately hold.

b. Couplings The mass eigenstates $H_{1,2,3}$ are, in general, a mixture of h_v , H_v , and S :

$$H_i = \sum_{\alpha} \xi_{H_i}^{H_{\alpha}} H_{\alpha}, \quad \text{for } i = 1, 2, 3, \quad H_{\alpha} = (h_v, H_v, S), \quad (\text{II.C.38})$$

with $\xi_{H_i}^{H_{\alpha}}$ being the 3×3 unitary matrix that rotates the Higgs bosons into the mass eigenstates. In particular, $|\xi_{H_i}^{H_{\alpha}}|^2$ defines the fraction of h_v , H_v , and S in H_i with the unitarity relations:

$$|\xi_{H_1}^{H_{\alpha}}|^2 + |\xi_{H_2}^{H_{\alpha}}|^2 + |\xi_{H_3}^{H_{\alpha}}|^2 = 1, \quad |\xi_{H_i}^{h_v}|^2 + |\xi_{H_i}^{H_v}|^2 + |\xi_{H_i}^S|^2 = 1. \quad (\text{II.C.39})$$

Similarly, for the CP-odd Higgs bosons, the unitary rotation is $A_i = \sum_{\alpha} \xi_{A_i}^{A_{\alpha}} A_{\alpha}$ where $i = 1, 2$, and $A_{\alpha} = (A_v, A_s)$. The fractions of A_v and A_s in the CP-odd mass eigenstates $A_{1,2}$ are given by $|\xi_{A_i}^{A_{\alpha}}|^2$, $i = 1, 2$, with $|\xi_{A_1}^{A_v}|^2 = |\xi_{A_2}^{A_s}|^2 = 1 - |\xi_{A_1}^{A_s}|^2 = 1 - |\xi_{A_2}^{A_v}|^2$.

In Table II.6, we express the tree-level reduced couplings of the NMSSM Higgs mass eigenstates to various pairs of SM particles, which are the ratios of the NMSSM Higgs couplings to the corresponding SM values. The charged Higgs couplings of $H^+ d_L u_R^c$ and $H^- u_L d_R^c$ are normalized to the SM top and bottom Yukawa couplings $\sqrt{2}m_t/v$ and $\sqrt{2}m_b/v$, respectively. In the NMSSM, the $H_i ZZ$ and $H_i WW$ couplings are always modified in the

Table II.6: Reduced Higgs couplings at tree level. The charged Higgs couplings of $H^+ d_L u_R^c$ and $H^- u_L d_R^c$ are normalized to the SM top and bottom Yukawa couplings $\sqrt{2}m_t/v$ and $\sqrt{2}m_b/v$, respectively.

	H_i	A_i		H^\pm
R_{uu}	$\xi_{H_i}^{h_v} + \xi_{H_i}^{H_v} / \tan \beta$	$\xi_{A_i}^{A_v} / \tan \beta$	$R_{d_L u_R^c}$	$-1 / \tan \beta$
R_{dd}	$\xi_{H_i}^{h_v} - \xi_{H_i}^{H_v} \tan \beta$	$\xi_{A_i}^{A_v} \tan \beta$	$R_{u_L d_R^c}$	$-\tan \beta$
R_{VV}	$\xi_{H_i}^{h_v}$			

same way at leading order. Therefore, we use VV to represent both WW and ZZ . The coupling of the CP-even Higgs bosons to the gauge boson sector VV is completely determined by the h_v -fraction of H_i : $|\xi_{H_i}^{h_v}|^2$, which plays an important role in understanding the coupling and branching fraction behavior of the SM-like Higgs boson. Note that $|\xi_{H_i}^{h_v}|^2 \leq 1$, therefore, the $H_i VV$ couplings, as well as the $H_i \rightarrow VV$ partial decay widths, are always suppressed compared to their SM values. However, the branching fractions of $H_i \rightarrow VV$ could still be similar or even enhanced compared to their SM values, since $H_i \rightarrow bb$ could be suppressed as well.

The Higgs to $\gamma\gamma$ and Higgs to gg couplings are both loop-induced. The dominant contribution to the $h_v\gamma\gamma$ coupling comes from the WW loop, with a sub-leading destructive contribution from the top loop. The $h_v gg$ coupling, on the other hand, is dominated by the top-loop contribution. The $H_i\gamma\gamma$ and $H_i gg$ couplings are modified similarly in the NMSSM, based on the reduced couplings as listed in Table II.6.

2. Parameter Scan and Constrained Regions

We will focus our scan on the parameters that are most relevant to the Higgs sector, namely, parameters appearing in the Higgs potential, as well as the stop mass parameters, which could induce a relatively large loop correction to the Higgs mass. Since the impact of other

SUSY sectors to the Higgs mass is typically small, we effectively decouple them by setting all other SUSY mass parameters to be 3 TeV and the other trilinear soft SUSY breaking parameters to be 0. Note that the sbottom and stau might modify the Higgs mass and certain couplings at loop level, which could have substantial effects in certain regions of parameter space. We defer a discussion of these regions to specific studies in the literature [259] and will only focus on the Higgs and stop sectors in the current study.

In the MSSM, the relevant Higgs and stop sector parameters are

$$m_A, \tan \beta, \mu, M_{3SQ}, M_{3SU}, A_t, \quad (\text{II.C.40})$$

as well as the Higgs vacuum expectation value $v = 246$ GeV. In the NMSSM, the tree level Higgs potential involves seven parameters: $(\lambda, \kappa, A_\lambda, A_\kappa, v_s, \tan \beta)$ and v . After replacing v_s by $\mu = \lambda v_s / \sqrt{2}$ and replacing A_λ by m_A as defined in Eq. (II.C.29), we are left with three new parameters compared to the MSSM case. We scan these parameters in the range of

$$\begin{aligned} 0 &\leq m_A \leq 200 \text{ GeV}, \\ 1 &\leq \tan \beta \leq 10, \\ 100 \text{ GeV} &\leq \mu \leq 1000 \text{ GeV}, \\ 0.01 &\leq \lambda, \kappa \leq 1, \\ -1200 \text{ GeV} &\leq A_\kappa \leq 200 \text{ GeV}, \\ 100 \text{ GeV} &\leq M_{3SQ}, M_{3SU} \leq 3000 \text{ GeV}, \\ -4000 \text{ GeV} &\leq A_t \leq 4000 \text{ GeV}, \end{aligned} \quad (\text{II.C.41})$$

unless otherwise stated. The range of m_A is chosen to guarantee that H_v and A_v are light. The ranges of μ , λ , κ and A_κ are chosen such that the CP-even and odd singlet masses are allowed to vary over a wide range. The stop sector mass and mixing parameters are chosen to cover both the minimal and maximal mixing scenarios. We restrict $\tan \beta$ to be in the range of 1 – 10 since regions with higher values of $\tan \beta$ do not contain a SM-like Higgs boson in the mass window of 124 – 128 GeV, as will be discussed in detail in Secs. II.C.3 and II.C.4.

The scan is performed by utilizing NMSSMTools 3.2.1 [260–262] to calculate the Higgs and SUSY spectrum, Higgs couplings, decay widths, branching fractions, and various Higgs production cross sections. The full constraints imposed for the scan procedure include:

- the latest LHC limits in various SM Higgs searches [263–267];
- bounds on MSSM Higgs search channels from LEP, the Tevatron, and the LHC [43, 268];
- stop and sbottom masses to be heavier than 100 GeV.

We did not impose bounds that are not directly relevant to the Higgs sector, for example, other SUSY particle searches, flavor physics, and dark matter relic density. Those bounds typically involve SUSY parameters of other NMSSM sectors which we did not scan. Although some significant reduction of the allowed parameter space may occur with these additional constraints, we do not expect our conclusions to be changed. We generated a large Monte Carlo sample over the multi-dimensional parameter space and tested each parameter point against the experimental constraints. For the following presentation, the allowed points (or regions) in the plots are indicative of consistent theoretical solutions satisfying the experimental constraints, but are not meant to span the complete space of possible solutions.

Given the discovery of a SM-like Higgs boson around 126 GeV, we study its implication by applying the following requirements step by step:

$$\text{Either } H_1, \text{ or } H_2, \text{ or } H_3 \text{ in the mass window of } 124 - 128 \text{ GeV}, \quad (\text{II.C.42})$$

$$\frac{\sigma \times \text{Br}(gg \rightarrow H_i \rightarrow \gamma\gamma)}{(\sigma \times \text{Br})_{\text{SM}}} \geq 0.8, \quad \frac{\sigma \times \text{Br}(gg \rightarrow H_i \rightarrow WW/ZZ)}{(\sigma \times \text{Br})_{\text{SM}}} \geq 0.4. \quad (\text{II.C.43})$$

The cases delineated in Eqs. (II.C.42) and (II.C.43) determine the defining feature of the regions described in this section and will, henceforth, be referred to as H_1 -126, H_2 -126 and H_3 -126, respectively.

Figure II.12 shows the allowed mass regions versus m_{H^\pm} for the CP-even Higgs bosons (left panels) and the CP-odd/charged Higgs bosons (right panels). The first and second row panels are for points that pass all the experimental constraints as itemized earlier, as well as H_1 and H_2 , respectively, satisfying both the mass and cross section requirements as listed in Eqs. (II.C.42) and (II.C.43). The third row panels are for points that pass all experimental

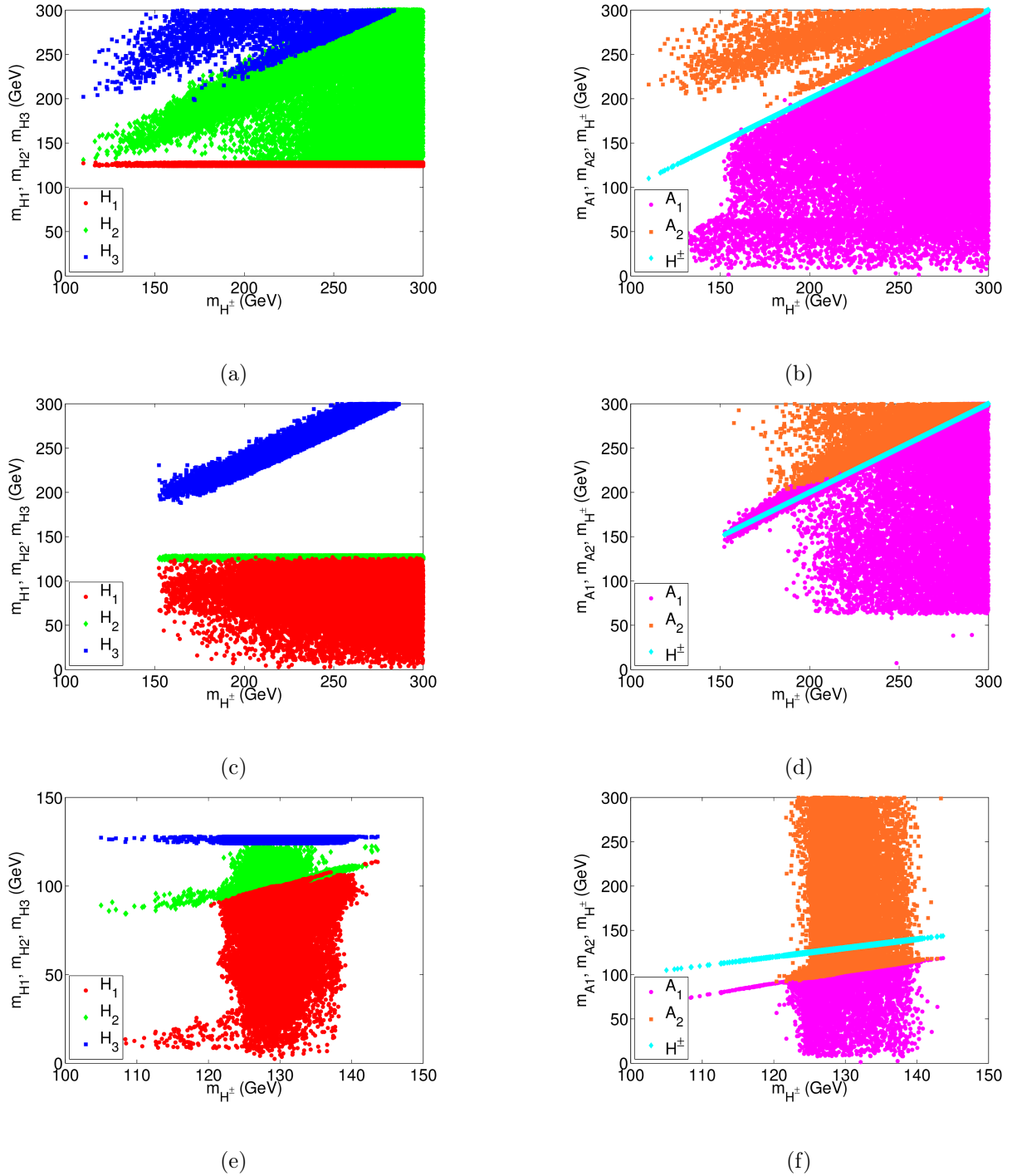


Figure II.12: The left panels show the allowed mass regions versus m_{H^\pm} for the CP-even H_1 (red), H_2 (green), and H_3 (blue). The right panels show the allowed mass regions versus m_{H^\pm} for the CP-odd A_1 (magenta), and A_2 (brown), and the charged Higgs H^\pm (cyan). The first and second row panels contain the points that pass all the experimental constraints as well as having H_1 and H_2 being SM-like. The third row panels contain the points that pass all the experimental constraints as well as Eq. (II.C.42), but not Eq. (II.C.43).

constraints as well as H_3 satisfying the mass requirement as listed in Eq. (II.C.42). We have chosen to plot the physical Higgs masses against the charged Higgs mass m_{H^\pm} , rather than the conventional choice of m_A as in the MSSM. Due to the relatively large loop corrections to the Higgs masses, the natural scale parameter choice in the NMSSM would be the loop corrected A_v mass $m_{A_{loop}}$, the NMSSM equivalent of the MSSM m_A (the physical mass for the CP-odd MSSM Higgs). A_v , however, has to mix with A_s to provide masses for the two CP-odd mass eigenstates A_1 and A_2 . The charged Higgs mass m_{H^\pm} , on the other hand, retains roughly the simple relationship with $m_{A_{loop}}$, described in Eq. (II.C.31), after loop corrections. Therefore, we choose the physical m_{H^\pm} as the scale parameter in Fig. II.12. In this figure, we scanned in the range $0 \text{ GeV} < m_{H^\pm}^{\text{tree}} < 300 \text{ GeV}$, rather than $0 \text{ GeV} < m_A < 200 \text{ GeV}$, to improve the coverage of the parameter region of our interest.

For H_1 being the SM-like Higgs in the mass window of $124 - 128 \text{ GeV}$ (see the first row of Fig. II.12), H_2 is typically in the mass range of $125 - 300 \text{ GeV}$, while $m_{H_3} \gtrsim 200 \text{ GeV}$. The charged Higgs mass is in the approximate range $125 - 300 \text{ GeV}$. Charged Higgs bosons with mass less than 150 GeV are mostly ruled out by the direct search for H^\pm produced in top decays. The light CP-odd Higgs could be very light, a few $\text{GeV} \lesssim m_{A_1} \lesssim 300 \text{ GeV}$, while $m_{A_2} \gtrsim 200 \text{ GeV}$. When $m_{A_1} < m_{H_1}/2$, the decay channel $H_1 \rightarrow A_1 A_1$ opens, leading to very interesting phenomenology, as will be discussed in detail in Sec. II.C.3. Note that the boundary of the H_2 and H_3 regions, as well as the boundary of the A_1 and A_2 regions show nice correlation with m_{H^\pm} . This is because the boundary is given by m_{H_v} as in Eq. (II.C.35) for the CP-even case, and by m_A for the CP-odd case, both of which scale with m_{H^\pm} . The singlet mixing with H_v and A_v will push/pull the mass eigenstates away from m_{H_v} and m_A , leaving a clear boundary. Given a H_2, H_3 pair (A_1, A_2 pair), the one whose mass is closer to the H_2 - H_3 (A_1 - A_2) boundary line is more H_v (A_v)-like.

For H_2 being the SM-like Higgs in the mass window of $124 - 128 \text{ GeV}$ (see the second row of Fig. II.12), a large fraction of the points contain H_1 in the mass range of $60 - 124 \text{ GeV}$. There is also a significant set of points with $m_{H_1} < m_{H_2}/2$, which turns on the decay channel $H_2 \rightarrow H_1 H_1$, as will be discussed in Sec. II.C.4. m_{H_3} is in the mass window of approximately $200 - 350 \text{ GeV}$, and grows roughly linearly with m_{H^\pm} , an indication of H_3 being mostly H_v -like. The points with m_{H_3} below $\sim 180 \text{ GeV}$ are removed by a combination

of the collider constraints and the cross section requirement of Eq. (II.C.43). This is very different from the H_1 -126 case, in which H_3 could be singlet dominant with mass as large as 1 TeV or higher. For the light CP-odd Higgs A_1 , it falls into two regions: one region with $60 \text{ GeV} \lesssim m_{A_1} \lesssim 300 \text{ GeV}$ ($m_{H^\pm} \gtrsim 200 \text{ GeV}$), with little dependence on m_{H^\pm} (for A_1 being mostly A_s); another region with $m_{A_1} \gtrsim 150 \text{ GeV}$ ($m_{H^\pm} \gtrsim 150 \text{ GeV}$), which grows linearly with m_{H^\pm} (for A_1 being A_v -like). A_2 typically has a mass of 200 GeV or higher, which also falls into two regions accordingly.

For H_3 being the SM-like Higgs in the mass window of 124 – 128 GeV (see the third row of Fig. II.12), both the singlet and H_v -dominant Higgs bosons need to be lighter than about 126 GeV. Given the tight experimental constraints on the light Higgs searches, as well as the fine-tuning between the mass parameters, this region turns out to be highly restrictive. While we can realize regions with m_{H_3} in the desired mass window, it is extremely difficult to satisfy the cross section requirement of Eq. (II.C.43). Panels in the third row of Fig. II.12 show points with H_3 in the mass window of 124 – 128 GeV. However, $\sigma \times \text{Br}(gg \rightarrow H_3 \rightarrow \gamma\gamma, WW/ZZ)/\text{SM}$ is less than 0.4 in general, and it is therefore hard to accommodate the observed Higgs signal as H_3 in the NMSSM.

In what follows, we will discuss the H_1 -126 and H_2 -126 cases in detail, exploring the relevant parameter space for each region, the composition of the 126 GeV SM-like Higgs and the other light NMSSM Higgs bosons, possible enhancement or suppression of various search channels as well as correlations between them.

3. H_1 as the SM-like Higgs Boson

a. Parameter Regions For H_1 to have SM-like cross sections for $gg \rightarrow H_1 \rightarrow \gamma\gamma, WW/ZZ$ within the experimentally observed ranges, H_1 needs to be either dominantly h_v or have a considerable singlet fraction with a suppressed $H_1 \rightarrow b\bar{b}$ partial width. H_v and S dominant states are typically heavier such that, usually, the lightest CP-even Higgs state is mostly h_v . This case is seldom realized in the MSSM low- m_A region ($m_A \lesssim 2m_Z$), since the light CP-even Higgs boson typically has suppressed couplings to WW and ZZ in this region. In the NMSSM, the tree-level diagonal mass term for h_v is

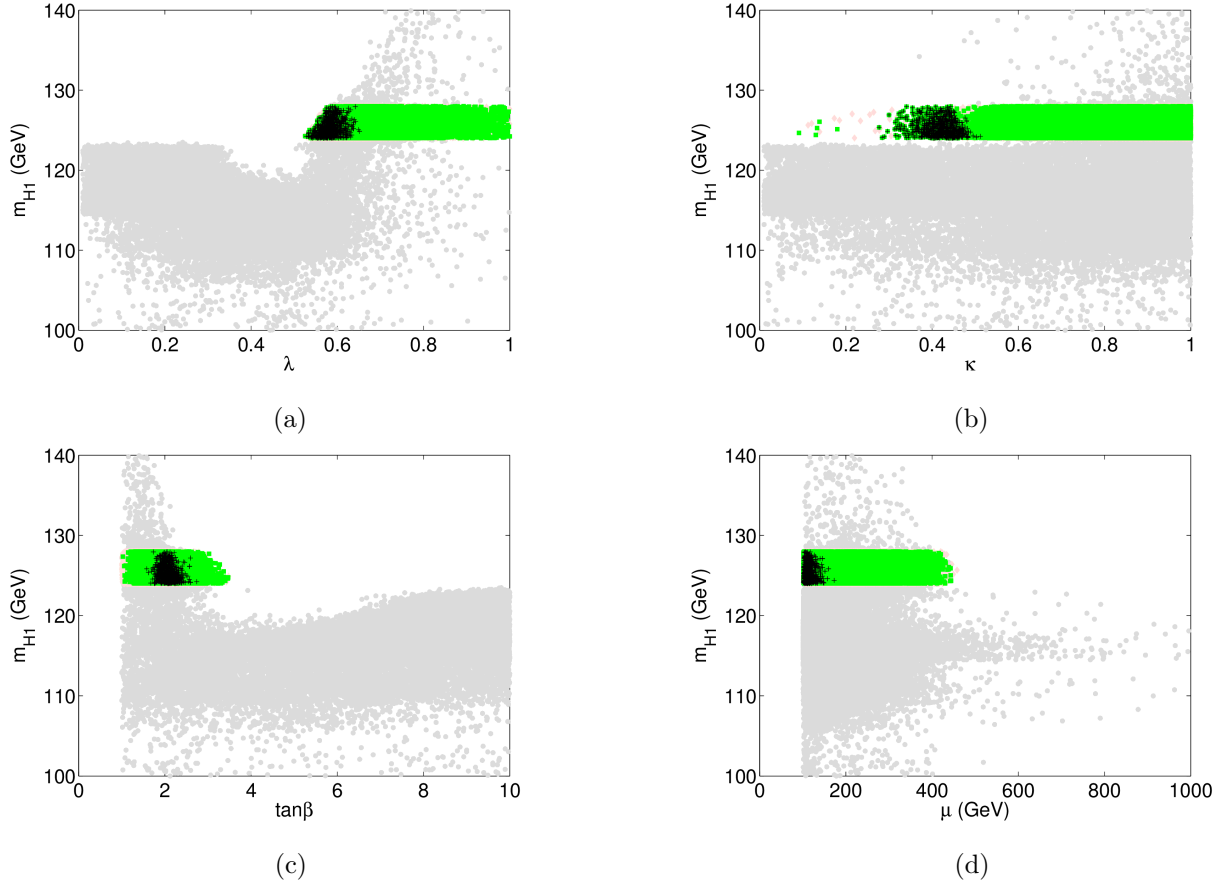


Figure II.13: The dependence of m_{H_1} on the following NMSSM parameters in the H_1 -126 case: λ , κ , $\tan\beta$, and μ . Grey points are those that pass the experimental constraints, pale-pink points are those with H_1 in the mass window $124 \text{ GeV} < m_{H_1} < 128 \text{ GeV}$ and green points are those with the cross section requirements further imposed. Black points are those that remain perturbative up to the Planck scale.

$m_{h_v}^2 = m_Z^2 \cos^2 2\beta + \frac{1}{2}(\lambda v)^2 \sin^2 2\beta$. Large λ and small $\tan \beta$ are preferred to push up the mass of h_v into the desired mass window. For small $\tan \beta$, even for small m_A , typically $m_{h_v}^2 < m_{H_v}^2$, resulting in the lighter MSSM-like CP-even Higgs being SM-like in the low- m_A region. In addition, mixture with the singlet in the NMSSM which produces, in particular, a suppressed $H_1 \rightarrow b\bar{b}$ partial decay width, could lead to a SM-like $\gamma\gamma$ and WW/ZZ branching fraction for H_1 as well. The push-down effect in mass eigenvalues from the singlet mixing also helps to realize the mostly h_v state being H_1 .

To show the effect of the narrowing down of the parameter regions due to the mass and cross section requirements, Fig. II.13 presents the dependence of m_{H_1} on λ , κ , $\tan \beta$, and μ , with gray dots for all points satisfying the experimental constraints, pale-pink points which pass the mass window requirement of Eq. (II.C.42), and green points, that almost overlap the pale-pink points, which pass both the mass and cross section requirements of Eqs. (II.C.42) and (II.C.43).

After requiring H_1 to fall into the mass region of 124 – 128 GeV, we are restricted to the parameter region of $\lambda \gtrsim 0.55$, $\kappa \gtrsim 0.3$ (with a small number of points down to 0.1), $1 \lesssim \tan \beta \lesssim 3.5$, $\mu \lesssim 500$ GeV, -1200 GeV $\lesssim A_\kappa \lesssim 200$ GeV with no restriction on m_A which is allowed to be in the entire region of 0 – 200 GeV (the corresponding region for A_λ is approximately –650 GeV to 300 GeV). The stop mass parameters M_{3SQ} , M_{3SU} and A_t are unrestricted as well. Further imposing the cross section requirement for $gg \rightarrow H_1 \rightarrow \gamma\gamma, WW$ and ZZ does not narrow down the allowed regions for these parameters further.

Also shown as the black points in Fig. II.13 are the parameter points where λ and κ remain perturbative up to the Grand Unified Theory (GUT) scale. They occupy a small region of $0.5 \lesssim \lambda \lesssim 0.65$, $0.3 \lesssim \kappa \lesssim 0.5$, $\tan \beta \sim 2$, $100 \lesssim \mu \lesssim 150$ GeV, $-150 \lesssim A_\kappa \lesssim 100$ GeV, and $150 \lesssim m_A \lesssim 200$ GeV ($-30 \lesssim A_\lambda \lesssim 230$ GeV). While M_{3SQ} and M_{3SU} are unconstrained, $|A_t|$ is restricted to be $\gtrsim 1200$ GeV. These parameter regions are summarized in Table II.7.

We have noted earlier that the light CP-odd Higgs A_1 could be very light. When it falls below half of the H_1 mass, $H_1 \rightarrow A_1 A_1$ opens up, which could dominate the H_1 decay width, compared to the usual case in which decay to $b\bar{b}$ dominates. Therefore, we further separate the H_1 -126 case into three regions:

Table II.7: NMSSM Parameter regions for the H_1 -126 case.

	$\tan \beta$	m_A (GeV)	μ (GeV)	λ	κ	A_λ (GeV)	A_κ (GeV)
H_1 -126	1~3.5	0~200	100~500	$\gtrsim 0.55$	$\gtrsim 0.3$	-650~300	-1200~200
perturb.	1.5 ~2.5	150~200	100~150	0.55~0.65	0.3~0.5	-30~230	-150~100
$m_{A_1} < \frac{m_{H_1}}{2}$	1~3.5	100~200	100~200	$\gtrsim 0.55$	$\gtrsim 0.5$	-150~150	-50~30

- H_1 Region IA: $m_{A_1} > m_{H_1}/2$ and $|\xi_{H_1}^{h_v}|^2 > 0.7$: green points in Figs. II.14-II.19.
- H_1 Region IB: $m_{A_1} > m_{H_1}/2$ and $|\xi_{H_1}^{h_v}|^2 < 0.7$: red points in Figs. II.14-II.19.
- H_1 Region II: $m_{A_1} < m_{H_1}/2$: magenta points in Figs. II.14-II.19.

To identify the NMSSM parameter regions that give a SM-like H_1 in the mass window of 124 – 128 GeV, in Fig. II.14, we show the viable regions in various combinations of NMSSM parameters. Grey points are those that pass the experimental constraints, pale-pink points are those with H_1 in the mass window $124 \text{ GeV} < m_{H_1} < 128 \text{ GeV}$, green and red points are for H_1 Region I with m_{A_1} above the $H_1 \rightarrow A_1 A_1$ threshold, and magenta points are for H_1 Region II with low m_{A_1} . Again, the black points are those where λ and κ remain perturbative up to the GUT scale.

The first two panels show the (a) λ versus m_A , and (b) κ versus m_A regions. For small values of m_A , λ has to be around 0.6–0.7, since too large a value of λ is ruled out by the charged Higgs mass bounds, while too small a value of λ results in m_{H_1} being less than 124 GeV. For larger values of m_A , the λ range is enlarged to $0.55 \lesssim \lambda \lesssim 1$. κ , on the other hand, has to be ~ 1 for small m_A , while smaller κ is allowed for larger m_A .

Panel (c) of Fig. II.14 shows the viable region in the λ versus κ plane. Given $\lambda \gtrsim 0.55$ and $\kappa \gtrsim 0.3$, the renormalization group running of λ , and κ , as well as of the Yukawa couplings $y_{t,b}$ and gauge couplings might reach the Landau pole before M_{GUT} . As noted in Ref. [35], a larger λ allows a highly natural light Higgs boson. For all the points that pass the mass and cross section requirements, only a small region of the λ - κ plane, as shown by the black points in panel (c) of Fig. II.14, remain perturbative up to the GUT scale around 10^{16} GeV. For

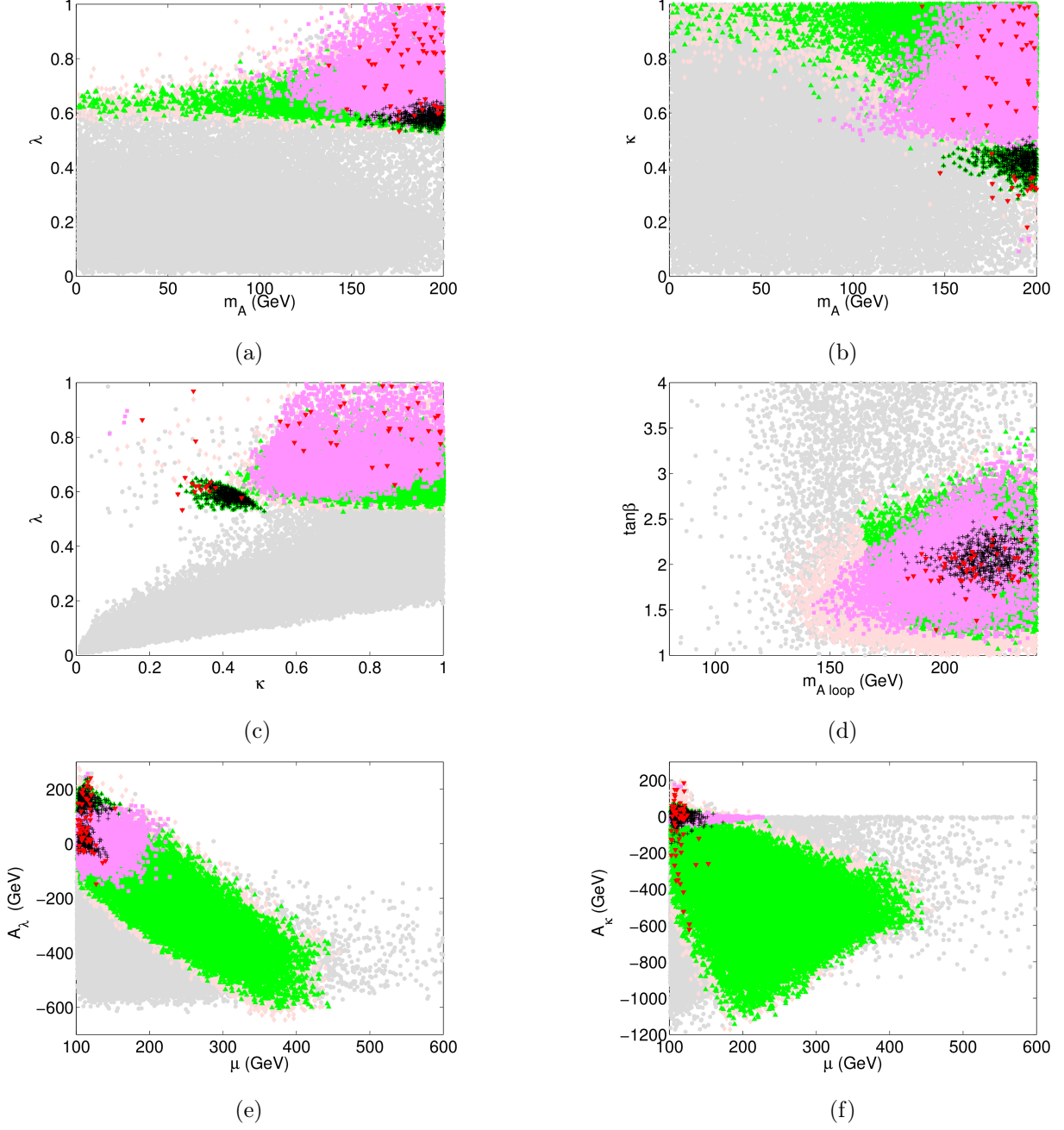


Figure II.14: Viable NMSSM parameter regions in the H_1 -126 case: (a) λ versus m_A , (b) κ versus m_A , (c) λ versus κ , (d) $\tan \beta$ versus $m_{A_{loop}}$, (e) A_λ versus μ , and (f) A_κ versus μ . Grey points are those that pass the experimental constraints, pale-pink points are those with H_1 in the mass window $124 \text{ GeV} < m_{H_1} < 128 \text{ GeV}$. Green points are for H_1 Region IA: $m_{A_1} > m_{H_1}/2$ and $|\xi_{H_1}^{h_v}|^2 > 0.7$. Red points are for H_1 Region IA: $m_{A_1} > m_{H_1}/2$ and $|\xi_{H_1}^{h_v}|^2 < 0.7$. Magenta points are for H_1 Region II: $m_{A_1} < m_{H_1}/2$. The black points are those where λ and κ remain perturbative up to the GUT scale.

larger values of κ , it reaches the Landau pole before the other couplings. While the running of λ is much slower, it has a large impact on the running of the gauge couplings and Yukawa couplings. Increasing the value of λ would accelerate the running of the top Yukawa coupling. However, for all the viable points that pass both the mass and cross section requirements, the scale at which at least one of the couplings becomes non-perturbative is typically larger than 10^7 GeV, much higher than the electroweak scale. Since adding new multiplets or other new physics could affect the running of the couplings and delay the Landau pole scale, in our study, we relax the perturbativity constraint and only place a loose upper bound of $\lambda, \kappa \leq 1$. All of our parameter points remain perturbative up to at least the scale of 10^7 GeV.

Panel (d) of Fig. II.14 shows the viable region in the $\tan\beta$ - $m_{A_{loop}}$ plane, where we have plotted $m_{A_{loop}}$ for better comparison with the MSSM.⁸ Unlike in the MSSM case, where constraints from collider direct Higgs searches and the light CP-even Higgs h^0 being SM-like require the parameters to be in the decoupling region of $m_A \gtrsim 300$ GeV [45], in the NMSSM, by contrast, with the push-down effect from the singlet mixing and the extra contribution from $\frac{1}{2}(\lambda v)^2 \sin^2 2\beta$ to the tree level mass squared for h_v , H_1 could be the SM-like Higgs in the low- m_A region: $m_{A_{loop}} \gtrsim 140$ GeV (while the tree-level m_A could be as low as a few GeV). The range of $\tan\beta$ is smaller compared to that of the MSSM:⁹ $1 \lesssim \tan\beta \lesssim 3$, since smaller $\tan\beta$ is preferred for providing a sizable contribution from the λ -term to the tree level Higgs mass $m_{h_v}^2$.

Panel (e) of Fig. II.14 shows a clear correlation between A_λ and μ . This is because a larger value of μ is needed to cancel the negative contribution from A_λ to keep $m_A^2 > 0$, as given in Eq. (II.C.29). Panel (f) of Fig. II.14 shows a weaker correlation between A_κ and μ . While larger μ is typically preferred for a larger negative A_κ , μ can not be too large since otherwise at least one of the CP-even Higgs masses squared becomes negative.

The magenta points in Fig. II.14 are in H_1 Region II: $m_{A_1} < m_{H_1}/2$. It maps out the region of small $|A_\kappa|$, $|A_\lambda|$ and μ : $-50 \lesssim A_\kappa \lesssim 30$ GeV, $-150 \lesssim A_\lambda \lesssim 150$ GeV, $100 \lesssim \mu \lesssim 200$ GeV. m_A is restricted to be in the range of 100 – 200 GeV ($m_{A_{loop}} \gtrsim 150$ GeV), and κ in the range of 0.5 – 1. Ranges for λ and $\tan\beta$, however, are not narrowed compared to the

⁸ m_A in the MSSM is the physical mass for the CP-odd Higgs A^0 , with loop corrections already included.

⁹ $\tan\beta \leq 3$ is excluded by the LEP Higgs searches in the MSSM [269].

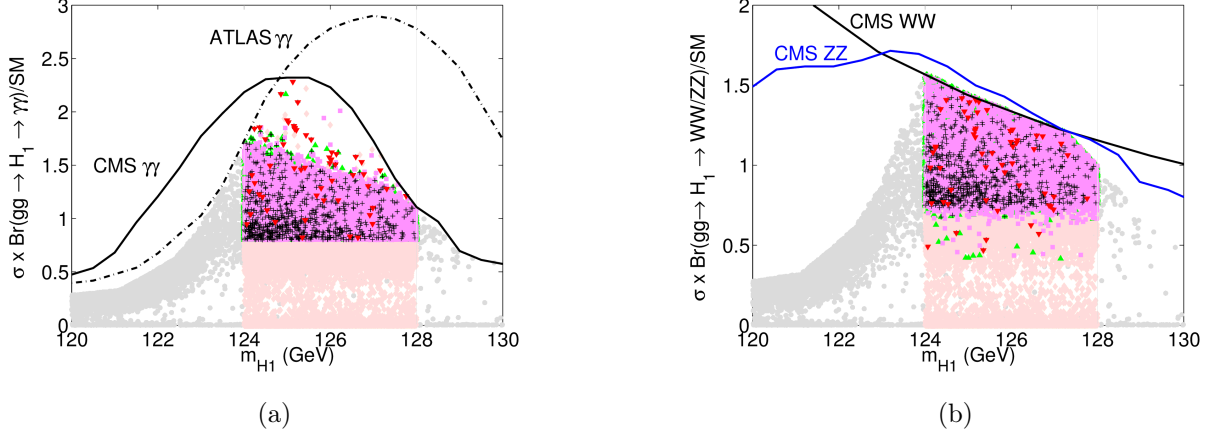


Figure II.15: The normalized $\sigma \times \text{Br}/\text{SM}$ for (a) $gg \rightarrow H_1 \rightarrow \gamma\gamma$ and (b) $gg \rightarrow H_1 \rightarrow WW/ZZ$ as a function of m_{H_1} in the H_1 -126 case. The current experimental constraints from the SM Higgs searches of the $\gamma\gamma$, WW and ZZ channels are also imposed. Color coding is the same as for Fig. II.14.

generic H_1 Region I, as shown as the green points in Fig. II.14.

Unlike in the MSSM case, where the mass parameters for the stop sector, M_{3SQ} and M_{3SU} , are correlated with the stop left-right mixing A_t to be close to the m_h^{max} scenario, $|A_t| \sim \sqrt{6M_{3SQ}M_{3SU}}$, there is no obvious correlation between M_{3SQ} , M_{3SU} , and A_t in the NMSSM. All the ranges are allowed for these parameters. This is because in the MSSM, we need large loop corrections to the Higgs mass from the stop sector to push it to the 124 – 128 GeV mass window, which requires either large stop masses around 5 – 10 TeV or large stop mixing. In the NMSSM, such a lift to the Higgs mass could be achieved by the $(\lambda v)^2$ contribution to the Higgs mass at tree level, resulting in a less constrained stop sector. The mass for the lightest stop can be as light as 100 – 200 GeV, with slightly larger mass splitting $\Delta m_{\tilde{t}} \gtrsim 200 - 300$ GeV anticipated for small $m_{\tilde{t}_1}$. However, once $m_{\tilde{t}_1} \gtrsim 400$ GeV, a degenerate stop mass spectrum can also be accommodated.

b. Production and Decays of the SM-like H_1 In Fig. II.15, we show the cross section ratios of NMSSM model to the Standard Model ($\sigma \times \text{Br}/\text{SM}$) for $gg \rightarrow H_1 \rightarrow \gamma\gamma$ in panel

(a) and $gg \rightarrow H_1 \rightarrow WW/ZZ$ in panel (b) as a function of m_{H_1} . The current 95% C.L. experimental exclusion limits for the SM Higgs searches in the $\gamma\gamma$, WW and ZZ channels are also imposed. While the $\gamma\gamma$ limit imposes strong constraints in the low m_{H_1} region, for m_{H_1} in the mass window of 124 – 128 GeV, the WW and ZZ cross section bounds are more important and rule out points with large $\sigma \times \text{Br}$. For the $\gamma\gamma$ channel, $\sigma \times \text{Br}/\text{SM}$ mainly varies in the range of 0.8 – 1.75, where the lower limit comes from our requirement of the signal region, as indicated by the current Higgs signal at both the ATLAS and CMS experiments [33, 34, 265]. Notice that for a few points, $\sigma \times \text{Br}/\text{SM}$ as large as 2 can be reached. For the WW/ZZ channel, $\sigma \times \text{Br}/\text{SM}$ varies mostly between the range of 0.7 – 1.6, with a few points that could reach a value of 0.5 or even smaller.

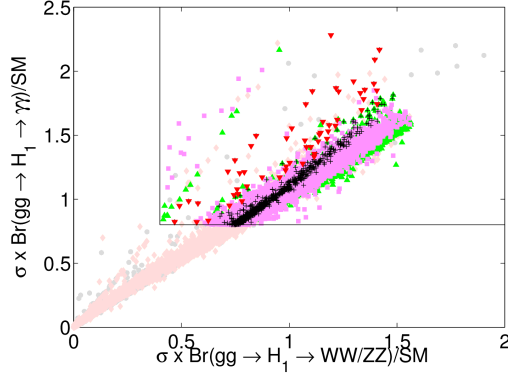
In the NMSSM, both the production cross section and decay branching fractions could deviate from their SM values. In the mass window of 124 – 128 GeV, $\sigma(gg \rightarrow H_1)/\sigma_{\text{SM}}$ typically varies between 0.6 – 1.4, although a suppression as small as 0.2 or an enhancement as large as 1.7 are also possible. For the decay branching fraction, $H_1 \rightarrow WW/ZZ$ ($\gamma\gamma$) is typically approximately 0.6–1.5 (0.6–2) of the SM value. There are a few points with very large enhancement factors, approximately 3–4 (5–6) for WW/ZZ ($\gamma\gamma$), which are needed to compensate the associated suppression from the gluon fusion production.

$H_1 \rightarrow \gamma\gamma$ and $H_1 \rightarrow WW/ZZ$ are highly correlated, as in the case of the MSSM scenario. This is because the loop generated $H_1\gamma\gamma$ coupling receives its dominant contribution from the W -loop and is therefore controlled by the same H_1WW coupling. Such correlation is shown in Fig. II.16, panel (a) for $\gamma\gamma$ versus VV . In the H_1 -126 case, most of the points fall into the region of

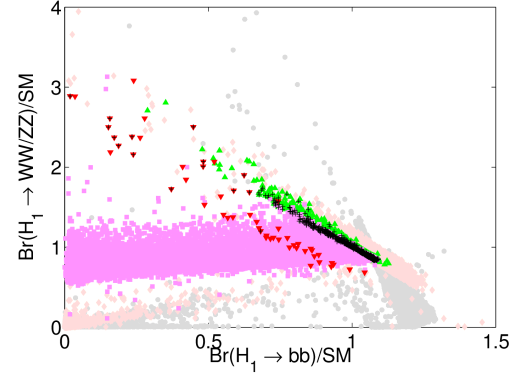
$$\frac{\sigma \times \text{Br}(gg \rightarrow H_1 \rightarrow \gamma\gamma)/(\sigma \times \text{Br})_{\text{SM}}}{\sigma \times \text{Br}(gg \rightarrow H_1 \rightarrow VV)/(\sigma \times \text{Br})_{\text{SM}}} = \frac{\text{Br}(H_1 \rightarrow \gamma\gamma)/\text{Br}_{\text{SM}}}{\text{Br}(H_1 \rightarrow VV)/\text{Br}_{\text{SM}}} \approx 1.1 \quad . \quad (\text{II.C.44})$$

However, there are a few scattered points with larger $\gamma\gamma : VV$ ratios. These points have an enhanced $H_1 \rightarrow \gamma\gamma$ partial width due to light stop contributions.

Unlike the correlation shown in the $\gamma\gamma$ versus VV channel, the correlation between the bb and VV channels exhibit interesting feature, as shown in Fig. II.16, panel (b), for $\frac{\text{Br}}{\text{Br}_{\text{SM}}}(H_1 \rightarrow bb)$ versus $\frac{\text{Br}}{\text{Br}_{\text{SM}}}(H_1 \rightarrow VV)$. For H_1 Region I, bb and WW are anti-correlated so that the VV channel is enhanced compared to the SM value only when the bb channel gets

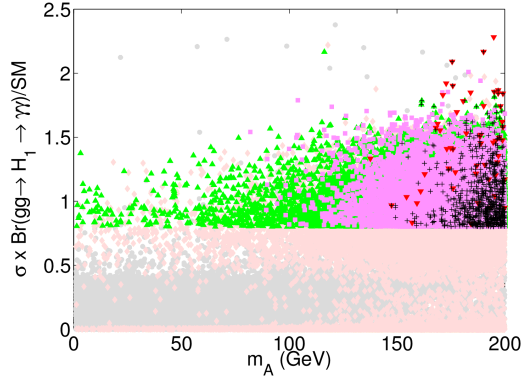


(a)

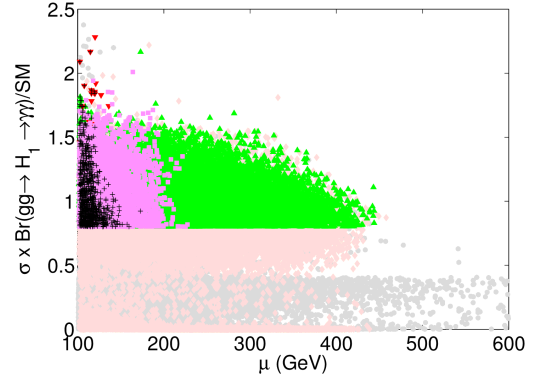


(b)

Figure II.16: The normalized $\sigma \times \text{Br}/\text{SM}$ for (a) $\gamma\gamma$ versus WW/ZZ channel and (b) the normalized $\text{Br}/\text{Br}_{\text{SM}}$ for WW/ZZ versus bb in the H_1 -126 case. Color coding is the same as for Fig. II.14.



(a)



(b)

Figure II.17: The normalized $\sigma \times \text{Br}/\text{SM}$ for $gg \rightarrow H_1 \rightarrow \gamma\gamma$ with (a) m_A dependence and (b) μ dependence in the H_1 -126 case. Color coding is the same as for Fig. II.14.

relatively suppressed. This is as expected since bb and VV are the two dominant H_1 decay channels for $m_{H_1} > 2m_{A_1}$.

For H_1 Region II with low m_{A_1} , however, no such correlation is observed. While $H_1 \rightarrow bb$ could be much suppressed compared to its SM value, $\text{Br}(H_1 \rightarrow VV)/\text{Br}_{\text{SM}}$ varies in the range of $0.5 - 1.5$, almost independently of $\text{Br}(H_1 \rightarrow bb)/\text{Br}_{\text{SM}}$. The opening of the $H_1 \rightarrow A_1 A_1$ channel in this mass window replaces $H_1 \rightarrow bb$ to keep $H_1 \rightarrow VV$ in the desired range to satisfy the cross section requirement.

The $\tau\tau$ and bb channels have also been searched for at the LHC, which indicate a weak SM Higgs signal of approximately $1 - 2\sigma$ [263, 264, 266, 267]. For the $\tau\tau$ channel, while the dominant contribution comes from the vector boson fusion (VBF) production, $gg \rightarrow H \rightarrow \tau\tau$ could be separated with a dedicated search [263, 266]. $H \rightarrow bb$ has been studied for both VH and ttH production, with better limits coming from VH associated production [264, 267]. In the NMSSM, since it is the same down-type Higgs H_d that couples to both the bottom quark and the tauon, $H_1 bb$ and $H_1 \tau\tau$ receive the same corrections (up to small difference in the radiative corrections that are non-universal for bottom and tau). Therefore, the bb and $\tau\tau$ channels are highly correlated: $\text{Br}(H_1 \rightarrow bb)/\text{Br}_{\text{SM}} \approx \text{Br}(H_1 \rightarrow \tau\tau)/\text{Br}_{\text{SM}}$. For VBF/VH $\rightarrow H_1 \rightarrow \tau\tau/bb$, $\sigma \times \text{Br}/\text{SM}$ is $\lesssim 1.1$. While for $gg \rightarrow H_1 \rightarrow \tau^+ \tau^-$, an enhancement as large as 1.5 of the SM value is possible, which is again from stop loop corrections to $gg \rightarrow H_1$. ttH_1 with $H_1 \rightarrow bb$ receives little enhancement, $\sigma \times \text{Br}/\text{SM} \lesssim 1.05$.

Fig. II.17 shows the parameter dependence of $\sigma \times \text{Br}/\text{SM}$ for $gg \rightarrow H_1 \rightarrow \gamma\gamma$ for m_A [panel (a)] and μ [panel (b)]. Larger values for $\sigma \times \text{Br}/\text{SM}$ is achieved for larger values of m_A and smaller values of μ . If a significant enhancement of $gg \rightarrow H_1 \rightarrow \gamma\gamma$ is observed in future experiments, m_A and μ (as well as A_λ) would be restricted to a narrower region.

c. Wave Function Overlap The deviation of the production and decay of H_1 can be traced back to the h_v , H_v and S fractions in H_1 , which is given by the wave function overlap $|\xi_{H_1}^{h_v}|^2$, $|\xi_{H_1}^{H_v}|^2$ and $|\xi_{H_1}^S|^2$, as defined in Eq. (II.C.38). Fig. II.18 shows $|\xi_{H_i}^S|^2$ versus $|\xi_{H_i}^{h_v}|^2$ for H_1 [panel (a)], H_2 [panel (b)] and H_3 [panel (c)]. Since $|\xi_{H_i}^{h_v}|^2 + |\xi_{H_i}^{H_v}|^2 + |\xi_{H_i}^S|^2 = 1$, the distance between the cross diagonal line and the points indicates the value of $|\xi_{H_i}^{H_v}|^2$. For the generic H_1 Region IA (green points), $|\xi_{H_1}^{h_v}|^2 + |\xi_{H_1}^S|^2 \sim 1$; the H_v -fraction in H_1 is almost 0.

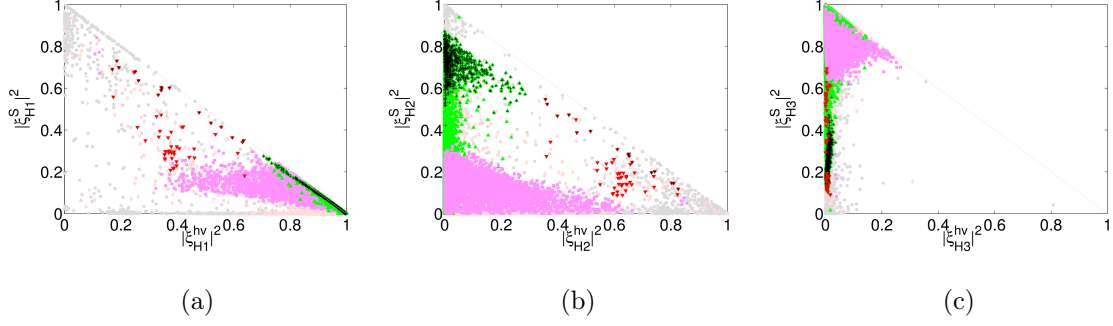


Figure II.18: $|\xi_{H_i}^S|^2$ versus $|\xi_{H_i}^{h_v}|^2$ for H_1 (a), H_2 (b) and H_3 (c) in the H_1 -126 case. Color coding is the same as for Fig. II.14.

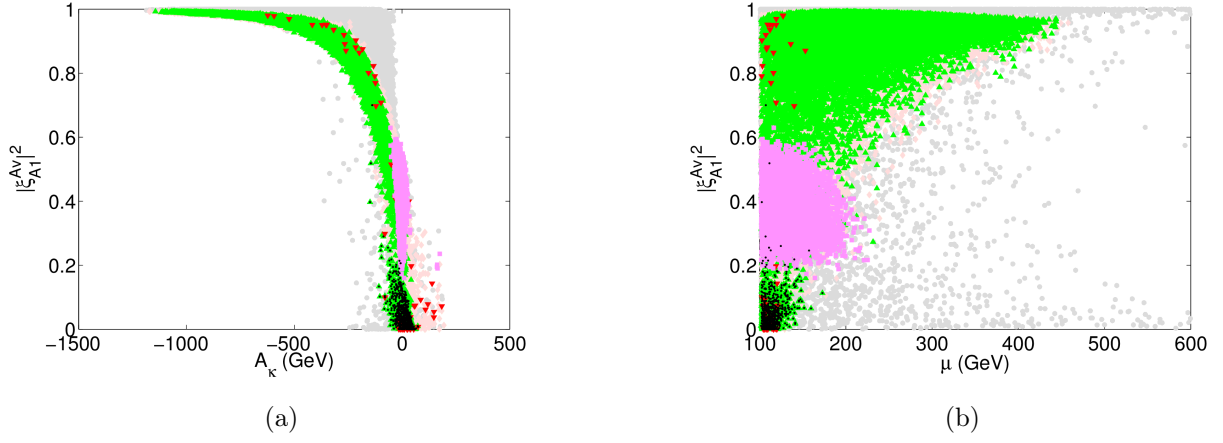


Figure II.19: A_v -fraction in the light CP-odd Higgs A_1 : $|\xi_{A_1}^{A_v}|^2 = 1 - |\xi_{A_2}^{A_v}|^2 = 1 - |\xi_{A_1}^{A_s}|^2$ in the H_1 -126 case. Color coding is the same as for Fig. II.14.

Typically, about 70% or more of H_1 is h_v , which couples exactly like the SM Higgs, while the singlet component varies between 0 to approximately 30%. For H_2 , it could be either H_v -dominant for those points with $|\xi_{H_2}^S|^2 \sim 0$, or a mixture of H_v and S for points with larger $|\xi_{H_2}^S|^2$. H_3 is mostly singlet-dominant, or with a small mixture of h_v for points close to the cross-diagonal line. It could also have a significant $H_v - S$ mixture for points with smaller $|\xi_{H_3}^S|^2$.

For the H_1 Region IB (red points), $|\xi_{H_1}^{h_v}|^2 < 0.7$, H_1 typically has a sizable fraction of H_v and S . H_2 is also a mixture of h_v , H_v and S , with H_3 being mostly a H_v - S mixture.

For H_1 in the low m_{A_1} region (magenta points of H_1 Region II), H_1 and H_2 are mostly a $h_v - H_v$ mixture, with H_1 being more h_v -like, and H_2 being more H_v -like. This region and Region IB share the property that they typically depend on a suppressed $H_1 b\bar{b}$ coupling proportional to $\xi_{H_i}^{h_v} - \xi_{H_i}^{H_v} \tan \beta$. The S fractions of Region II vary between 0 to 25% for both H_1 and H_2 , while it is the dominant component of H_3 .

Fig. II.19 shows the fraction of MSSM CP-odd Higgs A_v in the light CP-odd Higgs A_1 : $|\xi_{A_1}^{A_v}|^2$ as a function of A_κ [panel (a)] and μ [panel (b)]. The more negative A_κ becomes, the larger the diagonal mass term $m_{A_s}^2$ for the singlet A_s becomes, which results in A_1 becoming more and more A_v -like. The μ dependence also shows a trend of large μ leading to A_1 being more A_v -like, mainly due to the $-3\kappa/\lambda \mu A_\kappa$ contribution to the $m_{A_s}^2$ mass term. The A_s -fraction in A_1 , as well as the A_v -fraction in A_2 , is simply $1 - |\xi_{A_1}^{A_v}|^2$. For the points that satisfy the perturbativity requirement (black points), A_1 is mostly singlet like. For regions with small $m_{A_1} < m_{H_1}/2$ (magenta points), a significant fraction of A_1 , 40% to 80%, is singlet. While for generic H_1 Region I, A_1 could be either A_v -like (small m_A , large negative A_κ and A_λ , large μ , large κ) or A_s -like, depending on the NMSSM parameters. Note that while we are focusing on the low m_A region, which controls the mass scale for the MSSM-type CP-odd Higgs, the mass parameter for the CP-odd singlet Higgs could vary in a large range given the scanning parameter region. As a result, m_{A_1} is below 300 GeV, while the mass for the heavy CP-odd Higgs, m_{A_2} , could be as large as 1 TeV or higher.

4. H_2 as the SM-like Higgs Boson

a. Parameter Regions In the limit where the mixings between h_v , H_v and S are small, there are two cases that give rise to H_2 being SM-like: H_1 being singlet like and H_3 being mostly H_v ; or H_1 being mostly H_v -like and H_3 being mostly singlet. Including the loop corrections as well as mixture between h_v , H_v and S , the separation between these two cases becomes less distinct. The former case is similar to H_1 -126, except that the singlet is now the lightest state. The latter case is similar to the MSSM non-decoupling region, which requires a high level of fine-tuning to satisfy the experimental constraints, as well as mass and cross section requirements. As a result, in the NMSSM, while there are points with a relatively large H_v -fraction in H_1 , there is always a sizable S -fraction in H_1 as well.

Unlike the H_1 -126 case, where imposing the mass window on m_{H_1} already greatly narrows down the parameter regions while the cross section requirement usually does not provide further restriction, imposing the mass window in the H_2 -126 case ($124 \text{ GeV} < m_{H_2} < 128 \text{ GeV}$) does not greatly reduce the parameter space beyond the already restricted space from satisfying the experimental constraints. Requiring H_2 to have a SM-like $gg \rightarrow \gamma\gamma$, WW/ZZ rate, however, does further reduce the parameter space to be in the small $\tan\beta$, small μ , medium to large λ , and small $|A_\lambda|$ region, as summarized in Table. II.8. Note that compared to the H_1 -126 case, where m_A could be very small, in the H_2 -126 case, m_A is typically larger than about 100 GeV. We note, however, that $m_{A_{loop}}$ in both cases is greater than approximately 150 GeV. In the H_1 -126 case, the SM-like Higgs is pushed down and requires a larger stop-loop correction while in the present H_2 -126 case, the SM-like Higgs is pushed up and, as a result, requires less of a contribution from the stop sector. The stop mass parameters M_{3SQ} , M_{3SU} and A_t are therefore less restricted in the H_2 -126 case.

Also shown in Table II.8 is the region where λ and κ remain perturbative until the GUT scale. Unlike the H_1 -126 case in which $|A_t|$ is restricted to be $\gtrsim 1200 \text{ GeV}$, for the H_2 -126 case, $|A_t|$ is typically unrestricted.

While the light CP-odd Higgs A_1 is almost always heavier than $m_{H_2}/2$, the lightest CP-even Higgs H_1 could be lighter than $m_{H_2}/2$ such that the $H_2 \rightarrow H_1 H_1$ decay opens up. Although H_2 is typically h_v -like, it could obtain a relatively large S -fraction to suppress the

Table II.8: NMSSM Parameter region for the H_2 -126 case.

	$\tan \beta$	m_A (GeV)	μ (GeV)	λ	κ	A_λ (GeV)	A_κ (GeV)
$m_{H_2} \sim 126$	$\gtrsim 1$	0~200	100~300	0~0.75	0~1	-600~300	-1200~50
H_2 -126	1~3.25	100~200	100~200	0.4~0.75	$\gtrsim 0.05$	-300~300	-1200~50
perturb.	1.5~2.5	170~200	100~130	0.5~0.7	0.05~0.6	0~300	-300~50
$m_{H_1} < \frac{m_{H_2}}{2}$	1.25~2.5	125~200	100~150	0.5~0.75	$\gtrsim 0.3$	0~200	-500~-250

otherwise dominant decay mode $H_2 \rightarrow bb$. Therefore, we separate the H_2 -126 case into three regions:

- H_2 Region IA: $m_{H_1} > m_{H_2}/2$ and $|\xi_{H_2}^{h_v}|^2 > 0.5$: green points in Figs. II.20-II.23.
- H_2 Region IB: $m_{H_1} > m_{H_2}/2$ and $|\xi_{H_2}^{h_v}|^2 < 0.5$: red points in Figs. II.20-II.23.
- H_2 Region II: $m_{H_1} < m_{H_2}/2$: magenta points in Figs. II.20-II.23.

In Fig. II.20, we show the viable regions in various combinations of the NMSSM parameters. The first two panels show the (a) λ versus m_A , and (b) κ versus m_A regions. Small $m_A \lesssim 100$ GeV is not favored since the cross sections for $gg \rightarrow H_2 \rightarrow \gamma\gamma, WW/ZZ$ are suppressed. λ is typically in the range of 0.4 – 0.75. Smaller λ is not allowed due to the suppressed cross sections, while larger values of λ are not allowed due to charged Higgs mass bounds. κ varies over the whole range of 0 – 1, with larger values of m_A preferred for smaller κ .

Panel (c) of Fig. II.20 shows the viable region in the λ - κ plane. Regions with small λ satisfy the mass window but fail the cross section requirement. Also, shown in black, are those points that remain perturbative until the Planck scale, which spans a range of λ between 0.5 to 0.7 and κ between 0.1 and 0.5. Panel (d) of Fig. II.20 shows the viable region in the $\tan \beta$ - $m_{A_{loop}}$ plane. $\tan \beta$ falls into a range of 1.5 – 3.25, while $m_{A_{loop}}$ varies between 160 – 240 GeV (m_A varies between 100 – 200 GeV).

Panel (e) of Fig. II.20 shows a weak correlation between A_λ and μ . Regions of $A_\lambda \lesssim -300$ GeV fail the cross section requirement. There is also a correlation between A_κ and μ , as

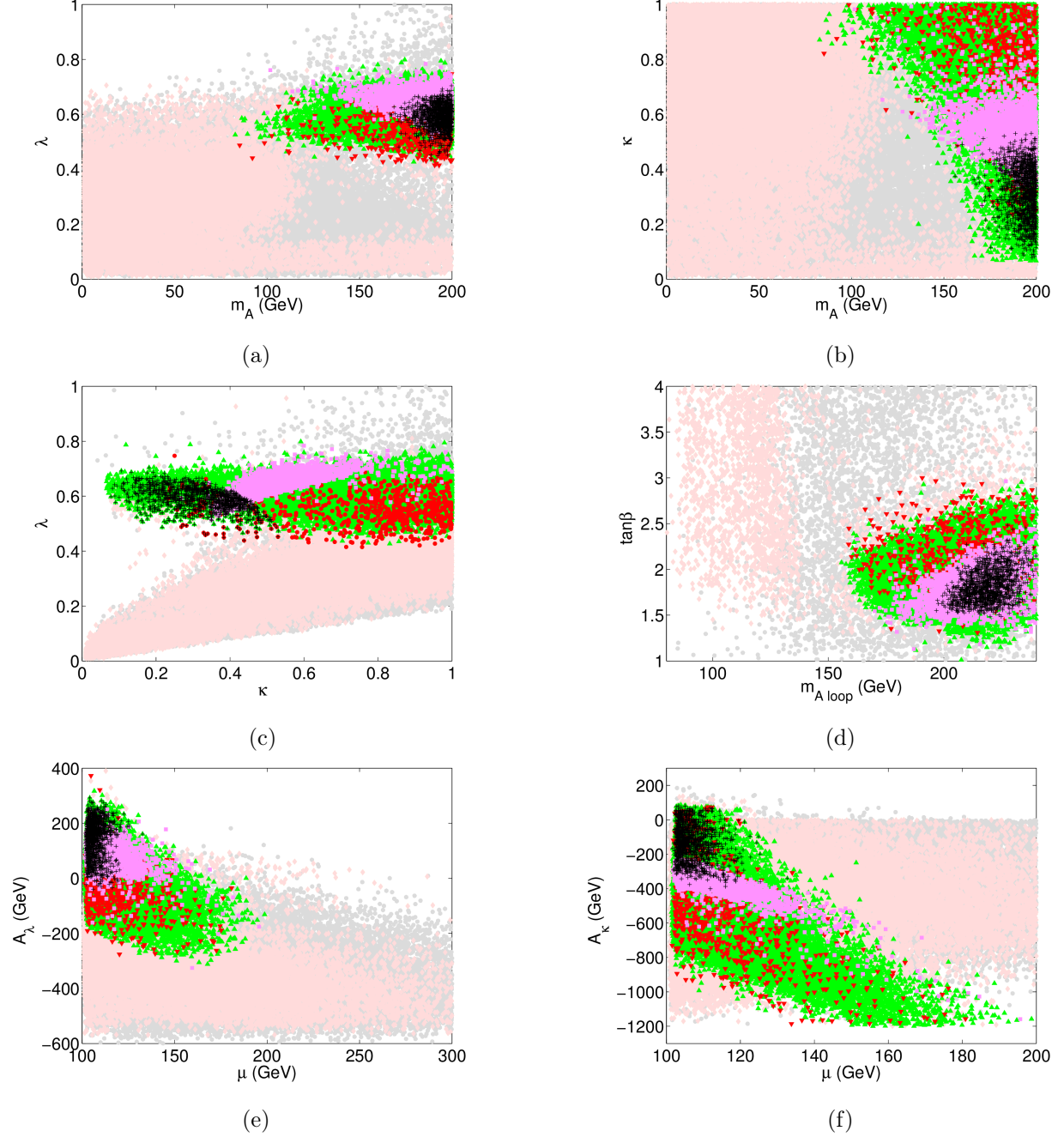


Figure II.20: Viable NMSSM parameter regions in the H_2 -126 case: (a) λ versus m_A , (b) κ versus m_A , (c) λ versus κ , (d) $\tan \beta$ versus $m_{A_{loop}}$, (e) A_λ versus μ , and (f) A_κ versus μ . Grey points are those that pass the experimental constraints, pale-pink points are those with H_2 in the mass window $124 \text{ GeV} < m_{H_2} < 128 \text{ GeV}$. Green points are for H_2 Region IA: $m_{H_1} > m_{H_2}/2$ with $|\xi_{H_2}^{h_v}|^2 > 0.5$. Red points are for H_2 Region IB: $m_{H_1} > m_{H_2}/2$ with $|\xi_{H_2}^{h_v}|^2 < 0.5$. Magenta points are for H_2 Region II: $m_{H_1} < m_{H_2}/2$. The black points are those where λ and κ remain perturbative up to the GUT scale.

shown in panel (f) of Fig. II.20. This is because in the H_2 -126 case, most H_1 are singlet-like. The CP-even singlet mass needs to be smaller than m_{h_v} and is typically controlled by the cancellation between a positive μ parameter and a negative A_κ term, as shown in Eq. (II.C.36). This correlation can be seen more clearly in H_2 Region II (magenta points) where finer cancellation is enforced.

The magenta points in Fig. II.20 are for H_2 Region II: $m_{H_1} < m_{H_2}/2$. They span the region of small $|A_\kappa|$, $|A_\lambda|$ and μ , intermediate κ , $m_A \sim 200$ GeV, and $1.5 \lesssim \tan \beta \lesssim 2$, as summarized in Table II.8.

b. Production and Decays for the SM-like H_2 The ranges of $\sigma \times \text{Br}/\text{SM}$ for $gg \rightarrow H_2 \rightarrow \gamma\gamma$, shown in Fig. II.21, is slightly large than that of the H_1 -126 case. An enhancement as large as a factor of 2 can be achieved in the present case. For $gg \rightarrow H_2 \rightarrow WW/ZZ$, the $\sigma \times \text{Br}/\text{SM}$ is typically in the range of 0.4 – 1.6, and bounded above by the current experimental searches in the WW/ZZ channels. Note that a relatively strong suppression of about 0.4 could be accommodated more easily than in the H_1 -126 case.

$H_2 \rightarrow \gamma\gamma$ and $H_2 \rightarrow WW/ZZ$ are also highly correlated, as shown in Fig. II.22, panel (a) for $\gamma\gamma$ versus WW/ZZ . There are several branches, corresponding to H_2 Region IA and IB as categorized in Sec. II.C.4.a. For Region IA (green points) with H_2 being mostly h_v -dominant, $\frac{\text{Br}(H_1 \rightarrow \gamma\gamma)/(\text{Br})_{\text{SM}}}{\text{Br}(H_1 \rightarrow WW)/(\text{Br})_{\text{SM}}} \approx 1.1$ for the lower branch of green points. However, there is another branch with a higher value of $\frac{\text{Br}(H_1 \rightarrow \gamma\gamma)/(\text{Br})_{\text{SM}}}{\text{Br}(H_1 \rightarrow WW)/(\text{Br})_{\text{SM}}} \approx 2$. Those points typically have an enhanced $H_2 \rightarrow \gamma\gamma$ compared to the SM value due to the light stop contributions. For Region IB (red points) with H_2 being a mixture of h_v , H_v and S , $\frac{\text{Br}(H_1 \rightarrow \gamma\gamma)/(\text{Br})_{\text{SM}}}{\text{Br}(H_1 \rightarrow WW)/(\text{Br})_{\text{SM}}} \approx 1.4$.

In Fig. II.22, panel (b), we show the correlation between the bb and VV channel: $\text{Br}(H_2 \rightarrow bb)/\text{Br}_{\text{SM}}$ versus $\text{Br}(H_2 \rightarrow VV)/\text{Br}_{\text{SM}}$. While most regions exhibit an anti-correlation as expected, in H_2 Region II (magenta points) with $m_{H_1} < m_{H_2}/2$, the branching fraction for the VV channel is almost independent of the bb channel. This is, similar to the magenta region in the H_1 -126 case, due to an opening up of the decay channel $H_2 \rightarrow H_1 H_1$, which compensates for the suppression of the bb channel while keeping the total decay width of H_2 close to the SM value.

The bb and $\tau\tau$ channels also exhibit a similar correlation behavior as in the H_1 -126 case:

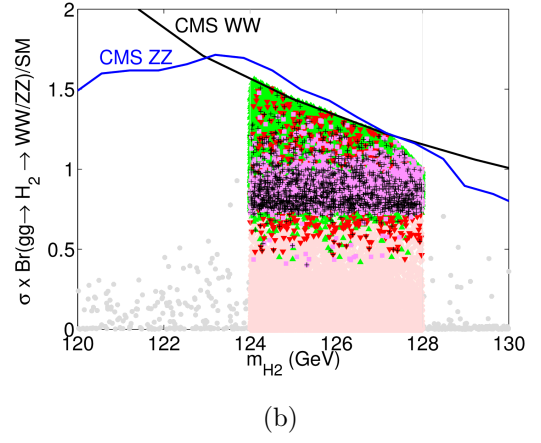
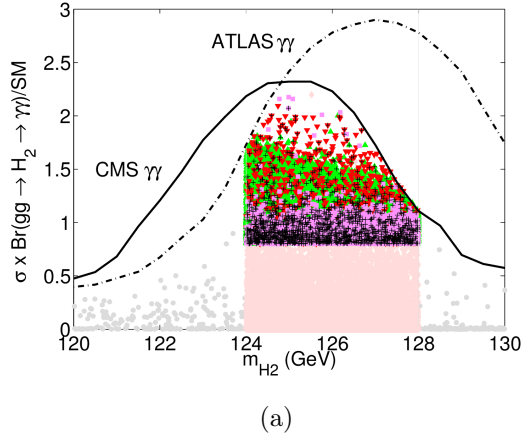


Figure II.21: The normalized $\sigma \times \text{Br}/\text{SM}$ for (a) $gg \rightarrow H_2 \rightarrow \gamma\gamma$ and (b) $gg \rightarrow H_2 \rightarrow WW/ZZ$ as a function of m_{H_2} in the H_2 -126 case. The current experimental constraints from the SM Higgs searches of the $\gamma\gamma$, WW and ZZ channels are also imposed. Color coding is the same as for Fig. II.20.

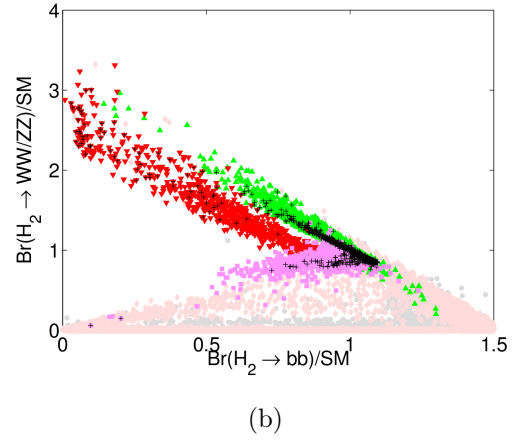
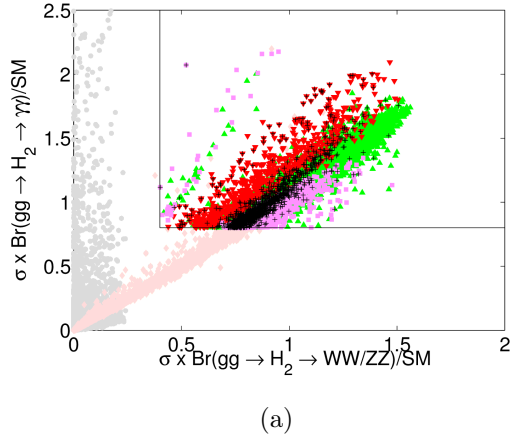


Figure II.22: The normalized $\sigma \times \text{Br}/\text{SM}$ for (a) $\gamma\gamma$ versus WW/ZZ channel, and the normalized $\text{Br}/\text{Br}_{\text{SM}}$ for (b) WW/ZZ versus bb in the H_2 -126 case. Color coding is the same as for Fig. II.20.

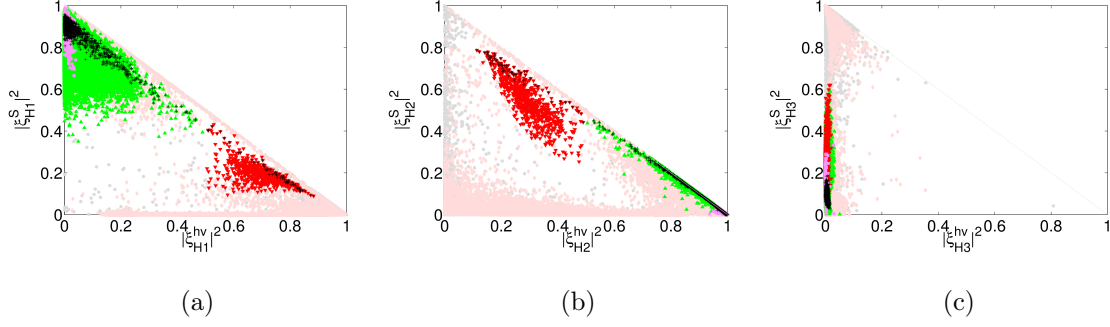


Figure II.23: $|\xi_{H_i}^S|^2$ versus $|\xi_{H_i}^{h_v}|^2$ for H_1 (a), H_2 (b) and H_3 (c) in the H_2 -126 case. Color coding is the same as for Fig. II.20.

$\text{Br}(H_2 \rightarrow bb)/\text{Br}_{\text{SM}} \approx \text{Br}(H_2 \rightarrow \tau\tau)/\text{Br}_{\text{SM}}$. For VBF and VH with $H_2 \rightarrow \tau\tau, bb$, $\sigma \times \text{Br}/\text{SM}$ is in the range of $0.4 - 1.1$ for H_2 Region IA and is much suppressed in Region IB and is $\lesssim 0.4$. For $gg \rightarrow H_2 \rightarrow \tau^+\tau^-$, most of the H_2 Region IA falls into the range of $0.4 - 1.4$, although an enhancement as large as 2 is possible. For Region IB, this channel is almost always suppressed with $\sigma \times \text{Br} \lesssim 0.8(\sigma \times \text{Br})_{\text{SM}}$. The process ttH_2 with $H_2 \rightarrow bb$ receives little enhancement, with $\sigma \times \text{Br}/\text{SM} \lesssim 1.06$ for Region IA and $\sigma \times \text{Br}/\text{SM} \lesssim 0.7$ for Region IB.

c. Wave Function Overlap Fig. II.23 shows $|\xi_{H_i}^S|^2$ versus $|\xi_{H_i}^{h_v}|^2$ for (a) H_1 , (b) H_2 and (c) H_3 . For H_2 Region II (magenta points), H_1 is mostly singlet, H_2 is mostly h_v and H_3 is mostly H_v .

For H_2 region IA (green points) with $|\xi_{H_2}^{h_v}|^2 > 0.5$, while H_2 is mostly h_v -like by definition, its H_v -fraction is almost always small. In contrast, while H_1 is dominated by S , it could have a relatively large H_v -fraction. H_3 is typically a mixture of S and H_v , with the H_v -fraction always being sizable: $|\xi_{H_3}^{H_v}|^2 \gtrsim 0.4$. The h_v -fraction in H_3 is almost negligible.

For H_2 region IB (red points) with $|\xi_{H_2}^{h_v}|^2 < 0.5$, the singlet fraction in H_2 could be significant, sometime even as large as 0.8. While the h_v -fraction in H_2 decreases, it increases accordingly in H_1 : $|\xi_{H_1}^{h_v}|^2 > 0.5$. This opens up the possibility of H_1 with sizable $H_1 WW/H_1 ZZ$ couplings that we will discuss in the next section. Both H_1 and H_2 could

have a fraction of H_v as large as 0.3–0.4. H_3 , on the other hand, is mostly a mixture of H_v and S , with the h_v -fraction being negligible.

The compositions of A_1 and A_2 are similar to that of the H_1 -126 case. Larger negative values of A_κ lead to a large fraction of A_1 being A_v . However, for $A_\kappa \sim 0$, A_1 could be mostly A_s .

5. LHC Phenomenology for the Non-SM-like Higgs Bosons

In the previous sections, we have presented two very interesting scenarios in the low- m_A region. The SM-like Higgs boson could be the lightest scalar particle (H_1 -126) while the next lightest one is an admixture of its MSSM partner and the singlet state. The alternative is that the SM-like Higgs boson is the second lightest (H_2 -126) while the lightest scalar is a H_v - S - h_v mixture. While the collider phenomenology of the SM-like Higgs boson has been shown earlier, it would be interesting to identify the signal features of the other low-mass Higgs bosons.

a. H_1 as the SM-like Higgs Boson In Fig. II.24(a), we show the dominant production cross sections of gg fusion and VBF for H_1 (red and pink points), H_2 (green and light green points) and H_3 (blue and light blue points), respectively, satisfying all the constraints for the H_1 -126 case at the 14 TeV LHC. The yellow lines indicate the corresponding cross sections with SM couplings. When the h_v -fraction is sizable, the production cross sections for H_2 could be similar to the SM-like rate. The cross sections could also be suppressed by two orders of magnitudes if the S -fraction is large, as for the H_3 case. The VBF process can be more significantly suppressed than that of gg fusion. The production cross section for the CP-odd states $A_{1,2}$ from gg fusion via triangle loop diagrams is shown in Fig. II.24(b). The rate can be similar to that of the SM-like Higgs boson and the spread of the cross section over the parameter scan is roughly about an order of magnitude, less pronounced than those for the CP-even cases. Although about an order magnitude lower, the production cross section from $b\bar{b}$ annihilation can be significantly larger than that of the SM value, due to the $\tan\beta$ enhancement.

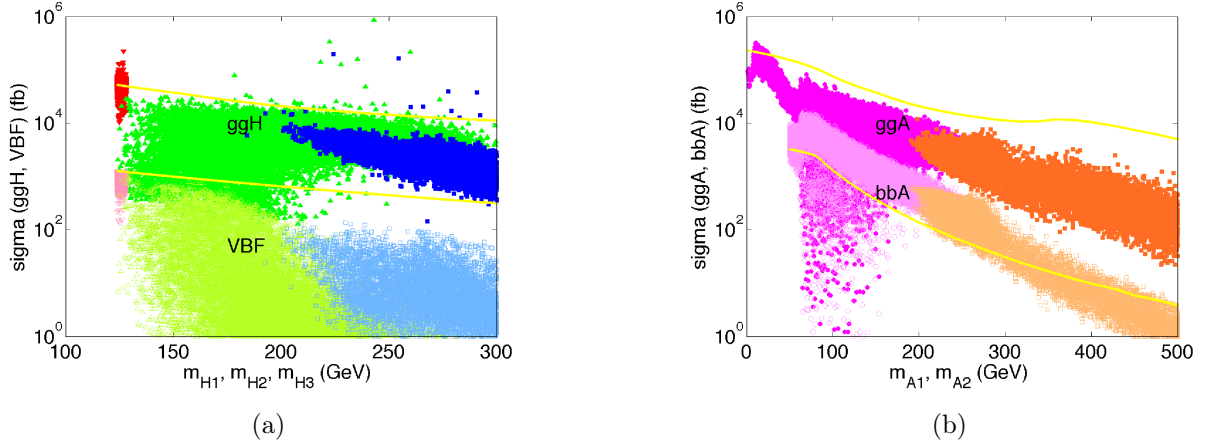


Figure II.24: Cross sections at the 14 TeV LHC in the H_1 -126 case for (a) $H_{1,2,3}$ production via gg fusion (VBF) denoted by red (pink), green (light green), blue (light blue) points, respectively, and for (b) $A_{1,2}$ production via gg fusion ($b\bar{b}$ fusion) denoted by purple (light purple), brown (light brown) points, respectively. The yellow lines indicate the cross sections with SM couplings.

In Fig. II.25, we further show the relevant branching fractions for $H_{1,2,3}$, $A_{1,2}$ and H^\pm to the SM particles (and $H_{2,3} \rightarrow \tilde{t}_1\tilde{t}_1$) for the case of H_1 -126. The yellow lines indicate the corresponding branching fraction values with SM couplings. The non SM-like Higgs bosons typically have suppressed decay branching fractions to the regular SM channels, in particular for H_3 , due to the opening up of new decay channels to lighter Higgs bosons pairs. The experimental searches for those new Higgs bosons at the LHC will continue to cover a broad parameter region. A_1 decays dominantly to $b\bar{b}$, with about 10% to $\tau^+\tau^-$, as shown in Fig. II.25(e). The phenomenological consequences of this decay have been studied in the literature [247, 270–272], emphasizing the $h \rightarrow A_1A_1 \rightarrow 4\tau, 4b, 2\tau 2b$ modes and we will not discuss them further here. One of the most striking results for the CP-odd Higgs decay, perhaps, is the potentially very large enhancement for the branching fraction $A_1 \rightarrow \gamma\gamma$, as seen in Fig. II.25(e). This is partly because of the reduced Γ_{tot} caused by the suppression of the $A_1\bar{b}b$ coupling, and partly because of the enhanced $\Gamma(A_1 \rightarrow \gamma\gamma)$ due to the loop contributions from the light charginos and charged Higgs bosons, and from the top and stop.

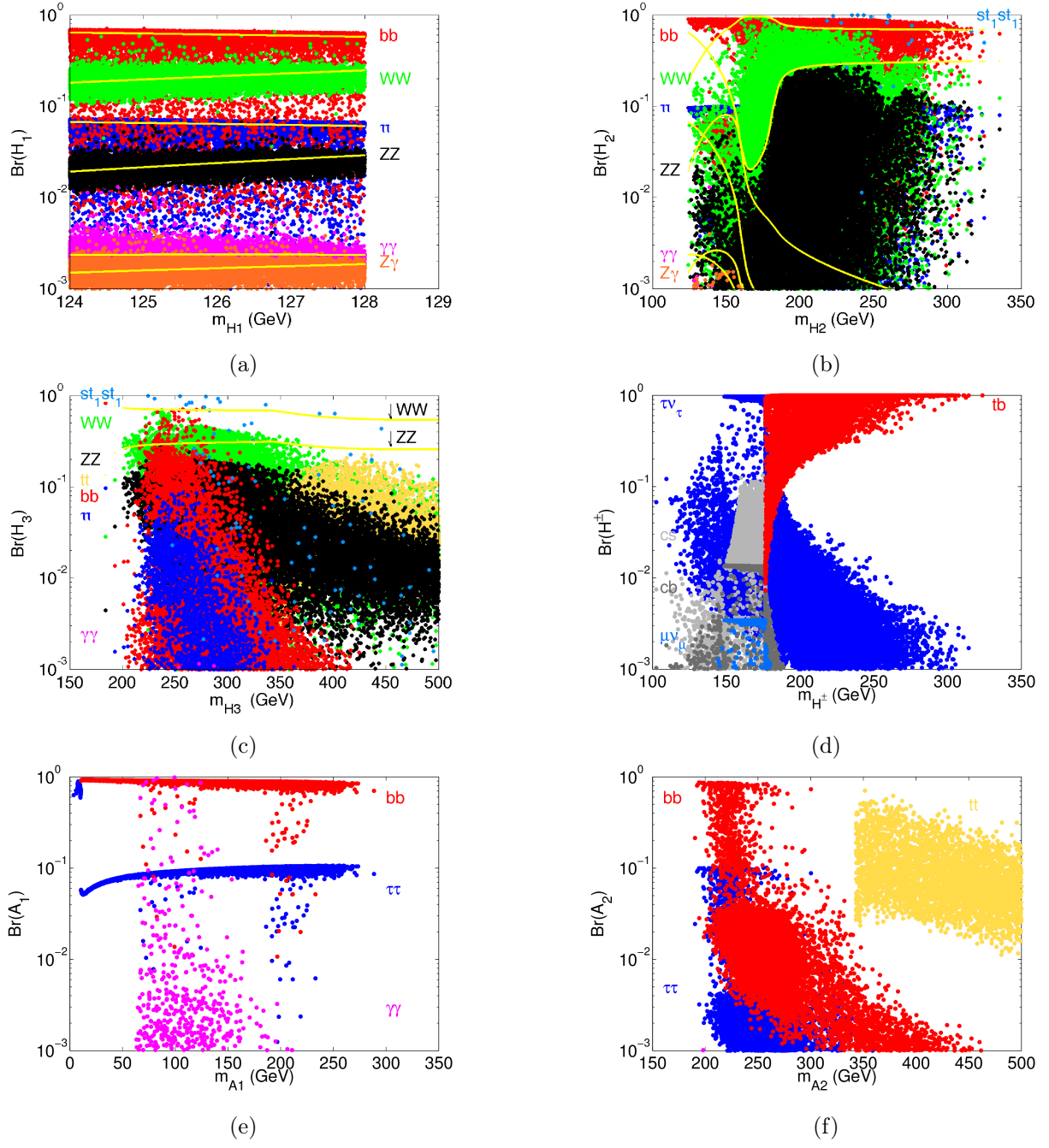


Figure II.25: Decay branching fractions for $H_{1,2,3}$, $A_{1,2}$ and H^\pm to the SM particles (and $H_{2,3} \rightarrow \tilde{t}_1 \tilde{t}_1$) in the case of H_1 -126. The yellow lines indicate the corresponding values with the SM couplings.

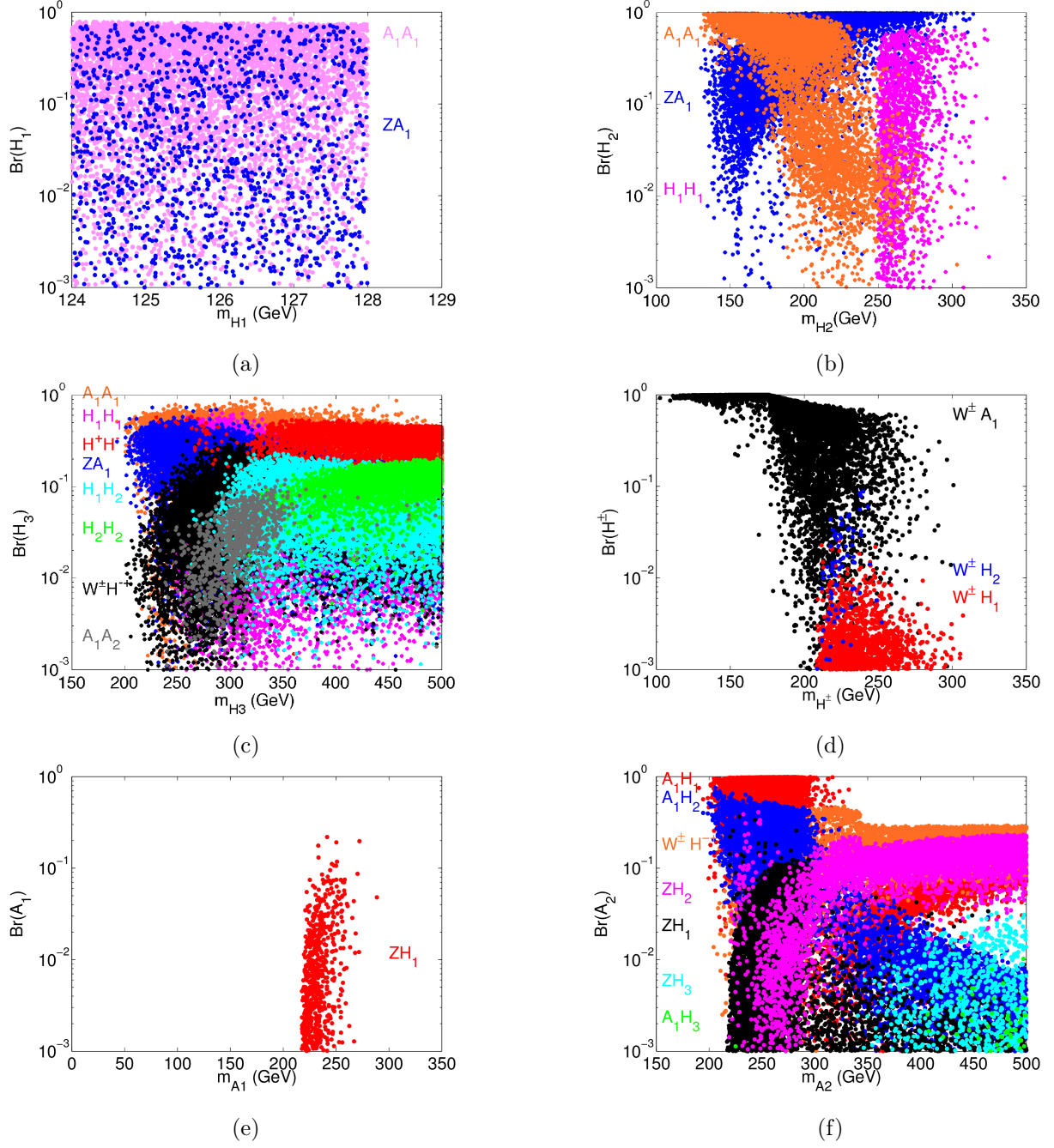


Figure II.26: Decay branching fractions for $H_{1,2,3}$, $A_{1,2}$ and H^\pm to Higgs bosons in the case of H_1 -126.

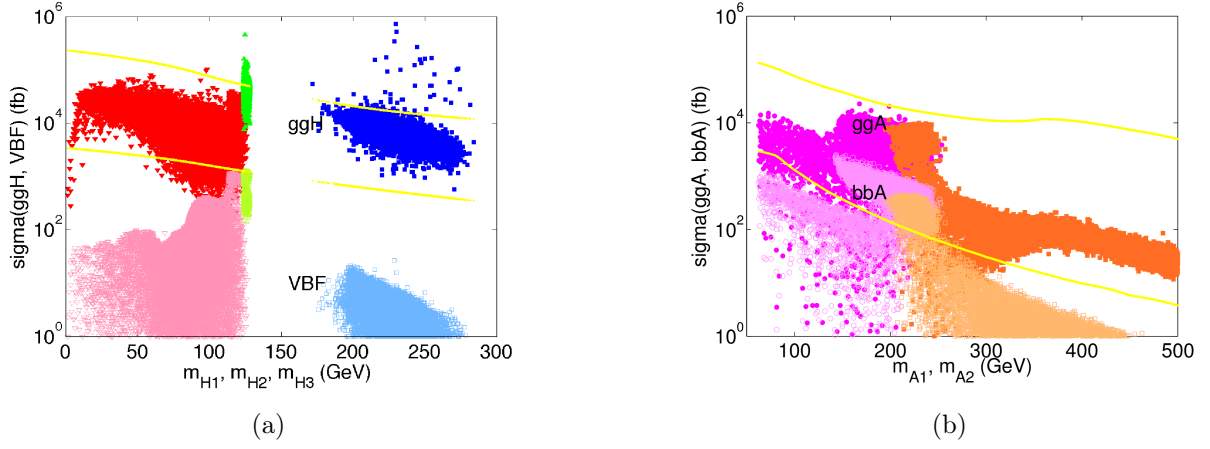


Figure II.27: Cross sections at the 14 TeV LHC in the H_2 -126 case. The color codes and the legends are the same as in Fig. II.24.

In the pure singlet limit, the dominant viable decay channel is $A_1 \rightarrow \gamma\gamma$ induced by the chargino loop and charged Higgs loop from their non-suppressed couplings with the singlet. However, the chargino in our case is always much lighter than the charged Higgs, granting non-zero $A_1\gamma\gamma$ coupling. The total width could be as low as around 10^{-6} GeV. This may lead to interesting scenarios with a proper LSP that produces a greatly suppressed low-end $\gamma\gamma$ continuum for an indirect dark matter search [273] such as Fermi-LAT.

Another interesting feature is that the CP-even heavy Higgs bosons could decay to a pair of stops when kinematically accessible. It is important to note that a heavier Higgs boson could decay to a pair of lighter Higgs bosons at a substantial rate and sometimes dominantly, as long as kinematically accessible. As shown in Fig. II.26 for the case of H_1 -126, we see that

$$H_1 \rightarrow A_1 A_1, \quad Z A_1, \quad (II.C.45)$$

$$H_2 \rightarrow A_1 A_1, \quad Z A_1, \quad H_1 H_1, \quad (II.C.46)$$

$$H_3 \rightarrow A_1 A_1, \quad H_1 H_1, \quad Z A_1, \quad W^\pm H^\mp, \quad A_1 A_2, \quad H_1 H_2, \quad H_2 H_2, \quad H^+ H^-, \quad (II.C.47)$$

$$H^\pm \rightarrow W^\pm A_1, \quad W^\pm H_2, \quad W^\pm H_1, \quad (II.C.48)$$

$$A_1 \rightarrow Z H_1, \quad (II.C.49)$$

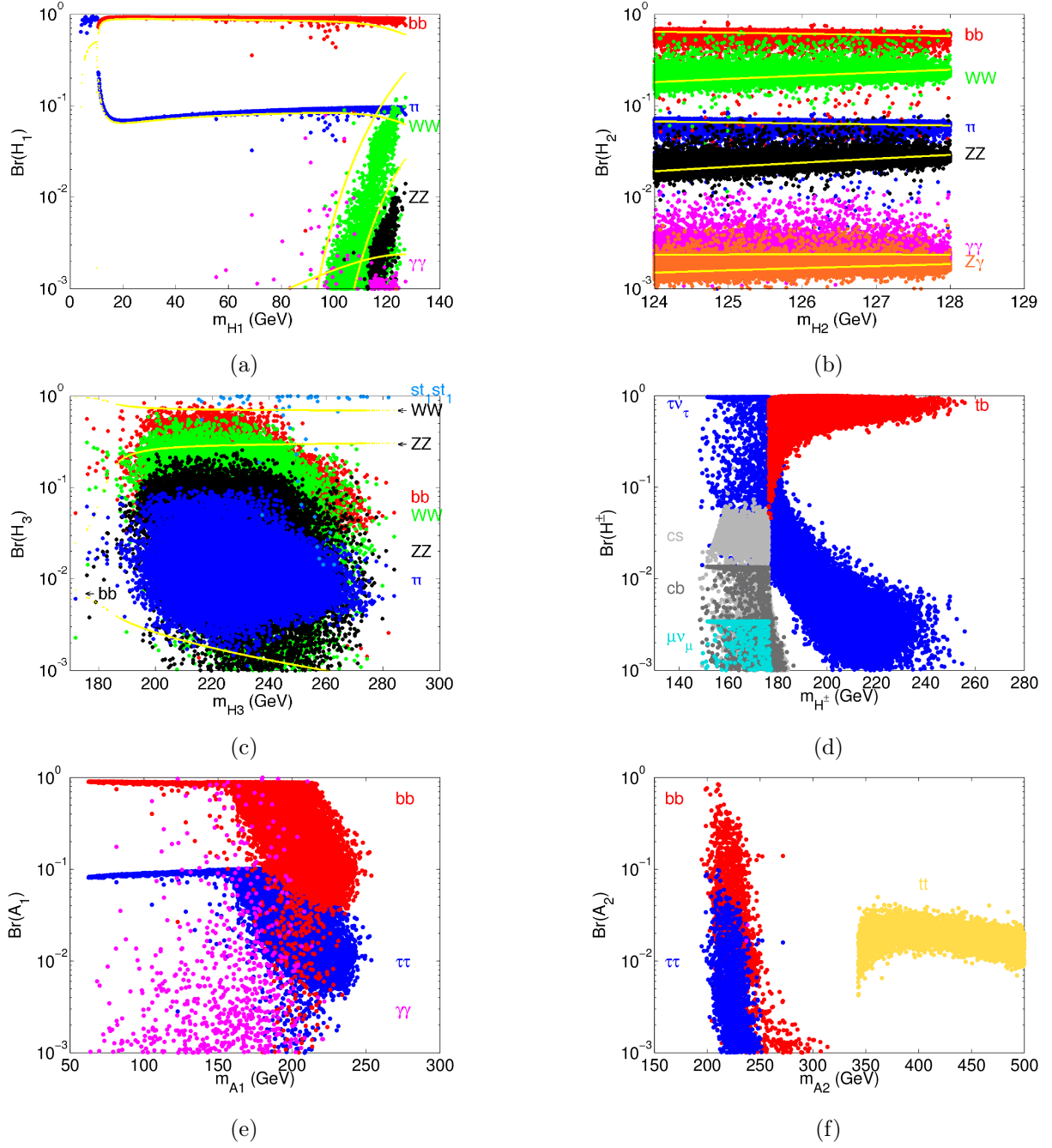


Figure II.28: Decay branching fractions for $H_{1,2,3}$, $A_{1,2}$ and H^\pm to the SM particles (and $H_3 \rightarrow \tilde{t}_1 \tilde{t}_1$) in the case of H_2 -126. The yellow lines indicate the corresponding values with the SM couplings.

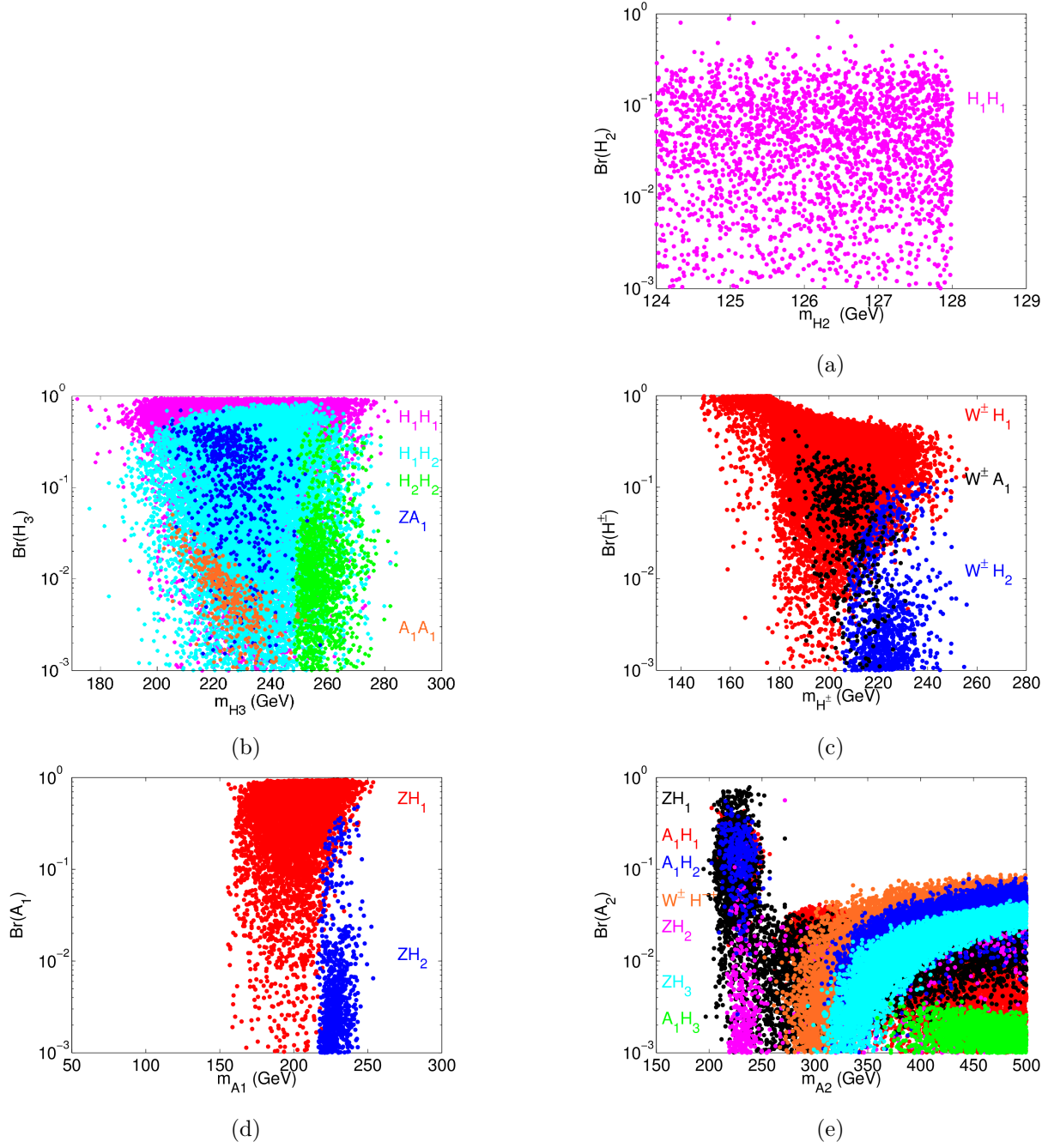


Figure II.29: Decay branching fractions for $H_{1,2,3}$, $A_{1,2}$ and H^\pm to Higgs bosons in the case of H_2 -126.

$$A_2 \rightarrow A_1 H_1, \quad A_1 H_2, \quad W^\pm H^\mp, \quad Z H_1, \quad Z H_2, \quad Z H_3, \quad A_1 H_3, \quad (\text{II.C.50})$$

roughly according to the sizes of the branching fractions at the low values of the mass. The relative branching fractions depend on phase space factors and the couplings dictated by the MSSM and singlet components. Consequently, the striking signals will be multiple heavy quarks, such as $4b$, $4t$ and $2b2t$, and will likely include $\tau^+\tau^-$ as well. While the final state with a W or Z may be a good channel from the event identification view point, the final states with multiple heavy quarks may be rather challenging to separate out from the large SM backgrounds.

b. H_2 as the SM-like Higgs Boson Similar results for the Higgs production and decay channels are shown in Figs. II.27–II.29, respectively, at the 14 TeV LHC for the H_2 -126 case. It is interesting to note that H_1 is non-SM-like, and lighter than H_2 , yet it could have as large a production cross section as H_2 . Although the branching fractions to WW , ZZ , and $\gamma\gamma$ are somewhat smaller than those for the SM, these clean signals can be searched for in the near future. For example, the H_1 could have a sufficient coupling with vector boson pairs to be responsible for the approximately 98 GeV excess at LEP [57, 269, 274].

Again, we find it very interesting that a heavier Higgs state could dominantly decay to a pair of lighter Higgs bosons. Note that H_1 is non-SM-like and light, so that there are no Higgs pair channels for it to decay to. We see, from Fig. II.29,

$$H_2 \rightarrow H_1 H_1, \quad (\text{II.C.51})$$

$$H_3 \rightarrow H_1 H_1, \quad H_1 H_2, \quad Z A_1, \quad A_1 A_1, \quad H_2 H_2, \quad (\text{II.C.52})$$

$$H^\pm \rightarrow W^\pm H_1, \quad W^\pm A_1, \quad W^\pm H_2, \quad (\text{II.C.53})$$

$$A_1 \rightarrow Z H_1, \quad Z H_2, \quad (\text{II.C.54})$$

$$A_2 \rightarrow Z H_1, \quad A_1 H_1, \quad A_1 H_2, \quad Z H_2, \quad W^\pm H^\mp, \quad Z H_3, \quad A_1 H_3, \quad (\text{II.C.55})$$

again roughly according to the sizes of the branching fractions at the low values of the mass. The collider signatures would be multiple heavy quarks, τ 's, and multiple gauge bosons as commented in the last section. The Higgs pair final states from the decay may serve as an important window for a new discovery.

It was previously noted [45, 275] that in the low- m_A region, the direct production of the Higgs boson pairs may be quite accessible at the LHC due to the model-independent

gauge couplings for $H^+H^-\gamma$ and $H^\pm AW^\mp$. Additional studies include processes such as $H_3 \rightarrow H_2H_1$ [276], low mass H^\pm with light A_1 [277], two low mass Higgs scenarios [278] and Higgs boson pair productions [279].

6. Summary and Outlook

In the framework of the Next to Minimal Supersymmetric Standard Model, we study the Higgs sector in light of the discovery of the SM-like Higgs boson at the LHC. We pay particular attention to the light Higgs states in the case when the parameter $m_A \lesssim 2m_Z$. Our results, coming from a broad parameter scan after implementing the current collider constraints from Higgs physics, lead to the following findings:

- The Higgs bosons in the NMSSM, namely three CP-even states, two CP-odd states, and two charged Higgs states, could all be rather light, near or below the electroweak scale (v), although the singlet-like state can be heavier. The SM-like Higgs boson could be either the lightest CP-even scalar as in Fig. II.12(a), or the second lightest CP-even scalar as in Fig. II.12(c), but is unlikely to be the heaviest scalar as in Fig. II.12(e).
- If we relax the perturbativity requirement by allowing the NMSSM parameters λ and κ to be larger (see Tables II.7 and II.8), the allowed region for the mass parameters would be enlarged significantly (e.g., black versus green, red and magenta points in Fig. II.13, Fig. II.14 and Fig. II.20, etc.).
- The SM-like Higgs signal at the LHC may be appreciably modified, as shown in Figs. II.24(a) and II.27(a) for production, and Figs. II.25(a) and II.28(b) for decay.
- Consequently, the $\gamma\gamma$ rate can be enhanced (Figs. II.15, II.17 and II.21). The naive correlations of $\gamma\gamma/VV$ and $VV/b\bar{b}$ ratios can be violated (Figs. II.16 and II.22). Furthermore, if the SM-like Higgs can decay to a pair of lighter Higgs bosons, the anti-correlation in the $VV/b\bar{b}$ ratio can be further broken (magenta regions of Figs. II.16(b) and II.22(b)).
- New Higgs bosons beyond the SM may be readily produced at the LHC. The production cross sections via gg fusion and VBF could be of the same orders of magnitude as those of the SM productions (Figs. II.24 and II.27). Their decay branching fractions to the SM

particles could be even larger than those of the SM (Figs. II.25 and II.28), depending on $\tan \beta$ and the size of their SM-like Higgs fractions (Figs. II.18 and II.23).

- The unique channels for the heavy Higgs signal are the decays to a pair of light Higgs bosons (Figs. II.26 and II.29). The striking signals will be multiple heavy quarks (t , b) and tau-leptons in the final states.

D. SUSY DARK MATTER IN MSSM

With the ever increasing experimental sensitivity of DM detection experiments, we are motivated to explore to what extent DM properties have been constrained by the results from particle accelerator experiments. Our goal is to systematically examine the complementarity between DM direct detection experiments, indirect detection searches, and collider experiments, and in particular explore the potential pivotal role played by the Higgs bosons. We perform a comprehensive study in the framework of the MSSM. We impose the following constraints on our model considerations:

- (1) **Relic abundance:** the neutralino LSP constitutes all the cold DM, consistent with the cosmological observations [78, 79].
- (2) **Collider constraints:** the MSSM parameter space satisfies all collider constraints from the Higgs boson searches and has a SM-like Higgs boson near 126 GeV.
- (3) **Flavor constraints:** the parameter space satisfies the flavor constraints from $b \rightarrow s\gamma$ [280], $B_s \rightarrow \mu^+\mu^-$ [281].

We further check the consistency of the annihilation rate at zero velocity $\langle \sigma_a v \rangle (v \rightarrow 0)$ with CMB observations, and the absence of gamma rays from nearby dwarf galaxies [72, 86]. It is known that the spin-independent WIMP-nucleon elastic scattering cross section obtained by the XENON-100 experiment [68] puts a very strong bound on the MSSM parameter space. We find that the surviving region has characteristic features, notably a Bino-like LSP. What is most interesting to us is that all these scenarios would lead to definitive predictions for the LHC experiments, that can be verified by the next generation of direct/indirect search

experiments such as LUX [69] and XENON-1T [70].

The rest of the section is organized as follows. In Section II.D.1, we discuss our technique for scanning the MSSM parameter space. In Section 4, we present our results, and discuss the experimental constraints from the Higgs and flavor searches. We also discuss the constraints on the parameter space imposed by the XENON-100 search for spin-independent scattering, as well as the Super-K and IceCube/DeepCore limits on spin-dependent scattering. We show that future experiments such as LUX and XENON-1T will likely probe the natural supersymmetric parametric space consistent with the LSP constituting all the DM. We present extensive discussions of our results in Section II.D.3 and finally draw our conclusions in Section II.D.4.

1. The MSSM Parameters Relevant to DM studies

In SUSY theories with conserved R-parity, the LSP is a viable WIMP DM candidate. For both theoretical and observational considerations [60, 61, 282–284], it is believed that the best candidate is the lightest Majorana mass eigenstate which is an admixture of the Bino (\tilde{B}), Wino (\tilde{W}_3), and Higgsinos ($\tilde{H}_{d,u}$), with the corresponding soft SUSY breaking mass parameters M_1 , M_2 , and the Higgs mixing μ , respectively. The neutralino mass matrix in the Bino-Wino-Higgsino basis is given by

$$M_{\text{neut}} = \begin{bmatrix} M_1 & 0 & -m_z \cos \beta \sin \theta_w & m_z \sin \beta \sin \theta_w \\ 0 & M_2 & m_z \cos \beta \cos \theta_w & -m_z \sin \beta \cos \theta_w \\ -m_z \cos \beta \sin \theta_w & m_z \cos \beta \cos \theta_w & 0 & -\mu \\ m_z \sin \beta \sin \theta_w & -m_z \sin \beta \cos \theta_w & -\mu & 0 \end{bmatrix},$$

where m_z is the Z boson mass, θ_w the Weinberg angle, and $\tan \beta = v_u/v_d$ is the ratio of the vacuum expectation values for the two Higgs doublets. The lightest neutralino is a linear combination of the superpartners

$$\chi_1^0 = N_{11}\tilde{B} + N_{12}\tilde{W}_3 + N_{13}\tilde{H}_d + N_{14}\tilde{H}_u, \quad (\text{II.D.56})$$

where N_{ij} are the elements of the matrix N that diagonalize M_{neut} :

$$N^* M_{\text{neut}} N^{-1} = \text{diag}\{m_{\chi_1^0}, m_{\chi_2^0}, m_{\chi_3^0}, m_{\chi_4^0}\}. \quad (\text{II.D.57})$$

The eigenvalues of M_{neut} are the masses of the four neutralinos. An interesting limit is $m_z \ll |M_1 \pm \mu|$ and $|M_2 \pm \mu|$, in which case, the mass eigenstates (neutralinos χ_i^0) are nearly pure gauge eigenstates (gauginos and Higgsinos). This also implies that large mixing of gaugino and Higgsino components for the mass eigenstates only takes place when M_1 and/or M_2 are nearly degenerate with μ . We will focus only on the lightest neutralino (henceforth denoted by χ_1^0) with a mass $m_{\chi_1^0}$. In particular, we assume that it constitutes the majority of the DM.

Intimately related to the neutralinos is the Higgs sector. The tree level Higgs masses in the MSSM can be expressed in terms of $\tan \beta$ and the CP-odd mass M_A . Radiative corrections enhance the Higgs mass significantly via the top quark Yukawa coupling, the third generation squark mass parameters M_{Q3} , M_{U3} , and the left-right squark mixing A_t . Flavor physics observations from the b -quark sector often serve as stringent constraints and we therefore include the sbottom sector parameters M_{D3} and the squark mixing A_b . The last potentially relevant sector is the stau, which could be light and contribute to the t -channel exchange, co-annihilations to control the relic density. We therefore generously vary the MSSM parameters in the ranges

$$\begin{aligned} 5 \text{ GeV} < |M_1| < 2000 \text{ GeV}, \quad 100 \text{ GeV} < |M_2, \mu| < 2000 \text{ GeV}, \\ 3 < \tan \beta < 55, \quad 80 \text{ GeV} < M_A < 1000 \text{ GeV}, \\ -4000 \text{ GeV} < A_t < 4000 \text{ GeV}, \quad 100 \text{ GeV} < M_{Q3}, M_{U3} < 3000 \text{ GeV}, \quad (\text{II.D.58}) \\ -4000 \text{ GeV} < A_b < 4000 \text{ GeV}, \quad 100 \text{ GeV} < M_{D3} < 3000 \text{ GeV}, \\ -4000 \text{ GeV} < A_\tau < 4000 \text{ GeV}, \quad 100 \text{ GeV} < M_{L3}, M_{E3} < 3000 \text{ GeV}. \end{aligned}$$

The lowest values of M_1 , M_2 and μ control the LSP mass for the WIMP DM. The lower values of 100 GeV for M_2 , μ are dictated by the LEP-2 bound from the largely model-independent chargino searches. The lower limit of $\tan \beta$ is close to the LEP-2 Higgs search exclusion. The lower limit of M_A is chosen to cover the non-decoupling Higgs sector as well

as above the LEP-2 bound on the charged Higgs. The upper limit of M_1 , M_2 , μ and the soft SUSY breaking masses in the stop and stau sectors are set with consideration of naturalness [37, 38, 285–288]. The other soft supersymmetry breaking parameters are less relevant for our DM considerations and we therefore set the other trilinear mass parameters to be zero, and the other soft SUSY breaking masses at 3 TeV.

While the natural value of μ is supposed to be close to the electroweak scale, we vary μ up to 2 TeV to capture some interesting features such as the scenario of “well-tempered neutralino” [289]. Letting $\mu \approx 2$ TeV would already allow for a severe fine tuning at the level of about 0.04% [285]. Although not our focus, we have included arbitrary signs for the M_1 , M_2 , μ parameters. This allows us to see the possible solutions with very specifically chosen parameter relations such as the “blind spots” scenarios [290–292].

We choose a flat prior for the scanning with a total number of scanned points around 10 million. Several different layers of scanning are performed to account for different experimental constraints and theoretical considerations, as seen by the corresponding color codes in our plots.

2. Current Constraints and the Scanning Results

The hints of DM detection from the DAMA, CoGeNT, and CRESST experiments have drawn significant interest in considering valid theoretical interpretations. The sensitivity of the DM direct searches have been steadily improving at an impressive pace, notably with the XENON collaboration [67, 68]. The indirect searches from WMAP, Fermi-LAT, and IceCube have also played crucial roles in exploring the nature of the DM particle.

Although the null results of searching for Supersymmetry at colliders have significantly tightened the viable SUSY parameter region, the bounds on WIMP DM properties are only limited within specific models, most notably in mSUGRA or CMSSM [100, 101]. The direct exploration of the electroweak gaugino sector at the LHC would be very challenging given the hostile background environment and the current search results depend on several assumptions [293, 294]. On the other hand, if we demand the correct WIMP LSP relic abundance from the current observations as in eq. (II.E.82), the SUSY parameter space of

eq. (IV.B.9) will be notably constrained in the Higgs and gaugino sectors. We assume a 10% theoretical uncertainty in the calculation of the DM relic density [89, 295]. Applying the Planck result for $\Omega_\chi h^2$ in eq. (II.E.82) combined with 10% theoretical uncertainty, we demand that the relic density in our model points be within the following 2σ window

$$0.0947 < \Omega_{\chi_1^0} h^2 < 0.1427 . \quad (\text{II.D.59})$$

We use the publicly available FEYNHIGGS code [296] as the spectrum calculator. The Higgs constraints are imposed using the HIGGSBOUNDS package [297] with our additional modifications. We modify the codes to include the most recent LHC constraints [263–267, 298–305]. The standard SLHA [306] output recorded is then supplied to the MICROMEAS code [307] which computes the DM relic density, direct/indirect search cross sections and flavor calculations. This is done to avoid any possible inconsistency due to the subtle differences in the spectrum calculator, particularly the lack of accuracy in the default approximate diagonalization routine for the neutralino mass matrix.

a. Constraints from the Higgs Searches and the Flavor Sector The discovery of a SM-like Higgs boson h as well as the upper limits on difference channels for the other Higgs bosons A, H, H^\pm shed much light on the electroweak sector, and can thus guide us for DM studies. When scanning over the SUSY parameter space as in eq. (IV.B.9), and requiring the correct WIMP LSP relic abundance to be within the 2σ window in eq. (II.D.59), we further require the theory to have a SM-like Higgs boson, and to accommodate all the current constraints from the Higgs searches:

$$\begin{aligned} &123 \text{ GeV} < m_h < 128 \text{ GeV}, \quad \sigma_{\gamma\gamma} > 0.8 \sigma_{\gamma\gamma}(SM), \\ &\text{plus Higgs search bounds from LEP, Tevatron, LHC,} \\ &\text{plus LEP bounds}^1 \text{ on the slepton mass } (\geq 80 \text{ GeV}) \\ &\text{and the squark and the chargino mass } (\geq 100 \text{ GeV}). \end{aligned} \quad (\text{II.D.60})$$

The Higgs diphoton rate being SM-like is one of our assumptions. We do not demand it to reach a large excess as indicated by the early LHC results, nor do we accept the deficit as

suggested by the latest CMS results [308, 309]. It is a statement of having a SM-like Higgs boson. Due to the correlation of the Higgs couplings, the requirement of the $\sigma_{\gamma\gamma}$ cross section effectively sets the SM-like values for σ_{WW} , σ_{ZZ} as well.

The absence of tree-level flavor changing neutral currents (FCNC) in the SM puts strong constraints on new physics. We consider two processes that have been observed to be consistent with the SM prediction and thus provide constraints on the MSSM parameter space. The first process is $b \rightarrow s\gamma$ [310], for which the branching fraction is sensitive to the charged Higgs boson and supersymmetric particles (e.g. chargino/stop) in the loop. The world average of the branching fraction of this channel [280] is $(3.43 \pm 0.21 \pm 0.07) \times 10^{-4}$, in good agreement with the standard model prediction [311–313] $(3.15 \pm 0.23) \times 10^{-4}$.

The second process is $B_s \rightarrow \mu^+\mu^-$, which receives a large contribution in the MSSM proportional to $(\tan^6 \beta / m_A^4)$ [314]. The LHCb collaboration has recently announced the first evidence [281] of this very rare decay and the branching ratio for this process was found to be $(3.2^{+1.4}_{-1.2} {}^{+0.5}_{-0.3}) \times 10^{-9}$ in good agreement with the standard model prediction of $(3.23 \pm 0.27) \times 10^{-9}$ [315]. We adopt world average of the branching fraction of this channel [280] $(3.2 \pm 1.0) \times 10^{-9}$ to put constraints on $\text{BR}(B_s \rightarrow \mu^+\mu^-)$.

We adopt the theoretical uncertainties from the SM predictions. We note that the uncertainties from experiments are of the same order of magnitude as the theoretical uncertainty for $\text{BR}(b \rightarrow s\gamma)$, and thus the latter becomes very important. In light of these precision results, we require our MSSM solutions to be within 2σ of the observed value²

$$\begin{aligned} 2.79 \times 10^{-4} < \text{BR}(b \rightarrow s\gamma) &< 4.07 \times 10^{-4}, \\ 1.1 \times 10^{-9} < \text{BR}(B_s \rightarrow \mu^+\mu^-) &< 5.3 \times 10^{-9}. \end{aligned} \tag{II.D.61}$$

¹The particle mass constraints applied here may still be evaded for certain limiting cases, if the lower lying particles have a mass splitting less than the order of GeV, for instance.

²It should be noted that the experimental measured value is an untagged value, while the theoretical prediction is CP averaged [316, 317].

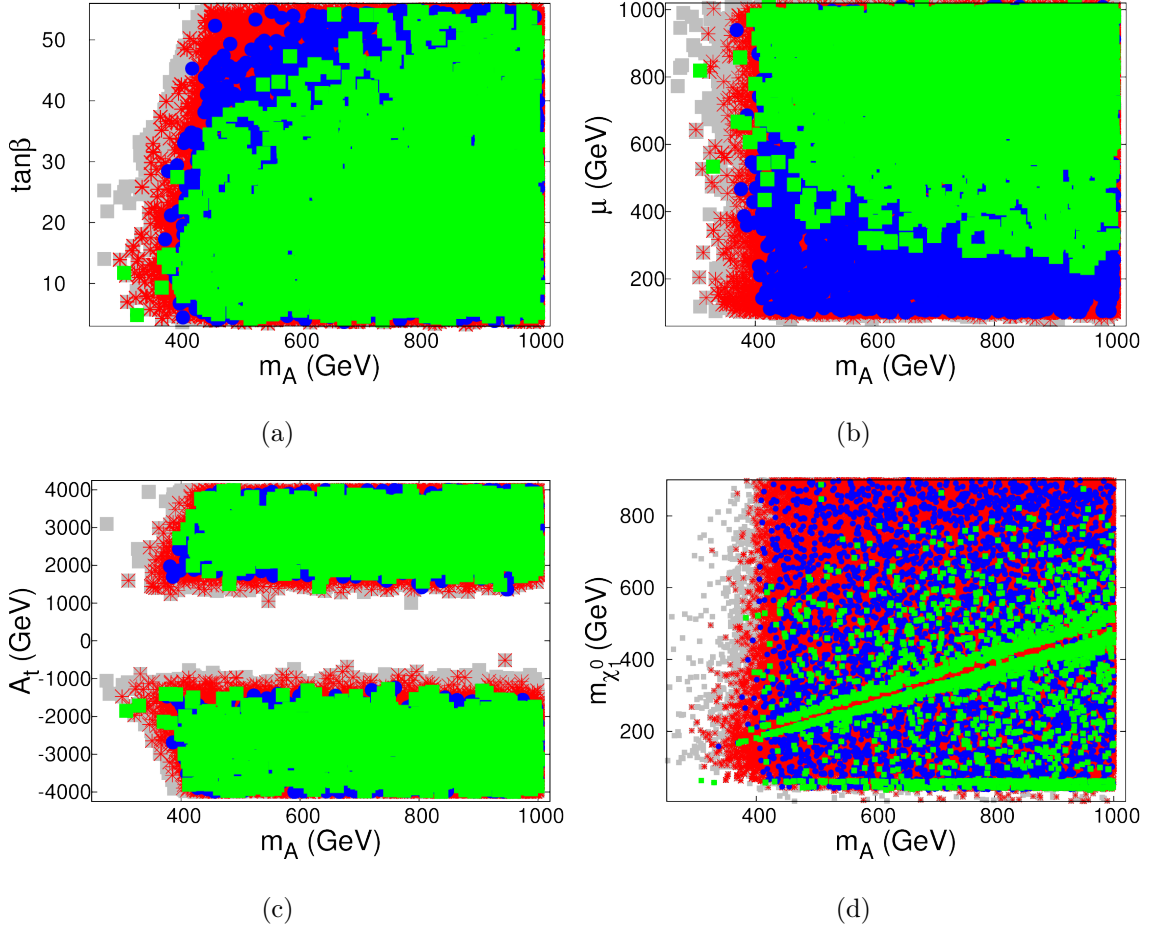


Figure II.30: Allowed parameter regions versus the CP-odd Higgs boson mass m_A , for (a) $\tan\beta$, (b) the Higgs mixing parameter μ , (c) stop mixing parameter A_t and (d) LSP DM mass m_{χ} , respectively. All points pass the collider and Higgs constraints of eq. (II.D.60). The grey squares require that the DM does not overclose the Universe; the red stars in addition satisfy the flavor constraints of eq. (II.D.61); the blue disks are consistent with the LSP being all of the DM (i.e. predicts the correct relic density of eq. (II.D.59)). The green squares pass the XENON-100 direct search bound in addition to the other requirements.

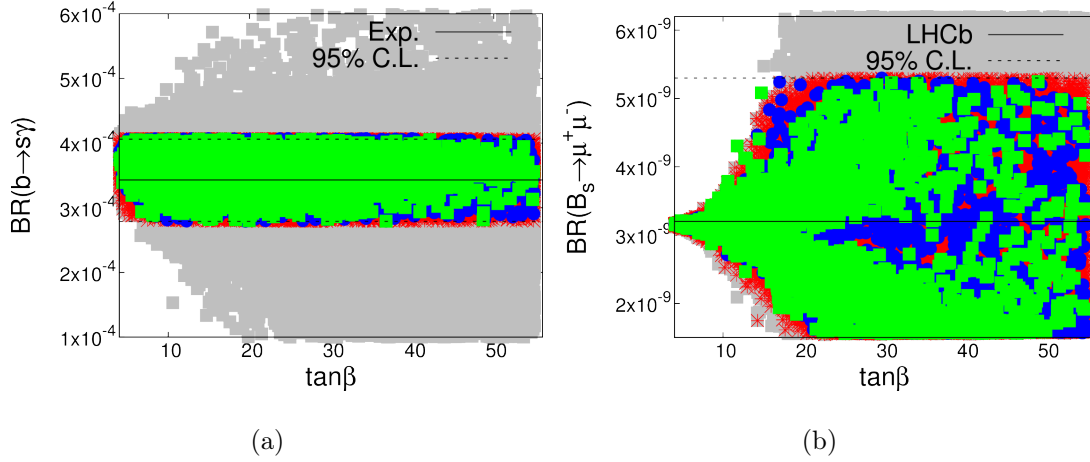


Figure II.31: Allowed branching fraction regions versus $\tan\beta$, for (a) $b \rightarrow s\gamma$, (b) $B_s \rightarrow \mu^+\mu^-$. The corresponding experimental central values and 2σ bands are plotted on each panel. Symbols and legends are the same as in Fig. II.30.

b. Confronting the Direct and Indirect Searches Thus far, the most stringent constraints on the spin-independent elastic scattering cross section (σ_p^{SI}) come from the XENON-100 experiment. The results from the XENON experiment challenge the signal hints from DAMA, CoGeNT and CRESST in the low mass region of $m_\chi \approx 10$ GeV, and cut deeply into the parameter space with $\sigma_p^{\text{SI}} \sim 2 \times 10^{-9}$ pb at $m_\chi \sim 60$ GeV. Limits on the spin-dependent cross section are not as constraining. We account for the bounds from the Super-Kamiokande [318], and the IceCube/DeepCore [319] experiments that are sensitive to the spin-dependent scattering of DM with Hydrogen at the sun's location. We also take into account bounds obtained by the Fermi satellite from the absence of gamma rays from the nearby dwarf galaxies.

c. Scanning Results We now present our results for the allowed parameter regions in Figs. II.30–II.37. In Fig. II.30, we show the parameter points passing the Higgs constraints in eq. (II.D.60) versus the CP-odd Higgs boson mass m_A , for (a) $\tan\beta$, (b) Higgs mixing parameter μ , (c) stop mixing parameter A_t and (d) DM mass $m_{\chi_1^0}$, respectively. These

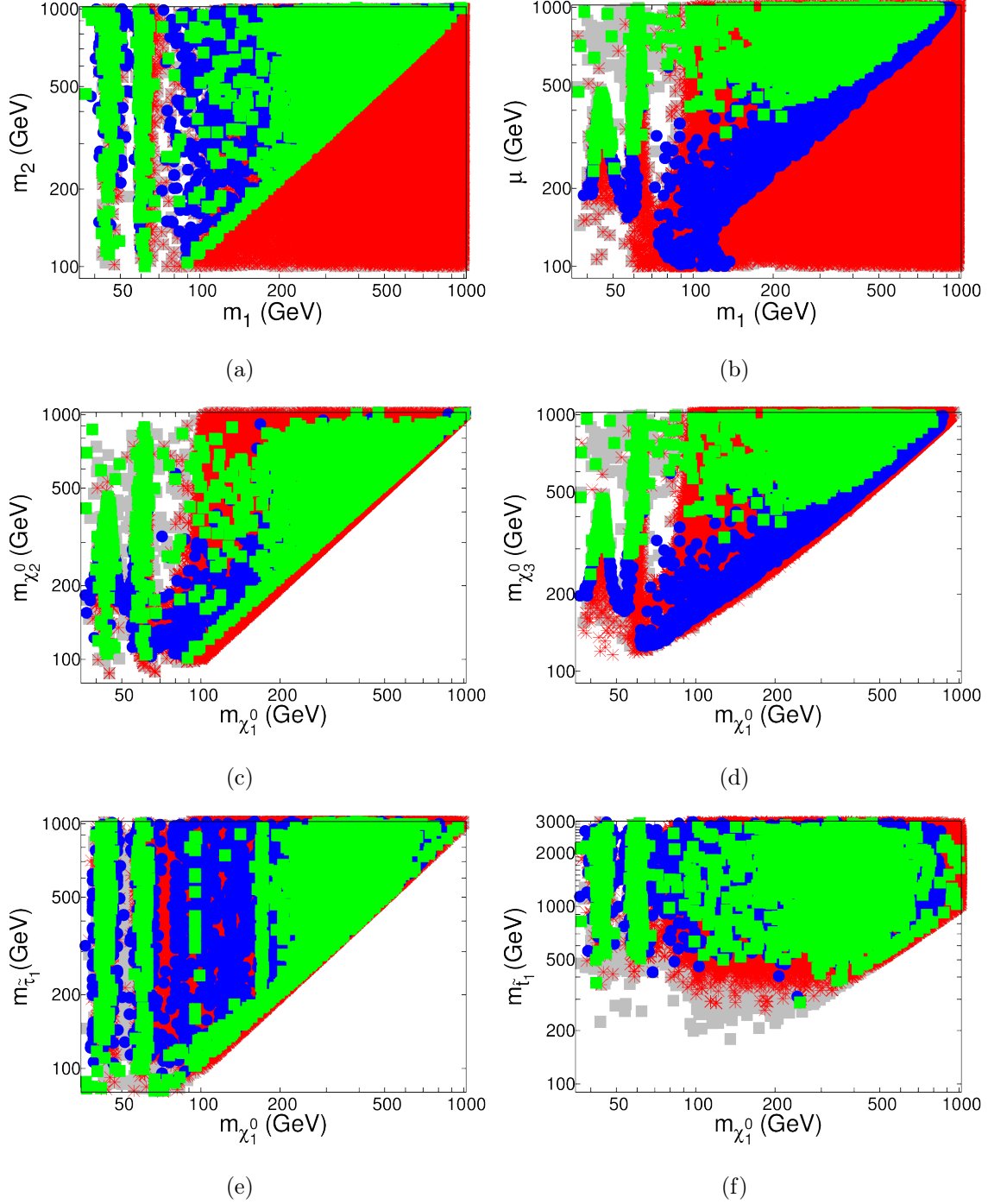


Figure II.32: Allowed parameter regions. Symbols and legends are the same as in Fig. II.30. (a) The Wino mass parameter M_2 and (b) the Higgsino mass parameter μ versus the Bino mass parameter M_1 ; (c) the second neutralino mass $m_{\chi_2^0}$ and (d) the third neutralino mass $m_{\chi_3^0}$ versus the lightest neutralino DM mass $m_{\chi_1^0}$; (e) the lighter stau mass $m_{\tilde{\tau}_1}$ and (f) lighter stop mass $m_{\tilde{t}_1}$ versus the DM mass $m_{\chi_1^0}$.

allowed parameter regions are shown in Fig. II.31 for branching fractions (a) $\text{BR}(b \rightarrow s\gamma)$ and (b) $\text{BR}(B_s \rightarrow \mu^+\mu^-)$ versus $\tan\beta$. We show from the same set of points, the Wino mass parameter M_2 and the Higgsino mass parameter μ versus the Bino mass parameter M_1 in Figs. II.32(a) and (b). We show the second and third neutralino masses $m_{\chi_2^0}$, $m_{\chi_3^0}$, the light stau mass and the light stop mass versus the LSP mass m_χ in Figs. II.32(c), (d), (e) and (f). In the above Figures II.30–II.32, all points satisfy the collider, and Higgs search requirements in eq. II.D.60. The grey squares show MSSM models that do not overclose the universe. The red stars in addition satisfy the flavor requirements in eq. (II.D.61). The blue disks represent the models that give the correct relic density in eq. (II.D.59). Finally, the green squares pass the severe XENON-100 direct search bound on the WIMP-proton spin-independent elastic scattering.

The results obtained here are consistent with the existing literature on the studies at the LHC [320, 321]. We make the following important observations:

(1). Higgs constraints (grey squares): We start with points that do not overclose the universe and satisfy the collider search requirements in eq. (II.D.60). We reproduced the known results that there are two surviving regions:

(i) The non-decoupling regime where $m_A \sim 95 - 130$ GeV, the heavy CP-even Higgs (H) is SM-like, and the light CP-even Higgs (h) is nearly degenerate in mass with the CP-odd Higgs (A). This region is particularly interesting since it leads to rich collider phenomenology and favors a light WIMP mass $m_\chi \lesssim 50$ GeV. These points are not shown on the plots since they are disfavored by the flavor constraints, as discussed next.

(ii) The decoupling regime where $m_A \gtrsim 250$ GeV, the light CP-even Higgs is SM-like, and the heavy CP-even Higgs is nearly degenerate in mass with the CP-odd Higgs. This regime is difficult to observe at the LHC when $m_A \gtrsim 400$ GeV and $\tan\beta \sim 10 - 20$ in traditional SM Higgs search channels due to severely suppressed couplings to the gauge bosons.

(2). Flavor constraints (red stars): The two decay processes $b \rightarrow s\gamma$ and $B_s \rightarrow \mu^+\mu^-$ are the most constraining ones. The experimental central values are plotted on the calculated branching fractions in Fig. II.31 on each panel, along with 2σ bands, which is summarized in eq. (II.D.61). These flavor constraints prefer lower $\tan\beta$ values and essentially remove the light Higgs (H^0, A^0, H^\pm) solutions in the non-decoupling region in our generic scan. The solutions with a light LSP of $m_\chi \lesssim 30$ GeV are also eliminated. Our results are in good agreement with the existing studies [106, 116]. Further improvements in the $B_s \rightarrow \mu^+\mu^-$ measurement would strongly constrain the large $\tan\beta$ and low m_A region. However, we have not tried to exhaust parameter choices with possible cancellations among different SUSY contributions, and some sophisticated scanning may still find solutions with certain degrees of fine-tuning [322].

(3). Relic density requirement (blue disks): Merely requiring that the LSP does not overclose the universe does not constrain the MSSM parameter space very much, as most clearly seen from the gray squares and red stars in Fig. II.32. This is because the Higgsino-like or Wino-like LSPs and NLSPs can annihilate efficiently through gauge bosons and Higgs bosons. Requiring the correct dark matter relic density at the present epoch does constrain the parameter space significantly. We see the preference for $\mu > M_1$ and $M_2 > M_1$, as in Figs. II.32(a) and (b). Otherwise the Higgsino or Wino LSP would annihilate too efficiently, and result in underabundant DM relic. Nevertheless, we do find a nearly degenerate region of a Bino LSP and Wino NLSPs as seen in Fig. II.32(c), which is best characterized by the “well-tempered” scenario [289]. This scenario, however, seems to be less implementable with Higgsino NLSPs as seen in Figs. II.32(b) and (d), if μ is not much greater 1 TeV. Importantly for our interests, we see prominent strips near $m_\chi \sim m_Z/2, m_h/2$ which are the Z and Higgs funnel regions. Interestingly, as seen in Fig. II.30(d), there is a region of depletion near $m_A \approx 2m_\chi$, indicating the very (too) efficient annihilation near the A^0 funnel in the s -channel that is removed by the correct relic density requirement. This is a result of a lower bound on the LSP-Higgsino component N_{13} that we will discuss later.

For the low mass dark matter that is favored by CoGent, DAMA, CRESST and CDMS experiments, the solutions are disfavored by precision electroweak observables, LEP con-

straints on SUSY direct searches, and constraints from the Higgs property³. In our analysis, we strictly apply the LEP bounds on the SUSY searches and the requirement for a SM-like Higgs boson as given in eq. (II.D.60), then there are no surviving points in the low mass DM region. However, as noted in Refs. [323–327], if one adopt the scenarios with a compressed spectrum, such as a mass difference $m_{\tilde{b}} - m_{\chi} < 5$ GeV to evade the LEP bounds, or relax the $h \rightarrow \gamma\gamma$ to be SM-like, new solutions in the low mass region could emerge.

(4). Direct search bounds (green, yellow and magenta squares): The results from DM direct searches can be translated to spin-independent cross sections and thus to the MSSM parameters. This is shown in Fig. II.33, where all the points in the colored shaded region give the correct relic abundance in eq. (II.D.59), satisfy the collider constraints in eq. (II.D.60) and the flavor constraints in eq. (II.D.61). The parameter space favored by the DAMA, CoGeNT, CRESST and CDMS experiments, as well as the stringent bound from the XENON-100 experiment are plotted. We see that the blue region is further excluded by the XENON-100 experiment⁴. As seen in Fig. II.30(a), lower $\tan\beta$ and higher m_A values are preferred. Figures II.30(b) and II.32(b) show the lower bound $\mu > 200$ GeV. This consequently leads to a heavier χ_3^0 as seen in II.32(d), while χ_2^0 could be still as light as the LSP χ_1^0 as seen in II.32(c).

The most important observation from our study is that the surviving points are quite characteristic. We can identify the following classes of predictive features for the LSP DM from Fig. II.33.

I-A (green) $\chi_1^0\chi_1^0 \rightarrow Z \rightarrow SM$ predicts $m_{\chi} \approx m_Z/2 \sim 45$ GeV, the Z -funnel [330].

I-B (green) $\chi_1^0\chi_1^0 \rightarrow h \rightarrow SM$ predicts $m_{\chi} \approx m_h/2 \sim 63$ GeV, the h -funnel.

I-C (green) $\chi_1^0\chi_1^0 \rightarrow H, A \rightarrow SM$ predicts $m_{\chi} \approx m_{A,H}/2 \sim 0.2 - 0.5$ TeV, the H/A -funnel.

The A-funnel is overall dominant comparing to the H-funnel.

II-A (yellow) Neutralino/chargino coannihilation [331, 332]: $\chi_i^0\chi_j^0, \chi_i^0\chi_j^{\pm} \rightarrow SM$.

II-B (magenta) Sfermion assistance [333–335]: $\chi_1^0\tilde{\tau}, \chi_1^0\tilde{t}, \chi_1^0\tilde{b} \rightarrow SM$; t -channel $\tilde{\tau}, \tilde{\nu}$ in $\chi_i^0\chi_j^0$.

³Our requirement of the $h \rightarrow \gamma\gamma$ rate in eq. (II.D.60) also limits the allowed Higgs branching fractions to SUSY particle pairs, especially for those solutions with kinematically allowed Higgs decays to NLSP pairs.

⁴It should be noted that the theoretical calculation of the spin-independent cross section may have significant uncertainties [328, 329].

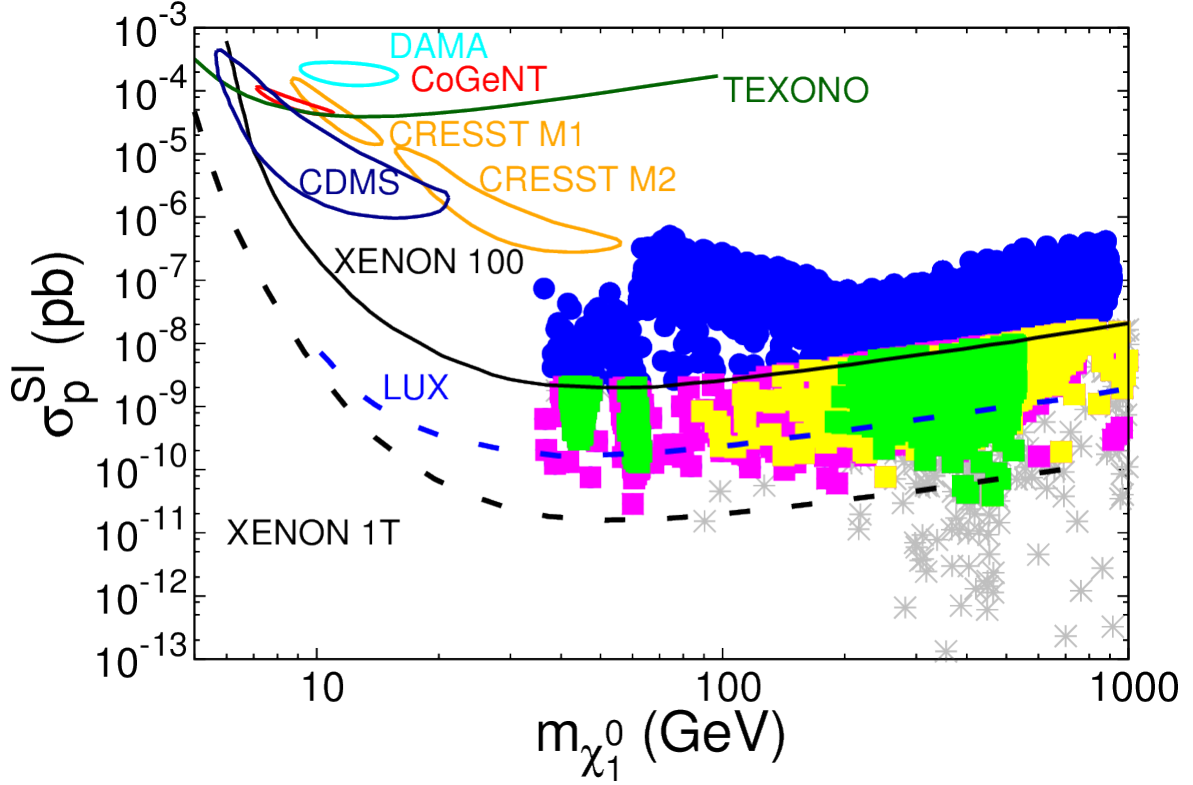


Figure II.33: Spin-independent cross section versus the DM mass $m_{\chi_1^0}$. All the points in the colored shaded region give the correct relic abundance in eq. (II.D.59), satisfy the collider constraints in eq. (II.D.60) and the flavor constraints in eq. (II.D.61). The green region represents the model points with the Z and Higgs resonances. The Z funnel and h funnel regions are clearly visible for WIMP masses around half the Z mass and half the Higgs mass. The yellow points represent the region of co-annihilation with Wino-like/Higgsino-like NLSPs. The magenta points represent the region with $\tilde{\tau}$, $\tilde{\nu}_\tau$, \tilde{b} , \tilde{t} contributions. The gray points represent the scenarios with special cancellations when M_1 and μ take opposite signs. The DAMA and CoGeNT contours (3σ) are shown for astrophysical parameters $v_0 = 220$ km/s, $v_{\text{esc}} = 600$ km/s, and for a local density $\rho_0 = 0.3$ GeV/cm³. CRESST contours are 2σ regions, from [65]. Also shown is the 90% confidence contour from the recent CDMS analysis [66]. The blue region is excluded by the XENON-100 experiment (90% exclusion curve from [68], for $v_0 = 220$ km/s, $v_{\text{esc}} = 544$ km/s, $\rho_0 = 0.3$ GeV/cm³). Recent results from the TEXONO [71] collaboration are shown. Expected exclusion bounds from the ongoing LUX experiment [69] and the future XENON-1T experiment [70] are also shown.

We categorize model points as scenario I if the difference between the mediator mass and twice the LSP mass is within 8% of the mediator mass, namely

$$|m_{Z,h,A} - 2m_{\chi_1^0}| \leq 0.08 m_{Z,h,A}. \quad (\text{II.D.62})$$

We categorize model points as scenario II-A if the difference between the LSP mass and neutralino NLSP⁵ mass is less than 15% of the LSP mass, namely $m_{\chi_2^0} - m_{\chi_1^0} < 0.15m_{\chi_1^0}$. Other cases are categorized as scenario II-B. Our classification and categorization have been verified by investigating a fraction of our generated model points and looking into their individual contributing annihilation channels. Two remarks are in order: First, the light sfermions needed in this category are still viable, especially for \tilde{t} , \tilde{b} , with respect to the direct LHC searches, because the mass splitting with the LSP is too small to result in significant missing transverse energy to be sensitive for the search. In case of compressed spectra, LHC searches on the monojet and monophoton could gain some sensitivity [336–341]. Second, this categorization based on simple kinematics has exemptions when the LSP coupling to the resonant mediator is very weak and thus the co-annihilation mechanism is dominant. We have kept track of those cases in the plot by examining the points individually.

(5). Indirect search bounds:

There exist cosmological bounds from the indirect search for DM signals. We present the annihilation cross section $\langle\sigma_a v\rangle$ in the limit $v \rightarrow 0$ (i.e. the v -independent component) versus the LSP DM mass in Fig. II.34(a), along with the 95% exclusion obtained by the Fermi-LAT satellite from the absence of gamma rays from the nearby dwarf galaxies [72]. We see that further improvement from the measurement by the Fermi-LAT will reach the current sensitivity range. The spin-dependent scattering cross section with a proton is shown in Fig. II.34(b), along with the 90% exclusion curves from the Super-Kamiokande experiment [318] and the IceCube constraint from DM annihilation in the Sun [319]. We see that IceCube results are cutting into the relevant parameter region closing the gap from the direct searches,

⁵This is almost always true because we have a very Bino-like LSP. For cases with $\tilde{\tau}_1$, \tilde{t}_1 NLSP with the sfermion coannihilation mechanism, they fall into scenario II-B automatically.

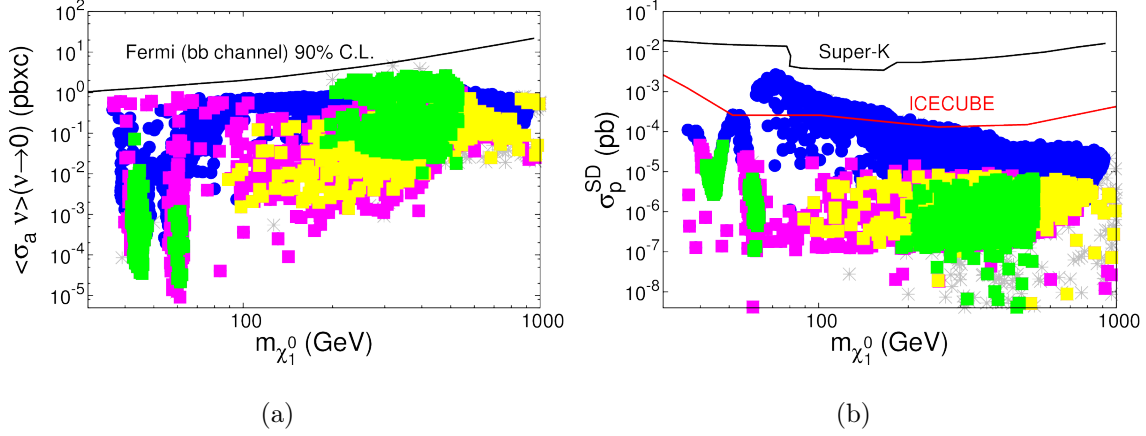


Figure II.34: (a) The annihilation cross section $\langle\sigma_a v\rangle$ in the limit $v \rightarrow 0$ along with the 95% exclusion obtained by the Fermi satellite from the absence of gamma rays from the nearby dwarf galaxies [72]. (b) The spin-dependent scattering cross section with a proton, along with the 90% exclusion curves from the Super-K [318] and IceCube [319] experiments. Legends are the same as in Fig. II.33.

although the bounds from the indirect searches are not quite as strong as that from XENON-100. It is worth mentioning that the local DM density in the Sun may be higher than the referral value [342] and thus would yield a slightly stronger exclusion from IceCube.

3. Discussions

a. The Nature of the DM Experimental results from the collider searches, the b -quark rare decays and the direct DM searches, combined with the relic density requirement have put very stringent constraints on the SUSY parameter space. This in turn could have significant implications for searches at future collider experiments. Of primary importance is the nature of the LSP. We show the gaugino and Higgsino fraction (N_{1i}^2) of the neutralino LSP versus its mass in Fig. II.35, consistent with all collider and flavor measurements as well as the correct relic density. From Fig. II.35(a), we note that the surviving points are mostly Bino-like (N_{11}^2 , as shown by the black dots), with lower fractions for Wino-like (N_{12}^2 , red dots) and

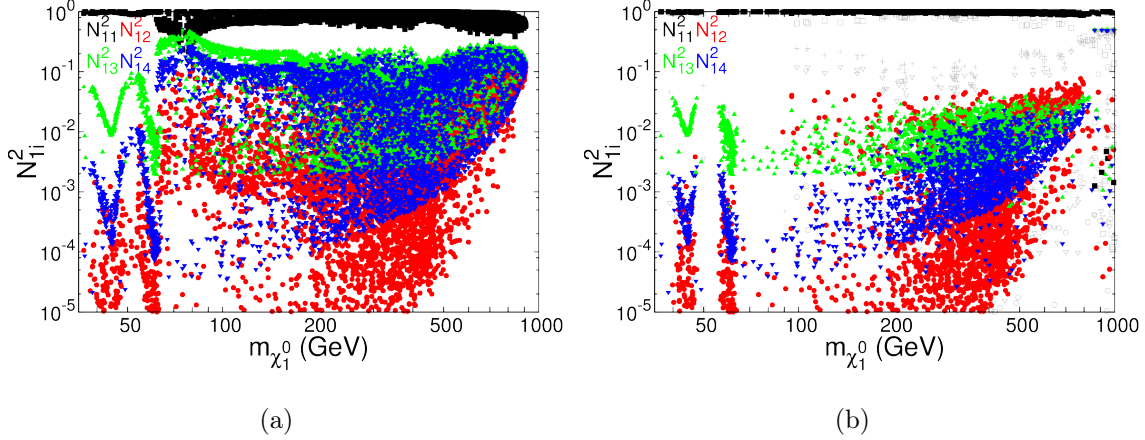


Figure II.35: The gaugino and Higgsino fractions of the LSP versus $m_{\chi_1^0}$ (a) consistent with the relic density, collider, and flavor constraints, (b) consistent with XENON-100 in addition to the other requirements. The gray points represent the results for M_1 and μ to have opposite signs and the corresponding fractions N_{11}^2 , N_{12}^2 , N_{13}^2 and N_{14}^2 are denoted by hollow squares, circles, daggers and hollow triangles, respectively.

Higgsino-like (N_{13}^2 , N_{14}^2 , green and blue dots, respectively). As noted earlier, this is because Wino-like and Higgsino-like LSP's annihilate very efficiently via SU(2) gauge interactions resulting in too little dark matter at the present epoch. Yet, the LSP could not be purely Bino-like since it would overclose the Universe. In the region $m_{\chi_1^0} \sim 40$ GeV–60 GeV, the line structures corresponding to the Higgsino components are easily identifiable with the Z and h exchanges.

The XENON-100 direct search plays a crucial role in fixing the DM properties. The surviving points are shown in Fig. II.35(b). We see that the Wino and Higgsino fractions of the LSP are further constrained. The \tilde{H}_d component comes in with the opposite signs with respect to the \tilde{H}_u and \tilde{W} components. Bino-like LSP becomes more pronounced and the Wino and Higgsino components consist of less than 7% each, rendering the “well-tempered” scenario [289] difficult to realize with large Bino-Wino or Bino-Higgsino mixing. The comparison between Fig. II.35(a) and (b) clearly shows the XENON-100 exclusion probes deeply into the Higgsino and Wino components. On the other hand, the \tilde{H}_d component N_{13}^2 must

be non-zero, and so is N_{14}^2 for \tilde{H}_u . The non-zero lower bound would have significant implications for direct searches as we will discuss next, although the precise values may depend on the choice of the ranges for M_1 , M_2 and μ .

It is important to note that a relative opposite sign between M_1 and μ could result in a subtle cancellation for the $h\chi\chi$ coupling [290, 292], and thus enlarge the allowed mixing parameters, reaching about 20% Wino/Higgsino mixtures, as shown by the grey points in Fig. II.35(b). This can happen only for a higher LSP mass when co-annihilations or H, A funnels are in effect.

b. Lower Limit on the Spin-Independent Cross Section With our assumptions in the MSSM framework and the well-constrained properties of the LSP, we would expect that the DM scattering cross section may be predicted. It is interesting to ask whether one may derive a lower limit for the spin-independent scattering cross section. This is quite achievable for the Higgs resonance situation. Much effort has been made to derive the neutralino recoil cross sections with nuclei in various SUSY models [283, 343–348]. This cross section mainly receives contributions from h , H exchanges and squark exchanges. Given the current experimental bounds on the masses of the squarks from the LHC [349, 350], the Higgs exchanges dominate. As a good approximation in the decoupling limit $\cos(\alpha - \beta) \simeq 0$, $\tan\beta \geq 3$ and a Bino-like LSP, the neutralino-nucleon cross sections via the Higgs exchanges are of the form [347]:

$$\sigma_{\chi N} \propto \begin{cases} \frac{|N_{11}|^2 |N_{13}|^2}{m_H^4 \cos^2 \beta} (f_{T_s} + \frac{2}{27} f_{TG})^2, & H \text{ exchange,} \\ \frac{|N_{11}|^2 |N_{14}|^2}{m_h^4} (f_{T_u} + \frac{4}{27} f_{TG})^2, & h \text{ exchange.} \end{cases} \quad (\text{II.D.63})$$

f_{T_s} , f_{T_u} and f_{TG} are parameters measured from nuclear physics experiments. The H exchange benefits from an enhancement factor $(N_{13}/\cos\beta)^2$. When the H is heavy, the h exchange proportional to N_{14}^2 becomes important. Due to our natural choices of parameters as in eq. (IV.B.9), there exist lower bounds on N_{13}^2 and N_{14}^2 , as shown in Fig. II.35, although unnaturally large values of μ and m_A could relax these bounds. Consequently, the LSP spin-independent cross sections at the Z, h funnels, which are mainly from the LSP scattering of

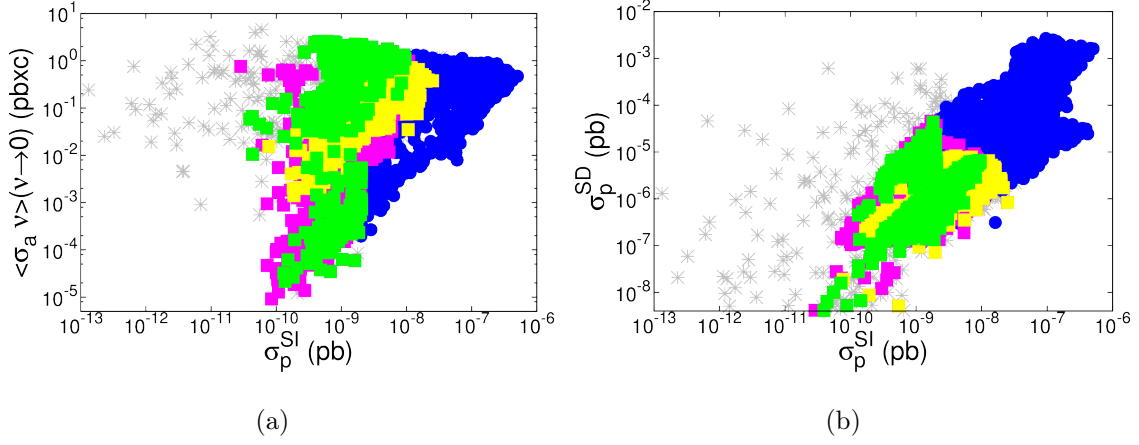


Figure II.36: (a) the annihilation cross section $\langle\sigma_a v\rangle(v \rightarrow 0)$ versus the spin independent cross section σ_p^{SI} . (b) the spin-dependent cross section σ_p^{SD} versus the spin independent cross section σ_p^{SI} . Legends are the same as in Fig. II.33.

a t -channel H exchange, reaches a lower bound, roughly

$$\sigma_p^{SI}(h, H) \gtrsim 10^{-10} \text{ pb.} \quad (\text{II.D.64})$$

As seen in Fig. II.33, this range (green dots) will be probed by the ongoing LUX experiment and will be fully covered by the proposed XENON-1T experiment. Similar argument could be also applicable to the H, A funnel regions, where t -channel h exchange could become dominant. However, an exception is that a subtle cancellation takes place when M_1 and μ take opposite signs [290–292]. As seen from the grey points in Fig. II.33(b), this can happen only for a higher LSP mass when co-annihilations or H, A funnels could be in effect.

In Ref. [54], a parameter-independent lower bound $\sigma_p^{SI} \gtrsim 2 \times 10^{-12} \text{ pb}$ could be obtained in the mass range $440 \text{ GeV} \lesssim m_\chi \lesssim 1020 \text{ GeV}$ and $\mu > 0$. In the most general pMSSM [115] with much larger M_2, μ parameters, the spin-independent cross section could go lower, depending on the mixing parameters.

c. Connection to the Indirect Searches The WIMP DM at the present epoch is non-relativistic and we can thus relate the current indirect search via LSP annihilation to that at freeze out [351]. The partial wave properties of the LSP annihilation allow us to understand the various contributions. Fig. II.36(a) shows the annihilation cross section $\langle\sigma_a v\rangle(v \rightarrow 0)$ versus the spin-independent cross section when scattering off a proton σ_p^{SI} . The model points in green squares near half the Z boson and near half the 126 GeV Higgs boson in Fig. II.34(a) correspond to the low branch of the green squares in Fig. II.36(a), due to the p -wave suppression. On the other hand, the s -channel annihilation through A in the mass window 200 GeV \sim 500 GeV in Fig. II.34(a) is through s -wave, and thus has a relatively high cross section (indicated by the high branch of green squares). Although the LSP couplings to H and A both are mainly through their Higgsino components N_{14} , the H exchange is via p -wave and thus yields a lower cross section as shown by the middle branch in Fig. II.36(a). Finally, we note that the LSP-NLSP co-annihilation (yellow squares) could yield higher cross sections for both direct, and indirect searches, depending on their Wino and Higgsino components. Figure II.36(b) shows the spin-dependent cross section versus the spin-independent cross section, for our different models. Some of the models represented by blue points have a large enough cross section to be probed by IceCube/DeepCore [319]. However, a large spin-dependent cross section implies a proportionally large spin-independent cross section. Thus, all models in blue are excluded by the XENON-100 experiment. Figure II.36 illustrates the connection between spin-dependent and spin-independent measurements, as well as the connection between direct searches and indirect searches. Further improvement of the indirect search sensitivity will soon reach the relevant parameter region, and will probe the A exchange contribution due to its s -wave dominance.

d. Implication of LSP for Higgs Physics A class of solutions exist with the LSP mass nearly half the mediator Z , h , H , A mass that undergoes a resonant enhancement in annihilation, in the Higgs funnel region. One may expect to see the mediator's invisible decay mode to LSP pairs in collider experiments. Unfortunately, these channels are kinematically suppressed near threshold by the non-relativistic velocity factor. Near the Z peak for example, the search for $Z \rightarrow \chi_1^0 \chi_1^0$ would prove impossible since the branching fraction would be

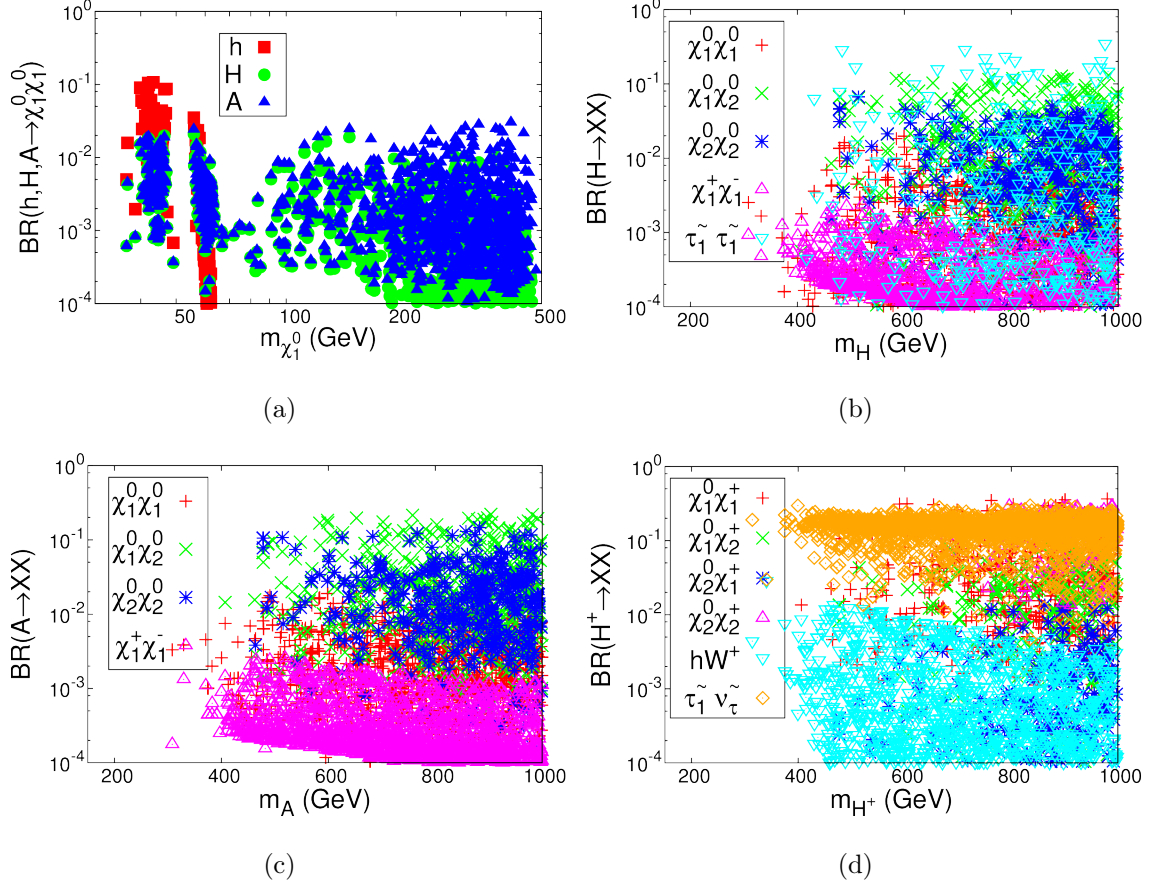


Figure II.37: Branching fractions to neutralinos and charginos (a) for h, H, A decays to LSP pair versus the LSP mass, (b) for H , (c) for A , and (d) for H^\pm versus its mass respectively.

smaller than 10^{-5} due to this suppression. On the other hand, invisible decay channels could be sizable for heavier parent particles. Shown in Fig. II.37(a) are the branching fractions of h, H, A to a pair of LSP $\chi_1^0\chi_1^0$ versus its mass, which would be the invisible mode in collider experiments. It is informative to note that the SM-like Higgs boson receives two distinctive contributions denoted by the red squares

$$\text{BR}_{\text{max}}(h \rightarrow \chi_1^0\chi_1^0) \sim \begin{cases} 1\% & m_\chi \approx 60 \text{ GeV}, \\ 10\% & m_\chi \approx 45 \text{ GeV}. \end{cases} \quad (\text{II.D.65})$$

The branching fraction near 60 GeV is rather small although this is clearly identifiable as the h -funnel region. The branching fraction near 45 GeV is about an order of magnitude larger because of the available kinematics, even though it is from the Z -funnel. This leads to the very interesting and challenging possibility of observing the Higgs invisible decay at the LHC [352–354], (a sensitivity of about 20% is considered feasible). The search sensitivity would be significantly improved at future e^+e^- colliders, reaching about a few percent at the ILC, and even 0.3% at the TLEP [355].

e. Consequences of Co-annihilation For the co-annihilation scenarios, some other SUSY particles are nearly degenerate with the LSP to ensure efficient annihilation. The common case is that the NLSP and NNLSP of the Winos (χ_1^\pm, χ_2^0) or the Higgsinos ($\chi_1^\pm, \chi_{2,3}^0$) are nearly degenerate with the Bino-like LSP, with appreciable mixing among them. On the other hand, the XENON-100 search bound puts a constraint on the sizes of the mixing as seen from Fig II.35(a) and (b). Nevertheless, the spin-independent cross sections are typically higher than those from the Higgs resonances, reaching $\sigma_p^{\text{SI}} \sim 10^{-8}$ pb (yellow region). The indirect detection cross sections are in general between the s -wave dominance (higher green band) and p -wave dominance (lower green band).

As shown in Figs. II.37(b)–(d), branching fractions for the other heavy Higgs bosons H, A to a pair of light SUSY particles could reach up to about 10% – 20%. These are the solutions for the correct relic density with co-annihilations. However, due to the mass degeneracy, the final decay products would be rather soft and would be difficult to observe with the LHC. Consequently, these also yield the invisible decay channels.

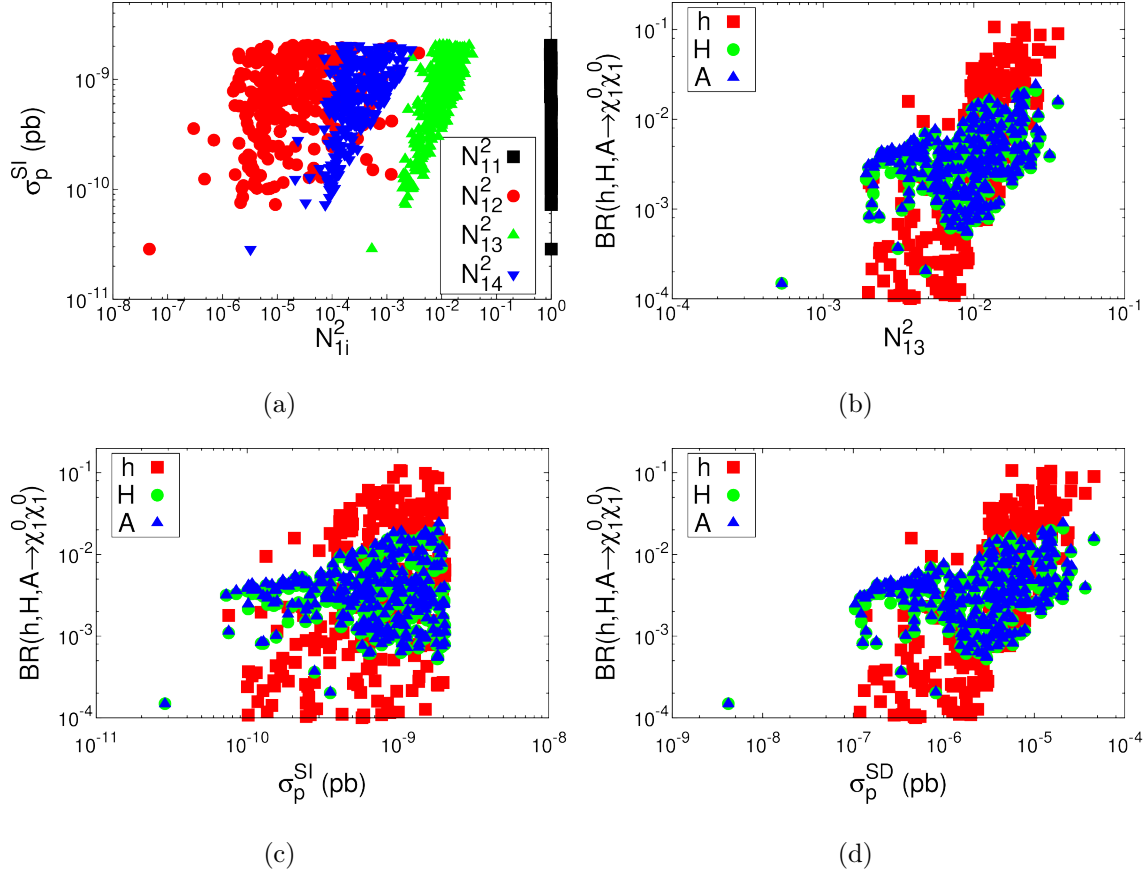


Figure II.38: (a) Spin-independent cross section versus the gaugino and Higgsino fractions N_{1i}^2 , and neutral Higgs decay branching fractions to DM pairs (b) versus the leading Higgsino fraction N_{13}^2 , (c) versus spin-independent cross section, and (d) versus spin-dependent cross section.

The coannihilation scenarios predict a rich spectrum near the LSP mass, leading to many different phenomena that can be explored by sparticles pair productions [294, 356, 357].

To conclude our discussion in this section, we bring a few crucial observables to comparison. First, in Fig. II.38(a), we show the spin-independent cross section labelled by the gaugino components N_{1i}^2 of Bino (black), Higgsinos (green and blue), and Wino (red). The lower right slopes of the N_{13}^2 and N_{14}^2 regions in this plot indicate the variable contributions from H -exchange and h -exchange, respectively, as discussed earlier in eq. (II.D.63). We then show the Higgs decay branching fractions versus the leading gaugino component N_{13}^2 in Fig. II.38(b). We see that the higher branching fractions naturally correspond to a higher value of the mixing parameter. In Figs. II.38(c) and (d), we reiterate the correlations among the observables by showing the neutral Higgs decay branching fractions versus spin-independent cross section and spin-dependent cross section, respectively. It is a generic feature that higher Higgs decay branching fractions correspond to higher cross sections. It is interesting to see that the spin-dependent cross section shows slightly more correlation with the Higgs BR's. We see the similarity between Figs. (b) and (d). This comes from the fact the Z -exchange in spin-dependent cross section is governed by N_{13}^2 while N_{14}^2 is rather small. It is important to emphasize that in anticipation of the improvement of the direct search in the near future, the LUX and XENON-1T experiments would be able to cover the full parameter space, pushing down to very small Higgs branching fractions, as shown in Fig. II.38(c).

4. Summary and Outlook

Within the framework of the MSSM, we investigated the possibility of the lightest supersymmetric particle being all the dark matter in light of the recent discovery of a SM-like Higgs boson, and the search for other Higgs bosons and SUSY particles at the LHC. We scanned through a wide range of the MSSM parameter space, and searched for model points wherein LSP has the correct properties to be the (WIMP) thermal DM. We applied the constraints on the MSSM Higgs sector from the LEP, Tevatron and LHC observations. We also imposed flavor constraints from the recent experimental results at the LHCb and BELLE, and

Table II.9: Connection between the SUSY DM properties and the Higgs bosons.

Type labels	DM mass $m_{\chi_1^0}$	Annihilation channels	Partial waves	$\langle\sigma v\rangle(v \rightarrow 0)$	Collider searches
I-A	$\sim m_Z/2$	$\chi_1^0\chi_1^0 \rightarrow Z$	p	low	$Z, h, H, A \rightarrow \chi_1^0\chi_1^0$
I-B	$\sim m_h/2$	$\chi_1^0\chi_1^0 \rightarrow h$	p	low	$h, H, A \rightarrow \chi_1^0\chi_1^0$
I-C	$\sim m_A/2$	$\chi_1^0\chi_1^0 \rightarrow A$	s	high	$H, A \rightarrow \chi_1^0\chi_1^0$
II-A	$m_{\chi_1^0} \sim m_{\chi_1^\pm}$ $\sim m_{\chi_2^0}$	$\chi_1^0\chi_2^0, \chi_1^0\chi_1^\pm$ $\chi_2^0\chi_2^0, \chi_1^+\chi_1^-$ $\rightarrow SM$	s+p	medium	$H, A \rightarrow \chi_1^0\chi_2^0$ $H, A \rightarrow \chi_2^0\chi_2^0$ $H^\pm \rightarrow \chi_1^0\chi_1^\pm$
II-B	$m_{\chi_1^0} \sim m_{\tilde{\tau}_1}$ $\sim m_{\tilde{\nu}_\tau}$	$\tilde{\tau}_1^+\tilde{\tau}_1^-, \tilde{\nu}_\tau\tilde{\nu}_\tau,$ $\chi_0^1\tilde{\tau}_1^\pm \rightarrow SM$	s+p	medium	$H, A \rightarrow \tilde{\tau}_1^+\tilde{\tau}_1^-$ $H^\pm \rightarrow \tilde{\tau}_1^\pm\tilde{\nu}_\tau$

found stringent bounds on the parameter space. The low LSP mass region may be closed, yielding a rough bound $m_\chi > 30$ GeV, unless for a compressed SUSY spectrum such as $m_{\tilde{g}} - m_\chi < 5$ GeV.

The XENON-100 experiment significantly constrains the viable parameter region via the spin-independent elastic WIMP-proton scattering cross section, as shown in Figs. II.30-II.33. Although not as sensitive, the indirect search experiments such as Fermi/LAT and IceCube have obtained impressive results to cut into the SUSY parameter region, as seen in Fig. II.34. We are able to identify the Higgs contributions and thus to make predictions for future searches at the LHC and ILC. There are also clear contributions from the co-annihilation channels. Table II.9 summarizes these distinctive MSSM model points, and the relation with the Higgs bosons. We reiterate the key points of our findings. For the resonance scenarios as in I-A, I-B and I-C,

- Z , h , H and A are the most important mediators at resonance to yield the correct relic abundance and give predictive narrow mass windows as shown in Fig. II.33, which we refer to as the Z , h and H/A -funnel regions. The spin-independent scattering in the Z , h funnel is dominated by the t -channel H exchange when $N_{13}^2 \gg N_{14}^2$, which is mostly the case seen in Fig. II.35(b).
- With our parameter scanning, the necessarily non-zero Wino, Higgsino components of the LSP (as seen in Fig. II.35) imply a lower bound for the WIMP scattering cross section mediated by h and H , as in eq. (II.D.64). In particular, the spin-independent cross sections may be fully covered by the next generation of direct search experiments for DM mass around 30 – 800 GeV such as LUX and XENON-1T, as seen in Fig. II.33 and Fig. II.38(c). An exception is the fine-tuned cancellation, the “blind spots” scenario, way above the Z , h funnels, as shown by the grey crosses in Fig. II.33.
- Z , h , H and A mediators determine the partial wave decomposition as listed in Table II.9 and predict a definite range of indirect search cross sections. It is especially sensitive to the A -exchange contribution, as seen in Fig. II.36(a).
- The invisible decays of h , H and A are expected, as plotted in Fig. II.37(a). Future studies at the LHC, and in particular, at the ILC may reveal the true nature of the DM particle, as seen in Figs. II.38(b-d).

Table II.10: Possible solutions for light (< 40 GeV) neutralino DM in MSSM and NMSSM.

	Models	DM (< 40 GeV)	Annihilation
Funnels	NMSSM	Bino/Singlino	$\tilde{\chi}_1^0 \tilde{\chi}_1^0 \rightarrow A_1, H_1 \rightarrow SM$
Co-ann.	MSSM & NMSSM	Bino/Singlino	$\tilde{\chi}_1^0 \tilde{\chi}_1^0 \rightarrow f \bar{f}; \tilde{\chi}_1^0 \tilde{f} \rightarrow V f; \tilde{f} \tilde{f}' \rightarrow f f'$

For the co-annihilation scenarios as in II-A and II-B,

- Although the “well-tempered” scenario with large Higgsino and Wino fractions is disfavored by the XENON-100 data, the co-annihilation may still be a valid solution to obtain the correct relic density. There may be several light SUSY particles such as neutralinos, charginos, or stau, leading to many rich phenomena that can be searched for at the LHC, and may be fully covered by the ILC.
- For highly degenerate NLSP, NNLSP, the decays of H , A and H^\pm as shown in Figs. II.37(b)-(d) could lead to large invisible modes, making the collider search for DM very interesting.

E. SUSY DARK MATTER IN NMSSM

Supersymmetric theories are well motivated to understand the large hierarchy between the electroweak scale and the Planck scale. The LSP can serve as a viable DM candidate. In the MSSM, the lightest neutralino serves as the best DM candidate (for a review, see, e.g., Ref. [358]). The absence of the DM signal from the direct detection in underground experiments as well as the missing energy searches at colliders, however, has significantly constrained theory parameter space. The relic abundance consideration leads to a few favorable scenarios for a (sub) TeV DM, namely $Z/h/A$ funnels, and LSP-sfermion coannihilation. For heavier gauginos, the “well-tempered” spectrum [289] may still be valid.

In this section, we explore the implications of a low mass neutralino LSP dark matter in the mass window $2 - 40$ GeV in the framework of the NMSSM (see Ref. [122] for a recent

review). The robust bounds on the chargino mass from LEP experiments disfavored the Wino-like and Higgsino-like neutralinos, and forced a light LSP largely Bino-like or Singlino-like, or an admixture of these two. However, those states do not annihilate efficiently to the SM particles in the early universe. Guided by the necessary efficient annihilation to avoid overclosing the universe, we tabulate in table II.10 the potentially effective processes, where the first row indicates the funnel processes near the light Higgs resonances, and the second row lists the coannihilation among the light SUSY states. There is another possibility of combined contributions from the s -channel Z -boson and SM-like Higgs boson, as well as the t -channel light stau (~ 100 GeV). For more details, see Refs. [323, 326, 327, 359–361].

With a comprehensive scanning procedure, we confirm three types of viable light DM solutions consistent with the direct/indirect searches as well as the relic abundance considerations: (i) A_1 , H_1 -funnels, (ii) LSP-stau coannihilation and (iii) LSP-sbottom coannihilation. Type-(i) may take place in any theory with a light scalar (or pseudo-scalar) near the LSP pair threshold; while Type-(ii) and (iii) could occur in the framework of MSSM as well. These possible solutions all have very distinctive features from the perspective of DM astrophysics and collider phenomenology. We present a comprehensive study on the properties of these solutions and focus on the observational aspects of them at colliders, including new phenomena in Higgs physics, missing energy searches and light sfermion searches. The decays of the SM-like Higgs boson may be modified appreciably and the new decay channels to the light SUSY particles may be sizable. The new light CP-even and CP-odd Higgs bosons will decay to a pair of LSPs as well as other observable final states, leading to rich new Higgs phenomenology at colliders. For the light sfermion searches, the signals would be very difficult to observe at the CERN LHC when the LSP mass is nearly degenerate with the parent. However, a lepton collider, such as the ILC, would be able to uncover these scenarios benefited from its high energy, high luminosity, and the clean experimental environment.

This section is organized as follows. In section II.E.1, we first define the LSP dark matter in the NMSSM, and outline its interactions with the SM particles. We list the relevant model parameters with broad ranges, and compile the current bounds from the collider experiments on them. We then search for the viable solutions in the low mass region by scanning a large volume of parameters. Having shown the existence of these interesting

solutions, we comment on the connection to the existing and upcoming experiments for the direct and indirect searches of the WIMP DM. Focused on the light DM solutions, we study the potential signals of the unique new Higgs physics, light sbottom and stau at the LHC in section II.E.2. We summarize our results and conclude in section II.E.3.

1. Light Neutralino Dark Matter

a. Neutralino Sector in the NMSSM In the NMSSM, the neutralino DM candidate is the lightest eigenstate of the neutralino mass matrix [122], which can be written as

$$M_{\tilde{N}^0} = \begin{pmatrix} M_1 & 0 & -g_1 \frac{v_d}{\sqrt{2}} & g_1 \frac{v_u}{\sqrt{2}} & 0 \\ & M_2 & g_2 \frac{v_d}{\sqrt{2}} & -g_2 \frac{v_u}{\sqrt{2}} & 0 \\ & & 0 & -\mu & -\lambda v_u \\ & * & & 0 & -\lambda v_d \\ & & & & 2 \frac{\kappa}{\lambda} \mu \end{pmatrix} \quad (\text{II.E.66})$$

in the gauge interaction basis of Bino \tilde{B} , Wino \tilde{W}^0 , Higgsinos \tilde{H}_d^0 and \tilde{H}_u^0 , and Singlino \tilde{S} . Here λ , κ are the singlet-doublet mixing and the singlet cubic interaction couplings, respectively [122], and we have adopted the convention of $v_d^2 + v_u^2 = (174 \text{ GeV})^2$. The light neutralino, assumed to be the LSP DM candidate, can then be expressed as

$$\tilde{\chi}_1^0 = N_{11} \tilde{B} + N_{12} \tilde{W}^0 + N_{13} \tilde{H}_d^0 + N_{14} \tilde{H}_u^0 + N_{15} \tilde{S}, \quad (\text{II.E.67})$$

where N_{ij} are elements of matrix N that diagonalize neutralino mass matrix $M_{\tilde{N}^0}$:

$$N^* M_{\tilde{N}^0} N^{-1} = \text{Diag}\{m_{\tilde{\chi}_1^0}, m_{\tilde{\chi}_2^0}, m_{\tilde{\chi}_3^0}, m_{\tilde{\chi}_4^0}, m_{\tilde{\chi}_5^0}\}, \quad (\text{II.E.68})$$

with increasing mass ordering for $m_{\tilde{\chi}_i^0}$.

Given the current chargino constraints, a favorable SUSY DM candidate could be either Bino-like, Singlino-like or Bino-Singlino mixed. In most cases, the DM follows the properties of the lightest (in absolute value) diagonal entry. Similar to Bino-Wino mixing via Higgsinos, Bino and Singlino do not mix directly: they mix through the Higgsinos. The mixing reaches maximum when $M_1 \sim 2\kappa/\lambda\mu$ from simple matrix argument. This Bino-Singlino mixing is

the only allowed large mixing with light DM candidate due to LEP bounds. A particularly interesting case is the Peccei-Quinn limit [246, 362, 363], when the singlet cubic coupling is small: $\kappa \rightarrow 0$, and both the singlet-like (CP-odd) Higgs boson and the Singlino can be light.

Under the limit of either a Bino-like LSP $N_{11} \approx 1$ or a Singlino-like LSP $N_{15} \approx 1$, the couplings of the physical Higgs bosons and the LSP are

$$\begin{aligned}
H_i \tilde{\chi}_1^0 \tilde{\chi}_1^0 \ (i = 1, 2, 3) : & \quad g_1 N_{11} [\xi_i^{h_v} (c_\beta N_{13} - s_\beta N_{14}) - \xi_i^{H_v} (s_\beta N_{13} + c_\beta N_{14})] \\
& + \sqrt{2} \lambda N_{15} [\xi_i^{h_v} (s_\beta N_{13} + c_\beta N_{14}) + \xi_i^{H_v} (c_\beta N_{13} - s_\beta N_{14})] - \sqrt{2} \kappa \xi_i^S N_{15}^2 \\
A_i \tilde{\chi}_1^0 \tilde{\chi}_1^0 \ (i = 1, 2) : & \quad -i g_1 N_{11} \xi_i^A [s_\beta N_{13} - c_\beta N_{14}] \\
& -i \sqrt{2} \lambda N_{15} \xi_i^A [c_\beta N_{13} + s_\beta N_{14}] - i \sqrt{2} \kappa \xi_i^{A_S} N_{15}^2,
\end{aligned} \tag{II.E.69}$$

where ξ_i are the mixing matrix elements for the Higgs fields with

$$H_i = \xi_i^{h_v} h_v + \xi_i^{H_v} H_v + \xi_i^S S, \quad A_i = \xi_i^A A + \xi_i^{A_S} A_S, \tag{II.E.70}$$

in the basis of (h_v, H_v, S) for the CP-even Higgs sector and (A, A_S) for the CP-odd Higgs sector.¹⁰ In the limit of a decoupling MSSM Higgs sector plus a singlet, the singlet-like Higgs has $\xi^S \approx 1$ and the SM-like Higgs has $\xi^{h_v} \approx 1$.

Specifically, in the Bino-like LSP scenario,

$$N_{11} \approx 1, \quad N_{15} \approx 0, \quad N_{13} \approx \frac{m_{ZSW}}{\mu} s_\beta, \quad N_{14} \approx -\frac{m_{ZSW}}{\mu} c_\beta, \tag{II.E.71}$$

$$H_i \tilde{\chi}_1^0 \tilde{\chi}_1^0 : g_1 N_{11} \frac{m_{ZSW}}{\mu} [\xi_i^{h_v} s_{2\beta} + \xi_i^{H_v} c_{2\beta}] - \sqrt{2} \kappa \xi_i^S N_{15}^2, \tag{II.E.72}$$

$$A_i \tilde{\chi}_1^0 \tilde{\chi}_1^0 : -i g_1 N_{11} \frac{m_{ZSW}}{\mu} \xi_i^A - i \sqrt{2} \kappa \xi_i^{A_S} N_{15}^2. \tag{II.E.73}$$

The couplings to the SM-like or MSSM-like Higgs bosons are proportional to the Bino-Higgsino mixing of the order $\mathcal{O}(m_{ZSW}/\mu)$. The coupling to the SM-like Higgs with $\xi_i^{h_v} \approx 1$, $\xi_i^{H_v} \ll 1$ is roughly $s_{2\beta} + \xi_i^{H_v} c_{2\beta}$, and is typically suppressed for $\tan \beta > 1$. The coupling to the MSSM-like Higgs with $\xi_i^{H_v} \approx 1$, $\xi_i^{h_v} \ll 1$, on the other hand, is unsuppressed. The couplings to the singlet-like (CP-even and CP-odd) Higgs bosons are suppressed by N_{15}^2 .

¹⁰In the basis of (h_v, H_v, S) , $h_v = \sqrt{2}[\cos \beta \operatorname{Re}(H_d^0) + \sin \beta \operatorname{Re}(H_u^0)]$ couples to the SM particles with exactly the SM coupling strength; while $H_v = \sqrt{2}[-\sin \beta \operatorname{Re}(H_d^0) + \cos \beta \operatorname{Re}(H_u^0)]$ does not couple to the SM W and Z . Similarly, A and A_S are the CP-odd MSSM Higgs and singlet Higgs, respectively [246].

In the Singlino-like LSP scenario,

$$N_{11} \approx 0, \quad N_{15} \approx 1, \quad N_{13} \approx -\frac{\lambda v}{\mu} c_\beta, \quad N_{14} \approx -\frac{\lambda v}{\mu} s_\beta, \quad (\text{II.E.74})$$

$$H_i \tilde{\chi}_1^0 \tilde{\chi}_1^0 : -\sqrt{2} \lambda N_{15} \frac{\lambda v}{\mu} [\xi_i^{h_v} s_{2\beta} + \xi_i^{H_v} c_{2\beta}] - \sqrt{2} \kappa \xi_i^S N_{15}^2, \quad (\text{II.E.75})$$

$$A_i \tilde{\chi}_1^0 \tilde{\chi}_1^0 : i\sqrt{2} N_{15} \frac{\lambda v}{\mu} \xi_i^A - i\sqrt{2} \kappa \xi_i^{AS} N_{15}^2. \quad (\text{II.E.76})$$

The couplings to the SM-like or MSSM-like Higgs bosons are proportional to the Singlino-Higgsino mixing of the order $\mathcal{O}(\lambda v/\mu)$. The contributions from the h_v and H_v components follow the same relation as in the Bino-like LSP case above. The coupling to the singlet-like Higgs can be approximated as $-\sqrt{2} \kappa N_{15}^2$, proportional to the Singlino component and the PQ symmetry-breaking parameter κ .

Neutralinos couple to fermion-sfermion through their Bino, Wino and Higgsino components, proportional to the corresponding $U(1)_Y$ Hyper charge, $SU(2)_L$ charge and $\tan \beta$ modified Yukawa couplings. For the Bino-like LSP, the coupling is dominated by the $U(1)_Y$ Hyper charge. For the Singlino-like LSP, the couplings to the SM fermions are more complex as the leading contributions depend on the mixing with the gauginos and Higgsinos.

b. Parameters and Constraints There are 15 parameters relevant to our low-mass DM consideration. In the Higgs sector with a doublet and a singlet, the tree-level parameters are $m_{A_{tree}}$,¹¹ $\tan \beta$, μ , λ , κ and A_κ , and loop-level correction parameters on the stop sector M_{Q3} , M_{U3} and A_t . These parameters also determine the Higgsino masses, Singlino mass and make strong connections between these particle sectors. The soft SUSY breaking gaugino mass M_1 governs the Bino mass. To explore the sfermion coannihilation with the LSP, we choose the third generation of stau and sbottom as benchmarks by including M_{L3} , M_{E3} and A_τ for stau, and M_{D3} and A_b for sbottom. The third generation sfermion sectors are expected to potentially have large mixing and small masses from the theoretical point of view, and as well are the least constrained sectors from the phenomenological perspective. We decouple other squarks and sleptons by setting their masses at 3 TeV and other trilinear mass terms

¹¹ $m_{A_{tree}}$ is the tree-level MSSM CP-odd Higgs mass parameter, defined as $m_{A_{tree}}^2 = \frac{2\mu}{\sin 2\beta} (A_\lambda + \frac{\kappa}{\lambda} \mu)$ [122, 364].

Table II.11: The parameters and ranges considered. The symbols “...” in entries indicate the scanning ranges the same as the ones in the general scan.

	General	Scenario-dedicated Scan		
	Scan	Sbottom	Stau	H_1 , A_1 -funnels
$m_{A_{\text{tree}}}$	[0,3000]
$\tan \beta$	[1,55]
μ	[100,500]
$ A_\kappa $	[0,1000]
λ	[0,1]	[0.01,0.6]
κ	[0,1]	either $\kappa \in [2, 30]\lambda/(2\mu)$ or $M_1 \in [2, 30]$, or both		
$ M_1 $	[0,500]			
M_{Q3}, M_{U3}	[0,3000]
$ A_t $	[0,4000]
M_{D3}	[0,3000]	[0,80]	3000	
$ A_b $	[0,4000]	...	0	
M_{L3}, M_{E3}	[0,3000]	3000	[0,500]	3000
$ A_\tau $	[0,4000]	0	[0,2000]	0

to be zero. The range for μ parameter is mainly motivated by the LEP lower bounds on the chargino mass. The upper bounds of superparticle mass parameters and the μ parameter are motivated by the naturalness argument [37, 285, 286, 288].

In the rest of the study, we employ a comprehensive random scan over these 15 parameters, which are summarized in table II.11. The second column presents the parameter ranges for our general scan. To effectively look for possible solutions, we also device several scenario-dedicated scans as listed in the other columns: sbottom-scan, stau-scan and A_1 , H_1 -funnels scan with certain relationship enforced and simplified parameters for different scenarios. The combinations for κ and M_1 are motivated by focusing on the Bino-like and Singlino-like LSP. In addition, we also choose several benchmarks as seeds and vary the DM mass parameters accordingly. This helps us to examine the possibility of Bino-Singlino mixture as well as solutions with fixed sfermion masses.

Focusing on the light DM scenarios motivated in table II.10, and guided by the relevant collider bounds to be discussed in the next section, we adopt the following theoretical and experimental constraints for the rest of the study:

- 2σ window of the SM-like Higgs boson mass: $122.7 - 128.7$ GeV, with linearly added estimated theoretical uncertainties of ± 2 GeV included.
- 2σ windows of the SM-like Higgs bosons cross sections for $\gamma\gamma$, ZZ , W^+W^- , $\tau^+\tau^-$ and $b\bar{b}$ final states with different production modes.
- Bounds on the other Higgs searches from LEP, the Tevatron and the LHC.
- LEP, Tevatron and LHC constraints on searches for supersymmetric particles, such as charginos, sleptons and squarks.
- Bounds on Z boson invisible width and hadronic width.
- B -physics constrains, including $b \rightarrow s\gamma$, $B_s \rightarrow \mu^+\mu^-$, $B \rightarrow \chi_s\mu^+\mu^-$ and $B^+ \rightarrow \tau^+\nu_\tau$, as well as Δm_s , Δm_d , $m_{\eta_b(1S)}$ and $\Upsilon(1S) \rightarrow a\gamma, h\gamma$.
- Theoretical constraints such as physical global minimum, no tachyonic solutions, and so on.

We use modified NMSSMTools 4.2.1 [260–262] to search for viable DM solutions that satisfy the above conditions.

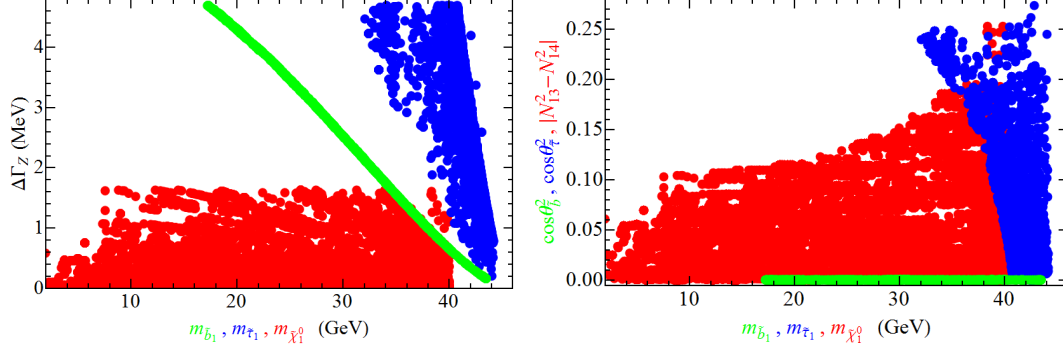


Figure II.39: Z boson partial decay widths (left panel) and coupling parameters $|N_{13}^2 - N_{14}^2|$, $\cos^2 \theta_{\tilde{b}}$, $\cos^2 \theta_{\tilde{\tau}}$ (right panel) to the pairs $\tilde{\chi}_1^0 \tilde{\chi}_1^0$ (red), $\tilde{b}_1 \tilde{b}_1$ (green) and $\tilde{\tau}_1 \tilde{\tau}_1$ (blue) versus the neutralino and sfermion masses. Constraints on $\Delta\Gamma_{\text{inv}}$ in eq. (II.E.77) and $\Delta\Gamma_{\text{tot}}$ in eq. (II.E.78) are imposed.

c. Highlights from Experimental Bounds The absence of deviations from the SM predictions on precision observables as well as null results on new physics direct searches put strong bounds on the parameters. We take them into account to guide our DM study. In this subsection, we highlight some specific collider constraints that are very relevant to our light neutralino DM study.

Bounds on light neutralino LSP

Precision measurements of Z -boson’s invisible width put strong constraint on the light neutralino LSP. The 95% C.L. upper limit on Z boson invisible width is [365]

$$\Delta\Gamma_{\text{inv}} < 2.0 \text{ MeV}. \quad (\text{II.E.77})$$

Z boson coupling to neutralino LSP pairs is proportional to $N_{14}^2 - N_{13}^2$ and vanishes when $\tan\beta = 1$. This coupling could also be small when the LSP is “decoupled” from Higgsinos, e.g., for a Bino-like LSP with $|\mu| \gg |M_1|, g_1 v_{u,d}$ or a Singlino-like LSP with $|\mu| \gg 2|\kappa/\lambda\mu|, |\lambda|v_{u,d}$.

We show the impact of eq. (II.E.77) on the relevant mass and coupling parameters in Fig. II.39. The left panel shows in red the scanning results of $\Gamma(Z \rightarrow \tilde{\chi}_1^0 \tilde{\chi}_1^0)$ as a function

of $m_{\tilde{\chi}_1^0}$. The resulting $|N_{13}^2 - N_{14}^2|$, which governs the $Z\tilde{\chi}_1^0\tilde{\chi}_1^0$ coupling, is shown in the right panel (red). Its typical value is near 0.1. The increasing in the allowed range for larger $m_{\tilde{\chi}_1^0}$ is due to the extra phase space suppression near the Z decay threshold. For $\tan\beta > 1$ and negligible Z decay phase space suppression, this requires $\mu \gtrsim 140$ GeV for the Bino limit shown in eq. (II.E.71) and $\mu/\lambda \gtrsim 540$ GeV for the Singlino limit shown in eq. (II.E.74).

The property of the neutralino LSP is constrained by the invisible decay branching fraction of the observed 126 GeV Higgs as well, with the 95% C.L. upper limit of Br_{inv} around 56% [366] from indirect fitting with current observed production and decays. Current direct searches on Higgs to invisible from ZH associated production and VBF set limits of $\text{Br}_{\text{inv}} < 75\%$ [367] and $\text{Br}_{\text{inv}} < 58\%$ [368]. Limits from other searching channels such as mono-jet and WH associated productions can also contribute (see, e.g., Ref. [369]) and are relatively weak as well.

Bounds on light sfermions

Superpartners of light quarks and leptons are in general excluded up to a few hundred GeV with arbitrary mass splittings [370] and are not suitable to be the NLSP to coannihilate with light neutralino LSP. The stop quark has been excluded up to 63 GeV at LEP [371] for arbitrary mixing angles and splittings. Sneutrino is in general unlikely to coannihilate with the light Bino-like LSP, because the Z -boson invisible width searches forbid light sneutrino. Only sbottom and stau could coannihilate with the light neutralino LSP.

Light sbottom and stau also contribute to the Z hadronic width. The current experimental precision on Z boson decay width is 2.4952 ± 0.0023 GeV [365], leading to

$$\Delta\Gamma_{\text{tot}} < 4.7 \text{ MeV at 95\% C.L.}, \quad (\text{II.E.78})$$

which includes a theoretical uncertainty of ~ 0.5 MeV based on a complete calculation with electroweak two-loop corrections [372].

The couplings of the Z to the sfermions depend on the mixing angles of the sfermions, which are originated from the left-right mixing in the sfermion mass matrices. We take the mixing angle $\theta_{\tilde{f}}$ convention that lighter mass eigenstate of the sfermions follows $\tilde{f}_1 = \cos\theta_{\tilde{f}}\tilde{f}_L + \sin\theta_{\tilde{f}}\tilde{f}_R$. The Z boson coupling to the sfermions can then be expressed as

$$Z\tilde{f}_1\tilde{f}_1 : g_f^L \cos^2\theta_{\tilde{f}} + g_f^R \sin^2\theta_{\tilde{f}}, \quad (\text{II.E.79})$$

Table II.12: Collider constraints on the sbottom and stau. Some of above constraints are from the Review of Particle Physics [370].

\tilde{f}	$m_{min}(\text{ GeV})$	Ref.	Condition
\tilde{b}	76	DELPHI [373]	$\tilde{b} \rightarrow b\tilde{\chi}^0$, all $\theta_{\tilde{b}}$, $\Delta m > 7 \text{ GeV}$
	89	ALEPH [371]	$\tilde{b} \rightarrow b\tilde{\chi}^0$, all $\theta_{\tilde{b}}$, $\Delta m > 10 \text{ GeV}$
	645	ATLAS [374, 375]	$\tilde{b} \rightarrow b\tilde{\chi}_1^0$, $m_{\tilde{\chi}_1^0} < 100 \text{ GeV}$, for $m_{\tilde{b}} > 100 \text{ GeV}$
$\tilde{\tau}$	26.3 (81.9)	DELPHI [373]	$\tilde{\tau} \rightarrow \tau\tilde{\chi}_1^0$, $\Delta m > m_{\tau}$ (15 GeV), all $\theta_{\tilde{\tau}}$

with $g_f^L = -(T_{3f} - Q_f \sin^2 \theta_w)$ and $g_f^R = Q_f \sin^2 \theta_w$ being the left-handed and right-handed chiral couplings of the corresponding SM fermions. To minimize the $Z\tilde{f}_1\tilde{f}_1$ coupling in order to suppress the contribution to Γ_{tot} , $\theta_{\tilde{f}}$ needs to be near the Z -decoupling value: $\tan^2 \theta_{\tilde{f}}^{\text{min}} = -g_f^L/g_f^R$. For a sbottom (down-type squark), $\tan^2 \theta_{\tilde{f}}^{\text{min}}$ equals 5.49, preferring the lighter sbottom to be right-handed. For a stau (slepton), $\tan^2 \theta_{\tilde{f}}^{\text{min}}$ equals 1.16, preferring the lighter stau to be an even mixture of $\tilde{\tau}_L$ and $\tilde{\tau}_R$.

The left panel of Fig. II.39 shows the scanning results of $\Gamma(Z \rightarrow \tilde{b}_1\tilde{b}_1, \tilde{\tau}_1\tilde{\tau}_1)$ as a function of $m_{\tilde{b}_1}$, $m_{\tilde{\tau}_1}$ after imposing $\Delta\Gamma_{\text{tot}} < 4.7 \text{ MeV}$. The resulting mixing parameters $\cos^2 \theta_{\tilde{f}}$ are shown in the right panel. For the light sbottom, it is almost completely right-handed with $\cos \theta_{\tilde{b}} \approx 0$, $m_{\tilde{b}_1} \gtrsim 16 \text{ GeV}$. For the light stau, a wide range of $\cos^2 \theta_{\tilde{\tau}} \lesssim 0.25$ can be accommodated with $m_{\tilde{\tau}_1} \gtrsim 32 \text{ GeV}$, especially for large $m_{\tilde{\tau}_1}$ when there is extra kinematic suppression in phase space.

Light sbottom and light stau are also constrained by many other collider searches, as summarized in table II.12. The LEP constraints on sfermion pair productions excludes sbottom and stau $\lesssim 80 - 90 \text{ GeV}$ with relatively large mass splitting $\Delta m = m_{\tilde{b},\tilde{\tau}} - m_{\tilde{\chi}_1^0} \gtrsim 5 \text{ GeV}$, independent of sfermion mixing angles. Once Δm becomes small ($\lesssim 5 \text{ GeV}$), the LEP constraints could be relaxed. Mono-photon searches at LEP could constrain the extreme degenerate LSP and NLSP sfermion. The limits, however, do not apply for GeV level mass

splitting due to hadronic activity veto applied in the analysis. There are currently no LHC bounds on stau yet. The existing analysis for sbottom searches at the LHC are optimized for heavy (> 100 GeV) sbottom and larger mass splitting. These bounds are applicable to the heavier sbottom \tilde{b}_2 after taking into account the branching fraction modifications for \tilde{b}_2 decay. To summarize, as a result of stringent collider constraints, the coannihilator sfermions considered in this section are in the rather narrow ranges

$$\text{Stau : } m_{\tilde{\tau}_1} = (32 - 45) \text{ GeV} \quad \text{with } \Delta m = m_{\tilde{\tau}} - m_{\tilde{\chi}_1^0} < (3 - 5) \text{ GeV, (II.E.80)}$$

$$\text{Sbottom : } m_{\tilde{b}_1} = (16 - 45) \text{ GeV} \quad \text{with } \Delta m = m_{\tilde{b}} - m_{\tilde{\chi}_1^0} < 7 \text{ GeV.} \quad (\text{II.E.81})$$

Bounds on light Higgs bosons

Current measurements of the Higgs properties at the LHC, in particular the discovery modes $H \rightarrow \gamma\gamma$ and $H \rightarrow ZZ^*$ both point to the 126 GeV Higgs being very SM-like. For the NMSSM, it is conceivable to have light Higgs bosons from the singlet Higgs fields, especially in the approximate PQ-symmetry limit of the NMSSM. These light Higgs bosons could be either CP-even or CP-odd. A light CP-even Higgs boson also appears in the non-decoupling solution of the MSSM [45]. They could give rise to new decay channels of the SM-like Higgs boson observed at the LHC and thus would be constrained by the current observations. If the light Higgs bosons are present in the main annihilation channels for the DM, such as in the case of A_1 , H_1 -funnels, slight mixing with the MSSM Higgs sector is required to ensure large enough cross sections for $\tilde{\chi}_1^0 \tilde{\chi}_1^0 \rightarrow A_1/H_1 \rightarrow \text{SM particles}$ in the early universe. If sizable spin-independent direct detection rate is desired and mainly mediated by singlet-like light CP-even Higgs boson, its sizable mixing with the MSSM CP-even sector is required as well. LEP experiments have made dedicated searches for light Higgs bosons and have tight constraints on the MSSM components of the light Higgs $\xi_1^{h_v}$ and $\xi_1^{H_v}$. NMSSMTools has incorporated all these constraints on the light Higgs bosons. Hadron collider searches on light CP-odd Higgs bosons are also included.

Relic abundance considerations

In the multi-variable parameter space in the NMSSM, the collider constraints presented in the previous sections serve as the starting point for viable solutions. In connection with the direct and indirect searches, the DM related observables, such as Spin-Independent (SI)

cross sections $\sigma_{p,n}^{\text{SI}}$, Spin-Dependent (SD) cross sections $\sigma_{p,n}^{\text{SD}}$, indirect search rate $\langle\sigma v\rangle$ and relic density Ωh^2 are calculated with MicrOmegas 2.2 [376] integrated with NMSSMTools. Furthermore, we choose the LSP to be neutralino and consider its contribution to the current relic abundance. As for a rather tight requirement, we demand the calculated relic density corresponding to the 2σ window of the observed relic density [377] plus 10% theoretical uncertainty [295, 378]. To be conservative, we also consider a loose requirement that the neutralino LSP partially provides DM relic, leaving room for other non-standard scenarios such as multiple DM scenarios [379–386]. We thus choose the tight (loose) relic density requirement as

$$0.0947 \text{ (0.001)} < \Omega_{\tilde{\chi}_1^0} h^2 < 0.142, \quad (\text{II.E.82})$$

d. DM Properties With a comprehensive scanning procedure over the 15 parameters as listed in Table II.11, we now present the interesting features of the viable LSP DM solutions and discuss their implications and consequences.

We show the DM relic density Ωh^2 (left panel) and the scaled¹² spin-independent cross section σ_p^{SI} (right panel) versus the neutralino DM mass in Fig. II.40. The red, green, and blue dots are the points in the A_1 , H_1 -funnels, sbottom, and stau coannihilation regions, respectively, which satisfy all constraints described in section II.E.1.b as well as direct detection limits from the LUX [387] and superCDMS [388]. The grey shaded region shows the sbottom coannihilation solutions that are excluded by direct detection. The horizontal line marks the lower limit for the tight relic abundance requirement. On the right panel, the color points (shaded regions) are the viable solutions that pass tight (loose) relic abundance constraints specified in eq. (II.E.82). To gain some perspectives, also shown there are the 68% and 95% C.L. signal contours from CDMS II [120], the current 95% C.L. exclusion and projected future exclusion limit from superCDMS, the current LUX result and future LZ expectation. The grey shaded region at the bottom is for the coherent neutrino-nucleus scattering backgrounds [389], below which the signal extraction would be considerably harder.

As seen from the left panel of Fig. II.40, all the three scenarios as in Table II.10 could

¹²DM direct detection observables are scaled with the ratio of the LSP relic density over the measured value.

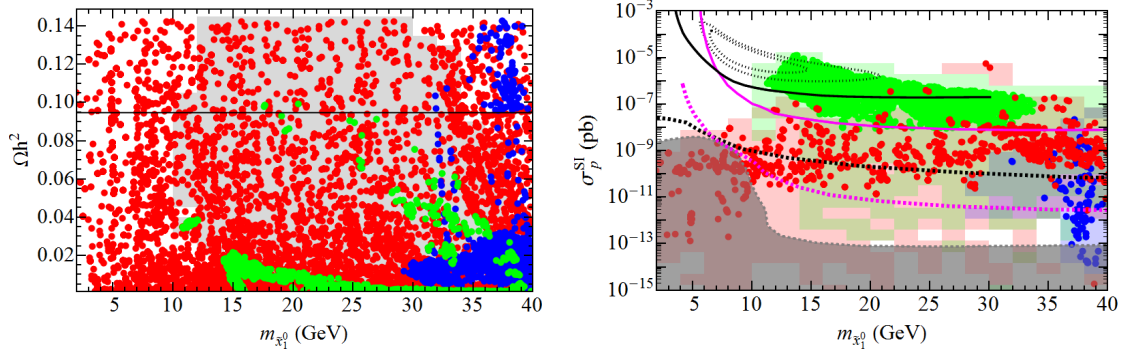


Figure II.40: Relic density (left panel) and scaled spin-independent cross section σ_p^{SI} (right panel) versus neutralino DM mass. All points pass constraints described in section II.E.1.b. The A_1 , H_1 -funnels, sbottom coannihilation, stau coannihilation solutions are shown in red, green and blue dots, respectively. Left panel: all points pass the LUX [387] and superCDMS [388] direct detection constraints. The grey shaded region shows the sbottom coannihilation solutions that are excluded by direct detection. The horizontal line is the lower limit for the tight relic requirement. Right panel: the color points (shaded regions) are the viable solutions that pass tight (loose) relic abundance constraints specified in eq. (II.E.82). Also shown are the 68% and 95% C.L. signal contours from CDMS II [120] (dotted black enclosed region), 95% C.L. exclusion and projected exclusion limits from superCDMS (solid and dashed black) and LUX/LZ (solid and dashed magenta). The grey shaded region at the bottom is for the coherent neutrino-nucleus scattering backgrounds [389].

provide the right amount of relic cold dark matter within the 2σ Planck region. However, results from the DM direct detection have led to important constraints, cutting deep into the regions consistent with the relic density considerations, in particular, for the sbottom coannihilation case. The direct detection in the sbottom coannihilation scenario receives a large contribution from the light sbottom exchange, typically of the order $10^{-8} \sim 10^{-5}$ pb, which is severely constrained by current searches from LUX and superCDMS. The large shaded grey region of sbottom coannihilation solutions on the left panel of Fig. II.40 is excluded by the direct detection constraints. This is also seen on the right panel of Fig. II.40 by the green dots mostly excluded by the direct detection. There is, however, a narrow dip region for $m_{\tilde{b}_1} - m_{\tilde{\chi}_1^0} < 3$ GeV when the direct detection rate could be suppressed below the current limit (for example, see [390]). These small mass splittings indicate late freeze-out of the coannihilator, resulting in a low relic density for the DM. For $m_{\tilde{b}_1} - m_{\tilde{\chi}_1^0} > m_b$, the direct detection rate decreases slowly as the splitting increases. The collider searches from LEP also exclude large mass splitting. Consequently, to survive direct detection, loose relic density and collider constraints, the mass splittings typically need either to be between 2 GeV to m_b , or be as large as allowed by the LEP searches. On the other hand, the A_1 , H_1 -funnels and stau coannihilation cases are not affected much by the direct detection constraints. Only a small fraction of A_1 , H_1 -funnels and stau coannihilation solution is excluded by the direct detection. For the A_1 , H_1 -funnel region, $m_{\tilde{\chi}_1^0}$ spans over the whole region of 2–40 GeV. For the sbottom (stau) coannihilation, only $m_{\tilde{\chi}_1^0} \gtrsim 10$ (30) GeV is viable due to the tight LEP constraints.

There are several recent studies on the possible “blind spot” for direct detection where large accidental cancellation in the neutralino Higgs couplings occurs [292, 359, 391]. Ref. [391] specifically pointed out the non-negligible cancellation between direct detection mediated by the light CP-even Higgs and the heavy CP-even Higgs with negative μ parameter. These constructions could further reduce the direct detection rate for our A_1 , H_1 -funnels and stau coannihilation solutions.

The left panel of Fig. II.41 shows the relic density versus the mass splitting $|m_{A_1, H_1} - 2m_{\tilde{\chi}_1^0}|/m_{A_1, H_1}$ for the A_1 , H_1 -funnel region. The deviation from the pole mass is typically less than 15% to satisfy the relic density constraints, with $|m_{A_1, H_1} - 2m_{\tilde{\chi}_1^0}| \lesssim 12$ GeV. The

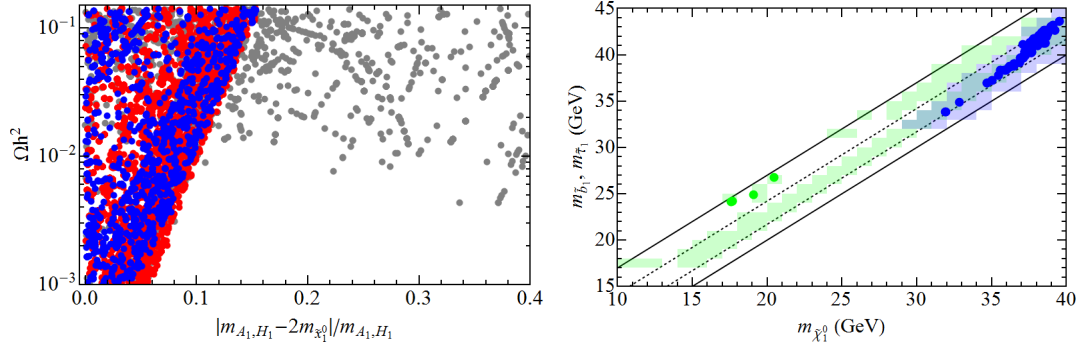


Figure II.41: Left panel: relic density versus the mass splitting $|m_{A_1, H_1} - 2m_{\tilde{\chi}_1^0}|/m_{A_1, H_1}$ for A_1 -funnel (red) and H_1 -funnel (blue). Grey points represent those with non-negligible s -channel Z boson contributions. Right panel: the sfermion masses versus neutralino LSP mass for the coannihilation regions. The shaded/dotted regions are those pass loose/tight relic density requirement for the sbottom coannihilation (green) and stau coannihilation (blue). The diagonal lines indicate the mass splittings of 0, 1.7 (m_τ), 4.2 (m_b), and 7 GeV as references.

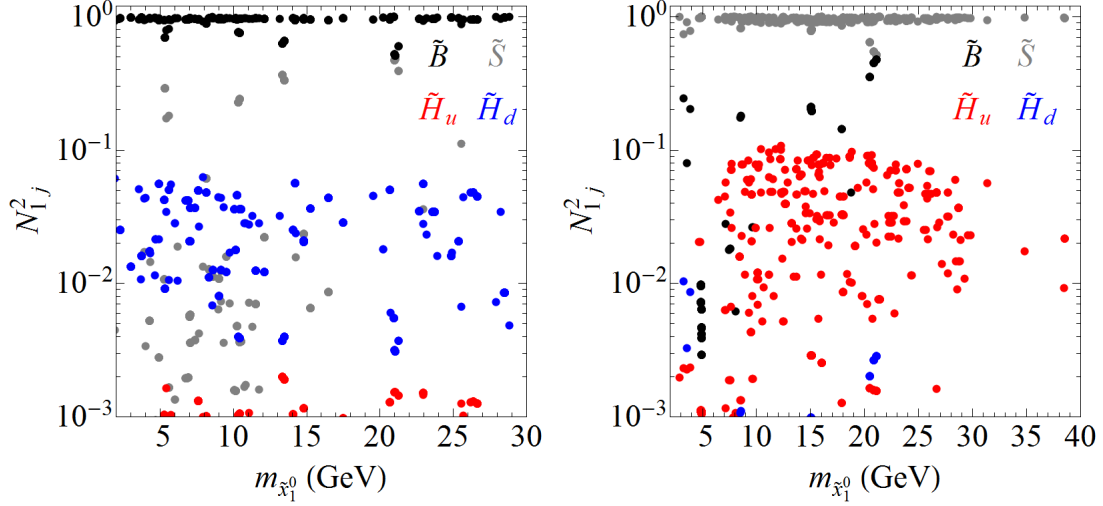


Figure II.42: The LSP DM candidate components N_{1j}^2 as a function of its mass in the A_1 , H_1 -funnel region with tight relic constraints. The left panel is for the Bino-like LSP ($N_{11}^2 > 0.5$) and the right panel is for Singlino-like LSP ($N_{15}^2 > 0.5$).

interplay among the LSP's couplings to the resonant Higgs mediator, the Higgs couplings to SM particles, and the resonance enhancement in the early universe determines the relic density. For larger deviations from the resonance region, there are non-negligible Z mediated contributions (indicated by grey points in Fig. II.41), which is emphasized in Ref. [359].

The right panel of Fig. II.41 shows the mass of sbottom/stau versus neutralino LSP for the sbottom/stau coannihilation regions. For the sbottom, imposing loose relic density requirement and collider constraints yields that $2 \text{ GeV} < m_{\tilde{b}_1} - m_{\tilde{\chi}_1^0} < 7 \text{ GeV}$. Most points that satisfy the direct detection fall in the region of $2 \text{ GeV} < m_{\tilde{b}_1} - m_{\tilde{\chi}_1^0} < m_b$, which typically have a suppressed relic density. Only very few points survive both the dark matter direct detection and tight relic density requirement with $m_{\tilde{\chi}_1^0} \sim 20 \text{ GeV}$ and $m_{\tilde{b}_1} - m_{\tilde{\chi}_1^0} \sim 6 \text{ GeV}$. For the stau, imposing direct detection bound does not restrict the mass regions further, while imposing the tight relic density requirement favors slightly larger stau masses.

It is informative to understand the DM LSP nature in terms of the gaugino, Higgsino and Singlino components N_{1j}^2 . This is shown in figures II.42 and Fig. II.43, for the A_1 , H_1 -funnel

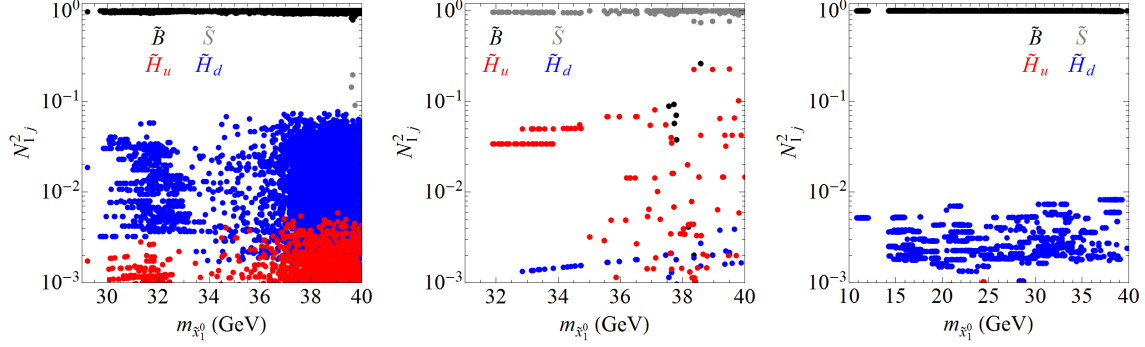


Figure II.43: The LSP DM candidate components N_{1j}^2 as a function of its mass for stau coannihilation with the Bino-like LSP (left panel) and the Singlino-like LSP (middle panel) and sbottom coannihilation (right panel) with the loose relic density constraint.

region and the stau, sbottom coannihilation regions, respectively, as a function of the LSP mass.

As seen in Fig. II.42, for the A_1 , H_1 -funnel case, the dark matter could either be Bino (dark black dots) or Singlino (light black dots) dominated, or as a mixture of these two. For a Bino-like LSP (left panel), the \tilde{H}_d component is typically larger: about 0.5%–5% while \tilde{H}_u component is suppressed, $\lesssim 0.1\%$. For a Singlino-like LSP (right panel), it features a larger \tilde{H}_u component: around 1% to 10%, while \tilde{H}_d fraction is much more suppressed. These features are direct results of the mixing matrix as shown in eq. (II.E.71) and eq. (II.E.74).

As seen in Fig. II.43, the stau coannihilation case can have the LSP being dominantly Bino-like (left panel) with a Higgsino fraction up to about 5% (mostly \tilde{H}_d), or dominantly Singlino-like (middle panel) with a Higgsino fraction up to about 20% (mostly \tilde{H}_u). The Singlino-like LSP case usually has a larger relic density due to the suppressed coupling to the stau coannihilator. The sbottom coannihilation case (right panel) has a much smaller fraction of Higgsino component 0.5% or less, with LSP being mostly Bino-like.

Finally, we want to comment on the degree of mass degeneracy for these solutions. For the funnel case, the requirement is mostly for hitting the resonance with the LSP pair. For a measure defined as $|m_{H_1/A_1} - 2m_{\tilde{\chi}_1^0}|/m_{H_1/A_1}$, about 10% mass split in the neutralino

and singlet-like Higgs sector is more than sufficient to provide viable solutions as shown in Fig. II.41. For the sfermion coannihilation, several requirements need to be satisfied simultaneously. One requirement is the nearly degenerate masses of the coannihilator and the LSP, as enforced by the LEP constraints and effective coannihilation. The other requirement is to have the appropriate amount of L-R mixing while keeping the heavier eigenstate heavier than hundreds of GeV, as enforced by Z -boson width constraint, collider searches on sfermions, and the decays of the SM-like Higgs boson. This tuning leads to the lack of solutions with Z -decoupling sfermions as shown in Fig. II.39. Overall, light neutralino solutions require certain level of tuning, and future searches are likely to either lead to discovery or push the solutions into much narrower and fine-tuned regions.

Direct and indirect detection

As already discussed in the last section, for the spin-independent (SI) direct detection of all these three scenarios with the loose relic density constraint, the signal rates vary in a large range. It is typically mediated by the CP-even Higgs bosons via t -channel exchange. The partons in the nucleon couple to the MSSM doublet Higgs bosons (or h_v and H_v) directly. The dark matter candidate, which is Bino-like or Singlino-like, couples to the doublet Higgs bosons through their Higgsino components only, as shown in eqs. (II.E.72) and (II.E.75). Their direct detection are usually suppressed because the singlet-like Higgs only couples to the SM fermions weakly, and the doublet Higgs bosons do not couple to the LSP pairs much. The signal rate could be extended well below the coherent neutrino backgrounds. Certain tuned scenarios could result in larger SI direct detection, for example, a very light CP-even Higgs with sizable doublet Higgs fraction [392, 393]. The detection rate for the sbottom coannihilation scenario, on the other hand, is naturally high, coming from the additional contribution through the sbottom exchange.¹³ The next generation direct detection experiments such as LZ and superCDMS would provide us valuable insights into very large portion of the allowed parameter space with the increased sensitivity of several orders of magnitude.

¹³A recent study shows that the pole region resides at $m_{\tilde{b}} = m_{\tilde{\chi}_1^0} - m_b$ instead of $m_{\tilde{b}} = m_b + m_{\tilde{\chi}_1^0}$ [390]. Given that the sbottom mass is always larger than the corresponding LSP mass, we are away from this pole region. In our analyses, we correct the direct detection cross sections calculated by MicrOMEGAs [376] by replacing the values for points near the fake pole of $m_{\tilde{b}} = m_b + m_{\tilde{\chi}_1^0}$ with points of the same sbottom mass away from the pole, which well approximates the results in Ref. [390] in the relevant regions.

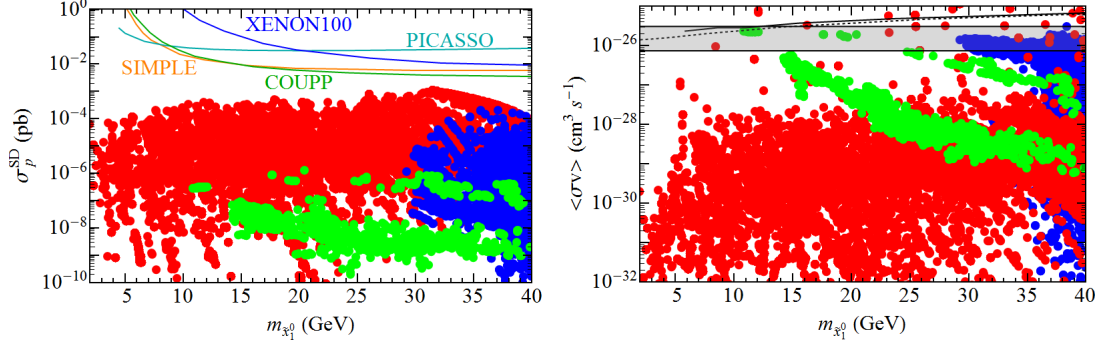


Figure II.44: The scaled proton spin-dependent direct detection rate (left panel) and the indirect detection rate (right panel) versus the neutralino DM mass. Red, green and blue dots are for the solutions in A_1 , H_1 -funnels, sbottom and stau coannihilation scenarios, respectively. The solid lines on the left panel correspond to exclusions on σ_p^{SD} from SIMPLE [394], PICASSO [395], COUPP [396], and XENON100 [397]. The solid (dashed) line on the right panel corresponds to exclusion on indirect detection rate from Fermi-LAT [72] with $b\bar{b}$ ($\tau^+\tau^-$) annihilation mode. The shaded region are the preferred low velocity annihilation cross section to account for the gamma ray excess with 35 GeV Majorana DM annihilating into $b\bar{b}$ [398].

We show the scaled proton Spin-Dependent (SD) cross section in the left panel of Fig. II.44. All the viable solutions has the spin-dependent cross sections of the order 10^{-4} pb or smaller, below the current limits from various dark matter direct detection experiments. For these solutions through the funnels and coannihilations, the usual connection among the annihilation, direct detection, indirect detection and collider searches through crossing diagrams is not always valid. It needs to be examined in a scenario and model specific manner. Due to the Majorana nature of the neutralino LSP, only the CP-even Higgs bosons could mediate the SI direct detection, and only the axial vector current through Z -boson contributes to the SD direct detection. In addition, there are squark contributions to the direct detection, which leads to large SI direct detection rate for sbottom coannihilation scenario as discussed in previous sections. As a result, the SD direct detection provides a complementary probe for the neutralino LSP's couplings to the Z boson. This is especially true even in some of the “blind spot” scenarios.

In the right panel of Fig. II.44 we show the low velocity DM annihilation rate in the current epoch for different light DM scenarios, together with the 95% C.L. exclusions on the indirect detection rate from Fermi-LAT [72]. Majority of our solutions satisfy the indirect detection constraints. Note that the low-velocity DM annihilation rate could be either larger or smaller than the usual WIMP thermal relic preferred value of $\sim 2 \times 10^{-26} \text{ cm}^3\text{s}^{-1}$ (assuming s -wave dominance). This is because the DM annihilation rate at low velocity does not necessarily correspond to the thermal averaged dark matter annihilation $\langle\sigma v\rangle$ around the time of the dark matter freezing out. When far away from the resonance, the s -channel CP-odd (CP-even) Higgs exchange corresponds to s -wave (p -wave) annihilation. While low velocity annihilation rate for the s -wave annihilation is similar to the thermal freezing out rate due to the velocity independence, the rate for p -wave annihilation today is much lower comparing to the early universe due to velocity suppression. Furthermore, this simple connection between mediator CP property and partial wave no longer holds when near the resonance region, when full kinematics needs to be taken into account in numerical studies. In particular, for the funnel region with $2m_{\tilde{\chi}_1^0} > m_{A_1, H_1}$ ($2m_{\tilde{\chi}_1^0} < m_{A_1, H_1}$), low velocity rate should be higher (lower) than the freezing out annihilation rate due to the increase (decrease) of resonant enhancement. The bulk of our funnel region solutions corresponds to the $2m_{\tilde{\chi}_1^0} < m_{A_1, H_1}$

case, as a result of the combined constraints imposed.

Interestingly, our results indicate that possible solutions exist for those regions preferred by the GeV gamma-ray excess from the Galactic Center, which is indicated by the grey region in the right panel of Fig. II.44. While the astro-physical sources for explanation of the excess could be very subtle with different subtraction scheme resulting in different shapes of excess, or even no excess, this observation has stimulated several interesting discussions recently [398–409]. As shown in later sections, the dominant decay for funnel mediators is $b\bar{b}$, which serves as a good candidate for the gamma-ray source. For the stau and sbottom coannihilations, the main annihilation channels for the LSP pairs are $\tau^+\tau^-$ and $b\bar{b}$, with the former yielding a different gamma ray spectrum. The predicted gamma-ray excess spectra could vary in shape in many different ways in a given model such as (N)MSSM due to various composition of annihilation products. With more data collected and analyzed, confirmation of the gamma-ray excess and a robust extraction of the excess shape would help pin down the source and shed light on the underlying theory. The three light neutralino LSP DM scenarios provide an important framework with their different annihilation modes, yielding a range of soft to hard gamma-ray spectra to confront the potential excess data.

2. LHC Observables

Collider experiments provide a crucial testing ground for the WIMP light dark matter scenarios. In the NMSSM, guided by the light A_1 and H_1 in the funnel region, the light sbottom and stau in the coannihilation regions, we discuss the collider implications of the three light dark matter solutions on observables related to the SM-like Higgs boson, searches for light scalars and Missing Transverse Energy (MET) signals.

a. Modifications to the SM-like Higgs Boson Properties The observation of a SM-like Higgs boson imposes strong constraints on the extensions of the SM Higgs sector. In particular, one of the CP-even Higgs bosons in the NMSSM is required to have very similar properties to the SM Higgs boson. As a result, any deviation of this SM-like Higgs boson from h_v state is tightly constrained. Moreover, decays of the SM-like Higgs boson to

these newly accessible states of $\tilde{\chi}_1^0\tilde{\chi}_1^0$, A_1A_1 , H_1H_1 , $\tilde{\tau}_1^+\tilde{\tau}_1^-$ and $\tilde{b}_1\tilde{b}_1^*$ could reduce the Higgs branching fractions to the SM particles, which are constrained by the current experimental results as well. Furthermore, new light charged sparticles such as sbottom and stau could modify the loop-induced Higgs couplings such as Higgs to diphoton.

We examine the cross sections of the dominant channels for the SM-like Higgs boson search, as well as the Higgs decay branching fractions to those new light states. In Fig. II.45, we show the ratios of the cross sections with respect to the SM value $\sigma/\sigma_{\text{SM}}$ of $gg \rightarrow H_{SM} \rightarrow WW/ZZ$ versus that of $gg \rightarrow H_{SM} \rightarrow \gamma\gamma$ for the 126 GeV SM-like Higgs. The $\gamma\gamma$ channel remains correlated with the WW/ZZ channel, with the cross section ratios to the SM values varying between 0.7 – 1.2. Since the W -loop dominates the Higgs to diphoton coupling, deviations from the diagonal line come from the variation of other loop contributions such as the (s)fermion-loop. Importantly, although we have new light charged states such as sbottom and stau that could modify the Higgs to diphoton coupling, it does not show large deviations. Their limited contributions result from indirect constraints imposed on the Higgs boson decays to these light sfermions pairs. Beyond the mass range of our current interest, dedicated scan for stau around 100 GeV may still give very large enhancement in the diphoton rate, as discussed in detail in Ref. [259].

We show the decay branching fractions of the SM-like Higgs boson to the new states in Fig. II.46. The left panel shows the branching fractions of $H_{SM} \rightarrow A_1A_1, H_1H_1$. We see that the exotic decays can be as large as 40% and still consistent with the current Higgs measurements. Given the possible decay final states of A_1 and H_1 to $\tau\tau$, $b\bar{b}$ or $\gamma\gamma$, dedicated searches for these exotic multi-body decays of the SM-like Higgs could be fruitful in studying these solutions. A generic 7-parameter fit with extrapolation shows the LHC 14 TeV could bound the exotic decays of the Higgs boson up to 14 – 18% (7 – 11%) with 330 (3000) fb^{-1} of integrated luminosity [196], assuming the couplings of the Higgs boson to W and Z not exceeding the SM values [172].

The right panel in Fig. II.46 shows the branching fractions of $H_{SM} \rightarrow \tilde{\chi}_1^0\tilde{\chi}_1^0$, $\tilde{\tau}_1^+\tilde{\tau}_1^-$ and $\tilde{b}_1\tilde{b}_1^*$ versus contributions to the Z -boson width. The invisible decay channel $\tilde{\chi}_1^0\tilde{\chi}_1^0$ (red) shows some correlations between Z and H_{SM} decay because both are mediated through the Higgsino component. The invisible branching fraction of the SM-like Higgs boson could be quite

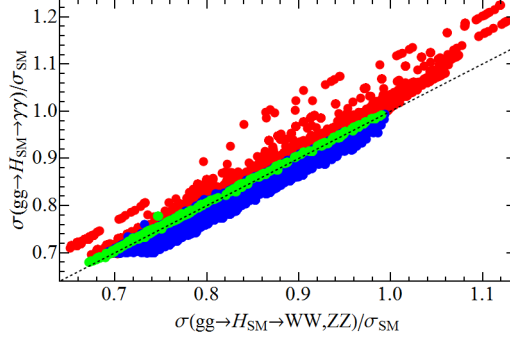


Figure II.45: The cross section ratios $\sigma(gg \rightarrow H_{SM} \rightarrow WW/ZZ)/\sigma_{SM}$ versus $\sigma(gg \rightarrow H_{SM} \rightarrow \gamma\gamma)/\sigma_{SM}$ for the SM-like Higgs. The A_1 , H_1 -funnels, sbottom coannihilation, stau coannihilation solutions are in red, green and blue dots, respectively. A black dashed line with slope 1 is shown as a reference.

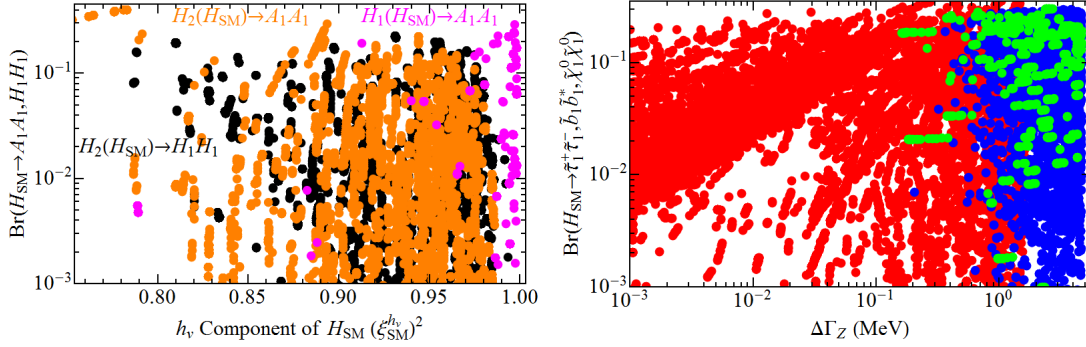


Figure II.46: Left panel: branching fractions of the SM-like Higgs boson decaying to new light Higgs channels $A_1 A_1$ (magenta and orange), and $H_1 H_1$ (black) versus the h_v fraction $(\xi_{SM}^{h_v})^2$ of the SM-like Higgs boson. Right panel: branching fractions of the SM-like Higgs boson decaying to $\tilde{\chi}_1^0 \tilde{\chi}_1^0$ (red), $\tilde{b}_1 \tilde{b}_1^*$ (green) and $\tilde{\tau}_1^+ \tilde{\tau}_1^-$ (blue) versus partial widths of these modes for Z boson.

sizable, reaching 30% – 40%. While the current LHC limits on the invisible Higgs decay via the ZH and VBF channels are relatively weak [366–368], future measurements will certainly improve the sensitivity to further probe this important missing energy channel [410–413].

The Higgs boson couplings to sfermion receive contributions from D-term, F-term and trilinear soft SUSY breaking terms, resulting in a generally non-correlated decay branching fractions to $\tilde{b}_1\tilde{b}_1^*$ (green) and $\tilde{\tau}_1^+\tilde{\tau}_1^-$ (blue) comparing to the corresponding decays of the Z boson. These decay branching fractions could be as large as 30%. However, given the small mass splitting between the mass of the sbottom/stau with that of the LSP, all the SM decay products would be too soft to be identifiable in the LHC environment. In practice, those channels could be counted as the invisible modes.

b. Non-SM Light Higgs Bosons Non-SM light Higgs bosons are particularly important in the A_1 , H_1 -funnel solutions and may as well exist for sbottom and stau coannihilation solutions. They are well-motivated in the PQ-limit NMSSM. These light scalars are usually singlet-dominant, but they have non-negligible mixing with the MSSM doublet Higgs bosons in the case of the A_1 , H_1 -funnel solutions.

The two panels on the left of Fig. II.47 show the couplings of A_1 and H_1 to quarks, gluons and gauge bosons, normalized to the SM values, versus the doublet fractions as defined in eq. (II.E.70). For A_1 , the couplings squared roughly scale with the MSSM CP-odd Higgs fraction $(\xi_1^A)^2$. The couplings to the up-type quarks are further suppressed by $1/\tan\beta$ while the couplings to the down-type quarks are enhanced by $\tan\beta$, which could reach ~ 0.1 for $|g_d/g_d^{\text{SM}}|^2$ despite the small $(\xi_1^A)^2$. Loop induced A_1 coupling to gluon is dominated by the bottom loop, therefore roughly the same order as the normalized $A_1 d\bar{d}$ coupling. The H_1 couplings to SM particles are through its h_v and H_v components. h_v couples in the same way as the SM Higgs, while H_v couples to the up- and down-type quarks with a factor of $1/\tan\beta$ and $\tan\beta$ of the corresponding SM Higgs couplings, and does not couple to W and Z at all. $H_1 d\bar{d}$ and $H_1 gg$ couplings squared span over a while range for a given $(\xi_1^{h_v})^2 + (\xi_1^{H_v})^2$, while $H_1 u\bar{u}$ and $H_1 VV$ scale with $(\xi_1^{h_v})^2 + (\xi_1^{H_v})^2$ almost linearly.

We show the leading decay branching fractions of the light Higgs bosons for the A_1 , H_1 -funnel cases in the two right panels of Fig. II.47. The decays of both CP-even and CP-odd

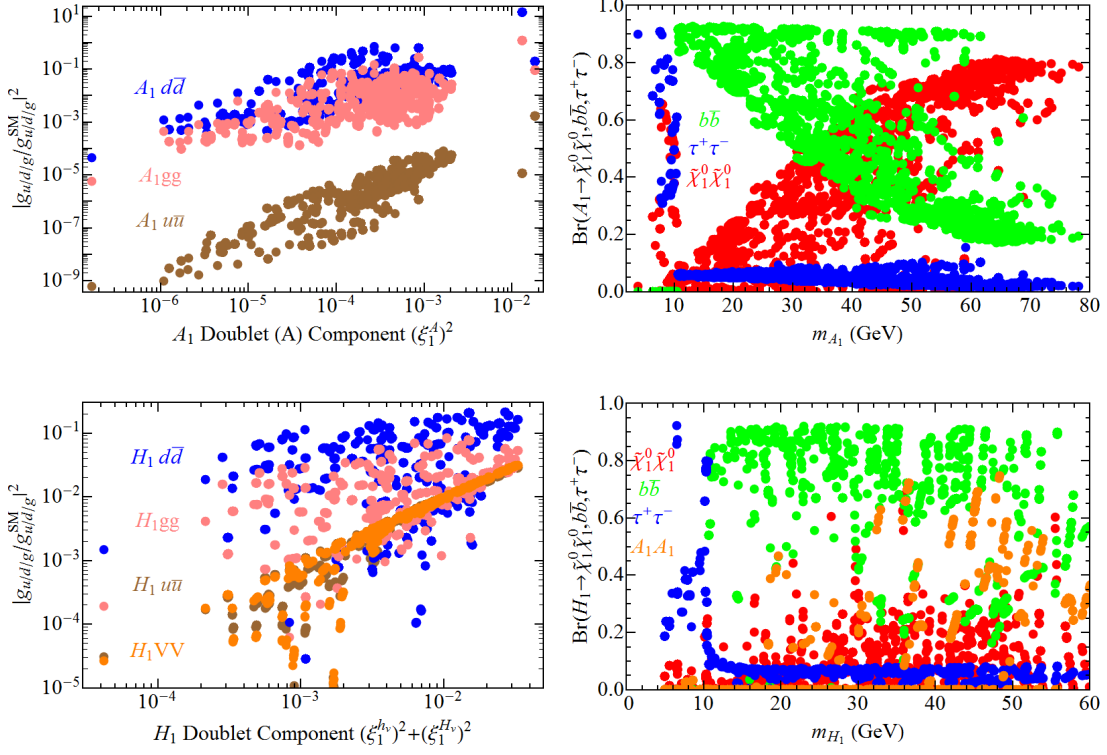


Figure II.47: Left panels: squared normalized couplings of the light CP-even, CP-odd Higgs bosons to up-type quarks (brown), down-type quarks (blue), gluon pair (pink) and weak boson pairs (orange) versus their doublet fraction: $(\xi_1^A)^2$ for A_1 (upper panel) and $(\xi_1^{h_v})^2 + (\xi_1^{H_v})^2$ for H_1 (lower panel) in the funnel regions. Right panels: branching fractions of light Higgs bosons A_1 , H_1 to $\tilde{\chi}_1^0 \tilde{\chi}_1^0$ (red), $b\bar{b}$ (green) and $\tau^+ \tau^-$ (blue) and $A_1 A_1$ (brown) final states for the funnel regions.

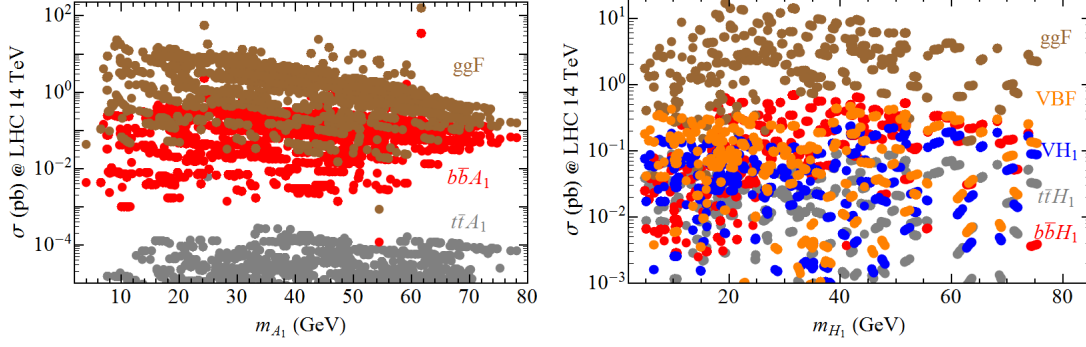


Figure II.48: Total cross sections at the 14 TeV LHC for the light A_1 (left panel) and H_1 (right panel), from the gluon fusion (ggF), Vector Boson Fusion (VBF), Vector boson associated production (VH_1), and $b\bar{b}$, $t\bar{t}$ associated production.

Higgs bosons show clear $\tau^+\tau^-$ dominance at lower masses and $b\bar{b}$ dominance once above the $b\bar{b}$ threshold. It is interesting to note that the invisible mode for $A_1 \rightarrow \tilde{\chi}_1^0 \tilde{\chi}_1^0$ is competitive to $\tau^+\tau^-$ below the $b\bar{b}$ threshold, and increasingly important for larger m_{A_1} comparing with the $b\bar{b}$ mode. This is because the higher DM mass, the more annihilation contribution through Z -boson (for example, the Z -funnel emphasized in Ref. [359]) could be in effect, allowing either larger deviation of the dark matter from A_1 pole and larger branching fraction of A_1 to LSP pair. For the H_1 decays on the other hand, the invisible mode $H_1 \rightarrow \tilde{\chi}_1^0 \tilde{\chi}_1^0$ is less competitive and typically below 30%. A new interesting channel $H_1 \rightarrow A_1 A_1$ opens up when kinematically allowed, which could reach as large as 80%.

These light Higgs bosons can be produced either indirectly from the decay of heavier Higgs bosons or directly from the SM-like processes through their suppressed MSSM doublet Higgs components. The former indirect production has many unique features. One of the important cases has been discussed in the previous section as $H_{SM} \rightarrow A_1 A_1$. Many other interesting channels have also been discussed in Refs. [369].

The direct production cross sections at the LHC could still be quite sizable, benefited from the large phase space and high parton luminosity at low x . We calculate the cross sections of these light Higgs bosons by extrapolating SM Higgs cross sections [414] to low

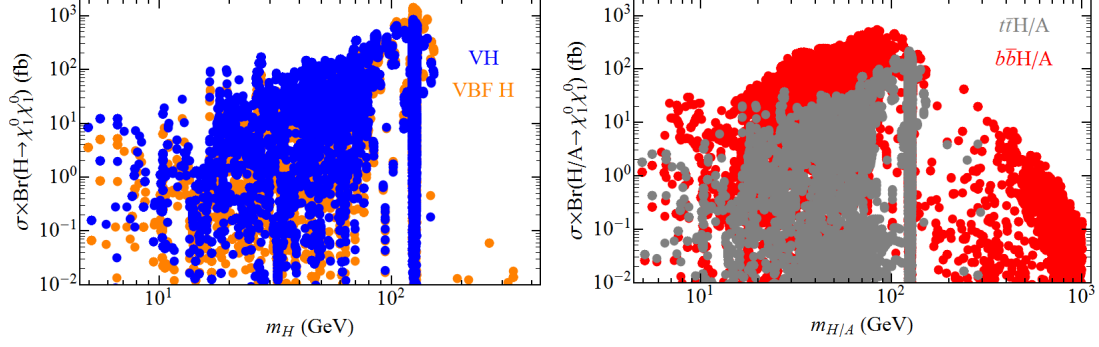


Figure II.49: Neutralino DM production from Higgs decays at the 14 TeV LHC as a function of Higgs boson mass. Left panel is for ZH , WH and VBF production, and right panel is for $t\bar{t}H/A$, $b\bar{b}H/A$ associated production.

mass regions and scaling with the corresponding squared couplings. The production cross sections for various channels are shown in Fig. II.48. The gluon fusion remains to be the leading production mode, and is typically of the order of pb. For the light A_1 , because its coupling to the top quark is suppressed by $\tan\beta$, the $t\bar{t}A_1$ cross section are as low as tens of ab, while $b\bar{b}A_1$ cross section could reach as high as pb level. For the light H_1 , it usually mixes more with the h_v , resulting in sub pb level $t\bar{t}H_1$ and $b\bar{b}H_1$ cross sections. The light CP-even Higgs boson also couples to the weak bosons. The VBF and Z/WH_1 associated production rate range from sub fb to sub pb.

As discussed in the last section, one of the promising channels to search at the LHC is the Higgs boson to invisible mode [367, 368]. This study can be naturally carried out with the Higgs bosons other than the SM-like one. In Fig. II.49 we show the cross sections for the Higgs bosons produced in channels of $t\bar{t}H/A$, $b\bar{b}H/A$, WH/ZH , as well as VBF, with the subsequent decay of Higgs bosons into a neutralino LSP pair as the invisible mode. For VH and VBF, the cross section rate could be as large as 10 fb to 1 pb for production via a relatively light Higgs, reaching a maximum near $m_{H_{SM}} \approx 125$ GeV. This is because VVH coupling is maximized for the SM-like Higgs. We note that given the fact that the SM-like Higgs boson must take up a large portion of h_v in the doublet, such associated production

will be correspondingly suppressed for other Higgs bosons. On the other hand, the $b\bar{b}H/A$ and $t\bar{t}H/A$ production cross sections reach their maximal allowed value around 80 GeV and fall below 1 fb for $m_{H/A} \gtrsim 600$ GeV.

We have also included contributions from the solutions of both A_1 , H_1 -funnels and coannihilations. In principle, the coannihilation regions do not necessarily have light Higgs bosons in presence, nor the Higgs bosons have large branching fractions to DM pairs. Nevertheless, Higgs bosons could help enhance the DM signals, especially for the Singlino-like one. These processes can be triggered in the LHC experiments with large MET plus the other companioning SM particles. Besides the typical search for $\ell\ell$ or $\ell\nu + \cancel{E}_T$ and VBF jets $+\cancel{E}_T$, other possible search channels include the heavy quark associated production $t\bar{t} + \cancel{E}_T$ and $b\bar{b} + \cancel{E}_T$. It is also known that one could take the advantage of the Initial State Radiation (ISR) of a photon or a jet for DM pair production. Such searches have been carried out in terms of effective operators [415] at the LHC for mono-photon and mono-jet searches. These searches should be interpreted carefully in our case through Higgs portal, due to the existence of the relatively light particles in the spectrum (see, e.g., Ref. [416]).

c. Light Sfermions It is of intrinsic interest to study the viability of the light sfermions at the LHC. Usual sfermion searches at the LHC tag the energetic visible part of the sfermion decay, requiring a larger mass gap between the sfermion and neutralino LSP. In this section, we discuss the LHC implications for these light sfermions with compressed spectra.

The light sbottom has to be very degenerate with the LSP to avoid the LEP constraints as shown in eq. (II.E.81): $\Delta m = m_{\tilde{b}_1} - m_{\tilde{\chi}_1^0} \lesssim 7$ GeV. This very special requirement has important kinematical and dynamical consequences and it leads to two distinctive regimes for the sbottom search at the LHC.

For $\Delta m > m_b$, the prompt decay of $\tilde{b}_1 \rightarrow b\tilde{\chi}_1^0$ would result in $2b + \cancel{E}_T$ final state for sbottom pair production. Given the softness of the b jets with energy of a few GeV, these events have to be triggered by demanding large \cancel{E}_T or a very energetic jet from initial or final state radiation. As a result, the b jet from sbottom though soft in the sbottom rest frame, can be boosted and can be even triggered on. However, the signal cross section is reduced by orders of magnitude with the requirement of large \cancel{E}_T or a energetic jet.

Table II.13: Summary of the ATLAS sbottom search results on the upper bound of signal cross section σ_{vis} [375], and the sbottom signal cross section σ_{sig} after selection cuts for the benchmark point of $m_{\tilde{b}_1} = 20$ GeV and $m_{\tilde{\chi}_1^0} = 14$ GeV from our study, in the two signal regions SRA and SRB.

	SRA			SRB
m_{CT}	≥ 250 GeV	≥ 300 GeV	≥ 350 GeV	
95% C.L. upper limit				
σ_{vis} (fb)	0.45	0.37	0.26	1.3
σ_{sig} (fb)	0.20	0.19	0.17	137

ATLAS has performed the sbottom searches for $2b + \cancel{E}_T$ and $b\bar{b}j + \cancel{E}_T$ final states [375] at the 8 TeV LHC with 20 fb^{-1} integrated luminosity, and a similar CMS analysis has used the 7 TeV data with H_T and variable α_T to reject backgrounds with 0, 1, 2 and 3 b -jets [417]. While current studies focus on the sbottom mass between $100 - 700$ GeV with $\Delta m \geq 15$ GeV, we adopted the same cuts used in their analyses to put bounds on the light sbottom in the sbottom coannihilation scenario.

For illustration, we choose a sbottom mass to be 20 GeV and a neutralino LSP mass to be 14 GeV. We generate the events using MadGraph5 [242] at parton level. In table II.13, we list the 95% C.L. upper limit on σ_{vis} from the ATLAS analysis [375] for two signal regions: SRA, mostly sensitive to $b\bar{b} + \cancel{E}_T$ final state, and SRB, mostly sensitive to $b\bar{b}j + \cancel{E}_T$ final state. This search mainly relies on large MET with two b -tagged jets and requires additional hard jet in SRB [375]. The last row of table II.13 gives the signal cross sections after all cuts, σ_{sig} , for the chosen benchmark point in the sbottom coannihilation region. We see that the $b\bar{b} + \cancel{E}_T$ search does not provide a meaningful bound for the light sbottom case, which could be attributed to the inefficient choice of the acceptance cuts, optimized for sbottom mass of hundreds of GeV. The $b\bar{b}j + \cancel{E}_T$ search in SRB, on the other hand, provides far more stringent bound that rules out the light sbottom prompt decay case with

$\Delta m = m_{\tilde{b}} - m_{\tilde{\chi}_1^0} > m_b$. Varying the light sbottom mass and neutralino LSP mass does not alter the results much since the triggers and cuts are on the order of hundred GeV.

For $\Delta m < m_b$, the tree-level 2-body decay is kinematically inaccessible and its decay lifetime is most likely longer than the QCD hadronization scale of $(10^{-12} - 10^{-13})$ second. A sbottom would first hadronize into a “R-hadron” [418]. If the R-hadron subsequently decays in the detector, the small mass difference would lead to very soft decay products with little MET and thus escape the detection at the LHC. These events may have to be triggered on by demanding a highly energetic jet from initial or final state radiation, recoiling against large MET. The requirement of large MET or a leading jet of hundreds of GeV reduces its signal cross section by several orders of magnitude. The overwhelming hadronic backgrounds at the LHC environment would render this weak signal impossible. If the R-hadron decays within the detector with favorable displacement, an interesting possibility of displaced vertex search at the LHC with high p_T jet recoiling against sbottom pairs may be sensitive to such a scenario, see Ref. [419]. If the R-hadron, on the other hand, is quasi-stable and is charged (CHARGed Massive Particle CHAMP), it could lead to a soft charged track in the detector. Searching for such signals is interesting, but typically challenging at the LHC [420]. On the other hand, such a light and long-live charged R-hadron has been excluded by CHAMP searches at the LEP.

In the stau coannihilation scenario, there is typically a light stau of mass between 32 and 45 GeV, which degenerates with the neutralino LSP with a small mass splitting of less than 3 – 5 GeV. It is known that searching for slepton signals at the LHC is extremely challenging because of the low signal rate and large SM backgrounds. The direct pair production for stau at the LHC is via the s -channel γ/Z exchanges. The electroweak coupling and p -wave behavior render the production rate characteristically small. With the leading decay of stau to tau plus LSP, the final state signal $\tilde{\tau}^+\tilde{\tau}^- \rightarrow \tau^+\tau^- + \cancel{E}_T$ encounters the overwhelming SM backgrounds such as $W^+W^- \rightarrow \tau^+\tau^- + \cancel{E}_T$. Furthermore, the nearly degenerate mass relation for our favorable DM solutions further reduces the missing energy, thus making the signal more difficult to identify over the SM backgrounds. For stau pair production in association with an additional energetic jet or photon, the extra jet/photon momentum kicks the stau pair and could result in a larger missing energy. However, $W^+W^- + n\text{j}$ background

would still be overly dominating, which makes the stau detection very challenging at the LHC. For some related studies, see Ref. [421].

The existing LHC searches on neutralino/chargino with cascaded decay via stau can be viewed as stau searches and the analyses relied on two tagged taus with MT2 cut. The minimal MT2 cut of $90 \sim 110$ GeV makes these searches insensitive to our light stau solutions which typically have a much smaller MT2.

3. Summary and Outlook

Identifying particle dark matter is of fundamental importance in particle physics. Searching for a light dark matter particle is always strongly motivated because of the interplay among the complementary detection of the underground direct search, indirect search with astroparticle means, and collider studies. Ultimately, the identification of a WIMP dark matter particle must undergo the consistency check for all of these three detection methods. In this section, we discussed the phenomenology of the light (< 40 GeV) neutralino DM candidates in the framework of the NMSSM. We performed a comprehensive scan over 15 parameters as shown in table II.11. We implemented the current constraints from the collider searches at LEP, the Tevatron and the LHC, the direct detection bounds, and the relic abundance considerations. We illustrated the qualitative nature of the neutralino dark matter solutions in table II.10. We provided extensive discussions for the complementarity among the underground direct detection, astro-physical indirect detection, and the searches at the LHC and ILC. Our detailed results are summarized as follows.

- *Viable light DM solutions:* we found solutions characterized by three scenarios: (i) A_1 , H_1 -funnels, (ii) stau coannihilation and (iii) sbottom coannihilation, as listed in Table II.10. The A_1 , H_1 -funnels and stau coannihilation could readily provide the right amount of dark matter abundance within the 2σ Planck region (figures 2 and 3). The sbottom coannihilation solutions typically result in a much lower relic density. This under-abundance could also occur for A_1 , H_1 -funnel solutions if $m_{A_1/H_1} \approx 2m_{\tilde{\chi}_1^0}$, and for stau coannihilation solutions if the LSP is Bino-like.

- *Features of the light DM solutions:* the neutralino LSP could either be Bino-like, Singlino-like or an admixture (figures II.42 and II.43). For the A_1 , H_1 -funnels, the light Higgs bosons A_1/H_1 are very singlet-like. They serve as the nearly resonant mediators for the DM annihilation. For the stau coannihilation, the stau usually needs large L-R mixing or Z decay kinematic suppression to avoid the Z boson total width constraint, and it could be as light as 32 GeV. For the sbottom coannihilation, the sbottom is mostly right handed and could be as light as 16 GeV given the Z total width consideration as well as other collider constraints (Fig. II.39).
- *Direct detection:* the direct detection rates for the three types of solutions vary in a large range. For the sbottom coannihilation with the right amount of DM relic abundance, the SI direct detection rate is usually high, due to the effective bottom content in the nuclei. The SD direct detection provides complementary probes to the DM axial-vector couplings to Z boson and light squark exchanges. The three kinds of solutions could have very low SI direct detection rate, some extend into the regime of the coherent neutrino-nucleus scattering background. The next generation of direct detection such as LZ, SuperCDMS and SNOLAB experiments would provide us valuable insights into very large portion of the allowed parameter space (figures II.40 and II.44).
- *Indirect detection:* the low velocity annihilation cross sections for these solutions also vary in a large range, usually prefer a rate lower than the canonical value of s -wave dominance assumption. For the A_1 , H_1 -funnels, the resonance feature allows some larger rates in the current epoch. Interestingly, it naturally provides a dark matter candidate for the GeV gamma-ray excess with ~ 35 GeV LSP pair that mainly annihilates into $b\bar{b}$. For sbottom and stau coannihilations, the corresponding annihilations are mainly into $b\bar{b}$ and $\tau^+\tau^-$, with the later yielding different gamma-ray spectra (Fig. II.44).
- *SM Higgs physics:* the decays of the SM-like Higgs boson may be modified appreciably (Fig. II.45), and its new decay channels to the light SUSY particles, including the invisible mode to the LSP DM particle, may be sizable (Fig. II.46).
- *New light Higgs physics:* the new light CP-even and CP-odd Higgs bosons will decay to the LSP DM particle, as well as other observable final states (Fig. II.47), leading to interesting new Higgs phenomenology at colliders. The search for a light singlet-like

Higgs boson is usually difficult at the LHC due to the low production rates (Fig. II.48) and the large SM backgrounds. The searches for pair produced singlet-like Higgs bosons via the decay of the SM-like Higgs as in Fig. II.46 and production of LSP pairs through Higgs portals as in Fig. II.49 may improve the signal sensitivity at the LHC.

- *Collider searches for the light sfermions:* for the sbottom coannihilation, our recast of the current LHC searches for heavier sbottom shows that the case of $\Delta m > m_b$ has been ruled out given the analysis of the sbottom pair production with a hard ISR jet. For the case of $\Delta m < m_b$, the long-lived charged R-hadron has been excluded by the LEP search, and the only viable case left would be a promptly decaying sbottom (or an R-hadron) that could escape the LHC search due to the softness in decay products, but will be covered at the ILC by searching for events with large missing energy plus charged tracks or displaced vertices.

For the stau coannihilation, searches at the LHC would be prohibitively difficult with the nearly degenerate masses. A lepton collider, however, comes to the rescue: For the case of $\Delta m < m_\tau$, the stau is most likely long-lived and has been excluded by the LEP search. For the case of $\Delta m > m_\tau$, the ILC will definitely be capable of covering this scenario.

F. SUSY DISPLACED DECAYS

We consider models with displaced decays motivated by the naturalness argument [160–164]:

- $\tilde{t} \rightarrow \bar{d}_i \bar{d}_j$ via baryonic RPV, including $\tilde{t} \rightarrow \bar{b} \bar{b}$ [151] (Figs. II.51, II.52)
- $\tilde{g} \rightarrow u_i d_j d_k$ via baryonic RPV (Fig. II.53)
- $\tilde{H} \rightarrow u_i d_j d_k$ (+soft) via baryonic RPV (Fig. II.54)
- $\tilde{q} \rightarrow q \tilde{G}$ in GMSB (Fig. II.55)
- $\tilde{g} \rightarrow g \tilde{G}$ in GMSB (Fig. II.56)
- $\tilde{t} \rightarrow t^{(*)} \tilde{G}$ in GMSB (Fig. II.57)
- $\tilde{H} \rightarrow h/Z \tilde{G}$ (+soft) in GMSB (Fig. II.58)
- $\tilde{g} \rightarrow q \bar{q} \tilde{B}$ in mini-split SUSY (Fig. II.59)

Some major options missing from this list are sleptons, electroweak gauginos, simplified spectra with leptonic RPV, and mini-split SUSY with gluino decays dominated by heavy flavor. As discussed in more detail below, some of these other possibilities are covered already by existing searches or recasts, and some we expect to have significant overlap with the above signals, but some would also be worth a closer look in future work.

The most powerful displaced decay limits within our selection of models typically come from the CMS tracker-based search for displaced dijets [138]. This search often remains sensitive to models with $c\tau$ much larger than the tracker radius, as well as to models with decay topologies different from the nominal dijets. For models where the long-lived particle is colored, hadronization implies a sizable charged fraction that can also be picked up by stable charged particle searches in events where the decay takes place outside of the detector. Similarly, these searches maintain some sensitivity for $c\tau$ much smaller than the 5–10 m outer detector radius. The overlap of exclusions between displaced decay searches and stable charged particle searches can then be significant, sometimes more than three orders of magnitude in lifetime. At the low end of the lifetime range, prompt searches also become sensitive. While it is not possible for us to precisely map out the lifetime range over which these searches remain efficient, conservative guesses again allow for significant overlap. This complementarity often allows for exclusions that span from prompt lifetimes to infinity with no gaps.

The main results of this section consist of a series of exclusion plots over the mass-lifetime plane of each displaced particle, Figs. II.51 through II.59. For the colored production models, the mass reach in the $c\tau$ range of $O(\text{mm}--\text{m})$ is usually comparable to, and in some cases better than, the ≈ 1 TeV reach from collider-stable charged particle searches. In particular stops, which are expected to have mass less than about 1 TeV in a natural model, have very little viable model space surviving in this lifetime range under these decay scenarios. For the electroweak Higgsino production, stable charged particle limits do not apply, and prompt searches are typically limited in sensitivity, but a large number of displaced searches yield powerful limits, especially in the GMSB case. We find that for $c\tau \sim 10$ cm, masses below about 600–800 GeV are excluded, giving serious tension with naturalness at those lifetimes. For natural masses near 100 GeV, the excluded lifetime ranges from $O(10 \text{ microns})$

to $O(10\text{ m})$ in RPV, and up to $O(100\text{ m})$ in GMSB, dominated there by CMS’s tracker-based displaced dilepton search [139].

For all models, the region of lifetimes around $c\tau \sim 10\text{ m}$ could in principle benefit from searches in the hadronic calorimeters and muon chambers, such as those performed by ATLAS [140, 141]. But the existing searches are highly limited in sensitivity by their focus on lower-mass models and by requiring very tight reconstruction cuts on both sides of the event. For the Higgsino models, improvements in this direction might be the only option for extending the sensitivity to higher lifetimes, without ultimately appealing to more standard-style SUSY searches that assume that both final-state Higgsinos escape the detector unseen.

The section is organized as follows. In the next sub-section, we review the existing LHC collider-stable and displaced particle searches that we use in our limit-setting. (This sub-section may be bypassed by a reader who is not interested in the details of these analyses.) Sec. II.F.2 specifies the motivations and features of the simplified SUSY models under investigation, and presents our derived limits. We conclude and present some ideas for future searches in section II.F.3. An appendix discusses the details and calibrations of our detector simulations used for recasting.

1. The LHC Searches Under Consideration

Displaced decay searches at the LHC are currently limited to a handful of specific new physics scenarios.¹⁴ Searches that target minimal SUSY include non-pointing photons in gauge mediation (assuming a mostly-bino LSP) [132, 133], the “disappearing track” signature of NLSP charginos in anomaly mediation [134, 434], displaced leptons from neutralino or stop decays with leptonic RPV [135, 136, 138], and late decays of gluino R-hadrons stopped in the calorimeters in mini-split SUSY [137, 145]. Other searches focus on models such as Hidden Valleys [138–141, 144, 146, 147] or light hidden-sector gauge bosons [142, 143]. Recently, ATLAS has also re-interpreted its prompt gluino limits, accounting for the effect of displacement on the signal acceptance [131], results that we put into broader context here.

¹⁴Displaced decay searches have also previously been carried at the Tevatron [422–430] and at LEP [431–433]. These searches have for the most part either been superseded by the LHC or do not have immediate relevance to the SUSY models we consider. We do not attempt to recast any of them. However, we practically assume that long-lived particles below 100 GeV should have been highly visible to some of these searches.

Table II.14: A summary of the LHC searches recast in this section.

	energy	lumi	refs	analysis
CMS heavy stable charged	7+8 TeV	5.0+18.8 fb ⁻¹	[129]	II.F.1.a
CMS displaced dijets	8 TeV	18.5 fb ⁻¹	[138, 435]	II.F.1.b
CMS displaced dileptons	8 TeV	19.6/20.5 fb ⁻¹	[139]	II.F.1.c
CMS displaced $e+\mu$	8 TeV	19.7 fb ⁻¹	[136]	II.F.1.d
ATLAS muon spectrometer	7 TeV	1.94 fb ⁻¹	[141]	II.F.1.e
ATLAS low-EM jets	8 TeV	20.3 fb ⁻¹	[140]	II.F.1.f
ATLAS μ +tracks	8 TeV	20.3 fb ⁻¹	[135]	II.F.1.g

CMS has re-interpreted its stable charged particle searches for a large ensemble of pMSSM models with long but finite lifetimes [130], and we apply a similar strategy to our more focused set of models.

From this modest but growing list of analyses, we select seven that appear to be of greatest relevance for the SUSY models studied in Section II.F.2: the CMS heavy stable charged particle search [129], the CMS displaced dijets search [138], the CMS displaced dileptons search [139], the CMS displaced electron and muon search [136], the ATLAS muon chamber search [141], the ATLAS low-EM jet search [140], and the ATLAS displaced muon plus tracks search [135]. Except for the ATLAS muon chamber, all of these have been performed with the full 8 TeV dataset. The following subsections summarize the relevant aspects of each analysis that we use for our recasts, as well as commentary on the reliability of these recasts where appropriate. Our approximate reproduction of each of these analyses relies on simplified detector simulations. Descriptions of these simulations and their calibration to known experimental results is provided in a corresponding set of subsections in the appendix. Table II.14 provides a compact overview, including the associated references and subsections.

a. CMS Heavy Stable Charged Particles Both ATLAS [128] and CMS [129] have conducted searches for heavy stable charged particles (HSCP) that traverse the entire detector, and appear as a “heavy muon” with anomalously small velocity or dE/dx in the detector material. We choose to focus on the CMS searches [129], though we expect very similar performance from the ATLAS searches. Stable squarks and gluinos have already been explicitly considered by both experiments, and will simply generalize these results to cases with finite lifetimes.

The only major subtlety when dealing with meta-stable colored particles is that they are only seen bound into R-hadrons [418]. The hadronization fractions can be estimated from simple models, and are likely fairly accurate for squarks given the extensive theoretical and experimental experience with heavy quarks. Hadronization of the color-octet gluino is less certain, but we assume here the default behavior in `Pythia8` [436]. (This results in a charged hadronization fraction of approximately 46%.) A more subtle issue is how these R-hadrons interact with the detector material, especially the chance that a charged R-hadron will pass through the calorimeters without a net charge exchange, and thus manage to trigger in the muon system. CMS considers two models: a nominal hadronic cloud interaction and a more extreme “charge-stripped” assumption where all R-hadrons emerge from the back of the calorimeter in a neutral state. Thankfully, the complicated interplay with the detector has been accounted for by CMS, and to extract our own finite-lifetime limits we can concentrate on simpler, geometric considerations.

We consider two of their search strategies. For the nominal hadronic interaction model, we take the tracker plus time-of-flight analysis. For the pessimistic charge-stripped assumption, we take the tracker-only analysis.

The tracker plus time-of-flight analysis relies dominantly on the muon trigger, and searches for anomalous track candidates that are matched between the muon chamber and inner tracker. This track must be reconstructed with $|\eta| < 2.1$ and $p_T > 70$ GeV, inverse-velocity above $1.225/c$ (measured using timing information), and a high dE/dx . There are also additional requirements on the mass inferred from the momentum and velocity measurements, which are constructed to be highly efficient for signal. In order to recast the cross section limit for a given model at finite lifetime, we form a conservative rescaling factor.

The numerator is the number of charged R-hadrons that would pass into the analysis given the above cuts, excepting the dE/dx cut, which we cannot model but which should also be highly efficient for signal. The denominator is the number of charged R-hadrons that pass these criteria and that also decay fully outside the detector. We only consider decaying R-hadrons where *none* of the visible decay products re-intercept the detector volume, as this may cause additional activity in the muon chambers and could have an unpredictable effect on the acceptance.¹⁵

In order to access the charge-suppressed scenario, the tracker-only analysis exploits a subtlety of the \cancel{E}_T trigger. A charged R-hadron may leave a track in the inner tracker, but if it leaves no track in the muon chamber and minimal calorimeter activity along its trajectory, the particle-flow algorithm used in triggering will assume that the track is spurious and not count it toward the \cancel{E}_T calculation. The R-hadron therefore adds to the apparent \cancel{E}_T . Because each R-hadron either leaves such a “trigger-invisible” track or is neutral to begin with, the apparent \cancel{E}_T is the total recoil p_T of the heavy particle pair.¹⁶ Offline, events from this \cancel{E}_T -triggered sample can be analyzed for inner tracks consistent with heavy stable particles. The basic track $|\eta|$ and p_T requirements are the same, but there is no velocity cut (as no timing information with respect to the muon chambers is available), and the dE/dx requirement is tightened. Again, we cannot model the dE/dx cut, so we assign an ad hoc velocity ceiling of $0.7c$, which puts us on the steep section of the Bethe-Bloch stopping power curve [438]. (Our final results are not very sensitive to the placement of this velocity cut.) We again form a rescaling factor for the infinite-lifetime cross section limits presented by CMS. For the numerator, we take the number of *events* where the recoil p_T exceeds 150 GeV

¹⁵CMS has also provided a full efficiency map of this analysis [130], which can be extremely useful in general recasts. However, we do not use this map since our physics models are identical to the ones that CMS studies, up to the finite lifetime. There could in principle be some interplay between the variation in stable particle acceptance and non-decay probability versus kinematics, which we are not simulating, but our treatment should be conservative. For example, slow particles would tend to decay earlier and become vetoed from the analysis, but slow stable particles (especially with $\beta \lesssim 0.4$) are anyway less efficiently accepted. Similarly, particles at higher $|\eta|$ must survive over a longer three-dimensional path length before exiting the detector, and again are more likely to be lost due to decay, but high- $|\eta|$ is also less efficient even for stable particles. Therefore, our naive approach, which effectively assumes a flat acceptance within the fiducial region, misses the fact that the particles that survive undecayed also tend to be in kinematic regions with higher acceptance. In any case, the turn-off of overall acceptance for this analysis due to decays at lower lifetimes is *exponential*, and we expect this behavior to dominate.

¹⁶For all SUSY pair production, processed through `Pythia8`, we damp the ISR, which has been shown to better-reproduce matched results [437].

and at least one R-hadron is charged and passes the reconstruction cuts. The denominator is the number of events that satisfy these criteria and where both R-hadrons decay fully outside the detector (including the non-intercept requirement on the visible daughters, as above).

b. CMS Displaced Dijets The CMS displaced dijet search [138, 435] uses a specialized trigger to capture events containing a pair of high- p_T jets containing displaced tracks at the level of several hundred microns. In the offline analysis, it counts the total number of jet-pairs that appear to be consistent with common vertices with a large number of such displaced tracks. For our recasts, we focus on the “High- L_{xy} ” analysis, which has 1.14 ± 0.54 expected background vertices and one observed, placing an upper limit of 3.7 signal vertices. We have found that the High- L_{xy} works well for all of our models, even ones with short decay lengths ($\langle L_{xy} \rangle < 20$ cm), and that the choice of High- L_{xy} versus the very similar Low- L_{xy} analyses has only minor impact on our results.

The jets used in the analysis have $p_T > 60$ GeV and $|\eta| < 2$, and the total event H_T must exceed 300 GeV at trigger level. (In practice we use a slightly tighter 320 GeV to account for the observed turn-on of the trigger with H_T measured offline [439].) Each pair of such jets is inspected for associated tracks with impact parameters larger than $500 \mu\text{m}$, and this set of displaced tracks is checked for consistency with a common vertex. At least one displaced track from each jet is required to fit that vertex, and there are a number of additional quality requirements on the vertex itself: total track-mass greater than 4 GeV, total track- p_T greater than 8 GeV, “significant” transverse distance L_{xy} from the primary vertex, and a multivariate likelihood-ratio discriminant cut. The discriminant is formed from distributions over the vertex track multiplicity, the fraction of tracks with positive impact parameters (based on the sign of the dot product of the track’s p_T vector and transverse displacement vector at the transverse point of closest approach to the beamline), and two additional variables based on a special clustering of track crossing points along a line starting at the detector’s center and oriented with the dijet p_T direction. The exact algorithm for this clustering is not given by CMS. For our reproduction of the analysis, we create a sliding window of full-width $0.15 \times L_{xy}$, and adjust it to surround a maximal number of crossing points. When

multiple window locations would surround different crossing point collections with equal multiplicities, we choose the one with the smallest RMS. For its multivariate discriminant, CMS includes both the cluster multiplicity and the RMS relative to the vertex L_{xy} . We determine the event-by-event value of the discriminant by using CMS’s own distributions for the four variables. (Our calibration distributions for these variables and the multivariate discriminant can be found in Appendix VI.E.5.)

The rest of the High- L_{xy} selection demands at most one prompt track per jet within the dijet candidate, less than 9% of the energy of each jet associated to prompt tracks, and a multivariate discriminant value greater than 0.8. In the analysis note [435] (which has identical results as the more recent preprint [138]), CMS’s new physics limit is phrased in terms of the number of dijet candidates that pass all of these requirements over the full 8 TeV run.

While this defines the basic search, we point out a few possible subtleties:

- CMS has only performed full simulation on models with dijet masses up to 350 GeV. We assume that there are no major obstacles to probing masses beyond 1 TeV. These may experience more tracking confusions due to the greater multiplicity of hits, but on the other hand should also be capable of surviving the analysis cuts with a smaller fraction of successfully-reconstructed tracks.
- For all of the physics models that CMS has studied, the displaced particle is neutral and leaves no tracker hits before its decay. It is unclear what would happen for charged displaced particles, such as R-hadrons, which would leave a signature sometimes called an “exploding track.” Presumably the extra hits would lead to additional confusions of the tracker algorithms. We simply exclude such cases from the analysis, effectively assuming zero efficiency. This is certainly an over-conservative treatment, especially, for decays that occur before crossing the first pixel layer.
- For some of our SUSY models, more than two jets can originate from the same displaced vertex. In principle, in the note [435] CMS considers all possible displaced dijet pairs, allowing the same jet to appear multiple times. Such a decay could therefore contribute much more than one dijet candidate. However, since the exact procedure is not unambiguously described in the CMS note, when a dijet pair passes the basic selection cuts

(before the High- L_{xy} selections), we remove its constituent jets from further consideration for constructing other dijet pairs.

- For most of our SUSY models, the displaced dijet candidate will be produced in a decay with additional activity, and will therefore by itself not reconstruct the decaying particle’s momentum vector. Since CMS’s cluster discriminant variables are constructed under the assumption that the vertex displacement vector and dijet momentum vector are well-aligned, there is a question of whether the discriminant is particularly inefficient for models where this is no longer true. We have found that any such effect is quite minor, and that the multivariate discriminant is mainly driven by the vertex track multiplicity variable.¹⁷
- When a decay contains bottom and/or charm quarks, it may generate multiple nearby displaced vertices rather than a single displaced vertex. CMS gives some explicit indication of how the reconstruction rate differs for heavy flavor decays, and it appears that such small secondary displacements do not play a significant role, but only for models down to $O(\text{cm})$ lifetimes. The behavior for shorter lifetimes is not specified. Due to the ambiguity, we simply ignore decays that contain heavy flavor and have $L_{xy} < 1 \text{ cm}$.
- It is clarified in the more recent analysis preprint [138] that no lepton identification is utilized, and that electrons and muons would function as jet constituents in this analysis. However, the earlier note [435], on which we base our analysis, is not explicit on this point. We have therefore excluded isolated leptons (as per the definition of [139]) from jet clustering. This may lead to slightly over-conservative limits when leptonic decays are available.

c. CMS Displaced Dileptons The CMS displaced dilepton search [139] is in some ways a simpler version of the displaced dijet search above.¹⁸ The analysis operates on pairs of isolated e^+e^- or $\mu^+\mu^-$, demanding that a pair reconstruct to a common highly-displaced vertex. The analysis is both background-free and has zero observed events, leading to a 95% limit of approximately 3 signal events.

¹⁷The same conclusion was reached in [156].

¹⁸We do not consider the superseded version of this search at lower luminosity and beam energy [440].

Electron-pair candidates in the event must consist of a leading (subleading) electron with $p_T > 40$ GeV (25 GeV). Muon-pair candidates must consist of muons with $p_T > 26$ GeV. Each lepton should be in the well-instrumented region of the tracker, at $|\eta| < 2.0$, and should have a “significant” transverse displacement of 12σ relative to the resolution. Since here we do not simulate track-by-track resolutions, we simply replace this last criterion with a fixed cut of $250\text{ }\mu\text{m}$. This choice appears to give conservative results for very low lifetimes. CMS further requires the leptons to be isolated from other tracks, excluding other identified leptons, using hollow cones of outer radius 0.3 built around the lepton candidates. Since our own lepton ID is “perfect” (up to the efficiency factors discussed in the appendix), we use solid cones. This again should furnish a conservative approximation, and should roughly approximate the ID failures that would occur in reality, e.g. for leptons inside of b/c -jets. Non-lepton tracks with $p_T > 1$ GeV count toward the isolation, and should tally to less than 10% of the lepton p_T . For muon-pairs, the two candidate tracks must be separated by $\Delta R > 0.2$, to operate in the region of high dimuon trigger efficiency. For electron-pairs, we here additionally require $\Delta R > 0.1$, assuming that the ECAL patterns of closely-spaced electrons could start to become difficult to reconstruct. A number of other basic quality cuts are applied: the dilepton pair should have invariant mass above 15 GeV to avoid hadronic resonances, the azimuthal angle between the dilepton momentum vector and its displaced vertex position vector should be less than $\pi/2$, and the 3D opening angle between a pair of candidate muon tracks should have a cosine greater than -0.79 to veto cosmics.

Given the simpler topology and cuts relative to the displaced dijet search, we should naively be more confident in the robustness in our recasting procedure for different models. Nonetheless, as discussed in Appendix VI.E.6, our modeled acceptances appear to be low for some of CMS’s benchmark models, possibly because we err on the conservative side for the lepton track-finding efficiencies at large decay radii. The “exploding track” question also persists in principle, but does not arise in any of the models that we consider. (Displaced dileptons only occur for our GMSB Higgsino models, in which case the long-lived particle is always neutral.) There is still some question about how this analysis would behave when additional tracks emerge from the same vertex, such as $h \rightarrow ZZ^* \rightarrow l^+l^- + \text{jets}$ from Higgsino decay. However, this model is the only case that we study where such a question would arise,

and the limits from this search are regardless not the most powerful for displaced Higgs decays.

d. CMS Displaced Electron and Muon The CMS displaced electron and muon search [136] uses a highly minimalistic and inclusive analysis, simply demanding the presence of exactly one electron and one muon, each with significant 2D impact parameter up to 2 cm. The analysis is broken down into three exclusive bins in joint impact parameters, with varying degrees of background. Consequently, the statistical analysis is somewhat more involved, as discussed below.

The electron and muon must each have $p_T > 25$ GeV, $|\eta| < 2.5$, and transverse impact parameter between 0.02 cm and 2 cm. The last requirement allows the analysis to focus on the region of tracking parameters where the efficiencies are largely the same as for prompt tracks. The two leptons must also be well-isolated. In addition to a basic particle isolation requirement, which we form by tallying all hadrons (charged and neutral) within $\Delta R < 0.3$ and demanding a relative p_T less than 10%, each lepton must also be isolated from jets with a p_T threshold of 15 GeV within $\Delta R < 0.5$. The leptons themselves must also be separated by at least this distance and have opposite charges.

The three exclusive signal regions consist of a high-displacement/lower-background region SR3 where both leptons' impact parameters are above 0.1 cm, an intermediate region SR2 where the event fails this criterion but still has impact parameters above 0.05 cm, and a low-displacement/higher-background SR1 where the event fails both of these criteria but still has impact parameters above 0.02 cm. The observed (expected) event counts are, respectively, 0 (0.051), 0 (1.01), and 19 (18.0). We have coded this three-bin statistical analysis as a toy Monte Carlo using a Poisson likelihood-ratio discriminator built from the central background predictions, and including the systematic uncertainties on the background (assumed Gaussian and uncorrelated) as perturbations on the simulated pseudo-experiments. This allows us to map out the 95% CL_S boundaries in the three-dimensional space of signal bin counts. Our statistical analysis is not exactly the same as that performed by CMS, but it should furnish an adequate approximation. We have verified this by reproducing sections of the leptonic RPV stop limits presented in the analysis note. Approximately speaking, high-

lifetime signals that are concentrated in SR2 and/or SR3 have a limit $N(\text{SR2})+N(\text{SR3}) < 3$, whereas low-lifetime signals that are concentrated in SR1 have a limit $N(\text{SR1}) < 13.5$.

Other than the nontrivial statistical analysis, this particular displaced search was one of the simplest for us to implement, since it is insensitive to efficiency degradations and nontrivial geometries that occur for decays in the body of the detector. Also, due to the fact that the focus is on decays that occur before traversing the pixels, the issue of whether the displaced particle is charged does not appear.

e. ATLAS Muon Spectrometer The ATLAS muon spectrometer search [141] (7 TeV, 2 fb^{-1}) is focused on models where particle decay lengths are several meters, and have high probability of decaying outside of the HCAL. It uses a novel vertex-finding algorithm [441] to identify the sprays of tracks from a displaced decay within the muon chambers. Events with two successfully identified candidates are used in the analysis, with zero events expected and zero observed (again, setting an upper limit of about 3 signal events).

To pass the analysis cuts, first of all both decays must occur within fiducial regions of the muon spectrometer. The identified decays must be well-isolated from tracks above 5 GeV out to $\Delta R < 0.4$, and from jets above 15 GeV out to $\Delta R < 0.7$. (Again, we do not consider displaced decays from charged particles, since the particle’s own track would veto it.)

This analysis appears to fill an important niche at lifetimes intermediate between the tracker radius and beyond the outer detector radius for colored long-lived particles, and uniquely probes out to the largest possible decay distances for long-lived particles that lack charged states. Nonetheless, we will see that the search is ultimately not very powerful. There are several reasons for this:

- Unlike all of the other analyses that we study here, it has not (yet) been performed at the full beam energy and luminosity. We will indicate how much this might help below by making a naive projection to 8 TeV, 20 fb^{-1} , assuming identical signal efficiencies and zero background.
- The ATLAS data acquisition becomes highly inefficient for particles traveling large distances at sub-light speeds, and loses the signal when a time delay of $\approx 7 \text{ ns}$ has accrued relative to a light-speed particle. For example, a particle traveling at $0.7c$ and decaying at

$r = 5$ m (at $\eta = 0$) accrues this much delay, and this velocity is already above the typical median for pair-produced heavy particles. The timing requirement therefore usually has an $O(1)$ impact on our signal acceptance.

- The analysis requires coincident behavior for both decays, and therefore pays every possible inefficiency factor twice. These include basic requirements such as neutral R-hadronization probabilities, the geometric constraints of the muon spectrometer, the vertexing efficiency, and the isolation requirements. The geometry in particular becomes a major factor when considering either very long or very short lifetimes, where it respectively leads to either a power suppression or an exponential suppression. Analyses that can rely on one candidate only need to be “lucky” once.

Regarding the last point, it would be very interesting to see if this analysis could be run with a single-candidate option. On the one hand, this would result in much higher background rates (effectively $O(10$ pb)) with the original reconstructions and cuts. On the other hand, many of the models that we consider here have quite appreciable cross sections, and because they have much higher masses than the baseline models that ATLAS studied, should lead to even more spectacular multi-track signatures in the muon spectrometer. Relaxing the isolation requirements somewhat, to allow more of the decay particles to point back to the HCAL, could also be beneficial. These HCAL signals would also be rather distinctive given that they would contribute mainly in the outermost layers. However, it is unclear whether ATLAS’s jet reconstruction requirements would anyway ignore such anomalous deposition patterns.

It should be also noted that the information on the performance of the displaced vertex reconstruction from ATLAS’s papers is limited to a rather small set of new physics models, using the common benchmark scenario of a Higgs-like scalar decaying to a pair of displaced pseudoscalars. Only four mass points with fairly similar kinematics are studied, the most energetic decays coming from a 140 GeV scalar decaying into a 40 GeV pseudoscalar. It is therefore unclear how this very complex search would perform on, say, a 1 TeV RPV gluino decaying into three jets. More so than most of our other recasts, this one must be then viewed cautiously and somewhat conditionally. Still, because of the search’s limitations discussed above, in practice it does not end up probing masses beyond a few hundred GeV.

f. ATLAS Low-EM Jets The ATLAS low-EM jets search [140] focuses on coincident jet-like signals confined entirely to the HCAL, with stringent cuts on nearby ECAL and tracker activity. It is sensitive to pairs of displaced decays within the HCAL volume. The analysis has a small but non-negligible background, leading to an upper limit of about 20 signal events.

For a pair of jets to pass into the analysis, the leading (subleading) jet must have $p_T > 60$ GeV (40 GeV). Each jet should have no associated tracks with $p_T > 1$ GeV within $\Delta R < 0.2$, and should have at least approximately 16 ($10^{1.2}$) times more energy recorded in the HCAL than in the ECAL. As discussed in Appendix VI.E.9, our default model of these isolation requirements uses a combination of a flat efficiency factor and an overconservative veto on decays in the HCAL body that produce particles pointing back to the ECAL. An alternative, looser version removes the latter requirement, and the two extremes define an approximate error band for our modeling of this analysis. We also automatically veto events containing charged long-lived particles, which as usual would leave a track. ATLAS further makes an explicit cut of 5 ns on the signal timing delay relative to what would be deposited by a particle moving at light-speed. Given that the linear distances involved are about half as large as those for the muon spectrometer analysis, this ends up having a relatively less detrimental effect (though still potentially $O(1)$) on the signal acceptance. Finally, there is a requirement that the event has $\cancel{E}_T < 50$ GeV in order to reject non-collision events, though this can severely impact many of our models with invisible LSPs.

Similar to the ATLAS muon spectrometer search, the requirement of coincident decays within the same detector system significantly limits the model reach. For our SUSY models, much of the candidate-by-candidate inefficiency comes from our somewhat ad hoc requirement that no decay particles can point back to the ECAL, and we take results with and without this requirement to define our uncertainty band. Still, we conclude that this search is not very competitive, even to a luminosity-scaled muon spectrometer search. It seems as if it is simply too constrained by geometry.

As in the previous subsection, it would potentially be useful if the search could be adapted for single-candidate acceptance instead of requiring decays with coincident properties. The fact that this would increase the background could be offset in several ways that should

maintain high signal acceptance. First of all, most of the SUSY models that we consider would deposit far more energy than ATLAS’s benchmark models. A search that is broken down into different jet E_T bins could already improve sensitivity. Second, these very energetic and wide-angle multibody decays might leave quite unusual 3D spatial and timing deposition patterns in the HCAL, possibly so unusual that even the relative ECAL deposition requirement could be relaxed. In fact, we are again already giving ATLAS the benefit of the doubt by assuming that such unusual jets would pass the reconstructions of their analysis. But the limited mass reach of the search by itself limits the possible impact of this subtlety.

It would also be very advantageous if the \cancel{E}_T cut could be eliminated. For GMSB and mini-split models in particular, the cut is a major handicap. It can also contribute a subtle geometric problem in models without true \cancel{E}_T . Under the zeroth-order assumption that a particle decaying within the HCAL has all of its energy absorbed at one point, the particle’s reconstructed momentum vector is effectively rescaled by its lab-frame energy. For sparticle pair production that is not exactly back-to-back in 3D space, true transverse momentum balances, but the energy-scaled transverse momentum need not. Again, this is mainly an issue for models with large masses, beyond the sensitivity of the original search. But it could become problematic if the search were to be extended.

g. ATLAS Displaced Muon Plus Tracks The ATLAS muon plus tracks search [135] uses the inner tracker to reconstruct highly displaced vertices containing at least one muon.¹⁹ The basic search, which counts the number of events containing at least one such vertex, is background-free. However, a looser version of the search relaxes the demand that the muon is matched to the displaced vertex candidate. This version is also background-free, and has improved signal acceptance, especially for models with a mixture of low-multiplicity leptonic decays and high-multiplicity hadronic decays (i.e., our GMSB Higgsino and stop models). We utilize this version for our recasts.

Vertices are reconstructed from displaced tracks originating within the inner region of the tracker, $r < 18$ cm and $|z| < 30$ cm. The tracks used toward the vertex reconstruction must

¹⁹We do not consider the superceded versions of this search at lower luminosity and beam energy [442, 443].

have $p_T > 1$ GeV and transverse impact parameter greater than 2 mm. A good candidate vertex must be reconstructed within the fiducial volume, have at least five associated tracks, a track-mass greater than 10 GeV. The muon selection is $p_T > 55$ GeV and $|\eta| < 1.07$, and transverse impact parameter greater than 1.5 mm.

Unlike the other ATLAS searches, this one requires neither very tight activity cuts nor coincident behavior for the decays. Consequently, it is much more powerful within its realm of applicability. Again, we conservatively ignore displaced particles produced in the decays of charged R-hadrons.

Because this is a tracker-based analysis, similar to the CMS displaced dijets, the possibility also exists for subtleties when heavy flavor secondary decays occur after the displaced decay. However, ATLAS states explicitly that vertices less than 1 mm from one another are merged. While the exact behavior for heavy flavor final-states is not given by ATLAS, we assume that this merging procedure effectively makes them insensitive to this issue.

2. Models and Limits

We now describe three of the well-known scenarios that lead to displaced sparticle decays, and present our new limits on several simplified models within those scenarios. In all three scenarios, we consider models with LSP or NLSP gluinos, which are common search targets due to their enormous pair production cross sections. For gauge mediation, we also consider the closely-related case of light-squark NLSPs. Otherwise, we focus on either stop pair production or Higgsino pair production, as both particles are expected to be below 1 TeV in a truly natural SUSY theory [160–164].²⁰ In most of what follows in this section, we restrict ourselves to presenting the basic search results, and reserve commentary on implications for Section II.F.3.

We generate event samples for most models with `Pythia8` [436], making extensive use of that program’s R-hadronization capabilities. Final-state particles from each lowest-level R-hadron or Higgsino decay are subsequently displaced before detector simulation and event reconstructions. For some of the colored production models where multibody decay kine-

²⁰We save explicit investigation of a left-handed sbottom (N)LSP for future work.

matics can be important, we have generated events in `MadGraph5` [444]. In this case, the `Pythia8` R-hadronization routine does not work because the R-odd colored particle has already decayed, and its daughters given color connections to other parts of the event. There, we identify final-state hadrons as descendants of the long-lived colored particles in an approximate way: each hadron is associated to the closest quark/gluon in ΔR as viewed the end of the parton shower, and the ancestry of that quark/gluon is traced by proxy.²¹

All pair production cross sections are normalized to their NLO+NLL predictions, including colored production through pure QCD [445] and electroweak Higgsino production [446]. These predictions are all conveniently tabulated for 7 and 8 TeV by the LHC SUSY Cross Section Working Group [447]. The Higgsino predictions assume nearly mass-degenerate Higgsino states with small mixings into the gauginos (assuming $M_{1,2} \sim 1$ TeV). Those cross sections are only provided up to 410 GeV, but we assume a flat K-factor for higher masses.

The generated particle-level events are passed through the detector simulations described in the Appendix and then subjected to the various analysis cuts described in Section II.F.1. The main output is a set of experimental acceptances for each individual simplified model (either per-decay or per-event), scanned over mass and lifetime. As an illustrative example, we provide our acceptances for the RPV $\tilde{t} \rightarrow \bar{d}\bar{s}$ model described below, passed through the CMS displaced dijet analysis. As can be seen, this specific analysis is most efficient for masses greater than a few hundred GeV and lifetimes at the $O(10\text{ cm})$ scale.

When constructing limits, for most of our recast experimental searches we provide a very rough error band on our predicted exclusion regions by varying these signal acceptance estimates up and down by a factor of 1.5 (not allowing those rescaled acceptances to exceed unity). This gives some indication of sensitivity to possible recasting errors. There are only two specific searches where we do not follow this protocol. The first such search is for stable charged particles, for which we do not explicitly include an error band. Our modeling here is fairly basic and conservative, and the acceptance anyway turns off exponentially fast at low lifetimes. We have also recast CMS’s over-conservative “charge stripped” limits, estimated

²¹ Using the simple 2-body $\tilde{t} \rightarrow \bar{d}_i \bar{d}_j$ as a cross-check, we find that the invariant mass of each stop is reconstructed to within about 10% and without bias, and that most search acceptances are only mildly sensitive to the ordering of decay and hadronization. The largest effects are on the tracker-based searches, with the efficiencies dropping by 10–15% for the sample decayed before hadronization, and therefore yielding conservative limits.

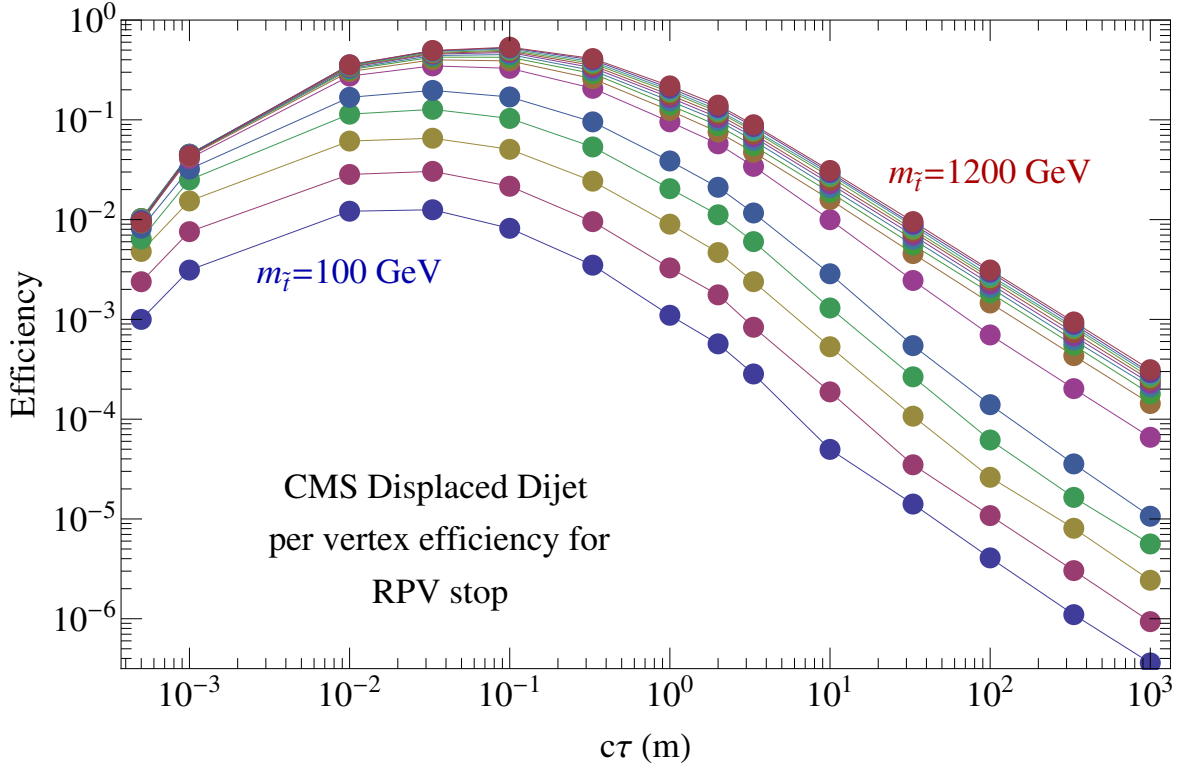


Figure II.50: Our central predictions for the CMS per-decay displaced dijet acceptances for $\tilde{t} \rightarrow \bar{d}\bar{s}$, using the detector model described in Appendix VI.E.5 and following the analysis described in Section II.F.1.b. The different colored lines are steps of 100 GeV in mass.

in a scenario where interactions in the calorimeters always strip off the R-hadron charges. The second search is for low-EM jets at ATLAS, where we have opted to instead define over-conservative and under-conservative treatments of the isolation against EM calorimeter activity, which we cannot reliably model. Here, we require either that no decay particles point back to the ECAL, or do not place any explicit isolation criterion (though in both cases we employ a flat $O(1)$ reconstruction efficiency factor given in Appendix VI.E.9).

a. Baryonic R-Parity Violation One of the simplest extensions to the MSSM is the introduction of R-parity-violating Yukawa superpotential couplings and/or a μ -term between the lepton doublet and down-type Higgs doublet superfields [1]. R-parity violation may also be introduced in the soft SUSY-breaking potential, or in the Kähler potential [151]. These are all typically set with zero coefficients in order to enforce R-parity. R-parity trivially prevents dimension-four proton decay and stabilizes the LSP, providing a possible dark matter candidate. However, these virtues are hardly strict requirements of the MSSM. Proton decay can be prevented by alternative stabilizing symmetries, which in any case may be required given the existence of potentially dangerous R-even operators at dimension-five [162]. Dark matter could easily arise from a different particle sector instead of the MSSM neutralino.

Violation of R-parity can lead to radical changes in collider phenomenology, depending sensitively on which operators are activated, on the magnitude and flavor structure of those operators, and on the identity of the LSP, which is no longer stable and no longer needs to be electromagnetically neutral. Broad ranges of coupling strengths allow for the LSP to decay at displaced locations within the LHC detector volumes. For example, for two-body sfermion decays into light SM fermions, mediated by one of the R-parity-violating Yukawas, a dimensionless coupling of $O(10^{-10} - 10^{-6})$ would yield a substantial population of measurably-displaced decays.

Proton stabilization allows the active RPV operators to violate either lepton number or baryon number, but not both. This partitions the RPV scenarios into two mutually-exclusive classes, which we can call leptonic RPV and baryonic RPV. The only explicit RPV displaced searches so far at the LHC have assumed leptonic RPV [135, 136, 138, 139], capitalizing on the presence of leptons in the final state to help with triggering and with controlling

backgrounds. Here we pursue the completely untested case of baryonic RPV. (However, we will put the leptonic RPV searches to an alternative use in the next subsection, applying them to gauge mediation models.)

We begin with the case of stop LSP. Minimalistically, the decay would be mediated by the usual Yukawa superpotential interaction of right-handed chiral quark/squark fields, $\lambda''_{ijk} U_i D_j D_k$ (ijk are flavor indices). This is the only baryon-number-violating interaction in the MSSM that respects SUSY at dimension-four. The required antisymmetrization over color indices requires a commensurate antisymmetrization over down-type flavor indices, leading to allowed decays $\tilde{t} \rightarrow \bar{d}\bar{s}$, $\bar{d}\bar{b}$, and $\bar{s}\bar{b}$. Recently, it has also been observed that stop decays may proceed through a different combination of chiral quark/squark fields, via dimension-five operator $Q_i Q_j D_k^\dagger$ in the Kähler potential [151]. The resulting component-field operators allow for a decay $\tilde{t} \rightarrow \bar{b}\bar{b}$, and indeed this is generally preferred since the decay amplitudes are chirally-suppressed (analogous to pion decay). Prompt decays $\tilde{t} \rightarrow \bar{d}_j \bar{d}_k$ have only just begun to be probed by the LHC, in the mass region 200–400 GeV [448]. It has been estimated that a search based on jet substructure could also push down into the lower-mass region currently not covered [449]. (For longer-term projections, also see [449] as well as [450].) The only other available limits are when the stops are detector-stable, the strongest (≈ 900 GeV) coming from the CMS and ATLAS charged R-hadron searches [128, 129].

Figs. II.51 and II.52 show the regions of mass and lifetime for $\tilde{t} \rightarrow \bar{d}_j \bar{d}_k$ that have now been excluded according to our recasts, taking the two extreme cases of only light-flavor decays and only $\bar{b}\bar{b}$ decays. The sensitivity is dominated by the charged R-hadron and displaced dijet searches, a pattern that will recur often in our colored sparticle limits. For both models there is nearly complete coverage out to almost 1 TeV, with a notable weak-spot at $c\tau \sim 10$ m and of course much weaker limits for displacements \lesssim mm. This weakening at low lifetimes is more pronounced for the $\bar{b}\bar{b}$ decays, partially because the CMS dijet search is intrinsically less efficient for heavy flavor decays due to the somewhat lower particle track multiplicities, but also because of the conservative choice in our modeling of displaced vertex reconstruction for b -jets, discussed in Section II.F.1.b. At lower lifetimes, we have also indicated the existing and projected prompt limits, applying a conservative sensitivity cutoff at 1 mm. (There should still be sensitivity from prompt searches for longer lifetimes, but

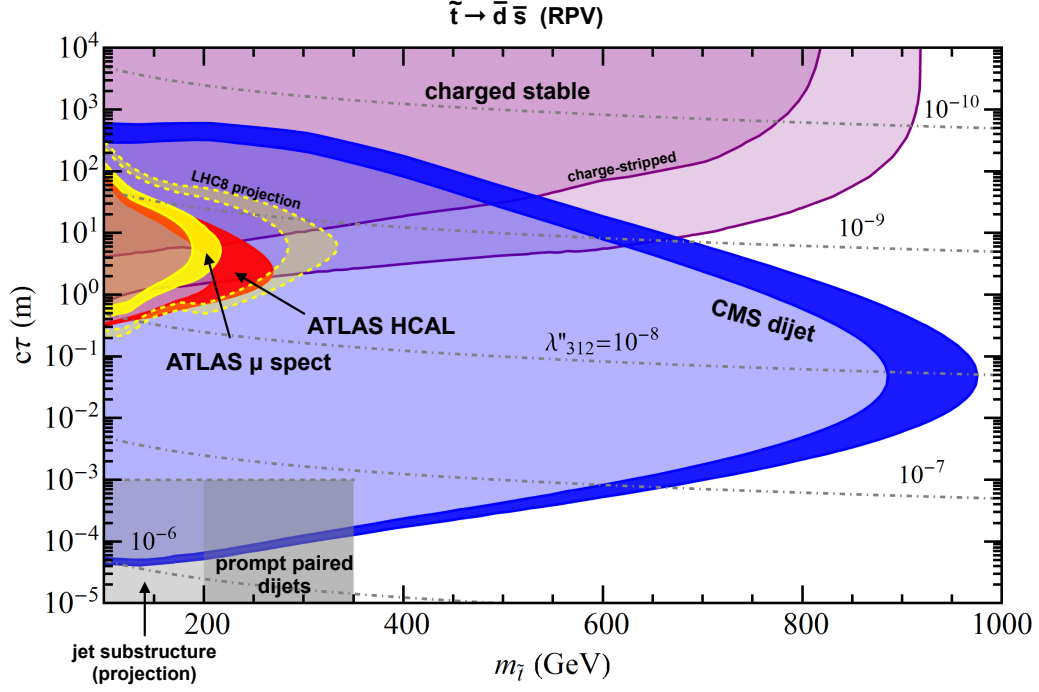


Figure II.51: Recast constraints on displaced $\tilde{t} \rightarrow \bar{d}_j \bar{d}_k$ via baryonic RPV. Colored bands indicate acceptance variations up/down by 1.5. The dot-dashed lines indicate contours of λ''_{312} , assumed to be the only contributing RPV coupling. Prompt limits (dark gray) are from [448], and low-mass search projections (light gray) are from [449]. They are conservatively cut off at 1 mm.

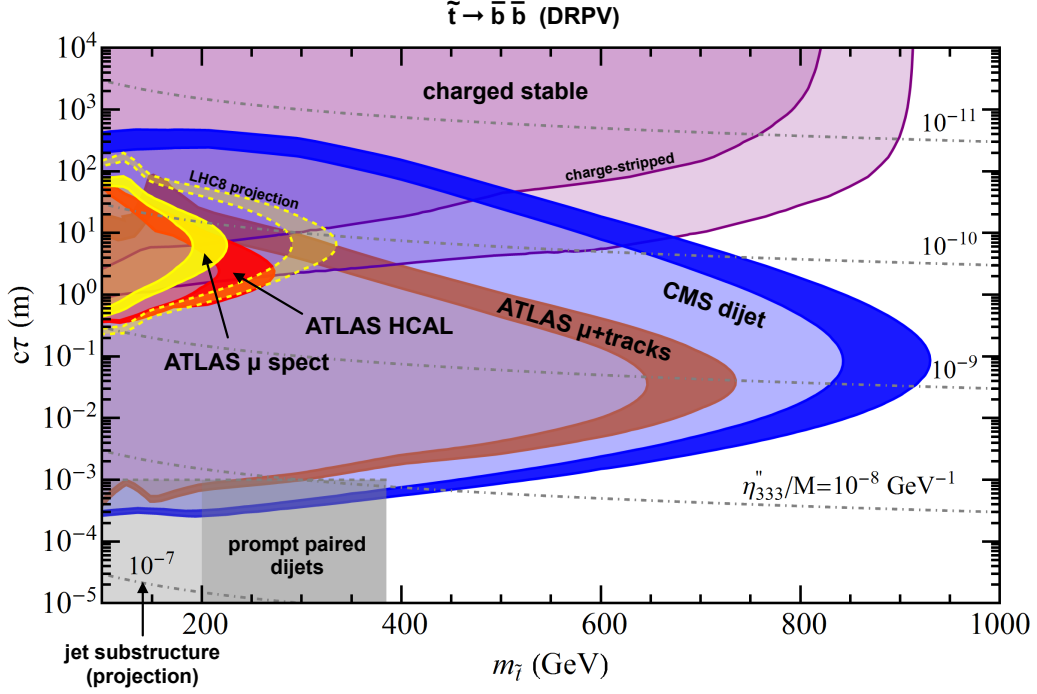


Figure II.52: Recast constraints on displaced $\tilde{t} \rightarrow \bar{b}\bar{b}$ in the Dynamical RPV framework. Colored bands indicate acceptance variations up/down by 1.5. The dot-dashed lines indicate contours of η''_{333}/M , assumed to be the only contributing RPV coupling. It arises from the Kähler potential operator $(\eta''_{333}/M)Q_3Q_3D_3^\dagger + (\text{h.c.})$. Prompt limits (dark gray) are from [448] (neglecting a possible improvement in the limits due to the higher b-jet multiplicity in the DRPV model), and low-mass search projections (light gray) are from [449]. They are conservatively cut off at 1 mm.

we do not have enough information to reliably model this.) Combining these three searches, unbroken coverage is achieved for *all* lifetimes for masses where the prompt searches are sensitive. Indeed, for stop masses up to a few hundred GeV, the CMS dijet search alone spans 6—7 orders of magnitude in lifetime. This amazing performance capitalizes heavily on the fact that millions of stop pairs would have been produced at such small masses, with sizable enough kinematic tails to pass the jet H_T and p_T cuts, and enough remaining rate to catch anomalously early or late decays from models at the edges of the exclusion region. Two other displaced searches, ATLAS muon chamber (including our naive 8 TeV projection) and ATLAS low-EM jets, are much less competitive for the reasons discussed in Sections II.F.1.e and II.F.1.f, though they do offer useful complementarity in that their limits are derived from completely different detector systems. Finally, we point out a sizable region in the $b\bar{b}$ decay case that is also covered by the ATLAS μ +tracks search, from a small population of events where one of the bottom decays produces a hard muon.²²

The next model that we consider is gluino LSP. Considering only traditional superpotential RPV, the gluino decays by first transitioning into a virtual squark and a corresponding real quark. The virtual squark then splits to two quarks through the UDD operator. The full 3-body decay is $\tilde{g} \rightarrow jjj$. There are again many options for flavor structure, which may be engineered both at the level of the λ''_{ijk} couplings and the squark mass spectrum. Here, we simply assume decays into light flavors, though decays involving b -quarks could again be subjected to weaker limits at low lifetimes, and decays involving t -quarks would also receive constraints from the displaced searches involving leptons. Otherwise, we expect fairly similar coverage. Of course, branching ratios into top also suffer additional phase space suppression.

Fig. II.53 shows our estimated exclusions for $\tilde{g} \rightarrow jjj$. The qualitative features are quite similar to the RPV stop decays, though the much higher cross sections yield a significantly extended mass reach for all searches. CMS dijets in particular reaches above 1.5 TeV, close to the production limit of $O(1)$ event in the entire run, and exceeding the mass reach of the stable R-hadron search by several hundred GeV. Notably, the displaced trijet configuration is very efficiently picked up by the CMS dijets search, which was designed for a very different

²²The muon in this search is triggered from the standalone muon spectrometer, and is not explicitly required to be isolated.

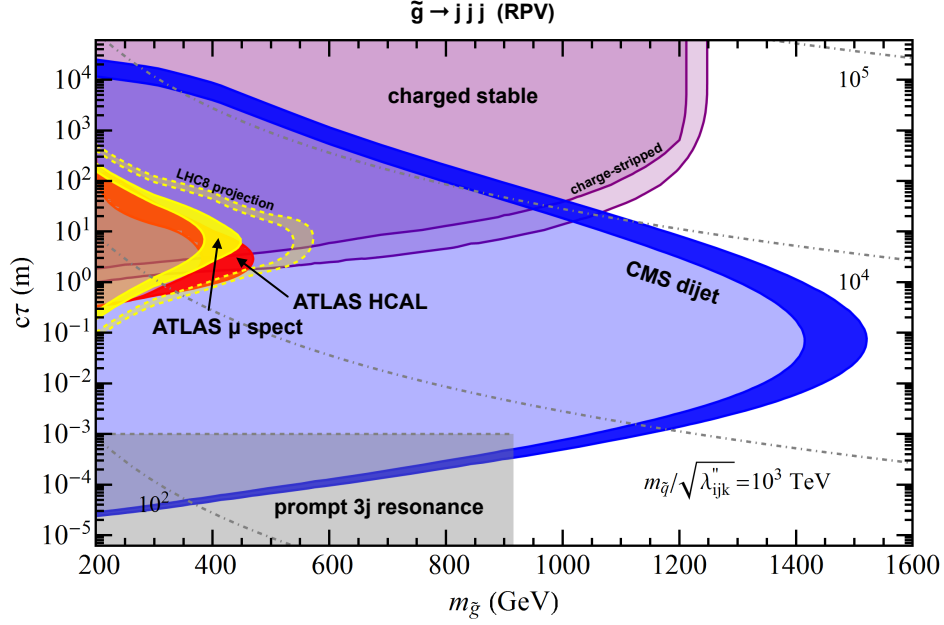


Figure II.53: Recast constraints on displaced $\tilde{g} \rightarrow jjj$ via baryonic RPV. Colored bands indicate acceptance variations up/down by 1.5. The dot-dashed lines indicate contours of $m_{\tilde{g}}/\sqrt{\lambda''_{ijk}}$. We have parametrized the decay assuming that one species of off-shell RH squark dominates, and splits into quarks via a single λ''_{ijk} coupling. All final-state quarks are also assumed to be from the first two generations. Prompt limits (gray) are derived from [451]. They are conservatively cut off at 1 mm.

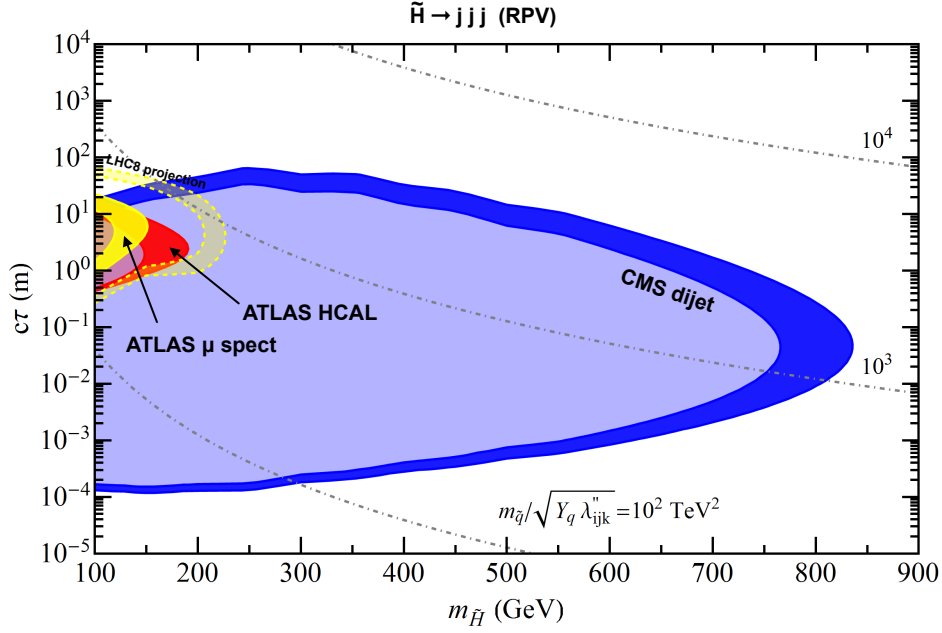


Figure II.54: Recast constraints on displaced $\tilde{H}^0 \rightarrow jjj$ via baryonic RPV. Colored bands indicate acceptance variations up/down by 1.5. The dot-dashed lines indicate contours of $m_{\tilde{q}}/\sqrt{Y_q \lambda''_{ijk}}$. We have parametrized the decay assuming that one species of off-shell RH squark dominates, coupling to the Higgsino according to its up-type or down-type Yukawa $Y_q \propto m_q/(v \sin \beta)$ or $m_q/(v \cos \beta)$, and splits into quarks via a single λ''_{ijk} coupling. All final-state quarks are also assumed to be from the first two generations.

signal. The weak spot at 10 m is still apparent, but much less pronounced since the CMS dijet search nearly matches the HSCP search sensitivity at that lifetime. It is also interesting to supplement with the limits from prompt searches [451, 452], which are similar for purely light-flavor decays and decays containing b -quarks. Again applying an ad hoc 1 mm cutoff on the lifetime sensitivity of the prompt searches, there is currently unbroken coverage for *all* possible lifetimes for masses potentially as high as 900 GeV.

The last baryonic RPV example model that we consider is a Higgsino multiplet “co-LSP.” The four Higgsino states are assumed to be only mildly mixed into heavier electroweak gauginos, and the multiplet split by $O(10 \text{ GeV})$ or less. The heavier Higgsinos undergo a soft

but prompt cascade via virtual gauge boson emission into the lightest, neutral Higgsino. The displaced decay of this lightest Higgsino proceeds in almost exact analogy with the gluino decay, though now the virtual squark is accessed via a super-Yukawa coupling instead of a super-QCD coupling. Again, the flavor structure of the decay can be nontrivial, but as a first pass we simply assume that the final quarks are all light. Decays involving tops deserve a dedicated investigation, especially in the context of a natural theory, though we anticipate fairly similar limits.

Fig. II.54 shows our estimated exclusions for $\tilde{H} \rightarrow jjj$. The qualitative picture from the displaced decay searches remains similar, though with reduced mass reach due to the smaller production cross sections. Unlike the preceding stop and gluino examples, there are no explicit limits on $\tilde{H} \rightarrow jjj$ in either prompt or stable charged particle searches. For the prompt case, we can compare to $\tilde{g} \rightarrow jjj$ searches [451, 452]. Using simple cross section scaling suggests that that promptly decaying RPV Higgsinos are genuinely unconstrained, since the Higgsino cross section is roughly 500 times smaller at a given mass. (A more aggressive dedicated prompt search could be useful, though would be highly challenging.) For the stable case, the LSP here is generically neutral, and hence does not leave a track. Therefore, our reported direct Higgsino production limits here are the first for *any* lifetime.

While we have only studied a small sample of possible spectra, these results clearly illustrate the power of the LHC in probing baryonic RPV in general via displaced decays. An obvious extension of our observations would be an application to a broader class of flavor assumptions, though as indicated we do not expect radically different sensitivity. The remaining extensions would be to consider different LSPs, and perhaps more model-dependent scenarios where the LSP is created in cascades in addition to prompt production. An LSP squark could represent a rather trivial example, since the production and decay could be very similar to the LSP stop. However, decays into the top quark could also open up, and the effective production cross section could also be highly enhanced by the multiplicity of nearby squark states (cascading promptly into one another) and/or by gluino exchanges. Direct LSP slepton production represents a qualitatively different direction, wherein a 4-body decay to $ljjj$ or νjjj (via virtual electroweakino and squark) might dominate, even for much larger values of the λ''_{ijk} . Finally, production of different electroweakinos, such

as a mostly-bino or mostly-wino, could be considered. In fact, the latter has recently been investigated in [156], and similarly finds very high mass reach using the CMS displaced dijets search. With the generality and power of the HSCP and dijets searches, the main missing pieces in covering the mass-lifetime plane for these varied models would be prompt and b-tagged searches (possibly recast from other models) and more aggressive muon-chamber and calorimeter searches, especially for the cases without long-lived charged states. Additional studies within the framework of dynamical RPV could also be interesting, since this allows for additional flavor and chirality structures in the decays.

b. General Gauge Mediation Traditional forms of gauge mediation assume fairly minimal messenger sector constructions, and consequently relatively predictive patterns of sparticle masses [125]. For example, relationships like $M_1:M_2:M_3 = \alpha_1:\alpha_2:\alpha_3$ for the three gauginos favor a bino-like NLSP and a much heavier gluino. A much more general perspective has been advocated in [453], acknowledging the full range of possible MSSM spectra derivable from arbitrary messenger sectors, perturbative or not. Practically speaking, the individual sfermion and gaugino soft masses become almost freely-adjustable, up to two sfermion sum rules and flavor universality, as well as vanishing A -terms at the mediation scale. Even more general model frameworks allow for the possibility of flavor nonuniversality effects, either by mixing into a supersymmetric composite sector [454–457], by gauging flavor symmetries [458], or by introducing large A -terms through non-minimal interactions between MSSM and messenger fields [459].

Such freedom of model-building in gauge mediation allows for a number of intriguing options for LHC phenomenology. Practically any superparticle can be made the NLSP, which then decays into its SM-partner and a light gravitino (i.e., Goldstino) at a rate controlled only by the fundamental SUSY-breaking mass scale, \sqrt{F} . Roughly speaking, when the SM partner is light,

$$c\tau \sim 0.3 \text{ mm} \left(\frac{100 \text{ GeV}}{\tilde{m}} \right)^5 \left(\frac{\sqrt{F}}{100 \text{ TeV}} \right)^4, \quad (\text{II.F.83})$$

implying displaced decays at the $O(\text{mm} - 10 \text{ m})$ scale for \sqrt{F} in the range of a few-hundred to a few-thousand TeV. With the traditional option of the bino-like neutralino as the NLSP,

the decays are dominated by photon and gravitino. Consequently, the experimental effort in displaced GMSB searches has focused on signals of displaced/delayed photons and missing energy [132, 133].²³ In [148, 460], it was pointed out that an NLSP neutralino with larger wino or Higgsino fraction would also yield displaced W , Z , and Higgs. The possibility of displaced NLSP stops was emphasized in [153, 461, 462], especially for stop masses near or below the top quark mass. The simplest remaining displaced NLSP options would be slepton decaying to lepton, squarks decaying to (non-top) quarks, and gluino decaying to gluon.²⁴ None of these other possibilities have been searched for in the case of displaced decays, though a number of searches have been performed for prompt decays and for the collider-stable cases. However, most NLSP possibilities are actually already under tight constraint, as we will see, again sometimes with coverage over the full range of possible lifetimes.

A notable exception is any variation on the slepton NLSP, such as the standard mostly- $\tilde{\tau}_R$ when the sleptons are degenerate up to Yukawa effects, or possibly $\tilde{e}_R/\tilde{\mu}_R$ if the staus can be made heavier [466]. These would be largely unconstrained by the displaced vertex searches due to the low track multiplicities and vertex masses, and searches for displaced activity in the calorimeters or muon chambers would usually fail to pick up the signal, for example because the associated slepton track would cause isolation failure. CMS’s displaced $e+\mu$ search [136] should yield some sensitivity for leptonic tau decays. Though we reserve for future work a more comprehensive study of the status of displaced slepton NLSPs in GMSB, we anticipate that planned searches for “kinked track” topologies will be important to more fully cover the parameter space, and that existing disappearing track searches might also provide some sensitivity.

The remaining NLSP options that yield a single SM final-state particle, without passing through an intermediate heavy SM decay (top or electroweak), are the non-top squarks and the gluino. As in the baryonic RPV models, presently the only potentially applicable tracker-based search is the CMS displaced dijets, but the nominal number of partons in the decay is

²³These are also necessarily the most model-dependent of the available signals, since a simplified model containing only the bino would have vanishing tree-level pair production cross section. The most powerful existing search [132] mainly capitalizes on pair production of mostly-winos cascading down into a mostly-bino, relying on the relationship $M_2/M_1 \simeq \alpha_2/\alpha_1$.

²⁴An NLSP sneutrino from light $\tilde{\ell}_L$ doublets would decay fully invisibly, making the displacement irrelevant for its experimental signatures. The distinctive phenomenology of such a scenario has been studied in [463–465].

not two. Here, in order for the displaced dijet search to be sensitive, the decay must undergo a hard enough final-state bremsstrahlung to create a second jet. Given the large strong production cross sections, this is an affordable penalty: of order $(\alpha_s/\pi) \log(\tilde{m}/(60 \text{ GeV}))$, times color factors, with the sparticle mass and jet p_T cut appearing inside the logarithm. Quantitatively, the chance to radiate a second jet is roughly at the 1–10% level. Of course, a search explicitly geared toward the one-jet topology could be more efficient, and the displaced dijet trigger would already capture this signal in cases where both decays occur within the inner 60 cm radius of the tracker and with at least $O(\text{mm})$ displacement. However, at the very high and very low lifetime ranges, the inefficiency induced by requiring an extra jet may be less than the inefficiency that would be induced by forcing both decays to occur at improbably short or long proper times. A more fruitful option for future analyses could be to exploit the traditional jet, H_T , and \cancel{E}_T triggers, and apply an offline search for individual displaced jets.²⁵

Proper simulation of the decays for the existing displaced dijet search requires some level of matrix element matching. This is performed automatically by the **Pythia8** shower in the case of $\tilde{q} \rightarrow q\tilde{\chi}^0$ with a massless neutralino LSP, while the desired decay $\tilde{q} \rightarrow q\tilde{G}$ is not matched. However, we have observed essentially identical rates and kinematics for extra jet production in \tilde{q} decays between explicit **MadGraph5** 2- and 3-body decay simulations with neutralino and gravitino LSPs, and close agreement with **Pythia8**'s matched predictions for the first shower emission. We therefore feel confident using the massless neutralino LSP as a proxy for the gravitino LSP for squark decays in **Pythia8**. For the gluino, such an analogous decay to neutralino does not exist at tree level, is not part of the **MadGraph5** MSSM model, and would not obviously be matched if forced to proceed in **Pythia8**. Instead, we compare the unmatched **Pythia8** predictions for its first shower emission to **MadGraph5**, both with gravitino LSP. We again find similar decay kinematic distributions, with **Pythia8** predicting a somewhat slower falloff out to $\Delta R(j, j) \sim \pi$. But the major difference is in the total emission rate, which **Pythia8** over-estimates by a factor of about 1.8. To approximately compensate for this, we rescale the individual vertex reconstruction efficiencies by 1/2. It should be understood that $O(10\%)$ modeling uncertainties on the displaced dijet reconstruc-

²⁵We thank Joshua Hardenbrook for emphasizing this possibility.

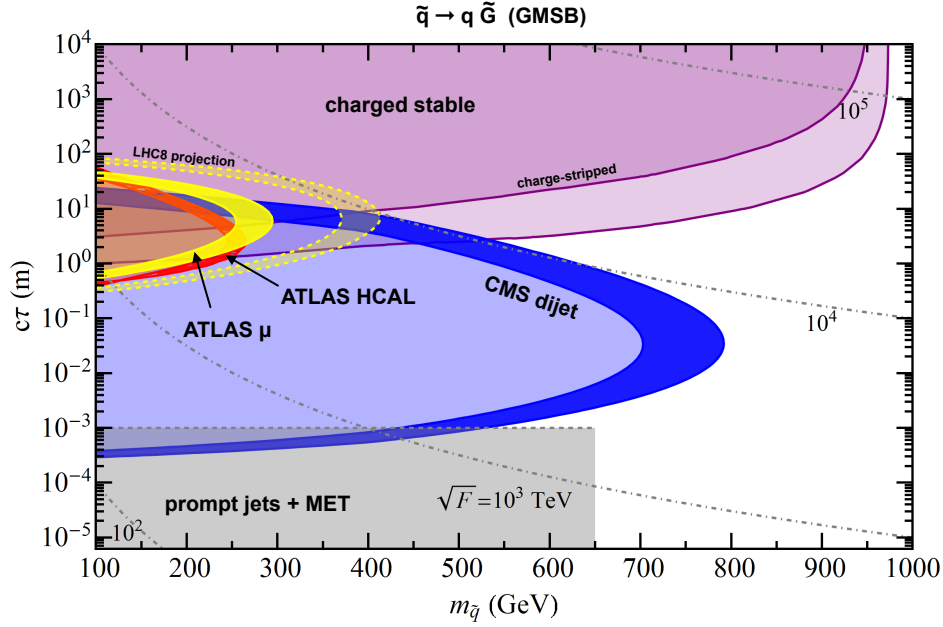


Figure II.55: Recast constraints on displaced $\tilde{q} \rightarrow q\tilde{G}$ in general GMSB, conservatively assuming contributions from only \tilde{d}_R and \tilde{s}_R . Colored bands indicate acceptance variations up/down by 1.5. The dot-dashed lines indicate contours of the SUSY-breaking scale \sqrt{F} . Prompt limits (gray) are derived from [467]. They are conservatively cut off at 1 mm.

tion efficiencies for GMSB gluinos should likely be applied, though we anyway effectively absorb this into our ad hoc systematic variations.

Starting with the squark NLSP, we display the results in Fig. II.55. We conservatively assume just two degenerate species, \tilde{d}_R and \tilde{s}_R . This is a technical possibility if the $SU(3)$ contributions to the sfermion masses are small, the $SU(2)$ contributions are large, and the third-generation squarks receive additional mass contributions. The exclusions are similar to those of the RPV stops (Figs. II.51 and II.52), although now with much stronger prompt jets+ \cancel{E}_T searches. Unbroken coverage over lifetime is achieved up to about 450—550 GeV, limited by the crossover between the HSCP and displaced dijet searches.

Next we consider the gluino NLSP in Fig. II.56. Comparing to the RPV results for $\tilde{g} \rightarrow jjj$ in Fig. II.53, we observe much weaker displaced decay limits and much stronger

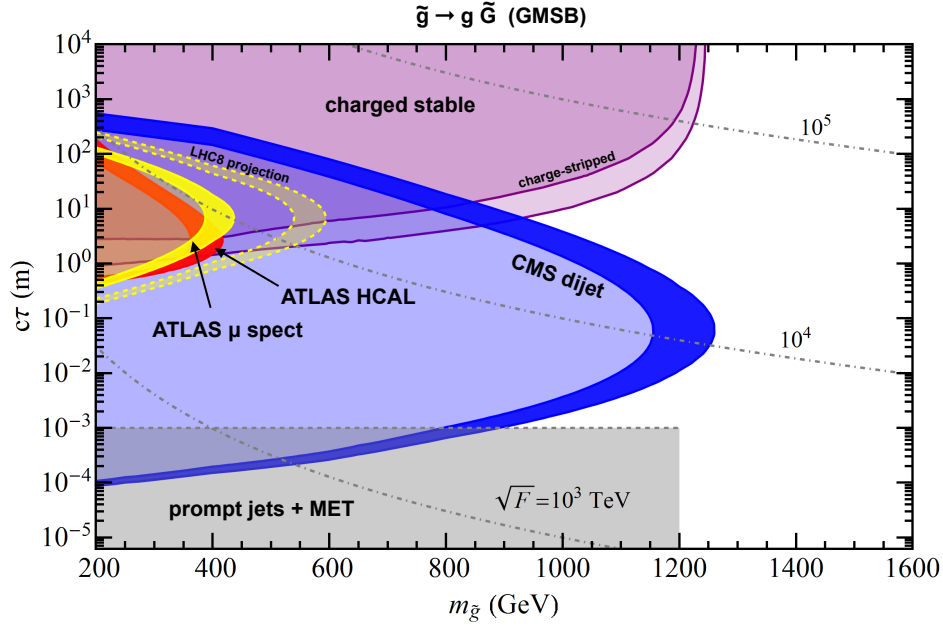


Figure II.56: Recast constraints on displaced $\tilde{g} \rightarrow g\tilde{G}$ in general GMSB. Colored bands indicate acceptance variations up/down by 1.5. The dot-dashed lines indicate contours of the SUSY-breaking scale \sqrt{F} . Prompt limits (gray) are derived from the $\tilde{q} \rightarrow q\tilde{G}$ of [467]. They are conservatively cut off at 1 mm.

prompt decay limits. The former is due to the requirement of additional hard radiation in the decay to pass the CMS displaced dijet reconstruction. The latter is due to the much more distinctive jets+ \cancel{E}_T signature. Most of the model space below 1200 GeV is covered, with expected weak spots at $O(\text{mm})$ and $O(1-10 \text{ m})$, though much of the surviving space at smaller lifetimes would likely be probed by a more detailed jets+ \cancel{E}_T recast, as in [131]. Full coverage over all lifetimes is only achieved for masses below 800 GeV.

We now move on to the naturalness-motivated options, starting with the NLSP stop in Fig. II.57. We consider stops of any mass above 100 GeV, including a range of masses below m_t and through the compressed region where $m_{\tilde{t}} = m_t$.²⁶ In these regions, the decays are dominantly 3-body $\tilde{t} \rightarrow Wb\tilde{G}$, with a large fraction of energy going into the effectively

²⁶Because of the smallness of the $t\tilde{t}\tilde{G}$ coupling, top quark decay into a light stop and \tilde{G} would be rare.

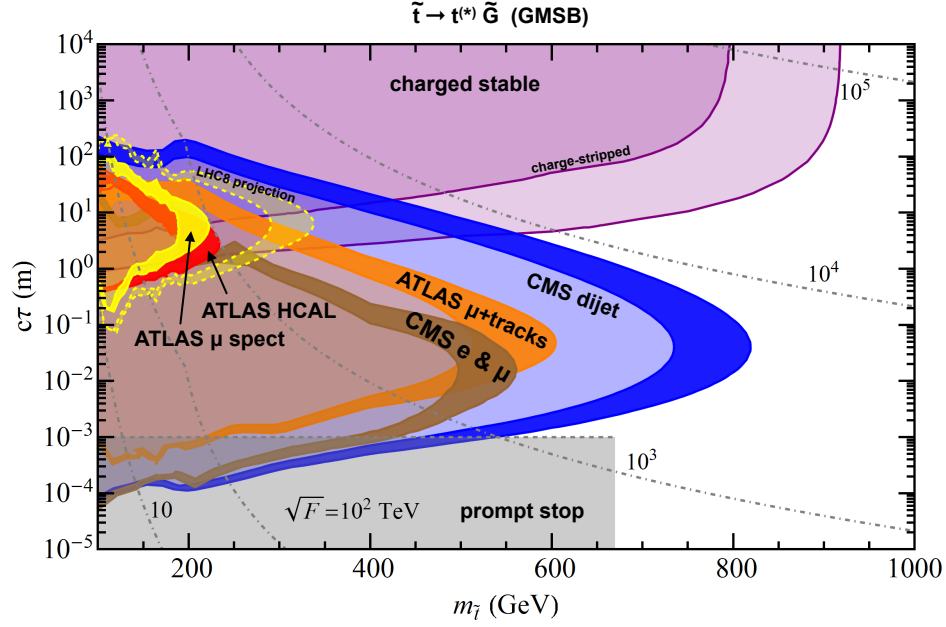


Figure II.57: Recast constraints on displaced $\tilde{t} \rightarrow t^{(*)} \tilde{G}$ in general GMSB. Colored bands indicate acceptance variations up/down by 1.5. The dot-dashed lines indicate contours of the SUSY-breaking scale \sqrt{F} . Prompt limits (gray) are derived from [468, 469]. They are conservatively cut off at 1 mm.

derivatively-coupled gravitino/Goldstino. Also, in addition to the by-now familiar searches that have appeared in all of our recasts above, the semileptonic decays of the stop open up sensitivity in the ATLAS μ +tracks search and the CMS displaced $e+\mu$ search. While the sensitivity regions for these searches are fully contained by CMS displaced dijets, corroborating coverage is provided by the leptonic searches over much of the excluded region. Adding in the prompt searches [468, 469], which likely give unbroken coverage between 100 GeV and 670 GeV,²⁷ we infer that GMSB stops of any lifetime are excluded below about 500 GeV. For lifetimes at the cm-scale, exclusions extend beyond 700 GeV, and, as noted before, out to about 900 GeV for lifetimes longer than $O(10\text{ m})$. (For other estimates of displaced stop exclusions in GMSB, see [157].)

Finally for GMSB, we consider Higgsino multiplet co-NLSPs. As in the RPV case above, we assume that all Higgsino states are nearby to one another (split by no more than $O(10\text{ GeV})$), with heavier states decaying promptly. The lightest Higgsino will preferentially decay to some mixture of $Z\tilde{G}$ and $h\tilde{G}$, with $\gamma\tilde{G}$ suppressed. The lifetime and branching fractions of the lightest Higgsino exhibit simple behavior if mixings with the bino and wino are small, and the scalar Higgs sector is close to the “decoupling limit.” For instance, when $\tan\beta = 1$, the lightest Higgsino coupling to either $Z\tilde{G}$ or $h\tilde{G}$ vanishes, depending on the relative signs of the μ parameter and $M_{1,2}$. For $\tan\beta \gg 1$, the $h\tilde{G}$ and $Z\tilde{G}$ decay modes have similar partial widths if $m_{\tilde{H}} \gtrsim m_h$.

We present the limits in these three extreme cases in Fig. II.58: a) pure $\tilde{H} \rightarrow Z\tilde{G}$, b) pure $\tilde{H} \rightarrow h\tilde{G}$, and c) large- $\tan\beta$. Though the HSCP searches again do not apply, the GMSB Higgsino brings into play all of our other displaced decay recasts, now including as well the CMS displaced dilepton search. For decays that include direct Z bosons, this last search can be seen to play a major role, competing significantly with and even beating the

²⁷The prompt searches face some subtleties. On the one hand, for stop masses well above m_t , existing searches for $\tilde{t} \rightarrow t\tilde{\chi}^0$ with massless neutralino should offer identical coverage. On the other hand, the decay kinematics near or below m_t can be significantly different than the corresponding decays to neutralinos. The expectation is that the GMSB limits there should be much stronger than the nominal limits, and not subject to the usual sensitivity gap with a compressed spectrum [470]. The major exception is a mostly- \tilde{t}_L stop, for which spin effects would reshape the \cancel{E}_T -sensitive distributions and weaken the limits in searches with semileptonic decays. Without recasting the most recent searches, it is not possible to precisely delineate this gap, though the results of [470] suggest that it may be several 10’s of GeV wide, centered in the vicinity of 200 GeV. Since the displaced searches are not designed to cut on \cancel{E}_T -sensitive tails, we do not expect such spin effects to be significant there.

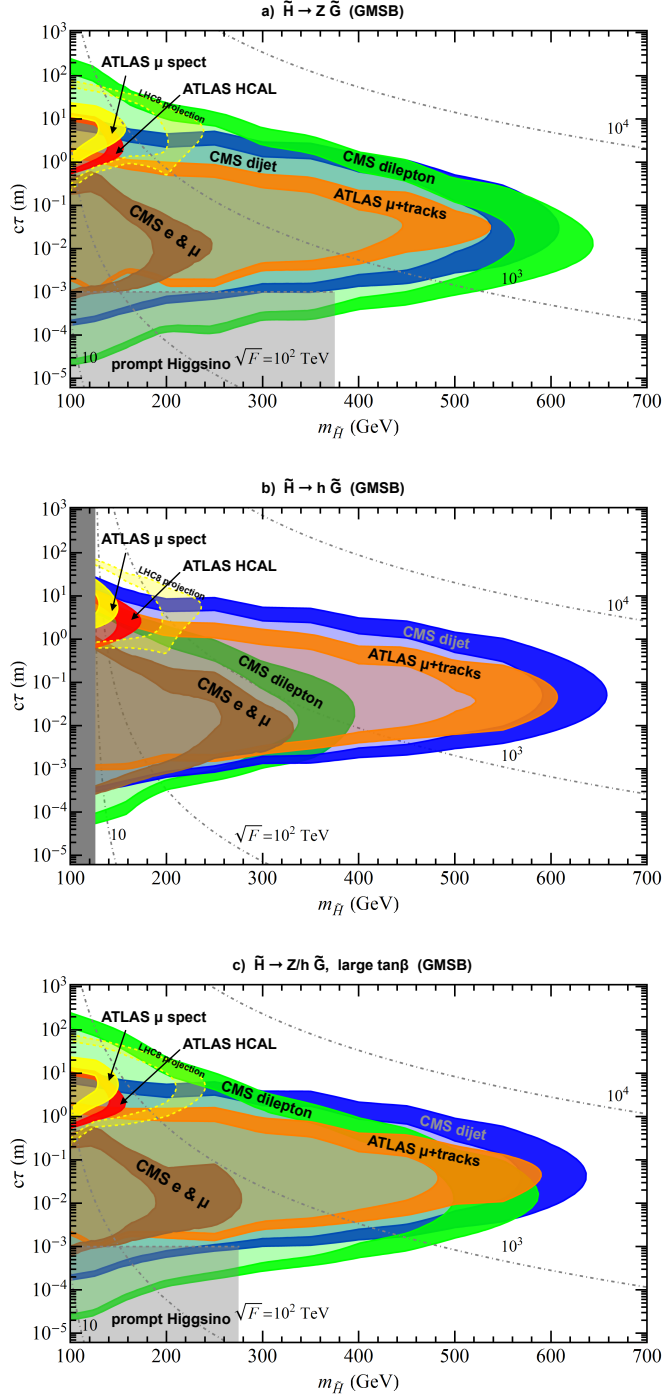


Figure II.58: Recast constraints on displaced \tilde{H}^0 decays via GMSB: a) pure $\tilde{H}^0 \rightarrow Z \tilde{G}$, b) pure $\tilde{H}^0 \rightarrow h \tilde{G}$, c) large- $\tan\beta$. Colored bands indicate acceptance variations up/down by 1.5. The dot-dashed lines indicate contours of the SUSY-breaking scale \sqrt{F} . Prompt limits (gray) are derived from [471]. They are conservatively cut off at 1 mm.

CMS dijet search. This is especially obvious at very low and very high lifetimes, where the dilepton search benefits from both lower track impact parameter thresholds and looser p_T reconstruction thresholds. Similarly, leptonic decays play a major role in the prompt searches [471], with maximal sensitivity for pure $\tilde{H} \rightarrow Z\tilde{G}$, capitalizing in part on 3- and 4-lepton channels. Taking the large- $\tan\beta$ case as a baseline example, $m_{\tilde{H}} = 100$ GeV is now covered from zero lifetime up to $c\tau \sim 100$ m, and $m_{\tilde{H}} = 300$ GeV is covered up to $c\tau \sim$ few m. The highest mass reach is for $c\tau \sim 10$ cm, extending out to about 600 GeV. For the pure $\tilde{H} \rightarrow h\tilde{G}$ case, our displaced search recasts represent the only extant limits, as was the case for the RPV Higgsinos.

We have touched upon most of the possible displaced NLSP decays in gauge mediation. The last obvious remaining option, which we now briefly discuss for completeness, would be wino co-NLSPs. In some ways, this should overlap significantly with our \tilde{H} results, but there are some notable differences. First, wino cross sections are about two times larger. Second, the \tilde{W}^0 has a significant branching fraction into photons, hence subjecting it to the displaced/delayed photon searches. Third, when the wino multiplet is somewhat separated in mass from the bino and Higgsino, the mass splitting between charged and neutral states is protected at leading order in the mass mixing by an accidental custodial symmetry, with the first nontrivial mixing contributions often comparable to or smaller than the electroweak radiative mass splitting of ≈ 170 MeV. This famously leads to the long-lived decays $\tilde{W}^\pm \rightarrow \pi^\pm \tilde{W}^0$, with $c\tau \simeq 5$ cm, searched for in [134, 434]. In such a case, there can be non-trivial competition between the above decay and $\tilde{W}^\pm \rightarrow W^\pm \tilde{G}$. There can also be peculiar cases with an initial stage decay $\tilde{W}^\pm \rightarrow \pi^\pm \tilde{W}^0$, leaving a disappearing track, followed by a secondary displaced decay $\tilde{W}^0 \rightarrow (\gamma/Z)\tilde{G}$. Finally, there are also some corners of parameter space with $m(\tilde{W}^\pm) < m(\tilde{W}^0)$ due to chargino and neutralino mixings [472], causing every event to contain two displaced W s. The signatures would be much more similar to those of $\tilde{H} \rightarrow Z\tilde{G}$, though missing the displaced dileptons and, if $c\tau > O(\text{cm})$, containing a track or track stub pointing to the displaced decay (similar to the slepton NLSPs). All together, the potentially rich displaced phenomenology of wino co-NLSPs in gauge mediation clearly deserves a more detailed investigation, and would bring together a surprisingly varied set of displaced search results.

c. Mini-Split SUSY The last model framework that we consider is mini-split supersymmetry, where the scalars of the MSSM (excepting the SM-like Higgs boson) are all raised to the 1000 TeV scale [126, 127, 473]. This scale could represent a sweet-spot between masses that are high enough to avoid flavor constraints with arbitrary sfermion mass matrix structure, but low enough to provide a 125 GeV Higgs from the stop loop corrections. The separation between MSSM scalars and fermions can arise automatically in several SUSY-breaking mediation scenarios (surveyed in [126] and discussed on general terms in [127]). However, while some of the important virtues of SUSY such as gauge coupling unification and dark matter can be preserved, the original motivation of naturalness is partially abandoned. The apparently finely-tuned Higgs mass might nonetheless be viewed as a byproduct of anthropic selection bias in the multiverse, in some ways similar to the unnaturally small cosmological constant [473], or as a compromise against much larger “tunings” within the available “model space” of broken SUSY theories [127].

While gauginos need not be present at any particular mass scale, the WIMP miracle is suggestive of TeV-scale masses, potentially within reach of the LHC. One of the most interesting targets is the gluino, since the flow of R-parity in its decay must pass through the heavy squarks, leading to suppressed matrix elements and extended lifetimes. Two types of LHC searches so far have directly targeted this signal: searches for R-hadrons stopped in the calorimeters and decaying out-of-time with respect to collisions [137, 145], and an ATLAS reinterpretation of its prompt jets+ \cancel{E}_T searches using models with displaced decays [131]. Neither of these are optimally sensitive, though the former strategy has the added benefit of permitting a lifetime measurement if a positive signal is observed, and the latter strategy can be carried out quickly with no changes to the event reconstruction and selection software. In addition, searches for anomalous tracks from collider-stable R-hadrons, which we have discussed above in the contexts of both RPV and GMSB, continue to apply.

Here we put all of these long-lived gluino searches into context for a couple of specific assumptions for the decay kinematics. In almost full generality, the gluino may decay into any flavor-combination of quark-antiquark pairs plus a \tilde{B} , \tilde{W} , or \tilde{H} . The exact admixture of these decays is highly model-dependent. Since the decay rate through any given off-shell squark channel scales like $1/m_{\tilde{q}}^4$, the lightest squark eigenstate would dominate if there is a somewhat

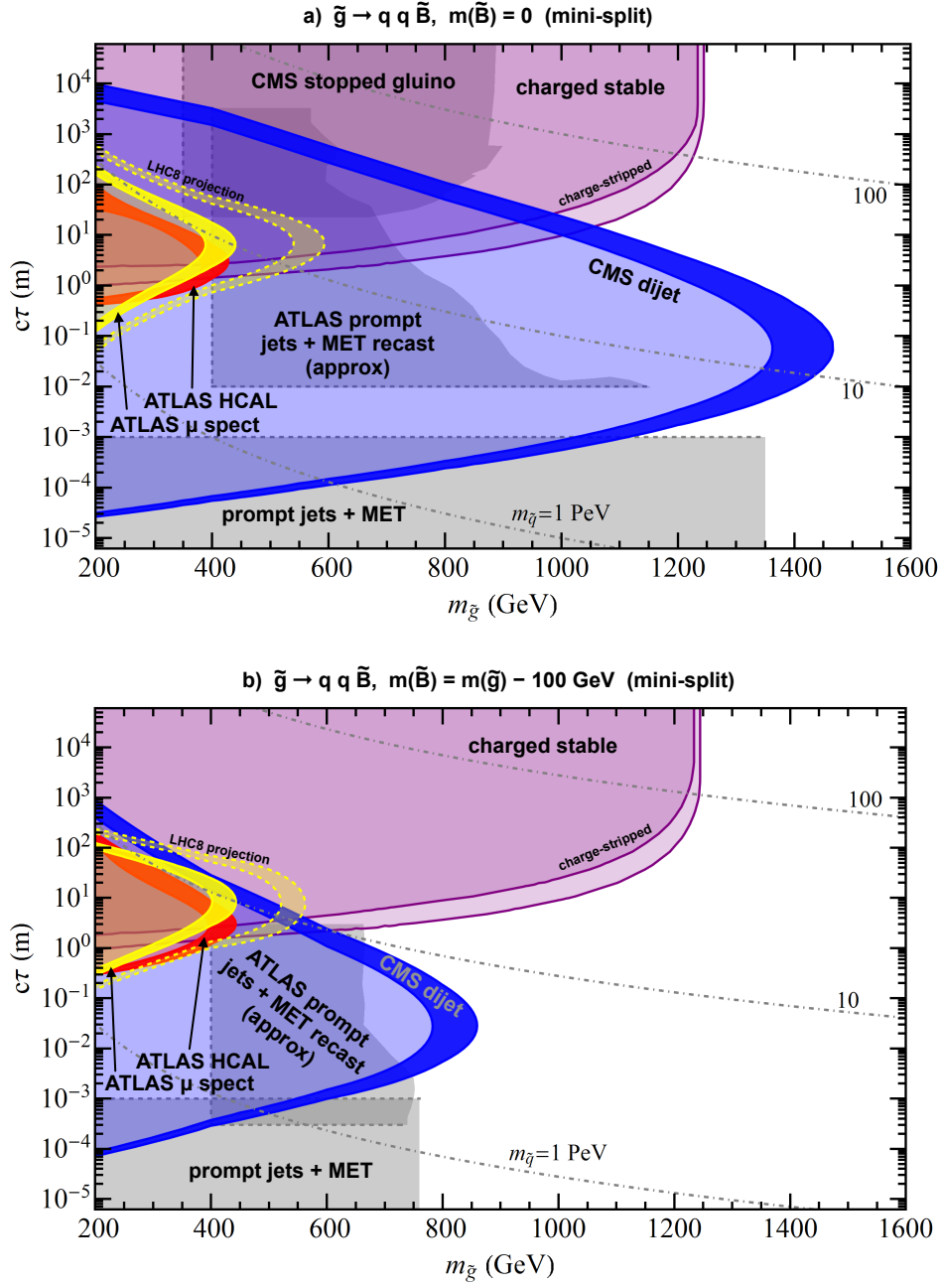


Figure II.59: Recast constraints on displaced $\tilde{g} \rightarrow q\bar{q}\tilde{B}$ in mini-split SUSY: a) $m_{\tilde{B}} = 0$, b) $m_{\tilde{B}} = m_{\tilde{g}} - 100$ GeV. Colored bands indicate acceptance variations up/down by 1.5. The dot-dashed lines indicate the intermediate squark mass, assuming that either d_R or s_R dominates the decay. Prompt limits (gray) are derived from [467, 474]. They are conservatively cut off at 1 mm. Additional displaced limits come from stopped R-hadron searches [145] and ATLAS’s recast prompt limits [131]. (The latter is only approximate, as it has not been strictly re-interpreted from ATLAS’s model assumptions to our exclusive $\tilde{g} \rightarrow q\bar{q}\tilde{B}$ final-state.)

spread-out scalar mass spectrum. Yukawa effects in the renormalization group may favor light third generation squarks, suggesting dominant decays $\tilde{g} \rightarrow t\bar{t}\tilde{\chi}^0$ or $\tilde{g} \rightarrow t\bar{b}\tilde{\chi}^- + \text{c.c.}$ [127], though flavor-anarchic soft masses could instead lead to lighter first- or second-generation squarks. Loop-induced decays $\tilde{g} \rightarrow g\tilde{\chi}^0$ might also become important [475], though again depending in detail on the squark mass spectrum, as well as on the gaugino mass spectrum. For our initial study here, we simply assume 100% 3-body branching fraction $\tilde{g} \rightarrow q\bar{q}\tilde{B}$ for $q = udc$ s. The only free parameters are then the gluino and neutralino masses, as well as the gluino lifetime set by the squark mass scale [127],

$$c\tau \approx 10^{-5} \text{ m} \left(\frac{m_{\tilde{q}}}{\text{TeV}} \right)^4 \left(\frac{\text{TeV}}{m_{\tilde{g}}} \right)^5. \quad (\text{II.F.84})$$

We reserve a more general survey of displaced mini-split phenomenology for future work.

Fig. II.59 shows our results, choosing either $m_{\tilde{B}} = 0$ or $m_{\tilde{B}} = m_{\tilde{g}} - 100 \text{ GeV}$. We find once again that, amongst explicit displaced decay searches, CMS displaced dijets offers superior sensitivity. For the light neutralino case, exclusions extend out as far as 1400 GeV, and for the heavy neutralino out to 800 GeV. The dedicated mini-split gluino searches, based on stopped R-hadron decays [137, 145] and ATLAS’s recasts of prompt searches [131],²⁸ do not tend to be competitive with this search combined with the HSCP searches. Interestingly, the ATLAS muon chamber and low-EM jets searches, which have tended to give universally weaker coverage, potentially offer more stable sensitivity as the visible activity gets squeezed out when $m_{\tilde{B}} \simeq m_{\tilde{g}}$. This owes largely to their focus on lower-mass signatures, which for compressed SUSY spectra becomes a major virtue. However, the overlap with HSCP coverage remains substantial.

3. Summary and Outlook

The initial 7 and 8 TeV runs of the LHC have launched an impressive exploration of the vast parameter space of the MSSM and its extensions, yielding the most sensitive searches to date and in many cases already probing up to TeV mass scales. In this section, we have sought to

²⁸The ATLAS recasts in [131] assume a model with 50% branching fractions into $q\bar{q}\tilde{\chi}^0$ and $g\tilde{\chi}^0$, respectively. Since our models here are pure $q\bar{q}\tilde{\chi}^0$, rigorous interpretation of the limits would require yet another layer of recasting. We do not attempt this, but use the ATLAS results only to indicate an approximate model reach.

initiate a systematic extension of this program into the similarly vast realm of SUSY with non-prompt final-stage decays, as occur in a number of common and well-motivated scenarios within the MSSM such as R-parity violation, gauge mediation, and mini-split spectra. This has been accomplished by recasting seven existing searches for stable charged particles and highly displaced decays, and combining these with prompt searches. Our present survey has focused mainly on signals containing a sizable fraction of hadronic decays, including “natural” spectra with light stops and Higgsinos. The overarching conclusion is that, while very few long-lived particle searches are explicitly designed to be sensitive to these signals, the extremely low backgrounds and reasonably high acceptances of those searches nonetheless allow us to place tight limits. Indeed, we have typically found large patches of parameter space where multiple distinct search channels overlap. That said, we have identified several places where significant improvements might still be possible.

We first list here some conclusions of our investigations regarding the performance of the searches:

- In the long-lifetime limit, several searches have been carried out for stable charged R-hadrons. They are usually still sensitive down to $c\tau \sim \text{meter}$, catching rare late-decaying particles, and providing substantial overlap with explicit displaced decay searches. Limits on squarks and gluinos extend up to about 1 TeV. However, there is of course no sensitivity to long-lived *neutral* particles, such as (N)LSP Higgsinos.
- The CMS displaced dijet search is extremely effective for essentially any decay topology involving any number of energetic quarks and gluons (including one or three, as well as many decays with leptons [138]). It is almost universally the most powerful displaced decay search when hadronic decays dominate, including decays involving weak bosons. For $c\tau \sim 10 \text{ cm}$, (stop) squark pairs are probed up to almost 1 TeV, gluinos typically up to above 1 TeV, and Higgsinos up to 600–800 GeV. Though the trigger p_T requirements are relatively harsh, good sensitivity is maintained for superparticles with strong or electroweak production cross sections down to 100 GeV mass, by picking up events on the high- p_T tails. It seems likely that similar search strategies, perhaps capitalizing on different sets of triggers and displaced vertex criteria, could expand the model reach. In particular, within our own set of models the original dijet requirement reduces by

$O(10-100)$ the acceptance for “monojet” decay topologies such as from $\tilde{q} \rightarrow q\tilde{G}$ and $\tilde{g} \rightarrow g\tilde{G}$ in GMSB. A standard jets+ \cancel{E}_T style trigger could much more efficiently pick up this signal, and a single displaced-jet requirement would likely eliminate the remaining background. It would also be very useful to investigate this style of search for more traditionally motivated signals such as $\tilde{\tau} \rightarrow \tau\tilde{G}$, which would require accepting low-multiplicity/low-mass vertices. For this signature and many others, it is important to understand what happens when the displaced particle is charged and can leave its own track segment.

- Existing ATLAS searches for displaced decays inside the calorimeters and muon chambers should in principle supplement the region $c\tau \sim \text{few meters}$, where both the stable charged track and displaced dijet searches are becoming weaker. However, these searches were highly optimized for low-mass pseudoscalar signals, and achieve relatively limited sensitivity for displaced SUSY models. It seems likely that these searches could be modified to better capitalize on the energetic signatures of superparticles with 100’s of GeV mass, where they are anyway most needed to extend the global search reach beyond $c\tau \sim 1 \text{ m}$, especially for long-lived neutral particles where stable charged track searches are unusable. This could possibly be done using existing data from the specialized ATLAS HCAL and muon triggers. Such modified searches would still need to achieve very high efficiency in order to become competitive with the other searches, possibly benefiting from a single-candidate mode rather than their standard double-candidate.
- We have also considered three searches that capitalize on relatively clean leptonic signatures: a displaced muon in association with a displaced tracker vertex (not necessarily geometrically overlapping), a displaced dilepton pair, and generic $e\mu+X$ signatures where the electron and muon are each displaced. Interestingly, the $\mu+\text{tracks}$ search shows non-trivial sensitivity even to fully hadronic decays, provided that they contain energetic bottom quarks. However, within the scope of models studied here, all of these searches truly become relevant for signals involving weak bosons, such as stop and Higgsino decays in GMSB. The displaced dilepton search in particular offers improved sensitivity relative to displaced dijets when Z bosons are available, since the former can be constructed with both lower impact parameter thresholds and lower p_T thresholds. The $\mu+\text{tracks}$ is

also highly competitive, though somewhat weaker in lifetime coverage due to geometric restrictions on the vertexing.²⁹

- A variety of prompt searches have been directly applied to the decay topologies that we consider here. It is, however, mostly unclear how effective these searches are when the decays become appreciably displaced, especially for searches involving leptons or traditional b - and τ -jets. A first analysis in this direction was performed by ATLAS [131] for gluinos in mini-split SUSY, indicating an approximately logarithmic degradation of mass reach with increasing lifetime (presumably stemming from the onset of a linear falloff in displaced decay acceptance when $c\tau > O(\text{m})$). For searches at CMS, which rely much more on tracking and vertexing in the construction and validation of particle-flow jets, more significant degradations might be expected. While we have shown that CMS’s dedicated displaced dijets search can much more efficiently pick up the gluino signal in the lifetime range where ATLAS shows results, we expect that there would be additional benefits to exploring other searches involving “many b -jets” and/or “many τ -jets” (possibly plus \cancel{E}_T), ideally with some allowances for uncharacteristically high displacements. Such searches would (or perhaps already do) bridge the possible weakening in fully hadronic coverage around $O(\text{mm})$ lifetime stemming from CMS’s $500\ \mu\text{m}$ displaced dijet impact parameter cut. As noted, the benefit of searching down to smaller nonzero displacements was already made clear in our GMSB Higgsino results, where displaced dileptons was able to push the lifetime reach down by as much as an order of magnitude.

We next discuss some of the physics implications of our findings:

- Natural supersymmetry with light, promptly-decaying stops has been coming under progressively more pressure from a series of LHC searches. Moving to scenarios with displaced stop decays into jj via baryonic RPV or $t^{(*)}\tilde{G}$ in GMSB, we are apparently forced into to even more unnatural regions of model space. This is particularly true in baryonic RPV, where prompt decay limits are currently very weak. However, very small λ'' and displaced stop decays are actually favored by cosmological arguments, as even $\lambda'' \gtrsim 10^{-6}$

²⁹It could be quite interesting to recast this search (as well as the displaced dijets) for the $\tilde{t} \rightarrow l^+ b$ leptonic RPV model, which was searched for in the $e\mu + X$ channel in [136]. There are likely other models we have not touched upon for which this search could be uniquely sensitive.

with sub-TeV stops would efficiently wipe out the baryon asymmetry of the universe in a standard thermal history with baryogenesis no lower than the weak scale [476]. It is therefore becoming very difficult to simultaneously accommodate naturalness, baryogenesis, and LHC direct searches in such a scenario. In GMSB, where an NLSP stop is rather nongeneric but has been an interesting logical possibility for some time [461], the region with $m_{\tilde{t}} < m_t$ is almost guaranteed to yield displaced decays (provided $\sqrt{F} \gtrsim 10$ TeV). The $m_{\tilde{t}} < m_t$ possibility is now fully closed, as is essentially all model space below 500 GeV.

- Natural supersymmetry with light Higgsinos is traditionally very challenging to probe via direct electroweak Higgsino production, though some limits are becoming available in general GMSB models where decays into Z bosons are appreciable [471]. In the presence of baryonic RPV, the multijet decays of the lightest Higgsino yield a very striking and highly constrained displaced signature, and furnish the only extant LHC direct production limits in that topology. The cosmological implications are more model-dependent, but again tend to disfavor the as-yet unprobed prompt decays [476]. RPV Higgsinos with $c\tau \gtrsim 10$ m would effectively act stable, and again become very difficult unless, as usual for neutralinos, they are produced in the decays of heavier colored superparticles and appear as \cancel{E}_T . In the GMSB case, as noted above, almost all of the searches that we have recast become sensitive, the only exception being stable charged particles. The mass/lifetime coverage is qualitatively similar to the RPV case, though the smaller fraction of visible energy, the typically smaller number of hard partons, and the smaller branching fractions into individual final states all contribute to slightly lower mass reach. Assuming that a natural Higgsino mass must be roughly below 400 GeV (naively corresponding to less than 5% fine-tuning of the Higgs boson mass), the displaced GMSB decay searches can probe a large fraction of the available space with \sqrt{F} between 10 TeV and a several 1000 TeV. In particular, for $m_{\tilde{H}} \simeq \text{few } 100 \text{ GeV}$, there is now a fairly firm constraint $\sqrt{F} \gtrsim 1000 \text{ TeV}$, unless the decay is dominated by $h\tilde{G}$.
- Mini-split SUSY with sub-TeV gluinos is close to being fully ruled-out for any squark mass scale. An immediate escape hatch is to compress the spectrum to $m_{\tilde{g}} - m_{\tilde{\chi}} \lesssim 100 \text{ GeV}$. We have also not studied in detail the limits on decays involving top quarks, though many

other searches then open up, and it would be surprising if the limits become appreciably weaker. Non-minimal decay topologies involving electroweak-ino cascades could also be interesting to study, but would likely only yield signals that are even more visible to displaced decay searches.

- Generic colored superparticles as (N)LSPs in either RPV or GMSB are to large degree ruled out for any lifetime if the mass is below about 1 TeV, again with the gluino limits tending to be several 100 GeV stronger than squark limits. Light RPV squarks with prompt decays would also face direct search difficulties similar to stops, but partially compensated by the higher multiplicity of flavor/chirality states.

What else remains to be done? Within the context of RPV (both baryonic and leptonic), a more thorough survey of the current status of different LSPs and flavor structures along the lines of [477] and [149, 478] seems warranted. Leptonic RPV in particular has a quite large set of possible couplings. Spectra with “electroweak” LSPs besides Higgsinos, namely sleptons or gauginos, also deserve further attention, as they can become much more visible than they would be if their decays were prompt. For general gauge mediation, we have emphasized in Section II.F.2.b that the full set of possible NLSPs is (rather remarkably) almost fully covered. The major exceptions are again sleptons and winos, with the latter offering an interestingly varied array of different signatures. We again expect that the existing set of displaced and prompt searches have much to say about all of the above models, though in many cases coverage may still be entirely lacking, unnecessarily weak, or ambiguous given the current limitations of making public the general analysis acceptances.

With the upcoming Run 2 of the LHC, the mass reach for the models that we have explicitly studied might be expected to roughly double, assuming that similar analyses will be undertaken. We encourage the experiments to continue their displaced decay search programs at an even greater level of breadth so that interesting signals are not left behind. We also hope that future recasts are better facilitated by more explicit discussions of analysis acceptances, less tied to one or two specific fully simulated models in limited kinematic ranges. Endeavors like ours should ideally not require as much from-scratch calibration, extrapolation, and guesswork, as detailed here in Section II.F.1 and in the Appendices below. Of course, the need to facilitate more general model interpretations becomes even more

pressing if a discovery is made. Works along the lines of CMS's stable charged particle efficiency maps [130] are a step in the right direction. But we emphasize that even coarse parametrizations such as the ones that we have developed can prove invaluable, especially if directly compared against full internal simulations by the collaborations. We hope that our work, which has further clarified the extreme power and broad model reach of these searches, spurs further activities in these directions, and we look forward to the next round of LHC displaced search results.

III. BSM PHYSICS AT THE ILC AND CEPC

A. ELECTROWEAK RESONANCES AT THE ILC

1. Z' observables at the ILC

A lepton collider with high luminosity could probe the Z' couplings through their interference with the SM. Here we study the sensitivity of different observables to a Z' at the 500 GeV and 1 TeV ILC. Previous studies include [223, 224, 227, 479–484].

We show our results in Fig. III.1. We apply an acceptance of polar angle for the charged leptons in region of $10^\circ < \theta < 170^\circ$ [485]. We require a minimal p_T of 20 GeV for jets. We include a 0.25% polarization uncertainty, 0.2% uncertainties on leptonic observables, and 0.5% uncertainties on hadronic observables [177]. Among those uncertainties associated with leptonic and hadronic final states, we assume that 0.14% are correlated and thus will cancel in asymmetry observables. The τ lepton, bottom quark, and top quark tagging efficiencies are set at 60%, 96% [177] and 70%.

We study the accuracies of the muon forward-backward asymmetry $A_{FB}[\mu^-\mu^+]$ and the cross section $\sigma[\mu^-\mu^+]$ for the dimuon final state¹, assuming the fixed (normal) beam polarization² $\mathcal{P}(e^-, e^+) = (+0.8, +0.3)$, using the formulae in (VI.E.34) and (VI.E.42). The muon forward-backward asymmetry in the SM is relatively large, as shown in the left panel of Fig. III.1. The difference in cross section is dominantly a summation of interference terms from different squared helicity amplitudes, and it is possible to have sizable interferences

¹Dielectron final states also involve t -channel exchanges.

²As discussed in Appendix VI.E.2 we define $\mathcal{P} > 0$ for predominantly left (right)-handed $e^-(e^+)$. We note this is opposite of the ILC convention for the positron polarization. We only use such convention in this section for simplicity of discussion. In other sections, especially for physics physics, we take the ILC convention.

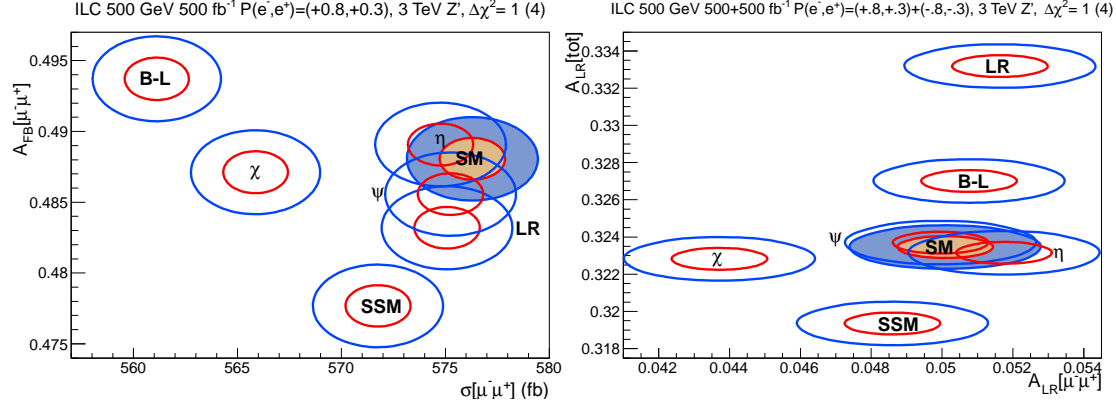


Figure III.1: The accuracies of ILC observables for a 500 GeV ILC. Details of the assumed uncertainties are discussed in the text. *Left panel:* $\Delta\chi^2 = 1(4)$ contours (red (blue)) of the simulated $e^-e^+ \rightarrow \mu^-\mu^+$ cross sections $\sigma[\mu^-\mu^+]$ and the forward-backward asymmetry $A_{FB}[\mu^-\mu^+]$ in the dimuon system, with 500 fb $^{-1}$ data at fixed beam polarization $P(e^-, e^+) = (+0.8, +0.3)$. *Right panel:* $\Delta\chi^2 = 1(4)$ contours (red (blue)) of the simulated polarization (left-right) asymmetry in the dimuon system $A_{LR}[\mu^-\mu^+]$, and the total polarization asymmetry $A_{LR}[tot]$ (including all of the final states except e^-e^+ and $\nu\bar{\nu}$), with 500 fb $^{-1}$ each for beam polarizations $P(e^-, e^+) = (+0.8, +0.3)$ and $P(e^-, e^+) = (-0.8, -0.3)$.

without changing the cross section much. A typical example is the Z'_{SSM} , shown in the figure, and similarly the Z'_{LR} . All of the leptonic cross sections are smaller than the SM. This is no longer true for hadronic final states, since $g_{L/R}^e g_{L/R}^{u/d}$ could have either sign. From this figure we can see that Z'_χ , Z'_{B-L} and Z'_{SSM} are well separated from the SM.

If the beam polarization can be flipped from normal polarization to the reversed polarization $\mathcal{P}(e^-, e^+) = (-0.8, -0.3)$, one can determine the polarization (left-right) asymmetry $A_{LR}[\mu^-\mu^+]$ for the dimuon channel, defined in (VI.E.45) and (VI.E.46), for which some of the systematics cancel. One can also observe the total polarization asymmetry $A_{LR}[tot]$ defined in (VI.E.47), for which one does not need to identify the final state (other than removing the dielectron) and which has higher statistics. However, there are some cancellations between final states. For example, some final states may have positive deviations from the SM while others have negative deviations. Both $A_{LR}[\mu^-\mu^+]$ and $A_{LR}[tot]$ are shown in the right panel of Fig. III.1, assuming 500 fb^{-1} for each polarization.³ For the $A_{LR}[tot]$, we sum all of the observed final states other than the dielectron⁴. A_{LR} has the merit that not only most of the luminosity uncertainty cancels, but also many systematic uncertainties, such as those associated with tagging efficiencies, acceptances, etc., cancel. Therefore, we only include the polarization and statistical uncertainties when treating the polarization asymmetries⁵. $A_{LR}[\mu^-\mu^+]$ is especially sensitive to Z'_χ , while $A_{LR}[tot]$ is useful for distinguishing Z'_{LR} .

There is some complementarity between the LHC and ILC observations, as can be seen in Figs. II.10 and III.1. For example, the LHC has limited discrimination between the LR, B-L, and SSM models, especially from the cleaner $A_{FB}[e^-e^+]$, while these could be well-separated using the ILC observables.

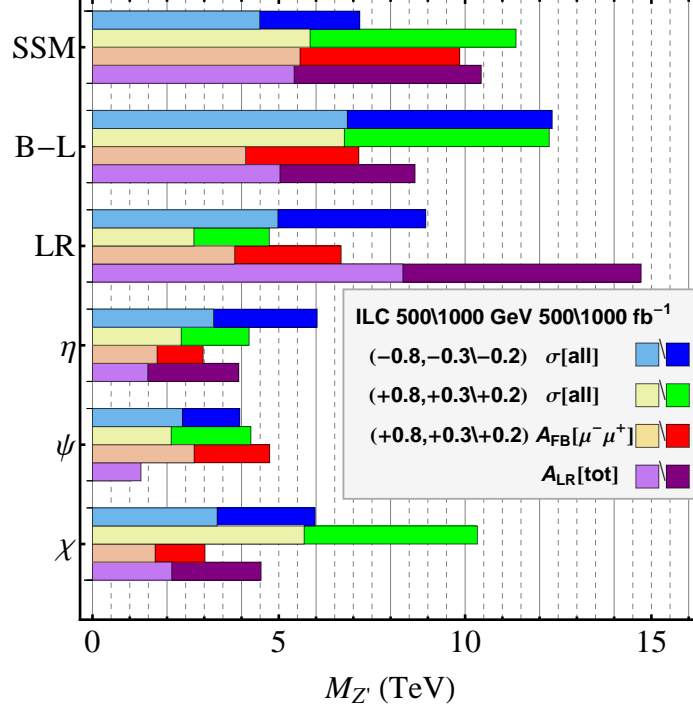


Figure III.2: The exclusion reach of the 500 GeV (1 TeV) ILC with 500 fb⁻¹ (1000 fb⁻¹) of integrated luminosity for both normal beam polarization $P(e^-, e^+) = (+0.8, +0.3)$ ($P(e^-, e^+) = (+0.8, +0.2)$) (brown (red) and yellow (green)) and reversed beam polarization $P(e^-, e^+) = (-0.8, -0.3)$ ($P(e^-, e^+) = (-0.8, -0.2)$) (cyan (blue)). We show the complementarities between different beam polarizations and observables σ including all channels other than the dielectron (cyan (blue) and yellow (green)) and A_{FB} from the dimuon final state (brown (red)). We also show the exclusion reach (magenta (purple)) from $A_{LR}[tot]$ for reversed beam polarizations, with 500+500 fb⁻¹ and 1000+1000 fb⁻¹ for the ILC 500 GeV and ILC 1000 GeV, respectively. The reaches from $A_{LR}[tot]$ would be reduced by $\sim 15\%$ for divided runs of 250+250 fb⁻¹ and 500+500 fb⁻¹.

2. Z' Beyond the LHC Reach

We show the exclusion (95% C.L.) reach of the ILC at 500 GeV and 1 TeV, including the case that the Z' is beyond the LHC reach, in Fig. III.2. We show the reach from both the normal and reversed beam polarizations obtained from the cross sections for $\mu^-\mu^+, \tau^-\tau^+$, 2 jets (from light quarks), $b\bar{b}$, and $t\bar{t}$, where we combine the χ^2 from each channel after including the appropriate systematic uncertainties. We also show the exclusion reach from the muon forward-backward asymmetry $A_{FB}[\mu^-\mu^+]$ and from $A_{LR}[tot]$. In the latter case we assume that the beam polarizations can be reversed and that a full luminosity run is made for each polarization. The uncertainties included are described in the previous section. We assume the deviations in the cross sections and asymmetries from the SM scale with $M_{Z'}^{-2}$. We conservatively estimate that corrections will reduce the exclusion reach by $\lesssim 2\%$. There is no single best exclusion observable; for some models like Z'_χ and Z'_{SSM} the normal polarization is better, for others like Z'_ψ , Z'_η and Z'_{LR} the reversed beam polarization or the forward-backward asymmetry has a larger reach. The polarization asymmetries, with a portion of systematic uncertainties cancelled, is especially stringent for the LR model.

3. Summary of the Z' at the ILC

For the ILC, the chiral couplings and Z' mass affect various observables through the interference of the Z' with SM contributions. Typical observables include the cross section σ , forward-backward asymmetry A_{FB} for di-fermion systems with charge identification, and polarization asymmetries A_{LR} for reversed beam polarizations. (Other possibilities include the polarized forward-backward asymmetry and the final state polarizations in $\tau^+\tau^-$ and $t\bar{t}$.) We show the cross section and forward-backward asymmetry for the dimuon system in the left panel of Fig. III.1. It shows good discrimination potential for Z'_χ , Z'_{B-L} and Z'_{SSM} from

³With the doubled run one would also have such new observables as $\sigma_L + \sigma_R$ in (VI.E.45), A_{FB} in (VI.E.42) with reversed polarization, or A_{LR}^{FB} in (VI.E.48). Alternatively, one could divide a 500 fb⁻¹ run into two 250 fb⁻¹ runs with opposite polarizations, in which case the outer contours in Fig. III.1 would correspond to $\Delta\chi^2 = 2.6$.

⁴The major contribution to $A_{LR}[tot]$ is from the hadronic final states, since the polarization asymmetry for dileptons is much smaller. One could also consider different final states separately to gain better statistical sensitivity (but with larger systematic uncertainties).

⁵Some parametric uncertainties in the SM parameters don't cancel. We ignore them here as they are expected to improve in the future [486].

other models and the SM background. The polarization asymmetry for the total (except for dielectron) cross section and the dimuon final states are also potentially very useful if the e^\pm polarizations can be reversed, as shown in the right panel of Fig. III.1. The asymmetry for the total cross section is especially important because it involves high statistics and reduced systematic uncertainties, since the final states do not need to be identified.

For the scenarios in which the Z' cannot be resonantly produced, we study the exclusion reach for the ILC from cross sections, forward-backward asymmetries, and polarization asymmetries. The results are shown in Fig. III.2, which also shows the complementarity between these observables.

In this preliminary study we have focused on the ability of various observables at the LHC and ILC to discriminate between several benchmark Z' models with minimal width. For $M_{Z'} \sim 3$ TeV the LHC should be able to observe a Z' through its leptonic decays, and obtain a measurement of its mass and width at the 10 GeV level. Some sensitivity to the chiral couplings (as illustrated by model discrimination) would be possible at the LHC and especially at the ILC, and the ILC reach would extend considerably higher as well.

However, there are a very large variety of possible models, including those with much weaker or stronger couplings than our benchmarks. Ideally, one would like to obtain as much information as possible in a model-independent way from the LHC, ILC, other colliders, and also from existing and future precision electroweak experiments.

B. HIGGS WIDTH AT THE ILC

In this section, we revisit the issue of to what extent an ILC, combined with expected LHC inputs, would be able to precisely determine the Higgs total width and individual couplings. We follow a systematic approach in a model-independent manner. We discuss the leading and subleading contributions for total width and perform studies on two typical processes at the ILC. We find the optimal results for the Higgs couplings, the invisible decay mode, and total width determinations. Finally, we consider the effects of adding mildly model-dependent assumptions, which can significantly improve the precision.

1. Formalism for Higgs Width Determination

a. General Approach to the Higgs Width The total width of the SM Higgs boson is predicted to be about 4.2 MeV. For such a narrow width, only a muon collider may provide a sufficiently small energy spread to directly measure the width [181, 487–489]. At the LHC and ILC, the smearing effects from energy spread for both the initial state and final state override the Breit-Wigner resonance distribution, although it may have a visible effect in differential cross section distributions involving interference with the background diagrams [166, 173, 174].

The Narrow Width Approximation (NWA) allows us to write a total s -channel cross section as a production cross section multiplied by the branching fraction (Br) of the Higgs boson decay

$$\sigma_{AB} \simeq \frac{\sigma(A \rightarrow h)\Gamma(h \rightarrow B)}{\Gamma_h} \propto \frac{g_A^2 g_B^2}{\Gamma_h}, \quad (\text{III.B.1})$$

where we have symbolically denoted the Higgs production via A with an AAh coupling (g_A), and the subsequent decay to B with a BBh coupling (g_B). There is a well-known “scaling degeneracy” of the NWA cross section, namely the cross section is invariant under the scaling of related couplings by κ and the total width of the resonant particle by κ^4 . This demonstrates the incapability of hadron colliders to determine the couplings and width in a model-independent fashion. With certain modest assumptions, one may obtain some bounds on the total width as recently discussed in [171, 172, 179, 196, 490].

When determining the accuracies from the measurements, we take the form of Eq. (III.B.1) in a general sense. We consider all available measurements from, for instance, AA -fusion, Ah -associated production etc. to extract g_A^2 . This form also allows for interchanging production and decay since g_A^2 and g_B^2 are on equal footing.

In order to break the “scaling degeneracy” without assumptions on the couplings, we must go beyond the simple form σ_{AB} . The most efficient process for this purpose is the inclusive Higgs production cross section from the coupling to A . This can be measured when we know the information about the incoming and outgoing particles aside from the Higgs boson in the process. The best-known example is the “Higgstrahlung” process $e^+e^- \rightarrow hZ$,

where one can construct the recoil mass by the well-measured Z decay products

$$M_{rec}^2 = (p_{e^+e^-} - p_Z)^2 = s + M_{Z^*}^2 - 2\sqrt{s}E_Z. \quad (\text{III.B.2})$$

The peak near m_h selects the signal events and the Higgs decay modes are all accounted for inclusively. Thus the inclusive cross section σ_Z^{inc} and equivalently g_Z^2 can be measured since the factor $\sum_{all} g_B^2/\Gamma_h$ is unity.

With the inclusive cross section σ_A^{inc} (equivalently g_A^2) measured, one can readily perform the extraction to the total width Γ_h by utilizing exclusive cross sections:

- directly measuring σ_{AA}

$$\Gamma_h = \frac{(g_A^2)^2}{(g_A^2 g_A^2/\Gamma_h)} \propto g_A^2 \frac{\sigma_A^{inc}}{\sigma_{AA}}; \quad (\text{III.B.3})$$

- indirectly determining σ_{AA} by inserting other cross section measurements from the ILC

$$\begin{aligned} \Gamma_h &= \frac{(g_A^2)^2 (g_B^2 g_C^2/\Gamma_h)}{(g_A^2 g_B^2/\Gamma_h)(g_A^2 g_C^2/\Gamma_h)} \propto g_A^2 \frac{\sigma_A^{inc} \sigma_{BC}}{\sigma_{AB} \sigma_{AC}} \\ &= \frac{(g_A^2)^2 (g_B^2 g_C^2/\Gamma_h)(g_D^2 g_E^2/\Gamma_h)}{(g_A^2 g_B^2/\Gamma_h)(g_C^2 g_D^2/\Gamma_h)(g_A^2 g_E^2/\Gamma_h)} \propto g_A^2 \frac{\sigma_A^{inc} \sigma_{BC} \sigma_{DE}}{\sigma_{AB} \sigma_{CD} \sigma_{AE}} \\ &= \dots; \end{aligned} \quad (\text{III.B.4})$$

- more generally, indirectly determining σ_{AA} by inserting other cross sections including those from the LHC

$$\Gamma_h = \frac{(g_A^2)^2}{g_A^2 g_B^2/\Gamma_h} \left(\frac{g_B^2}{g_A^2} \right) \propto g_A^2 \frac{\sigma_A^{inc}}{\sigma_{AB}} \left(\frac{\text{Br}_B}{\text{Br}_A} \right). \quad (\text{III.B.5})$$

We note that in the above method as expressed in Eqs. (III.B.3), (III.B.4) and (III.B.5), the right hand sides are fully expressed by experimental observables⁶, which can be easily and consistently used to determine precision on derived quantities such as Γ_h . In principle, the longer the chain of measured cross-sections is in our expressions above, the more sources of uncertainties we must be concerned with, but this may allow us to utilize quantities with minimal individual uncertainties which can be advantageous. The most important channels to measure depend on the center of mass energy. Current plans for the ILC foresee an initial stage of running at 250 GeV, which maximizes the Higgstrahlung cross section, and a higher-energy phase at 500 GeV with perhaps 1 TeV running at an upgraded machine where

⁶We keep g_A^2 to make clear the transition between Eq. (III.B.1) and Eq. (III.B.3). As stated earlier, it is a direct translation from observable σ_A^{inc} .

weak boson fusion takes over. This leads to rich physics interplay between combinations of contributing channels which we discuss in the following subsections Sec. III.B.1.b and Sec. III.B.1.c.

Determining the couplings other than g_A^2 from σ_A^{inc} , can be done directly once Γ_h is known. With any exclusive cross section measurement σ_{AB} or σ_{BA} , we can write

$$g_B^2 \propto \frac{\sigma_{AB}\Gamma_h}{g_A^2}. \quad (\text{III.B.6})$$

However, one needs to be cautious when determining g_B^2 using this relation. Γ_h is a derived quantity and may depend heavily on σ_{AB} as well. For proper treatment of errors, we will evaluate precision on these quantities consistently by global fitting as described in Sec. III.B.3.a and Appendix VI.G. Discussions in this subsection and following subsections clearly point out leading and sub-leading contributions and will provide guidance for current and future studies.

b. The ILC at 250 GeV With ILC only

For an electron-positron machine running near 250 GeV the leading Higgs production mechanism is the ‘‘Higgstrahlung’’ process $e^+e^- \rightarrow hZ$. For Z decaying to electrons and particularly to muons we can have very good resolution on recoil mass and a clear excess over expected background. Detailed simulations estimate that the inclusive cross section $\sigma(Zh)$ can be determined to a statistical uncertainty of 2.5% with 250 fb^{-1} of integrated luminosity [183, 184, 491].

Unfortunately, σ_{ZZ} can not be measured with great precision at the ILC due to the limited statistics from the small Z leptonic branching fractions. As such, the total width determined from Eq. (III.B.3) has large uncertainties. However, we can make several measurements from which an equivalent ratio of couplings to widths is derivable, as shown in Eq. (III.B.4). For a Standard-Model-like Higgs boson, couplings to b -quarks and to W and Z bosons are expected to dominate, leading to high statistics for those channels. Since we are mainly interested in ratios of coupling constants and the Higgs width, σ_{WZ} and σ_{ZW} give us equivalent information and can potentially both be measured. To use Eq. (III.B.4) we must have at least one cross section that involves a Higgs coupling to non- Z particles at

both vertices. At the ILC this generally requires producing the Higgs via WW fusion. This mechanism becomes dominant at higher energies but remains relatively small at 250 GeV. Nonetheless, Dürig et al. estimate that $\sigma(e^+e^- \rightarrow h\nu\nu \rightarrow b\bar{b}\nu\nu) = \sigma_{Wb}$ can be measured with 10.5% accuracy [492]. Then by measuring σ_{Zb} and σ_{WZ} one has an alternative and likely more precise determination of the Higgs width

$$\Gamma_h \propto g_Z^2 \frac{\sigma_Z^{inc} \sigma_{Wb}}{\sigma_{ZW} \sigma_{Zb}}. \quad (\text{III.B.7})$$

Incorporating LHC data

The LHC Run II will accumulate a significant amount of integrated luminosity and the Higgs property will be studied to a high accuracy. Although, as discussed in Sec. III.B.1.a, it cannot resolve the inclusive Higgs measurement, we can use ratios of cross sections from the LHC in conjunction with ILC data to improve our results as described by Eq. (III.B.5). The ATLAS and CMS collaborations have conducted simulations to estimate the sensitivity of various cross section and ratio measurements with 300 fb⁻¹ of data and in some cases up to 3000 fb⁻¹ [493–495]. In particular, with 300 fb⁻¹ of data the LHC is expected to measure the Higgs decays to $\gamma\gamma$, ZZ , WW , bb and $\tau\tau$ with $\sim 5 - 20\%$ accuracy. We can use these numbers along with measurements of σ_{Zb} , $\sigma_{Z\gamma}$, σ_{ZW} and $\sigma_{Z\tau}$ at the ILC to determine the total width as well. Generically, either the relevant ILC cross section or the ratio coming from the LHC will have limited sensitivity so the individual combinations will have only moderate uncertainty for the total Higgs width, but in combination with each other and the pure ILC combinations above an improved result for the width can be achieved, as will be discussed in section III.B.3.

Invisible Decays of the Higgs One further decay channel which it is interesting to include is the partial width for Higgs decaying to invisible particles. In the SM this is a tiny branching fraction due to $h \rightarrow ZZ \rightarrow 4\nu$ ($\text{Br} \sim 0.2\%$). However it may be enhanced by new physics such as Higgs portal scenarios for dark-matter [496]. The invisible decay cross section can be measured to high precision at the ILC. This is done by again using the recoil mass and the absence of visible final particles except for the recoiling matter, which will be a Z for our purposes at the 250 GeV ILC. Since we only expect to measure one cross section involving the coupling to invisible particles, the invisible decay measurement does not constrain the

total Higgs width in a model-independent analysis. Rather, other measurements largely fix g_Z and Γ_h which then constrain g_{inv} , the effective coupling to invisible final states. However, as will be discussed in Sec. III.B.3.b, the invisible width can become an important constraint when applying very moderate assumptions. We have performed a fast simulation of the invisible decay sensitivity, which is detailed in Sec. III.B.2.a.

c. The ILC at 500 GeV and Beyond Beyond 250 GeV the Higgstrahlung cross section falls off and the fusion cross sections grow. At 500 GeV WW fusion is the leading process with a cross section of approximately ~ 130 fb. The total Zh inclusive cross section is ~ 100 fb, however the he^+e^- component is only about 3% of this and similarly for the muon decay mode. At this energy, ZZ fusion to e^+e^-h contributes roughly twice as much cross section as hZ with $Z \rightarrow e^+e^-, \mu^+\mu^-$ [497]. The inclusive cross section cannot be measured as well for leptonic decays of the Z but including hadronic decays it may be possible to establish σ_Z^{inc} at 3% using 500 GeV data [498]. At 1 TeV the fusion cross-sections completely dominate the production signal. For a SM-like Higgs the best individual determination of the width is expected to come from measuring σ_{Wb} , σ_{WW} and σ_{Zb} with high precision. These can be put in the form of Eq. (III.B.4)

$$\Gamma_h \propto g_Z^2 \frac{\sigma_Z^{inc} \sigma_{Wb}^2}{\sigma_{Zb}^2 \sigma_{WW}}. \quad (\text{III.B.8})$$

Based on the statistical uncertainty expected in these channels, one finds the precision on the total width can be known with a $\sim 6\%$ error as reported in Ref. [177], and as confirmed using the numbers in Sec. III.B.3.a. This error is dominated by the uncertainty on the inclusive cross section, which is squared in our formula, and that of the cross section σ_{WW} . Although the remaining measurements, σ_{Wb} and σ_{Zb} both enter quadratically, they are expected to be known to the sub-percent level and thus add only a small contribution to the total uncertainty. These uncertainties assume that the 250 GeV run has been completed in order to obtain the best resolution on σ_{Zb} and on σ_{Zh} . One should, however, bear in mind that these are statistical uncertainties based on SM productions and decays rates; this

formula is sensitive to additional theoretical and systematic uncertainties, and to deviations from the SM.

Assuming the numbers used above, we can ask if any other channels will contribute significantly to the total model-independent width. The best candidate is one used for the 250 GeV analysis as in Eq. (III.B.7).

This derivation depends linearly on the sub-percent cross sections noted above and is therefore less sensitive to any additional sources or error not included in the purely statistical determinations currently in use. It makes use of σ_{WZ} rather than σ_{WW} . Although σ_{WW} has a large cross section at 500 GeV, σ_{WZ} can be determined from several different measurements at 250 and 500 GeV. We have carried out a detailed simulation of signal and background for one of these processes which we outline in Sec. III.B.2.b.

The best constraints will come by measuring as many channels as possible, including the available information from the LHC. However, only minor improvements beyond Eq. (III.B.4) are possible at 500 GeV for an approximately SM-like Higgs. The uncertainty on the inclusive cross section becomes the largest source of error and total width depends on it quadratically, as seen in Eqs. (III.B.3), (III.B.4) and (III.B.5). Due to this dependence the error on σ_Z^{inc} contributes 5% to the total width uncertainty, and improving this key measurement is crucial to any substantial improvements on the total width. As a result, we argue that inclusive measurement from ZZ -fusion at a 500 GeV and 1 TeV ILC deserves detailed studies for potential improvements.

2. Simulations

Many analyses for specific ILC channels exist in the literature, in particular the recently published ILC TDR [177] and the Snowmass Report [498]. We now present two new studies in this section, that contribute to our determination of the width as motivated in sections Sec. III.B.1.b and Sec. III.B.1.c.

a. Invisible Decays of the Higgs at 250 GeV We perform a quick simulation of the invisible signal to estimate the sensitivity. For event generation we use the ILC-Whizard

setup provided through the detector simulation package SGV3 [499]. Beam profiles for several energies have been generated by GuineaPIG [500], these include effects from Beamstrahlung and ISR. These profiles are interfaced with Whizard 1.95 [501]. The output from this event generator is showered and hadronized by Pythia and the final state particles are passed to SGV, which performs a fast detector simulation. Detected particles are grouped into jets by SGV, for which we set an initially low separation cutoff. The Higgs is taken to be SM-like in its couplings with a mass of 126 GeV. We assume a beam polarization of -0.8 for the electron and $+0.3$ for the positron, consistent with standard assumptions used in the ILC TDR [177]. The simulation includes generator level cuts of $M_{jj} > 10$ GeV and $|M_{ll}| > 4$ GeV where j are outgoing quarks or gluons and ll applies to final-final state lepton pairs and to initial-final state pairs of the same charge. To check our simulations we have performed a calculation of the $Zh \rightarrow b\bar{b}\nu\nu$ signal in our setup following the analysis of Ref. [502], which used a full detector simulation. We find good agreement on the expected number of events.

For a signal sample we use the Standard Model process $e^+e^- \rightarrow Zh, h \rightarrow ZZ \rightarrow 4\nu$ as a template and scale it according to a parameterized branching fraction

$$\sigma_{Zh \rightarrow Z+inv} = \sigma_{Zh} \times \text{Br}_{inv}. \quad (\text{III.B.9})$$

We perform this analysis at the 250 GeV energy scale and concern ourselves only with the Higgstrahlung production process. We consider two analysis channels: Z decaying to leptons (e^+e^- and $\mu^+\mu^-$) and Z decaying to jets. The latter has lower resolution of the peak but benefits from large statistics. In Fig. III.3 we present simulation results showing the recoil mass peak overlaying the major backgrounds in both channels.

We perform our analysis by imposing the following requirements: In the leptonic Z case we require exactly two detected charged tracks, which are identified as either opposite sign muons or opposite sign electrons. The invariant mass of this lepton pair, M_{ll} must be between 80 and 100 GeV. The recoil mass must satisfy $120 < M_{rec} < 150$ GeV. The magnitude of the 3-momentum of the pair must be less than 50 GeV. Finally, the total detected momentum and total detected energy must both be within 10 GeV of the momentum and energy of the lepton pair.

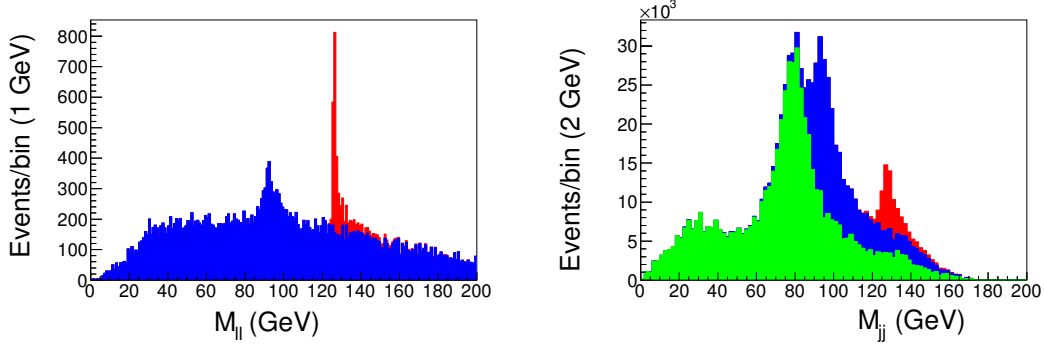


Figure III.3: Recoil mass distributions for the invisible decay of the Higgs boson (assuming 100% branching fraction) for 250 fb^{-1} at 250 GeV. The Higgs signal is shown in red while the background in blue. In the left panel: recoil mass for $Z \rightarrow e^+e^-$; in the right panel: recoil mass for $Z \rightarrow jj$. The cuts are described in Sec. III.B.2.a.

For the hadronic Z decays, we first use the Durham algorithm (k_t algorithm) to merge all detected particles down to two jets, which must have an invariant mass $70 < M_{jj} < 110$ GeV. The recoil mass must satisfy $120 < M_{rec} < 160$ GeV. The transverse momentum of the jet pair must be greater than 20 GeV. To reduce the background from leptonically decaying W s we veto events where the highest energy charged track is greater than 35 GeV.

The main background for the leptonic Z comes from $e^+e^- \rightarrow ll\nu\nu$. In the hadronic case we see approximately equal backgrounds from $e^+e^- \rightarrow qq\nu\nu$ and $e^+e^- \rightarrow qql\nu$. We also consider $e^+e^- \rightarrow qqll$, although it adds a negligible number of events to either channel after cuts. We present the expected number of events from signal and background in Table III.1 below. The numbers shown are for 250 fb^{-1} of integrated luminosity and a 100% branching fraction to invisible particles for the Higgs.

We will take the statistical uncertainty in a given channel to be $\sqrt{N_S + N_B}$ where N_S and N_B are the expected number of signal and background events, respectively. Based on our numbers, given a 10% branching fraction to invisible decays, one could measure the studied cross section with a 5.4% relative accuracy. The cross section for 1% branching fraction could be measured with 52% relative uncertainty. A branching fraction greater than 3.5%

Table III.1: Expected number of events in invisible Higgs searches for leptonically and hadronically decaying Z at a 250 GeV ILC with 250 fb^{-1} of data.

Process	$Z \rightarrow ee$	$Z \rightarrow \mu\mu$	$Z \rightarrow jj$
$ee \rightarrow Zh$	1810	1970	41900
$ee \rightarrow ll\nu\nu$	4730	3000	6220
$ee \rightarrow qq\nu\nu$	0	0	20700
$ee \rightarrow qql\nu$	0	0	22600
$ee \rightarrow qqll$	0	0	84

can be excluded at 95% confidence in the leptonic channel alone and as low as 0.9% can be excluded for the hadronic channel.

b. Estimated Sensitivity for σ_{ZW} at 500 GeV To augment the sensitivity of σ_{ZW} , we carry out a Monte Carlo simulation of the signal $e^+e^- \rightarrow e^+e^-h \rightarrow e^+e^-W^+W^-$ at the ILC running at 500 GeV. In particular, we include signal events generated by ZZ fusion graphs, which are small at 250 GeV but comprise the majority of events at 500 GeV.

This signal has several nice features. At 500 GeV, after cuts, approximately two thirds of the signal is generated by ZZ fusion, and one third comes from the Higgstrahlung process. We search for an on-shell Higgs decaying to one on-shell and one off-shell W . Each W then decays either hadronically to two jets or leptonically to a charged lepton and a neutrino. We consider the all-hadronic and semi-leptonic cases for the two W s taken together; the all leptonic-mode makes up only a small fraction ($\sim 9\%$) of total WW decays. For both the hadronic and semi-leptonic cases the event is essentially fully reconstructible, with the neutrino momentum assumed to be equal to the missing momentum in the semi-leptonic case.

Our simulation framework is the same as described in the previous subsection. For each event, we first identify the two highest energy charged tracks which have been identified

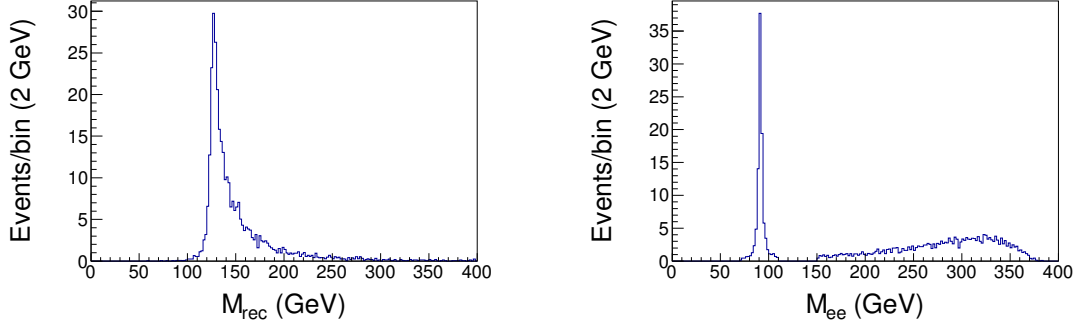


Figure III.4: Kinematic distributions for the signal $e^+e^- \rightarrow e^+e^-h \rightarrow e^+e^-W^+W^- \rightarrow e^+e^-4j$, after the hadronic decay selection criteria are applied for 500 fb^{-1} at 500 GeV. In the left panel: the recoil mass using outgoing electrons; in the right panel: invariant mass of the recoil electron pair.

as electrons by SGV. If these are not opposite in charge sign we consider the next highest energy electron track until we find one that is of opposite sign to the highest energy track. Otherwise we discard the event. If these tracks are identified with a jet that includes seen hadronic particles, we subtract the track momentum from the jet and use the observed track momentum as the electron momentum, otherwise we identify the electron momentum with the jet. After this process we define the number of jets with hadronic particles and energy greater than 5 GeV to be N_{hj} (number of hadronic jets). We also consider potential muon tracks. Muons are not specifically identified by SGV, they appear as charged tracks that are not identified as electrons or hadronic states.

For our event selection, we first require that either $70 < M_{ee} < 110 \text{ GeV}$, which we consider a Higgstrahlung event, or $M_{ee} > 150$, which we take as a fusion event. The distributions for the recoil mass and the invariant mass for our signal are shown in Fig. III.4, one can clearly see the Higgstrahlung and fusion regions in the latter.

If there are more than 3 initial jets, and $M_h > 115 \text{ GeV}$, and $E_{miss} < 50 \text{ GeV}$ we treat the event as a fully hadronic decay. Otherwise we consider it as semi-leptonic and require that it have at least two hadronic jets and one additional electron or muon track.

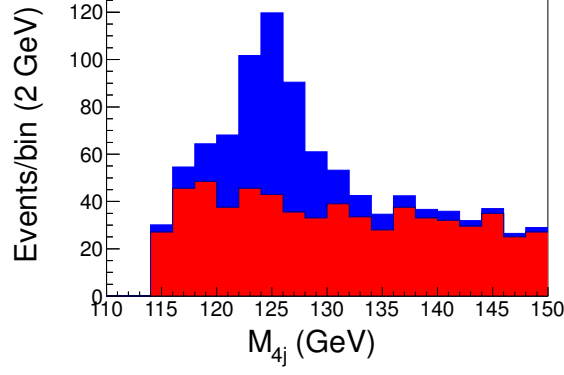


Figure III.5: Invariant mass of the 4 jets identified with a Higgs in the all-hadronic analysis for 500 fb^{-1} at 500 GeV. The Higgs signal is shown in red on top of the primary background arising from $e^+e^- \rightarrow e^+e^-q\bar{q}$ in blue.

c. Fully Hadronic Reconstruction For the fully hadronic case we merge the existing jets according to the Durham algorithm until there are only four. The Durham jet definition is a sequential combination algorithm which merges the nearest sub-jets at each step according to the distance parameter

$$Y \equiv 2 \min[E_1^2, E_2^2](1 - \cos \theta_{12}). \quad (\text{III.B.10})$$

We denote by Y_{45} the distance parameter at which the fifth jet is merged into the fourth and similarly for Y_{34} . We then take the pair of jets which has an invariant mass closest to the physical W mass and treat this as the on-shell W . The remaining pair are then regarded as the off-shell W . The sum of the two W momenta is identified with the Higgs, with corresponding mass M_h . Figure III.5 shows a simulation of the signal M_h along with the dominant background.

The six outgoing particles of the signal provide a number of angular variables which can be useful in discriminating against background. The decay of a Higgs through a pair of W s has been analyzed in detail in Ref. [503] and we adopt the angular variables described therein. We first boost to the rest frame of the Higgs. Then for each W we boost to the rest

frame of that W and compute the angle between one of the jets from its decay and the boost direction of the W with respect to the Higgs rest frame. We choose whichever jet gives an angle less than $\frac{\pi}{2}$ and call these angles θ_{j1}, θ_{j2} for the two W s. A third angle, ϕ_j , describes the angle between the planes of decay of the W s in the Higgs rest frame.

We adopt a similar treatment for the incoming and outgoing electrons. We again begin in the Higgs rest frame and define θ_{l1}, θ_{l2} as the angles between the incoming/outgoing electron associated with each Z , and the boost direction of the Z with respect to the Higgs, in the Z rest frame. Then ϕ_l is the angle between the incoming and outgoing lepton pair “decay” planes⁷.

With these reconstructions and definitions, we impose the following cuts: The recoil mass must be between 110 and 250 GeV. The 4-jet reconstructed Higgs mass, M_{had} must be less than 150 GeV. We choose these cuts because the recoil mass provides a sharper resolution at the low mass edge while the jet reconstruction is better for the high mass cut-off. The off-shell reconstructed W must have an invariant mass less than 70 GeV and its momentum in the rest frame of the Higgs ($|P_W^{rest}|$) must be less than 45 GeV. The on-shell W should have an invariant mass between 55 and 100 GeV. For further discrimination against the backgrounds we rely on a likelihood function L . This function differs in the Higgstrahlung (L_h) and ZZ fusion (L_f) analysis regions. L_h and L_f take as inputs $\theta_{j1}, \theta_{j2}, \theta_{l1}, \theta_{l2}, \phi_j, \phi_l, |P_W^{rest}|, Y_{34}, N_{hj}, M_W^{off}$, and M_h . L_f also uses M_{ee} . These functions are defined as the logarithm of the ratio of background to signal probability distributions in the input variables. We have only used simple functions, such as Gaussians and exponentials, to approximately fit these distributions and have not tried to include complicated correlations, so a more detailed analysis might improve their efficacy.

d. Semi-leptonic Reconstruction For the semi-leptonic decays, we proceed in analogous fashion. We require at least one additional electron or muon candidate and take the highest energy track among those found as our decay-product lepton. (Disregarding the two which are selected as recoiling electrons.) As before, we subtract this track from a hadronic

⁷There is a seventh physical angle describing the orientation of the Higgs decay relative to the Z s involved in producing it, but this does not seem to show any useful structure in the backgrounds or signal. This is expected for the signal since the scalar Higgs cannot transmit angular correlation information.

Table III.2: Cuts applied in hadronic and semi-leptonic analysis for $e^+e^- \rightarrow e^+e^-h \rightarrow e^+e^-W^+W^-$.

Variable	Hadronic		Semi-Leptonic	
	Higgstrahlung	Fusion	Higgstrahlung	Fusion
M_{rec}	$> 110, < 250$		> 115	
M_h	< 150		$> 100, < 150$	
M_W^{off}	< 70		$> 10, < 60$	
$ P_W^{rest} $	< 45			
M_W^{on}	$> 55, < 100$			
L	L_b	L_f	L_b	L_f

jet if necessary. We identify the missing energy and momentum with the neutrino. We then merge the hadronic jets down to two, discarding the event if there is initially only one. The sum of the hadronic jets is considered to be one W while the other is the sum of the charged lepton and the neutrino. The Higgs is then the sum of the two W s and W^{on} is whichever has an invariant mass nearer the physical W mass. Angles are defined as in the all-hadronic case except that, for the leptonically decaying W , θ_{j2} and ϕ_j are defined by the charged lepton instead of the nearer jet to the boost direction in the W rest frame. We do not attempt to reconstruct the tau decays. The Higgstrahlung and fusion regions are defined as before and we apply the following cuts: The recoil mass must be greater than 115 GeV. The candidate Higgs mass, constructed from two jets plus a charged lepton plus missing energy, must be between 100 and 150 GeV. The off-shell W should have an invariant mass between 10 and 60 GeV. Further cuts are imposed by likelihood functions, which depend on $\theta_{j1}, \theta_{j2}, \theta_{l1}, \theta_{l2}, \phi_j, \phi_l, M_W^{off}$, and M_h and, for the fusion case, M_{ee} . Our cuts are summarized in Table III.2.

Table III.3: Expected number of events from $h \rightarrow WW$ signal and backgrounds with 500 fb⁻¹ at 500 GeV ILC.

Process	Expected Events			
	All Hadronic		Semi-leptonic	
	Higgstrahlung	ZZ Fusion	Higgstrahlung	ZZ Fusion
$eeh \rightarrow ee4j$	85	183	0	0
$eeh \rightarrow eeqq\ell\nu$	1	1	52	111
$ee \rightarrow eeqq$	65	100	39	59
$ee \rightarrow ee4q/eeqqgg$	38	85	2	1
$ee \rightarrow eeqq\ell\nu$	1	9	8	41
$ee \rightarrow qq\ell\nu$	< 18	< 18	< 18	< 18
Total Background	104(+18)	194(+18)	49(+18)	101(+18)
$\delta\sigma$	16%	11%	19%	13%

e. Sensitivity To estimate our sensitivity we include a number of backgrounds which are expected to contribute significantly after cuts. We model the processes $e^+e^- \rightarrow e^+e^-q\bar{q}$, $e^+e^- \rightarrow q\bar{q}l\nu$, $e^+e^- \rightarrow e^+e^-jjjj$, and $e^+e^- \rightarrow e^+e^-q\bar{q}l\nu$. Among these $e^+e^- \rightarrow e^+e^-q\bar{q}$ is the most significant in both the fully hadronic and semi-leptonic channels. Not surprisingly, $e^+e^- \rightarrow e^+e^-4j$ also contributes significantly to the fully hadronic analysis background and $e^+e^- \rightarrow e^+e^-q\bar{q}l\nu$ to the semi-leptonic background. We provide the expected number of events from various sources which pass our cuts in Table III.3 below, assuming 500 fb⁻¹ of integrated luminosity.

The last row before the total background sum sets an upper limit on any background contributions from $e^+e^- \rightarrow q\bar{q}l\nu$. No events in our generated sample for this process pass the cuts, but due to the large initial cross section we are not sensitive to a number of observed events smaller than ~ 18 .

A further consideration is the effect of Higgs decays to b -quark pairs, which are expected to present a large branching fraction for a SM-like scalar. These decays can potentially pass our cuts and contribute to the excess over non-Higgs backgrounds but they could limit our ability to measure the pure WW signal. However, this concern can be largely addressed with b -tagging techniques. We do not include an explicit b -tagging simulation in our analysis, however, reasonable estimates show that the net effect of b -quark decays and b -tagging is small and we will proceed based on the assumption that this background can be neglected. See Appendix VI.H for a more detailed discussion of these effects.

Based on the numbers above we estimate the sensitivity to the combined all-hadronic and semi-leptonic signals using

$$\delta\sigma_{eeh \rightarrow eeWW} = \frac{\sqrt{N_S + N_B}}{N_S} \quad (\text{III.B.11})$$

where N_S and N_B are the expected number of signal and background events respectively. This gives an uncertainty on the signal cross section $\delta\sigma_{eeh \rightarrow eeWW} = 6.8\%$. However, we can additionally make use of Higgstrahlung signal events where the Z decays to muons. This should give us essentially the same number of signal events as the Higgstrahlung to electrons channel. If we very conservatively assume that the background is also the same, we can

bring the error down to $\delta\sigma_{eeh\rightarrow eeWW} = 6.0\%$. Assuming no new background would bring our error down to 5.6%. For the results below we will use $\delta\sigma_{ZW} = 6\%$ for this channel.

3. Achievable Accuracies at the ILC

a. Model-Independent Fitting The expected statistical uncertainty on various other cross sections at the ILC have been calculated by several authors [177, 498]. We will make use of numbers presented for the Snowmass Community Study for cross sections other than those we have calculated ourselves. Table III.4 lists the ILC uncertainties we use in our analysis below. Table III.5 lists the most relevant LHC uncertainties in our study. These include assumptions about future theoretical and systematic errors. ATLAS and CMS use different extrapolation assumptions to obtain their high luminosity precisions. We have combined them in a conservative way to estimate the effect of both experiments, for details of the combination in Appendix. VI.G.

Our procedure for this model-independent fit is described in Appendix VI.G, especially in Eq. (VI.G.62). This fit also determines the relative error on the various coupling constants g_A . The results are given below in Table III.13 and Fig. III.6. We present the expected errors at the 250, 500 and 1000 GeV stages of running with integrated luminosities of 250 fb⁻¹, 500 fb⁻¹, and 1000 fb⁻¹ respectively, henceforth labeled as ILC250, ILC500 and ILC1000 scenarios. For each scenario we include projected sensitivities with and without the addition of information from the LHC. For the invisible decays we present the case for a 10% invisible branching fraction and for 1%. As mentioned in Sec. III.B.1.b, the addition of the invisible search does not constrain the other Higgs couplings or total width in a model-independent fit.

Using the σ_{ZW} determination above we can compute the Higgs width in terms of Eq. (III.B.8). σ_{ZW} can be further constrained by measurements of the process $e^+e^- \rightarrow Zh, h \rightarrow WW$ at 250 GeV and $e^+e^- \rightarrow \nu\nu h, h \rightarrow ZZ$ at 500 GeV. Combining the information from these channels we estimate that σ_{ZW} can be determined to a relative error of $\delta\sigma_{ZW} = 4.6\%$. Using the available estimates for $\delta\sigma_{Zb}$ and $\delta\sigma_{Wb}$ one finds that the total error on Γ_h using Eq. (III.B.8) is 6.8%. This is nearly the same as the error achievable using Eq. (III.B.4).

Table III.4: Estimated relative errors for various cross sections at the ILC. The first and second rows indicate the production energy and mechanism respectively for the Higgs while the first column shows the decay modes. Numbers are taken from the ILC Snowmass Whitepaper [498] except for simulation studies presented in this section. The Br_{inv} is absolute error.

\sqrt{s} and \mathcal{L} (P_{e^-} , P_{e^+})	ILC250 (-0.8 , $+0.3$)		ILC500 (-0.8 , $+0.3$)		ILC1000 (-0.8 , $+0.2$)
Decay\ Production	Zh	$\nu\nu h$	Zh/eeh	$\nu\nu h$	$\nu\nu h$
<i>inclusive</i> (%)	2.6		3.0		
$b\bar{b}$ (%)	1.2	11	1.8	0.66	0.5
$c\bar{c}$ (%)	8.3		13	6.2	3.1
$\tau^+\tau^-$ (%)	4.2		5.4	9.0	2.3
gg (%)	7		11	4.1	1.6
WW (%)	6.4		6	2.4	3.1
ZZ (%)	19		25	8.2	4.1
$\gamma\gamma$	29 – 38		29 – 38	20 – 26	8.5
$\text{Br}_{inv}(\%)$	0.5-0.7				

Table III.5: Relative uncertainties of relevant quantities from projections of ATLAS and CMS experiments for LHC 14 TeV with 300 fb⁻¹ and 3000 fb⁻¹ (HL_LHC) integrated luminosity from Snowmass studies [196]. See the text and Appendix VI.G for combination details.

		$\gamma\gamma$ (%)	WW^* (%)	ZZ^* (%)	$b\bar{b}$ (%)	$\tau^+\tau^-$ (%)
LHC 300 fb ⁻¹	ATLAS	9-14	8-13	6-12	N/A	16-22
	CMS	6-12	6-11	7-11	11-14	8-14
	Combined	12	10	10	14	14
HL_LHC 3000 fb ⁻¹	ATLAS	4-10	5-9	4-10	N/A	12-19
	CMS	4-8	4-7	4-7	5-7	5-8
	Combined	7	7	6	7	8

As can be seen from Table III.13 and Fig. III.6, the results for ILC alone fitting are comparable with the model-independent fitting in Ref. [196]. Our study for the invisible Higgs decays in Sec. III.B.2.a and ZZ -fusion Higgs to WW both improves the ILC measurements when comparing Table III.4 with Ref. [177]. The combination with LHC measurements from Table III.5 improves almost all couplings precisions for 250 GeV ILC. The improvement for total width in this case receives contributions from several channels at the LHC as described in Eq. (III.B.5). Especially for g_γ and g_g , which are statistically limited at the ILC, the LHC can provide sizable gains. With ILC 500 data many of these benefits become marginal due to increased sensitivity from ILC channels alone. Still, the improvement in the g_γ remains significant. Including an ILC run at 1 TeV leads to further gains in the fermion and photon channels and essentially obviates the effect of LHC information.

As noted before, the largest contribution to the total width error derives from the uncertainty on the inclusive cross section. Further studies on ZZ -fusion inclusive measurement at the ILC for 500 GeV and 1 TeV should be valuable. Approximately half of the expected sen-

Table III.6: Model-independent precisions (1σ) of the width and couplings constants expected for a SM-like Higgs at three stages of ILC run. All results assume completion of previous stage of ILC runs. Results in combination with LHC projections are in parenthesis. We combine 300 fb^{-1} estimates for the LHC with the 250 GeV ILC run, and 3000 fb^{-1} with the 500 GeV run and 1 TeV run. The absolute value of uncertainty on Br_{inv} is given for an input Br_{inv} of 10% (1%).

Relative Error %	ILC250	+ILC500	+ILC1000
Γ	12 (9.3)	4.8 (4.8)	4.5 (4.5)
g_Z	1.3 (1.3)	0.99 (0.99)	0.98 (0.98)
g_W	5.0 (3.5)	1.1 (1.1)	1.1 (1.1)
g_γ	20 (6.2)	9.5 (3.8)	4.1 (2.9)
g_g	6.5 (4.3)	2.3 (2.0)	1.5 (1.5)
g_b	5.4 (4.1)	1.5 (1.5)	1.3 (1.3)
g_c	6.9 (5.8)	2.8 (2.8)	1.8 (1.8)
g_τ	5.8 (4.6)	2.8 (2.1)	1.6 (1.6)
$\text{Br}_{inv}(\%)$	0.6 (0.5)		

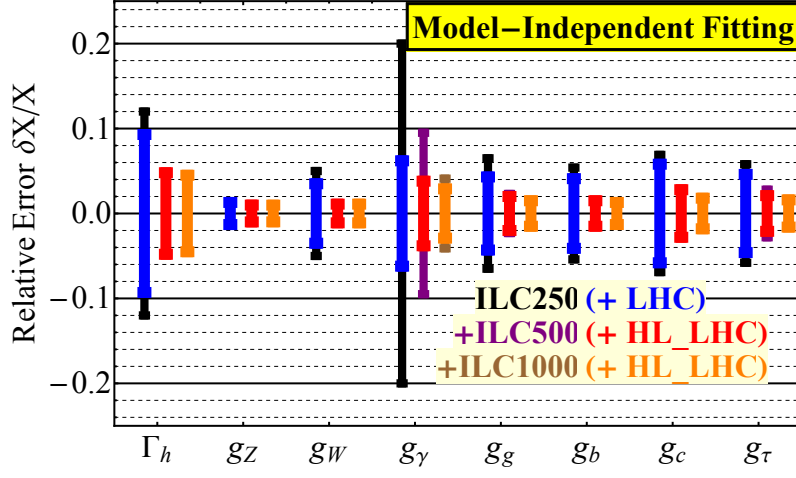


Figure III.6: Model-independent uncertainties of the Higgs boson couplings from ILC 250 GeV with (blue) and without (black) LHC data with 250 fb⁻¹ of integrated luminosity; at 500 GeV (red/purple) with 500 fb⁻¹; and at 1 TeV (orange/brown) with 1000 fb⁻¹. Results at 250 GeV are combined with LHC 14 TeV using 300 fb⁻¹ projections while those at 500 GeV and 1 TeV use 3000 fb⁻¹ projections. For details see Table III.13 and the text.

sitivity ($\sim 3\%$) on the inclusive measurement at 500 GeV comes from Higgstrahlung events with Z decaying to electrons or muons. If the fusion cross-section, which is roughly twice as many events, can be utilized efficiently the overall precision at 500 GeV might be pushed down to nearly the 2% level, which in combination with the 250 GeV measurement could determine the inclusive cross-section at less than 2%.

b. Model-Dependent Constraints Thus far we have proceeded with a strictly model-independent method for fixing the couplings, treating Γ_h as an independent parameter. Effectively, this means we allow for arbitrarily large Higgs decays into “buried” channels which are not constrained at the ILC. One may improve on the results by adding the reasonable assumption that any buried channels in the clean environment of the ILC are negligibly small compared to the total width, i.e., if we assume that the total width is the sum over partial widths arising from the coupling constants fitted above. This would be true for a SM-like Higgs. By including the search for invisible decays we can make this assumption considerably more robust.

In Table III.7 and Fig. III.7 we present expected sensitivities with the assumption that, including the invisible channel, all significant decay modes are observable. We include LHC information in Table III.5 for all columns. Two cases are shown for each energy:

1. MDA (Model-Dependent Case A) shows the case where no excess is observed and only an upper limit on the invisible decay cross section can be set. Since in this case the invisible signal is consistent with zero, we only show the upper limit on the branching fraction.
2. MDB (Model-Dependent Case B) shows the case assuming a tree-level custodial symmetry relation $g_{hWW}^2/g_{hZZ}^2 = \cos^2\theta_w$.⁸

MDA fitting results show strong improvement in the coupling precisions compared to the model-independent extraction as well as a large reduction on the total width error, with gains at both energy scales. We note here for the MDA fit the total width is no longer a fitting parameter, but rather a derived quantity as shown in Eq. (VI.G.63). The rarest

⁸This condition holds for Higgs singlet and doublet models. However, this condition does not necessarily hold for triplet models with custodial symmetry [505, 506].

Table III.7: Model-dependent precisions for coupling constants achievable at the ILC, combined with LHC (HL_LHC) under two different assumptions for ILC250 (ILC500 and ILC1000). MDA assumes no invisible decays above background. MDB assumes $g_{hWW}^2/g_{hZZ}^2 = \cos^2\theta_w$. Note that in MDA Γ_h is no longer a free parameter, and in MDB g_W and g_Z are essentially the same parameter, g_V . SM theoretical uncertainties are shown in the second column, from Ref. [414, 504]. Uncertainty on Br_{inv} is absolute value and input of Br_{inv} is set at 10%.

	SM Theo.	ILC250		+ILC500		+ILC1000	
	Error on	MDA	MDB	MDA	MDB	MDA	MDB
	Br(%)	($\pm\%$)	($\pm\%$)	($\pm\%$)	($\pm\%$)	($\pm\%$)	($\pm\%$)
Γ_h	+3.9, -3.8	1.5	7.8	0.84	4.4	0.67	4.2
g_Z	± 4.2	0.75	1.3	0.44	0.99	0.41	0.98
g_W	± 4.1	2.8		0.38		0.25	
g_γ	± 4.9	6.0	6.1	3.6	3.8	2.7	2.9
g_g	± 10.1	2.7	3.9	1.5	1.9	0.89	1.4
g_b	± 3.4	1.4	3.3	0.75	1.4	0.59	1.3
g_c	± 12.2	4.3	5.2	2.5	2.7	1.4	1.8
g_τ	± 5.6	2.3	3.7	1.6	2.0	1.1	1.5
Br_{inv}	—	< 0.52	0.60	< 0.52	0.57	< 0.52	0.57

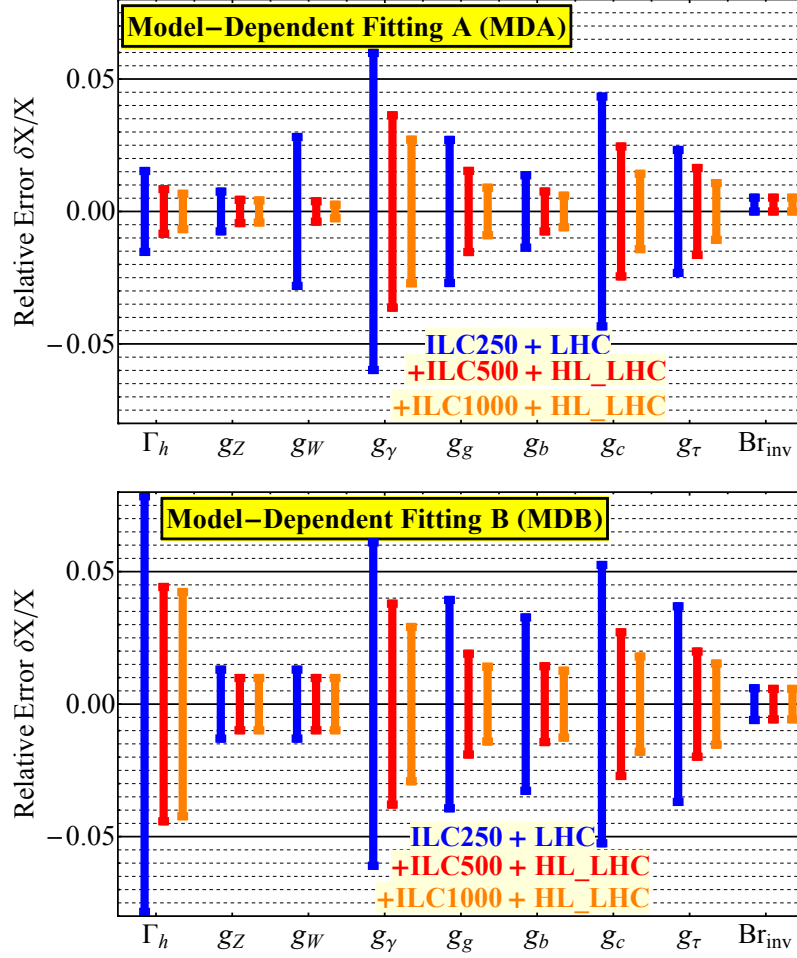


Figure III.7: Model-dependent uncertainties of the Higgs boson couplings from ILC250 (blue), ILC500 (red) and ILC1000 (orange) runs under assumption MDA (first panel) and MDB (second panel). Estimates include projected information from the LHC. For details, see caption of Table III.7 and the text. Uncertainty on Br_{inv} is absolute value and input of Br_{inv} is set at 10%.

channels show the least improvement comparing to the Model-Independent fit, which is to be expected since they are least sensitive to the overall width. This assumption, that “buried” channels are a negligible contribution is valid in many models. Still, searches for exotic Higgs decays are well-motivated [369] and should start with a concerted effort given the clean environment at a lepton collider where many can be explicitly “unburied”. MDB fitting also shows improved precisions for the 250 GeV run. Most obviously, the g_W precision is set to the same level as the g_Z , and this in turn better constrains other couplings to quarks and leptons. The improvement on the total width is not as dramatic as in MDA since the large branching fraction to bb and other modes still gives a significant contribution. With the addition of ILC 500 information MDB has little effect on the expected precisions. That is, the ILC model-independent measurements of g_W and g_Z are already comparable and small so the assumption that they are equal does not affect the fit much. As in the model-independent approach, ILC1000 can improve the sensitivity for fermionic, photonic and gluon couplings in MDA or MDB. We list in the second column the theoretical uncertainties on the total width Γ_h and branching fractions of a 126 GeV SM Higgs from Ref. [414, 504]. Roughly twice the uncertainty on coupling constants enters into the Brs. One can see that for both MDA and MDB the statistical precisions on couplings are comparable to theoretical uncertainties. In principle the theory errors are reducible but effort will be needed to make maximum use of the potential at a Higgs factory.

4. Summary and Outlook

In this section we have outlined a systematic approach to the determination of the Higgs total width and measurable coupling parameters in a model-independent manner at the ILC in Sec. III.B.1, and illustrated the complementarity for operating the ILC at 250 GeV, 500 GeV and 1 TeV. We have performed detailed simulations for two channels which can play an important role in determining the total width with high precision in model-independent and model-dependent scenarios. We first included the invisible decay channels at 250 GeV, and carried out new analyses of the $e^+e^- \rightarrow e^+e^-h$ with $h \rightarrow W^+W^-$ at 500 GeV. In Sec. III.B.3, we estimated the achievable accuracies on coupling constants and total width

at the ILC. We also emphasized the benefits and importance of combining measured cross sections from the LHC and the ILC, which results in improved precision, especially for the total width at 250 GeV ILC and precisions for g_γ and g_g for 250 GeV as well as 500 GeV ILC. With the statistics assumed for a 1 TeV ILC run, LHC information leads to only small improvements.

Our specific findings can be summarized as follows.

1. At 250 GeV the key measurement of the inclusive Higgstrahlung cross section, which enters all the partial width determinations in this approach, can be made with high precision as discussed in Sec. III.B.1.b. However, the precision on the total width is limited by the error on other exclusive cross sections, such as $e^-e^+ \rightarrow e^-e^+h \rightarrow e^-e^+ZZ^*$ and $e^-e^+ \rightarrow \nu\nu h \rightarrow \nu\nu W^+W^-$. This is where the additional information for the coupling ratios from the LHC provides important enhancement of the achievable precision as discussed in Sec. III.B.3.a. As shown in Table III.13, any couplings can be measured in a fully model-independent way at this energy to the $(3 - 5)\%$ level. Under the minimal assumption that the searches for visible and invisible modes comprise all significant decay channels or custodial symmetry, these couplings can be measured at the $(1 - 3)\%$ percent level.
2. At 500 GeV the total width can be largely determined by measuring a few channels due to the high precision expected for Higgs decays to $b\bar{b}$ produced via Higgstrahlung and WW fusion as discussed in Sec. III.B.1.c. We have shown that the exclusive cross section for ZZ fusion process with subsequent decay of the Higgs boson to WW^* (σ_{ZW}) can also be determined with good precision and used in place of the σ_{WW} measurement to achieve nearly the same precision on the total width in a way which is less sensitive to additional errors in the $b\bar{b}$ decay channels as shown in Sec. III.B.2.b. At this energy, assuming the 250 GeV run has been completed, one can make model-independent determinations of the coupling constants at the $(1 - 3)\%$ level as shown in Table III.13. Adding the assumption that all significant modes have been seen can reduce these errors to the sub-percent level for some couplings as shown in Table III.7. At this point any further improvement of the Higgs total width is limited by the uncertainty in the inclusive cross section for Zh production. Improving this key measurement would require either a longer

run at 250 GeV or detailed study at 500 GeV. At this stage efforts to reduce theoretical uncertainties are needed to consistently interpret the experimental results in terms of theoretical parameters.

3. A 1 TeV ILC run with high luminosity can improve the fermion, photon and gluon coupling measurements by $\sim 25 - 50\%$ except for g_b .
4. Good precision for Higgs to invisible, $0.5 - 0.7\%$, can be reached at the Zh threshold at 250 GeV, as shown in Sec. [III.B.2.a](#).
5. At a higher ILC energy above 250 GeV, the fusion channels will become more important. In particular, the inclusive ZZ fusion process at higher energy could provide further improvement for the model-independent coupling precision, and should be carefully studied with respect to the various sources of backgrounds.

C. HIGGS COUPLINGS AT THE ILC

In this work we perform a fast detector simulation analysis of the inclusive ZZ fusion channel measurement at 500 GeV and 1 TeV. We simulate the predominant backgrounds and a SM-like Higgs signal and calculate the signal sensitivity using a cut-based analysis and multivariate Log-likelihood analysis. We find that with the cut-based analysis, we can reach a sensitivity on the cross section to 2.9% level. The multivariate analysis further improves the precision of the cross section measurement to 2.3%.

The rest of the section is organized as follows: In Sec. [III.C.1](#), we discuss the kinematic features for identifying the signal and perform a detailed analyses for the ZZ fusion process at 500 GeV and 1 TeV energies including backgrounds. In Sec. [III.C.2](#) we discuss the effects of this additional information on the model-independent Higgs width and couplings. We also illustrate the potential use of these couplings in constraining higher-dimensional operators. We summarize our results in Sec. [III.C.3](#). Appendix [VI.C](#) is included to address issues relating to potential signal and backgrounds with a single photon in the final state.

1. Sensitivity Analysis

We consider the signal process $e^-e^+ \rightarrow e^-e^+h$ via ZZ fusion. We assume that the incoming leptons are described by the nominal beam energy moving along the beam axis in the positive and negative directions respectively. Then the outgoing electrons are each characterized by a 3-dimensional vector and there are six independent degrees of freedom measured in our final state. We choose the dimensionful variables to be the invariant mass of the final electron-positron pair m_{ee} and the recoil mass, given by

$$m_{rec}^2 \equiv s - 2\sqrt{s}E_{ee} + m_{ee}^2. \quad (\text{III.C.12})$$

The recoil mass provides the most distinct signal feature since it displays the resonance peak at the Higgs mass $m_h \simeq 126$ GeV observable on top of a continuum background. The electron-pair mass m_{ee} favors a large value $m_{ee} \gtrsim 250$ (600) GeV at a 500 (1000) GeV center of mass energy. This is distinct from the Higgsstrahlung mode where the pair mass is strongly peaked at the Z resonance. Despite a broad distribution for the ee pair mass in the ZZ fusion, it still provides some discriminating power against the diffuse electron background.

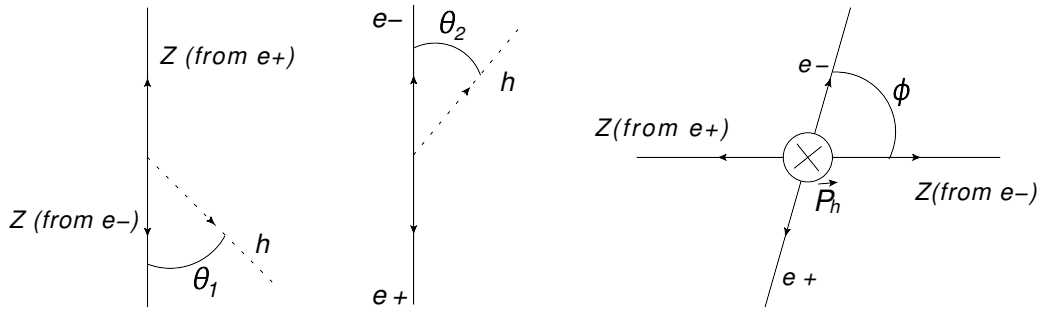


Figure III.8: Angles θ_1 , θ_2 and ϕ as defined in the text. The label e^- (e^+) represents the outgoing electron (positron) and the Z momentum is given by the difference between outgoing and incoming electrons (positrons). The arrows represent momentum directions. The Higgs momentum is perpendicular to the plane in the right panel.

The remaining kinematic degrees of freedom can be described by four angles. One of these, the azimuthal angle of the Higgs boson around the beam axis, is irrelevant to our

analysis due to the rotational symmetry of the initial state around the beamline when the beam is not transversely polarized. The other three angles, illustrated in Fig. III.8, are chosen as follows: θ_1 is the angle between the intermediate Z coming from the initial electron and the Higgs boost direction in the rest frame of the Higgs. θ_2 is the angle between the final state electron and the Higgs boost direction in the rest frame of the outgoing e^-e^+ pair. These angles take advantage of the scalar nature of the Higgs. The distributions for $\cos\theta_1$ and $\cos\theta_2$ are rather flat since the Higgs boost direction has no preference to align with the spins of the incoming Z s or outgoing electrons. There is some correlation between these two angles and mild enhancement at larger $|\cos\theta|$, which corresponds to a more collinear configuration. This is mitigated by the relatively large virtuality of the Z propagators. In contrast the most important backgrounds show much stronger correlation and peaks at high $|\cos\theta|$ arising from highly collinear regions of phase space which tend to dominate their production. The third variable, ϕ , is defined as the angle between the plane defined by the ZZ pair and the plane defined by the outgoing e^-e^+ pair when viewed along the Higgs boost direction. It is a measure of coplanarity. Here the signal shows a preference for small values of ϕ , indicating coplanar emission of the outgoing e^-e^+ pair with the Z propagators and with the incoming leptons. This strong correlation is expected since the Higgs does not carry away any spin information. The backgrounds will generally have a more complex spin structure which is not strongly coplanar.

In practice, the outgoing electrons of our signal will tend to radiate photons, an effect we treat with showering. This radiation degrades our signal resolution. To ameliorate this, nearby photons are clustered according to a recombination algorithm and identified with a single electron as described in detail in the next section.

Given our inclusive signal process, the backgrounds are of the form $e^-e^+ \rightarrow e^-e^+X$. Obviously, the single photon radiation $X = \gamma$ arising from the Bhabha scattering is by far the largest. Although the majority of events should be removed by the requirement of a large recoil mass m_X , beamstrahlung and the effects of the initial state radiation (ISR), as well as the final state radiation (FSR), will produce additional largely collinear photons. This generates a long tail in the recoil mass spectrum due to unobserved photons, mainly along the beam pipe. To keep this class of backgrounds under control, we introduce a cut on

the transverse momentum p_T of the outgoing e^-e^+ pair. Photons which are lost down the beam-pipe should only contribute small p_T differences to the observed final state. Thus the final state e^-e^+ intrinsically has no p_T as long as collinear photons from final state showering are correctly regrouped with the electrons. The signal, in contrast, has a non-zero p_T from the recoiling Higgs.

This leaves a background from $e^-e^+\gamma$ where the extra photon is not close enough to either electron to be grouped with it by the clustering algorithm. We find it most convenient to simply veto events, in addition to the e^-e^+ pair, with a single isolated photon

$$E_\gamma > 10 \text{ GeV}, \quad \theta_\gamma > 6^\circ, \quad (\text{III.C.13})$$

where θ_γ is the polar angle with respect to the beam. The effectiveness of this cut is illustrated in Table III.8 for the 500 GeV and 1 TeV run. (See the next section in Tables III.9 and III.11 for numerical definitions of the cuts.) Simple cuts on invariant mass and p_T reduce the $e^-e^+\gamma$ induced background by three orders of magnitude but it remains 30 times larger than our signal. However the single photon veto reduces this by more than 90%.

Table III.8: Cross section (fb) for signal $e^-e^+ \rightarrow h$ and background $e^-e^+\gamma$ after sequence of cuts. The cuts are specified in Table III.9 and Table III.11 for 500 GeV and 1 TeV case respectively.

Cuts (fb)	generator level	m_{rec}, m_{ee}	$p_{T(ee)}$	veto isolated single γ
e^-e^+h (500 GeV)	11.5	4.11	3.48	3.48
$e^-e^+\gamma$ (500 GeV)	165000	317	67.2	1.32
e^-e^+h (1 TeV)	24.1	9.75	8.49	8.18
$e^-e^+\gamma$ (1 TeV)	175000	1570	344	4.73

In principle this affects our inclusiveness. However, the Standard Model processes which could produce such a signal, such as $h \rightarrow \gamma\gamma$ (where one photon is lost down the beam pipe) and $h \rightarrow Z\gamma$ constitute branching fractions of 2.3×10^{-3} and 1.6×10^{-3} respectively. As

will be seen, the ultimate precision for the inclusive Higgs production measurement is at the $\sim 2\%$ level so that Higgs decays to $\gamma\gamma$ or $Z\gamma$ would have to be enhanced by more than an order of magnitude compared to the Standard Model to be seen in the model-independent inclusive measurement. Any such large signal enhancements will be seen at the LHC, to the extent that they are not already excluded by current results. See the Appendix for further discussion.

After these cuts some background can remain due to poorly measured final state particles. Particularly at 1 TeV center of mass energies, errors on the detected momentum of the final state can sometimes fake a recoil mass and a high p_T that passes our other cuts. This is necessarily an issue to be determined in detail by experimentalists when working with an actual machine and is only parameterized by assumptions on detector smearing and efficiency in our simulation. We find that badly measured states are typically associated with very high-energy photons. Either these photons are not detected at all due to imperfect calorimeter efficiency, or they are reported but with significant error on their transverse momenta. Mismeasured low energy photons will not usually cause a big enough error to satisfy our previous cuts. Thus it is useful to veto events with very high-energy detected photons, which are relatively rare in the signal.

Again, one may worry about introducing a bias against photons from Higgs decay, but this problem can be addressed. When an event has a high-energy photon we first boost it into the rest frame of the Higgs, as determined by the momentum of the outgoing lepton pair. If the photon’s energy in the Higgs frame is less than half the Higgs mass, then it potentially comes from a Higgs decay, and we do not subject it to the high-energy veto. Thus only events with “eligible” photons, γ^* which could not have come from the Higgs decay, are cut.

a. Simulation Framework To estimate the expected number of events and derive the sensitivity reach at a given energy and luminosity we use the ILC-Whizard setup provided through the detector simulation package SGV3 [499]. Beam profiles for several energies have been generated by GuineaPIG [500], which includes effects from Beamstrahlung and ISR. These profiles are interfaced with Whizard 1.95 [501] to generate parton level samples. The parton level samples are then passed to Pythia which performs showering and hadronization

to final state particles [244]. SGV is a fast detector simulation which has been found to agree well with full simulation results.

To avoid collinear and soft divergences, at the parton level we require that the Energy of a final state photon be greater than 10 GeV, and that the invariant masses of final lepton-antilepton pairs and of lepton-photon pairs be greater than 4 GeV. We also require that the invariant mass of a final state (anti-)electron with an initial (anti-)electron, or of a final photon with an initial lepton, be greater than 4 GeV. More collinear photons will be generated via the showering routines in Pythia.

After simulating tracking and calorimeter hits SGV attempts to identify charged and neutral particles and groups these into jet-like objects according to a sequential recombination algorithm. We use the JADE algorithm, which defines a distance between objects

$$y_{ij} \equiv \frac{2E_i E_j (1 - \cos \theta_{ij})}{E_{vis}^2}, \quad (\text{III.C.14})$$

where E_i and E_j are the energies of two objects and E_{vis} is the total seen energy of the event. Nearby objects are merged into subjects until all subjects are separated by $y_{ij} > 0.01$.

In selecting our observables we first identify the two highest energy electron/positron tracks in an event and discard it if there are fewer than two detected (anti-)electrons. We also require that these particles have opposite signs. If nearby calorimeter hits included in the subjet which contains the track are only identified as photons, then we use the “jet” momentum and energy for our reconstructed lepton. If the subjet contains any particles identified as hadrons then we use only the track momentum in order to minimize cases where hadron jets overlap with the recoiling electrons. For the purposes of the isolated photon cut described above, we define an isolated photon as a “jet” object which contains only photons and no charged tracks or hadronic calorimeter hits.

In the case of pure photon plus electron/positron backgrounds we simulate both $e^-e^+ \rightarrow e^-e^+\gamma$ and $e^-e^+ \rightarrow e^-e^+\gamma\gamma$ at the matrix element level. After showering there is some overlap in the signals described by these two processes. In the spirit of matching calculations done for hadron colliders we discard events from $e^-e^+ \rightarrow e^-e^+\gamma$ which produce two isolated photons after the clustering procedure.

Table III.9: Cuts applied at ILC 500 GeV.

Cut 1	$122 \text{ GeV} < m_{\text{rec}} < 145 \text{ GeV}$
	$110 \text{ GeV} < m_{ee} < 370 \text{ GeV}$
	$p_{T(ee)} > 40 \text{ GeV}$
	veto 1 iso. photon
	$E_{\gamma}^* < 200 \text{ GeV}$
Cut 2	$\phi < 1.5$

b. 500 GeV Analysis We proceed with a sensitivity analysis for the ILC running at a 500 GeV center of mass energy. We apply an initial beam polarization of -0.8 for the electron and $+0.3$ for the positron, following the ILC TDR [177]. We first perform a purely cut-based analysis with the cuts listed in Table III.9. E_{γ}^* represents only photon hits with energy greater than 65 GeV in the rest frame of the Higgs.

Figure III.9 displays the signal and background distributions in m_{rec} , m_{ee} and the three angular variables, after applying Cut 1 as listed. As can be seen, the angular variables show considerable distinction from the background which can be used to enhance our sensitivity. Cut 2 acts on these angles.

For this analysis we define the signal sensitivity according to the statistical 1σ relative error on the signal,

$$\frac{\delta\sigma}{\sigma} = \frac{\sqrt{N_s + N_b}}{N_s}, \quad (\text{III.C.15})$$

where $N_{s,b} = L\sigma_{s,b}$ are the expected number of signal and background events after cuts respectively. We assume the integrated luminosity $L = 500 \text{ fb}^{-1}$ at this energy. The statistical significance is then inversely related to the signal sensitivity as $N_s/\sqrt{N_s + N_b}$. The effect of our cuts on the cross section for signal and background processes is given in Table III.10.

We find that this cut based analysis can measure the inclusive ZZ fusion signal to a relative error of 8%. At this energy the dominant background after our cuts is $e^-e^+\nu_e\bar{\nu}_e$,

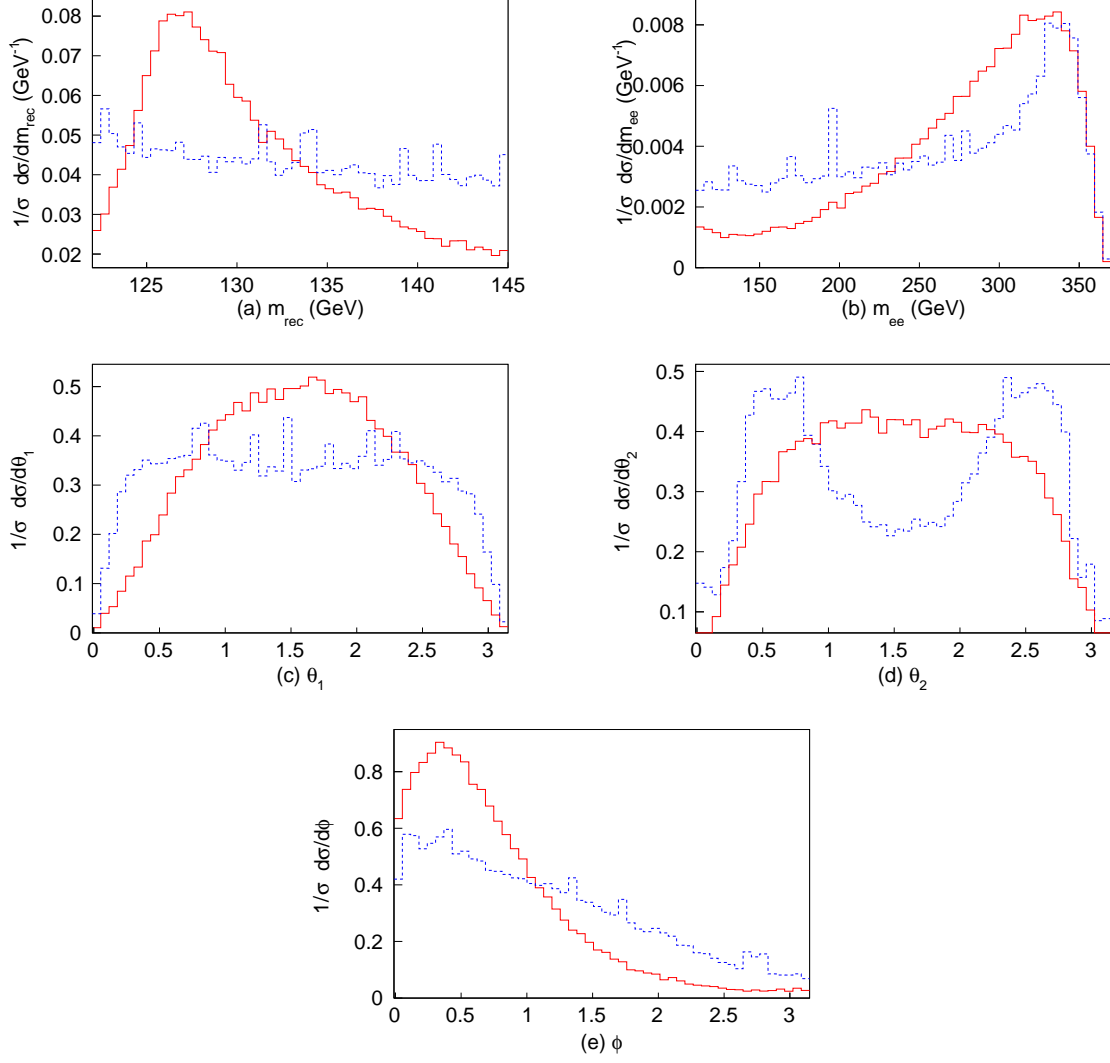


Figure III.9: Comparison of signal (solid red) and total background (dashed blue) distributions for variables m_{rec} , m_{ee} , θ_1 , θ_2 and ϕ at $\sqrt{s} = 500$ GeV. Cut1 in Table III.9 is applied. For clarity, both signal and background distributions are normalized to unity.

Table III.10: Cross sections for signal and background processes at ILC 500 GeV.

Process	Generator Level (fb)	Cut1 (fb)	Cut2 (fb)
$ee \rightarrow eeh(\text{Signal})$	11.5	3.48	3.11
$ee \rightarrow ee\nu_e\nu_e$	659	23.9	16.0
$ee \rightarrow ee\nu_{\mu,\tau}\nu_{\mu,\tau}$	78.6	1.02	0.70
$ee \rightarrow eeqq$	1850	9.33	6.88
$ee \rightarrow eell$	4420	5.18	4.42
$ee \rightarrow ee\gamma\gamma$	1640	1.18	0.60
$ee \rightarrow ee\gamma$	165000	1.32	0.66
Total Background	174000	41.9	29.2
$\delta\sigma/\sigma$	-	8.7%	8.2%

over 80% of which is from the process $e^-e^+ \rightarrow W^-W^+$. The large cross section of $e^-e^+ \rightarrow W^-W^+$ is favored by the beam polarization we have used at 500 GeV ILC. It is possible to reduce this background with a polarization that favors right-handed electrons, however, this also reduces the signal and we do not find any significant gain in sensitivity with the reversed polarization. It is possible to enhance sensitivity with an analysis that is sensitive to shape and to correlations between variables. This is particularly useful when the signal and background display distinct features which are not sharp enough to be efficiently cut on, as in Fig. III.9.

c. 1-TeV Analysis We next extend our analysis to a 1 TeV center of mass energy with 1000 fb^{-1} integrated luminosity. The polarization is assumed to be $(-0.8, +0.2)$ as suggested by the Snowmass Higgs report [196]. The ZZ fusion process is enhanced with increased center of mass energy. However, due to radiation from the energetic e^- and e^+ , the Higgs mass peak in the m_{rec} distribution is much more smeared than in the 500 GeV

Table III.11: Cuts applied at ILC 1 TeV.

Cut 1	$95 \text{ GeV} < m_{\text{rec}} < 300 \text{ GeV}$
	$500 \text{ GeV} < m_{ee} < 870 \text{ GeV}$
	$p_{T(ee)} > 50 \text{ GeV}$
	veto 1 iso. photon
	$E_{\gamma}^* < 200 \text{ GeV}$
Cut 2	$0.14 < \theta_2 < 3.0$
	$\phi < 1.5$

case, and photon radiation backgrounds become more significant. The angular variables θ_2 and ϕ show greater distinctions between signal and background. To maximize significance we apply cuts as listed in Table III.11.

Figure III.10 compares the signal and total background distributions after Cut1. Table III.12 shows the expected cross sections after Cut1 and Cut2. Despite the degradation of the recoil mass peak we gain significance from enhanced statistics and a somewhat improved signal to background ratio. The cut-based analysis can reach a sensitivity of 3.1%.

d. Multivariate Log-Likelihood Analyses To improve upon the cut-based results for reaching the optimal sensitivity, we perform a multivariate analysis (MVA), by evaluating a five-dimensional Log-likelihood as a function of the deviation from the SM. Assuming Poisson statistics in each bin, the Log-likelihood is defined as

$$LL(\mathbf{n}; \boldsymbol{\nu}) = 2 \sum_{i=1}^{N_{bins}} \left[n_i \ln\left(\frac{n_i}{\nu_i}\right) + \nu_i - n_i \right] \quad (\text{III.C.16})$$

where ν_i is the expected number of events in bin i for the SM signal plus background, and n_i is the number of events in bin i for the SM signal scaled by factor r (signal $\times r$) plus

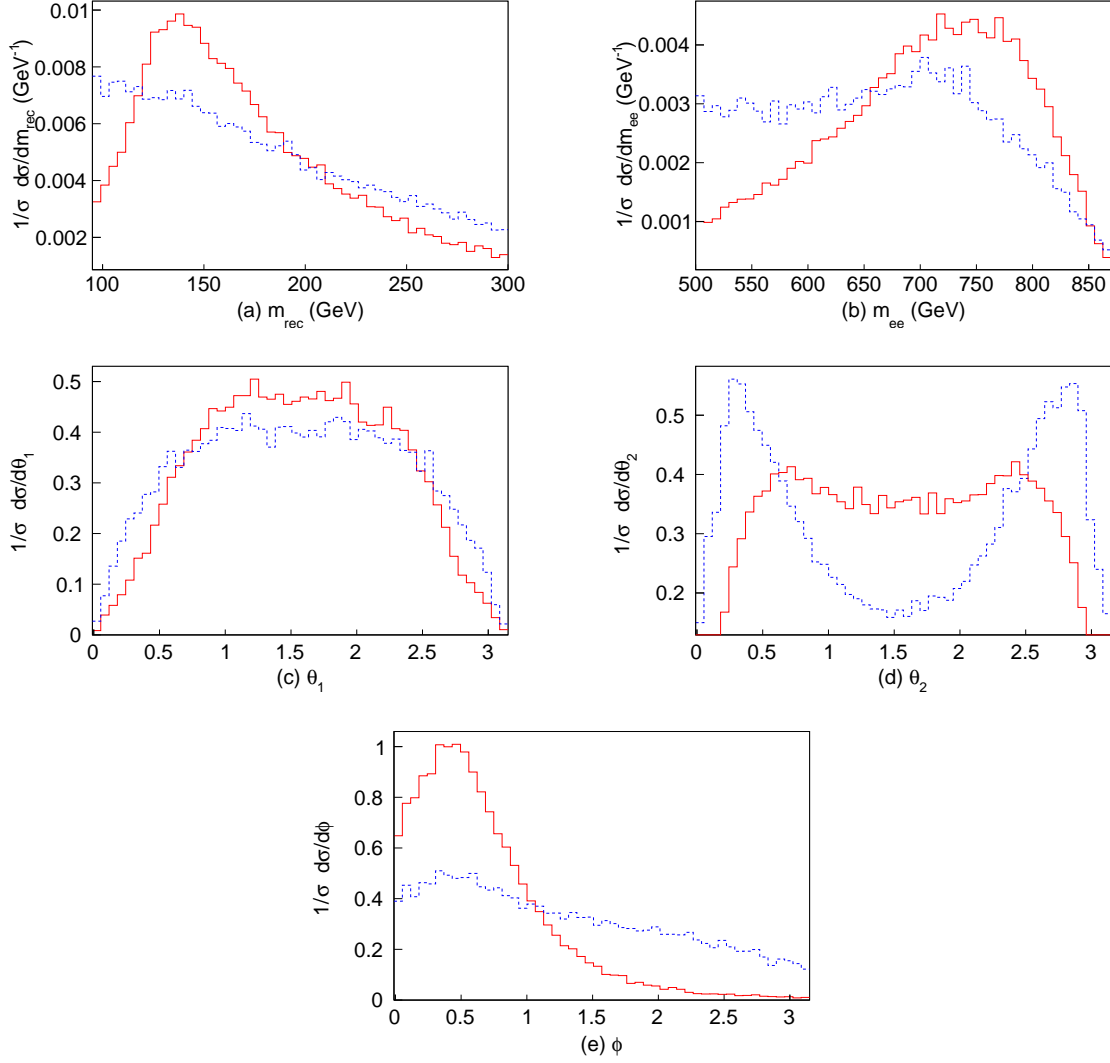


Figure III.10: Comparison of signal (solid red) and total background (dashed blue) distributions for variables m_{rec} , m_{ee} , θ_1 , θ_2 and ϕ at $\sqrt{s} = 1$ TeV. Cut1 in Table III.11 is applied. For clarity, both signal and background distributions are normalized to unity.

Table III.12: Cross sections for signal and background processes at ILC 1 TeV with 1000 fb^{-1} of integrated luminosity.

Process	Generator Level (fb)	Cut1(fb)	Cut2(fb)
$ee \rightarrow eeh(\text{Signal})$	24.1	8.18	7.52
$ee \rightarrow ee\nu_e\nu_e$	978	31.5	17.2
$ee \rightarrow ee\nu_{\mu,\tau}\nu_{\mu,\tau}$	93.9	3.24	1.64
$ee \rightarrow eeqq$	2830	24.1	13.6
$ee \rightarrow eell$	6690	13.7	10.8
$ee \rightarrow ee\gamma\gamma$	3180	2.68	1.10
$ee \rightarrow ee\gamma$	175000	4.73	2.28
Total Background	189000	80.0	46.6
$\delta\sigma/\sigma$	-	3.6%	3.1%

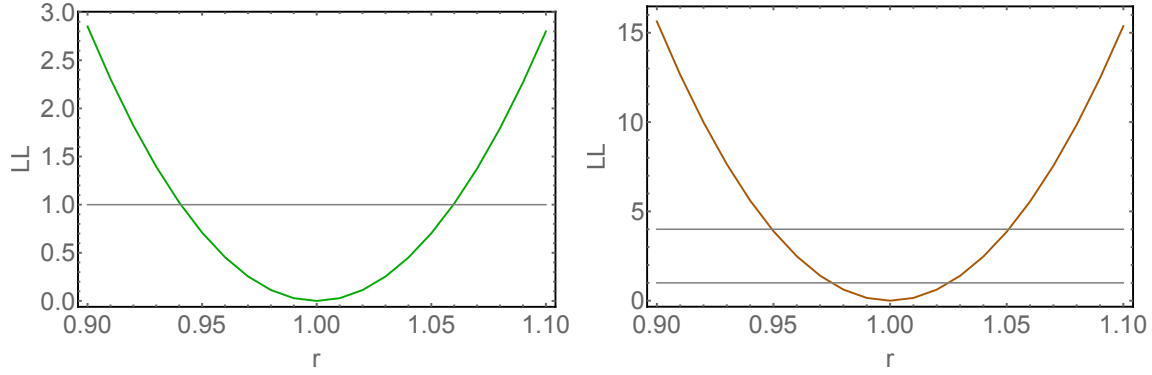


Figure III.11: 5-dimensional Log-likelihood as a function of the relative cross section r defined below Eq. (III.C.16) for (*left panel*): 500 GeV case and (*right panel*): 1 TeV case. For both analyses, Cut1 is applied.

background. We evaluate the region around $r = 1$ and our 1σ deviation from the Standard Model value corresponds to $\Delta LL = 1$.

Rather than applying Cut2 on the angular distributions, we apply Cut1 and evaluate the Log-likelihood in the five dimensional phase space defined by the variables m_{rec} , m_{ee} , θ_1 , θ_2 , and ϕ . In the analysis, we perform a 3125-bin analysis by dividing the phase space along each variable evenly into five bins. Figure III.11 shows the Log-likelihood as a function of r . In the 500 GeV analysis, we find the sensitivity on signal cross section improved to 6.0%. For the 1 TeV case, the multivariate analysis increases the sensitivity to 2.5%. The likelihood profile for the 500 GeV (1 TeV) case is shown in the left (right) panel of Fig. III.11.

2. Impact on Higgs Physics

a. Higgs Width and Coupling Fits Based on our results, the sensitivities on σ_z^{inc} which can be reached by studying the ZZ fusion channel at 500 GeV and 1 TeV ILC are 6.0% (8.2%) and 2.5% (3.1%) based upon MVA (cut-based) analyses, respectively. In combination this yields a 2.3% (2.9%) combined uncertainty on σ_z^{inc} from this production mode.

This is comparable to the current estimated precision of the ILC from studies [185] of Zh associate production. That is, σ_z^{inc} of 2.0% achieved by combining 2.6% and 3.0% uncertainties from 250 GeV and 500 GeV [498]). Thus, by combining the ZZ fusion and Zh measurements we estimate a final sensitivity σ_z^{inc} to 1.5%, a 25% improvement over the Zh channel alone. This improvement refines many other derived quantities in the model-independent fit. We demonstrate the improvement for a few representative quantities in Table III.13. We have performed a global 10-parameter model-independent fit following Ref. [182]. We compute sensitivities for the ILC alone and in combination with projected HL(High Luminosity)-LHC results. We take the optimistic projections for HL-LHC precision on cross sections from the CMS detector based on Ref. [196]. As discussed in detail in Ref. [182], twice the error of σ_z^{inc} propagates into the Γ_{tot} determination and this error dominates for stages beyond the 250 GeV phase of the ILC. Our study at the ILC 250+500+1000 stage relatively improves the total width precision by 16%, Higgs to ZZ coupling by 25%, Higgs to WW coupling by 16%, and Higgs to $b\bar{b}$ coupling by 8%. For other couplings with less precision the σ_z^{inc} is not

Table III.13: The improvement on selected coupling precisions by incorporating our ZZ fusion analysis from a typical 10-parameter model-independent fit. We show both the ILC exclusive results and ILC combined with the optimistic CMS HL-LHC input [196]. For details of fitting scheme and combination scheme, see Ref. [182]. The results for ILC 250/500/1000 (GeV) assume 250/500/1000 fb^{-1} integrated luminosities.

Relative Error %	ILC 250+500		ILC 250+500+1000	
$\delta\sigma_{Zh}$	6.0%		2.5%	
Improvement		with HL-LHC		with HL-LHC
Γ	$4.8 \rightarrow 4.7$	$4.8 \rightarrow 4.6$	$4.5 \rightarrow 3.7$	$4.5 \rightarrow 3.7$
g_Z	$0.99 \rightarrow 0.94$	$0.99 \rightarrow 0.94$	$0.98 \rightarrow 0.75$	$0.98 \rightarrow 0.75$
g_W	$1.1 \rightarrow 1.1$	$1.1 \rightarrow 1.1$	$1.1 \rightarrow 0.89$	$1.1 \rightarrow 0.88$
g_b	$1.5 \rightarrow 1.5$	$1.5 \rightarrow 1.5$	$1.3 \rightarrow 1.2$	$1.3 \rightarrow 1.1$

the largest source of uncertainty and less improvement is expected.

b. Operator Analysis New physics beyond the Standard Model (BSM) could give rise to modifications of the Higgs couplings. The proper framework to describe such possibilities in a model-independent manner is the effective field theory (EFT) approach. With respect to the SM gauge symmetry, such effects are expressed by dimension-six Higgs operators after integrating out heavy particles or loop functions [507–510].⁹ The operators modifying Higgs to ZZ couplings are naturally of particular interest in our case. This is partly because it will be one of the most precisely determined quantities through a recoil-mass measurement and partly because it is one of the key couplings that could help reveal the underlying dynamics of electroweak symmetry breaking. Certain operators may have different momentum-dependence and thus measurements of differential cross sections may be more sensitive to the new effects.¹⁰ The ILC is expected to have several operational stages with different center of mass energies, and the high precision measurement achievable from ZZ fusion will contribute to our knowledge of these different operators.¹¹

To demonstrate this important feature, we consider the following two representative operators

$$\mathcal{O}_H = \partial^\mu(\phi^\dagger\phi)\partial_\mu(\phi^\dagger\phi), \quad \mathcal{O}_{HB} = g'D^\mu\phi^\dagger D^\nu\phi B_{\mu\nu}, \quad (\text{III.C.17})$$

with

$$\mathcal{L}^{dim-6} \supset \frac{c_H}{2\Lambda^2}\mathcal{O}_H + \frac{c_{HB}}{\Lambda^2}\mathcal{O}_{HB}, \quad (\text{III.C.18})$$

where ϕ is the SM $SU(2)_L$ doublet and Λ is the new physics scale. The coefficients c_H and c_{HB} are generically of order unity. Following the convention for comparison with existing studies [510, 513–517], we adopt the scaled coefficients $\bar{c}_H = \frac{v^2}{\Lambda^2}c_H$ and $\bar{c}_{HB} = \frac{m_W^2}{\Lambda^2}c_{HB}$. This translates to generic values of $\bar{c}_H \approx 0.06$ and $\bar{c}_{HB} \approx 0.006$ for $\Lambda = 1$ TeV.

The operator \mathcal{O}_H modifies the Higgs- ZZ coupling in a momentum-independent way at lowest order. This operator renormalizes the Higgs kinetic term and thus modifies the Higgs

⁹For recent reviews of these operators, see e.g., Refs. [438, 511–513]. Many of these operators not only contribute to Higgs physics, but also modify EW precision tests simultaneously [514–517].

¹⁰For discussions of the effects on Higgs decays due to these operators, see Ref. [518].

¹¹Assuming existence of a single operator at a time, limits can be derived, see e.g. [519].

coupling to any particles universally [520, 521]. Equivalently, one may think of rescaling the standard model coupling constant. In contrast, the operator \mathcal{O}_{HB} generates a momentum-dependent Higgs- ZZ coupling. This leads to a larger variation of the production rate versus c.m. energy for the Zh process than the ZZ fusion because of the energy difference in the intermediate Z bosons. Consequently, the corresponding deviations of the cross sections are approximately,

$$\begin{aligned}
\text{ILC 250 GeV : } \quad \frac{\Delta\sigma}{\sigma}(Zh) &\approx -\bar{c}_H - 4.5 \bar{c}_{HB}, \\
\text{ILC 500 GeV : } \quad \frac{\Delta\sigma}{\sigma}(Zh) &\approx -\bar{c}_H - 25 \bar{c}_{HB}, \\
&\quad \frac{\Delta\sigma}{\sigma}(e^-e^+h) \approx -\bar{c}_H + 1.1 \bar{c}_{HB}, \\
\text{ILC 1 TeV : } \quad \frac{\Delta\sigma}{\sigma}(e^-e^+h) &\approx -\bar{c}_H + 2.4 \bar{c}_{HB}.
\end{aligned} \tag{III.C.19}$$

Such operators receive direct constraints from the LHC from similar production processes [514, 515], off-shell Higgs to ZZ measurement [522], etc., all of which lack desirable sensitivities due to the challenging hadron collider environment. Based on an analysis of current data the coefficient \bar{c}_{HB} is excluded for values outside the window $(-0.045, 0.075)$ ¹² and \bar{c}_H is far less constrained [514, 515].

We only list above the cross sections which can be precisely measured at different ILC stages, with corresponding polarizations taken into account. The distinction between ZZ fusion(e^-e^+h) and Zh -associated production with Z decaying to electron-positron pairs is easily made by applying a minimal m_{ee} cut above m_Z .

In Fig. III.12 we plot the expected constraints on the constants \bar{c}_H and \bar{c}_{HB} from the Zh and ZZ processes measured at the ILC, assuming only these two constants among the six-dimensional terms are non-zero. We show the 95% C.L. contours for different measurements. The dashed(dot-dashed) blue line represents the contour from Zh -associated measurement at ILC 250 GeV(500 GeV). The red line represents the contour from combined ZZ fusion measurements at ILC 500 GeV and 1 TeV. One can see that at a given energy for a simple production mode only a linear combination of the two operators is constrained, resulting

¹²The window is $(-0.053, 0.044)$ for single operator analysis. This smallness of the difference between the marginalized analysis and single operator analysis illustrates that this operator mainly affects Higgs physics and thus other electroweak precision observables do not provide much information.

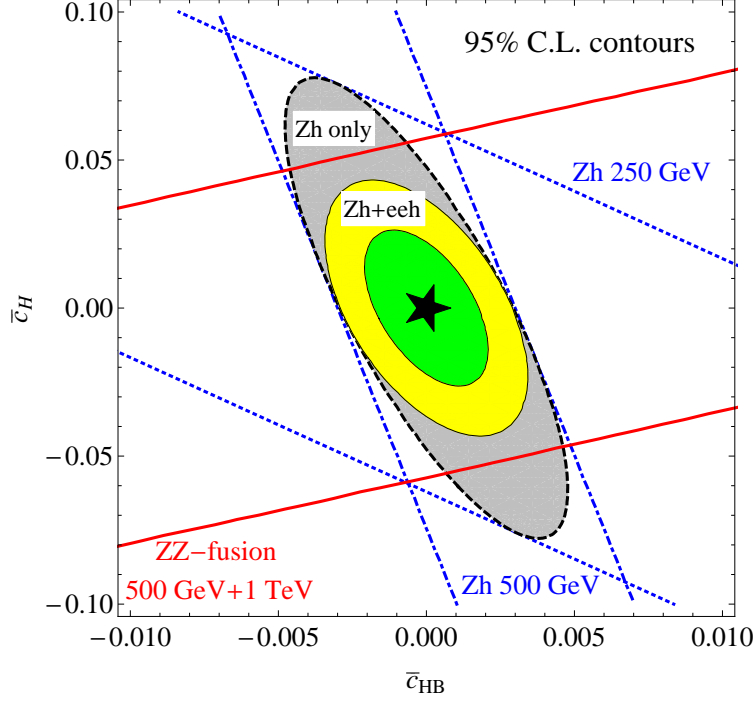


Figure III.12: Constraints on coefficients of dimension-six operators \bar{c}_H and \bar{c}_{HB} with and without the inclusion of ZZ fusion channel. The dashed and dot-dashed lines represent 2σ deviations from zero in the Zh channel at 250 and 500 GeV (blue lines), respectively. The solid (red) lines indicates the constraint from ZZ fusion for 500 GeV plus 1 TeV. The outer (black-dashed) contour shows the constraint from combined Zh measurements and the middle (yellow) and inner (green) contours show the combined 2σ and 1σ results with ZZ fusion included.

in a flat-direction in the contours. However, measurements of Zh at two different energies would allow us to measure both simultaneously, as shown in the gray contour. Moreover, the addition of the ZZ information at 1 TeV would offer *significant* improvements as shown in the yellow contour. This allows us to measure \bar{c}_H and \bar{c}_{HB} at the level of 0.04 and 0.004 respectively. Much of the improvement comes from the fact that in ZZ fusion, in contrast to Zh -associate production, the \mathcal{O}_{HB} operator contributes with opposite sign of \mathcal{O}_H operator. We note here such indirect measurements would strongly constrain BSM physics which are otherwise difficult to test, such as singlet-Higgs assisted baryogenesis [523], “neutral naturalness” [521, 524, 525], etc.

3. Summary and Outlook

To summarize, the ZZ fusion channel for Higgs measurement could provide valuable information for precision studies of the Higgs width and couplings because of the logarithmic increase of the total cross section versus the center of mass energy. Although the signal suffers from large radiation induced smearing at high energies it can be observed with good precision at a 1 TeV run and benefits from a multi-variate analysis. We have also demonstrated the sensitivity to probe higher-dimensional operators at the ILC, which are usually not covered by conventional global fits. We find:

- The inclusive cross section of the ZZ fusion channel can be measured to 2.5% at 1 TeV. This is competitive with the best estimate of Higgsstrahlung measurement at 250 GeV, as shown in Sec. III.C.1.c and Sec. III.C.1.d.
- Combing the ZZ fusion and Higgsstrahlung channels, the model-independent measurement of the inclusive cross section can be improved to 1.5% with a commensurate improvement of the Higgs width determination, as shown in Sec. III.C.2.a.
- Sensitivities on the inclusive cross section σ_Z^{inc} at multiple energies also offers the possibility to distinguish contributions from different higher-dimensional operators induced by BSM physics. We demonstrate the ability to simultaneously constrain two operators whose effects are difficult to observe at the LHC, as shown in Sec. III.C.2.b. Including the ZZ fusion channel provides as large as 50% relative improvement for the constraint on the

chosen operators compared to the Zh -associated production channel alone.

In the preceding analysis and discussion, we have shown the appreciable impact of including the ZZ fusion channel at the ILC for Higgs physics. Full detector simulations may be desirable to further the study of this signal mode.

D. HIGGS WIDTH AND COUPLINGS AT THE CEPC

Table III.14: Estimated precisions of Higgs boson property measurements at the CEPC. All the numbers refer to relative precision except for M_H and $\text{BR}(H \rightarrow \text{inv})$ for which ΔM_H and 95% CL upper limit are quoted respectively.

ΔM_H	Γ_H	$\sigma(ZH)$	$\sigma(\nu\nu H) \times \text{BR}(H \rightarrow b\bar{b})$
5.5 MeV	2.8%	0.51%	2.8%

Decay mode	$\sigma(ZH) \times \text{BR}$	BR
$H \rightarrow b\bar{b}$	0.28%	0.58%
$H \rightarrow c\bar{c}$	2.2%	2.3%
$H \rightarrow g\bar{g}$	1.6%	1.7%
$H \rightarrow \tau\tau$	1.2%	1.3%
$H \rightarrow W\bar{W}$	1.5%	1.6%
$H \rightarrow Z\bar{Z}$	4.3%	4.3%
$H \rightarrow \gamma\gamma$	9.0%	9.0%
$H \rightarrow \mu\mu$	17%	17%
$H \rightarrow \text{inv}$	0.28%	0.28%

Table III.14 summarizes the estimated precisions of Higgs property measurements discussed in this section. For the leading Higgs boson decay modes, namely $b\bar{b}$, $c\bar{c}$, $g\bar{g}$, $W\bar{W}$,

ZZ and $\tau\tau$, percent level precisions are expected. As it has been discussed this level of precision is required to attain sensitivity to many beyond SM physics scenarios.

All $\sigma \times \text{BR}$ measurements results are based on simple counting experiments. The best achievable statistical uncertainties for 5 ab^{-1} are 0.25% for $\sigma(e^+e^- \rightarrow ZH) \times \text{BR}(H \rightarrow b\bar{b})$ and 0.5% for $\sigma(e^+e^- \rightarrow ZH)$. Even for these measurements, statistics will be the dominant source of uncertainties. Systematic uncertainties from the efficiency/acceptance of the detector, the luminosity and the beam energy determination are expected to be small. The integrated luminosity can be measured with a 0.1% precision, a benchmark already achieved at LEP [526], and can be potentially improved in the future. The center-of-mass energy will be known better than 1 MeV, resulting negligible uncertainties on the theoretical cross section predictions and experimental recoil mass measurements. In summary, all aforementioned measurements will have uncertainties that are statistically dominated at CEPC.

In order to extract the implications of the predicted measurement precision shown in Table III.14 on possible new physics models, constraints on additional contributions to Higgs couplings are derived. The Standard Model makes specific predictions for the Higgs couplings to the SM fermions, $g(hff; \text{SM})$, and to the SM gauge bosons $g(hVV; \text{SM})$ ¹³. The deviation from the Standard Model couplings will be parameterized using:

$$\kappa_f = \frac{g(hff)}{g(hff; \text{SM})}, \quad \kappa_V = \frac{g(hVV)}{g(hVV; \text{SM})} \quad (\text{III.D.20})$$

In addition to couplings which are present at tree level, the Standard Model also predicts effective couplings $h\gamma\gamma$ and hgg , in terms of other SM parameters. Change can be induced by the possible shifts in the Higgs couplings described above. In addition, they can also be altered by loop contributions from new physics states. Hence, they will be introduced as two independent couplings, with their ratios to the SM predictions denoted as κ_γ and κ_g .

Furthermore, it is possible that the Higgs can decay directly into new physics particles. In this case, two type of new decay channels will be distinguished:

I. Invisible decay. This is a specific channel in which Higgs decay into invisible particles.

This can be searched for and, if detected, measured.

¹³For the discussion of coupling fits and their implications, " h " is used to denote the 125 GeV Higgs boson.

II. Exotic decay. This includes all the other new physics channels. Whether they can be observed, and, if so, to what precision, depends sensitively on the particular final states. In one extreme, they can be very distinct and can be measured very well. In another extreme, they can be in a form which is completely swamped by the background. Whether postulating a precision for the measurement of the exotic decay or treating it as an independent parameter (essentially assuming it can not be measured directly) is an assumption one has to make. Results in both cases will be presented. In the later case, it is common to use the total width Γ_h as an equivalent free parameter.

In general, possible deviations of all Standard Model Higgs couplings should be considered. However, in the absence of obvious light new physics states with large couplings to the Higgs boson and other SM particles, a very large deviation ($> \mathcal{O}(1)$) is unlikely. In the case of smaller deviations, the Higgs boson phenomenology will not be sensitive to the deviations κ_e , κ_u , κ_d and κ_s . Therefore, they will not be considered here.

CEPC will not be able to directly measure the Higgs coupling to top quarks. A deviation of this coupling from its SM value does enter $h\gamma\gamma$ and hgg amplitudes. However, this can be viewed as parameterized by κ_γ and κ_g already. Therefore, there will be no attempt to include κ_t as an independent parameter. In summary of the previous discussions, the following set of 10 independent parameters is considered:

$$\kappa_b, \kappa_c, \kappa_\tau, \kappa_\mu, \kappa_Z, \kappa_W, \kappa_\gamma, \kappa_g, \text{BR}_{\text{inv}}, \Gamma_h. \quad (\text{III.D.21})$$

In this 10 parameter list, the relation $\sum_i \Gamma_i = \Gamma_h$ is used to replace the exotic decay branching ratio with the total width.

Several assumptions can be made that can lead to a reduced number of parameters (see also [165, 180]). For instance a 9 parameter fit can be defined assuming lepton universality:

$$\kappa_b, \kappa_c, \kappa_\tau = \kappa_\mu, \kappa_Z, \kappa_W, \kappa_\gamma, \kappa_g, \text{BR}_{\text{inv}}, \Gamma_h. \quad (\text{III.D.22})$$

This can be further reduced to 7 parameters, by assuming the absence of exotic and invisible decays (excluding $h \rightarrow ZZ \rightarrow \nu\nu\nu\nu$) [180, 196]:

$$\kappa_b, \kappa_c, \kappa_\tau = \kappa_\mu, \kappa_Z, \kappa_W, \kappa_\gamma, \kappa_g. \quad (\text{III.D.23})$$

In addition to the previously mentioned assumptions, which reduce the number of parameters, there are also several classes of parameter space constraining assumptions, which can be combined in various ways with the former. These assumptions could also lead to possible extraction of coupling strengths from the LHC and enhancement of coupling precision projections for lepton colliders in a more model dependent manner. One such example is to assume $\kappa_W, \kappa_Z \leq 1$ [170, 172]. This assumption on the κ_V ratios is valid on a large class of Higgs sector extensions, including MSSM, 2HDM, NMSSM, etc. [527].

We remark here on the rational of considering a variety of fits with different assumptions. Different fits achieve different goals. In practice, the relative usefulness of them depends on the scenario and the goal. For example, in a specific and complete model, the Higgs couplings can be determined by a smaller number of more fundamental parameters. This leads to relations among the Higgs couplings. One can set the strongest limit by taking full advantage of these relations. Deviations produced by such an underlying model can be detected most sensitively in a such constrained fit. On the other extreme, model independent fit gives a model independent limit on the broadest possible model space. It helps to capture deviations that can be missed by a constrained fit. At the same time, it produces the weakest limits. In practice, it is likely something in between these two extremes that will be the most useful. As it was previously mentioned, there are many ways of imposing constraints. Even stronger ones then discussed above can be considered. However, the purpose of this note is not to access the reach in all possible models, which is an impossible task. We are aiming at giving an overall picture of the capability of CEPC. Similar problems have been encountered in all previous studies of Higgs factories. A relatively common set of assumptions have been used as benchmarks, such as the ones discussed above. Therefore, for comparison purpose, we will focus on a 10-parameter model independent fit, and 7-parameter constrained fit recommended by the LHC Higgs cross section group [180].

The LHC and especially the HL-LHC will provide valuable and complementary information about the Higgs boson properties. For example, the LHC is capable of directly measuring the top Yukawa coupling through the $t\bar{t}h$ process [167, 168]. In addition, the LHC could use differential cross sections to differentiate top-loop contributions and other heavy particle-loop contributions to the Higgs to gluon coupling [528–531], and similarly

to separate the dimension-four and dimension-six (with higher momentum dependence) operator contributions to the Higgs to vector boson couplings [514]. For the purpose of the coupling fit in our framework, the LHC with its large statistics, helps improving precision on rare processes such as Higgs to diphoton couplings. Note that a large portion of the systematics intrinsic to a hadron collider would be cancelled by taking ratios of measured cross sections. For example, combining the ratio of the rates $pp \rightarrow h \rightarrow \gamma\gamma$ and $pp \rightarrow h \rightarrow ZZ^*$ and the measurement of hZZ coupling at the CEPC can significantly improve the measurement of κ_γ . These are the most useful inputs from the LHC to combine with CEPC. Similar studies with the ILC can be found in Refs. [182, 490, 532].

The 10-parameter fit and the 7-parameter fit for several integrated luminosities are shown in Tables III.15 and III.16, respectively. In addition, the combinations with expectations (with theoretical uncertainties included) from HL-LHC from Ref. [533] are shown in the same tables as well.¹⁴ We assume HL-LHC will operate at 14 TeV center-of-mass energy and accumulate an integrated luminosity of 3000 fb⁻¹.

The CEPC Higgs properties measurements mark a giant step beyond the HL-LHC. First of all, in contrast to the LHC, a lepton collider Higgs factory is capable of measuring the absolute width and coupling strengths of the Higgs boson. A comparison with the HL-LHC is only possible with model dependent assumptions. One of such comparison is within the framework of a 7-parameter fit, shown in Fig. III.13. Even with this set of restrictive assumptions, the advantage of the CEPC is still significant. The measurement of κ_Z is more than a factor 10 better. The CEPC can also improve significantly on a set of channels which suffers from large background at the LHC, such as κ_b , κ_c , and κ_g . We emphasize that this is comparing with the HL-LHC projection with aggressive assumptions about systematics. Such uncertainties are typically under much better control at lepton colliders. Within this 7 parameter set, the only coupling which HL-LHC can give a competitive measurement is κ_γ , for which the CEPC's accuracy is limited by statistics. This is also the most valuable input that the HL-LHC can give to the Higgs coupling measurement at the CEPC, which underlines the importance of combining the results of these two facilities.

¹⁴We note here that LHC and CEPC have different sources of theoretical uncertainties, for detailed discussion, see Refs. [165, 196, 534–536].

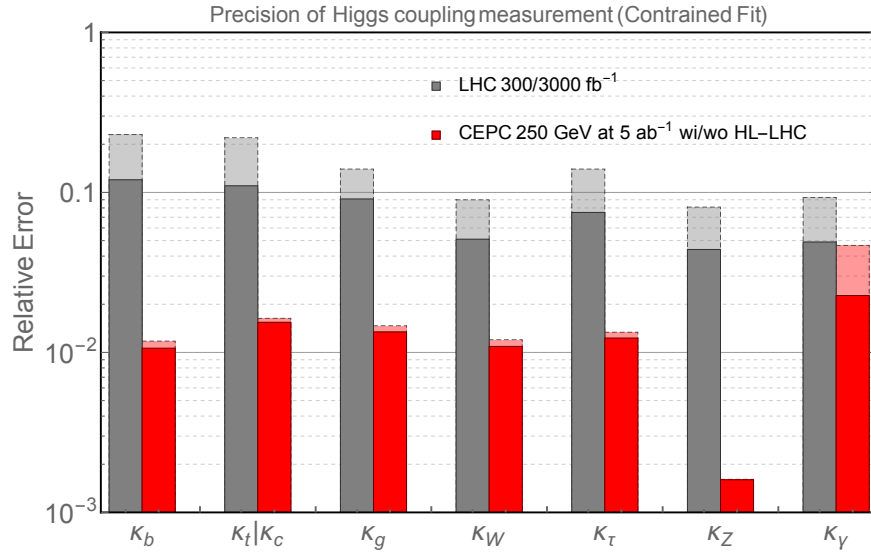


Figure III.13: The 7 parameter fit result, and comparison with the HL-LHC. The projections for CEPC at 250 GeV with 5 ab^{-1} integrated luminosity are shown. The CEPC results without combination with HL-LHC input are shown with dashed edges. The LHC projections for an integrated luminosity of 300 fb^{-1} are shown in dashed edges.

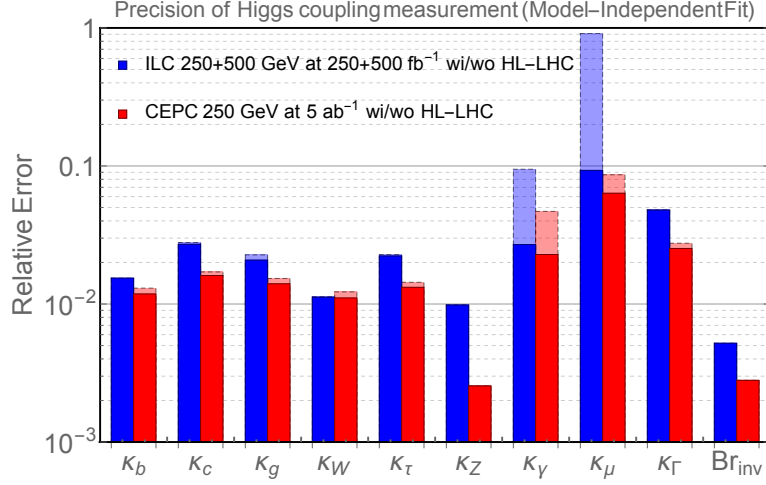


Figure III.14: The 10 parameter fit result and comparison with the ILC. The CEPC at 250 GeV with 5 ab^{-1} integrated luminosity and the ILC 250+500 GeV at 250+500 fb^{-1} are shown. The CEPC and ILC result without combination with HL-LHC input as shown in dashed edges.

We also remark on the couplings which are left out in this fit. The most obvious omission is the BR_{inv} . The CEPC with 5 ab^{-1} can measure this to a high accuracy of 0.25%, as shown in Table III.15. At the same time, the HL-LHC can only manage a much lower accuracy 6 – 17% [196].

As we have discussed above, one of the greatest advantages of lepton collider Higgs factory is the capability of determining the Higgs coupling *model independently*. The projection of such a determination at the CEPC is shown in Fig. III.14. For comparison, we have also put in the projection from the combination ILC 250 GeV and 500 GeV runs, based on the baseline designed luminosities. The advantage of the higher integrated luminosity at a circular lepton collider is apparent. The CEPC has a clear advantage in the measure of κ_Z . It is also much stronger in κ_μ and BR_{inv} measurements.

Table III.15: Coupling measurement precision in percent from the 10 parameter fit described in the text for several benchmark integrated luminosity of CEPC, and corresponding results after combination with the HL-LHC. All the numbers refer to are relative precision except for BR_{inv} for which 95% CL upper limit are quoted respectively.

	CEPC				CEPC+HL-LHC			
Luminosity (ab^{-1})	0.5	2	5	10	0.5	2	5	10
Γ_h	8.7	4.4	2.8	1.9	6.2	3.7	2.5	1.8
κ_b	4.1	2.1	1.3	0.92	2.8	1.7	1.2	0.87
κ_c	5.4	2.7	1.7	1.2	4.2	2.4	1.6	1.2
κ_g	4.8	2.4	1.5	1.1	3.2	2.0	1.4	1.0
κ_W	3.9	1.9	1.2	0.87	2.4	1.6	1.1	0.82
κ_τ	4.5	2.3	1.4	1.0	3.2	1.9	1.3	0.97
κ_Z	0.81	0.40	0.26	0.18	0.81	0.40	0.26	0.18
κ_γ	15	7.4	4.7	3.3	2.7	2.5	2.3	2.0
κ_μ	28	14	8.6	6.1	8.9	7.7	6.3	5.1
BR_{inv}	0.88	0.44	0.28	0.20	0.88	0.44	0.28	0.20

Table III.16: Coupling measurement precision in percent from the 7 parameter fit described in the text for several benchmark integrated luminosity of CEPC, and corresponding results after combination with the HL-LHC.

	CEPC				CEPC+HL-LHC			
Luminosity (ab^{-1})	0.5	2	5	10	0.5	2	5	10
κ_b	3.7	1.9	1.2	0.83	2.3	1.5	1.1	0.78
κ_c	5.1	3.2	1.6	1.2	4.0	2.3	1.5	1.1
κ_g	4.7	2.3	1.5	1.0	2.9	1.9	1.3	0.99
κ_W	3.8	1.9	1.2	0.84	2.3	1.6	1.1	0.80
κ_T	4.2	2.1	1.3	0.94	2.9	1.8	1.2	0.90
κ_Z	0.51	0.25	0.16	0.11	0.49	0.25	0.16	0.11
κ_γ	15	7.4	4.7	3.3	2.6	2.5	2.3	2.0

IV. BSM PHYSICS AT VLHC AND MUON COLLIDER

A. ELECTROWEAK RESONANCES AT VLHC

Typical Z' models with electroweak couplings should be observable¹ at the LHC as resonances in the dilepton channels for masses up to $\sim 4\text{--}5$ TeV for $\sqrt{s} = 14$ TeV and an integrated luminosity of 100 fb^{-1} . There have been extensive studies of diagnostic possibilities² of the Z' couplings at the LHC utilizing the cross sections

$$\sigma^f \equiv \sigma[f\bar{f}] \equiv \sigma_{pp \rightarrow Z' \rightarrow f\bar{f}} = \sigma_{Z'} B(Z' \rightarrow f\bar{f}) \quad (\text{IV.A.1})$$

for decays into the final state $f\bar{f}$ for $f = \ell, \tau, t, b$ (with $\ell = e, \mu$), as well as forward-backward or charge asymmetries, rapidity distributions, and possible final state polarizations for $\tau^-\tau^+$ or $t\bar{t}$. Other possible probes include $\Gamma_{Z'}$ from the lineshape, and various rare decay modes and associated productions.

We can classify them into three classes:

- Cross sections, such as $\sigma^\ell, \sigma^b, \sigma^t, \sigma^j$ (including line shape of the invariant mass)³;
- Forward-backward (charge) asymmetries, such as $A_{\ell^+\ell^-}^{FB}, A_{t\bar{t}}^{FB}$;
- Radiations, especially W -boson radiations, such as $\sigma_{\ell^+\ell^-W^\pm}^F, \sigma_{\ell^+\ell^-W^\pm}^B, \sigma_{b\bar{b}W^\pm}$, etc.

To gain a sense of what might be achievable at the VLHC, we show the total cross section σ and leptonic cross section of the benchmark models in Fig. IV.8 for three different energies of proton-proton collider. We use two cyan lines in the lower plot to show the Z' discovery

¹The reach is reduced if the dilepton branching ratios are significantly reduced due to BSM decay channels [27, 28].

²See, for example, [27, 28, 220–239]. Other studies are reviewed in [17, 19, 23].

³In presence of $Z - Z'$ mixing, new modes such as $\sigma_{W^+W^-}^{Z'}$ and $\sigma_{Zh}^{Z'}$ are also possible.

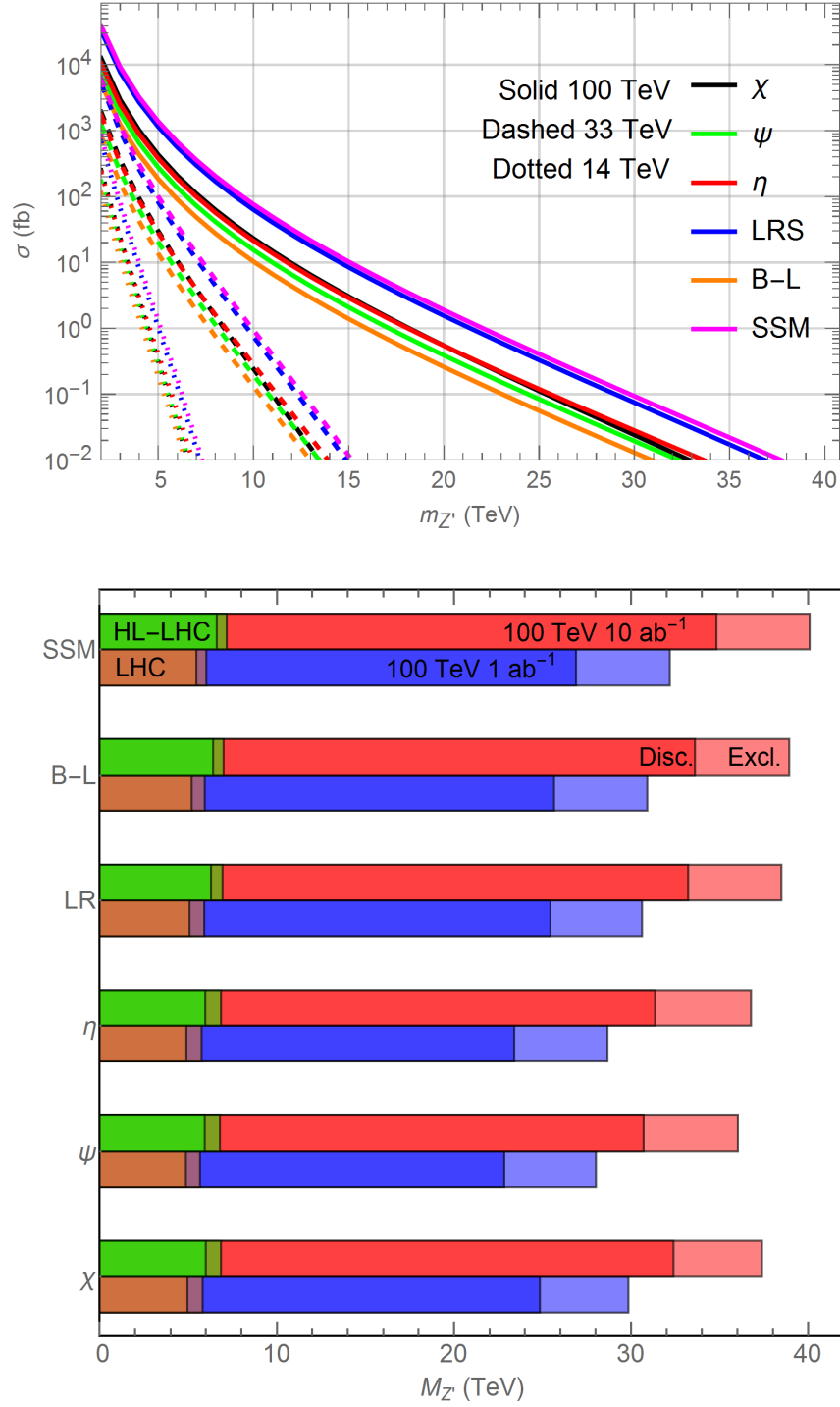


Figure IV.1: Top panel: the production cross sections for benchmark Z' 's for pp collider at 14, 33, and 100 TeV. Bottom panel: the discovery and exclusion reaches of Z' for VLHC 100 TeV at 1 ab^{-1} (blue) and 10 ab^{-1} (red) and LHC 14 TeV at 300 fb^{-1} (orange) and 3000 fb^{-1} (green) through dilepton (e, μ) channels.

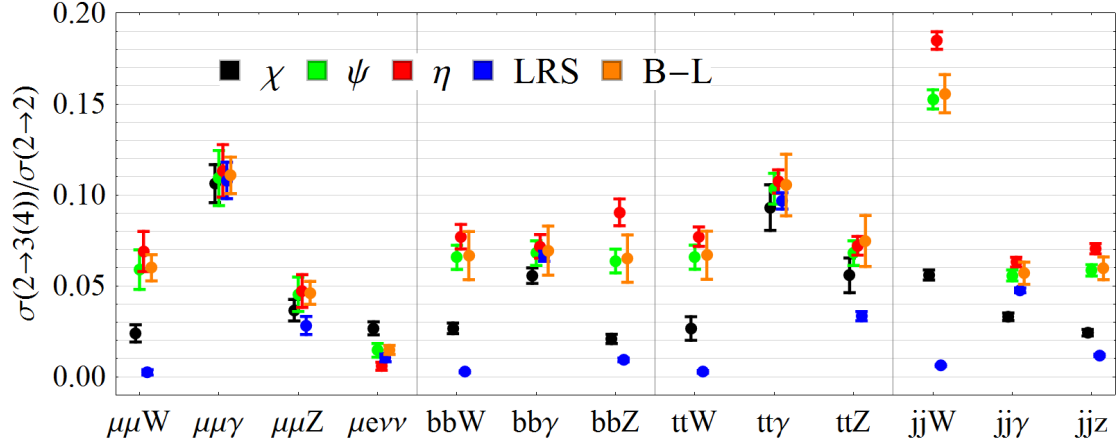


Figure IV.2: The ratios of the $2 \rightarrow 3(4)$ process cross sections over corresponding $2 \rightarrow 2$ process cross sections. The 68% C.L. error bars account for signal statistical uncertainties only, assuming 1 ab^{-1} integrated luminosity. This figure is to show what maximal amount of Z' information we may learn from weak boson radiations.

and exclusion with combining the clean leptonic modes σ^μ and σ^e . We can see that at 1 ab^{-1} the 100 TeV VLHC could discover (exclude) up to $24 \sim 29$ ($30 \sim 34$) TeV Z' for various benchmark models. As for our benchmark of 10 TeV Z' , total cross section are around $1 \sim 10 \text{ fb}$, and the leptonic cross sections are of the order hundreds of ab at 100 TeV VLHC. This implies large statistics are achievable and observables such as forward-backward asymmetry could be obtained with good precision.

Each cross section is a measure of the product of production vertex couplings and decay vertex couplings over the total width. Denoting the subprocesses with their production and decay chiral couplings, LL and RR types contribute to the forward leptons, and LR and RL types contribute to the backward leptons. Forward and backward leptons/anti-lepton obey $1 + \cos\theta^2$ and $1 - \cos\theta^2$ angular distribution in the Z' C.M. frame with respect to the quark/anti-quark direction, respectively.

To optimize what we can learn about the Z' from the VLHC, we consider utilizing the radiations from initial and final states. Because Z' is an $SU(3)$ singlet, the gluon radiation

from initial and final state provide no diagnostic power on the couplings. Consequently we consider electroweak gauge boson radiations only, namely W -boson, Z -boson and photon. We show the ratio of the cross section of Z' production with radiation over that of corresponding Z' mode in Fig. IV.2. These ratios for radiations from $pp \rightarrow Z' \rightarrow \mu^- \mu^+, b\bar{b}, t\bar{t}$ and $j\bar{j}$. We associate statistical uncertainties to these ratios with error bars assuming 1 ab^{-1} integrated luminosity. We note here that we have not consider any specific decay modes of the radiated gauge boson. Neither do we include any uncertainties in the background in this illustrative figure. In this sense, what we are showing are what we may maximally learn from these possible radiations.

The W -boson radiation is of most interest because it can naturally act as a polarization tagger; only left-handed fermions radiates W -boson and all fermions can be approximately viewed as massless at such high energy. Consequently, the forward lepton mode with initial state W -boson radiation (ISR- W) corresponds to LL subprocess ($\sigma_{\ell^+\ell^-W^\pm}^F$) and backward lepton mode with W -boson radiation corresponds to LR subprocess ($\sigma_{\ell^+\ell^-W^\pm}^B$). The sum of LL and LR is shown in the $\mu\mu W$ ratio in Fig. IV.2. Final State W -boson Radiation (FSR- W) in leptonic Z' decay modes are indicated by $\mu e \nu \bar{\nu}$. For hadronic decay modes, $b\bar{b}W$ and $t\bar{t}W$ are ISR- W only while $j\bar{j}W$ includes both ISR- W , FSR- W and their interference. This cause the ratio of $j\bar{j}W$ are higher than both $t\bar{t}W$ and $b\bar{b}W$. We note that throughout this section, unless specified, we still use the convention of j representing light quark u, d, c, s and gluon jets assuming b tagging and t tagging are available at VLHC .

The Z -boson and photon radiations also potentially provide some diagnostic power. The Z -boson diagnostic power comes from its different couplings to left chiral and right chiral fermions. Clearly, this would be weaker than that of W -boson radiations from its nature of maximal parity violation. The photon radiation diagnostic power comes from different electric charges of up-type quark, down-type quarks and leptons and for this reason is expected not to be strong. Moreover, the Z -boson radiation and photon radiation are a combined effect of ISR, FSR and interference.

One might also consider these additional FSR radiations help probe the invisible Z' . Taking neutrino for example, the FSR either result in $Z + \cancel{E}_T$ or $\ell + \cancel{E}_T$. The transverse mass of this system does not have an intrinsic mass scale as the mother $Z' \rightarrow \nu \bar{\nu}$ has

zero intrinsic missing transverse energy. Subjecting to different sources of background, this mono- Z boson search could help probe the invisible decays of the Z' [537], especially when a effective Z tagger with low mistagging rate from jets become feasible.

The total unknown parameters of Z' models with negligible $Z - Z'$ mixing, family universality and $U(1)'$ commutes with $SU(2)$ are six (seven). These are Z' mass, (Z' width,) and 5 chiral charges/couplings. Z' -mass (and width) can be measured from leptonic Z' lineshape, and improved by other channels. The remaining five chiral couplings requires at least four (five) linearly independent observables, note Z' width can already be counted as an observable toward chiral couplings determinations assuming minimal Z' width with only fermion pair decay modes.

Cross sections σ^ℓ , σ^b , σ^t and σ^j provides three linearly independent observables. Lepton forward-backward asymmetry provides a fourth observable to determine these five chiral couplings. We note there these observables all depends on chiral couplings squared with negligible interference with background. In fact, the leptonic forward-backward asymmetry as a function of lepton pair invariant mass provide additional information about the signs of these couplings through interfere with SM background. Top forward-backward asymmetry and radiations provides additional observables to increase the diagnostic power. More, with these additional observables, one can relax the assumption about minimal width, relax the assumption of commuting $U(1)'$ and $SU(2)$ generator, etc. We perform numerical studies to estimate the precision on these observables in the following section IV.A.1 and section IV.A.2 and perform parameter fit in section IV.A.3 to show the VLHC diagnostic power on Z' .

1. Gold-plated Modes: Leptonic Final States

The leptonic Z' processes at the VLHC provide the largest discovery potential and diagnostic power comparing to other modes. They enjoy little QED background at pp collider. Many observables are accessible in these leptonic modes. In this section, we consider the three types of observables mentioned in the previous section, including leptonic Z' cross sections, dilepton invariant mass distribution, lepton forward-backward (charge) asymmetry and leptonic Z' ISR- W . The forward-backward asymmetry can also be studied as a function of dilepton

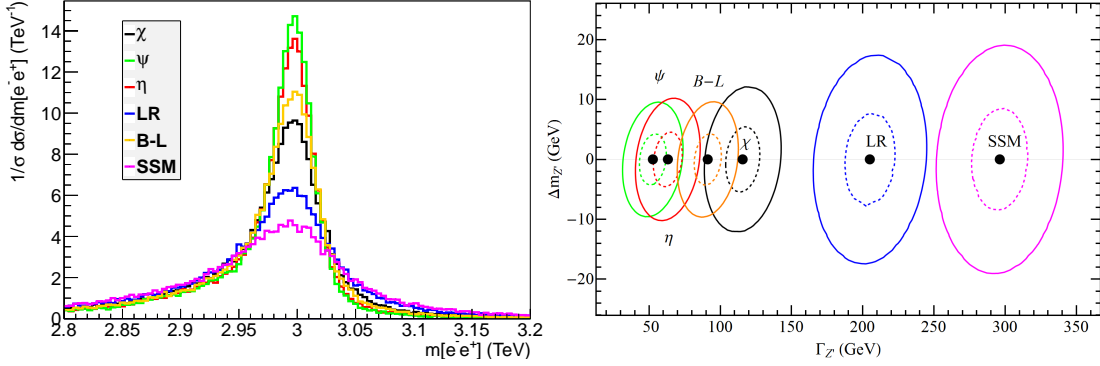


Figure IV.3: *Left panel:* the invariant mass distribution of the dielectron system for the benchmark models for a 10 TeV Z' at the 100 TeV VLHC ; *Right panel:* the 90% C.L. contour of fitting precision on Z' mass and width from electron positron pair final state at integrated luminosity of $1(5) \text{ ab}^{-1}$.

invariant mass to reveal the relative signs of the products of the couplings. The leptonic Z' ISR- W can be further decomposed into forward lepton piece and backward lepton piece. We study the VLHC sensitivity on these interesting and important observables here. For all of the following studies, we use Madgraph5 [242] for parton level event generation using models generated by FeynRules [243], showered by Pythia6.4 [244] and detector simulated by Delphes3 [245]. We choose CTEQ6.1 Parton Distribution Function (PDF) in five flavor scheme. We conservatively assume the detector of VLHC the same as ATLAS detector, a common assumption recommend by Snowmass.

a. Dilepton Invariant Mass The dilepton invariant mass bump would be the smoking gun for a Z' discovery. This partial cross section distribution over dilepton mass carries the Z' mass, width information as shown in figure IV.3. On the left panel, we show this distribution for our 10 TeV Z' benchmark models. The spread is a PDF convoluted Z' Breit-Wigner distribution smeared by Gaussian distribution from detector effects. The energy resolution on the electrons for our detector assumption is 1% with electron positron pair

acceptance $\sim 78\%$. We require these leptons p_T greater than 100 GeV. We show the fitting precision on the Z' width and mass from this distribution on the right panel of Fig. IV.3, assuming 1 ab^{-1} integrated luminosity. The precision can be further improved by combining the dimuon final state.

We show that $\sim 1\%$ precision on mass and $10\% - 20\%$ precision on Z' width can be achieved. For this invariant mass distribution fit we neglect the background for two reasons. One reason is the dielectron background cross section is small, approximately one order of magnitude smaller than the signal. The second reason is distribution follow polynomial tails nicely and can be removed by SM calculation with little theoretical uncertainties and further improved by data-driven methods.

We note the resolution on Z' width largely depends on the lepton energy resolution. The Z' benchmark model widths varies from 52 GeV for Z'_ϕ to 296 GeV for Z'_{SSM} . As long as the energy resolution is not much larger than the Z' width, we shall have sensitivities to it. For our fitting procedure, we assume no systematic uncertainties on the energy resolution of leptons, due to lack of detector information. We should emphasis here width is of peculiar importance to understanding Z' properties. It sets the overall strength of the couplings, otherwise all measured cross sections would be invariant with a proper scaling of Z' parameters with allowance of unobserved decays.

b. Forward-backward Asymmetry The forward-backward asymmetry the first and foremost probe we have for the chiral structure of Z' couplings. We show the angular distribution of the dielectron system in the left panel of Fig. IV.4. This angular distribution is a direct probe of the spin of the underlying resonance and forward-backward asymmetry. Assuming a vector resonance, the angular distribution is equivalent to forward-backward asymmetry. On the right panel of this figure, we show the precision on this leptonic forward-backward asymmetry versus the leptonic cross section σ^l precision. We assume an $10\%(6\%) \oplus 2\%$ systematic uncertainties for the cross section measurement for 1 (5) ab^{-1} integrated luminosity.

We assume the $10\%(6\%)$ systematic uncertainties which usually contains PDF uncertainties and some other correlated systematic uncertainties can be canceled by taking the

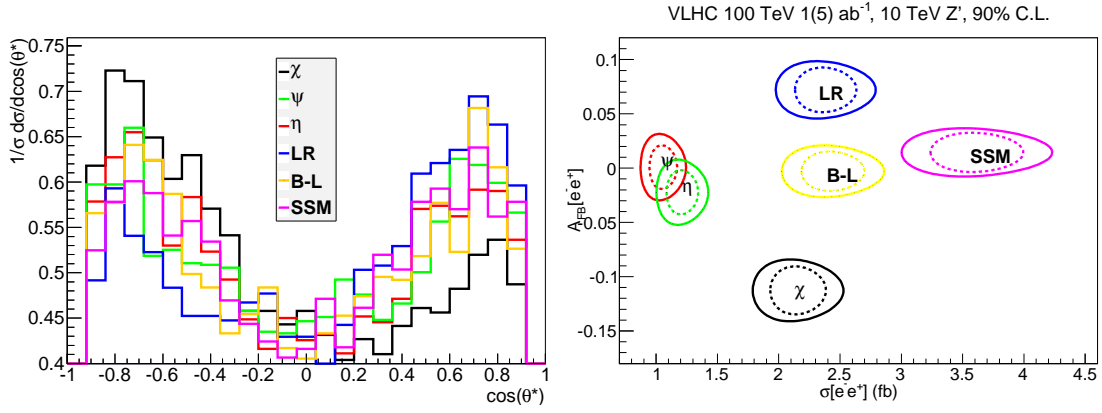


Figure IV.4: *Left panel:* the angular distribution of the electrons in the CM frame with respect to the rapidity (boost) direction of the system in the lab frame, integrated over the dielectron rapidity y . *Right panel:* the 90% C.L. fitted curve for leptonic cross section and leptonic forward-backward asymmetry. The solid and dashed lines corresponds to 1 (5) ab^{-1} with systematic uncertainties specified in the text.

Table IV.1: The comparison of leptonic forward-backward asymmetry of two bins with $m_{\ell-\ell^+}$ in the window of $9.5 \sim 9.9$ TeV and $10.1 \sim 10.5$ TeV. If the asymmetries increase (decrease) we list “+” (“-”). We also list the significance of this comparison.

	χ	ψ	η	LR	B-L	SSM
sign	-	-	-	+	+	+
significance @ 10 ab ⁻¹	0.9	2.7	1.4	4.3	1.5	2.4

ratio of cross sections to obtain forward-backward asymmetry, these captures the advantages of such quantities in ratios. We keep this assumption throughout this section. This is to say, we assume 2% systematic uncertainties for all the other quantities except when they can be expressed as in form of ratios. Note here we assume 2% residual systematic uncertainties associated with leptonic forward-backward asymmetry. The background cross section is less than one tenth of the benchmark signals. We assume the uncertainties associated with background subtraction included in this 2% uncertainty.

There are two factors that downgrades the forward-backward asymmetry of the dilepton system. The first factor is the direction of quark identification. At pp collider, *a priori* one can not tell the initial state quark/anti-quark direction. The best we can do it so associate the Z' boosting direction as the quark direction, utilizing the fact that energetic valence quarks contributes most to the production. Still there is large possibility of wrongly assign the direction at such high energy collider at the VLHC . The second factor is from collider acceptance which removes very forward and backward leptons. This can be clearly seen on the left panel of Fig. IV.4 in the $|\cos\theta| \sim 1$ regions. This factor downgrades the ratio of A_{FB} from 0.75 to 0.65 for a lepton sample obeys $(1 + \cos\theta)^2$. The overall effect of these two factors downgrades the asymmetry by a factor of $\sim 75\%$ for 10 TeV Z' .

Another crucial observable associated with the leptonic forward backward asymmetry as a function of dilepton invariant mass. This is one of the few observables that are sensitive to the sign of the couplings through its interference with the SM background. It worthy

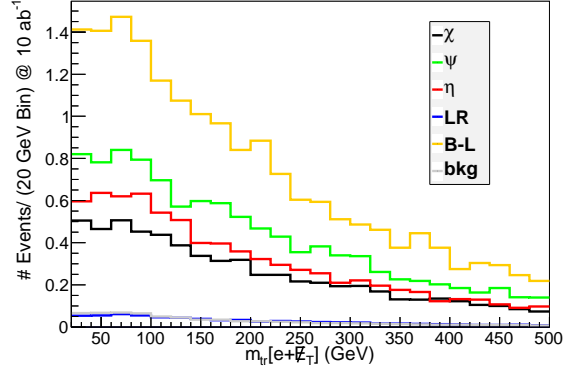


Figure IV.5: The transverse mass distribution of the $e^\pm + \cancel{E}_T$ system in the $\mu^-\mu^+ + e^\pm + \cancel{E}_T$ final state. Signal and background are not stacked. The dimuon invariant mass $m_{\mu^-\mu^+}$ are restricted in the window of $9 \sim 11$ TeV.

mention here the intrinsic forward-backward asymmetry of the SM background is 0.30. A simple comparison of the forward backward asymmetry between two bins with $m_{\ell^-\ell^+} \leq m_{Z'}$ and $m_{\ell^-\ell^+} \geq m_{Z'}$ would be sufficient to extract such information. We show such comparison in Table. IV.1, where the two bins are taken at $9.5 \sim 9.9$ TeV and $10.1 \sim 10.5$ TeV.

c. Weak Boson Radiation Weak boson radiation is another interesting probe for underlying Z' chiral structures. We can see that W -boson radiation provides better diagnostic power than Z -boson and photon radiations. The ISR- W from $pp \rightarrow Z' \rightarrow \mu^-\mu^+$ process can be observed for $\mu^-\mu^+W^\pm$ final state and FSR- W can be observed for $m\mu^\pm\ell^\mp + \cancel{E}_T$ final state, especially $m\mu^\pm e^\mp + \cancel{E}_T$ final state for reduction of background and possible mixture with ISR- W .

In this section, we present our study on ISR- W in the $\mu^-\mu^+W^\pm$ process. We first consider the leptonic W for purpose of clean background. For simplicity, we show the result for $\mu^-\mu^+ + e^\pm + \cancel{E}_T$ final state in Fig. IV.5 and Table. IV.2. Other processes in $\ell^-\ell^+ + \ell^\pm + \cancel{E}_T$ shall provide similar significance.

We consider the irreducible SM background with a same final state. We require the $\mu^-\mu^+$

Table IV.2: The results of the initial state W -boson radiation. We list the parton level cross sections in the first two rows, and in the last row the cross section after showering, detector simulation and cuts specified in the text for the $\mu^-\mu^+ + e^\pm + \cancel{E}_T$ final state.

	SM bkg	χ	ψ	η	LR	B-L	SSM
$\sigma(\mu^-\mu^+) \text{ (ab)}$	—	990	520	600	1100	1200	1800
$\sigma(\mu^-\mu^+W^\pm) \text{ (ab)}$	—	26	31	42	3.0	73	190
$\sigma(\mu^-\mu^+ + e^\pm + \cancel{E}_T)_{cut} \text{ (ab)}$	0.08	0.69	0.87	1.1	0.08	2.0	4.9

pair invariant mass in the mass window of $9 \sim 11$ TeV, the transverse mass of the electron greater than 20 GeV, and the final state electron/positron p_T greater than 100 GeV. Though one would expect a sharp transverse mass peak near the W -boson mass, this is washed out by the energy resolutions on the final state leptons and ISR jets. The transverse mass as a result does not provide much signal background discrimination. As shown in Table. IV.2, the leptonic ISR- W for most benchmark models are accessible with $\geq 5 \text{ ab}^{-1}$ luminosity.

We would like to comment on the hadronic ISR- W as well. These channels would require hadronic W tagger to establish the signal from QCD ISR background. The effectiveness of these hadronic W taggers heavily depends on the detector performance on the $\eta - \phi$ plane. Current assumption of the detector is 0.1×0.1 resolution. This, however, may not be enough to resolve highly boosted W s. In addition, to distinguish between hadronic W and hadronic Z would be very hard. As a result, the $\mu^-\mu^+$ with hadronic W and hadronic Z will be mixed and reduce the diagnostic power greatly.

2. Crucial Modes for Coupling Determination: Hadronic Final States

The Z' hadronic final states are crucial for coupling determination, as it directly provide information on the size of products of up-type and down-type hadronic couplings. At the VLHC , the QCD background is quite challenging. We list our study on the signal and

background for $b\bar{b}$, $t\bar{t}$ and jj final states in Table. IV.3.

We simulate the SM QCD background in five flavor scheme and exclusive background for $b\bar{b}$ for purpose of statistics and cross check. We show the parton level cross sections of our benchmark models in the table. We only list the background cross section after cuts due to high efficiency from these basic cuts. The SM QCD background for large dijet invariant mass mainly from t -channel process. A stringent cut on the large jet p_T reduces them greatly. For our study, we require 3 TeV minimal p_T for the leading jet in p_T in the final state. We construct the invariant mass of jets by including all jets with p_T greater than 100 GeV. We only select events with this invariant mass in the window of $8.5 \sim 11.5$ TeV. For $b\bar{b}$ and $t\bar{t}$ channels we require at least one tagged bottom quark and top quark, respectively. Additionally, this tagged jet is required to have p_T greater than 3 TeV.

We also show the significance on these hadronic channels at 10 ab^{-1} . We can see that these tagged channels $b\bar{b}$ and $t\bar{t}$ has a much higher significance than jj final state.

We would like to note different possibilities in the hadronic final state. One is possible charm tagging. A charm quark with large boosting factor in principle can be tagged using a similar method for b-tagging. In fact, in some cases a charm quark can fake a bottom quark. Energetic Z' with known mass actually provide well-defined sample of bottom quarks and charm quarks with know boosting factor. As a result, charm tagging actually provide additional probe for the Z' chiral couplings.

3. Diagnosis Power of the VLHC

With sensitivities at the VLHC for observables belong to all three classes discussed earlier in the discussion, we gathered more than enough observables to perform a relative model-independent fitting. We keep the assumption of negligible $Z - Z'$ mixing, family universality and $SU(2)$ commuting $U(1)'$. We perform a 5-parameter fitting, namely these introduced in Eq. I.B.5 and show the result in Fig. IV.6. The result is shown in terms of chiral couplings squared. As discussed earlier, only the interference with the background could potentially reveal the sign of the couplings. The observables in use are σ^l , σ^b , σ^t , A_{FB}^l , ISR- W in leptonic mode and Z' total width.

Table IV.3: The hadronic cross sections for benchmark models and SM background, before and after cuts described in the text. The statistical significance of each modes at 10 fb^{-1} are listed for corresponding modes. The background before cuts are huge and as a results not listed, since cuts are very effective in removing these t -channel dominated QCD background.

	SM bkg	χ	ψ	η	LR	B-L	SSM
$\sigma^b \text{ (fb)}$	—	3.3	1.6	1.8	9.5	0.4	8.5
$\sigma_{cut}^b \text{ (fb)}$	9.1	0.38	0.19	0.23	1.0	0.05	0.93
$S/\sqrt{B}@10 \text{ ab}^{-1}$	—	13	6.5	7.5	34	1.5	31
$\sigma^t \text{ (fb)}$	—	0.66	1.6	2.9	5.4	0.42	6.5
$\sigma_{cut}^t \text{ (fb)}$	11	0.13	0.32	0.58	1.1	0.08	1.3
$S/\sqrt{B}@10 \text{ ab}^{-1}$	—	4.0	9.6	18	33	2.5	39
$\sigma^j \text{ (fb)}$	—	7.9	6.4	9.6	30	1.7	30
$\sigma_{cut}^j \text{ (fb)}$	7.5×10^3	3.7	3.0	4.4	14	0.8	13
$S/\sqrt{B}@10 \text{ ab}^{-1}$	—	4.5	3.4	5.0	16	0.9	15

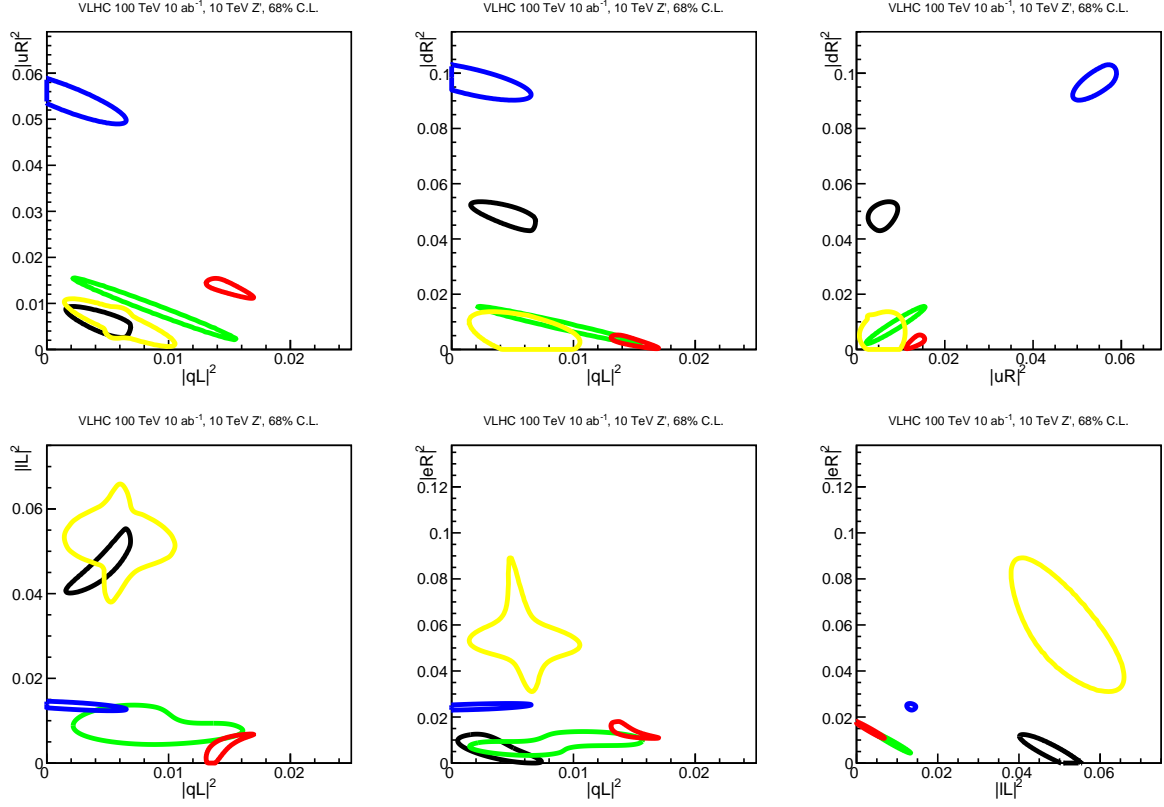


Figure IV.6: 5(6)-parameter fit contour at 68% C.L. for our benchmark models. The color for different benchmark models are the same as in Fig. IV.8.

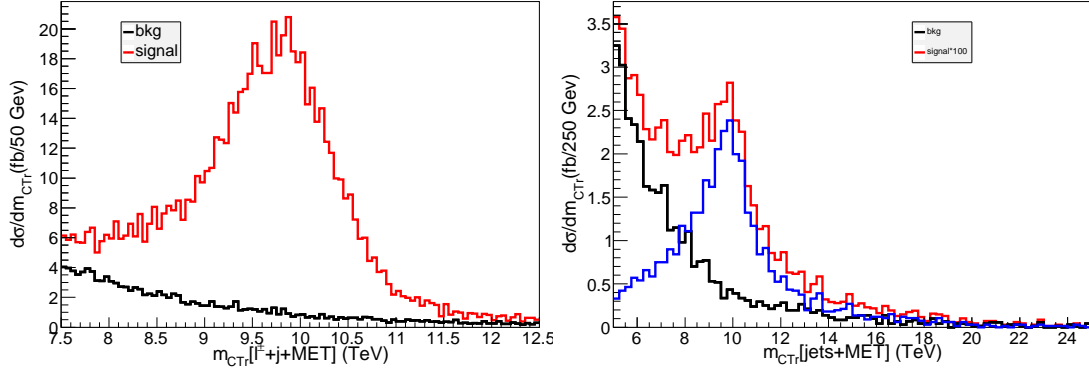


Figure IV.7: Left panel: clustered transverse mass distribution of the lepton and \cancel{E}_T plus leading jet system for $Z' \rightarrow W^+W^-$ signal and background. Right panel: clustered transverse mass distribution of the jets and \cancel{E}_T system for $Z' \rightarrow zh$ signal and background.

We show the fitting result in series of two dimensional plots. The separation of fitted regions of different benchmark models show the diagnostic power of the VLHC .

4. In the Presence of $Z - Z'$ Mixing

In presence of $Z - Z'$ mixing, new decay channels of $Z' \rightarrow W^+W^-$ and $Z' \rightarrow Zh$ are open. Some additional decay modes to new Higgs states are possible as well, as many Z' models introduces new Higgs states to give mass for $U(1)'$ gauge boson. As discussed in earlier section, such mixing is strongly constrained by the Elctroweak precision observables.

For $Z - Z'$ mass mixing, the decay branching fraction of $Z' \rightarrow W^+W^-$ and $Z' \rightarrow Zh$ will be the same in the large Z' mass limit such as predicted by Goldstone equivalence theorem. We discuss the observability of both Z' decay modes at the VLHC in this section.

There are three possible combinations of this pair of W bosons, including fully leptonic decay, semi-leptonic decay and fully hadronic decay. The fully hadronic decay mode requires dedicated W -tagging to dijet background from both the SM and Z' itself, whereas the former is expected to be very large as in the Z' dijet searches. As a result, we consider fully leptonic

decay and semi-leptonic decay mode in this subsection.

The W pair fully leptonic decay is characterized by pair of oppositely charged leptons with missing energy. The missing energy is made up by a pair of neutrinos from different mother W boson.

The W pair semi-leptonic decay is characterized by large \cancel{E}_T with energetic jets (dijets) and charged lepton. It has little ambiguity and larger rate comparing to the full leptonic decays. On the right panel of Fig. IV.7 we show the clustered transverse mass distribution for the $\ell + jet + \cancel{E}_T$ system with a clear peak and endpoint at the Z' mass. We note here the typical energy of the hadronic W boson is greater or equal to 5 TeV, resulting in very clustered dijet system. Using an anti- k_T algorithm with $R = 0.5$, these dijets from hadronic W bosons are most likely clustered into one jet. We thus define the clustered as the $\ell + jet + \cancel{E}_T$ system to avoid additional mass gains and endpoint smearing from ISR, so here we only include the leading jet with p_T greater than 100 GeV. We can see that the clustered transverse mass alone can serve as a most effective signal background discriminator, characterized by a broad peak with FWHM around 1.5 TeV. Clearly the smearing effects shifts the endpoint behavior of the clustered transverse momentum, but still the signal Jacobian peak stands out of the continuous background.

The $Z' \rightarrow Zh$ decay mode bears quite interesting phenomenology as well. For such a heavy Z' , the decay product of both the h boson and Z boson are highly boosted. The Higgs bosons decay mostly hadronically, with around 80% Br being purely hadronic decays with significant Br to the $b\bar{b}$ final state. One interesting possibilities is to require two bottom tagging within the boosted Higgs jet using jet substructure. This possibilities is to be tested at the LHC 13 TeV. A challenge at the VLHC is it would be hard to reconstruct the displaced vertices for very boosted bottom quarks, as the corresponding impact parameter has large uncertainties. Developments on higher magnetic field, higher resolutions on trackers and calorimeters will certainly improve the performance on boosted b-tagging. For our study, we conservatively assume no boosted di-bottom Higgs tagger, and thus the hadronic Higgs boson will be a jet (jets). One then would put more requirements on the boost Z boson from Z' decay, namely on the invisible Z boson or dileptonic Z boson. Consequently, we focus on two signal regions here: 1) jet(s) plus \cancel{E}_T ; 2) jet(s) plus dilepton. An interesting possibilities

is to make use of the semi-leptonic decays of the bottom jet [538].

B. HIGGS WIDTH AT A MUON COLLIDER

At a muon collider, due to the much stronger coupling of the Higgs to muons than to electrons, an s -channel production of a Higgs boson [186] will likely lead to clear signals for several channels, and thus its total decay width may be directly measured by fitting its scanned data.

In this section, we propose a realistic scanning and fitting procedure to determine the Higgs boson width at a muon collider. We demonstrate the complementarity for the two leading signal channels $h \rightarrow b\bar{b}$, WW^* . The combined results lead to a highly accurate determination for the width, mass and the s -channel production cross section. This is undoubtedly invaluable for determining the Higgs interactions and testing the theory of the electroweak symmetry breaking to an unparalleled precision.

1. Resonant Profile for a Higgs Boson

For a resonant production $\mu^+\mu^- \rightarrow h$ and a subsequent decay to a final state X with a collider c.m. energy $\sqrt{\hat{s}}$, the Breit-Wigner formula reads

$$\sigma(\mu^+\mu^- \rightarrow h \rightarrow X) = \frac{4\pi\Gamma_h^2 \text{Br}(h \rightarrow \mu^+\mu^-) \text{Br}(h \rightarrow X)}{(\hat{s} - m_h^2)^2 + \Gamma_h^2 m_h^2}, \quad (\text{IV.B.2})$$

where Br denotes the corresponding decay branching fraction. At a given energy, the cross section is governed by three parameters: m_h for the signal peak position, Γ_h for the line shape profile, and the product $B \equiv \text{Br}(h \rightarrow \mu^+\mu^-) \text{Br}(h \rightarrow X)$ for the event rate.

In reality, the observable cross section is given by the convolution of the energy distribution delivered by the collider. Assume that the $\mu^+\mu^-$ collider c.m. energy (\sqrt{s}) has a flux distribution

$$\frac{dL(\sqrt{s})}{d\sqrt{\hat{s}}} = \frac{1}{\sqrt{2\pi}\Delta} \exp\left[-\frac{(\sqrt{\hat{s}} - \sqrt{s})^2}{2\Delta^2}\right],$$

with a Gaussian energy spread $\Delta = R\sqrt{s}/\sqrt{2}$, where R is the percentage beam energy resolution; then, the effective cross section is

$$\begin{aligned} \sigma_{\text{eff}}(s) &= \int d\sqrt{\hat{s}} \frac{dL(\sqrt{s})}{d\sqrt{\hat{s}}} \sigma(\mu^+\mu^- \rightarrow h \rightarrow X) \\ &\propto \begin{cases} \Gamma_h^2 B / [(s - m_h^2)^2 + \Gamma_h^2 m_h^2] & (\Delta \ll \Gamma_h), \\ B \exp[-\frac{(m_{h^0} - \sqrt{s})^2}{2\Delta^2}] (\frac{\Gamma_h}{\Delta}) / m_h^2 & (\Delta \gg \Gamma_h). \end{cases} \end{aligned} \quad (\text{IV.B.3})$$

For $\Delta \ll \Gamma_h$, the line shape of a Breit-Wigner resonance can be mapped out by scanning over the energy as given in the first equation. For $\Delta \gg \Gamma_h$ on the other hand, the physical line shape is smeared out by the Gaussian distribution of the beam energy spread, and the signal rate will be determined by the overlap of the Breit-Wigner and the luminosity distributions, as seen in the second equation above.

Unless stated otherwise, we focus on the SM Higgs boson with the mass and total width as

$$m_{h^0} = 126 \text{ GeV}, \quad \Gamma_h = 4.21 \text{ MeV}. \quad (\text{IV.B.4})$$

For definitiveness in this study, we assume two sets of representative values for the machine parameters [539]

$$\text{Case A :} \quad R = 0.01\% \ (\Delta = 8.9 \text{ MeV}), \ L = 0.5 \text{ fb}^{-1}, \quad (\text{IV.B.5})$$

$$\text{Case B :} \quad R = 0.003\% \ (\Delta = 2.7 \text{ MeV}), \ L = 1 \text{ fb}^{-1}. \quad (\text{IV.B.6})$$

We see that their corresponding beam energy spread Δ is comparable to the Higgs total width. In Fig. IV.4, we show the effective cross section versus the $\mu^+\mu^-$ collider c.m. energy for the SM Higgs boson production. A pure Breit-Wigner resonance is shown by the dotted curve. The solid and dashed curves include the convolution of the luminosity distribution for the two beam energy resolutions and are integrated over $\sqrt{\hat{s}}$. For simplicity, we have taken the branching fractions $h \rightarrow \mu^+\mu^-$ to be the SM value and the final state $h \rightarrow X$ to be 100%. The beam energy resolution manifests its great importance in comparison between the solid and dashed curves in this figure.

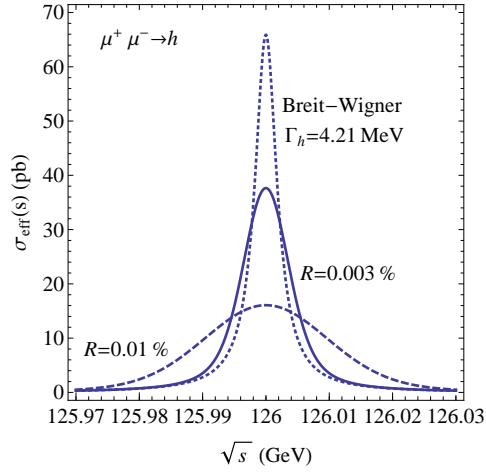


Figure IV.8: Effective cross section for $\mu^+\mu^- \rightarrow h$ versus the collider energy \sqrt{s} for the SM Higgs boson production with $m_{h^0} = 126$ GeV. A Breit-Wigner line shape with $\Gamma_h = 4.21$ MeV is shown (dotted curve). The solid and dashed curves compare the two beam energy resolutions of cases A and B.

Table IV.4: Effective cross sections (in pb) at the resonance $\sqrt{s} = m_{h^0}$ for two choices of beam energy resolutions R and two leading decay channels, with the SM branching fractions $\text{Br}_{b\bar{b}} = 56\%$ and $\text{Br}_{WW^*} = 23\%$ [504].

R (%)	$\mu^+\mu^- \rightarrow h$	$h \rightarrow b\bar{b}$		$h \rightarrow WW^*$	
	σ_{eff} (pb)	σ_{Sig}	σ_{Bkg}	σ_{Sig}	σ_{Bkg}
0.01	16	7.6	15	3.7	0.051
0.003	38	18		5.5	

2. Width Determination for the SM Higgs Boson

An excellent beam energy resolution for a muon collider would make a direct determination of the Higgs boson width possible in contrast to the situations in the LHC and ILC. Because of the expected narrow width for a SM Higgs boson, one still needs to convolute the idealistic Breit-Wigner resonance with the realistic beam energy spectrum as illustrated in Eq. (IV.B.3). We first calculate the effective cross sections at the peak for the two cases of energy resolutions A and B. We further evaluate the signal and SM background for the leading channels

$$h \rightarrow b\bar{b}, \quad WW^*. \quad (\text{IV.B.7})$$

We impose a polar angle acceptance for the final-state particles,

$$10^\circ < \theta < 170^\circ. \quad (\text{IV.B.8})$$

Tightening up the polar angle to $20^\circ - 160^\circ$ will further reduce the signal by 4.6%, and the background by 6.7% (15%) for the $b\bar{b}$ (WW^*) final states. We assume a 60% single b -tagging efficiency and require at least one tagged b jet for the $b\bar{b}$ final state. The backgrounds are assumed to be flat with cross sections evaluated right at 126 GeV using Madgraph5. This appears to be an excellent approximation over the energy range of the current interest about 100 MeV. We tabulate the results in Table IV.4. The background rate of $\mu^+\mu^- \rightarrow Z^*/\gamma^* \rightarrow b\bar{b}$ is 15 pb, and the rate of $\mu^+\mu^- \rightarrow WW^* \rightarrow 4 \text{ fermions}$ is only 51 fb, as shown in Table IV.4. Here, we consider all the decay modes of WW^* because of its clear signature at a muon collider. The four-fermion backgrounds from $Z\gamma^*$ and $\gamma^*\gamma^*$ are smaller to begin with and can be greatly reduced by kinematical considerations such as by requiring the invariant mass of one pair of jets to be near m_W and setting a lower cut for the invariant mass of the other pair. While the $b\bar{b}$ final state has a larger signal rate than that for WW^* by about a factor of three, the latter has a much improved signal (S) to background (B) ratio, about 100:1 near the peak.

For a given beam resolution, we assume that a scan procedure over the collider c.m. energy \sqrt{s} is available. The current Higgs mass statistical error is about 0.4 GeV [33, 34] with an

integrated luminosity of about 10 fb^{-1} . Toward the end of the LHC run with about 100 times more luminosity accumulated, it is conceivable to improve the statistical error of the mass determination by about an order of magnitude. Then, the systematic errors would have to be controlled to the best level. It was argued that an ILC could reach a similar or better accuracy [540]. We thus proceed to scan over the energy in the range

$$126 \text{ GeV} \pm 30 \text{ MeV} \text{ in 20 scanning steps.} \quad (\text{IV.B.9})$$

The energy scanning step is set at 3 MeV, roughly the same size of the Δ and Γ_h .

We first generate ideal data in accordance with a Breit-Wigner resonance at this mass convoluted with Gaussian distribution of the beam energy integrated over $\sqrt{\hat{s}}$, as discussed before. These data are then randomized with a Gaussian fluctuation with standard deviation \sqrt{N} , where N is the number of events expected for a given integrated luminosity, summing both signal and background. The simulated events over the scanning points are plotted with statistical errors for the assumed integrated luminosity as in Eqs. (IV.B.5) and (IV.B.6).

The results are shown by the solid curves in Fig. IV.9, for cases A and B as in Eq. (IV.B.5) (left panels) and Eq. (IV.B.6) (right panels). The $b\bar{b}$ and W^+W^- final states are separately shown by the upper and lower panels, respectively.

We adopt a χ^2 fit over the scanning points with three model-independent free parameters in the theory Γ_h , B and m_{h^0} by minimizing the χ^2 . The fitting accuracies for the Higgs properties can be illustrated by the standard deviation, denoted by $\delta\Gamma_h$, δB , and δm_h . These standard deviations are estimated by the standard method of projecting the $\chi^2_{min} + 1$ sphere to corresponding parameters. To see the effects from the available luminosity, we show our results for the SM Higgs width determination in Fig. IV.10 for both cases by varying the luminosity. The achievable accuracies with the scanning scheme as specified in Eq. (IV.B.9) by combining two leading channels are summarized in Table IV.5 for three representative luminosities per step with the same 20-step scanning scheme.

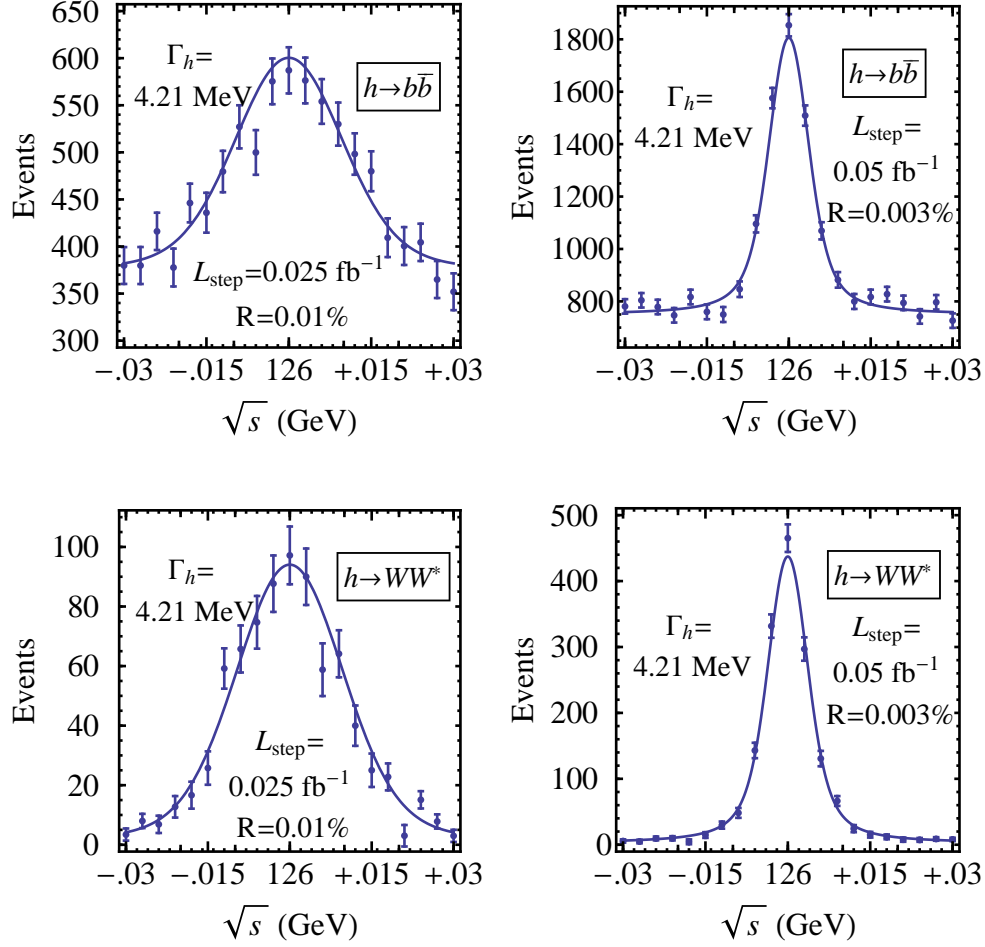


Figure IV.9: Number of events of the Higgs signal plus backgrounds and statistical errors expected for cases A and B as a function of the collider energy \sqrt{s} in $b\bar{b}$ and WW^* final states with a SM Higgs $m_{h^0} = 126$ GeV and $\Gamma_h = 4.21$ MeV.

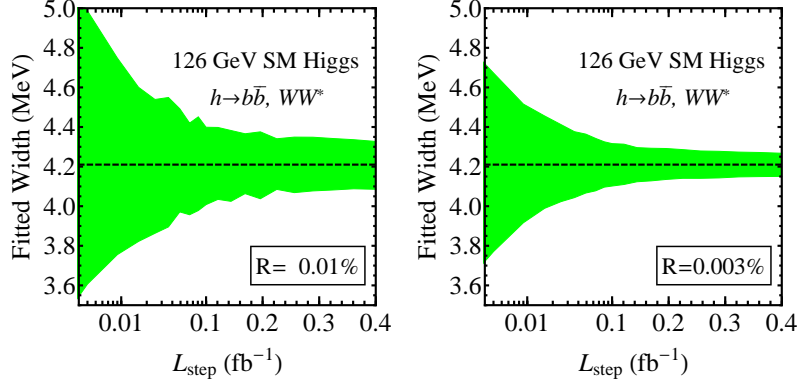


Figure IV.10: Fitted values and errors for the SM Higgs width versus the luminosity per step with the scanning scheme as specified in Eq. (IV.B.9).

Table IV.5: Fitting accuracies for one standard deviation of Γ_h , B , and m_h of the SM Higgs with the scanning scheme as specified in Eq. (IV.B.9) for three representative luminosities per step. Results with the default luminosities for cases A and B described in Eqs. (IV.B.5) and (IV.B.6) are in boldface.

$\Gamma_h = 4.21 \text{ MeV}$	$L_{\text{step}} \text{ (fb}^{-1}\text{)}$	$\delta\Gamma_h \text{ (MeV)}$	δB	$\delta m_h \text{ (MeV)}$
$R = 0.01\%$	0.005	0.73	6.5%	0.25
	0.025	0.35	3.0%	0.12
	0.2	0.17	1.1%	0.06
$R = 0.003\%$	0.01	0.30	4.4%	0.12
	0.05	0.15	2.0%	0.06
	0.2	0.08	1.0%	0.03

Table IV.6: The effective cross sections (in pb) for the exotic Higgs, with $\text{Br}_{b\bar{b}} = 18\%$ and $\text{Br}_{WW^*} = 7.3\%$.

R (%)	$\mu^+\mu^- \rightarrow h$ σ_{eff} (pb)	$h \rightarrow b\bar{b}$		$h \rightarrow WW^*$	
		σ_{Sig}	σ_{Bkg}	σ_{Sig}	σ_{Bkg}
0.01	18	2.6	15	1.3	0.051
0.003	20	3.0		1.5	

3. Width Determination for a Broader Higgs Boson

We now explore the unique feature of the direct width measurement for a broader resonance at a muon collider. For definitiveness, we still work with a Higgs-like particle with a mass at 126 GeV, but with a total width of ten times larger than that of the SM value, $\Gamma_h = 42$ MeV. We shall consider scenarios in which the signal at the LHC of this particle (assuming a SM Higgs) would be unchanged.

In Fig. IV.11, we present the similar analyses as in Fig. IV.9 for a broader Higgs. There are two features of this figure compared to the SM Higgs in Fig. IV.9. First, the increase of Higgs width requires a broader scan range to reconstruct the Breit-Wigner resonant distribution. We choose to scan the same number of 20 scan steps with a step size of 10 MeV, while keeping the same total integrated luminosity. It is seen from the figure that the physical line shape of the Higgs boson is essentially mapped out by the scanning. Second, since the signal rate at the LHC is governed by partial widths to initial (i) and final (f) states $\propto \Gamma_i \Gamma_f / \Gamma_h$, the rate could be kept the same when increasing the Higgs total width by a factor κ while scaling the partial widths up by a factor of $\sqrt{\kappa}$. This would correspondingly reduce the cross section for the signal at a muon collider as seen in Eq. (IV.B.2). Under this constraint, the results for the branching fractions and the effective peak cross sections of a broader Higgs at a muon collider are listed in Table IV.6.

Although a larger Higgs width would be easier to resolve with a fine energy resolution,

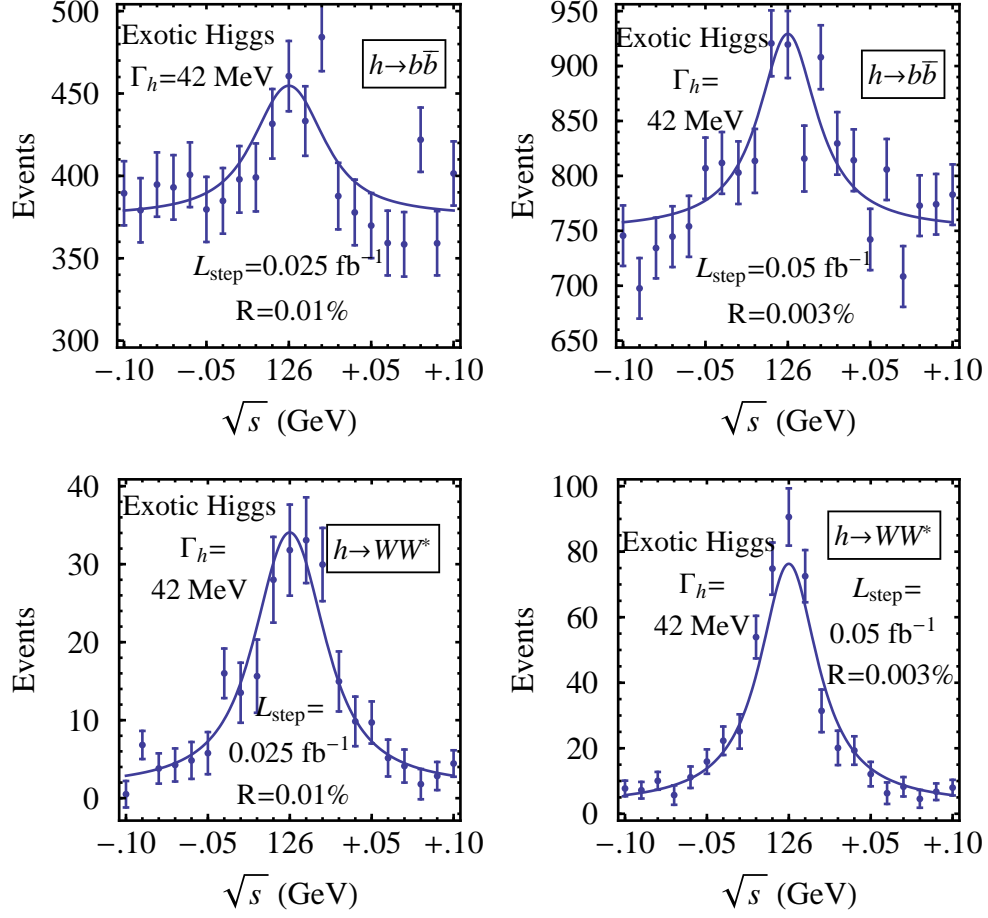


Figure IV.11: Number of events of the Higgs signal plus backgrounds and statistical errors expected for cases A and B as a function of the collider energy \sqrt{s} in $b\bar{b}$ and WW^* final states with an exotic Higgs $m_{h^0} = 126$ GeV and $\Gamma_h = 42$ MeV.

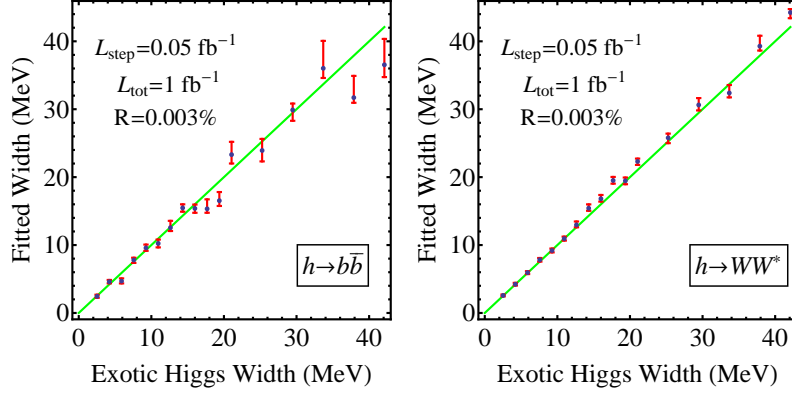


Figure IV.12: Fitted values and errors for the Higgs width versus the input values. The step size is set as a rounded half-integer value between 3 MeV – 10 MeV in accordance with the Higgs width 0.6 – 10 times the SM value.

it is a practical concern when a larger range of the scanning energy is needed with a fixed total luminosity. In Fig. IV.12, we explore this issue by plotting the width determination with statistical errors for a fixed total luminosity at 1 fb^{-1} and varying Higgs widths. The events from the $b\bar{b}$ channel and WW^* channel are shown individually. It turns out that a smaller width could receive better accuracies in the scanning process due to the larger signal rate than that at a larger width as mentioned above. We summarize the fitting accuracies in Table IV.7.

Table IV.7: Fitting accuracies for the exotic Higgs properties. The scanning scheme is the same as in Fig. IV.12.

$\Gamma_h = 2.5 - 42 \text{ MeV}$	$\delta\Gamma_h \text{ (MeV)}$	δB	$\delta m_h \text{ (MeV)}$
$b\bar{b}$	0.33 – 1.1	2.8% – 11%	0.07 – 1.2
WW^*	0.14 – 0.67	2.2% – 5.2%	0.05 – 0.71

4. Summary and Outlook

The direct measurement of the Higgs width with high precision will be invaluable to explore new physics through this “Higgs lamp post.” For instance, varying the parameters $\tan\beta$, M_A in the MSSM within the current LHC constraints, the SM-like Higgs width could change by 20%. Models with Higgs invisible decays would increase the width. Generic Higgs multiplet models allow an increase in total width, as illustrated in the triplet Georgi-Machacek model. Composite Higgs models also alter the Higgs width from the SM value.

The mass and cross section can be simultaneously determined along with the Higgs width to a high precision. The results obtained are largely free from theoretical uncertainties. Uncertainties of the signal evaluation do not alter the width and mass fitting. The major systematic uncertainty comes from our knowledge of beam properties. The uncertainty associated with the beam energy resolution R will directly add to our statistical uncertainties of Higgs width. This uncertainty can be well-calibrated by experimentalists as well as by measuring the Z boson peak rate. Our estimated accuracies are by and large free from detector resolutions. Other uncertainties associated with b tagging, acceptance, etc., will enter into our estimation of signal strength B directly. These uncertainties will affect our estimation of total width Γ_h indirectly through statistics, leaving a minimal impact in most cases. It is worthy it to mention that our scanning scheme for the SM Higgs case is by simply adopting the projected accuracy for the Higgs mass measurement from the LHC and ILC. A prescanning with the muon collider to narrow down the mass window could also increase the achievable accuracies, as a tradeoff for the total luminosity available.

Moreover, our study on the width and mass measurements can be applicable to new particles predicted in many theories. For example, the CP -odd and the other CP -even Higgs states in the minimal supersymmetric standard model and in two-Higgs-doublet-models may all be suitably studied at a muon collider. The achievable high accuracy would help to resolve nearly degenerate Higgs states.

C. HIGGS FROM RADIATIVE RETURN AT A MUON COLLIDER

The exact center-of-mass energy required for an optimal heavy Higgs signal depends on the unknown heavy Higgs mass, in particular for the s -channel resonant production at a muon collider. The situation may be remedied if instead we consider associated production of a Higgs boson with other particles. A particularly interesting process is the “radiative return” (RR) process. In the case of the Higgs boson production, the processes under consideration are

$$\mu^+\mu^- \rightarrow \gamma H, \gamma A, \quad (\text{IV.C.10})$$

where H (A) is a heavy neutral CP-even (CP-odd) state, respectively. When the center of mass energy of the muon collider is above the heavy Higgs resonance, the photon emission from the initial state provides an opportunity of the heavy Higgs boson “back” to the resonance. For this, one does not need to know the mass of the (unknown) heavy scalar. This mechanism alone could also provide an excellent channel to measure the invisible decay of the heavy Higgs boson. Without losing generality, we illustrate our main points with a notation in the context of a two-Higgs-doublet model (2HDM) [541], where the vacuum expectation values (vev) of both the doublets contribute to the W - and Z -masses.⁴

In Sec. IV.C.2, we first present the radiative return production of heavy Higgs boson in $\mu^+\mu^-$ collision in detail. We also consider the production $l^+l^- \rightarrow ZH$ and $l^+l^- \rightarrow AH$ ($l = e, \mu$) in Sec. IV.C.3. To make the illustration more concrete, we compare these production modes in Sec. IV.C.4 in the framework of 2HDM. Because of the rather clean experimental environment and the model-independent reconstruction of the Higgs signal events at lepton colliders. Finally, we summarize our results and conclude in Sec. IV.C.5.

1. Production Mechanisms

Perhaps the most useful feature of a muon collider is the potential to have s -channel resonant production of the Higgs boson [181, 186, 198, 487, 489]. As has been already mentioned in the

⁴For discussion on RR for other new physics searches at lepton colliders, see Refs. [542–545].

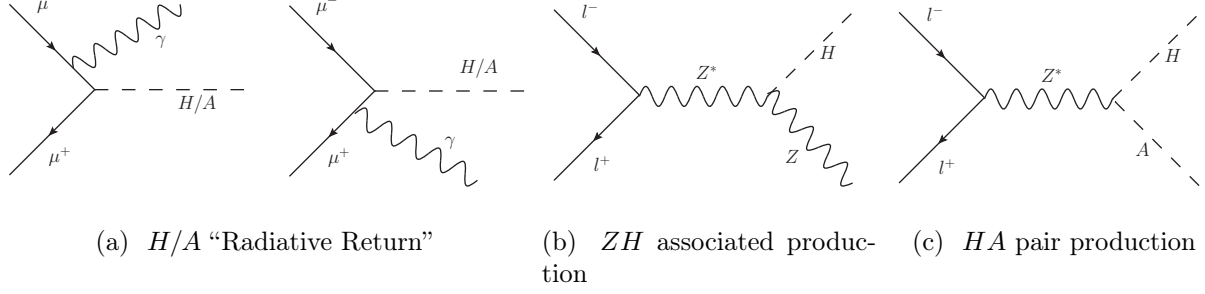


Figure IV.13: Main production mechanisms of heavy Higgs boson H/A at lepton colliders.

previous section, such a machine undoubtedly has its merits in analyzing in detail the already discovered Higgs boson near 125 GeV. When it comes to identifying a heavier additional (pseudo)scalar, however, we do not have any *a priori* knowledge about the mass, rendering the new particle search rather difficult. If one envisions a rather wide-ranged scanning, it would require to devote a large portion of the design integrated luminosity [488, 489]. In this section, we discuss the three different production mechanisms for the associated production of the heavy Higgs boson. Besides the “radiative return” as in Eq. (IV.C.10), we also consider

$$\mu^+\mu^- \rightarrow Z^* \rightarrow ZH \text{ and } HA. \quad (\text{IV.C.11})$$

The relevant Feynman diagrams are all shown in Fig. VI.1.

We first parametrize the relevant heavy Higgs boson couplings as

$$\begin{aligned} \mathcal{L}_{int} = & -\kappa_\mu \frac{m_\mu}{v} H \bar{\mu} \mu + i\kappa_\mu \frac{m_\mu}{v} A \bar{\mu} \gamma_5 \mu \\ & + \kappa_Z \frac{m_Z^2}{v} H Z^\mu Z_\mu \\ & + \frac{g}{2 \cos \theta_W} \sqrt{(1 - \kappa_Z^2)} (H \partial^\mu A - A \partial^\mu H) Z_\mu. \end{aligned} \quad (\text{IV.C.12})$$

The two parameters κ_μ and κ_Z characterize the coupling strength with respect to the SM Higgs boson couplings to $\mu^+\mu^-$ and ZZ . The coupling κ_μ controls the heavy Higgs resonant production and the radiative return cross sections, while κ_Z controls the cross sections for ZH associated production and heavy Higgs pair HA production. We have used κ_μ as the common scale parameter for Yukawa couplings of both the CP-even H and the CP-odd A , although

Table IV.8: Parametrization and their 2HDM models correspondence.

Coupling	$\kappa \equiv g/g_{\text{SM}}$	Type-II & lepton-specific	Type-I & flipped
$g_{H\mu^+\mu^-}$	κ_μ	$\sin \alpha / \cos \beta$	$\cos \alpha / \sin \beta$
$g_{A\mu^+\mu^-}$	κ_μ	$\tan \beta$	$-\cot \beta$
g_{HZZ}	κ_Z	$\cos(\beta - \alpha)$	$\cos(\beta - \alpha)$
g_{HAZ}	$1 - \kappa_Z^2$	$\sin(\beta - \alpha)$	$\sin(\beta - \alpha)$

in principle they could be different. For the HAZ coupling we have used the generic 2HDM relation: κ_Z is proportional to $\cos(\beta - \alpha)$ and the HAZ coupling is proportional to $\sin(\beta - \alpha)$.⁵ In the heavy Higgs decoupling limit of 2HDM at large m_A , $\kappa_Z \equiv \cos(\beta - \alpha) \sim m_Z^2/m_A^2$ is highly suppressed and $\kappa_\mu \approx \tan \beta$ ($-\cot \beta$) in Type-II [546, 547] and lepton-specific [548–551] (Type-I [541, 546] and flipped [548–551]) 2HDM. Note that many SUSY models, including MSSM and NMSSM, are essentially Type-II 2HDM, subject to fewer tree-level parameters for the Higgs potential and potentially large supersymmetric loop corrections. We tabulate our choices of parameters and their 2HDM correspondences in Table. IV.8. We reiterate that such a notation can be carried over to any scenario where there is another multiplet in addition to the SM Higgs doublet contributing to the W - and Z -masses, whereby the WW and ZZ couplings of the two neutral CP-even scalars are connected by a unitary relationship, with some SU(2) Clebsch-Gordan coefficients arising in addition.

We choose the following configuration as shown in Table IV.9 for the muon collider parameters and the detector acceptance, to study feasibilities of these different production channels. The beam energy spread is defined as

$$\frac{d\mathcal{L}(\sqrt{s})}{d\sqrt{\hat{s}}} = \frac{1}{2\pi\Delta} \exp\left[-\frac{(\sqrt{s} - \sqrt{\hat{s}})^2}{2\Delta^2}\right], \quad (\text{IV.C.13})$$

with $\Delta = R\sqrt{s}/\sqrt{2}$.

⁵Customarily, $\tan \beta$ is the ratio of the two vev's, and α is the mixing angle of the two scalar states.

Table IV.9: Muon Collider Parameters [552] assuming four collider years of running. The photon energy resolution is set as SiD from ILC TDR [485].

$\sqrt{s} = 1.5 \text{ GeV}$	500 fb^{-1}
$\sqrt{s} = 3.0 \text{ GeV}$	$1,760 \text{ fb}^{-1}$
Beam energy spread:	$R = 0.1\%$
Polar angle acceptance:	$10^\circ < \theta < 170^\circ$
$p_{T\min}$ for photon:	10 GeV
Photon Energy Resolution:	$0.17/\sqrt{E} \oplus 0.01$
$p_{T\min}$ for lepton:	20 GeV
ΔR_{\min} for leptons:	0.2

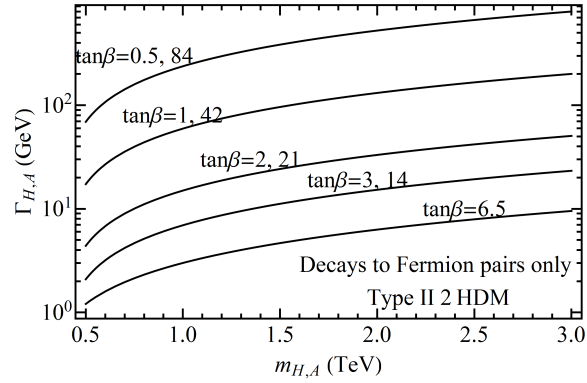


Figure IV.14: Total width of heavy Higgs boson in Type II 2HDM as a function of Higgs mass for a variety values of $\tan \beta = \kappa_\mu$. We only consider partial widths to fermion pairs here. The total width is symmetric with respect to $\sqrt{m_t/m_b}$.

2. Radiative Return

Due to the “radiative return”, when the heavy Higgs boson mass is below the center of mass energy of the muon collider, the photon emission from the initial state provides an opportunity of the heavy Higgs boson “back” to resonance. The signature is quite striking: a mono-chromatic photon plus other recoil particles. The “recoil mass” is a sharp resonant peak at $m_{H/A}$, manifesting itself from the continuous background. This photon’s energy is subject to the beam energy spread and detector energy smearing. The tagging of the heavy Higgs boson from its decay product, if necessary, provides extra handle on reducing the background and increasing the significance.

a. Signal and Background The characteristics of this RR signal is a photon with the energy given by

$$E_\gamma = \frac{\hat{s} - m_{H/A}^2}{2\sqrt{\hat{s}}}, \quad (\text{IV.C.14})$$

from which one constructs a recoil mass peaked at the heavy Higgs mass $m_{H/A}$. The energy of this photon is smeared by the following factors: detector photon energy resolution, collider beam energy spread, additional (soft) ISR/FSR, and heavy Higgs total width. Our choice of the detector photon energy resolution and beam energy spread are as shown in Table IV.9. The beam energy spread and (soft) ISR are of GeV level [552]. When the Higgs boson mass is significantly below the beam energy, the recoil mass construction receives large smearing due to the energy resolution for the very energetic photon.

Besides the Higgs boson mass, the other most important parameter is the total width, which effectively smears the mono-chromatic photons as well. We calculate the total width as a sum of the partial widths to fermion pairs for Type II 2HDM in Fig. IV.14. In this model, $\kappa_\mu = \tan \beta$ in the decoupling limit. The total width is minimized when $\tan \beta = \sqrt{m_t/m_b}$. Because of the quadratic dependence, there are typically two values to give the same width $\tan \beta_1 \cdot \tan \beta_2 = m_t/m_b$. Numerically we take $m_t/m_b = 42$. We can see that typically the total width ranges from a few GeV to hundreds of GeV. The total width of heavy Higgs boson could remain small in lepton-specific 2HDM. We thus choose three representative values for the total width: 1, 10, and 100 GeV for later discussions.

The inclusive cross section for mono-photon background is very large in comparison with the radiative return signal. The background is mainly from the Möller scattering with ISR/FSR $\mu^+\mu^- \rightarrow \mu^+\mu^-\gamma$, and the W exchange with ISR $\mu^+\mu^- \rightarrow \nu\nu\gamma$. The signal background ratio is typically of the order 10^{-3} for a 3 TeV muon collider. As a result, for the discovery through the RR process, we need to rely on some exclusive processes, or to the least veto mono-photon plus missing energy and mono-photon plus dimuon exclusive channels.

It should be noted that, in a 2HDM, the heavy neutral scalar H may decay into both $t\bar{t}$, $b\bar{b}$ and $\tau^+\tau^-$ modes, where the branching ratios depend on $\tan\beta$. We adopt the Type-II 2HDM for illustration. We show in Fig. IV.15 the total cross sections (left panel) for $\mu^+\mu^- \rightarrow H/A\gamma \rightarrow q\bar{q}\gamma$ (for $q = t, b$) for $\tan\beta = 5, 40$, with the basic cuts applied on the photon. It is clear from the plots that while the rates for $t\bar{t}\gamma$ is considerably suppressed for large values of $\tan\beta$, it can be of comparable magnitude (or even larger) to that for $b\bar{b}\gamma$ for relatively low $\tan\beta$. Judicious criteria for event selection, therefore, need to be developed for both channels. In the rest of the present study, however, only the $b\bar{b}$ mode is considered for simplicity.

To be more specific, we choose the $b\bar{b}$ final state as a benchmark with heavy Higgs boson decay branching fraction (Br) to this final state to be 80%. We also assume 80% b -tagging efficiency and require at least one b -jet tagged. In fact, any visible decay of the heavy Higgs boson except for the dimuon final state, negligible in most of models, would be very efficient in background suppression. One could also interpret our assumption as that 80% of the decays of the Higgs boson could be utilized.

We employ Madgraph5 [242] and for parton level signal and background simulations and tuned Pythia 6.4 [244] mainly for ISR and FSR, and further implement detector smearing and beam energy spread with our own code. We show the recoil mass distribution for the heavy Higgs boson mass of 0.5, 1, 1.5, 2, 2.5, 2.9 TeV each with 1, 10, 100 GeV width at a 3 TeV muon collider in Fig. IV.15 (right panel). Both cross sections of the signal and the background at fixed beam energy increase as the recoil mass increases due to the infrared nature of the photon radiation. The spread of recoil mass peak increases at a lower mass, due to the larger photon energy detector resolution smearing at a higher photon energy. We

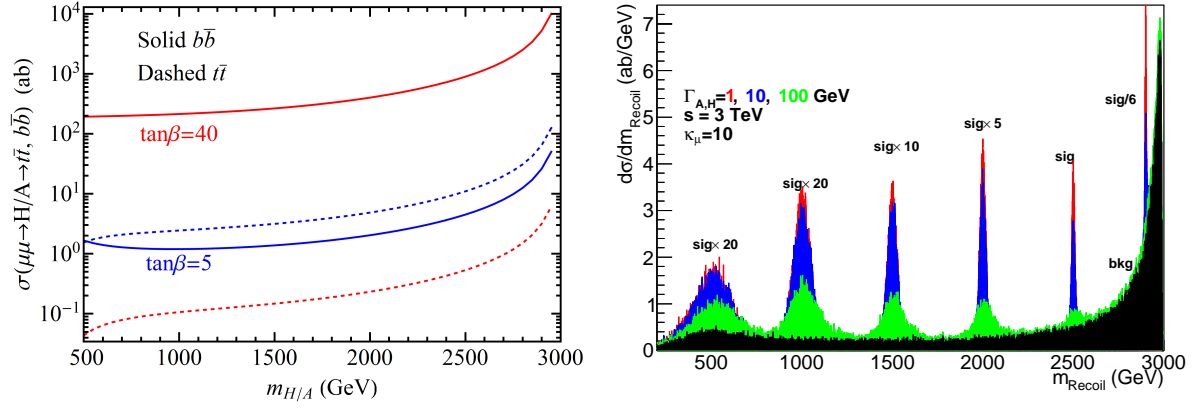


Figure IV.15: Left panel: total cross section for $H/A \rightarrow b\bar{b}$ (solid lines) and $t\bar{t}$ (dashed lines) as a function of $m_{H/A}$ at $\sqrt{s} = 3$ TeV, in Type-II 2HDM scenario for $\tan\beta = 5$ (blue) and 40 (red). Right panel: recoil mass distribution for heavy Higgs mass of 0.5, 1, 1.5, 2, 2.5, 2.9 TeV with total width 1 (red), 10 (blue), and 100 (green) GeV at a 3 TeV muon collider. The beam energy resolution and photon energy resolution are as shown in Table. IV.9. ISR and FSR are included but not beamstrahlung. Background (black) includes all events with a photon that has $p_T > 10$ GeV. Note that signal and background have different multiplication factors for clarity.

can see that the pronounced mass peaks look promising for the signal observation, and the RR process is a plausible discovery production mechanism that does not rely on the precise knowledge of the new heavy Higgs boson mass. We discuss the observability of this mode in next subsection.

b. Estimated Sensitivities To quantify the reach of the signal observation, we choose different bin sizes according to the spread of the photon energy distribution. This is because the recoil mass spread is broader than the photon energy smearing, as scaled by a factor of $\sqrt{\hat{s}}/m_{H/A}$. This implies the Higgs mass resolution would be much worse than the photon energy resolution if the mass is far away from the beam energy. We find the bin sizes in step of 1 GeV that optimize statistical significance of signal at $\kappa_\mu = 10$ over the background. With this optimal choice of number of bins, we show the 2σ exclusion (solid) and 5σ discovery (dashed) limits from RR in Fig. IV.16 for both 1.5 TeV and 3 TeV muon colliders as described in Table IV.9, for three different benchmark heavy Higgs width values 1, 10, and 100 GeV in red, blue, and green, respectively. The results show that the RR production mode could cover a large κ_μ ($\tan\beta$ in Type II 2HDM) region. To put these results into perspective, we reproduce the LHC curves for the discovery reach on the $m_A - \tan\beta$ plane in solid black lines for 300 fb^{-1} and 3000 fb^{-1} [193]. These LHC discovery projections are mainly from searches on heavier Higgs bosons decaying into SM particles such as $\tau^+\tau^-$ and $t\bar{t}$, in the maximal mixing scenario in the MSSM. This “wedge” shape indicates the LHC’s limitation in discovering heavy Higgs bosons in the medium $\tan\beta$ range, roughly when the production rate is minimal for the MSSM as a Type-II 2HDM. It is important to see the significant extension at the high energy muon collider via the RR process over the LHC coverage in the heavy Higgs parameter space.

3. ZH Associated Production and HA Pair Production

The ZH associated production and HA pair production of Eq. (IV.C.11) at tree level are mediated by an off-shell Z boson. The cross section for the ZH associated production is proportional to κ_Z^2 . On the other hand, the HA pair production is proportional to $1 - \kappa_Z^2$

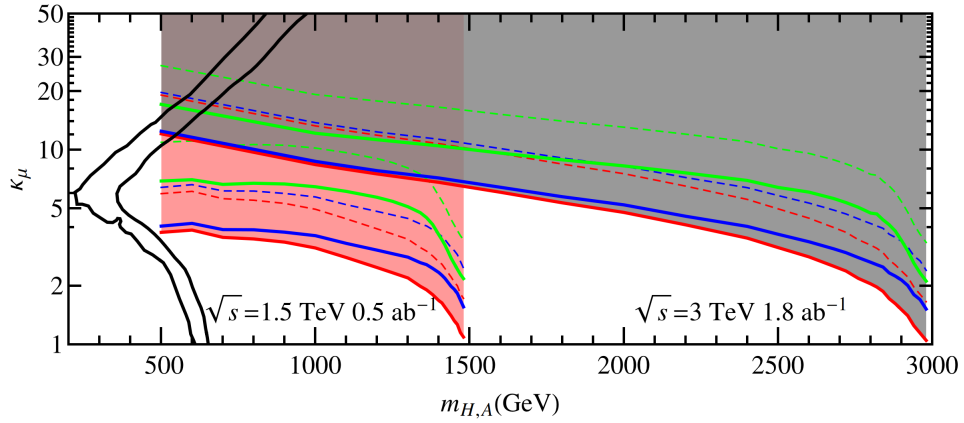


Figure IV.16: Estimated 2σ exclusion limits (solid) and 5σ discovery limits (dashed) in the Higgs mass and κ_μ plane, shown as shaded region. We include the cases with Higgs width 1 (red), 10 (blue), and 100 (green) GeV. We overlay the 3 TeV muon collider reach (gray shade) over 1.5 TeV muon collider results (pink shade). For comparison, the two solid black wedged curves reproduce the LHC coverage in m_A - $\tan\beta$ plane for 300 fb^{-1} and 3000 fb^{-1} , respectively.

in generic 2HDM models. These two channels bear some complementarity with each other. To quantify our study, we assume 90% tagging efficiency for the visible Z decays in the ZH associated production. We also studied the leptonic Z boson decay mode, where requirement on lepton p_T , angle and separation are imposed as described in Table IV.9. For simplicity, we take both the CP-even and CP-odd heavy Higgs bosons to have the same mass.

In Fig. IV.17 we show the event contours with 10 events (solid) and 50 events (dashed) for both ZH and HA channels in the $m_{H,A}-\kappa_Z$ plane. As expected, once crossing the kinematical threshold, the HA channel would be sensitive to a large range of κ_Z value. For instance, even for $\kappa \sim 0.97$, one still have 6% of the full cross section which leads to about 15 events. The kinematically favored channel ZH associated production is more sensitive than the HA pair production, expanding to a larger m_H region, as long as $\kappa_Z > 0.1$. A higher energy collider would extend the mass coverage to the multiple TeV kinematical limit, with a proportionally larger κ_Z value as seen in the figures.

4. Comparison of Different Modes

Kinematically, the RR process and the ZH associated production have quite different threshold behavior due to the massless nature of the photon. The closer the Higgs boson mass is to the energy threshold, the more effective the RR channel would be with respect to the ZH associated production. Well above the threshold on the other hand, these two processes scale with the energy in the same way as $1/s$. Dynamically, the RR process is only dependent on κ_μ , while both ZH associated production and HA pair production mainly depend on κ_Z . These two parameters are essentially independent of each other, characterizing the muon Yukawa coupling and the Higgs-gauge coupling, respectively.

It would be nevertheless informative to put side-by-side the reach of the two theory parameters via these two processes. Our results are summarized in Fig. IV.18, where we choose a 3 TeV muon collider to illustrate this comparison in the parameter plane $\kappa_\mu-\kappa_Z$. The shaded regions labeled by different values of the heavy Higgs mass show the higher signal rate from the RR process than both the ZH associated production and HA pair production. The nearly flat region for 1.4 TeV H and A represents the good sensitivity from

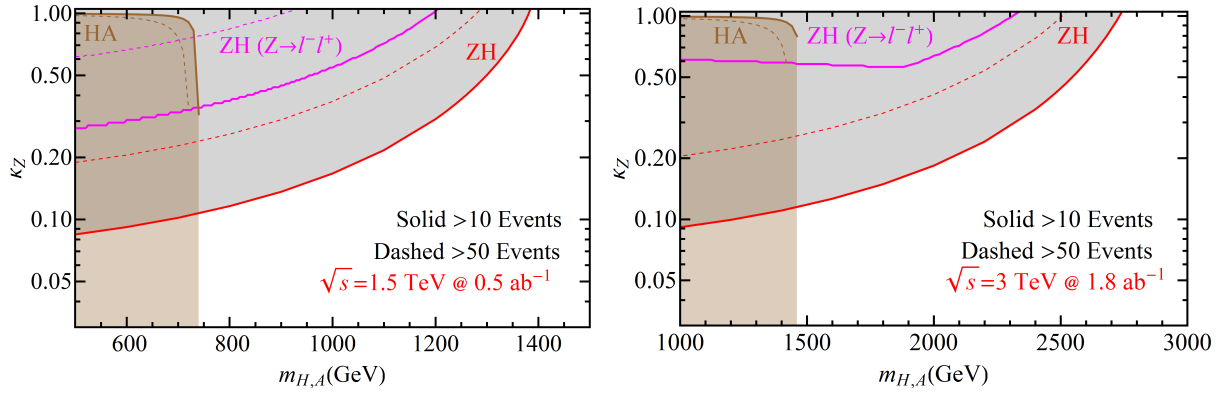


Figure IV.17: Sensitivity to the Higgs coupling κ_Z versus the Higgs mass for the ZH associated production (red for all visible Z decays, magenta for the leptonic Z decay only) and HA pair production (brown) for the muon collider defined as in Table IV.9 at the center of mass energy 1.5 TeV (left panel) and 3 TeV (right panel). Shaded regions bounded by solid (dashed) curves are regions with more than 10 (50) signal events being produced, indicating the exclusion (discovery) reach.

HA pair production in the low κ_Z region. As expected, the RR process is more sensitive for a heavier Higgs boson near the energy threshold, which would be especially important in the decoupling regime for ZH/HA processes. At higher (lower) energies, the mass reach scales up (down), but with a lower (higher) luminosity need scaled by $1/s$.

Only after specifying the underlying theory for the heavy Higgs bosons, and requiring the lighter Higgs boson in agreement with the current LHC measurement, these two parameters could be constrained in a correlated manner, subject to the experimental accuracy. The allowed κ_Z region is tightly constrained by the currently observed SM-like Higgs boson. We reproduce the allowed parameter regions from Ref. [178] for four types of 2HDM with current LHC data (solid) and projection after LHC-300 fb^{-1} (dashed). This illustrates that the RR processes is very much favored in 2HDM models, where the lighter SM-like Higgs boson carries most of the couplings to the electroweak gauge bosons.

5. Summary and Outlook

We studied the signature and sensitivity for heavy Higgs boson signals from three production modes at a high energy muon collider. Compared to the s -channel resonance at $\sqrt{s} = m_h$, these different production mechanisms do not rely on *a priori* knowledge of the Higgs boson mass, and thus avoid the broad scanning procedure. We find that radiative return (RR) is of particular interest. This signal (γH) is characterized by a mono-chromatic photon that yields a reconstructed recoil mass peak at the heavy Higgs boson mass. We performed numerical simulations for this signal and its SM backgrounds and showed the coupling-mass parameter space κ_μ - m (SUSY equivalent of $\tan\beta - M_A$) covered by such search at a high energy muon collider to be substantially extended over the LHC expectation with the direct observation of the heavy Higgs boson. Comparing with other modes of ZH and HA production at a lepton collider, the RR process is advantageous, especially for the “decoupled” scenarios in many 2HDM-like models. We further discussed its potential for measuring the invisible decays of the heavy Higgs boson and found some sensitivity especially for larger values of κ_μ . The RR process could certainly provide us an interesting option comparing to traditional scanning procedure for heavy Higgs boson discovery at a high energy muon collider.

Because of the lepton universality for gauge interactions, the processes $\mu^+\mu^- \rightarrow ZH, HA$ would be the same as those in e^+e^- collisions at the same c.m. energy since the contributions to both processes are overwhelmingly from the s -channel Z -exchange. Thus the advantage of the RR process (γH) would also apply when compared with a high energy e^+e^- collider, where the RR process is essentially absent.

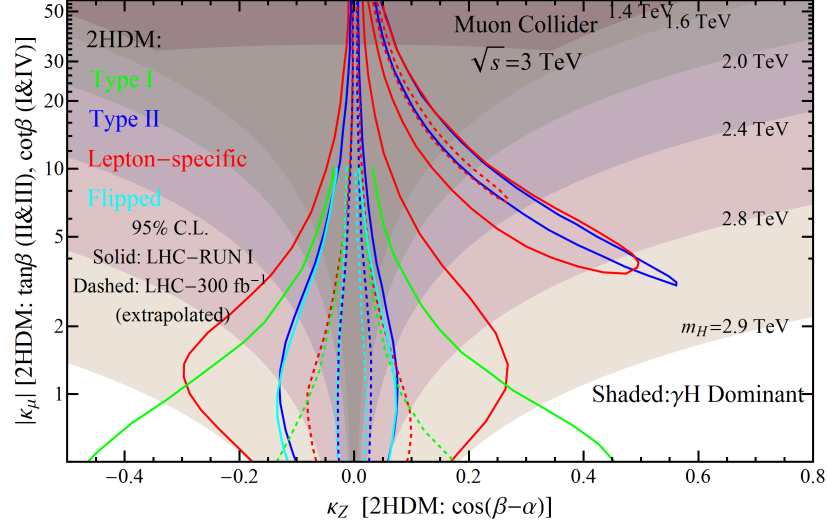


Figure IV.18: Comparison of sensitivities between different production mechanisms in the parameter plane κ_μ - κ_Z for different masses of the heavy Higgs boson at the 3 TeV muon collider. The shaded regions show the higher signal rate from the RR process than both the ZH associated production and HA pair production. We also reproduce the allowed parameter regions (extracted from Ref. [178]) for four types of 2HDM with current LHC data (solid) and projection after LHC-300 fb^{-1} (dashed).

V. CONCLUSIONS

In this chapter, we collect the key features of many of the studies discussed in previous chapters, detailed features of the each analysis can be found in the corresponding sections.

Dijet resonances: We study the colored resonance production at the LHC in a most general approach. We classify the possible colored resonances based on group theory decomposition, and construct their effective interactions with light partons. The production cross section from annihilation of valence quarks or gluons may be on the order of 400–1000 pb at LHC energies for a mass of 1 TeV with nominal couplings, leading to the largest production rates for new physics at the TeV scale, and simplest event topology with dijet final states. We apply the new dijet data from the LHC experiments to put bounds on various possible colored resonant states. The formulation is readily applicable for future searches including other decay modes.

Electroweak resonances: In this work, we study the physics potential for the Z' at the VLHC. We choose different benchmark models for the Z' , namely Z'_χ , Z'_ϕ , Z'_η , Z'_{LR} , Z'_{B-L} and Z'_{SSM} , and include also the mass mixing through the SM Higgs boson with additional $U(1)'$ charge. The latter introduces $Z' \rightarrow W^+W^-$ and $Z' \rightarrow Zh$ decay modes, in addition to the fermion decay modes. In conclusion, the newly observed Higgs-like particle at the LHC strongly motivates a muon collider as the Higgs factory. We proposed methods and evaluated the attainable accuracy to directly measure the Higgs width by scanning and fitting the s -channel resonance. The unparalleled precision would test the Higgs interactions to a high precision and undoubtedly take us to a deeper understanding of the electroweak-symmetry-breaking sector.

Multi-Higgs at colliders: We study the Higgs sector of the NMSSM in light of the discovery of the SM-like Higgs boson at the LHC. We perform a broad scan over the NMSSM

parameter space and identify the regions that are consistent with current Higgs search results at colliders. In contrast to the commonly studied “decoupling” scenario in the literature where the Minimal Supersymmetric Standard Model CP-odd Higgs boson mass is large $m_A \gg m_Z$, we pay particular attention to the light Higgs states in the case when $m_A \lesssim 2m_Z$. The Higgs bosons in the NMSSM, namely three CP-even states, two CP-odd states, and two charged Higgs states, could all be rather light, near or below the electroweak scale, although the singlet-like states can be heavier. The SM-like Higgs boson could be either the lightest CP-even scalar or the second lightest CP-even scalar, but is unlikely to be the heaviest scalar. These NMSSM parameter regions have unique properties and offer rich phenomenology. The decay branching fractions for the SM-like Higgs boson may be modified appreciably. The correlations of $\gamma\gamma/VV$ and $VV/b\bar{b}$ can be substantially altered. The new Higgs bosons may be readily produced at the LHC and may decay to non-standard distinctive final states, most notably a pair of Higgs bosons when kinematically accessible. We evaluate the production and decay of the Higgs bosons and comment on further searches at the LHC to probe the Higgs sector of the NMSSM. The Higgs sector in the NMSSM provides a well motivated theoretical framework consistent with the Higgs boson discovery and the searches at the LHC. The low- m_A parameter region yields multiple light Higgs bosons that lead to rich phenomenology at colliders. Although strongly constrained by the current searches, it is also highly predictive. Dedicated studies for this very interesting sector, in particular for a multiple Higgs boson final state at the LHC, will allow a search for this scenario to be completed in the near future.

SUSY dark matter: We investigate DM in the context of the MSSM. We scan through the MSSM parameter space and search for solutions that (a) are consistent with the Higgs discovery and other collider searches; (b) satisfy the flavor constraints from B physics; (c) give a DM candidate with the correct thermal relic density; and (d) are allowed by the DM direct detection experiments. For the surviving models with our parameter scan, we find the following features: (1) The DM candidate is largely a Bino-like neutralino with non-zero but less than 20% Wino and Higgsino fractions; (2) The relic density requirement clearly pins down the solutions from the Z and Higgs resonances (Z, h, H, A funnels) and co-annihilations; (3) Future direct search experiments will likely fully cover the Z, h funnel

regions, and H, A funnel regions as well except for the “blind spots”; (4) Future indirect search experiments will be more sensitive to the CP-odd Higgs exchange due to its s -wave nature; (5) The branching fraction for the SM-like Higgs decay to DM can be as high as 10%, while those from heavier Higgs decays to neutralinos and charginos can be as high as 20%. We show that collider searches provide valuable information complementary to what may be obtained from direct detections and astroparticle observations. In particular, the Z - and h -funnels with a predicted low LSP mass should be accessible at future colliders. Overall, the Higgs bosons may play an essential role as the portal to the dark sector. We conclude that understanding the nature of DM requires us to consider results from a number of different experiments. Future collider searches and the next generation of direct detection experiments will likely cover the conventional parameter range of the MSSM if the LSP constitutes all of the DM. The recent exciting discovery of the SM-like Higgs boson, and searches for beyond the SM physics at the energy frontier will serve as a new “lamp post” and guide in DM searches complementary to what may be obtained from direct detection and astro-particle observations at the cosmic frontier.

Light SUSY dark matter: We study the neutralino being the LSP as a cold DM candidate with a mass less than 40 GeV in the framework of the NMSSM. We find that with the current collider constraints from LEP, the Tevatron and the LHC, there are three types of light DM solutions consistent with the direct/indirect searches as well as the relic abundance considerations: (i) A_1 , H_1 -funnels, (ii) stau coannihilation and (iii) sbottom coannihilation. Type-(i) may take place in any theory with a light scalar (or pseudo-scalar) near the LSP pair threshold; while Type-(ii) and (iii) could occur in the framework of MSSM as well. We present a comprehensive study on the properties of these solutions and point out their immediate relevance to the experiments of the underground direct detection such as superCDMS and LUX/LZ, and the astro-physical indirect search such as Fermi-LAT. We also find that the decays of the SM-like Higgs boson may be modified appreciably and the new decay channels to the light SUSY particles may be sizable. The new light CP-even and CP-odd Higgs bosons will decay to a pair of LSPs as well as other observable final states, leading to interesting new Higgs phenomenology at colliders. For the light sfermion searches, the signals would be very challenging to observe at the LHC given the current

bounds. However, a high energy and high luminosity lepton collider, such as the ILC, would be able to fully cover these scenarios by searching for events with large missing energy plus charged tracks or displaced vertices. Overall, a light WIMP DM candidate remains to be of great interest both experimentally and theoretically. A light neutralino DM in the NMSSM may result in rich physics connecting all the current and the upcoming endeavors of the underground direct detection, astro-physical indirect searches, and collider signals related to the Higgs bosons and new light sfermions.

SUSY displaced decays: Supersymmetry searches at the LHC are both highly varied and highly constraining, but the vast majority are focused on cases where the final-stage visible decays are prompt. Scenarios featuring superparticles with detector-scale lifetimes have therefore remained a tantalizing possibility for sub-TeV SUSY, since explicit limits are relatively sparse. Nonetheless, the extremely low backgrounds of the few existing searches for collider-stable and displaced new particles facilitates recastings into powerful long-lived superparticle searches, even for models for which those searches are highly non-optimized. In this section, we assess the status of such models in the context of baryonic R-parity violation, gauge mediation, and mini-split SUSY. We explore a number of common simplified spectra where hadronic decays can be important, employing recasts of LHC searches that utilize different detector systems and final-state objects. The LSP/NLSP possibilities considered here include generic colored superparticles such as the gluino and light-flavor squarks, as well as the lighter stop and the quasi-degenerate Higgsino multiplet motivated by naturalness. We find that complementary coverage over large swaths of mass and lifetime is achievable by superimposing limits, particularly from CMS’s tracker-based displaced dijet search and heavy stable charged particle searches. Adding in prompt searches, we find many cases where a range of sparticle masses is now excluded from zero lifetime to infinite lifetime with no gaps. In other cases, the displaced searches furnish the only extant limits at any lifetime.

Higgs width at the ILC: We outline a systematic approach to the determination of the Standard Model-like Higgs boson total width and measurable coupling parameters in a model-independent manner at the ILC and illustrate the complementarity for operating the ILC at 250 GeV near the Zh threshold and at 500 GeV and 1 TeV utilizing the WW, ZZ fusion processes. We perform detailed simulations for an important contributing channel

to the coupling determination and for invisible decays. Without model assumptions, and combining the information for the coupling ratios from the LHC, the total width can be determined to an accuracy of about 6%, and the couplings for the observable channels can be measured to the (3–5)% level at 250 GeV, reaching (1–3)% level including the 500 GeV results, with further improvements possible with a 1 TeV run. The best precision for the branching fraction measurement of the Higgs to invisible modes can be reached at 0.5–0.7% around the Zh threshold. Further studies from ZZ fusion at higher energies may provide significant improvement for the measurements. With modest theory assumptions, the width and coupling determinations can be further improved to the percent or sub-percent level.

Higgs couplings from ZZ -fusion at the ILC: We evaluate the $e^-e^+ \rightarrow e^-e^+ + h$ process through the ZZ fusion channel at the ILC operating at 500 GeV and 1 TeV center of mass energies. We perform realistic simulations on the signal process and background processes. With judicious kinematic cuts, we find that the inclusive cross section can be measured to 2.9% after combining the 500 GeV at 500 fb⁻¹ and 1 TeV at 1 ab⁻¹ runs. A multivariate log-likelihood analysis further improves the precision of the cross section measurement to 2.3%. We discuss the overall improvement to model-independent Higgs width and coupling determinations and demonstrate the use of different channels in distinguishing new physics effects in Higgs physics. Our study demonstrates the importance of the ZZ fusion channel to Higgs precision physics, which has often been neglected in the literature.

Higgs boson at muon collider: In the light of the discovery of a 126 GeV Standard-Model-like Higgs boson at the LHC, we evaluate the achievable accuracies for direct measurements of the width, mass, and the s -channel resonant production cross section of the Higgs boson at a proposed muon collider. We find that with a beam energy resolution of $R = 0.01\%$ (0.003%) and integrated luminosity of 0.5 fb⁻¹ (1 fb⁻¹), a muon collider would enable us to determine the Standard-Model-like Higgs width to ± 0.35 MeV (± 0.15 MeV) by combining two complementary channels of the WW^* and $b\bar{b}$ final states. A non-Standard-Model Higgs with a broader width is also studied. The unparalleled accuracy potentially attainable at a muon collider would test the Higgs interactions to a high precision.

Higgs boson at muon collider through radiative return: Higgs boson properties could be studied with a high accuracy at a muon collider via the s -channel resonant pro-

duction. We consider the situation where the center-of-mass energy of the muon collider is off the resonance above the Higgs mass. We discuss the discovery potential for a generic heavy Higgs boson and compare different production mechanisms, including the “radiative return”, Z -boson associated production and heavy Higgs pair production. These production mechanisms do not sensitively rely on *a priori* knowledge of the heavy Higgs boson mass. We include various types of Two Higgs Doublet Models for the comparison. We conclude that the radiative return process could provide an important option for both the heavy Higgs discovery and direct measurement of invisible decays at a high energy muon collider.

Acknowledgement: I would like acknowledge many people who have played crucial roles in my graduate study, including,

- My advisor: Tao Han;
- My committee: Joseph Boudreau, Adam Leibovich, Ira Rothstein, Michael Wood-Vasey;
- My friends and colleagues in Pittsburgh, Madison, Fermilab, Zhejiang University and other institutions: Aryes Freitas, Steven Dytman, James Mueller, Josh Sayre, Sussane Westhoff, Brock Tweedie, Richard Ruiz, Chien-yi Chen, Zhouni Qian, Junmou Chen, Chao Wang, Cindy Cercone, Leyla Hirschfeld, Laura Provolt, Vernon Barger, Lisa Everett, Dan Chung, Frank Petriello, Ian Lewis, Gabe Shaughnessy, Zhe Dong, Linda Dolan, Peisi Huang, Yuxuan Wang, Xian Wu, Yan Wang, Fei Meng, Wenjiang Ma, Qiang Fu, Peng Zhou, Peng Xiao, Chris Hill, Estia Eichten, Stephen Parke, Marcela Carena, Joe Lykken, Bogdan Dobrescu, Roni Harnik, Paddy Fox, Anthony Difranzo, Pilar Coloma, Claudia Frugiuele, Elisabetta Furlan, Prateek Agrawal, Katrin Gemmler, Jack Kearney, Raoul Rontsch, Ran Zhou, Felix Yu, Olivia Vizcarra, Carlos Wagner, Lian-Tao Wang, Shufang Su, Ian Low, Kaoru Hagiwara, C.P. Yuan, Bo Feng, Guo-huai Zhu, Zhibai Zhang, Yihong Wang, Junqi Wang, Wenchao Wang, Xiaobo Tong, Chunqiang Shao, Yehua Liu, and many more;
- My fiancée: Linghong Zhang;
- My family members: Gen Liu, Caihua Xi, Yiqing Liu, Qingrong Meng, Zhu Liu, Caihong Xi, Meng Xi, Jiwei Xi, Caiji Xi and many more.

I especially want to thank my advisor Tao Han, without whom I cannot imagine my accomplishing Ph.D. and continuing in academia. Words fail me in describing how much I have been learning from him and how grateful I am for his mentorship. I owe him my eternal gratitude.

Zhen Liu

April 2015

VI. APPENDIX

A. CLEBSCH-GORDAN COEFFICIENTS

Here we exhibit the Clebsch-Gordan Coefficients relations that are needed in color resonance calculation for general $SU(N)$ groups. Typical initial state group structure includes $N \otimes N$, $N \otimes \bar{N}$, $N \otimes A$ and $A \otimes A$, whereas A denotes the adjoint representation of $SU(N)$.

We assume that the Clebsch-Gordan coefficients obey the following orthogonality relationship:

$$\text{Tr}[K^a \bar{K}_b] = \delta_b^a, \quad (\text{VI.A.1})$$

where $K^a = \bar{K}_a^\dagger$. The Clebsch-Gordan coefficients couple the different irreducible representations together in a gauge invariant way. Hence, depending on the interaction, the indices a take on different values. For example, according to our conventions in Eqs. (II.A.5) and (II.A.6):

$$a = \begin{cases} 1, \dots, \frac{N(N-1)}{2} & \text{couplings to the antisymmetric combination of } N \otimes N \text{ boson} \\ 1, \dots, \frac{N(N+1)}{2} & \text{couplings to the symmetric combination of } N \otimes N \text{ boson} \\ 1, \dots, N^2 - 1 & \text{couplings to the new fermion from } N \otimes A \end{cases} \quad (\text{VI.A.2})$$

Using this orthogonality condition, the following identities are used for the appropriate couplings:

$$\text{Tr}[K^a \bar{K}_a] = \begin{cases} \frac{N(N-1)}{2} & \text{couplings to the antisymmetric combination of } N \otimes N \text{ boson} \\ \frac{N(N+1)}{2} & \text{couplings to the symmetric combination of } N \otimes N \text{ boson} \\ N^2 - 1 & \text{couplings to the new fermion from } N \otimes A \end{cases} \quad (\text{VI.A.3})$$

Specifically for $SU(3)$ couplings, the color antisymmetric (symmetric) coupling of two quarks is the triplet-(sextet) scalar or vector diquark. Then we have for the diquark interactions in Eq. (II.A.5) and excited quark interactions in Eq. (II.A.6)

$$\text{Tr}[K^a \bar{K}_a] = \begin{cases} 3 & \text{couplings to the triplet diquark} \\ 6 & \text{couplings to the sextet diquark} \\ 8 & \text{couplings to the triplet and sextet excited quarks} \end{cases} \quad (\text{VI.A.4})$$

The complete symmetric invariant symbol of $SU(3)$ algebra satisfy

$$d^{ABC} d^{ABC} = 2C_F(N^2 - 4) \quad (\text{VI.A.5})$$

where as $C_F = (N^2 - 1)/2N$ is the eigenvalue of the quadratic $SU(N)$ Casimir operator acting on the fundamental representation. For $SU(3)$, $C_F = 4/3$.

B. FEYNMAN RULES

Here we give the explicit Feynman rules for the interacting vertices constructed in the text, as in Sec. II.A.2.

The diquark Feynman rules are in Eq. (B.1) and (B.2): Q_{N_D} may be E_{N_D} , D_{N_D} , or U_{N_D} , depending on the initial state. The labels $q, q' = u, d$ indicate whether the initial state quarks are up-type or down-type and α, β are generation indices. For the triplet diquark the Clebsch-Gordan coefficients are antisymmetric $K_{ab}^j = -K_{ba}^j$, and for the antisextet diquark they are symmetric $K_{ab}^j = K_{ba}^j$. C is the charge conjugation matrix.

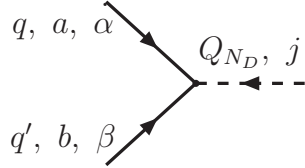
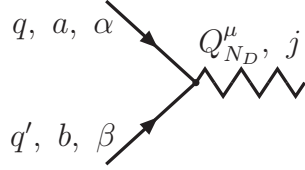
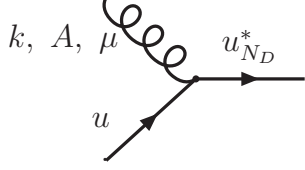
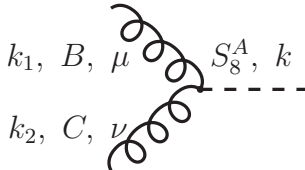
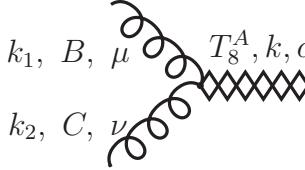
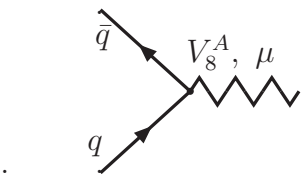
	$-i(1 + \delta_{qq'})\lambda_{\alpha\beta}^{Q_{ND}} K_{ab}^j C P_\tau$	(B.1)
	$q = q' : -i\lambda_{\alpha\beta}^{Q_{ND}} (K_{ab}^j P_R - K_{ba}^j P_L) C \gamma_\mu$ $q \neq q' : -i\lambda_{\alpha\beta}^{Q_{ND}} K_{ab}^j P_\tau C \gamma_\mu$	(B.2)
	$-2i\frac{g_s}{\Lambda} K_{ND,A} (\not{k}\gamma_\mu - k_\mu)(\lambda_L^U P_L + \lambda_R^U P_R)$	(B.3)
	$-4ig_s d^{ABC} \frac{\kappa_S}{\Lambda_S} ((k_1 \cdot k_2) g_{\mu\nu} - k_{2\mu} k_{1\nu})$	(B.4)
	$-2ig_s d^{ABC} \frac{\kappa_T}{\Lambda_T} (k_{1\alpha} k_{2\beta} g_{\mu\nu} - k_{1\nu} k_{2\beta} g_{\alpha\mu}$ $+ (k_1 \cdot k_2) g_{\alpha\mu} g_{\beta\nu} - k_{1\alpha} k_{2\mu} g_{\beta\nu}$ $+ 2f g_{\alpha\beta} ((k_1 \cdot k_2) g_{\mu\nu} - k_{2\mu} k_{1\nu}))$	(B.5)
	$V_8^0 : -ig_s T^A \gamma^\mu (g_L^{U/D} P_L + g_R^{U/D} P_R)$ $V_8^+ : -ig_s T^A \gamma^\mu (C_L V_L^{CKM} P_L + C_R V_R^{CKM} P_R)$	(B.6)

Figure VI.1: Feynman rules for the vertices of resonant particle couplings to quarks and gluons. All the momenta are incoming and $\tau = L, R$.

The excited quark Feynman rules in Eq. (B.3): equally applicable for both $u_{N_D}^*$ and $d_{N_D}^*$. The spin summation for a spin-2 tensor state (T_8^A) of mass M obeys the relation [553]:

$$\begin{aligned} \Sigma \epsilon_{\mu\nu}(k) \epsilon_{\rho\sigma}^*(k) &= B_{\mu\nu,\rho\sigma}(k) = \left(g_{\mu\rho} - \frac{k_\mu k_\rho}{M^2} \right) \left(g_{\nu\sigma} - \frac{k_\nu k_\sigma}{M^2} \right) \\ &+ \left(g_{\mu\sigma} - \frac{k_\mu k_\sigma}{M^2} \right) \left(g_{\nu\rho} - \frac{k_\nu k_\rho}{M^2} \right) - \frac{2}{3} \left(g_{\mu\nu} - \frac{k_\mu k_\nu}{M^2} \right) \left(g_{\rho\sigma} - \frac{k_\rho k_\sigma}{M^2} \right). \end{aligned}$$

C. CONSIDERATION OF ONE PHOTON SENSITIVITY

As discussed in the main text, we find it useful to simply veto events with a single, isolated photon in addition to an electron-positron pair. This cut reduces the potentially large background arising from Bhabha scattering plus radiation which can pass the invariant mass and p_T cuts. This cut also reduces signal events where the Higgs decays to a single photon plus invisible particles, or a single photon plus additional particles which are lost down the beam pipe. In general we do not expect this to be a relevant effect since our final sensitivity for the model-independent cross section is 2.5% while the Standard Model processes which might contribute to such events are at the level of 10^{-3} branching fractions or less. Only order of magnitude enhancements to these channels from exotic physics would be relevant to our analysis and such enhancements are constrained by exclusive searches at the LHC and in future at the ILC.

Nevertheless, there may be some exotic model which would produce an observable effect in the inclusive measurement which is not ruled out by other searches. We note that if one wishes to preserve sensitivity to exotic channels which could produce a single isolated photon, it is possible to institute cuts which will remove almost all of the background while preserving a substantial fraction of any such Higgs decays. We find that, in the reconstructed Higgs rest frame, the isolated photon in the background sample is not isotropically distributed. The background photon usually appears collinear to the Higgs boost direction, and/or confined to be near the radial plane containing the beam and the Higgs boost vector. This is because the photon is recoiling against the e^-e^+ pair with a possible boost along the beam axis due to additional unseen photons. We also find that measurement errors on the photon are

typically larger in the polar angle than in the azimuthal direction. Thus one can largely remove this background by cutting on the polar (with respect to the Higgs boost) and azimuthal (measured with respect to the Higgs-beam plane) angles of a single extra photon in the Higgs rest frame. We find the problematic background can be reduced to the level of a few fb while preserving $\sim 60\%$ of any hypothetical Higgs decay signal,¹ since the photon from such a decay would be isotropically distributed in the Higgs rest frame. Hence any new physics signal large enough to affect the inclusive rate would still be observable, although underestimated.

We note that a cut similar in spirit to this one is already present in the widely used analysis of Higgsstrahlung inclusive measurement at the 250 GeV ILC [184]. In that case additional single photons were removed by a “ p_T balance” cut when the p_T of an isolated photon accounted for the bulk of the e^-e^+ pair p_T . However, since this more complicated approach does not materially change our results we present the simpler case of simply vetoing the single isolated photon as described in the main text.

D. Z' AT THE LHC

Here we establish our notation and summarize the basic formalism for the production and decay of a Z' into a fermion pair at the LHC by the process $p_A p_B \rightarrow f\bar{f} + X$. We define $s = (p_A + p_B)^2$ and $\hat{s} = (p_f + p_{\bar{f}})^2$, where in our examples we take $s = (14 \text{ TeV})^2$ and $\hat{s} = (3 \text{ TeV})^2$. y is the $f\bar{f}$ rapidity, with $y > 0$ along the \vec{p}_A direction (i.e., the $f\bar{f}$ boost direction). θ^* is the angle of f in the $f\bar{f}$ rest frame, defined² with respect to y (i.e., with respect to \vec{p}_A for $y > 0$ and \vec{p}_B for $y < 0$), and $z = \cos\theta^*$. We ignore the transverse momentum p_T of the $f\bar{f}$ system.

Let $f_{q_i}(x)[f_{\bar{q}_i}(x)]$ be the proton PDF of the i^{th} flavor quark [antiquark] q_i [\bar{q}_i], evaluated at the scale μ^2 , which we will take to be \hat{s} . The tree-level cross section for Drell-Yan production

¹This fraction is relative to other decay channels not affected by the cut, since other cuts will affect all decays equally.

²The θ^* convention is opposite that in [220] for $y < 0$, which was motivated by the simultaneous study of $p\bar{p}$.

is then

$$\frac{d\sigma}{d\hat{s} dy dz} = \frac{1}{\hat{s}} \sum_{i=u,d,c,s,b} \left[p_i(\hat{s}, y) \frac{d\sigma(q_i \bar{q}_i \rightarrow f \bar{f})}{dz} + \bar{p}_i(\hat{s}, y) \frac{d\sigma(\bar{q}_i q_i \rightarrow f \bar{f})}{dz} \right], \quad (\text{VI.D.6})$$

where³

$$p_i(\hat{s}, y) \equiv x_A x_B f_{q_i}(x_A) f_{\bar{q}_i}(x_B), \quad \bar{p}_i(\hat{s}, y) \equiv x_A x_B f_{\bar{q}_i}(x_A) f_{q_i}(x_B), \quad (\text{VI.D.7})$$

with

$$x_{A,B} \equiv \sqrt{\frac{\hat{s}}{s}} e^{\pm y}. \quad (\text{VI.D.8})$$

For family-independent couplings and ignoring quark masses, we can absorb the heavier quark PDFs into $p_{u,d}$, i.e., we redefine $p_u + p_c \rightarrow p_u$ and $p_d + p_s + p_b \rightarrow p_d$, and similarly for $\bar{p}_{u,d}$, with $\sum_{i=u,d,c,s,b} \rightarrow \sum_{i=u,d}$. We also define the distribution functions integrated over rapidity

$$P_i(\hat{s}, y_1, y_2) = \int_{y_1}^{y_2} p_i(\hat{s}, y) dy, \quad \bar{P}_i(\hat{s}, y_1, y_2) = \int_{y_1}^{y_2} \bar{p}_i(\hat{s}, y) dy, \quad (\text{VI.D.9})$$

where $0 \leq y_1 < y_2 \leq y_{max}$.

The differential cross sections in (VI.D.6) due to s -channel γ , Z , and Z' are given by

$$\frac{d\sigma(q_i \bar{q}_i \rightarrow f \bar{f})}{dz} = \frac{C_f}{384\pi\hat{s}} \left\{ [G_{LL}^i + G_{RR}^i] (1+z)^2 + [G_{LR}^i + G_{RL}^i] (1-z)^2 \right\}, \quad (\text{VI.D.10})$$

where C_f is the color factor (1 for leptons and 3 for quarks), and⁴

$$G_{ab}^i(\hat{s}) = \left| e^2 q^i q^f + \frac{g_a^{1i} g_b^{1f} \hat{s}}{\hat{s} - M_Z^2 + iM_Z \Gamma_Z} + \frac{g_a^{2i} g_b^{2f} \hat{s}}{\hat{s} - M_{Z'}^2 + iM_{Z'} \Gamma_{Z'}} \right|^2 \quad (\text{VI.D.11})$$

for $a, b = L, R$. The expression for $\frac{d\sigma(\bar{q}_i q_i \rightarrow f \bar{f})}{dz}$ is the same except $(1 \pm z)^2 \rightarrow (1 \mp z)^2$. We have ignored the masses of the initial and final fermions in (VI.D.10), which is an adequate approximation except for the t quark. For our simulations, the top quarks mass is approximately included. The massive top quark will also affect the top charge tagging

³Higher order QCD K factors $K(\hat{s}, y)$ can be included in p_i and \bar{p}_i . We have not implemented the K factors in the present study. They will potentially increase the sensitivity through an increase in cross section, and may alter the angular distribution slightly.

⁴ G_{ab}^i and the analogous C_{ab}^i defined in (VI.D.14) should more properly be written as G_{ab}^{if} and C_{ab}^{if} , respectively. We usually suppress the dependence on the final state fermion for notational simplicity.

efficiency through its leptonic decays. For simplicity, we will evaluate the SM couplings for both the LHC and ILC cases at M_Z .

Near the Z' pole it is often adequate to ignore the γ and Z , in which case

$$G_{ab}^i(\hat{s}) \rightarrow \hat{s}^2 |D(\hat{s})|^2 C_{ab}^i, \quad (\text{VI.D.12})$$

where

$$|D(\hat{s})|^2 = \frac{1}{(\hat{s} - M_{Z'}^2)^2 + M_{Z'}^2 \Gamma_{Z'}^2} \quad (\text{VI.D.13})$$

is the Breit-Wigner propagator-squared and

$$C_{ab}^i \equiv |g_a^i|^2 |g_b^f|^2, \quad a, b = L, R. \quad (\text{VI.D.14})$$

1. Narrow Width Approximation

We first consider Z' production, ignoring interference effects, in the narrow width approximation (NWA),

$$|D(\hat{s})|^2 \rightarrow \frac{\pi}{M_{Z'} \Gamma_{Z'}} \delta(\hat{s} - M_{Z'}^2). \quad (\text{VI.D.15})$$

This is a reasonable first approximation for a multi-TeV scale Z' with electroweak couplings, for which typically $\Gamma_{Z'}/M_{Z'} = \mathcal{O}(1\%)$ unless there are important non-SM decay channels.

The cross section is then

$$\begin{aligned} \frac{d\sigma}{dy dz} &\rightarrow \frac{C_f}{384 M_{Z'} \Gamma_{Z'}} \sum_{i=u,d} \{ [p_i C_N^i + \bar{p}_i C_F^i] (1+z)^2 + [p_i C_F^i + \bar{p}_i C_N^i] (1-z)^2 \} \\ &= \frac{C_f}{384 M_{Z'} \Gamma_{Z'}} \sum_{i=u,d} \{ p_i^+ C_+^i (1+z^2) + 2p_i^- C_-^i z \}, \end{aligned} \quad (\text{VI.D.16})$$

where

$$p_i^\pm \equiv p_i \pm \bar{p}_i, \quad P_i^\pm \equiv P_i \pm \bar{P}_i, \quad (\text{VI.D.17})$$

and

$$\begin{aligned} C_N^i &\equiv C_{LL}^i + C_{RR}^i, & C_F^i &\equiv C_{LR}^i + C_{RL}^i \\ C_\pm^i &\equiv C_N^i \pm C_F^i = (C_{LL}^i + C_{RR}^i) \pm (C_{LR}^i + C_{RL}^i). \end{aligned} \quad (\text{VI.D.18})$$

Integrating over angles (one could include a cut on maximum $|z|$):

$$\begin{aligned}\frac{d\sigma}{dy} &= \int_{-1}^{+1} \frac{d\sigma}{dy dz} dz = \frac{C_f}{144 M_{Z'} \Gamma_{Z'}} \{p_u^+ C_+^u + p_d^+ C_+^d\} \\ \sigma &= \left(\int_{y_1}^{y_2} + \int_{-y_2}^{-y_1} \right) \frac{d\sigma}{dy} dy = \frac{C_f}{72 M_{Z'} \Gamma_{Z'}} \{P_u^+ C_+^u + P_d^+ C_+^d\}.\end{aligned}\tag{VI.D.19}$$

These results are sometimes rewritten in terms of the Z' partial widths

$$\begin{aligned}\Gamma(Z' \rightarrow f\bar{f}) &= \frac{C_f M_{Z'}}{24\pi} (|g_L^f|^2 + |g_R^f|^2) \\ \Gamma(Z' \rightarrow q_i \bar{q}_i) &= \frac{M_{Z'}}{8\pi} (|g_L^i|^2 + |g_R^i|^2),\end{aligned}\tag{VI.D.20}$$

so that

$$\frac{d\sigma}{dy} = \frac{4\pi^2}{3M_{Z'}^3} [p_u^+ \Gamma(Z' \rightarrow u\bar{u}) + p_d^+ \Gamma(Z' \rightarrow d\bar{d})] B(Z' \rightarrow f\bar{f}),\tag{VI.D.21}$$

where $B(Z' \rightarrow f\bar{f}) \equiv \Gamma(Z' \rightarrow f\bar{f})/\Gamma_{Z'}$ is the branching ratio into $f\bar{f}$. Similarly,

$$\sigma \equiv \sigma_{Z'} B(Z' \rightarrow f\bar{f}) = \frac{8\pi^2}{3M_{Z'}^3} [P_u^+ \Gamma(Z' \rightarrow u\bar{u}) + P_d^+ \Gamma(Z' \rightarrow d\bar{d})] B(Z' \rightarrow f\bar{f})\tag{VI.D.22}$$

is the total cross section into $f\bar{f}$. (We will sometimes denote σ by σ^f or by $\sigma[f\bar{f}]$.) Since $\Gamma_{Z'}$ is not known a priori (except in specific models) one cannot directly constrain the absolute couplings from σ^f , although one can obtain ratios of couplings by comparing different final states. However, if $\Gamma_{Z'}$ can be measured independently from the lineshape to a precision of around 25 GeV as shown in the left panel of Fig. III.1, then $\sigma^f \Gamma_{Z'} = \sigma_{Z'} \Gamma(Z' \rightarrow f\bar{f})$ does contain information on the absolute couplings. Another difficulty is that the cross section for a given f depends on the combination $C_+^u + C_+^d (P_d^+/P_u^+)$. In principle, one could separate $C_{u,d}^+$ by using the rapidity dependence, but in practice there is little sensitivity for $M_{Z'} \gtrsim 3$ TeV. (Similar statements apply to the rapidity dependence of the angular distribution.) The u and d couplings could, however, be separated if one can observe $b\bar{b}$ and $t\bar{t}$ (assuming family-universality).

In addition to $\Gamma_{Z'}$, the total cross sections suffer from PDF, luminosity, K factor, and other systematic uncertainties. These difficulties are reduced for ratios of rates for different final states, angular distributions, and final state polarizations.

2. Angular Distribution

Define the forward (F) and backward (B) cross sections for rapidity y as

$$F(y) \equiv \int_0^1 \frac{d\sigma}{dy dz} dz, \quad B(y) \equiv \int_{-1}^0 \frac{d\sigma}{dy dz} dz. \quad (\text{VI.D.23})$$

Recall that positive z corresponds to f in the direction of the rapidity, so that F and B are symmetric under $y \rightarrow -y$. It is also useful to define F and B integrated over a range of $|y|$:

$$F \equiv \left(\int_{y_1}^{y_2} + \int_{-y_2}^{-y_1} \right) F(y) dy, \quad B \equiv \left(\int_{y_1}^{y_2} + \int_{-y_2}^{-y_1} \right) B(y) dy. \quad (\text{VI.D.24})$$

The forward-backward asymmetries are then

$$\begin{aligned} A_{FB}(y) &\equiv \frac{F(y) - B(y)}{F(y) + B(y)} = \frac{3}{4} \frac{p_u^- C_-^u + p_d^- C_-^d}{p_u^+ C_+^u + p_d^+ C_+^d} \\ A_{FB} &\equiv \frac{F - B}{F + B} = \frac{3}{4} \frac{P_u^- C_-^u + P_d^- C_-^d}{P_u^+ C_+^u + P_d^+ C_+^d}, \end{aligned} \quad (\text{VI.D.25})$$

for which the $\Gamma_{Z'}$, luminosity, and some of the PDF uncertainties cancel. Of course, $A_{FB}(0) = 0$ for pp since $p_-^i = 0$, but $A_{FB}(y)$ can be nonzero for $y \neq 0$ [220]. For large positive y , for example, the cross section is dominated by $q_i \bar{q}_i$, with little dilution from $\bar{q}_i q_i$, leading to the possibility of a large asymmetry. Of course, the cross section is smaller at high y , so that one should try to optimize the $y_{1,2}$ range.

The forward-backward asymmetry is equivalent to the charge asymmetry A_c defined by

$$A_{FB} = A_c \equiv \frac{\sigma(|y_f| > |y_{\bar{f}}|) - \sigma(|y_f| < |y_{\bar{f}}|)}{\sigma(|y_f| > |y_{\bar{f}}|) + \sigma(|y_f| < |y_{\bar{f}}|)}, \quad (\text{VI.D.26})$$

at least in the absence of cuts.

3. Final State Polarization

One can also consider final state polarizations⁵, defined as

$$P_f = \frac{\sigma^{f_R} - \sigma^{f_L}}{\sigma^{f_R} + \sigma^{f_L}}, \quad (\text{VI.D.27})$$

where σ^{f_R} and σ^{f_L} are respectively the rates for producing right and left-helicity f .

In addition to (VI.D.18) it is convenient to define the combinations

$$\begin{aligned} C_L^i &\equiv C_{LL}^i + C_{LR}^i, & C_R^i &\equiv C_{RL}^i + C_{RR}^i \\ \hat{C}_L^i &\equiv C_{LL}^i - C_{RL}^i, & \hat{C}_R^i &\equiv C_{LR}^i - C_{RR}^i, \end{aligned} \quad (\text{VI.D.28})$$

and

$$\begin{aligned} C_P^i &\equiv C_L^i - C_R^i = C_{LL}^i - C_{RR}^i + C_{LR}^i - C_{RL}^i \\ \hat{C}_P^i &\equiv \hat{C}_L^i - \hat{C}_R^i = C_{LL}^i - C_{RR}^i - C_{LR}^i + C_{RL}^i, \end{aligned} \quad (\text{VI.D.29})$$

with

$$C_L^i + C_R^i = \hat{C}_L^i + \hat{C}_R^i = C_N^i + C_F^i = C_+^i. \quad (\text{VI.D.30})$$

Then, ignoring the mass of f ,

$$P_f = - \frac{\sum_{i=u,d} \left\{ p_i^+ \hat{C}_P^i (1+z^2) + 2p_i^- C_P^i z \right\}}{\sum_{i=u,d} \left\{ p_i^+ C_+^i (1+z^2) + 2p_i^- C_-^i z \right\}}. \quad (\text{VI.D.31})$$

One can integrate the numerator and denominator separately over the desired ranges of y and z . The polarization of \bar{f} is opposite to that of f for $m_f \sim 0$.

⁵Here we list just the polarizations. In practice, it might be best to consider the actual observables that depend on the polarization, i.e., the angular distributions of the f and \bar{f} decay products.

4. Beyond the Narrow Width Approximation

Define the combinations $G_{N,F}^i, G_{\pm}^i, G_{L,R}^i, \hat{G}_{L,R}^i, G_P^i$, and \hat{G}_P^i of the parameters $G_{ab}^i(\hat{s})$ in (VI.D.11) in analogy with the combinations of C_{ab}^i in (VI.D.18), (VI.D.28), and (VI.D.29). Then

$$\begin{aligned} \frac{d\sigma}{d\hat{s} dy dz} &= \frac{C_f}{384\pi\hat{s}^2} \sum_{i=u,d} \left\{ [p_i G_N^i + \bar{p}_i G_F^i] (1+z)^2 + [p_i G_F^i + \bar{p}_i G_N^i] (1-z)^2 \right\} \\ &= \frac{C_f}{384\pi\hat{s}^2} \sum_{i=u,d} \left\{ p_i^+ G_+^i (1+z^2) + 2p_i^- G_-^i z \right\}, \end{aligned} \quad (\text{VI.D.32})$$

Other relevant observables (for $m_f = 0$) are then

$$\begin{aligned} \frac{d\sigma}{d\hat{s} dz} &= \frac{C_f}{192\pi\hat{s}^2} \sum_{i=u,d} \left\{ P_i^+ G_+^i (1+z^2) + 2P_i^- G_-^i z \right\} \\ \frac{d\sigma}{d\hat{s} dy} &= \frac{C_f}{144\pi\hat{s}^2} \left\{ p_u^+ G_+^u + p_d^+ G_+^d \right\} \\ \frac{d\sigma}{d\sqrt{\hat{s}}} &= 2\sqrt{\hat{s}} \frac{d\sigma}{d\hat{s}} = \frac{C_f}{36\pi\hat{s}^{3/2}} \left\{ P_u^+ G_+^u + P_d^+ G_+^d \right\} \\ A_{FB}(\hat{s}, y) &= \frac{3}{4} \frac{p_u^- G_-^u + p_d^- G_-^d}{p_u^+ G_+^u + p_d^+ G_+^d} \\ P_f &= - \frac{\sum_{i=u,d} \left\{ p_i^+ \hat{G}_P^i (1+z^2) + 2p_i^- G_P^i z \right\}}{\sum_{i=u,d} \left\{ p_i^+ G_+^i (1+z^2) + 2p_i^- G_-^i z \right\}}. \end{aligned} \quad (\text{VI.D.33})$$

One can separately integrate the numerator and denominator of A_{FB} over the desired ranges of \hat{s} and y to obtain the integrated asymmetry. Similarly, the numerator and denominator of P_f can be separately integrated over the desired ranges of \hat{s} , y , and z . The polarization of \bar{f} is opposite to that of f for $m_f \sim 0$.

E. Z' AT THE ILC

We now consider $e^-e^+ \rightarrow f\bar{f}$ at CM energy \sqrt{s} . The final fermion f can be μ, τ, b, t or possibly c, s , or unidentified quark. (We do not consider $f = e$ because that involves t channel exchange as well as s channel.) Define

$$G_{ab}^e(s) = \left| e^2 q^e q^f + \frac{g_a^{1e} g_b^{1f} s}{s - M_Z^2 + iM_Z \Gamma_Z} + \frac{g_a^{2e} g_b^{2f} s}{s - M_{Z'}^2 + iM_{Z'} \Gamma_{Z'}} \right|^2, \quad (\text{VI.E.34})$$

in analogy to (VI.D.11). We assume $M_Z \ll \sqrt{s} \ll M_{Z'}$, so we can ignore Γ_Z and $\Gamma_{Z'}$.

1. No Polarization

In the absence of polarization for the e^\mp the observables are

$$\begin{aligned} \frac{d\sigma(s)}{dz} &= \frac{C_f}{128\pi s} \{ [G_{LL}^e + G_{RR}^e] (1+z)^2 + [G_{LR}^e + G_{RL}^e] (1-z)^2 \} \\ &= \frac{C_f}{128\pi s} \{ G_+^e (1+z^2) + 2G_-^e z \} \\ \sigma(s) &= \frac{C_f}{48\pi s} G_+^e \\ A_{FB}(s) &= \frac{3}{4} \frac{G_-^e}{G_+^e} \\ P_f &= -\frac{\hat{G}_P^e (1+z^2) + 2G_P^e z}{G_+^e (1+z^2) + 2G_-^e z}, \end{aligned} \quad (\text{VI.E.35})$$

where the various G_{ab}^e combinations are defined in analogy to the combinations of C_{ab}^i in (VI.D.18), (VI.D.28), and (VI.D.29). As usual, one can integrate numerator and denominator of P_f over z to obtain the average polarization $P_f = -\hat{G}_P^e/G_+^e$.

Although we are mainly concerned with the regime $M_Z \ll \sqrt{s} \ll M_{Z'}$ it is nevertheless useful to display the asymmetries and polarizations at the Z or Z' pole, ignoring interferences. For $s = M_Z^2$,

$$\begin{aligned} A_{FB}(M_Z^2) &\rightarrow \frac{3}{4} A_e^1 A_f^1 \\ P_f(M_Z^2) &\rightarrow -\frac{A_f(1+z^2) + 2A_e z}{(1+z^2) + 2A_e A_f z} \rightarrow -A_f^1 \end{aligned} \quad (\text{VI.E.36})$$

with

$$A_f^1 \equiv \frac{(g_L^{1f})^2 - (g_R^{1f})^2}{(g_L^{1f})^2 + (g_R^{1f})^2} = \frac{2 g_V^{1f} g_A^{1f}}{(g_V^{1f})^2 + (g_A^{1f})^2}. \quad (\text{VI.E.37})$$

The second form for P_f is the average polarization. Similar expressions hold at the Z' pole, with $A_f^1 \rightarrow A_f^2$ and $g_a^{1f} \rightarrow g_a^{2f}$.

2. Fixed Initial State Polarization

For V and A interactions (and ignoring m_e), only the combinations $e_L^- e_R^+$ and $e_R^- e_L^+$ contribute yield nonzero amplitudes (unlike, S , P , and T , which are sensitive to $e_L^- e_L^+$ and $e_R^- e_R^+$). We define the initial state polarizations

$$\mathcal{P}^- = \eta_L^- - \eta_R^-, \quad \mathcal{P}^+ = \eta_R^+ - \eta_L^+, \quad (\text{VI.E.38})$$

where η_L^- and $\eta_R^- = 1 - \eta_L^-$ are respectively the fractions of L and R -helicity e^- , and similarly for e^+ . Note that (neglecting m_e) $\mathcal{P}^- = \mathcal{P}^+ \sim 1$ for e^\mp produced in weak charge current processes. Also note that the definition of \mathcal{P}^- is conventional for $e^- e^+$, though it is opposite in sign from usual polarization definitions. Some useful relations are

$$\eta_{L,R}^- = \frac{1 \pm \mathcal{P}^-}{2}, \quad \eta_{L,R}^+ = \frac{1 \mp \mathcal{P}^+}{2} \quad (\text{VI.E.39})$$

$$\frac{\eta_L^- \eta_R^+}{\eta_L^- \eta_R^+ + \eta_R^- \eta_L^+} = \frac{1 + \mathcal{P}_{eff}}{2}, \quad \frac{\eta_R^- \eta_L^+}{\eta_L^- \eta_R^+ + \eta_R^- \eta_L^+} = \frac{1 - \mathcal{P}_{eff}}{2}, \quad (\text{VI.E.40})$$

where the effective polarization is defined as

$$\mathcal{P}_{eff} \equiv \frac{\mathcal{P}^- + \mathcal{P}^+}{1 + \mathcal{P}^- \mathcal{P}^+} = \frac{\eta_L^- \eta_R^+ - \eta_R^- \eta_L^+}{\eta_L^- \eta_R^+ + \eta_R^- \eta_L^+}. \quad (\text{VI.E.41})$$

For example, $\mathcal{P}^- = 0.80$ and $\mathcal{P}^+ = 0.30$ yields $\mathcal{P}_{eff} \sim 0.89$, while $(\mathcal{P}^-, \mathcal{P}^+) = (0.80, 0.60) \Rightarrow \mathcal{P}_{eff} \sim 0.95$.

The relevant observables for fixed polarizations are

$$\begin{aligned}
\frac{d\sigma}{dz} &= \frac{C_f}{32\pi s} \left\{ [\eta_L^- \eta_R^+ G_{LL}^e + \eta_R^- \eta_L^+ G_{RR}^e] (1+z)^2 \right. \\
&\quad \left. + [\eta_L^- \eta_R^+ G_{LR}^e + \eta_R^- \eta_L^+ G_{RL}^e] (1-z)^2 \right\} \\
\sigma &= \frac{C_f}{12\pi s} [\eta_L^- \eta_R^+ G_L^e + \eta_R^- \eta_L^+ G_R^e] \\
A_{FB} &= \frac{3}{4} \frac{G_-^e + \mathcal{P}_{eff} \hat{G}_P^e}{G_+^e + \mathcal{P}_{eff} G_P^e} \rightarrow \frac{3}{4} A_f \frac{A_e + \mathcal{P}_{eff}}{1 + \mathcal{P}_{eff} A_e} \\
P_f &= - \frac{[\hat{G}_P^e + \mathcal{P}_{eff} G_-^e] (1+z^2) + 2[G_P^e + \mathcal{P}_{eff} G_+^e] z}{[G_+^e + \mathcal{P}_{eff} G_P^e] (1+z^2) + 2[G_-^e + \mathcal{P}_{eff} \hat{G}_P^e] z} \\
&\rightarrow - \frac{[A_f + \mathcal{P}_{eff} A_e A_f] (1+z^2) + 2[A_e + \mathcal{P}_{eff}] z}{[1 + \mathcal{P}_{eff} A_e] (1+z^2) + 2[A_e A_f + \mathcal{P}_{eff} A_f] z} \\
&\rightarrow -A_f.
\end{aligned} \tag{VI.E.42}$$

The second forms for A_{FB} and P_f are valid at the Z or Z' pole (the superscript 1 or 2 on $A_{e,f}$ is implied). The third form for P_f is obtained by integrating the numerator and denominator over z .

3. Polarization Asymmetries

Denote the cross sections for the polarizations \mathcal{P}^\mp defined in the previous section by σ_L , and let σ_R represent the cross section for reversed polarizations

$$\eta_{L,R}^- \rightarrow \bar{\eta}_{L,R}^-, \quad \eta_{L,R}^+ \rightarrow \bar{\eta}_{L,R}^+, \tag{VI.E.43}$$

with

$$\bar{\eta}_{L,R}^- = \eta_{R,L}^-, \quad \bar{\eta}_{L,R}^+ = \eta_{R,L}^+, \tag{VI.E.44}$$

so that $\mathcal{P}^\mp \rightarrow -\mathcal{P}^\mp$. For example,

$$\begin{aligned}
\sigma_L &= \frac{C_f}{12\pi s} \{ \eta_L^- \eta_R^+ G_L^e + \eta_R^- \eta_L^+ G_R^e \} \\
\sigma_R &= \frac{C_f}{12\pi s} \{ \bar{\eta}_L^- \bar{\eta}_R^+ G_L^e + \bar{\eta}_R^- \bar{\eta}_L^+ G_R^e \} = \frac{C_f}{12\pi s} \{ \eta_R^- \eta_L^+ G_L^e + \eta_L^- \eta_R^+ G_R^e \}.
\end{aligned} \tag{VI.E.45}$$

For $\mathcal{P}^\pm = 0$ these both reduce to the unpolarized cross section σ .

The polarization (left-right) asymmetry is defined as

$$A_{LR} \equiv \frac{\sigma_L - \sigma_R}{\sigma_L + \sigma_R} = \mathcal{P}_{eff} \frac{G_P^e}{G_+^e} \rightarrow \mathcal{P}_{eff} A_e, \quad (\text{VI.E.46})$$

where the second form is valid on the Z or Z' pole. (At the pole, A_{LR} is independent of the final state, allowing the determination of A_e from the total cross section polarization asymmetry.) It is also useful to define the total polarization asymmetry

$$A_{LR}^{tot} \equiv \frac{\sigma_L^{tot} - \sigma_R^{tot}}{\sigma_L^{tot} + \sigma_R^{tot}} = \mathcal{P}_{eff} \frac{\sum_f C_f G_P^{ef}}{\sum_f C_f G_+^{ef}} \rightarrow \mathcal{P}_{eff} A_e, \quad (\text{VI.E.47})$$

where we have added the superscript to emphasize the final state f . The sum can be taken over $f = \mu, \tau, u, d, c, s, b$, and t (if one ignores m_t). A_{LR}^{tot} is convenient in that one does not have to identify the final state (other than removing $f = e$, which also has t -channel contributions) and because one therefore has much higher statistics. However, the asymmetries between different final states may partially cancel away from the poles.

Assuming that the e^- and e^+ polarizations can each be turned off or reversed without affecting the magnitudes, one could in principle determine G_P^e/G_+^e (or the analogous quantity in (VI.E.47)), \mathcal{P}_{eff} , \mathcal{P}^- , and \mathcal{P}^+ experimentally by measuring the asymmetries obtained by reversing the polarizations ($\mathcal{P}^-, \mathcal{P}^+$), ($\mathcal{P}^-, 0$), and ($0, \mathcal{P}^+$) (the Blondel scheme [554]).

Another useful observable is the left-right forward-backward asymmetry

$$A_{LR}^{FB} \equiv \frac{F_L - B_L - F_R + B_R}{F_L + B_L + F_R + B_R} = \frac{3}{4} \mathcal{P}_{eff} \frac{\hat{G}_P^e}{G_+^e} \rightarrow \frac{3}{4} \mathcal{P}_{eff} A_f, \quad (\text{VI.E.48})$$

where

$$F_{L,R} \equiv \int_0^1 \frac{d\sigma_{L,R}}{dz} dz, \quad B_{L,R} \equiv \int_{-1}^0 \frac{d\sigma_{L,R}}{dz} dz. \quad (\text{VI.E.49})$$

One can also define the final state polarization left-right asymmetry:

$$\begin{aligned} P_f^{LR} &\equiv \frac{\sigma_L^{fR} - \sigma_L^{fL} - \sigma_R^{fR} + \sigma_R^{fL}}{\sigma_L^{fR} + \sigma_L^{fL} + \sigma_R^{fR} + \sigma_R^{fL}} = -\mathcal{P}_{eff} \frac{G_-^e(1+z^2) + 2G_+^e z}{G_+^e(1+z^2) + 2G_-^e z} \\ &\rightarrow -\mathcal{P}_{eff} \frac{A_e A_f(1+z^2) + 2z}{(1+z^2) + 2A_e A_f z} \rightarrow -\mathcal{P}_{eff} A_e A_f. \end{aligned} \quad (\text{VI.E.50})$$

The set of recastings performed in section II.F are all based on a small set of custom detector simulation codes. These are meant to capture the main features relevant to each analysis while bypassing the many highly complex details of the real detector response.

Since the displaced SUSY models studied here have never appeared in public collaboration results, calibration of our simulations must rely on the specific physics models that appear in the experimental literature. Our aim has been to build simulations that reproduce the known experimental acceptances for new physics at the $O(1)$ level, which we are often able to accomplish even with very minimal treatment of detector issues. In most cases this level of agreement is adequate to define reasonable estimates of the true sensitivity contours in the mass-lifetime plane, as the sensitivity can be an extremely steep function in both variables. However, typically we can achieve even $O(10\%)$ agreement with the experimental results, either “out of the box” or by adjusting ad hoc efficiency factors. A single tuning of the latter type is often able to reproduce the results for a broad range of models.

Below, we provide complete descriptions of our detector simulations and their calibrations.

4. CMS Heavy Stable Charged Particles

The simulation required for the CMS heavy stable charged particle search [129] can be quite minimal, since CMS searches for the same physics signal that we do: long-lived stop and gluino R-hadrons. The only novelty that we introduce is the finite lifetime, which effectively adds an additional factor to the overall R-hadron acceptance. Decays must occur completely outside of the muon system, with no visible particles from the decay pointing back. We define the outer edge of this active volume simply as a cylinder with 8 m radius and 10 m half-length.⁶

Calibration is trivial, as we define our analysis in Section II.F.1.a to reproduce the results of [129] for long lifetimes.

5. CMS Displaced Dijets

The CMS displaced dijet search [138, 435] utilizes that detector’s highly precise tracking capabilities. Nonetheless, the tracker is not perfect, especially in the extreme cases of $O(m)$

⁶Reference [130] recommends using a slightly smaller radius of 7 m and a slightly longer half-length of 11 m.

displacements. At such large displacements, particles may not traverse enough detector layers to furnish a reconstructable string of hits, or may lead to hit patterns that not usable given a detector geometry and track-finding software that is highly optimized for tracks originating very close to the beampipe. In particular, CMS observes a dramatic drop in tracking efficiency versus vertex radius in simulation [555], falling to zero beyond 60 cm. The tracker also becomes highly inefficient for soft particles, especially for transverse momenta that are small enough for the particles to spiral-out. The efficiency experiences a rapid turn-on near 1 GeV.

It is not possible to reproduce the tracking and vertex-finding performance in detail here. Instead, we rely on simplistic parametrizations, and validate them against the results presented in the analysis note [435]. As a “zeroth-order” approximation, we could consider the tracker to be perfect within some fiducial volume. Our most naive version applies hard cutoffs at $r = 60$ cm and $p_T = 1$ GeV. Based on the discussions in [139, 435], and Fig. 3 in [139], we also include a corresponding longitudinal position cutoff at $z = 55$ cm, as well as a cutoff in transverse impact parameter at 30 cm. However, we have found by comparing to [435] that this zeroth-order treatment is far too idealized. CMS’s new physics models with $O(\text{cm})$ lifetimes are reproduced fairly well, with reconstruction rate estimates already typically within about 25% of CMS’s. (This result by itself indicates the amazing performance of the CMS tracker system for charged particles originating near the beampipe.) But the efficiencies for the longer $O(\text{m})$ lifetimes come out too large by up to a factor of 3.5, and distributions of variables such as the reconstructed vertex radius often significantly disagree.

We therefore use a slightly more aggressive parametrization for our nominal detector simulation. We continue to apply a hard cutoff at $p_T = 1$ GeV. For the geometric limitations, instead of hard cutoffs, we apply a nontrivial track-finding probability. We construct this probability by starting off with a prompt tracking efficiency of 90%, and multiplying it by the product of three linearly-falling probability factors, one each for r , z , and transverse impact parameter. Each factor starts at unity, and falls to zero at the geometric cutoff. Finally, in addition to these track-by-track efficiencies, we apply an efficiency for identifying each candidate vertex. This efficiency is the square of a linear falloff function versus radius,

intercepting zero at 60 cm. The combination of these ad hoc efficiency factors significantly improves our predicted rates and distributions relative to CMS.⁷

For the rest of the detector, we use a very minimal treatment to capture the essential elements of the geometry. The tracker is surrounded by imaginary surfaces corresponding the ECAL and HCAL faces. The ECAL face corresponds to a closed cylinder of radius 1.3 m and half-length 3 m. The HCAL face corresponds to a closed cylinder of radius 1.8 m and half-length 3.75 m. Charged particles that fail tracking due to the above inefficiencies are analytically propagated through the 3.8 T magnetic field to the appropriate calorimeter face: ECAL for electrons, HCAL for charged hadrons (failed muon tracks are discarded). Photons and neutral hadrons are propagated to the appropriate calorimeter face along straight lines. Particles are absorbed at the calorimeter face, and replaced by anonymous massless pseudoparticles carrying the original particle energy, but with momentum oriented to toward the impact point.⁸ For successfully reconstructed tracks, we use the momentum vector at their extrapolated point of closest transverse approach to the beamline (where the 2D impact parameter is defined). Track and calorimeter energy/momentum measurements are treated as perfect, since the effects of energy smearing are subdominant to our other modeling uncertainties. The tracks and calorimeter pseudoparticles are the inputs into our jet clustering, excluding any identified isolated electrons or muons as defined in the next subsection.

We plot our calibration results of the per-decay reconstruction rate (“acceptance times efficiency” in CMS’s language) relative to CMS in Fig. VI.2. These comparisons are based on the set of Hidden Valley [557] inspired simplified models used by CMS, consisting of a heavy Higgs-like scalar, produced through gluon fusion, that decays into a pair of long-lived pseudoscalars. The pseudoscalars then undergo displaced decays into dijets. (We have not undertaken calibrations against the $\tilde{\chi}^0 \rightarrow \mu jj$ signatures that are studied in the more recent

⁷The additional ad hoc vertexing efficiency causes a more rapid degradation of reconstruction rates versus radius than what is reported by CMS in their supplementary online materials [556]. However, an alternative approach of convolving the reported rates versus radius with our simulated number of decays versus radius similarly disagrees with the CMS analysis note [435]. We do not attempt to resolve this apparent discrepancy, but have chosen to parametrize our simulation to reproduce the integrated rates of the note, rather than the differential rates of the online material. This is in any case the more conservative choice.

⁸For photons and electrons produced from displaced vertices in between the ECAL and HCAL faces, the energy is deposited without propagation, and the momentum vector pointed towards the vertex. Any particle produced within the HCAL body is also absorbed in this way. For this purpose we assign an outer HCAL surface of radius 2.8 m and half-length 5.5 m. Particles produced outside of this volume are ignored.

CMS Displaced Dijets

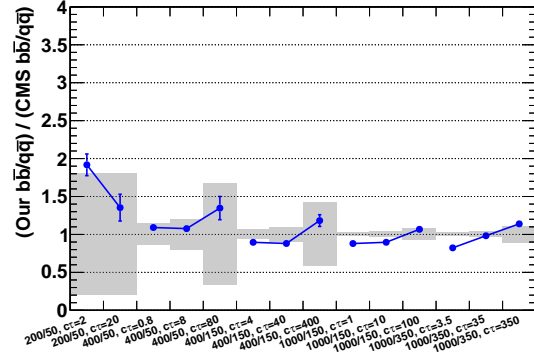
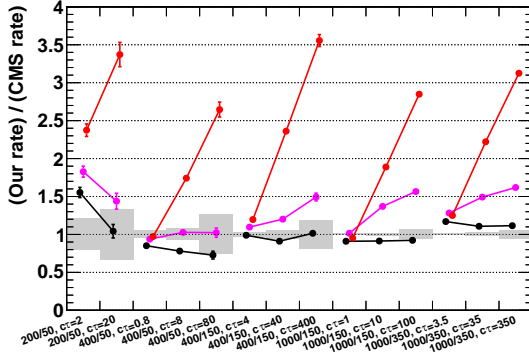


Figure VI.2: A comparison of our detector simulation to the CMS displaced dijet analysis, illustrating the ratio of individual displaced decay reconstruction rates to CMS for light quark decays (**left**) and the ratio of ratios between b -quarks and light quarks (**right**). The 14 benchmark models are labeled by scalar / pseudoscalar masses in GeV and by $c\tau$ in cm. On the left plot, we show our nominal simulation (black), our nominal simulation without the vertexing efficiency factor (pink), and our “zeroth-order” simulation with perfect tracking within the fiducial volume (red). Error bars are monte carlo statistics from our simulations. Grey bands indicate CMS’s efficiency uncertainties.

preprint [138].) The steep slopes for our zeroth-order detector’s reconstruction rates relative to CMS indicates that simulation’s failure to correctly account for inefficiencies at high displacements. A remnant of this slope remains after applying our tracking efficiencies but before applying our vertexing efficiencies. The nominal detector is generally in agreement with CMS for all lifetimes to within 20%, with the notable exception of the 200 GeV scalar model. We do not consider this a serious issue, as this model has high sensitivity to initial-state radiation modeling. The other models exhibit a good spread of overall masses, mass hierarchies, and lifetimes. In particular, the 400/50 and 1000/150 models tend to produce dijets near the edge of the jet clustering radius, and we see that we tend to slightly underestimate their reconstruction rates relative to models with widely-separated jets. Nonetheless, the highest dijet mass covered is 350 GeV, whereas some of our SUSY models go above 1 TeV. We assume that there are no dramatic changes in efficiencies as we scale up in mass, though a broader set of simulated models from CMS would help to clarify the actual behavior.

Fig VI.2 also indicates our ability to reproduce reconstructions with heavy flavor, by showing a double-ratio of reconstruction rates. The numerator is our estimated ratio of rates for $X \rightarrow b\bar{b}$ relative to X decays to light flavors. The denominator is CMS’s estimate of the same ratio. For this analysis, we pretend that the secondary displacements from the bottoms either cannot be resolved or are effectively ignored by the adaptive vertex finder. The agreement is generally seen to be quite reasonable, with a handful of outliers disagreeing at more than 20%. The fact that we achieve such good agreement without separately displacing the bottoms strongly suggests that the dominant differences in light flavor and heavy flavor efficiencies stems from the different visible particle multiplicities and kinematics. There remains a question of whether small primary displacements at the mm-level may have resolvable secondary displacements according to CMS’s adaptive vertex fitter, such that only the “best” of the truth vertices from each decay actually contributes. (E.g., $\tilde{t} \rightarrow b\bar{b}$ could produce up to three separate vertices, one from the radiation before the b ’s hadronize, and two more from the b -hadron decays.) Presumably, this would degrade the efficiency, since fewer tracks would be usable from any given decay. However, CMS does not provide enough information to infer exactly what happens for primary displacements below the cm-scale. In the main results in section II.F, we only consider the extremely conservative

assumption that vertices with bottom/charm quarks and sub-cm displacements experience complete reconstruction failure.

Finally, we comment on our modeling of the variables that go into CMS’s multivariate vertex/cluster discriminant variable. The discriminant is defined as a ratio of products of normalized p.d.f.’s over four variables: vertex track multiplicity, vertex positive IP fraction, cluster track multiplicity, and cluster RMS. The “cluster” is formed as described in Section II.F.1.b. We plot our predicted Hidden Valley signal distributions for the four variables and the multivariate discriminant in Fig. VI.3, along with the CMS predictions. For both our own simulation and CMS’s, we form the discriminant using CMS’s p.d.f.’s. (The signal discriminant distribution that would be predicted by CMS is generated by us through toy monte carlo from the individual variables’ histograms.) The agreements are mostly reasonable, though there can be differences in the tails. The fraction of events passing the discriminant cuts are nonetheless nearly identical to CMS. The signal’s discriminant distributions at high values appear to be mostly driven by the multiplicity variables, which we model relatively well.

6. CMS Displaced Dileptons

For the CMS displaced dilepton search [139], we use the same detector simulation discussed in the previous subsection, though without the vertex reconstruction penalty as a function of radius. We also apply the p_T -dependent lepton ID efficiencies provided in the appendix of [558], though we divide these by 0.9 to approximately deconvolve the prompt track-finding efficiency which we have already accounted for.

Similar to the displaced dijet search, the benchmark models feature a Higgs-like scalar decaying to a pair of long-lived pseudoscalars, but with the latter decaying to e^+e^- or $\mu^+\mu^-$. Unlike the displaced dijet search, detailed tables of acceptances and efficiencies are not provided. However, a handful of specific numbers are given, and the observed cross section limits can also be used to infer overall reconstruction rates.

For the 1000 GeV / 150 GeV models, CMS’s individual pseudoscalar reconstruction rates for $c\tau = 1$ cm in the electron (muon) decay channel are given as 36% (46%). Our predictions

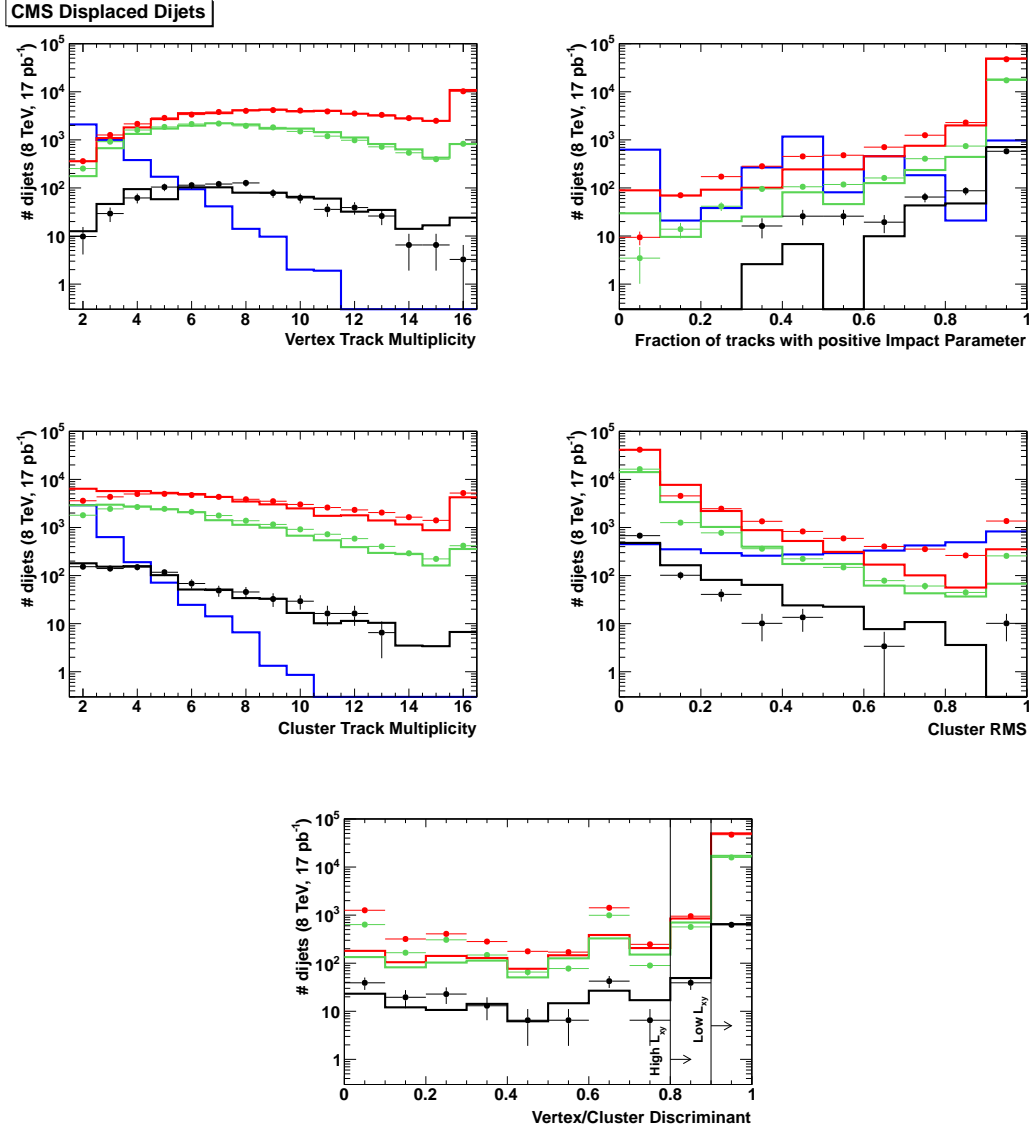


Figure VI.3: A comparison of our detector simulation to the CMS displaced dijet analysis, illustrating expected reconstructed dijet counts versus several discriminator variables (Fig. 1 of [435]). Continuous histograms indicate CMS predictions for QCD background (blue) and different scalar / pseudoscalar masses: 1000 GeV / 350 GeV with $c\tau = 35$ cm (red), 400 GeV / 150 GeV with $c\tau = 40$ cm (green), and 200 GeV / 50 GeV with $c\tau = 20$ cm (black); all with $\sigma \rightarrow 10 \mu\text{b}$ for visualization. Data points with error bars are our simulation predictions, and are color-matched and normalized to the corresponding CMS model histogram. The multivariate discriminant cuts for High- L_{xy} and Low- L_{xy} signal regions are also indicated.

are in decent agreement, at 36% (40%). For $c\tau = 20$ cm in the electron (muon) decay channel, CMS gives 14% (20%). Our predictions here are 9% (10%), indicating too-low reconstruction rates by $O(1)$. This is likely due to our ad hoc track-finding efficiency's linear falloff being too steep for this analysis. Indeed the supplementary online material of [559] indicates fairly stable reconstruction efficiency for this model out to $r \simeq 50$ cm, where our simulation would predict nearly zero. It seems quite likely that the low track multiplicity of the decay contributes to a higher rate of successful displaced track reconstructions, relative to that of the displaced dijets. However, we conservatively continue to use our tracking efficiency factors derived for the latter analysis, especially as in some SUSY models the lepton pair may be produced in association with hadronic tracks from the same vertex. This does not lead to a runaway loss of efficiency at high lifetime for simple dilepton decays, as we will see.

The calculation of limits from the signal reconstruction rates is in principle nontrivial, involving incorporation of backgrounds and various sources of systematic errors. However, given that the analysis is ultimately both background-free (as inferred from a control region) and has zero observed events, and that the naive Poissonian 95% C.L. limit for such an experiment is ≈ 3 signal events, we can perform a back-of-the-envelope estimate of the reconstruction rates. The explicit CMS per-candidate rates discussed above are reproduced at the 10% level using this method, providing a good cross-check. Fig. VI.4 illustrates our estimated relative rates for a few example models. The general behavior is that our simulation appears to be less efficient than reality, especially at very low and very high lifetimes. The former is perhaps unsurprising given our coarse modeling of the impact parameter cut, and the latter could be due to our overzealous tracking efficiency falloff. Nonetheless, some of the model points still appear to exceed the CMS rate, even at higher lifetimes, motivating us to keep these somewhat artificial effects to help prevent us from inferring too-strong limits on SUSY models.

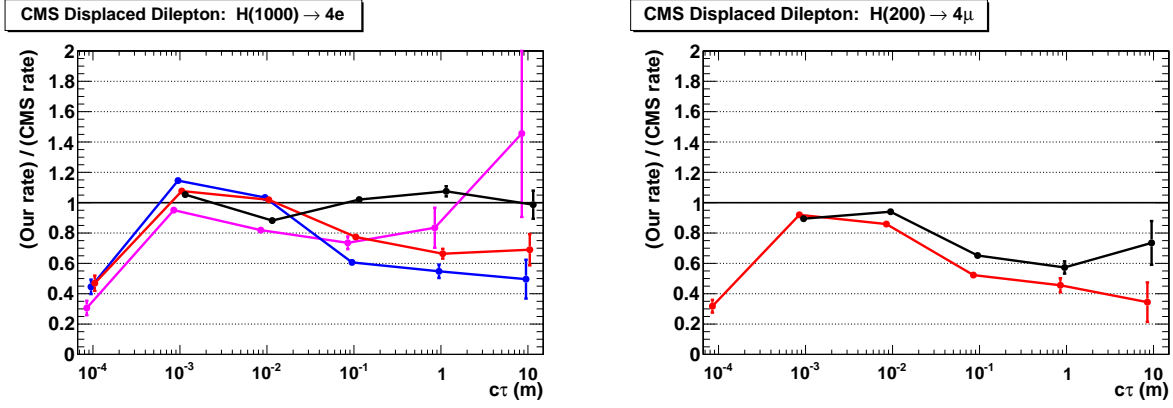


Figure VI.4: A comparison of our detector simulation to the CMS displaced dilepton analysis by inverting their reported limits, illustrating the approximate ratio of event reconstruction rates to CMS for 1000 GeV scalar cascade decays to electrons (**left**) and 200 GeV scalar cascade decays to muons (**right**) versus pseudoscalar lifetime (based on the limits presented in Figs. 4 and 5 of [139]). On the left plot, we show pseudoscalar masses of 20 GeV (pink), 50 GeV (blue), 150 GeV (red), and 350 GeV (black). On the right plot, we show pseudoscalar masses of 20 GeV (red) and 50 GeV (black). Error bars are monte carlo statistics from our simulations. All models are evaluated at $c\tau$ in powers of 10, but are offset slightly horizontally for clarity.

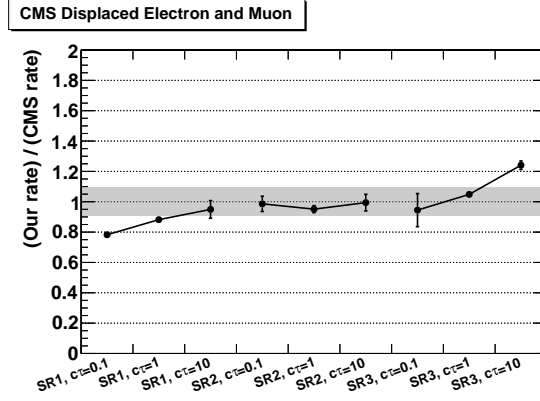


Figure VI.5: A comparison of our detector simulation to the CMS displaced electron and muon analysis, illustrating the ratio of individual displaced decay reconstruction rates to CMS for the 500 GeV stop benchmark model. The bins are labeled by analysis signal region (SR1 for lower impact parameters, through SR3 for higher impact parameters) and by the stop’s $c\tau$ in cm. Grey bands indicate CMS’s efficiency uncertainties, with the stop cross section uncertainty quadrature-subtracted.

7. CMS Displaced Electron and Muon

For the CMS displaced electron and muon search [136], we continue to use the detector simulation described in Appendix VI.E.5. To better match the efficiencies reported by CMS in the present analysis, we apply a flat event-by-event weight of 0.80.

The physics model studied by CMS is RPV stop pair production, but with each stop decaying into bl^+ , with equal branching fractions into each of the three lepton generations. It is not explicitly stated in this analysis whether the displaced leptons could suffer any loss of efficiency if produced from the decay of a charged stop-hadron, leading to an “exploding track” topology rather a displaced vertex with no string of hits tracing back to the primary vertex. In any case, since the analysis focuses on impact parameters below 2 cm, it is mostly sensitive to decays that occur before reaching the pixels. We treat charged and neutral stop-hadrons identically, assuming that this is not a major issue. CMS gives explicit reconstruction rates for a 500 GeV stop at lifetimes of 0.1 cm, 1 cm, and 10 cm. Our detector

simulation does a good job of reproducing all of these numbers to 20% accuracy, as indicated in Fig. VI.5.

8. ATLAS Muon Spectrometer

The ATLAS muon spectrometer search [141] is again very difficult to model without access to both a full ATLAS detector simulation and the exact reconstruction algorithms. Here, we simply parametrize all of these with fixed efficiency factors. Our simulation defines an active trigger volume within $r = [4.0, 6.5]$ m and $|\eta| < 1.0$. Displaced particles that decay in this region are given a 50% chance to fire the muon RoI cluster trigger. For events passing the trigger, two displaced decays must be reconstructed in either the muon barrel or muon endcap, respectively defined as the volumes $r = [4.0, 7.5]$ m and $|\eta| < 1.0$, or $|\eta| = [1.0, 2.5]$ and $z = [8, 14]$ m. Both of these decays must also occur within the data acquisition timing window, designed to follow particles moving through the detector at the speed of light. We choose a maximum delay of 7 ns, which we have independently calibrated to the extremely timing-sensitive ATLAS 120 GeV/ 40 GeV model results. Our calibrated choice of maximum delay indeed corresponds to the end of the efficiency plateau versus time for the trigger [560]. We assign each displaced vertex that survives this cut a reconstruction rate of 40%, irrespective of which ones were capable of firing the RoI trigger. Finally, in order to very approximately account for possible isolation failures when a displaced decay points back to the detector volume, we limit the amount of visible transverse energy flowing back into the HCAL to 15 GeV. For this purpose, we define the outer surface of the HCAL as a cylinder of radius 4.25 m and half-length 6 m. This cut tends to have only modest effect on ATLAS scalar models, but could become important for our SUSY models at higher mass.

Similar to the CMS displaced dilepton analysis above, we calibrate against the ATLAS models by extracting their overall efficiencies from the reported limits. Given that this analysis is background-free, the limits are assumed to correspond to ≈ 3 signal events. The result of this comparison is shown in Fig. VI.6. We are able to reproduce all of the ATLAS results to within about 20%. (The one outlier point occurs on a very steep part of the efficiency curve.)

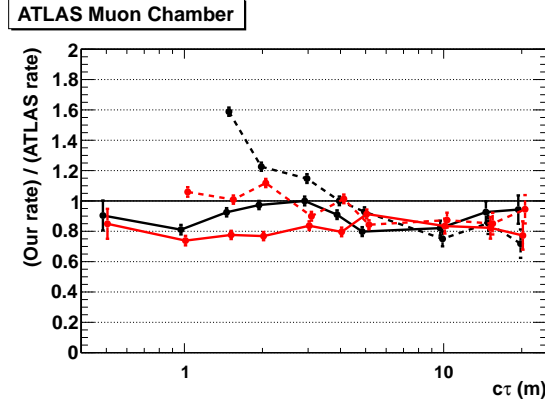


Figure VI.6: A comparison of our detector simulation to the ATLAS muon chamber analysis using their reported limits, illustrating the ratio of event reconstruction rates to ATLAS versus pseudoscalar lifetime (based on the limits presented in Fig. 3 of [141]). We show scalar / pseudoscalar masses of 120 GeV / 20 GeV (solid black), 120 GeV / 40 GeV (dashed black), 140 GeV / 20 GeV (solid red), and 140 GeV / 40 GeV (dashed red). Error bars are monte carlo statistics from our simulations. All models are evaluated at common $c\tau$ of (0.5,1,1.5,2,3,4,5,10,15,20) m, but are offset slightly horizontally for clarity.

9. ATLAS Low-EM Jets

For our SUSY models to pass the ATLAS low-EM jets search [140], both displaced decays must occur within an effective HCAL volume: a “barrel” with $|\eta| < 1.7$ and $r = [2.25, 3.35]$ m; or an “endcap” with $|\eta| < 2.5$, $r < 2.0$ m, and $z = [4.25, 5.0]$ m. To approximate ATLAS’s isolation cuts against activity in the ECAL and tracker, we apply a flat efficiency factor of 0.55 per displaced decay.⁹ (As usual, events with one or two charged displaced particles, which would leave high- p_T tracks, are not considered.)

Our detector simulation assumes perfect and immediate absorption of the visible decay energy within our active HCAL volume. However, we conservatively veto events where any visible final-state particle from either displaced decay points back towards the ECAL volume, which we take to be $r < 2.0$ m and $|z| < 4.0$ m. The effect of this veto is modest for most of ATLAS’s Hidden Valley models, but notably has a nearly 50% effect on the acceptance for the highest mass models, actually improving our agreement (see below). The cut is especially relevant for our SUSY models, which generally contain many more decay particles produced at large angles. Practically, for us the cut serves as a proxy for any number of unknown requirements on the energy pattern and timing in the HCAL, in addition to the explicit limits on the nearby ECAL activity. As such, it serves as our largest source of modeling uncertainty on this analysis.

To validate our detector simulation and calibrate the efficiency factor, we compare to ATLAS’s physics models, which again feature singly-produced Higgs-like scalars that promptly decay into a pair of pseudoscalars with displaced decays. The pseudoscalars dominantly decay into heavy quarks, with an $O(10\%)$ branching ratio to τ -leptons, though we use a simpler model with decays only to light quarks. (Our model therefore does not include energy losses to neutrinos, which we do not expect to be a major effect.) We have found good agreement with the reconstruction efficiencies of the eight benchmark models, detailed in the appendix of [140], though for 100 GeV scalars our efficiencies come out $O(1)$ smaller. In any case, these models barely pass the E_T cuts, and are significantly more sensitive to the detailed turn-on of the efficiency with scalar mass. We have also studied the efficiency versus

⁹ATLAS’s reported efficiencies are smaller than this. However, those also fold in the efficiencies for passing the p_T cuts within their studied physics models.

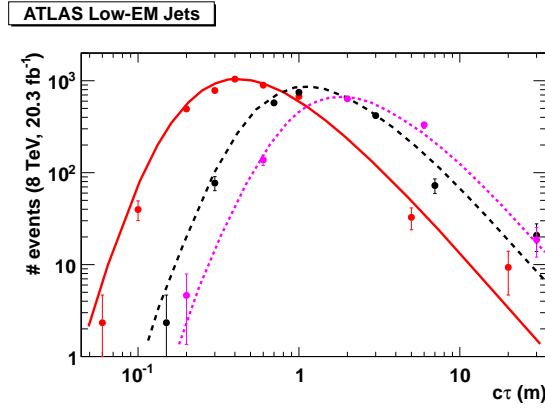


Figure VI.7: A comparison of our detector simulation to the ATLAS low-EM jet analysis, illustrating expected event counts versus pseudoscalar lifetime (Fig. 4 of [140]). Curves indicate ATLAS predictions for different scalar / pseudoscalar masses: 126 GeV / 10 GeV (red solid), 126 GeV / 25 GeV (black dashed), and 140 GeV / 40 GeV (pink dotted). Data points with error bars are our simulation predictions, and are color-matched to the corresponding ATLAS model curve.

pseudoscalar lifetime for three of the mass points. The agreement is illustrated in Fig. VI.7, and is typically at the 10% level.

10. ATLAS Displaced Muon Plus Tracks

Similar to our simulation of the CMS displaced dijet analysis, for the ATLAS muon plus tracks search [135] we assign each track a reconstruction probability. We ignore all tracks from vertices with $r > 18$ cm or $z > 30$ cm, as well as cylindrical regions near the beampipe or the pixel layers: $r = [2.5, 3.8]$ cm, $[4.5, 6.0]$ cm, $[8.5, 9.5]$ cm, and $[12, 13]$ cm. Within the active tracking volume, we use a tracking efficiency of $0.85 \times (1 - r/(24 \text{ cm})) \times (1 - z/(30 \text{ cm}))$. For muon identification, which requires a very high-quality inner track, we apply an additional fixed efficiency factor of 70%. We apply another fixed factor of 70% for successfully matching a muon to a displaced vertex. These ad hoc factors reproduce the qualitative vertex reconstruction efficiency behavior versus (r, z) in Fig. 3 of [135], as well as the ratio between event selection efficiencies before/after the muon-vertex matching requirement in Table 5 of that note.¹⁰ The latter is particularly relevant for the version of the analysis that we run for our recasts, which does not require the muon-vertex matching used in the nominal analysis.

ATLAS studies a set of SUSY models with leptonic RPV, where squark pairs promptly decay into jets plus long-lived LSP neutralinos, which then each undergo a displaced decay into a muon plus two quarks. Three mass points are considered: MH (700 GeV / 494 GeV), ML (700 GeV / 108 GeV), and HL (1000 GeV / 108 GeV). Fig. VI.8 shows the event reconstruction efficiencies versus lifetime for these models after full selection cuts, as predicted by our simulation and by ATLAS’s full simulation. (The individual vertex reconstruction efficiencies are approximately half of the event reconstruction efficiencies, and show nearly identical behavior.) The large gap in efficiencies between MH and ML/HL is reproduced, as is the shift in the peak versus lifetime and the falloffs at low and high lifetimes. However, the $\approx 30\%$ gap between ML and HL is not reproduced, except at higher lifetimes, where

¹⁰The table suggests that the vertex reconstruction efficiencies, before track multiplicity and vertex mass cuts, are close to one. However, matching between outer muons and inner tracks, as well as between muons and vertices, exhibits these nontrivial efficiencies.

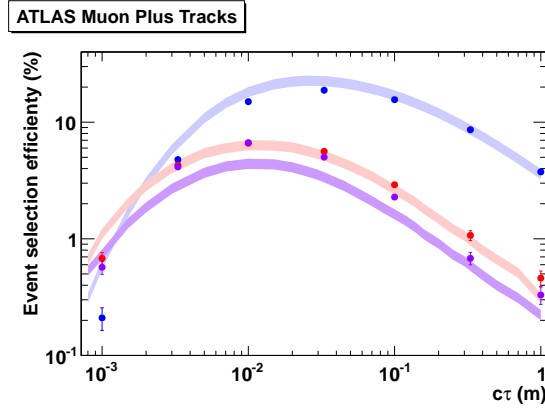


Figure VI.8: A comparison of our detector simulation to the ATLAS muon plus tracks analysis, illustrating expected event reconstruction efficiencies versus neutralino lifetime (Fig. 4 of [135]). Colored bands indicate ATLAS predictions for different squark / neutralino masses: 700 GeV / 494 GeV (blue), 700 GeV / 108 GeV (red), and 1000 GeV / 108 GeV (purple). Data points with error bars are our simulation predictions, and are color-matched to the corresponding ATLAS model curve.

the higher boost of HL tends to feel the tracking efficiency losses at large radii. (The higher boost would also lead to smaller impact parameters at a given decay radius, but this is largely offset by the time-dilated decay length.) The difference in modeling is possibly attributable to the fact that our simulation does not account for how displaced tracking and vertexing efficiencies change with track density, nor to possible issues in impact parameter reconstruction at small angles, all of which the lighter neutralino could be particularly sensitive to. (To get a sense of this sensitivity, deleting one track from each vertex would cause the efficiency to fall by 20% due to failures of the cut on the number of tracks.) There could also be effects on the global muon reconstruction. Nonetheless, the size of the mismodeling is below $O(1)$, and appears to be mainly relevant for relatively low-mass decays at relatively high boost.

F. RELIC DENSITY CALCULATION

When the Hubble expansion $H = \dot{a}/a$ became much larger than the interaction rate $\Gamma = n_\chi \langle \sigma_a v \rangle$, the WIMPs (χ^0), once in thermal equilibrium with the rest of the Universe, decoupled from equilibrium. The number density of WIMPs at a time t , $n_\chi(t)$, is obtained by solving the Boltzmann equation

$$\frac{1}{a^3} \frac{d(a^3 n_\chi)}{dt} = -\langle \sigma_a v \rangle [n_\chi^2 - n_{\text{eq}}^2], \quad (\text{VI.F.51})$$

where $\langle \sigma_a v \rangle$ is the WIMP annihilation rate averaged over velocities, and n_{eq} is the equilibrium number density of WIMPs:

$$n_{\text{eq}} = \frac{g}{2\pi^2} \int_{m_\chi}^{\infty} dE \frac{E \sqrt{E^2 - m_\chi^2}}{1 + e^{E/T}}. \quad (\text{VI.F.52})$$

g measures the number of relativistic degrees of freedom, and T is the temperature.

Define the dimensionless variables $Y = n_\chi/s$ and $x = m_\chi/T$, where s is the entropy density given by

$$s = \frac{2\pi^2}{45} g_s T^3. \quad (\text{VI.F.53})$$

Here and henceforth, we adopt the natural units $k_b = \hbar = c = 1$. g_s is different from g only at late times, after neutrinos have decoupled from equilibrium, and e^\pm annihilation leads to

the photons being heated relative to the neutrinos. However, dY/dx is very small at late times, and with good accuracy, we may set $g = g_s$ when computing the relic abundance. The entropy per comoving volume is conserved, and hence

$$\frac{d(a^3 s)}{dt} = \frac{d(g a^3 T^3)}{dt} = 0 \quad (\text{VI.F.54})$$

We may then rewrite eq. (VI.F.51) in terms of Y as:

$$\frac{dY}{dt} = -\langle \sigma_a v \rangle s [Y^2 - Y_{\text{eq}}^2], \quad (\text{VI.F.55})$$

where $Y_{\text{eq}} = n_{\text{eq}}/s$. From eq. (VI.F.54), we see that $g a^3 T^3 = \text{constant}$, and therefore,

$$-\frac{\dot{T}}{T} = H + \frac{\dot{g}}{3g}. \quad (\text{VI.F.56})$$

The Hubble parameter $H(T)$ is given by the expression

$$H = \left[\frac{8\pi G}{3} \rho_\gamma \right]^{1/2} = \left[\frac{8\pi^3 G}{90} \right]^{1/2} g^{1/2} T^2 \quad (\text{VI.F.57})$$

Differentiating $x = m_\chi/T$ with respect to time, we find

$$\begin{aligned} \dot{x} = \left(-\dot{T}/T \right) x &= Hx \left[1 + \frac{\dot{g}_s}{3Hg_s} \right] \\ &\approx Hx \left[1 - \frac{1}{3} \frac{d(\ln g_s)}{d(\ln T)} \right], \end{aligned} \quad (\text{VI.F.58})$$

where we simplified the second term on line 1 by substituting $\dot{x} \approx Hx$ (provided $\dot{g}_s \ll 3Hg_s$), and therefore $\dot{g} \approx -HT(dg/dT)$ [561]. Note that g changes significantly at the epoch of quark-hadron transition. We may now rewrite eq. (VI.F.55) in terms of x :

$$\begin{aligned} \frac{dY}{dx} &= \frac{-\langle \sigma_a v \rangle s(x)}{H(x)x \left[1 - \frac{1}{3} \frac{d(\ln g)}{d(\ln T)} \right]} \\ &= -\sqrt{\frac{\pi}{45G}} \langle \sigma_a v \rangle m_\chi \frac{g^{1/2}}{\left[1 - \frac{1}{3} \frac{d(\ln g)}{d(\ln T)} \right]} \frac{Y^2 - Y_{\text{eq}}^2}{x^2}. \end{aligned} \quad (\text{VI.F.59})$$

We solve eq. (VI.F.59) numerically to obtain the present day value Y_0 , once the form of $g(T)$ and $\langle \sigma_a v \rangle$ are known. The dark matter relic density is then computed as:

$$\Omega_\chi h^2 = \frac{m_\chi Y_0 s_0}{(\rho_{\text{crit}}/h^2)}, \quad (\text{VI.F.60})$$

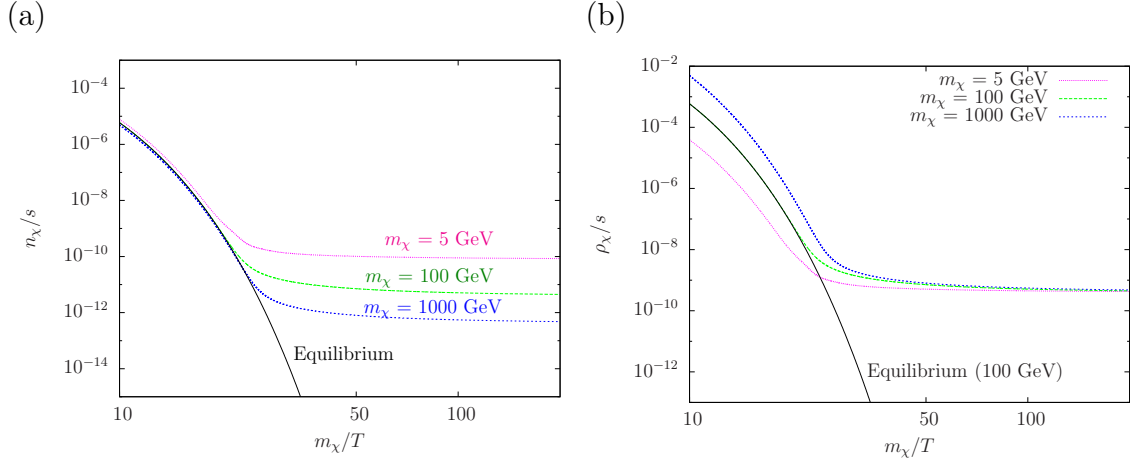


Figure VI.9: Evolution with temperature and yielding the correct WIMP relic density $\Omega_\chi h^2 = 0.11$ with illustrative values of the WIMP mass $m_\chi = 5, 100, \text{ and } 1000 \text{ GeV}$, (a) WIMP number density, and (b) WIMP mass density. The equilibrium lines are for $m_\chi = 100 \text{ GeV}$.

where $s_0 \approx 2893 \text{ cm}^{-3}$ is the present day entropy density and $\rho_{\text{crit}} \approx 1.054 \times 10^{-5} h^2 \text{ GeV/cm}^3$ is the critical density.

After performing a numerical integration of the Boltzmann equation as formulated in eq. (VI.F.59), we show the WIMP number density in Fig. VI.9(a) and the WIMP relic (mass) density in Fig. VI.9(b), for various WIMP mass values. The dark straight-falling line gives the densities if the particle keeps in thermal equilibrium with the environment for $m_\chi = 100 \text{ GeV}$. It is known that the freeze-out temperature for a relatively light WIMP particle is

$$x_f = m_\chi/T \approx 20. \quad (\text{VI.F.61})$$

The horizontal curves in Figs. VI.9(a) and (b) present the WIMP number density and mass density after freeze-out for $m_\chi = 5 - 1000 \text{ GeV}$, leading to the correct relic density.

G. COMBINATION METHOD AND χ^2 DEFINITION

We list the LHC projections for most relevant modes in Table III.5. All ATLAS and CMS projections are shown in ranges corresponding to different assumptions about systematic and theoretical uncertainties. For ATLAS, the ranges represent projections with and without theoretical uncertainties. For CMS, the ranges represent projections with and without reductions of systematic and theoretical uncertainties. The lower range corresponds to assumptions that systematical uncertainties will scale as $1/\sqrt{\mathcal{L}}$ and theoretical uncertainties will be halved. We estimate the theoretical and systematic uncertainties based on these ranges, for example, range $a - b$ indicates theoretical uncertainty is $\sqrt{b^2 - a^2}$ for ATLAS. Similarly, for CMS projections in range $a - b$, $\sqrt{b^2 - a^2}$ is approximately the theoretical uncertainty plus the systematic uncertainty added in quadrature. We take the lower of these two quantities from ATLAS and CMS as an estimated systematic plus theoretical uncertainty. We combine both experimental results from the lower range to approximate the statistical gain and add in the estimated theory plus systematics term quadratically. These conservative combined results are shown in Table III.5. As one can see, most of them are only slightly better than conservative individual experimental projections, indicating the large contribution from systematic and theoretical uncertainties. We use these combined results as our input for LHC measurement for the fitting described below. Note that some portion of the theoretical uncertainties, including PDF and scaling effects, can be cancelled when taking the ratios of measurements from the LHC. Once these projections on ratios from experiments become available, LHC input in form of ratios will further help determine the Higgs couplings.

For the model-independent fittings, we have 9 parameters, these are Γ_h , g_b , g_c , g_g , g_W , g_τ , g_Z , g_γ , and Br_{inv} . In the absence of actual experimental data, we take the central values of the measured cross sections to be equal to their standard model values. Let \hat{g}_A be the fitted parameter normalized by its standard model value. All of these take a central value of one.

For the model-independent fittings, the χ^2 we used can be expressed in Eq. (VI.G.62), where sum over σ means summing over all the independently measured cross sections. These

cross sections includes LHC, ILC at 250 GeV and 500 GeV. σ_Z^{inc} is the inclusive Zh associated production cross section measured at 250 GeV ILC. For the LHC measurements, we take all of the sensitivity projections for $\gamma\gamma$, WW^* and ZZ^* from glu-glu-fusion and $b\bar{b}$ from ZH associated production. As for $\tau^+\tau^-$, we take half the sensitivity to be from glu-glu-fusion and the other half from weak boson fusion [263, 562]. For ILC input, we take the conservative value as well. For example, we take $\sigma_{Z\gamma}$ to be 38% where the estimation is in the range of 29% – 38%.

$$\chi^2 = \sum_{\sigma} \left(\frac{1 - \hat{g}_A^2 \hat{g}_B^2 / \hat{\Gamma}_h}{\delta\sigma_{AB}} \right)^2 + \left(\frac{1 - \hat{g}_Z^2}{\delta\sigma_Z^{inc}} \right)^2 + \left(\frac{1 - \hat{g}_Z^2 \hat{\text{Br}}_{inv}}{\delta\sigma_{Zh \rightarrow Z+inv}} \right)^2 \quad (\text{VI.G.62})$$

For model-dependent fittings, we have 8 parameters, these are Br_{inv} , g_b , g_c , g_g , g_W , g_τ , g_Z , and g_γ . Again, all of the couplings are normalized to one. Br_{inv} has a central value of zero. Notice that Γ_h is no longer a fitting parameters here, instead it is determined by the other fitting parameters, as shown in Eq. (VI.G.63). This is a result of assuming that a sum over all Br gives the normalized total width. χ^2 for the model-dependent case can be written as in Eq. (VI.G.64).

$$\hat{\Gamma}_h = \left(\sum_i \text{Br}_i \hat{g}_i^2 + (1 - \sum_i \text{Br}_i) \right) (1 - \text{Br}_{inv}) + \text{Br}_{inv} \quad (\text{VI.G.63})$$

$$\chi^2 = \sum_{\sigma} \left(\frac{1 - \hat{g}_X^2 \hat{g}_Y^2 / \hat{\Gamma}_h}{\delta\sigma_{AB}} \right)^2 + \left(\frac{1 - \hat{g}_Z^2}{\delta\sigma_Z^{inc}} \right)^2 + \left(\frac{\hat{g}_Z^2 \text{Br}_{inv}}{\delta\sigma_{Zh \rightarrow Z+inv}} \right)^2 \quad (\text{VI.G.64})$$

We note here that ILC measurements include systematic but not theoretical uncertainties. For our results shown in Tables III.13 and III.7, theoretical errors should be included for a consistent comparison with models.

H. ANALYSIS FOR $B\bar{B}$ BACKGROUNDS

A potential complication to our signal which we do not explicitly include is the “background” coming from $h \rightarrow b\bar{b}$ decays. Kinematically, these events are very similar to the WW signal

Table VI.1: Additional events expected from $h \rightarrow b\bar{b}$ with the cuts described in Sec. III.B.2.b. No b -tagging has been applied for this table.

	All Hadronic		Semi-leptonic	
	Higgstrahlung	ZZ Fusion	Higgstrahlung	ZZ Fusion
$eeh \rightarrow eebb$	100	112	33	42

except for the details of the 4-jet substructure. With the cuts described above, a SM-like $h \rightarrow b\bar{b}$ process would contribute events as in the Table VI.1.

Although adding to the excess over non-Higgs SM backgrounds, these events would degrade our ability to precisely measure the g_W coupling. However, we can make use of the strong b -tagging capabilities expected at the ILC to reduce this problem [563]. Tagging algorithms can be characterized in terms of their b -acceptance efficiency, ϵ_b , vs. their mistagging efficiency, which it is useful to divide into c -mistagging, ϵ_c , and light-jet-mistagging ϵ_j . These efficiencies describe the percentage of true b -quark (or c -quark or light parton) originating jets which are positively tagged by the algorithm. The efficiencies are generally a function of a cut parameter in the tagging algorithm which can be adjusted to favor greater purity or greater inclusiveness in the tagging.

We can exclude much of the $b\bar{b}$ background by instituting a veto on events with one or more b -tags. Based on simulations of ILC tagging efficiency, we take $\epsilon_b = 0.7$, $\epsilon_c = 0.1$ and $\epsilon_j = 0.005$ as a plausible working point. Then for a $b\bar{b}$ background resolved to two jets only 10% of events will pass the b -tag veto. This also applies to roughly a fifth of the large $ee \rightarrow qq$ background. (Backgrounds from $c\bar{c}$ will be reduced by a factor of $\sim 20\%$ as well.) Thus, although the Higgs decays are now being added to the background, the total number of expected background events can be slightly reduced. For the signal we would expect a small reduction in expected events, mostly due to W 's decaying to c and s quarks. In the semi-leptonic analysis this would lead to about 5% reduction of the signal. For the all-hadronic analysis, estimation of tagging efficiencies is somewhat ambiguous since we have

multiple jets arising from a single b parton. If we treat each of the four jets according to the efficiencies above, with all jets arising from the $b\bar{b}$ backgrounds having a “true” identity as a b -jet, then it is advantageous to veto events with more than one b -tag while keeping those with up to one b -tag. This would preserve virtually all of the signal while reducing the $b\bar{b}$ backgrounds by $\sim 92\%$.

The net result of adding $h \rightarrow b\bar{b}$ decays and b -tagging is thus a very small change to the expected cross-section sensitivity, on the order of $1 - 2\%$ correction.

BIBLIOGRAPHY

- [1] R. Barbier, C. Berat, M. Besancon, M. Chemtob, A. Deandrea, *et al.*, “R-parity violating supersymmetry”, *Phys.Rept.* **420** (2005) 1–202, [arXiv:hep-ph/0406039](#).
- [2] J. L. Hewett and T. G. Rizzo, “Low-Energy Phenomenology of Superstring Inspired E(6) Models”, *Phys.Rept.* **183** (1989) 193.
- [3] J. C. Pati and A. Salam, “Lepton Number as the Fourth Color”, *Phys.Rev.* **D10** (1974) 275–289.
- [4] N. Cabibbo, L. Maiani, and Y. Srivastava, “Anomalous Z Decays: Excited Leptons?”, *Phys.Lett.* **B139** (1984) 459.
- [5] U. Baur, I. Hinchliffe, and D. Zeppenfeld, “Excited Quark Production at Hadron Colliders”, *Int.J.Mod.Phys.* **A2** (1987) 1285.
- [6] P. H. Frampton and S. L. Glashow, “Chiral Color: An Alternative to the Standard Model”, *Phys.Lett.* **B190** (1987) 157.
- [7] S. P. Martin, “A Tumbling top quark condensate model”, *Phys.Rev.* **D46** (1992) 2197–2202, [arXiv:hep-ph/9204204](#).
- [8] C. T. Hill and E. H. Simmons, “Strong dynamics and electroweak symmetry breaking”, *Phys.Rept.* **381** (2003) 235–402, [arXiv:hep-ph/0203079](#).
- [9] B. A. Dobrescu, K. Kong, and R. Mahbubani, “Leptons and photons at the LHC: Cascades through spinless adjoints”, *JHEP* **0707** (2007) 006, [arXiv:hep-ph/0703231](#).
- [10] J. Bagger, C. Schmidt, and S. King, “Axigluon Production in Hadronic Collisions”, *Phys.Rev.* **D37** (1988) 1188.
- [11] C. T. Hill, “Topcolor: Top quark condensation in a gauge extension of the standard model”, *Phys.Lett.* **B266** (1991) 419–424.
- [12] R. Chivukula, A. G. Cohen, and E. H. Simmons, “New strong interactions at the Tevatron?”, *Phys.Lett.* **B380** (1996) 92–98, [arXiv:hep-ph/9603311](#).

- [13] K. Agashe, A. Belyaev, T. Krupovnickas, G. Perez, and J. Virzi, “LHC Signals from Warped Extra Dimensions”, *Phys.Rev.* **D77** (2008) 015003, [arXiv:hep-ph/0612015](#).
- [14] S. Cullen, M. Perelstein, and M. E. Peskin, “TeV strings and collider probes of large extra dimensions”, *Phys.Rev.* **D62** (2000) 055012, [arXiv:hep-ph/0001166](#).
- [15] P. Burikham, T. Figy, and T. Han, “TeV-scale string resonances at hadron colliders”, *Phys.Rev.* **D71** (2005) 016005, [arXiv:hep-ph/0411094](#).
- [16] L. A. Anchordoqui, H. Goldberg, and T. R. Taylor, “Decay widths of lowest massive Regge excitations of open strings”, *Phys.Lett.* **B668** (2008) 373–377, [arXiv:0806.3420](#).
- [17] P. Langacker, “The Physics of Heavy Z' Gauge Bosons”, *Rev. Mod. Phys.* **81** (2009) 1199–1228, [arXiv:0801.1345](#). %%CITATION = 0801.1345;%%
- [18] M. Cvetič and S. Godfrey, “Discovery and identification of extra gauge bosons”, [arXiv:hep-ph/9504216](#).
- [19] A. Leike, “The Phenomenology of extra neutral gauge bosons”, *Phys.Rept.* **317** (1999) 143–250, [arXiv:hep-ph/9805494](#).
- [20] M. Cvetič and P. Langacker, “Z-prime physics and supersymmetry”, [arXiv:hep-ph/9707451](#).
- [21] J. Erler, P. Langacker, S. Munir, and E. Rojas, “Improved Constraints on Z-prime Bosons from Electroweak Precision Data”, *JHEP* **0908** (2009) 017, [arXiv:0906.2435](#).
- [22] P. Langacker, “The Physics of New U(1)-prime Gauge Bosons”, *AIP Conf.Proc.* **1200** (2010) 55–63, [arXiv:0909.3260](#).
- [23] P. Nath, B. D. Nelson, H. Davoudiasl, B. Dutta, D. Feldman, *et al.*, “The Hunt for New Physics at the Large Hadron Collider”, *Nucl.Phys.Proc.Suppl.* **200-202** (2010) 185–417, [arXiv:1001.2693](#).
- [24] J. Jaeckel and A. Ringwald, “The Low-Energy Frontier of Particle Physics”, *Ann.Rev.Nucl.Part.Sci.* **60** (2010) 405–437, [arXiv:1002.0329](#).
- [25] F. del Aguila, J. de Blas, and M. Perez-Victoria, “Electroweak Limits on General New Vector Bosons”, *JHEP* **1009** (2010) 033, [arXiv:1005.3998](#).
- [26] R. Diener, S. Godfrey, and I. Turan, “Constraining Extra Neutral Gauge Bosons with Atomic Parity Violation Measurements”, *Phys.Rev.* **D86** (2012) 115017, [arXiv:1111.4566](#).
- [27] J. Kang and P. Langacker, “ Z' discovery limits for supersymmetric E(6) models”, *Phys.Rev.* **D71** (2005) 035014, [arXiv:hep-ph/0412190](#).

- [28] C.-F. Chang, K. Cheung, and T.-C. Yuan, “Supersymmetric Decays of the Z' Boson”, *JHEP* **1109** (2011) 058, [arXiv:1107.1133](#).
- [29] R. Robinett and J. L. Rosner, “Mass Scales In Grand Unified Theories ”, *Phys.Rev.* **D26** (1982) 2396.
- [30] J. R. Ellis, J. Gunion, H. E. Haber, L. Roszkowski, and F. Zwirner, “Higgs Bosons in a Nonminimal Supersymmetric Model”, *Phys.Rev.* **D39** (1989) 844.
- [31] M. Drees, “Supersymmetric Models with Extended Higgs Sector”, *Int.J.Mod.Phys.* **A4** (1989) 3635.
- [32] H. P. Nilles, M. Srednicki, and D. Wyler, “Weak Interaction Breakdown Induced by Supergravity”, *Phys.Lett.* **B120** (1983) 346.
- [33] **ATLAS** Collaboration, G. Aad *et al.*, “Observation of a new particle in the search for the Standard Model Higgs boson with the ATLAS detector at the LHC”, *Phys.Lett.* **B716** (2012) 1–29, [arXiv:1207.7214](#).
- [34] **CMS** Collaboration, S. Chatrchyan *et al.*, “Observation of a new boson at a mass of 125 GeV with the CMS experiment at the LHC”, *Phys.Lett.* **B716** (2012) 30–61, [arXiv:1207.7235](#).
- [35] L. J. Hall, D. Pinner, and J. T. Ruderman, “A Natural SUSY Higgs Near 126 GeV”, *JHEP* **1204** (2012) 131, [arXiv:1112.2703](#).
- [36] M. Carena, S. Gori, N. R. Shah, and C. E. Wagner, “A 125 GeV SM-like Higgs in the MSSM and the $\gamma\gamma$ rate”, *JHEP* **1203** (2012) 014, [arXiv:1112.3336](#).
- [37] H. Baer, V. Barger, P. Huang, and X. Tata, “Natural Supersymmetry: LHC, dark matter and ILC searches”, *JHEP* **1205** (2012) 109, [arXiv:1203.5539](#).
- [38] M. W. Cahill-Rowley, J. L. Hewett, A. Ismail, and T. G. Rizzo, “The Higgs Sector and Fine-Tuning in the pMSSM”, *Phys.Rev.* **D86** (2012) 075015, [arXiv:1206.5800](#).
- [39] S. F. King, M. Muhlleitner, R. Nevzorov, and K. Walz, “Natural NMSSM Higgs Bosons”, *Nucl.Phys.* **B870** (2013) 323–352, [arXiv:1211.5074](#).
- [40] K. Agashe, Y. Cui, and R. Franceschini, “Natural Islands for a 125 GeV Higgs in the scale-invariant NMSSM”, *JHEP* **1302** (2013) 031, [arXiv:1209.2115](#).
- [41] H. E. Haber, “Nonminimal Higgs sectors: The Decoupling limit and its phenomenological implications”, [arXiv:hep-ph/9501320](#).
- [42] **ATLAS** Collaboration, G. Aad *et al.*, “Search for neutral MSSM Higgs bosons decaying to $\tau^+\tau^-$ pairs in proton-proton collisions at $\sqrt{s} = 7$ TeV with the ATLAS detector”, *Phys.Lett.* **B705** (2011) 174–192, [arXiv:1107.5003](#).

- [43] “Search for neutral mssm higgs bosons in $\sqrt{s} = 7$ tev pp collisions at atlas”, Tech. Rep. ATLAS-CONF-2012-094, CERN, Geneva, Jul 2012.
- [44] CMS Collaboration, S. Chatrchyan *et al.*, “Search for a Higgs boson decaying into a b-quark pair and produced in association with b quarks in proton-proton collisions at 7 TeV”, [arXiv:1302.2892](#).
- [45] N. D. Christensen, T. Han, and S. Su, “MSSM Higgs Bosons at The LHC”, *Phys.Rev.* **D85** (2012) 115018, [arXiv:1203.3207](#).
- [46] U. Ellwanger, “A Higgs boson near 125 GeV with enhanced di-photon signal in the NMSSM”, *JHEP* **1203** (2012) 044, [arXiv:1112.3548](#).
- [47] S. King, M. Muhlleitner, and R. Nevzorov, “NMSSM Higgs Benchmarks Near 125 GeV”, *Nucl.Phys.* **B860** (2012) 207–244, [arXiv:1201.2671](#).
- [48] J.-J. Cao, Z.-X. Heng, J. M. Yang, Y.-M. Zhang, and J.-Y. Zhu, “A SM-like Higgs near 125 GeV in low energy SUSY: a comparative study for MSSM and NMSSM”, *JHEP* **1203** (2012) 086, [arXiv:1202.5821](#).
- [49] J. F. Gunion, Y. Jiang, and S. Kraml, “The Constrained NMSSM and Higgs near 125 GeV”, *Phys.Lett.* **B710** (2012) 454–459, [arXiv:1201.0982](#).
- [50] U. Ellwanger and C. Hugonie, “Higgs bosons near 125 GeV in the NMSSM with constraints at the GUT scale”, *Adv.High Energy Phys.* **2012** (2012) 625389, [arXiv:1203.5048](#).
- [51] K. Choi, S. H. Im, K. S. Jeong, and M. Yamaguchi, “Higgs mixing and diphoton rate enhancement in NMSSM models”, [arXiv:1211.0875](#).
- [52] K. S. Jeong, Y. Shoji, and M. Yamaguchi, “Singlet-Doublet Higgs Mixing and Its Implications on the Higgs mass in the PQ-NMSSM”, *JHEP* **1209** (2012) 007, [arXiv:1205.2486](#).
- [53] T. Graf, R. Grober, M. Muhlleitner, H. Rzehak, and K. Walz, “Higgs Boson Masses in the Complex NMSSM at One-Loop Level”, *JHEP* **1210** (2012) 122, [arXiv:1206.6806](#).
- [54] K. Kowalska, S. Munir, L. Roszkowski, E. M. Sessolo, S. Trojanowski, *et al.*, “The Constrained NMSSM with a 125 GeV Higgs boson – A global analysis”, [arXiv:1211.1693](#).
- [55] D. A. Vasquez, G. Belanger, C. Boehm, J. Da Silva, P. Richardson, *et al.*, “The 125 GeV Higgs in the NMSSM in light of LHC results and astrophysics constraints”, *Phys.Rev.* **D86** (2012) 035023, [arXiv:1203.3446](#).
- [56] D. E. Lopez-Fogliani, “Light Higgs and neutralino dark matter in the NMSSM”, *J.Phys.Conf.Ser.* **384** (2012) 012014.

- [57] G. Belanger, U. Ellwanger, J. F. Gunion, Y. Jiang, S. Kraml, *et al.*, “Higgs Bosons at 98 and 125 GeV at LEP and the LHC”, *JHEP* **1301** (2013) 069, [arXiv:1210.1976](#).
- [58] G. Belanger, U. Ellwanger, J. Gunion, Y. Jiang, and S. Kraml, “Two Higgs Bosons at the Tevatron and the LHC?”, [arXiv:1208.4952](#).
- [59] J. F. Gunion, Y. Jiang, and S. Kraml, “Could two NMSSM Higgs bosons be present near 125 GeV?”, *Phys.Rev.* **D86** (2012) 071702, [arXiv:1207.1545](#).
- [60] G. Jungman, M. Kamionkowski, and K. Griest, “Supersymmetric dark matter”, *Phys.Rept.* **267** (1996) 195–373, [arXiv:hep-ph/9506380](#).
- [61] G. Bertone, D. Hooper, and J. Silk, “Particle dark matter: Evidence, candidates and constraints”, *Phys.Rept.* **405** (2005) 279–390, [arXiv:hep-ph/0404175](#).
- [62] M. Drees and G. Gerbier, “Mini-Review of Dark Matter: 2012”, [arXiv:1204.2373](#).
- [63] **DAMA, LIBRA Collaboration** Collaboration, R. Bernabei *et al.*, “New results from DAMA/LIBRA”, *Eur.Phys.J.* **C67** (2010) 39–49, [arXiv:1002.1028](#).
- [64] **CoGeNT Collaboration**, C. Aalseth, P. Barbeau, J. Colaresi, J. Collar, J. Diaz Leon, *et al.*, “Search for an Annual Modulation in a P-type Point Contact Germanium Dark Matter Detector”, *Phys.Rev.Lett.* **107** (2011) 141301, [arXiv:1106.0650](#).
- [65] **CRESST Collaboration**, G. Angloher *et al.*, “Results from 730 kg days of the CRESST-II Dark Matter Search”, *Eur.Phys.J.* **C72** (2012) 1971, [arXiv:1109.0702](#).
- [66] **CDMS Collaboration**, R. Agnese *et al.*, “Dark Matter Search Results Using the Silicon Detectors of CDMS II”, [arXiv:1304.4279](#).
- [67] **XENON10 Collaboration**, J. Angle *et al.*, “A search for light dark matter in XENON10 data”, *Phys.Rev.Lett.* **107** (2011) 051301, [arXiv:1104.3088](#).
- [68] **XENON100 Collaboration**, E. Aprile *et al.*, “Dark Matter Results from 225 Live Days of XENON100 Data”, *Phys.Rev.Lett.* **109** (2012) 181301, [arXiv:1207.5988](#).
- [69] **LUX Collaboration**, D. Akerib *et al.*, “The Large Underground Xenon (LUX) Experiment”, [arXiv:1211.3788](#).
- [70] **XENON1T Collaboration**, E. Aprile, “The XENON1T Dark Matter Search Experiment”, [arXiv:1206.6288](#).
- [71] **TEXONO Collaboration**, H. Li *et al.*, “Limits on spin-independent couplings of WIMP dark matter with a p-type point-contact germanium detector”, [arXiv:1303.0925](#).

- [72] **Fermi-LAT** Collaboration, M. Ackermann *et al.*, “Constraining Dark Matter Models from a Combined Analysis of Milky Way Satellites with the Fermi Large Area Telescope”, *Phys.Rev.Lett.* **107** (2011) 241302, [arXiv:1108.3546](#).
- [73] **AMS** Collaboration, “First result from the alpha magnetic spectrometer on the international space station: Precision measurement of the positron fraction in primary cosmic rays of 0.5–350 gev”, *Phys. Rev. Lett.* **110** Apr (2013) 141102.
- [74] **H.E.S.S.** Collaboration, A. Abramowski *et al.*, “Search for photon line-like signatures from Dark Matter annihilations with H.E.S.S”, *Phys.Rev.Lett.* **110** (2013) 041301, [arXiv:1301.1173](#).
- [75] **MAGIC** Collaboration, J. Aleksić *et al.*, “Searches for Dark Matter annihilation signatures in the Segue 1 satellite galaxy with the MAGIC-I telescope”, *JCAP* **1106** (2011) 035, [arXiv:1103.0477](#).
- [76] **VERITAS** Collaboration, T. Arlen *et al.*, “Constraints on Cosmic Rays, Magnetic Fields, and Dark Matter from Gamma-Ray Observations of the Coma Cluster of Galaxies with VERITAS and Fermi”, *Astrophys.J.* **757** (2012) 123, [arXiv:1208.0676](#).
- [77] **Planck Collaboration** Collaboration, P. Ade *et al.*, “Planck 2013 results. XVI. Cosmological parameters”, [arXiv:1303.5076](#).
- [78] **WMAP** Collaboration, D. Larson, J. Dunkley, G. Hinshaw, E. Komatsu, M. Nolta, *et al.*, “Seven-Year Wilkinson Microwave Anisotropy Probe (WMAP) Observations: Power Spectra and WMAP-Derived Parameters”, *Astrophys.J.Suppl.* **192** (2011) 16, [arXiv:1001.4635](#).
- [79] G. Hinshaw, D. Larson, E. Komatsu, D. Spergel, C. Bennett, *et al.*, “Nine-Year Wilkinson Microwave Anisotropy Probe (WMAP) Observations: Cosmological Parameter Results”, [arXiv:1212.5226](#).
- [80] S. Galli, F. Iocco, G. Bertone, and A. Melchiorri, “CMB constraints on Dark Matter models with large annihilation cross-section”, *Phys.Rev.* **D80** (2009) 023505, [arXiv:0905.0003](#).
- [81] G. Hutsi, J. Chluba, A. Hektor, and M. Raidal, “WMAP7 and future CMB constraints on annihilating dark matter: implications on GeV-scale WIMPs”, *Astron.Astrophys.* **535** (2011) A26, [arXiv:1103.2766](#).
- [82] S. Galli, F. Iocco, G. Bertone, and A. Melchiorri, “Updated CMB constraints on Dark Matter annihilation cross-sections”, *Phys.Rev.* **D84** (2011) 027302, [arXiv:1106.1528](#).
- [83] A. Natarajan, “A closer look at CMB constraints on WIMP dark matter”, *Phys.Rev.* **D85** (2012) 083517, [arXiv:1201.3939](#).
- [84] G. Giesen, J. Lesgourgues, B. Audren, and Y. Ali-Haïmoud, “CMB photons shedding light on dark matter”, *JCAP* **1212** (2012) 008, [arXiv:1209.0247](#).

- [85] C. Evoli, S. Pandolfi, and A. Ferrara, “CMB constraints on light dark matter candidates”, [arXiv:1210.6845](#).
- [86] A. Geringer-Sameth and S. M. Koushiappas, “Exclusion of canonical WIMPs by the joint analysis of Milky Way dwarfs with Fermi”, *Phys.Rev.Lett.* **107** (2011) 241303, [arXiv:1108.2914](#).
- [87] R. Cotta, A. Drlica-Wagner, S. Murgia, E. Bloom, J. Hewett, *et al.*, “Constraints on the pMSSM from LAT Observations of Dwarf Spheroidal Galaxies”, *JCAP* **1204** (2012) 016, [arXiv:1111.2604](#).
- [88] A. Fowlie, A. Kalinowski, M. Kazana, L. Roszkowski, and Y. S. Tsai, “Bayesian Implications of Current LHC and XENON100 Search Limits for the Constrained MSSM”, *Phys.Rev.* **D85** (2012) 075012, [arXiv:1111.6098](#).
- [89] L. Roszkowski, E. M. Sessolo, and Y.-L. S. Tsai, “Bayesian Implications of Current LHC Supersymmetry and Dark Matter Detection Searches for the Constrained MSSM”, *Phys.Rev.* **D86** (2012) 095005, [arXiv:1202.1503](#).
- [90] Y.-L. S. Tsai, Q. Yuan, and X. Huang, “A generic method to constrain the dark matter model parameters from Fermi observations of dwarf spheroids”, [arXiv:1212.3990](#).
- [91] J. L. Feng, K. T. Matchev, and F. Wilczek, “Neutralino dark matter in focus point supersymmetry”, *Phys.Lett.* **B482** (2000) 388–399, [arXiv:hep-ph/0004043](#).
- [92] J. D. Wells, “PeV-scale supersymmetry”, *Phys.Rev.* **D71** (2005) 015013, [arXiv:hep-ph/0411041](#).
- [93] N. Arkani-Hamed and S. Dimopoulos, “Supersymmetric unification without low energy supersymmetry and signatures for fine-tuning at the LHC”, *JHEP* **0506** (2005) 073, [arXiv:hep-th/0405159](#).
- [94] G. Giudice and A. Romanino, “Split supersymmetry”, *Nucl.Phys.* **B699** (2004) 65–89, [arXiv:hep-ph/0406088](#).
- [95] G. F. Giudice, T. Han, K. Wang, and L.-T. Wang, “Nearly Degenerate Gauginos and Dark Matter at the LHC”, *Phys.Rev.* **D81** (2010) 115011, [arXiv:1004.4902](#).
- [96] M. Farina, M. Kadastik, D. Pappadopulo, J. Pata, M. Raidal, *et al.*, “Implications of XENON100 and LHC results for Dark Matter models”, *Nucl.Phys.* **B853** (2011) 607–624, [arXiv:1104.3572](#).
- [97] D. Albornoz Vasquez, G. Belanger, R. Godbole, and A. Pukhov, “The Higgs boson in the MSSM in light of the LHC”, *Phys.Rev.* **D85** (2012) 115013, [arXiv:1112.2200](#).

- [98] M. Kadastik, K. Kannike, A. Racioppi, and M. Raidal, “Implications of the 125 GeV Higgs boson for scalar dark matter and for the CMSSM phenomenology”, *JHEP* **1205** (2012) 061, [arXiv:1112.3647](#).
- [99] A. Bottino, N. Fornengo, and S. Scopel, “Phenomenology of light neutralinos in view of recent results at the CERN Large Hadron Collider”, *Phys.Rev.* **D85** (2012) 095013, [arXiv:1112.5666](#).
- [100] J. Ellis and K. A. Olive, “Revisiting the Higgs Mass and Dark Matter in the CMSSM”, *Eur.Phys.J.* **C72** (2012) 2005, [arXiv:1202.3262](#).
- [101] H. Baer, V. Barger, and A. Mustafayev, “Neutralino dark matter in mSUGRA/CMSSM with a 125 GeV light Higgs scalar”, *JHEP* **1205** (2012) 091, [arXiv:1202.4038](#).
- [102] J.-J. Cao, Z.-X. Heng, J. M. Yang, Y.-M. Zhang, and J.-Y. Zhu, “A SM-like Higgs near 125 GeV in low energy SUSY: a comparative study for MSSM and NMSSM”, *JHEP* **1203** (2012) 086, [arXiv:1202.5821](#).
- [103] J.-J. Cao, Z. Heng, J. M. Yang, and J. Zhu, “Higgs decay to dark matter in low energy SUSY: is it detectable at the LHC?”, *JHEP* **1206** (2012) 145, [arXiv:1203.0694](#).
- [104] A. Choudhury and A. Datta, “Many faces of low mass neutralino dark matter in the unconstrained MSSM, LHC data and new signals”, *JHEP* **1206** (2012) 006, [arXiv:1203.4106](#).
- [105] G. Belanger, S. Biswas, C. Boehm, and B. Mukhopadhyaya, “Light Neutralino Dark Matter in the MSSM and Its Implication for LHC Searches for Staus”, *JHEP* **1212** (2012) 076, [arXiv:1206.5404](#).
- [106] A. Arbey, M. Battaglia, A. Djouadi, and F. Mahmoudi, “The Higgs sector of the phenomenological MSSM in the light of the Higgs boson discovery”, *JHEP* **1209** (2012) 107, [arXiv:1207.1348](#).
- [107] J. Cao, Z. Heng, J. M. Yang, and J. Zhu, “Status of low energy SUSY models confronted with the LHC 125 GeV Higgs data”, *JHEP* **1210** (2012) 079, [arXiv:1207.3698](#).
- [108] H. Baer, V. Barger, A. Lessa, and X. Tata, “Discovery potential for SUSY at a high luminosity upgrade of LHC14”, *Phys.Rev.* **D86** (2012) 117701, [arXiv:1207.4846](#).
- [109] R. Allahverdi, B. Dutta, and K. Sinha, “Non-thermal Higgsino Dark Matter: Cosmological Motivations and Implications for a 125 GeV Higgs”, *Phys.Rev.* **D86** (2012) 095016, [arXiv:1208.0115](#).
- [110] S. Mohanty, S. Rao, and D. Roy, “Predictions of a Natural SUSY Dark Matter Model for Direct and Indirect Detection Experiments”, *JHEP* **1211** (2012) 175, [arXiv:1208.0894](#).

- [111] H. Baer, “Radiative natural supersymmetry with mixed axion/higgsino cold dark matter”, [arXiv:1210.7852](#).
- [112] J. Hisano, K. Ishiwata, and N. Nagata, “Direct Search of Dark Matter in High-Scale Supersymmetry”, [arXiv:1210.5985](#).
- [113] L. J. Hall, Y. Nomura, and S. Shirai, “Spread Supersymmetry with Wino LSP: Gluino and Dark Matter Signals”, [arXiv:1210.2395](#).
- [114] W. Altmannshofer, M. Carena, N. R. Shah, and F. Yu, “Indirect Probes of the MSSM after the Higgs Discovery”, *JHEP* **1301** (2013) 160, [arXiv:1211.1976](#).
- [115] M. W. Cahill-Rowley, J. L. Hewett, A. Ismail, and T. G. Rizzo, “More Energy, More Searches, but the pMSSM Lives On”, [arXiv:1211.1981](#).
- [116] A. Arbey, M. Battaglia, A. Djouadi, and F. Mahmoudi, “An update on the constraints on the phenomenological MSSM from the new LHC Higgs results”, *Physics Letters B* **720** (2013) , pp. 153–160, [arXiv:1211.4004](#).
- [117] C. Strege, G. Bertone, F. Feroz, M. Fornasa, R. R. de Austri, *et al.*, “Global Fits of the cMSSM and NUHM including the LHC Higgs discovery and new XENON100 constraints”, [arXiv:1212.2636](#).
- [118] K. Kowalska, L. Roszkowski, and E. M. Sessolo, “Two ultimate tests of constrained supersymmetry”, [arXiv:1302.5956](#).
- [119] J. H. Davis, C. McCabe, and C. Boehm, “Quantifying the evidence for Dark Matter in CoGeNT data”, [arXiv:1405.0495](#).
- [120] **CDMS Collaboration** Collaboration, R. Agnese *et al.*, “Silicon Detector Dark Matter Results from the Final Exposure of CDMS II”, *Phys.Rev.Lett.* **111** (2013) 251301, [arXiv:1304.4279](#).
- [121] T. Daylan, D. P. Finkbeiner, D. Hooper, T. Linden, S. K. N. Portillo, *et al.*, “The Characterization of the Gamma-Ray Signal from the Central Milky Way: A Compelling Case for Annihilating Dark Matter”, [arXiv:1402.6703](#).
- [122] U. Ellwanger, C. Hugonie, and A. M. Teixeira, “The Next-to-Minimal Supersymmetric Standard Model”, *Phys.Rept.* **496** (2010) 1–77, [arXiv:0910.1785](#).
- [123] <https://twiki.cern.ch/twiki/bin/view/AtlasPublic/SupersymmetryPublicResults>.
- [124] <https://twiki.cern.ch/twiki/bin/view/CMSPublic/PhysicsResultsSUS>.
- [125] G. F. Giudice and R. Rattazzi, “Theories with Gauge-Mediated Supersymmetry Breaking”, *Phys. Rept.* **322** (1999) 419–499, [hep-ph/9801271](#). %%CITATION = HEP-PH/9801271;%%.

- [126] A. Arvanitaki, N. Craig, S. Dimopoulos, and G. Villadoro, “Mini-Split”, *JHEP* **1302** (2013) 126, [arXiv:1210.0555](#).
- [127] N. Arkani-Hamed, A. Gupta, D. E. Kaplan, N. Weiner, and T. Zorawski, “Simply Unnatural Supersymmetry”, [arXiv:1212.6971](#).
- [128] **ATLAS Collaboration** Collaboration, G. Aad *et al.*, “Searches for Heavy Long-Lived Charged Particles with the ATLAS Detector in Proton-Proton Collisions at $\sqrt{s} = 8$ TeV”, [arXiv:1411.6795](#).
- [129] **CMS Collaboration** Collaboration, S. Chatrchyan *et al.*, “Searches for Long-Lived Charged Particles in pp Collisions at $\sqrt{s}=7$ and 8 TeV”, *JHEP* **1307** (2013) 122, [arXiv:1305.0491](#).
- [130] The CMS Collaboration, “Reinterpreting the Results of the Search for Long-Lived Charged Particles in the pMSSM and Other BSM Scenarios”. CMS PAS EXO-13-006.
- [131] The ATLAS Collaboration, “Limits on Metastable Gluinos from ATLAS SUSY Searches at 8 TeV”. ATLAS-CONF-2014-037.
- [132] **ATLAS Collaboration** Collaboration, G. Aad *et al.*, “Search for Non-Pointing and Delayed Photons in the Diphoton and Missing Transverse Momentum Final State in 8 TeV pp Collisions at the LHC Using the ATLAS Detector”, [arXiv:1409.5542](#).
- [133] **CMS Collaboration** Collaboration, S. Chatrchyan *et al.*, “Search for Long-Lived Particles Decaying to Photons and Missing Energy in Proton-Proton Collisions at $\sqrt{s} = 7$ TeV”, *Phys.Lett.* **B722** (2013) 273–294, [arXiv:1212.1838](#).
- [134] **ATLAS Collaboration** Collaboration, G. Aad *et al.*, “Search for Charginos Nearly Mass Degenerate with the Lightest Neutralino Based on a Disappearing-Track Signature in pp Collisions at $\sqrt{s}=8$ TeV with the ATLAS Detector”, *Phys.Rev.* **D88** (2013), no. 11, 112006, [arXiv:1310.3675](#).
- [135] The ATLAS Collaboration, “Search for Long-Lived, Heavy Particles in Final States with a Muon and a Multi-Track Displaced Vertex in Proton-Proton Collisions at $\sqrt{s} = 8$ TeV with the ATLAS Detector”. ATLAS-PHYS-PUB-2013-092.
- [136] **CMS Collaboration** Collaboration, V. Khachatryan *et al.*, “Search for “Displaced Supersymmetry” in Events with an Electron and a Muon with Large Impact Parameters”, [arXiv:1409.4789](#).
- [137] **ATLAS Collaboration** Collaboration, G. Aad *et al.*, “Search for Long-Lived Stopped R-Hadrons Decaying Out-of-Time with pp Collisions Using the ATLAS Detector”, *Phys.Rev.* **D88** (2013), no. 11, 112003, [arXiv:1310.6584](#).

- [138] **CMS Collaboration** Collaboration, V. Khachatryan *et al.*, “Search for Long-Lived Neutral Particles Decaying to Quark-Antiquark Pairs in Proton-Proton Collisions at $\sqrt{s} = 8$ TeV”, [arXiv:1411.6530](#).
- [139] **CMS Collaboration** Collaboration, V. Khachatryan *et al.*, “Search for Long-Lived Particles that Decay into Final States Containing Two Electrons or Two Muons in Proton-Proton Collisions at $\sqrt{s} = 8$ TeV”, [arXiv:1411.6977](#).
- [140] The ATLAS Collaboration, “Search for Pair Produced Long-Lived Neutral Particles Decaying in the ATLAS Hadronic Calorimeter in pp Collisions at $\sqrt{s} = 8$ TeV”. ATLAS-CONF-2014-041.
- [141] **ATLAS Collaboration** Collaboration, G. Aad *et al.*, “Search for a Light Higgs Boson Decaying to Long-Lived Weakly-Interacting Particles in Proton-Proton Collisions at $\sqrt{s} = 7$ TeV with the ATLAS Detector”, *Phys.Rev.Lett.* **108** (2012) 251801, [arXiv:1203.1303](#).
- [142] **ATLAS Collaboration** Collaboration, G. Aad *et al.*, “Search for Displaced Muonic Lepton Jets from Light Higgs Boson Decay in Proton-Proton Collisions at $\sqrt{s} = 7$ TeV with the ATLAS Detector”, *Phys.Lett.* **B721** (2013) 32–50, [arXiv:1210.0435](#).
- [143] **ATLAS Collaboration** Collaboration, G. Aad *et al.*, “Search for Long-Lived Neutral Particles Decaying into Lepton Jets in Proton-Proton Collisions at $\sqrt{s} = 8$ TeV with the ATLAS Detector”, [arXiv:1409.0746](#).
- [144] **LHCb collaboration** Collaboration, R. Aaij *et al.*, “Search for Long-Lived Particles Decaying to Jet Pairs”, [arXiv:1412.3021](#).
- [145] **CMS Collaboration**, V. Khachatryan *et al.*, “Search for Decays of Stopped Long-Lived Particles Produced in Proton-Proton Collisions at $\sqrt{s} = 8$ TeV”, [arXiv:1501.05603](#).
- [146] M. J. Strassler and K. M. Zurek, “Echoes of a Hidden Valley at Hadron Colliders”, *Phys.Lett.* **B651** (2007) 374–379, [arXiv:hep-ph/0604261](#).
- [147] M. J. Strassler and K. M. Zurek, “Discovering the Higgs Through Highly-Displaced Vertices”, *Phys.Lett.* **B661** (2008) 263–267, [arXiv:hep-ph/0605193](#).
- [148] P. Meade, M. Reece, and D. Shih, “Long-Lived Neutralino NLSPs”, *JHEP* **1010** (2010) 067, [arXiv:1006.4575](#).
- [149] P. W. Graham, D. E. Kaplan, S. Rajendran, and P. Saraswat, “Displaced Supersymmetry”, *JHEP* **1207** (2012) 149, [arXiv:1204.6038](#).
- [150] P. Jaiswal, K. Kopp, and T. Okui, “Higgs Production Amidst the LHC Detector”, *Phys.Rev.* **D87** (2013), no. 11, 115017, [arXiv:1303.1181](#).

- [151] C. Csaki, E. Kuflik, and T. Volansky, “Dynamical R-Parity Violation”, *Phys.Rev.Lett.* **112** (2014) 131801, [arXiv:1309.5957](#).
- [152] D. G. Cerde so, V. Mart n-Lozano, and O. Seto, “Displaced vertices and long-lived charged particles in the NMSSM with right-handed sneutrinos”, *JHEP* **1405** (2014) 035, [arXiv:1311.7260](#).
- [153] L. Covi and F. Dradi, “Long-Lived Stop at the LHC with or without R-Parity”, *JCAP* **1410** (2014), no. 10, 039, [arXiv:1403.4923](#).
- [154] M. R. Buckley, V. Halyo, and P. Lujan, “Don’t Miss the Displaced Higgs at the LHC Again”, [arXiv:1405.2082](#).
- [155] A. Falkowski, Y. Hochberg, and J. T. Ruderman, “Displaced Vertices from X-ray Lines”, [arXiv:1409.2872](#).
- [156] Y. Cui and B. Shuve, “Probing Baryogenesis with Displaced Vertices at the LHC”, [arXiv:1409.6729](#).
- [157] M. Cahill-Rowley, “Long-Lived Sparticles in the Gravitino pMSSM”.
Talk at ATLAS Searches Workshop (LBNL, 1 January 2014).
- [158] P. Schwaller, D. Stolarski, and A. Weiler, “Emerging Jets”, [arXiv:1502.05409](#).
- [159] S. Jung and H.-S. Lee, “Untracked Signals of Supersymmetry at the LHC”, [arXiv:1503.00414](#).
- [160] S. Dimopoulos and G. Giudice, “Naturalness Constraints in Supersymmetric Theories with Nonuniversal Soft Terms”, *Phys.Lett.* **B357** (1995) 573–578, [arXiv:hep-ph/9507282](#).
- [161] A. G. Cohen, D. Kaplan, and A. Nelson, “The More Minimal Supersymmetric Standard Model”, *Phys.Lett.* **B388** (1996) 588–598, [arXiv:hep-ph/9607394](#).
- [162] C. Brust, A. Katz, S. Lawrence, and R. Sundrum, “SUSY, the Third Generation and the LHC”, *JHEP* **1203** (2012) 103, [arXiv:1110.6670](#). %%CITATION = ARXIV:1110.6670;%%.
- [163] M. Papucci, J. T. Ruderman, and A. Weiler, “Natural SUSY Endures”, *JHEP* **1209** (2012) 035, [arXiv:1110.6926](#).
- [164] Y. Kats, P. Meade, M. Reece, and D. Shih, “The Status of GMSB After 1/fb at the LHC”, *JHEP* **1202** (2012) 115, [arXiv:1110.6444](#). %%CITATION = ARXIV:1110.6444;%%.
- [165] **LHC Higgs Cross Section Working Group** Collaboration, S. Heinemeyer *et al.*, “Handbook of LHC Higgs Cross Sections: 3. Higgs Properties”, [arXiv:1307.1347](#).

- [166] L. J. Dixon and Y. Li, “Bounding the Higgs Boson Width Through Interferometry”, *Phys.Rev.Lett.* **111** (2013) 111802, [arXiv:1305.3854](#).
- [167] **ATLAS** Collaboration, G. Aad *et al.*, “Search for $H \rightarrow \gamma\gamma$ produced in association with top quarks and constraints on the Yukawa coupling between the top quark and the Higgs boson using data taken at 7 TeV and 8 TeV with the ATLAS detector”, *Phys.Lett.* **B740** (2015) 222–242, [arXiv:1409.3122](#).
- [168] **CMS** Collaboration, V. Khachatryan *et al.*, “Search for the associated production of the Higgs boson with a top-quark pair”, *JHEP* **1409** (2014) 087, [arXiv:1408.1682](#).
- [169] D. Curtin, R. Essig, S. Gori, P. Jaiswal, A. Katz, *et al.*, “Exotic decays of the 125 GeV Higgs boson”, *Phys.Rev.* **D90** (2014), no. 7, 075004, [arXiv:1312.4992](#).
- [170] M. Duhrssen, S. Heinemeyer, H. Logan, D. Rainwater, G. Weiglein, *et al.*, “Extracting Higgs boson couplings from CERN LHC data”, *Phys.Rev.* **D70** (2004) 113009, [arXiv:hep-ph/0406323](#).
- [171] M. E. Peskin, “Comparison of LHC and ILC Capabilities for Higgs Boson Coupling Measurements”, [arXiv:1207.2516](#).
- [172] B. A. Dobrescu and J. D. Lykken, “Coupling spans of the Higgs-like boson”, *JHEP* **1302** (2013) 073, [arXiv:1210.3342](#).
- [173] F. Caola and K. Melnikov, “Constraining the Higgs boson width with ZZ production at the LHC”, *Phys.Rev.* **D88** (2013) 054024, [arXiv:1307.4935](#).
- [174] J. M. Campbell, R. K. Ellis, and C. Williams, “Bounding the Higgs width at the LHC using full analytic results for $gg \rightarrow 2e\,2\mu$ ”, [arXiv:1311.3589](#).
- [175] M. Bicer, H. Duran Yildiz, I. Yildiz, G. Coignet, M. Delmastro, *et al.*, “First Look at the Physics Case of TLEP”, [arXiv:1308.6176](#).
- [176] **ILD Concept Group - Linear Collider** Collaboration, T. Abe *et al.*, “The International Large Detector: Letter of Intent”, [arXiv:1006.3396](#).
- [177] H. Baer, T. Barklow, K. Fujii, Y. Gao, A. Hoang, *et al.*, “The International Linear Collider Technical Design Report - Volume 2: Physics”, [arXiv:1306.6352](#).
- [178] V. Barger, L. L. Everett, H. E. Logan, and G. Shaughnessy, “Scrutinizing h(125) in Two Higgs Doublet Models at the LHC, ILC, and Muon Collider”, *Phys.Rev.* **D88** (2013) 115003, [arXiv:1308.0052](#).
- [179] V. Barger, M. Ishida, and W.-Y. Keung, “Total Width of 125 GeV Higgs Boson”, *Phys.Rev.Lett.* **108** (2012) 261801, [arXiv:1203.3456](#).

- [180] **LHC Higgs Cross Section Working Group** Collaboration, A. David *et al.*, “LHC HXSWG interim recommendations to explore the coupling structure of a Higgs-like particle”, [arXiv:1209.0040](#).
- [181] T. Han and Z. Liu, “Direct Measurement of the Higgs Boson Total Width at a Muon Collider”, *Phys.Rev.* **D87** (2013) 033007, [arXiv:1210.7803](#).
- [182] T. Han, Z. Liu, and J. Sayre, “Potential Precision on Higgs Couplings and Total Width at the ILC”, *Phys.Rev.* **D89** (2014) 113006, [arXiv:1311.7155](#).
- [183] **ILD Design Study Group** Collaboration, H. Li *et al.*, “HZ Recoil Mass and Cross Section Analysis in ILD”, [arXiv:1202.1439](#).
- [184] H. Li, “Higgs Recoil Mass and Higgs-Strahlung Cross-Section Study for the ILD LOI”, [arXiv:1007.2999](#).
- [185] A. Miyamoto, “A measurement of the total cross section of σ_{Zh} at a future e^+e^- collider using the hadronic decay mode of Z ”, [arXiv:1311.2248](#).
- [186] V. D. Barger, M. Berger, J. Gunion, and T. Han, “s channel Higgs boson production at a muon muon collider”, *Phys.Rev.Lett.* **75** (1995) 1462–1465, [arXiv:hep-ph/9504330](#).
- [187] J. Gunion and H. E. Haber, “Higgs Bosons in Supersymmetric Models. 1.”, *Nucl.Phys.* **B272** (1986) 1.
- [188] W. Konetschny and W. Kummer, “Nonconservation of Total Lepton Number with Scalar Bosons”, *Phys.Lett.* **B70** (1977) 433.
- [189] T. Cheng and L.-F. Li, “Neutrino Masses, Mixings and Oscillations in SU(2) x U(1) Models of Electroweak Interactions”, *Phys.Rev.* **D22** (1980) 2860.
- [190] G. Lazarides, Q. Shafi, and C. Wetterich, “Proton Lifetime and Fermion Masses in an SO(10) Model”, *Nucl.Phys.* **B181** (1981) 287–300.
- [191] J. Schechter and J. Valle, “Neutrino Masses in SU(2) x U(1) Theories”, *Phys.Rev.* **D22** (1980) 2227.
- [192] R. N. Mohapatra and G. Senjanovic, “Neutrino Masses and Mixings in Gauge Models with Spontaneous Parity Violation”, *Phys.Rev.* **D23** (1981) 165.
- [193] F. Gianotti, M. Mangano, T. Virdee, S. Abdullin, G. Azuelos, *et al.*, “Physics potential and experimental challenges of the LHC luminosity upgrade”, *Eur.Phys.J.* **C39** (2005) 293–333, [arXiv:hep-ph/0204087](#).
- [194] I. M. Lewis, “Closing the Wedge with 300 fb^{-1} and 3000 fb^{-1} at the LHC: A Snowmass White Paper”, [arXiv:1308.1742](#).

- [195] T. Li, “Decoupling MSSM Higgs Sector and Heavy Higgs Decay”, *Phys.Lett.* **B728** (2014) 77–84, [arXiv:1309.6713](#).
- [196] S. Dawson, A. Gritsan, H. Logan, J. Qian, C. Tully, *et al.*, “Higgs Working Group Report of the Snowmass 2013 Community Planning Study”, [arXiv:1310.8361](#).
- [197] B. Coleppa, F. Kling, and S. Su, “Exotic Decays Of A Heavy Neutral Higgs Through HZ/AZ Channel”, [arXiv:1404.1922](#).
- [198] E. Eichten and A. Martin, “The Muon Collider as a H/A factory”, *Phys.Lett.* **B728** (2014) 125–130, [arXiv:1306.2609](#).
- [199] **ATLAS** Collaboration, G. Aad *et al.*, “Search for New Particles in Two-Jet Final States in 7 TeV Proton-Proton Collisions with the ATLAS Detector at the LHC”, *Phys.Rev.Lett.* **105** (2010) 161801, [arXiv:1008.2461](#).
- [200] L. A. Anchordoqui, H. Goldberg, D. Lust, S. Nawata, S. Stieberger, *et al.*, “Dijet signals for low mass strings at the LHC”, *Phys.Rev.Lett.* **101** (2008) 241803, [arXiv:0808.0497](#).
- [201] R. S. Chivukula, M. Golden, and E. H. Simmons, “Six jet signals of highly colored fermions”, *Phys.Lett.* **B257** (1991) 403–408.
- [202] C. W. Bauer, Z. Ligeti, M. Schmaltz, J. Thaler, and D. G. Walker, “Supermodels for early LHC”, *Phys.Lett.* **B690** (2010) 280–288, [arXiv:0909.5213](#).
- [203] V. Barger, T. Han, and D. G. Walker, “Top Quark Pairs at High Invariant Mass: A Model-Independent Discriminator of New Physics at the LHC”, *Phys.Rev.Lett.* **100** (2008) 031801, [arXiv:hep-ph/0612016](#).
- [204] E. Ma, M. Raidal, and U. Sarkar, “Probing the exotic particle content beyond the standard model”, *Eur.Phys.J.* **C8** (1999) 301–309, [arXiv:hep-ph/9808484](#).
- [205] R. S. Chivukula and H. Georgi, “Composite Technicolor Standard Model”, *Phys.Lett.* **B188** (1987) 99.
- [206] J. M. Arnold, M. Pospelov, M. Trott, and M. B. Wise, “Scalar Representations and Minimal Flavor Violation”, *JHEP* **1001** (2010) 073, [arXiv:0911.2225](#).
- [207] R. Mohapatra, N. Okada, and H.-B. Yu, “Diquark Higgs at LHC”, *Phys.Rev.* **D77** (2008) 011701, [arXiv:0709.1486](#).
- [208] K. Babu, R. Mohapatra, and S. Nasri, “Unified TeV Scale Picture of Baryogenesis and Dark Matter”, *Phys.Rev.Lett.* **98** (2007) 161301, [arXiv:hep-ph/0612357](#).
- [209] S. Atag, O. Cakir, and S. Sultansoy, “Resonance production of diquarks at the CERN LHC”, *Phys.Rev.* **D59** (1999) 015008.

- [210] O. Cakir and M. Sahin, “Resonant production of diquarks at high energy pp , ep and e^+e^- colliders”, *Phys.Rev.* **D72** (2005) 115011, [arXiv:hep-ph/0508205](#).
- [211] A. Celikel, M. Kantar, and S. Sultansoy, “A Search for sextet quarks and leptogluons at the LHC”, *Phys.Lett.* **B443** (1998) 359–364.
- [212] E. Eichten, I. Hinchliffe, K. Lane, and C. Quigg, “Signatures for Technicolor”, *Phys.Rev.* **D34** (1986) 1547.
- [213] M. I. Gresham and M. B. Wise, “Color octet scalar production at the LHC”, *Phys.Rev.* **D76** (2007) 075003, [arXiv:0706.0909](#).
- [214] A. Idilbi, C. Kim, and T. Mehen, “Factorization and resummation for single color-octet scalar production at the LHC”, *Phys.Rev.* **D79** (2009) 114016, [arXiv:0903.3668](#).
- [215] A. V. Manohar and M. B. Wise, “Flavor changing neutral currents, an extended scalar sector, and the Higgs production rate at the CERN LHC”, *Phys.Rev.* **D74** (2006) 035009, [arXiv:hep-ph/0606172](#).
- [216] P. Fileviez Perez, R. Gavin, T. McElmurry, and F. Petriello, “Grand Unification and Light Color-Octet Scalars at the LHC”, *Phys.Rev.* **D78** (2008) 115017, [arXiv:0809.2106](#).
- [217] J. Pumplin, D. Stump, J. Huston, H. Lai, P. M. Nadolsky, *et al.*, “New generation of parton distributions with uncertainties from global QCD analysis”, *JHEP* **0207** (2002) 012, [arXiv:hep-ph/0201195](#).
- [218] T. Han, I. Lewis, and T. McElmurry, “QCD Corrections to Scalar Diquark Production at Hadron Colliders”, *JHEP* **1001** (2010) 123, [arXiv:0909.2666](#).
- [219] E. Eichten, K. D. Lane, and M. E. Peskin, “New Tests for Quark and Lepton Substructure”, *Phys.Rev.Lett.* **50** (1983) 811–814.
- [220] P. Langacker, R. W. Robinett, and J. L. Rosner, “New Heavy Gauge Bosons in $p p$ and p anti- p Collisions”, *Phys.Rev.* **D30** (1984) 1470.
- [221] A. Czarnecki, M. Jezabek, and J. H. Kuhn, “Lepton Spectra From Decays Of Polarized Top Quarks ”, *Nucl.Phys.* **B351** (1991) 70–80.
- [222] F. del Aguila, M. Cvetič, and P. Langacker, “Determination of Z-prime gauge couplings to quarks and leptons at future hadron colliders”, *Phys.Rev.* **D48** (1993) 969–973, [arXiv:hep-ph/9303299](#).
- [223] F. Del Aguila and M. Cvetič, “Diagnostic power of future colliders for Z-prime couplings to quarks and leptons: e^+e^- versus $p p$ colliders”, *Phys.Rev.* **D50** (1994) 3158–3166, [arXiv:hep-ph/9312329](#).

- [224] F. Del Aguila, M. Cvetič, and P. Langacker, “Reconstruction of the extended gauge structure from Z-prime observables at future colliders”, *Phys.Rev.* **D52** (1995) 37–43, [arXiv:hep-ph/9501390](#).
- [225] M. Dittmar, A.-S. Nicollerat, and A. Djouadi, “Z-prime studies at the LHC: An Update”, *Phys.Lett.* **B583** (2004) 111–120, [arXiv:hep-ph/0307020](#).
- [226] M. S. Carena, A. Daleo, B. A. Dobrescu, and T. M. Tait, “Z’ gauge bosons at the Tevatron”, *Phys.Rev.* **D70** (2004) 093009, [arXiv:hep-ph/0408098](#).
- [227] **LHC/LC Study Group** Collaboration, G. Weiglein *et al.*, “Physics interplay of the LHC and the ILC”, *Phys.Rept.* **426** (2006) 47–358, [arXiv:hep-ph/0410364](#).
- [228] F. Petriello and S. Quackenbush, “Measuring Z’ couplings at the CERN LHC”, *Phys.Rev.* **D77** (2008) 115004, [arXiv:0801.4389](#).
- [229] S. Godfrey and T. A. Martin, “Identification of Extra Neutral Gauge Bosons at the LHC Using b- and t-Quarks”, *Phys.Rev.Lett.* **101** (2008) 151803, [arXiv:0807.1080](#).
- [230] P. Osland, A. Pankov, A. Tsytrinov, and N. Paver, “Spin and model identification of Z’ bosons at the LHC”, *Phys.Rev.* **D79** (2009) 115021, [arXiv:0904.4857](#).
- [231] Y. Li, F. Petriello, and S. Quackenbush, “Reconstructing a Z-prime Lagrangian using the LHC and low-energy data”, *Phys.Rev.* **D80** (2009) 055018, [arXiv:0906.4132](#).
- [232] R. Diener, S. Godfrey, and T. A. Martin, “Discovery and Identification of Extra Neutral Gauge Bosons at the LHC”, [arXiv:0910.1334](#).
- [233] R. Diener, S. Godfrey, and T. A. Martin, “Unravelling an Extra Neutral Gauge Boson at the LHC using Third Generation Fermions”, *Phys.Rev.* **D83** (2011) 115008, [arXiv:1006.2845](#).
- [234] S. Gopalakrishna, T. Han, I. Lewis, Z.-g. Si, and Y.-F. Zhou, “Chiral Couplings of W’ and Top Quark Polarization at the LHC”, *Phys.Rev.* **D82** (2010) 115020, [arXiv:1008.3508](#).
- [235] J. Erler, P. Langacker, S. Munir, and E. Rojas, “Z’ Bosons at Colliders: a Bayesian Viewpoint”, *JHEP* **1111** (2011) 076, [arXiv:1103.2659](#).
- [236] E. L. Berger, Q.-H. Cao, C.-R. Chen, and H. Zhang, “Top Quark Polarization As A Probe of Models with Extra Gauge Bosons”, *Phys.Rev.* **D83** (2011) 114026, [arXiv:1103.3274](#).
- [237] C.-W. Chiang, N. D. Christensen, G.-J. Ding, and T. Han, “Discovery in Drell-Yan Processes at the LHC”, *Phys.Rev.* **D85** (2012) 015023, [arXiv:1107.5830](#).

- [238] E. Accomando, D. Becciolini, A. Belyaev, S. Moretti, and C. Shepherd-Themistocleous, “Z’ at the LHC: Interference and Finite Width Effects in Drell-Yan”, [arXiv:1304.6700](#).
- [239] E. L. Berger, Q.-H. Cao, J.-H. Yu, and H. Zhang, “Measuring Top-Quark Polarization in Top-Pair + Missing Energy Events”, [arXiv:1305.7266](#).
- [240] **ATLAS** Collaboration, ATLAS-CONF-2013-017, “Search for high-mass dilepton resonances in 20/fb of pp collisions at $\sqrt{s} = 8$ TeV with the ATLAS experiment”, 2013.
- [241] **CMS** Collaboration, EXO12061, “Search for Resonances in the Dilepton Mass Distribution”, 2013.
- [242] J. Alwall, M. Herquet, F. Maltoni, O. Mattelaer, and T. Stelzer, “MadGraph 5 : Going Beyond”, *JHEP* **1106** (2011) 128, [arXiv:1106.0522](#), * Temporary entry *.
- [243] N. D. Christensen and C. Duhr, “FeynRules - Feynman rules made easy”, *Comput.Phys.Commun.* **180** (2009) 1614–1641, [arXiv:0806.4194](#).
- [244] T. Sjostrand, S. Mrenna, and P. Z. Skands, “PYTHIA 6.4 Physics and Manual”, *JHEP* **0605** (2006) 026, [arXiv:hep-ph/0603175](#).
- [245] S. Ovin, X. Rouby, and V. Lemaitre, “DELPHES, a framework for fast simulation of a generic collider experiment”, [arXiv:0903.2225](#).
- [246] D. Miller, R. Nevzorov, and P. Zerwas, “The Higgs sector of the next-to-minimal supersymmetric standard model”, *Nucl.Phys.* **B681** (2004) 3–30, [arXiv:hep-ph/0304049](#).
- [247] V. Barger, P. Langacker, H.-S. Lee, and G. Shaughnessy, “Higgs Sector in Extensions of the MSSM”, *Phys.Rev.* **D73** (2006) 115010, [arXiv:hep-ph/0603247](#).
- [248] **LEP Higgs Working Group for Higgs boson searches, ALEPH Collaboration, DELPHI Collaboration, L3 Collaboration, OPAL Collaboration**, “Search for charged Higgs bosons: Preliminary combined results using LEP data collected at energies up to 209-GeV”, [arXiv:hep-ex/0107031](#).
- [249] **ALEPH** Collaboration, A. Heister *et al.*, “Search for charged Higgs bosons in e^+e^- collisions at energies up to $\sqrt{s} = 209$ -GeV”, *Phys.Lett.* **B543** (2002) 1–13, [arXiv:hep-ex/0207054](#).
- [250] S. Heinemeyer, O. Stal, and G. Weiglein, “Interpreting the LHC Higgs Search Results in the MSSM”, *Phys.Lett.* **B710** (2012) 201–206, [arXiv:1112.3026](#).
- [251] A. Arbey, M. Battaglia, A. Djouadi, and F. Mahmoudi, “The Higgs sector of the phenomenological MSSM in the light of the Higgs boson discovery”, *JHEP* **1209** (2012) 107, [arXiv:1207.1348](#).

- [252] R. Benbrik, M. Gomez Bock, S. Heinemeyer, O. Stal, G. Weiglein, *et al.*, “Confronting the MSSM and the NMSSM with the Discovery of a Signal in the two Photon Channel at the LHC”, *Eur.Phys.J.* **C72** (2012) 2171, [arXiv:1207.1096](#).
- [253] K. Hagiwara, J. S. Lee, and J. Nakamura, “Properties of 125 GeV Higgs boson in non-decoupling MSSM scenarios”, *JHEP* **1210** (2012) 002, [arXiv:1207.0802](#).
- [254] J. Ke, H. Luo, M.-x. Luo, K. Wang, L. Wang, *et al.*, “Revisit to Non-decoupling MSSM”, [arXiv:1211.2427](#).
- [255] M. Drees, “A Supersymmetric Explanation of the Excess of Higgs–Like Events at the LHC and at LEP”, *Phys.Rev.* **D86** (2012) 115018, [arXiv:1210.6507](#).
- [256] CMS Collaboration, S. Chatrchyan *et al.*, “Search for a light charged Higgs boson in top quark decays in pp collisions at $\sqrt{s} = 7$ TeV”, *JHEP* **1207** (2012) 143, [arXiv:1205.5736](#).
- [257] ATLAS Collaboration, G. Aad *et al.*, “Search for charged Higgs bosons decaying via $H^+ \rightarrow \tau\nu$ in top quark pair events using pp collision data at $\sqrt{s} = 7$ TeV with the ATLAS detector”, *JHEP* **1206** (2012) 039, [arXiv:1204.2760](#).
- [258] ATLAS Collaboration, G. Aad *et al.*, “Search for a light charged Higgs boson in the decay channel $H^+ \rightarrow c\bar{s}$ in $t\bar{t}$ events using pp collisions at $\sqrt{s} = 7$ TeV with the ATLAS detector”, [arXiv:1302.3694](#).
- [259] M. Carena, S. Gori, N. R. Shah, C. E. Wagner, and L.-T. Wang, “Light Stau Phenomenology and the Higgs $\gamma\gamma$ Rate”, *JHEP* **1207** (2012) 175, [arXiv:1205.5842](#).
- [260] U. Ellwanger, J. F. Gunion, and C. Hugonie, “NMHDECAY: A Fortran code for the Higgs masses, couplings and decay widths in the NMSSM”, *JHEP* **0502** (2005) 066, [arXiv:hep-ph/0406215](#).
- [261] U. Ellwanger and C. Hugonie, “NMHDECAY 2.0: An Updated program for sparticle masses, Higgs masses, couplings and decay widths in the NMSSM”, *Comput.Phys.Commun.* **175** (2006) 290–303, [arXiv:hep-ph/0508022](#).
- [262] G. Belanger, F. Boudjema, C. Hugonie, A. Pukhov, and A. Semenov, “Relic density of dark matter in the NMSSM”, *JCAP* **0509** (2005) 001, [arXiv:hep-ph/0505142](#).
- [263] “Search for the standard model higgs boson in $h \rightarrow \tau\tau$ decays in proton-proton collisions with the atlas detector”, Tech. Rep. ATLAS-CONF-2012-160, CERN, Geneva, Nov 2012.
- [264] “Search for the standard model higgs boson produced in association with a vector boson and decaying to bottom quarks with the atlas detector”, Tech. Rep. ATLAS-CONF-2012-161, CERN, Geneva, Nov 2012.

- [265] “Observation and study of the higgs boson candidate in the two photon decay channel with the atlas detector at the lhc”, Tech. Rep. ATLAS-CONF-2012-168, CERN, Geneva, Dec 2012.
- [266] “Higgs to tau tau (sm) (hcp)”, Tech. Rep. CMS-PAS-HIG-12-043, CERN, Geneva, 2012.
- [267] “Search for the standard model higgs boson produced in association with w or z bosons, and decaying to bottom quarks for hcp 2012”, Tech. Rep. CMS-PAS-HIG-12-044, CERN, Geneva, 2012.
- [268] “Higgs to tau tau (mssm) (hcp)”, Tech. Rep. CMS-PAS-HIG-12-050, CERN, Geneva, 2012.
- [269] **ALEPH Collaboration, DELPHI Collaboration, L3 Collaboration, OPAL Collaboration, LEP Working Group for Higgs Boson Searches** Collaboration, S. Schael *et al.*, “Search for neutral MSSM Higgs bosons at LEP”, *Eur.Phys.J.* **C47** (2006) 547–587, [arXiv:hep-ex/0602042](#).
- [270] R. Dermisek and J. F. Gunion, “Consistency of LEP event excesses with an $h \rightarrow aa$ decay scenario and low-fine-tuning NMSSM models”, *Phys.Rev.* **D73** (2006) 111701, [arXiv:hep-ph/0510322](#).
- [271] R. Dermisek and J. F. Gunion, “The NMSSM Close to the R-symmetry Limit and Naturalness in $h \rightarrow aa$ Decays for $m(a) < 2m(b)$ ”, *Phys.Rev.* **D75** (2007) 075019, [arXiv:hep-ph/0611142](#).
- [272] M. Carena, T. Han, G.-Y. Huang, and C. E. Wagner, “Higgs Signal for $h \rightarrow aa$ at Hadron Colliders”, *JHEP* **0804** (2008) 092, [arXiv:0712.2466](#).
- [273] G. Chalons, M. J. Dolan, and C. McCabe, “Neutralino dark matter and the Fermi gamma-ray lines”, *JCAP* **1302** (2013) 016, [arXiv:1211.5154](#).
- [274] **LEP Working Group for Higgs boson searches, ALEPH Collaboration, DELPHI Collaboration, L3 Collaboration, OPAL Collaboration**, R. Barate *et al.*, “Search for the standard model Higgs boson at LEP”, *Phys.Lett.* **B565** (2003) 61–75, [arXiv:hep-ex/0306033](#).
- [275] N. D. Christensen, T. Han, and T. Li, “Pair Production of MSSM Higgs Bosons in the Non-decoupling Region at the LHC”, *Phys.Rev.* **D86** (2012) 074003, [arXiv:1206.5816](#).
- [276] Z. Kang, J. Li, T. Li, D. Liu, and J. Shu, “Probing the CP-even Higgs Sector via $H_3 \rightarrow H_2 H_1$ in the Natural NMSSM”, [arXiv:1301.0453](#).
- [277] J. Rathsmann and T. Rossler, “Closing the Window on Light Charged Higgs Bosons in the NMSSM”, *Adv.High Energy Phys.* **2012** (2012) 853706, [arXiv:1206.1470](#).

- [278] D. G. Cerdeno, P. Ghosh, and C. B. Park, “Probing the two light Higgs scenario in the NMSSM with a low-mass pseudoscalar”, [arXiv:1301.1325](#).
- [279] J. Cao, Z. Heng, L. Shang, P. Wan, and J. M. Yang, “Pair Production of a 125 GeV Higgs Boson in MSSM and NMSSM at the LHC”, [arXiv:1301.6437](#).
- [280] **Heavy Flavor Averaging Group** Collaboration, Y. Amhis *et al.*, “Averages of B-Hadron, C-Hadron, and tau-lepton properties as of early 2012”, [arXiv:1207.1158](#).
- [281] **LHCb** Collaboration, R. Aaij *et al.*, “First evidence for the decay $B_s \rightarrow \mu^+ \mu^-$ ”, *Phys. Rev. Lett.* **110**, **021801** (2013) [arXiv:1211.2674](#).
- [282] J. R. Ellis, J. Hagelin, D. V. Nanopoulos, K. A. Olive, and M. Srednicki, “Supersymmetric Relics from the Big Bang”, *Nucl.Phys.* **B238** (1984) 453–476.
- [283] M. W. Goodman and E. Witten, “Detectability of Certain Dark Matter Candidates”, *Phys.Rev.* **D31** (1985) 3059.
- [284] K. Griest, “Cross-Sections, Relic Abundance and Detection Rates for Neutralino Dark Matter”, *Phys.Rev.* **D38** (1988) 2357.
- [285] R. Barbieri and G. Giudice, “Upper Bounds on Supersymmetric Particle Masses”, *Nucl.Phys.* **B306** (1988) 63.
- [286] R. Kitano and Y. Nomura, “Supersymmetry, naturalness, and signatures at the LHC”, *Phys.Rev.* **D73** (2006) 095004, [arXiv:hep-ph/0602096](#).
- [287] V. Barger, P. Langacker, H.-S. Lee, and G. Shaughnessy, “Higgs Sector in Extensions of the MSSM”, *Phys.Rev.* **D73** (2006) 115010, [arXiv:hep-ph/0603247](#).
- [288] J. L. Feng, “Naturalness and the Status of Supersymmetry”, *Ann.Rev.Nucl.Part.Sci.* **63** (2013) 351–382, [arXiv:1302.6587](#).
- [289] N. Arkani-Hamed, A. Delgado, and G. Giudice, “The Well-tempered neutralino”, *Nucl.Phys.* **B741** (2006) 108–130, [arXiv:hep-ph/0601041](#).
- [290] M. Perelstein and B. Shakya, “Fine-Tuning Implications of Direct Dark Matter Searches in the MSSM”, *JHEP* **1110** (2011) 142, [arXiv:1107.5048](#).
- [291] P. Grothaus, M. Lindner, and Y. Takanishi, “Naturalness of Neutralino Dark Matter”, [arXiv:1207.4434](#).
- [292] C. Cheung, L. J. Hall, D. Pinner, and J. T. Ruderman, “Prospects and Blind Spots for Neutralino Dark Matter”, [arXiv:1211.4873](#).
- [293] **CMS** Collaboration, S. Chatrchyan *et al.*, “Search for electroweak production of charginos and neutralinos using leptonic final states in pp collisions at $\sqrt{s} = 7$ TeV”, *JHEP* **1211** (2012) 147, [arXiv:1209.6620](#).

- [294] T. Han, S. Padhi, and S. Su, “Electroweakinos in the Light of the Higgs Boson”, [arXiv:1309.5966](#).
- [295] A. Chatterjee, M. Drees, and S. Kulkarni, “Radiative Corrections to the Neutralino Dark Matter Relic Density - an Effective Coupling Approach”, *Phys.Rev.* **D86** (2012) 105025, [arXiv:1209.2328](#).
- [296] S. Heinemeyer, W. Hollik, and G. Weiglein, “FeynHiggs: A Program for the calculation of the masses of the neutral CP even Higgs bosons in the MSSM”, *Comput.Phys.Commun.* **124** (2000) 76–89, [arXiv:hep-ph/9812320](#).
- [297] P. Bechtle, O. Brein, S. Heinemeyer, G. Weiglein, and K. E. Williams, “HiggsBounds: Confronting Arbitrary Higgs Sectors with Exclusion Bounds from LEP and the Tevatron”, *Comput.Phys.Commun.* **181** (2010) 138–167, [arXiv:0811.4169](#).
- [298] “Evidence for a particle decaying to w^+w^- in the fully leptonic final state in a standard model higgs boson search in pp collisions at the lh”, Tech. Rep. CMS-PAS-HIG-12-042, CERN, Geneva, 2012.
- [299] “Updated results on the new boson discovered in the search for the standard model higgs boson in the zz to 4 leptons channel in pp collisions at $\sqrt{s} = 7$ and 8 tev”, Tech. Rep. CMS-PAS-HIG-12-041, CERN, Geneva, 2012.
- [300] “Combination of standard model higgs boson searches and measurements of the properties of the new boson with a mass near 125 gev”, Tech. Rep. CMS-PAS-HIG-12-045, CERN, Geneva, 2012.
- [301] “An update of combined measurements of the new higgs-like boson with high mass resolution channels”, Tech. Rep. ATLAS-CONF-2012-170, CERN, Geneva, Dec 2012.
- [302] “Observation of an excess of events in the search for the standard model higgs boson in the $h \rightarrow zz^* \rightarrow 4l$ channel with the atlas detector”, Tech. Rep. ATLAS-CONF-2012-169, CERN, Geneva, Dec 2012.
- [303] “Study of the channel $h \rightarrow z^*z \rightarrow \ell^+\ell^-q\bar{q}$ in the mass range 120-180 gev with the atlas detector at $\sqrt{s}=7$ tev”, Tech. Rep. ATLAS-CONF-2012-163, CERN, Geneva, Nov 2012.
- [304] “Updated atlas results on the signal strength of the higgs-like boson for decays into ww and heavy fermion final states”, Tech. Rep. ATLAS-CONF-2012-162, CERN, Geneva, Nov 2012.
- [305] “Update of the $h \rightarrow ww^{(*)} \rightarrow e\nu\mu\nu$ analysis with 13 fb^{-1} of $\sqrt{s} = 8$ tev data collected with the atlas detector”, Tech. Rep. ATLAS-CONF-2012-158, CERN, Geneva, Nov 2012.
- [306] B. Allanach, C. Balazs, G. Belanger, M. Bernhardt, F. Boudjema, *et al.*, “SUSY Les Houches Accord 2”, *Comput.Phys.Commun.* **180** (2009) 8–25, [arXiv:0801.0045](#).

- [307] G. Belanger, F. Boudjema, A. Pukhov, and A. Semenov, “MicrOMEGAs 2.0: A Program to calculate the relic density of dark matter in a generic model”, *Comput.Phys.Commun.* **176** (2007) 367–382, [arXiv:hep-ph/0607059](#).
- [308] “Measurements of the properties of the higgs-like boson in the two photon decay channel with the atlas detector using 25 fb⁻¹ of proton-proton collision data”, Tech. Rep. ATLAS-CONF-2013-012, CERN, Geneva, Mar 2013.
- [309] “Updated measurements of the higgs boson at 125 gev in the two photon decay channel”, Tech. Rep. CMS-PAS-HIG-13-001, CERN, Geneva, 2013.
- [310] R. Barbieri and G. Giudice, “b → s gamma decay and supersymmetry”, *Phys.Lett.* **B309** (1993) 86–90, [arXiv:hep-ph/9303270](#).
- [311] M. Misiak, H. Asatrian, K. Bieri, M. Czakon, A. Czarnecki, *et al.*, “Estimate of B(anti-B → X(s) gamma) at O(alpha(s)**2)”, *Phys.Rev.Lett.* **98** (2007) 022002, [arXiv:hep-ph/0609232](#).
- [312] T. Becher and M. Neubert, “Analysis of Br(anti-B → X(s gamma)) at NNLO with a cut on photon energy”, *Phys.Rev.Lett.* **98** (2007) 022003, [arXiv:hep-ph/0610067](#).
- [313] M. Benzke, S. J. Lee, M. Neubert, and G. Paz, “Factorization at Subleading Power and Irreducible Uncertainties in $\bar{B} \rightarrow X_s \gamma$ Decay”, *JHEP* **1008** (2010) 099, [arXiv:1003.5012](#).
- [314] K. Babu and C. F. Kolda, “Higgs mediated $B^0 \rightarrow \mu^+ \mu^-$ in minimal supersymmetry”, *Phys.Rev.Lett.* **84** (2000) 228–231, [arXiv:hep-ph/9909476](#).
- [315] A. J. Buras, J. Girrbach, D. Guadagnoli, and G. Isidori, “On the Standard Model prediction for BR(Bs,d to mu+ mu-)”, *Eur.Phys.J.* **C72** (2012) 2172, [arXiv:1208.0934](#).
- [316] K. De Bruyn, R. Fleischer, R. Knegjens, P. Koppenburg, M. Merk, *et al.*, “Branching Ratio Measurements of B_s Decays”, *Phys.Rev.* **D86** (2012) 014027, [arXiv:1204.1735](#).
- [317] K. De Bruyn, R. Fleischer, R. Knegjens, P. Koppenburg, M. Merk, *et al.*, “Probing New Physics via the $B_s^0 \rightarrow \mu^+ \mu^-$ Effective Lifetime”, *Phys.Rev.Lett.* **109** (2012) 041801, [arXiv:1204.1737](#).
- [318] **Super-Kamiokande** Collaboration, S. Desai *et al.*, “Search for dark matter WIMPs using upward through-going muons in Super-Kamiokande”, *Phys.Rev.* **D70** (2004) 083523, [arXiv:hep-ex/0404025](#).
- [319] **IceCube** Collaboration, M. Aartsen *et al.*, “Search for dark matter annihilations in the Sun with the 79-string IceCube detector”, [arXiv:1212.4097](#).
- [320] N. D. Christensen, T. Han, and S. Su, “MSSM Higgs Bosons at The LHC”, *Phys.Rev.* **D85** (2012) 115018, [arXiv:1203.3207](#).

- [321] M. Carena, S. Heinemeyer, O. Stal, C. Wagner, and G. Weiglein, “MSSM Higgs Boson Searches at the LHC: Benchmark Scenarios after the Discovery of a Higgs-like Particle”, [arXiv:1302.7033](#).
- [322] T. Han, T. Li, S. Su, and L.-T. Wang, “Non-Decoupling MSSM Higgs Sector and Light Superpartners”, [arXiv:1306.3229](#).
- [323] A. Arbey, M. Battaglia, and F. Mahmoudi, “Light Neutralino Dark Matter in the pMSSM: Implications of LEP, LHC and Dark Matter Searches on SUSY Particle Spectra”, *Eur.Phys.J.* **C72** (2012) 2169, [arXiv:1205.2557](#).
- [324] C. Boehm, P. S. B. Dev, A. Mazumdar, and E. Pukartas, “Naturalness of Light Neutralino Dark Matter in pMSSM after LHC, XENON100 and Planck Data”, *JHEP* **1306** (2013) 113, [arXiv:1303.5386](#).
- [325] A. Arbey, M. Battaglia, and F. Mahmoudi, “Supersymmetry with Light Dark Matter confronting the recent CDMS and LHC Results”, [arXiv:1308.2153](#).
- [326] G. Belanger, G. D. La Rochelle, B. Dumont, R. M. Godbole, S. Kraml, *et al.*, “LHC constraints on light neutralino dark matter in the MSSM”, [arXiv:1308.3735](#).
- [327] K. Hagiwara, S. Mukhopadhyay, and J. Nakamura, “10 GeV neutralino dark matter and light stau in the MSSM”, [arXiv:1308.6738](#).
- [328] J. R. Ellis, K. A. Olive, and C. Savage, “Hadronic Uncertainties in the Elastic Scattering of Supersymmetric Dark Matter”, *Phys.Rev.* **D77** (2008) 065026, [arXiv:0801.3656](#).
- [329] E. Accomando, R. L. Arnowitt, B. Dutta, and Y. Santoso, “Neutralino proton cross-sections in supergravity models”, *Nucl.Phys.* **B585** (2000) 124–142, [arXiv:hep-ph/0001019](#).
- [330] G. Belanger, F. Boudjema, A. Cottrant, R. Godbole, and A. Semenov, “The MSSM invisible Higgs in the light of dark matter and g-2”, *Phys.Lett.* **B519** (2001) 93–102, [arXiv:hep-ph/0106275](#).
- [331] J. Edsjo and P. Gondolo, “Neutralino relic density including coannihilations”, *Phys.Rev.* **D56** (1997) 1879–1894, [arXiv:hep-ph/9704361](#).
- [332] J. Edsjo, M. Schelke, P. Ullio, and P. Gondolo, “Accurate relic densities with neutralino, chargino and sfermion coannihilations in mSUGRA”, *JCAP* **0304** (2003) 001, [arXiv:hep-ph/0301106](#).
- [333] J. R. Ellis, T. Falk, and K. A. Olive, “Neutralino - Stau coannihilation and the cosmological upper limit on the mass of the lightest supersymmetric particle”, *Phys.Lett.* **B444** (1998) 367–372, [arXiv:hep-ph/9810360](#).

- [334] J. R. Ellis, T. Falk, K. A. Olive, and M. Srednicki, “Calculations of neutralino-stau coannihilation channels and the cosmologically relevant region of MSSM parameter space”, *Astropart.Phys.* **13** (2000) 181–213, [arXiv:hep-ph/9905481](#).
- [335] J. R. Ellis, K. A. Olive, and Y. Santoso, “Calculations of neutralino stop coannihilation in the CMSSM”, *Astropart.Phys.* **18** (2003) 395–432, [arXiv:hep-ph/0112113](#).
- [336] M. Carena, A. Freitas, and C. Wagner, “Light Stop Searches at the LHC in Events with One Hard Photon or Jet and Missing Energy”, *JHEP* **0810** (2008) 109, [arXiv:0808.2298](#).
- [337] A. Rajaraman, W. Shepherd, T. M. Tait, and A. M. Wijangco, “LHC Bounds on Interactions of Dark Matter”, *Phys.Rev.* **D84** (2011) 095013, [arXiv:1108.1196](#).
- [338] P. J. Fox, R. Harnik, J. Kopp, and Y. Tsai, “Missing Energy Signatures of Dark Matter at the LHC”, *Phys.Rev.* **D85** (2012) 056011, [arXiv:1109.4398](#).
- [339] A. Delgado, G. F. Giudice, G. Isidori, M. Pierini, and A. Strumia, “The light stop window”, *Eur.Phys.J.* **C73** (2013) 2370, [arXiv:1212.6847](#).
- [340] T. Lin, E. W. Kolb, and L.-T. Wang, “Probing dark matter couplings to top and bottom at the LHC”, [arXiv:1303.6638](#).
- [341] H. An, L.-T. Wang, and H. Zhang, “Dark matter with t -channel mediator: a simple step beyond contact interaction”, [arXiv:1308.0592](#).
- [342] P. Salucci, F. Nesti, G. Gentile, and C. Martins, “The dark matter density at the Sun’s location”, *Astron.Astrophys.* **523** (2010) A83, [arXiv:1003.3101](#).
- [343] M. Srednicki and R. Watkins, “Coherent Couplings Of Neutralinos To Nuclei From Squark Mixing”, *Phys.Lett.* **B225** (1989) 140.
- [344] G. Gelmini, P. Gondolo, and E. Roulet, “Neutralino dark matter searches”, *Nucl.Phys.* **B351** (1991) 623–644.
- [345] M. Drees and M. M. Nojiri, “Neutralino relic density in minimal $n = 1$ supergravity”, *Phys. Rev. D* **47** Jan (1993) 376–408.
- [346] M. Drees and M. M. Nojiri, “New contributions to coherent neutralino - nucleus scattering”, *Phys.Rev.* **D47** (1993) 4226–4232, [arXiv:hep-ph/9210272](#).
- [347] M. Drees and M. Nojiri, “Neutralino - nucleon scattering revisited”, *Phys.Rev.* **D48** (1993) 3483–3501, [arXiv:hep-ph/9307208](#).
- [348] J. R. Ellis, A. Ferstl, and K. A. Olive, “Reevaluation of the elastic scattering of supersymmetric dark matter”, *Phys.Lett.* **B481** (2000) 304–314, [arXiv:hep-ph/0001005](#).

- [349] “Search for direct top squark pair production in events with a single isolated lepton, jets and missing transverse energy at $\sqrt{s} = 8$ tev”, Tech. Rep. CMS-PAS-SUS-12-023, CERN, Geneva, 2012.
- [350] **ATLAS** Collaboration, G. Aad *et al.*, “Multi-channel search for squarks and gluinos in $\sqrt{s} = 7$ TeV pp collisions with the ATLAS detector”, [arXiv:1212.6149](#).
- [351] V. Barger, W.-Y. Keung, and G. Shaughnessy, “Spin Dependence of Dark Matter Scattering”, *Phys.Rev.* **D78** (2008) 056007, [arXiv:0806.1962](#).
- [352] H. Davoudiasl, T. Han, and H. E. Logan, “Discovering an invisibly decaying Higgs at hadron colliders”, *Phys.Rev.* **D71** (2005) 115007, [arXiv:hep-ph/0412269](#).
- [353] Y. Bai, P. Draper, and J. Shelton, “Measuring the Invisible Higgs Width at the 7 and 8 TeV LHC”, *JHEP* **1207** (2012) 192, [arXiv:1112.4496](#).
- [354] G. Belanger, B. Dumont, U. Ellwanger, J. Gunion, and S. Kraml, “Status of invisible Higgs decays”, [arXiv:1302.5694](#).
- [355] A. Blondel, A. Chao, W. Chou, J. Gao, D. Schulte, *et al.*, “Report of the ICFA Beam Dynamics Workshop ‘Accelerators for a Higgs Factory: Linear vs. Circular’ (HF2012)”, [arXiv:1302.3318](#).
- [356] E. Arganda, J. L. Diaz-Cruz, and A. Szykman, “Split Supersymmetry with Non-Universal Higgs Masses”, [arXiv:1211.0163](#).
- [357] B. Dutta, T. Kamon, N. Koley, K. Sinha, K. Wang, *et al.*, “Top Squark Searches Using Dilepton Invariant Mass Distributions and Bino-Higgsino Dark Matter at the LHC”, [arXiv:1302.3231](#).
- [358] G. Jungman, M. Kamionkowski, and K. Griest, “Supersymmetric dark matter”, *Phys.Rept.* **267** (1996) 195–373, [arXiv:hep-ph/9506380](#).
- [359] T. Han, Z. Liu, and A. Natarajan, “Dark matter and Higgs bosons in the MSSM”, *JHEP* **1311** (2013) 008, [arXiv:1303.3040](#).
- [360] M. R. Buckley, D. Hooper, and J. Kumar, “Phenomenology of Dirac Neutralino Dark Matter”, *Phys.Rev.* **D88** (2013) 063532, [1307.3561](#).
- [361] A. Pierce, N. R. Shah, and K. Freese, “Neutralino Dark Matter with Light Staus”, [arXiv:1309.7351](#).
- [362] R. Peccei and H. R. Quinn, “CP Conservation in the Presence of Instantons”, *Phys.Rev.Lett.* **38** (1977) 1440–1443.
- [363] R. Barbieri, L. J. Hall, A. Y. Papaioannou, D. Pappadopulo, and V. S. Rychkov, “An Alternative NMSSM phenomenology with manifest perturbative unification”, *JHEP* **0803** (2008) 005, [arXiv:0712.2903](#).

- [364] N. D. Christensen, T. Han, Z. Liu, and S. Su, “Low-Mass Higgs Bosons in the NMSSM and Their LHC Implications”, *JHEP* **1308** (2013) 019, [arXiv:1303.2113](#).
- [365] **ALEPH Collaboration, DELPHI Collaboration, L3 Collaboration, OPAL Collaboration, SLD Collaboration, LEP Electroweak Working Group, SLD Electroweak Group, SLD Heavy Flavour Group** Collaboration, S. Schael *et al.*, “Precision electroweak measurements on the Z resonance”, *Phys.Rept.* **427** (2006) 257–454, [arXiv:hep-ex/0509008](#).
- [366] G. Belanger, B. Dumont, U. Ellwanger, J. Gunion, and S. Kraml, “Status of invisible Higgs decays”, *Phys.Lett.* **B723** (2013) 340–347, [arXiv:1302.5694](#).
- [367] **ATLAS Collaboration** Collaboration, G. Aad *et al.*, “Search for Invisible Decays of a Higgs Boson Produced in Association with a Z Boson in ATLAS”, [arXiv:1402.3244](#).
- [368] **CMS Collaboration** Collaboration, S. Chatrchyan *et al.*, “Search for invisible decays of Higgs bosons in the vector boson fusion and associated ZH production modes”, [arXiv:1404.1344](#).
- [369] D. Curtin, R. Essig, S. Gori, P. Jaiswal, A. Katz, *et al.*, “Exotic Decays of the 125 GeV Higgs Boson”, [arXiv:1312.4992](#).
- [370] **Particle Data Group** Collaboration, J. Beringer *et al.*, “Review of Particle Physics (RPP)”, *Phys.Rev.* **D86** (2012) 010001.
- [371] **ALEPH Collaboration** Collaboration, A. Heister *et al.*, “Search for scalar quarks in e^+e^- collisions at \sqrt{s} up to 209-GeV”, *Phys.Lett.* **B537** (2002) 5–20, [arXiv:hep-ex/0204036](#).
- [372] A. Freitas, “Two-loop fermionic electroweak corrections to the Z -boson width and production rate”, *Phys.Lett.* **B730** (2014) 50–52, [arXiv:1310.2256](#).
- [373] **DELPHI Collaboration** Collaboration, J. Abdallah *et al.*, “Searches for supersymmetric particles in e^+e^- collisions up to 208-GeV and interpretation of the results within the MSSM”, *Eur.Phys.J.* **C31** (2003) 421–479, [arXiv:hep-ex/0311019](#).
- [374] **ATLAS Collaboration** Collaboration, G. Aad *et al.*, “Search for scalar bottom pair production with the ATLAS detector in pp Collisions at $\sqrt{s} = 7$ TeV”, *Phys.Rev.Lett.* **108** (2012) 181802, [arXiv:1112.3832](#).
- [375] **ATLAS Collaboration**, G. Aad *et al.*, “Search for direct third-generation squark pair production in final states with missing transverse momentum and two b -jets in $\sqrt{s} = 8$ TeV pp collisions with the ATLAS detector”, *JHEP* **1310** (2013) 189, [arXiv:1308.2631](#).

- [376] G. Belanger, F. Boudjema, A. Pukhov, and A. Semenov, “Dark matter direct detection rate in a generic model with micrOMEGAs 2.2”, *Comput.Phys.Commun.* **180** (2009) 747–767, [arXiv:0803.2360](#).
- [377] **Planck** Collaboration, P. Ade *et al.*, “Planck 2013 results. XVI. Cosmological parameters”, *Astron.Astrophys.* **571** (2014) A16, [arXiv:1303.5076](#).
- [378] L. Roszkowski, E. M. Sessolo, and Y.-L. S. Tsai, “Bayesian Implications of Current LHC Supersymmetry and Dark Matter Detection Searches for the Constrained MSSM”, *Phys.Rev.* **D86** (2012) 095005, [arXiv:1202.1503](#).
- [379] K. R. Dienes and B. Thomas, “Dynamical Dark Matter: I. Theoretical Overview”, *Phys.Rev.* **D85** (2012) 083523, [arXiv:1106.4546](#).
- [380] K. R. Dienes and B. Thomas, “Dynamical Dark Matter: II. An Explicit Model”, *Phys.Rev.* **D85** (2012) 083524, [arXiv:1107.0721](#).
- [381] M. Baldi, “Multiple dark matter as a self-regulating mechanism for dark sector interactions”, *Annalen der Physik* **524** (2012) 602–617, [arXiv:1204.0514](#).
- [382] M. Aoki, M. Duerr, J. Kubo, and H. Takano, “Multi-Component Dark Matter Systems and Their Observation Prospects”, *Phys.Rev.* **D86** (2012) 076015, [arXiv:1207.3318](#).
- [383] D. Chialva, P. B. Dev, and A. Mazumdar, “Multiple dark matter scenarios from ubiquitous stringy throats”, *Phys.Rev.* **D87** (2013), no. 6, 063522, [arXiv:1211.0250](#).
- [384] H. Baer, V. Barger, and D. Mickelson, “Direct and indirect detection of higgsino-like WIMPs: concluding the story of electroweak naturalness”, *Phys.Lett.* **B726** (2013) 330–336, [arXiv:1303.3816](#).
- [385] S. Bhattacharya, A. Drozd, B. Grzadkowski, and J. Wudka, “Two-Component Dark Matter”, *JHEP* **1310** (2013) 158, [arXiv:1309.2986](#).
- [386] K. J. Bae, H. Baer, and E. J. Chun, “Mixed axion/neutralino dark matter in the SUSY DFSZ axion model”, *JCAP* **1312** (2013) 028, [arXiv:1309.5365](#).
- [387] **LUX Collaboration** Collaboration, D. Akerib *et al.*, “First results from the LUX dark matter experiment at the Sanford Underground Research Facility”, [arXiv:1310.8214](#).
- [388] **SuperCDMS Collaboration** Collaboration, R. Agnese *et al.*, “Search for Low-Mass WIMPs with SuperCDMS”, [arXiv:1402.7137](#).
- [389] J. Billard, L. Strigari, and E. Figueroa-Feliciano, “Implication of neutrino backgrounds on the reach of next generation dark matter direct detection experiments”, *Phys.Rev.* **D89** (2014) 023524, [arXiv:1307.5458](#).

- [390] P. Gondolo and S. Scopel, “On the sbottom resonance in dark matter scattering”, [1307.4481](#).
- [391] P. Huang and C. E. M. Wagner, “Blind Spots for neutralino Dark Matter in the MSSM with an intermediate m_A ”, [arXiv:1404.0392](#).
- [392] P. Draper, T. Liu, C. E. Wagner, L.-T. Wang, and H. Zhang, “Dark Light Higgs”, *Phys.Rev.Lett.* **106** (2011) 121805, [arXiv:1009.3963](#).
- [393] J. Cao, C. Han, L. Wu, P. Wu, and J. M. Yang, “A light SUSY dark matter after CDMS-II, LUX and LHC Higgs data”, *JHEP* **1405** (2014) 056, [arXiv:1311.0678](#).
- [394] M. Felizardo, T. Girard, T. Morlat, A. Fernandes, A. Ramos, *et al.*, “Final Analysis and Results of the Phase II SIMPLE Dark Matter Search”, *Phys.Rev.Lett.* **108** (2012) 201302, [arXiv:1106.3014](#).
- [395] **PICASSO Collaboration** Collaboration, S. Archambault *et al.*, “Constraints on Low-Mass WIMP Interactions on ^{19}F from PICASSO”, *Phys.Lett.* **B711** (2012) 153–161, [arXiv:1202.1240](#).
- [396] **COUPP Collaboration** Collaboration, E. Behnke *et al.*, “First Dark Matter Search Results from a 4-kg CF_3I Bubble Chamber Operated in a Deep Underground Site”, *Phys.Rev.* **D86** (2012) 052001, [arXiv:1204.3094](#).
- [397] **XENON100 Collaboration** Collaboration, E. Aprile *et al.*, “Limits on spin-dependent WIMP-nucleon cross sections from 225 live days of XENON100 data”, *Phys.Rev.Lett.* **111** (2013), no. 2, 021301, [arXiv:1301.6620](#).
- [398] A. Berlin, D. Hooper, and S. D. McDermott, “Simplified Dark Matter Models for the Galactic Center Gamma-Ray Excess”, [arXiv:1404.0022](#).
- [399] P. Agrawal, B. Batell, D. Hooper, and T. Lin, “Flavored Dark Matter and the Galactic Center Gamma-Ray Excess”, [arXiv:1404.1373](#).
- [400] E. Izaguirre, G. Krnjaic, and B. Shuve, “The Galactic Center Excess from the Bottom Up”, [arXiv:1404.2018](#).
- [401] S. Ipek, D. McKeen, and A. E. Nelson, “A Renormalizable Model for the Galactic Center Gamma Ray Excess from Dark Matter Annihilation”, [arXiv:1404.3716](#).
- [402] K. Kong and J.-C. Park, “Bounds on Dark Matter Interpretation of Fermi-LAT GeV Excess”, [arXiv:1404.3741](#).
- [403] P. Ko, W.-I. Park, and Y. Tang, “Higgs portal vector dark matter for GeV scale γ -ray excess from galactic center”, [arXiv:1404.5257](#).
- [404] C. Boehm, M. J. Dolan, and C. McCabe, “A weighty interpretation of the Galactic Centre excess”, [arXiv:1404.4977](#).

- [405] M. Abdullah, A. DiFranzo, A. Rajaraman, T. M. P. Tait, P. Tanedo, *et al.*, “Hidden On-Shell Mediators for the Galactic Center Gamma-Ray Excess”, [arXiv:1404.6528](#).
- [406] D. Marzocca and A. Urbano, “Composite Dark Matter and LHC Interplay”, [arXiv:1404.7419](#).
- [407] D. K. Ghosh, S. Mondal, and I. Saha, “Confronting the Galactic Center Gamma Ray Excess With a Light Scalar Dark Matter”, [arXiv:1405.0206](#).
- [408] A. Martin, J. Shelton, and J. Unwin, “Fitting the Galactic Center Gamma-Ray Excess with Cascade Annihilations”, [arXiv:1405.0272](#).
- [409] A. Berlin, P. Gratia, D. Hooper, and S. D. McDermott, “Hidden Sector Dark Matter Models for the Galactic Center Gamma-Ray Excess”, [arXiv:1405.5204](#).
- [410] D. Choudhury and D. Roy, “Signatures of an invisibly decaying Higgs particle at LHC”, *Phys.Lett.* **B322** (1994) 368–373, [arXiv:hep-ph/9312347](#).
- [411] O. J. Eboli and D. Zeppenfeld, “Observing an invisible Higgs boson”, *Phys.Lett.* **B495** (2000) 147–154, [arXiv:hep-ph/0009158](#).
- [412] H. Davoudiasl, T. Han, and H. E. Logan, “Discovering an invisibly decaying Higgs at hadron colliders”, *Phys.Rev.* **D71** (2005) 115007, [arXiv:hep-ph/0412269](#).
- [413] J. R. Espinosa, M. Muhlleitner, C. Grojean, and M. Trott, “Probing for Invisible Higgs Decays with Global Fits”, *JHEP* **1209** (2012) 126, [arXiv:1205.6790](#).
- [414] **LHC Higgs Cross Section Working Group** Collaboration, S. Dittmaier *et al.*, “Handbook of LHC Higgs Cross Sections: 1. Inclusive Observables”, [arXiv:1101.0593](#).
- [415] J. Goodman, M. Ibe, A. Rajaraman, W. Shepherd, T. M. Tait, *et al.*, “Constraints on Dark Matter from Colliders”, *Phys.Rev.* **D82** (2010) 116010, [arXiv:1008.1783](#).
- [416] G. Busoni, A. De Simone, J. Gramling, E. Morgante, and A. Riotto, “On the Validity of the Effective Field Theory for Dark Matter Searches at the LHC, Part II: Complete Analysis for the s-channel”, [arXiv:1402.1275](#).
- [417] **CMS Collaboration** Collaboration, S. Chatrchyan *et al.*, “Search for supersymmetry in final states with missing transverse energy and 0, 1, 2, or at least 3 b-quark jets in 7 TeV pp collisions using the variable α_T ”, *JHEP* **1301** (2013) 077, [arXiv:1210.8115](#).
- [418] G. R. Farrar and P. Fayet, “Phenomenology of the Production, Decay, and Detection of New Hadronic States Associated with Supersymmetry”, *Phys.Lett.* **B76** (1978) 575–579.

- [419] Z. Liu and B. Tweedie, “New LHC Constraints on Displaced Superparticles”, 2014, appear soon.
- [420] B. Batell, C. E. M. Wagner, and L.-T. Wang, “Constraints on a Very Light Sbottom”, [arXiv:1312.2590](#).
- [421] R. L. Arnowitt, B. Dutta, T. Kamon, N. Kolev, and D. A. Toback, “Detection of SUSY in the stau-neutralino coannihilation region at the LHC”, *Phys.Lett.* **B639** (2006) 46–53, [arXiv:hep-ph/0603128](#).
- [422] **CDF Collaboration** Collaboration, T. Aaltonen *et al.*, “Search for Long-Lived Massive Charged Particles in 1.96 TeV $p\bar{p}$ Collisions”, *Phys.Rev.Lett.* **103** (2009) 021802, [arXiv:0902.1266](#).
- [423] **CDF Collaboration** Collaboration, T. Aaltonen *et al.*, “Signature-Based Search for Delayed Photons in Exclusive Photon Plus Missing Transverse energy Events from $p\bar{p}$ Collisions with $\sqrt{s} = 1.96$ TeV”, *Phys.Rev.* **D88** (2013), no. 3, 031103, [arXiv:1307.0474](#).
- [424] **CDF Collaboration** Collaboration, T. Aaltonen *et al.*, “Search for Heavy Metastable Particles Decaying to Jet Pairs in $p\bar{p}$ Collisions at $\sqrt{s} = 1.96$ TeV”, *Phys.Rev.* **D85** (2012) 012007, [arXiv:1109.3136](#).
- [425] The CDF Collaboration, “Search for Long-Lived Parents of the Z^0 Boson”. CDF NOTE 7244.
- [426] **D0 Collaboration** Collaboration, V. M. Abazov *et al.*, “Search for Charged Massive Long-Lived Particles at $\sqrt{s} = 1.96$ TeV”, *Phys.Rev.* **D87** (2013), no. 5, 052011, [arXiv:1211.2466](#).
- [427] **D0 Collaboration** Collaboration, V. Abazov *et al.*, “Search for Resonant Pair Production of Long-Lived Particles Decaying to $b\bar{b}$ in $p\bar{p}$ Collisions at $\sqrt{s} = 1.96$ TeV”, *Phys.Rev.Lett.* **103** (2009) 071801, [arXiv:0906.1787](#).
- [428] **D0 Collaboration** Collaboration, V. Abazov *et al.*, “Search for Long-Lived Particles Decaying into Electron or Photon Pairs with the D0 Detector”, *Phys.Rev.Lett.* **101** (2008) 111802, [arXiv:0806.2223](#).
- [429] **D0 Collaboration** Collaboration, V. Abazov *et al.*, “Search for Stopped Gluinos from $p\bar{p}$ Collisions at $\sqrt{s} = 1.96$ TeV”, *Phys.Rev.Lett.* **99** (2007) 131801, [arXiv:0705.0306](#).
- [430] **D0 Collaboration** Collaboration, V. Abazov *et al.*, “Search for Neutral, Long-Lived Particles Decaying into Two Muons in $p\bar{p}$ Collisions at $\sqrt{s} = 1.96$ TeV”, *Phys.Rev.Lett.* **97** (2006) 161802, [arXiv:hep-ex/0607028](#).

- [431] **ALEPH Collaboration** Collaboration, R. Barate *et al.*, “Search for a Scalar Top Almost Degenerate with the Lightest Neutralino in e^+e^- Collisions at \sqrt{s} up to 202 GeV”, *Phys.Lett.* **B488** (2000) 234–246.
- [432] **ALEPH Collaboration** Collaboration, R. Barate *et al.*, “Search for Sleptons in e^+e^- Collisions at Centre-of-Mass Energies up to 184 GeV”, *Phys.Lett.* **B433** (1998) 176–194.
- [433] **ALEPH Collaboration** Collaboration, R. Barate *et al.*, “Search for Gauge Mediated SUSY Breaking Topologies at $\sqrt{s} \sim 189$ GeV”, *Eur.Phys.J.* **C16** (2000) 71–85.
- [434] **CMS Collaboration** Collaboration, S. Chatrchyan *et al.*, “Search for Disappearing Tracks in Proton-Proton Collisions at $\sqrt{s} = 8$ TeV”, [arXiv:1411.6006](#).
- [435] The CMS Collaboration, “Search for Long-Lived Neutral Particles Decaying to Dijets”.
CMS PAS EXO-12-038.
- [436] T. Sjostrand, S. Mrenna, and P. Z. Skands, “A Brief Introduction to PYTHIA 8.1”, *Comput.Phys.Comm.* **178** (2008) 852–867, [arXiv:0710.3820](#). %%CITATION = ARXIV:0710.3820;%%.
- [437] R. Corke and T. Sjostrand, “Improved Parton Showers at Large Transverse Momenta”, *Eur.Phys.J.* **C69** (2010) 1–18, [arXiv:1003.2384](#).
- [438] **Particle Data Group** Collaboration, K. Olive *et al.*, “Review of Particle Physics”, *Chin.Phys.* **C38** (2014) 090001.
- [439] Zuranski, Andrzej, “Long-Lived Searches at CMS”.
Talk for CMS Long-Lived Exotica Group (8 November 2013).
- [440] **CMS Collaboration** Collaboration, S. Chatrchyan *et al.*, “Search in Leptonic Channels for Heavy Resonances Decaying to Long-Lived Neutral Particles”, *JHEP* **1302** (2013) 085, [arXiv:1211.2472](#).
- [441] **ATLAS Collaboration** Collaboration, G. Aad *et al.*, “Standalone Vertex Finding in the ATLAS Muon Spectrometer”, *JINST* **9** (2014) P02001, [arXiv:1311.7070](#).
- [442] **ATLAS Collaboration** Collaboration, G. Aad *et al.*, “Search for Long-Lived, Heavy Particles in Final States with a Muon and Multi-Track Displaced Vertex in Proton-Proton Collisions at $\sqrt{s} = 7$ TeV with the ATLAS Detector”, *Phys.Lett.* **B719** (2013) 280–298, [arXiv:1210.7451](#).
- [443] **ATLAS Collaboration** Collaboration, G. Aad *et al.*, “Search for Displaced Vertices Arising from Decays of New Heavy Particles in 7 TeV pp Collisions at ATLAS”, *Phys.Lett.* **B707** (2012) 478–496, [arXiv:1109.2242](#).

- [444] J. Alwall, R. Frederix, S. Frixione, V. Hirschi, F. Maltoni, *et al.*, “The automated computation of tree-level and next-to-leading order differential cross sections, and their matching to parton shower simulations”, *JHEP* **1407** (2014) 079, [arXiv:1405.0301](#).
- [445] W. Beenakker, S. Brensing, M. Kramer, A. Kulesza, E. Laenen, *et al.*, “Supersymmetric Top and Bottom Squark Production at Hadron Colliders”, *JHEP* **1008** (2010) 098, [arXiv:1006.4771](#).
- [446] B. Fuks, M. Klasen, D. R. Lamprea, and M. Rothering, “Precision Predictions for Electroweak Superpartner Production at Hadron Colliders with RESUMMINO”, *Eur.Phys.J.* **C73** (2013) 2480, [arXiv:1304.0790](#).
- [447] <https://twiki.cern.ch/twiki/bin/view/LHCPhysics/SUSYCrossSections>.
- [448] **CMS Collaboration** Collaboration, V. Khachatryan *et al.*, “Search for Pair-Produced Resonances Decaying to Jet Pairs in Proton-Proton Collisions at $\sqrt{s} = 8$ TeV”, [arXiv:1412.7706](#).
- [449] Y. Bai, A. Katz, and B. Tweedie, “Pulling Out All the Stops: Searching for RPV SUSY with Stop-Jets”, *JHEP* **1401** (2014) 040, [arXiv:1309.6631](#).
- [450] D. Duggan, J. A. Evans, J. Hirschauer, K. Kaadze, D. Kolchmeyer, *et al.*, “Sensitivity of an Upgraded LHC to R-Parity Violating Signatures of the MSSM”, [arXiv:1308.3903](#).
- [451] The ATLAS Collaboration, “Search for Massive Particles Decaying into Multiple Quarks with the ATLAS Detector in $\sqrt{s} = 8$ TeV *pp* Collisions”. ATLAS-CONF-2013-091.
- [452] **CMS Collaboration** Collaboration, S. Chatrchyan *et al.*, “Searches for Light- and Heavy-Flavour Three-Jet Resonances in *pp* Collisions at $\sqrt{s} = 8$ TeV”, *Phys.Lett.* **B730** (2014) 193–214, [arXiv:1311.1799](#).
- [453] P. Meade, N. Seiberg, and D. Shih, “General Gauge Mediation”, *Prog. Theor. Phys. Suppl.* **177** (2009) 143–158, [arXiv:0801.3278](#). %%CITATION = 0801.3278;%%
- [454] R. Sundrum, “SUSY Splits, But Then Returns”, *JHEP* **1101** (2011) 062, [arXiv:0909.5430](#).
- [455] C. Csaki, L. Randall, and J. Terning, “Light Stops from Seiberg Duality”, *Phys.Rev.* **D86** (2012) 075009, [arXiv:1201.1293](#).
- [456] T. Gherghetta, B. von Harling, and N. Setzer, “A Natural Little Hierarchy for RS from Accidental SUSY”, *JHEP* **1107** (2011) 011, [arXiv:1104.3171](#).
- [457] G. Larsen, Y. Nomura, and H. L. Roberts, “Supersymmetry with Light Stops”, *JHEP* **1206** (2012) 032, [arXiv:1202.6339](#).

- [458] N. Craig, M. McCullough, and J. Thaler, “Flavor Mediation Delivers Natural SUSY”, *JHEP* **1206** (2012) 046, [arXiv:1203.1622](#).
- [459] J. A. Evans and D. Shih, “Surveying Extended GMSB Models with $m_h=125$ GeV”, *JHEP* **1308** (2013) 093, [arXiv:1303.0228](#).
- [460] P. Meade, M. Reece, and D. Shih, “Prompt Decays of General Neutralino NLSPs at the Tevatron”, *JHEP* **1005** (2010) 105, [arXiv:0911.4130](#). %%CITATION = ARXIV:0911.4130;%%.
- [461] C.-L. Chou and M. E. Peskin, “Scalar Top Quark as the Next-to-Lightest Supersymmetric Particle”, *Phys.Rev.* **D61** (2000) 055004, [arXiv:hep-ph/9909536](#).
- [462] Y. Kats and D. Shih, “Light Stop NLSPs at the Tevatron and LHC”, *JHEP* **1108** (2011) 049, [arXiv:1106.0030](#).
- [463] A. Katz and B. Tweedie, “Signals of a Sneutrino (N)LSP at the LHC”, *Phys. Rev.* **D81** (2010) 035012, [arXiv:0911.4132](#). %%CITATION = 0911.4132;%%.
- [464] A. Katz and B. Tweedie, “Leptophilic Signals of a Sneutrino (N)LSP and Flavor Biases from Flavor-Blind SUSY”, *Phys.Rev.* **D81** (2010) 115003, [arXiv:1003.5664](#).
- [465] L. Covi and S. Kraml, “Collider Signatures of Gravitino Dark Matter with a Sneutrino NLSP”, *JHEP* **08** (2007) 015, [hep-ph/0703130](#). %%CITATION = HEP-PH/0703130;%%.
- [466] L. Calibbi, A. Mariotti, C. Petersson, and D. Redigolo, “Selectron NLSP in Gauge Mediation”, *JHEP* **1409** (2014) 133, [arXiv:1405.4859](#).
- [467] **ATLAS Collaboration** Collaboration, G. Aad *et al.*, “Search for Squarks and Gluinos with the ATLAS Detector in Final States with Jets and Missing Transverse Momentum Using $\sqrt{s} = 8$ TeV Proton–Proton Collision Data”, *JHEP* **1409** (2014) 176, [arXiv:1405.7875](#).
- [468] **ATLAS Collaboration**, G. Aad *et al.*, “Search for Top Squark Pair Production in Final States with One Isolated Lepton, Jets, and Missing Transverse Momentum in $\sqrt{s}=8$ TeV pp Collisions with the ATLAS Detector”, *JHEP* **1411** (2014) 118, [arXiv:1407.0583](#).
- [469] The CMS Collaboration, “Exclusion Limits on Gluino and Top-Squark Pair Production in Natural SUSY Scenarios with Inclusive Razor and Exclusive Single-Lepton Searches at 8 TeV”. CMS PAS SUS-14-011.
- [470] C. Kilic and B. Tweedie, “Cornering Light Stops with Dileptonic m_{T2} ”, *JHEP* **1304** (2013) 110, [arXiv:1211.6106](#).

- [471] **CMS Collaboration** Collaboration, V. Khachatryan *et al.*, “Searches for Electroweak Neutralino and Chargino Production in Channels with Higgs, Z , and W Bosons in pp Collisions at 8 TeV”, *Phys.Rev.* **D90** (2014) 092007, [arXiv:1409.3168](#).
- [472] G. D. Kribs, A. Martin, and T. S. Roy, “Supersymmetry with a Chargino NLSP and Gravitino LSP”, *JHEP* **01** (2009) 023, [arXiv:0807.4936](#). %%CITATION = 0807.4936;%%.
- [473] N. Arkani-Hamed and S. Dimopoulos, “Supersymmetric Unification Without Low Energy Supersymmetry and Signatures for Fine-Tuning at the LHC”, *JHEP* **0506** (2005) 073, [arXiv:hep-th/0405159](#).
- [474] The CMS Collaboration, “Search for Supersymmetry in Hadronic Final States Using M_{T2} with the CMS Detector at $\sqrt{s} = 8$ TeV”. CMS PAS SUS-13-019.
- [475] P. Gambino, G. Giudice, and P. Slavich, “Gluino Decays in Split Supersymmetry”, *Nucl.Phys.* **B726** (2005) 35–52, [arXiv:hep-ph/0506214](#).
- [476] K. Barry, P. W. Graham, and S. Rajendran, “Displaced Vertices from R-Parity Violation and Baryogenesis”, *Phys.Rev.* **D89** (2014), no. 5, 054003, [arXiv:1310.3853](#).
- [477] J. A. Evans and Y. Kats, “LHC Coverage of RPV MSSM with Light Stops”, *JHEP* **1304** (2013) 028, [arXiv:1209.0764](#).
- [478] P. W. Graham, S. Rajendran, and P. Saraswat, “Supersymmetric Crevices: Missing Signatures of R-Parity Violation at the LHC”, *Phys.Rev.* **D90** (2014), no. 7, 075005, [arXiv:1403.7197](#).
- [479] **ECFA/DESY LC Physics Working Group** Collaboration, E. Accomando *et al.*, “Physics with e^+e^- linear colliders”, *Phys.Rept.* **299** (1998) 1–78, [arXiv:hep-ph/9705442](#).
- [480] S. Godfrey, P. Kalyniak, and A. Tomkins, “Distinguishing between models with extra gauge bosons at the ILC”, [arXiv:hep-ph/0511335](#).
- [481] P. Osland, A. Pankov, and A. Tsytrinov, “Identification of extra neutral gauge bosons at the International Linear Collider”, *Eur.Phys.J.* **C67** (2010) 191–204, [arXiv:0912.2806](#).
- [482] L. Linssen, A. Miyamoto, M. Stanitzki, and H. Weerts, “Physics and Detectors at CLIC: CLIC Conceptual Design Report”, [arXiv:1202.5940](#).
- [483] H. Baer *et al.*, “Physics at the International Linear Collider, Technical Design Report”, 2012.
- [484] M. Battaglia, F. Coradeschi, S. De Curtis, and D. Dominici, “Indirect Sensitivity to Heavy Z' Bosons at a Multi-TeV e^+e^- Collider”, [arXiv:1203.0416](#).

- [485] T. Behnke, J. E. Brau, P. N. Burrows, J. Fuster, M. Peskin, *et al.*, “The International Linear Collider Technical Design Report - Volume 4: Detectors”, [arXiv:1306.6329](#).
- [486] A. Freitas, K. Hagiwara, S. Heinemeyer, P. Langacker, K. Moenig, *et al.*, “Exploring Quantum Physics at the ILC”, [arXiv:1307.3962](#).
- [487] V. D. Barger, M. Berger, J. Gunion, and T. Han, “Higgs Boson physics in the s channel at $\mu^+ \mu^-$ colliders”, *Phys.Rept.* **286** (1997) 1–51, [arXiv:hep-ph/9602415](#).
- [488] A. Conway and H. Wenzel, “Higgs Measurements at a Muon Collider”, [arXiv:1304.5270](#).
- [489] Y. Alexahin, C. M. Ankenbrandt, D. B. Cline, A. Conway, M. A. Cummings, *et al.*, “Muon Collider Higgs Factory for Snowmass 2013”, [arXiv:1308.2143](#).
- [490] M. Klute, R. Lafaye, T. Plehn, M. Rauch, and D. Zerwas, “Measuring Higgs Couplings at a Linear Collider”, *Europhys.Lett.* **101** (2013) 51001, [arXiv:1301.1322](#).
- [491] H. Li, F. Richard, R. Poeschl, and Z. Zhang, “Precision Measurements of SM Higgs Recoil Mass and Cross Section for $s^{*1/2}$ of 230-GeV and 250-GeV at ILC”, [arXiv:0901.4893](#).
- [492] C. Durig, “Talk given at lcws12, arlington, texas”,.
- [493] **ATLAS** Collaboration, “Physics at a High-Luminosity LHC with ATLAS”, [arXiv:1307.7292](#).
- [494] **CMS** Collaboration, “Projected Performance of an Upgraded CMS Detector at the LHC and HL-LHC: Contribution to the Snowmass Process”, [arXiv:1307.7135](#).
- [495] **ATLAS** Collaboration, “Projections for measurements of Higgs boson cross sections, branching ratios and coupling parameters with the ATLAS detector at a HL-HLC”, Tech. Rep. ATL-PHYS-PUB-2013-014, CERN, Geneva, 2013.
- [496] B. Patt and F. Wilczek, “Higgs-field portal into hidden sectors”, [arXiv:hep-ph/0605188](#).
- [497] J. Gunion, T. Han, and R. Sobey, “Measuring the coupling of a Higgs boson to $Z Z$ at linear colliders”, *Phys.Lett.* **B429** (1998) 79–86, [arXiv:hep-ph/9801317](#).
- [498] D. Asner, T. Barklow, C. Calancha, K. Fujii, N. Graf, *et al.*, “ILC Higgs White Paper”, [arXiv:1310.0763](#).
- [499] M. Berggren, “SGV 3.0 - a fast detector simulation”, [arXiv:1203.0217](#).
- [500] D. Schulte, “Beam-beam simulations with GUINEA-PIG”, 1999.
- [501] W. Kilian, T. Ohl, and J. Reuter, “WHIZARD: Simulating Multi-Particle Processes at LHC and ILC”, *Eur.Phys.J.* **C71** (2011) 1742, [arXiv:0708.4233](#).

- [502] H. Ono and A. Miyamoto, “A study of measurement precision of the Higgs boson branching ratios at the International Linear Collider”, *Eur.Phys.J.* **C73** (2013) 2343, [arXiv:1207.0300](#).
- [503] B. A. Dobrescu and J. D. Lykken, “Semileptonic decays of the standard Higgs boson”, *JHEP* **1004** (2010) 083, [arXiv:0912.3543](#).
- [504] S. Dittmaier, S. Dittmaier, C. Mariotti, G. Passarino, R. Tanaka, *et al.*, “Handbook of LHC Higgs Cross Sections: 2. Differential Distributions”, [arXiv:1201.3084](#).
- [505] H. Georgi and M. Machacek, “DOUBLY CHARGED HIGGS BOSONS”, *Nucl.Phys.* **B262** (1985) 463.
- [506] H. E. Logan and M.-A. Roy, “Higgs couplings in a model with triplets”, *Phys.Rev.* **D82** (2010) 115011, [arXiv:1008.4869](#).
- [507] S. Weinberg, “Phenomenological Lagrangians”, *Physica* **A96** (1979) 327.
- [508] C. N. Leung, S. Love, and S. Rao, “Low-Energy Manifestations of a New Interaction Scale: Operator Analysis”, *Z.Phys.* **C31** (1986) 433.
- [509] W. Buchmuller and D. Wyler, “Effective Lagrangian Analysis of New Interactions and Flavor Conservation”, *Nucl.Phys.* **B268** (1986) 621–653.
- [510] K. Hagiwara, R. Szalapski, and D. Zeppenfeld, “Anomalous Higgs boson production and decay”, *Phys.Lett.* **B318** (1993) 155–162, [arXiv:hep-ph/9308347](#).
- [511] G. Giudice, C. Grojean, A. Pomarol, and R. Rattazzi, “The Strongly-Interacting Light Higgs”, *JHEP* **0706** (2007) 045, [arXiv:hep-ph/0703164](#).
- [512] B. Grzadkowski, M. Iskrzynski, M. Misiak, and J. Rosiek, “Dimension-Six Terms in the Standard Model Lagrangian”, *JHEP* **1010** (2010) 085, [arXiv:1008.4884](#).
- [513] R. Contino, M. Ghezzi, C. Grojean, M. Muhlleitner, and M. Spira, “Effective Lagrangian for a light Higgs-like scalar”, *JHEP* **1307** (2013) 035, [arXiv:1303.3876](#).
- [514] J. Ellis, V. Sanz, and T. You, “Complete Higgs Sector Constraints on Dimension-6 Operators”, *JHEP* **1407** (2014) 036, [arXiv:1404.3667](#).
- [515] J. Ellis, V. Sanz, and T. You, “The Effective Standard Model after LHC Run I”, *JHEP* **1503** (2015) 157, [arXiv:1410.7703](#).
- [516] A. Biekäutter, A. Knochel, M. Krämer, D. Liu, and F. Riva, “Vices and virtues of Higgs effective field theories at large energy”, *Phys.Rev.* **D91** (2015) 055029, [arXiv:1406.7320](#).
- [517] A. Falkowski and F. Riva, “Model-independent precision constraints on dimension-6 operators”, *JHEP* **1502** (2015) 039, [arXiv:1411.0669](#).

- [518] M. Beneke, D. Boito, and Y.-M. Wang, “Anomalous Higgs couplings in angular asymmetries of $H \rightarrow Z\ell^+\ell^-$ and $e^+e^- \rightarrow HZ$ ”, *JHEP* **1411** (2014) 028, [arXiv:1406.1361](#).
- [519] N. Craig, M. Farina, M. McCullough, and M. Perelstein, “Precision Higgsstrahlung as a Probe of New Physics”, *JHEP* **1503** (2015) 146, [arXiv:1411.0676](#).
- [520] V. Barger, T. Han, P. Langacker, B. McElrath, and P. Zerwas, “Effects of genuine dimension-six Higgs operators”, *Phys.Rev.* **D67** (2003) 115001, [arXiv:hep-ph/0301097](#).
- [521] N. Craig, S. Knapen, and P. Longhi, “Neutral Naturalness from Orbifold Higgs Models”, *Phys.Rev.Lett.* **114** (2015), no. 6, 061803, [arXiv:1410.6808](#).
- [522] A. Azatov, C. Grojean, A. Paul, and E. Salvioni, “Taming the off-shell Higgs boson”, *Zh.Eksp.Teor.Fiz.* **147** (2015) 410–425, [arXiv:1406.6338](#).
- [523] D. Curtin, P. Meade, and C.-T. Yu, “Testing Electroweak Baryogenesis with Future Colliders”, *JHEP* **1411** (2014) 127, [arXiv:1409.0005](#).
- [524] Z. Chacko, H.-S. Goh, and R. Harnik, “The Twin Higgs: Natural electroweak breaking from mirror symmetry”, *Phys.Rev.Lett.* **96** (2006) 231802, [arXiv:hep-ph/0506256](#).
- [525] G. Burdman, Z. Chacko, H.-S. Goh, and R. Harnik, “Folded supersymmetry and the LEP paradox”, *JHEP* **0702** (2007) 009, [arXiv:hep-ph/0609152](#).
- [526] **ALEPH, DELPHI, L3, OPAL, LEP Electroweak** Collaboration, S. Schael *et al.*, “Electroweak Measurements in Electron-Positron Collisions at W-Boson-Pair Energies at LEP”, *Phys.Rept.* **532** (2013) 119–244, [arXiv:1302.3415](#).
- [527] J. F. Gunion, H. E. Haber, G. L. Kane, and S. Dawson, “The Higgs Hunter’s Guide”, *Front.Phys.* **80** (2000) 1–448.
- [528] A. Banfi, A. Martin, and V. Sanz, “Probing top-partners in Higgs+jets”, *JHEP* **1408** (2014) 053, [arXiv:1308.4771](#).
- [529] A. Azatov and A. Paul, “Probing Higgs couplings with high p_T Higgs production”, *JHEP* **1401** (2014) 014, [arXiv:1309.5273](#).
- [530] C. Grojean, E. Salvioni, M. Schlaffer, and A. Weiler, “Very boosted Higgs in gluon fusion”, *JHEP* **1405** (2014) 022, [arXiv:1312.3317](#).
- [531] M. Buschmann, C. Englert, D. Goncalves, T. Plehn, and M. Spannowsky, “Resolving the Higgs-Gluon Coupling with Jets”, *Phys.Rev.* **D90** (2014) 013010, [arXiv:1405.7651](#).
- [532] M. E. Peskin, “Estimation of LHC and ILC Capabilities for Precision Higgs Boson Coupling Measurements”, [arXiv:1312.4974](#).

- [533] “Projections for measurements of Higgs boson signal strengths and coupling parameters with the ATLAS detect or at a HL-LHC”, Tech. Rep. ATL-PHYS-PUB-2014-016, CERN, Geneva, Oct 2014.
- [534] A. Denner, S. Heinemeyer, I. Puljak, D. Rebuszi, and M. Spira, “Standard Model Higgs-Boson Branching Ratios with Uncertainties”, *Eur.Phys.J.* **C71** (2011) 1753, [arXiv:1107.5909](#).
- [535] L. G. Almeida, S. J. Lee, S. Pokorski, and J. D. Wells, “Study of the standard model Higgs boson partial widths and branching fractions”, *Phys.Rev.* **D89** (2014), no. 3, 033006, [arXiv:1311.6721](#).
- [536] G. P. Lepage, P. B. Mackenzie, and M. E. Peskin, “Expected Precision of Higgs Boson Partial Widths within the Standard Model”, [arXiv:1404.0319](#).
- [537] A. Hook and A. Katz, “Unbroken $SU(2)$ at a 100 TeV collider”, *JHEP* **1409** (2014) 175, [arXiv:1407.2607](#).
- [538] M. Son, C. Spethmann, and B. Tweedie, “Diboson-Jets and the Search for Resonant Zh Production”, *JHEP* **1208** (2012) 160, [arXiv:1204.0525](#).
- [539] D. Neuffer, “The First Muon Collider - 125 GeV Higgs Factory?”, *AIP Conf.Proc.* **1507** (2012) 849–853.
- [540] V. D. Barger, M. Berger, J. Gunion, and T. Han, “Precision Higgs boson mass determination at lepton colliders”, *Phys.Rev.Lett.* **78** (1997) 3991–3994, [arXiv:hep-ph/9612279](#).
- [541] H. Haber, G. L. Kane, and T. Sterling, “The Fermion Mass Scale and Possible Effects of Higgs Bosons on Experimental Observables”, *Nucl.Phys.* **B161** (1979) 493.
- [542] S. Kumar Rai and S. Raychaudhuri, “Single photon signals for warped quantum gravity at a linear $e^+ e^-$ collider”, *JHEP* **0310** (2003) 020, [arXiv:hep-ph/0307096](#).
- [543] D. Choudhury, S. K. Rai, and S. Raychaudhuri, “Tagging sneutrino resonances at a linear collider with associated photons”, *Phys.Rev.* **D71** (2005) 095009, [arXiv:hep-ph/0412411](#).
- [544] B. Mukhopadhyaya and S. K. Rai, “Associated single photons as signals for a doubly charged scalar at linear $e^- e^-$ colliders”, *Phys.Lett.* **B633** (2006) 519–525, [arXiv:hep-ph/0508290](#).
- [545] S. K. Rai, “Associated Photons and New Physics Signals at Linear Colliders”, *Mod.Phys.Lett.* **A23** (2008) 73–89, [arXiv:0802.2209](#).
- [546] L. J. Hall and M. B. Wise, “FLAVOR CHANGING HIGGS - BOSON COUPLINGS”, *Nucl.Phys.* **B187** (1981) 397.

- [547] J. F. Donoghue and L. F. Li, “Properties of Charged Higgs Bosons”, *Phys.Rev.* **D19** (1979) 945.
- [548] V. D. Barger, J. Hewett, and R. Phillips, “New Constraints on the Charged Higgs Sector in Two Higgs Doublet Models”, *Phys.Rev.* **D41** (1990) 3421–3441.
- [549] M. Aoki, S. Kanemura, K. Tsumura, and K. Yagyu, “Models of Yukawa interaction in the two Higgs doublet model, and their collider phenomenology”, *Phys.Rev.* **D80** (2009) 015017, [arXiv:0902.4665](#).
- [550] A. Pich and P. Tuzon, “Yukawa Alignment in the Two-Higgs-Doublet Model”, *Phys.Rev.* **D80** (2009) 091702, [arXiv:0908.1554](#).
- [551] G. Branco, P. Ferreira, L. Lavoura, M. Rebelo, M. Sher, *et al.*, “Theory and phenomenology of two-Higgs-doublet models”, *Phys.Rept.* **516** (2012) 1–102, [arXiv:1106.0034](#).
- [552] J.-P. Delahaye, C. Ankenbrandt, A. Bogacz, S. Brice, A. Bross, *et al.*, “Enabling Intensity and Energy Frontier Science with a Muon Accelerator Facility in the U.S.: A White Paper Submitted to the 2013 U.S. Community Summer Study of the Division of Particles and Fields of the Amer”, [arXiv:1308.0494](#).
- [553] T. Han, J. D. Lykken, and R.-J. Zhang, “On Kaluza-Klein states from large extra dimensions”, *Phys.Rev.* **D59** (1999) 105006, [arXiv:hep-ph/9811350](#).
- [554] A. Blondel, “A Scheme To Measure The Polarization Asymmetry At The Z Pole In LEP”, *Phys.Lett.* **B202** (1988) 145.
- [555] CMS Collaboration, S. Chatrchyan *et al.*, “Description and Performance of Track and Primary-Vertex Reconstruction with the CMS Tracker”, *JINST* **9** (2014), no. 10, P10009, [arXiv:1405.6569](#).
- [556] <https://twiki.cern.ch/twiki/bin/view/CMSPublic/PhysicsResultsEX012038>.
- [557] T. Han, Z. Si, K. M. Zurek, and M. J. Strassler, “Phenomenology of Hidden Valleys at Hadron Colliders”, *JHEP* **0807** (2008) 008, [arXiv:0712.2041](#).
- [558] The CMS Collaboration, “Search for RPV SUSY in the Four-Lepton Final State”. . CMS PAS EXO-13-010.
- [559] The CMS Collaboration, “Search for Long-Lived Particles Decaying to Final States that Include Dileptons”. . CMS PAS EXO-12-037.
- [560] The ATLAS Collaboration, “Triggering on Long-Lived Neutral Particles in the ATLAS Detector”. ATLAS-PHYS-PUB-2009-082.

- [561] G. Steigman, B. Dasgupta, and J. F. Beacom, “Precise Relic WIMP Abundance and its Impact on Searches for Dark Matter Annihilation”, *Phys.Rev.* **D86** (2012) 023506, [arXiv:1204.3622](#).
- [562] **CMS Collaboration** Collaboration, “Search for the Standard-Model Higgs boson decaying to tau pairs in proton-proton collisions at $\sqrt{s} = 7$ and 8 TeV”, Tech. Rep. CMS-PAS-HIG-13-004, CERN, Geneva, 2013.
- [563] **LCFI** Collaboration, D. Bailey *et al.*, “The LCFIVertex package: Vertexing, flavour tagging and vertex charge reconstruction with an ILC vertex detector”, *Nuclear Instruments and Methods in Physics Research A* **610** (2009) 573–589, [arXiv:0908.3019](#).